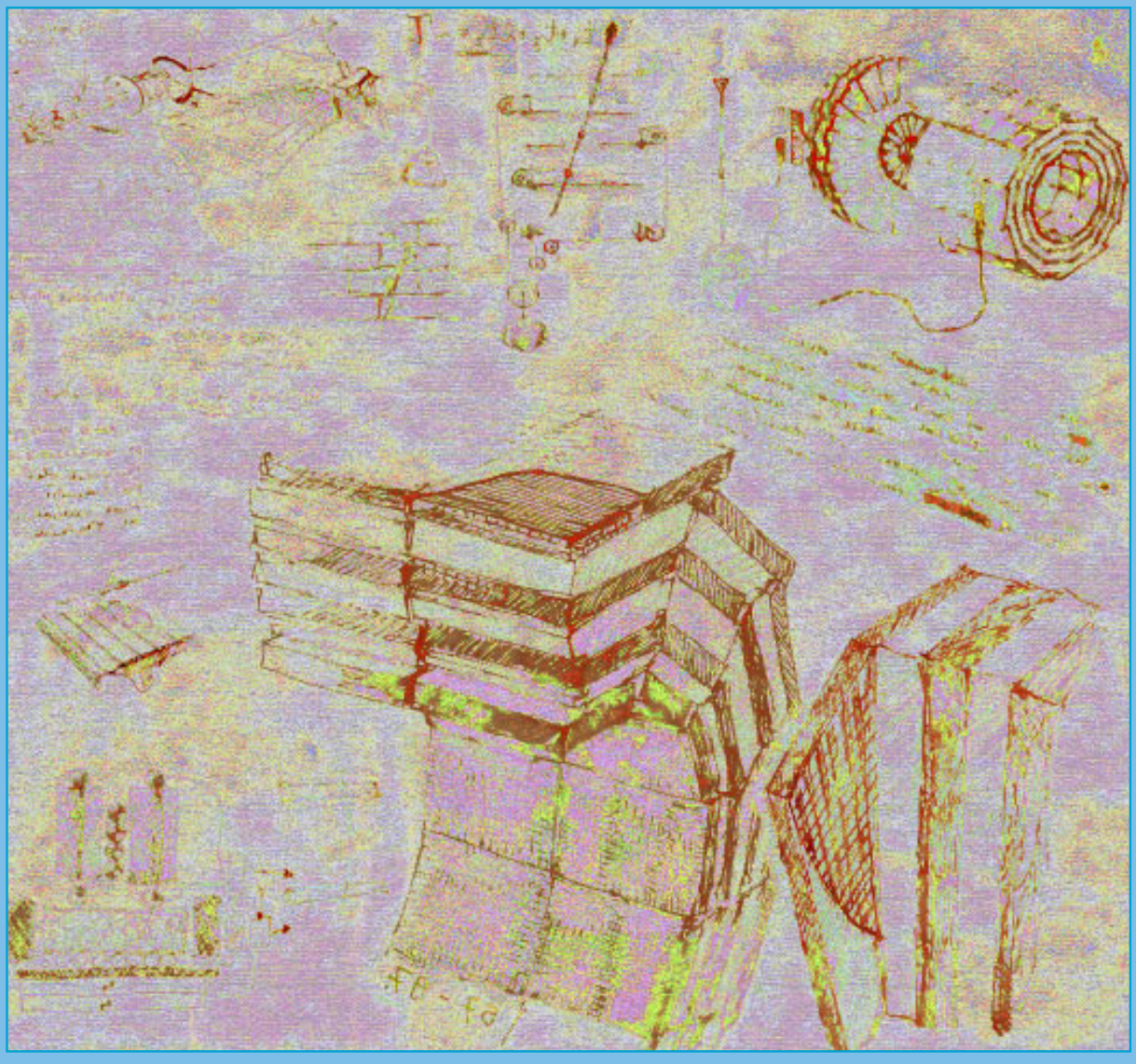
LABORATOIRE EUROPÉEN POUR LA PHYSIQUE DES PARTICULES
CERN EUROPEAN LABORATORY FOR PARTICLE PHYSICS

CERN/LHCC 97-32
CMS TDR 3
15 December 1997

CMS



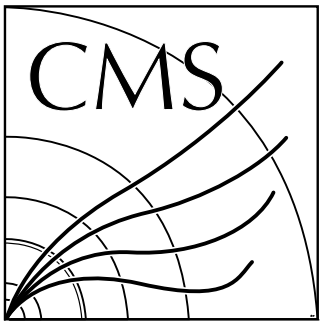
The Muon Project

Technical Design Report

Cover in Leonardo da Vinci style.

Turning the image, see:

Top right:	CSC wiring machine
Top center:	Beam crossing identification
Top left:	Laser levels for alignment
Bottom right:	An early cosmic ray detector from 1957
Bottom middle:	Detection of signals on CSC and RPC strips
Bottom left:	A section of the CMS MUON detector



CERN/LHC 97-32
CMS TDR 3
15 December 1997

CMS

The Compact Muon Solenoid

Muon Technical Design Report

CMS Spokesperson
M. Della Negra
CERN
michel.della.negra@cern.ch

CMS Technical Coordinator
E. Radermacher
CERN
ernst.radermacher@cern.ch

Muon Project Manager
F. Gasparini
Padova
fgasparini@padova.infn.it

Muon Project Manager
G. Mitselmakher
Florida/FNAL
mitselmakher@phys.ufl.edu

TDR Editorial Board

J. G. Layter – *Editor*
F. Gasparini
R. Loveless
G. Mitselmakher
H. Reithler

Acknowledgments

Consultants for Specific Chapters

I. Azhgirey, F. Hahn, S. Haider, M. Huhtinen, D. Peach, F. Perriollat, R. Schmidt, V. Talanov, A. Uzunian

Data Processing Environment

I. Gaines, J. Hanlon, W. Jank, J.-P. Porte, N. Sinanis

Text Processing

T. Grozis, O. Rademakers

Cover Design

S. Cittolin

CMS Collaboration

Yerevan Physics Institute, Yerevan, ARMENIA
G.L. Bayatian, N.K. Grigorian, V.G. Khachatrian, A. Margarian, A.M. Sirunian, S.S. Stepanian

Institut für Hochenergiephysik der OeAW, Wien, AUSTRIA
W. Adam, R. Fruehwirth, J. Hrubec, M. Kloimwieder, A. Kluge, M. Krammer, N. Neumeister, H. Pernegger, M. Pernicka, P. Porth, D. Rakoczy, H. Rohringer, L. Rurua[1], J. Scherzer, F. Szoncsó, A. Taurok, G. Walzel, T. Wildschek, C.-E. Wulz

Byelorussian State University, Minsk, BELARUS
V.V. Petrov, V.S. Prosolovich

Institute of Nuclear Problems, Minsk, BELARUS
V.G. Baryshevsky, A.A. Fedorov, M.V. Korzhik, O.V. Missevitch

National Centre of Particle and High Energy Physics, Minsk, BELARUS
G.V. Basalyga, N.E. Chekhlova, V.A. Chekhovsky, O.V. Dvornikov, I.F. Emelianchik, A.P. Khomich, V.L. Kolpaschikov, A.S. Kurilin, V.I. Kuvshinov, A.V. Litomin, V.A. Mossolov, A.K. Panfilenko, A.V. Raspereza, S.I. Reutovich, N.M. Shumeiko, A.V. Solin, R.V. Stefanovich, V.J. Stepanets, S.V. Sushkov, S.S. Vetokhin, Y. Yurenya, V.B. Zalessky, F.E. Zyazyulya

Research Institute of Applied Physical Problems, Minsk, BELARUS
F.A. Ermalitsky, P.V. Kuchinsky, V.M. Lomako

Université Libre de Bruxelles, Brussels, BELGIUM
O. Bouhali, J. Sacton, J. Stefanescu, C. Vander Velde, P. Vanlaer

Vrije Universiteit Brussel, Brussels, BELGIUM
O. Devroede, J. Lemonne, S. Tavernier, F. Udo, W. Van Doninck, L. Van Lancker, V. Zhukov

Université Catholique de Louvain, Louvain-la-Neuve, BELGIUM
K. Bernier, D. Favart, J. Govaerts, G. Grégoire

Université de Mons-Hainaut, Mons, BELGIUM
I. Boulogne, E. Daubie, Ph. Herquet, R. Windmolders

Universitaire Instelling Antwerpen, Wilrijk, BELGIUM
W. Beaumont, T. Beckers, J. De Troy, Ch. Van Dyck, F. Verbeure

Institute for Nuclear Research and Nuclear Energy, Sofia, BULGARIA
T. Anguelov, G. Antchev[2], I. Atanasov, D. Bourilkov, L. Dimitrov, V. Genchev, G. Georgiev, P. Hristov, P. Iaydjiev, I. Ivanov, L. Penchev, V. Penev, A. Shklovskaja, G. Sultanov, I. Vankov

University of Sofia, Sofia, BULGARIA
C.V. Cheshkov, A. Gritskov, A. Jordanov, L. Litov, P. Petev, V. Spassov, R. Tsenov, G. Velev

Institute of High Energy Physics, Beijing, CHINA, PR
G.M. Chen, Y. Chen, B.S. Cheng, Y.F. Gu, Y.N. Guo, J.T. He, B.N. Jin, Z.J. Ke, J. Li, W.G. Li, X.N. Li, J. Liu, B.W. Shen, C.Q. Shen, P.R. Shen, X.Y. Shen, H.Y. Sheng, H.Z. Shi, X.F. Song, Y.Y. Wang, Y.R. Wu, R.S. Xu, B.Y. Zhang, S.Q. Zhang, W.R. Zhao, J.P. Zheng, G.Y. Zhu

Peking University, Beijing, CHINA, PR
Y. Ban, J.E. Chen, H. Liu, S. Liu, B. Lou, S. Qian, Y. Ye

University for Science and Technology of China, Hefei, Anhui, CHINA, PR
Q. An, Z. Bian, C. Li, Ch. Shi, L. Sun, X. Wang, Z. Wang, J. Wu, S. Ye, Z. Zhang

Technical University of Split, Split, CROATIA
N. Godinovic, M. Milin[3], I. Puljak, I. Soric, M. Stipcevic[3], J. Tudoric-Ghemo

University of Split, Split, CROATIA
Z. Antunovic, M. Dzelalija

University of Cyprus, Nicosia, CYPRUS
A. Hasan, P.A. Razis, A. Vorvolakos

Charles University, Praha , CZECH REPUBLIC
M. Finger, T. Kracikova, A. Linka, J. Picek, M. Slunecka, M. Sulc

Czech Technical University, Praha, CZECH REPUBLIC
M. Laub, R. Nova'k, M. Vognar, J. Zicha

Institute of Computing Machines, Praha, CZECH REPUBLIC
M. Tomasek

Institute of Scientific Instruments, Brno, CZECH REPUBLIC
J. Dupak, P. Hanzelka, M. Horacek, A. Srnka

Nuclear Research Institute, Rez, CZECH REPUBLIC
A. Janata

Institute of Chemical Physics and Biophysics, Tallinn, ESTONIA
R. Aguraiuja, A. Hall, E. Lippmaa, J. Subbi

Department of Physics, University of Helsinki, Helsinki, FINLAND
S. Lehti, T. Lindén

Helsinki Institute of Physics, Helsinki, FINLAND
O. Bouianov, N. Eiden, C. Eklund, L. Eronen, J. Hahkala, M. Heikkinen, V. Karimäki[2],
R. Kinnunen, J. Klem, M. Kotamäki, T. Mäenpää, E. Pietarinen, S. Ruotsalainen, H. Saarikoski,
K. Skog, J. Tuominiemi

Department of Physics & Microelectronics Instrumentation Laboratory, University of Oulu, Oulu, FINLAND
A. Keranen, L. Palmu, M. Piila, K. Remes, R. Skantsi, E. Suhonen, T. Tuuva

Tampere University of Technology, Tampere, FINLAND
J. Niittylahti, O. Vainio

University of Jyväskylä, Jyväskylä, FINLAND
J. Äystö, R. Julin, V. Ruuskanen

Laboratoire d'Annecy-le-Vieux de Physique des Particules, IN2P3-CNRS, Annecy-le-Vieux, FRANCE
G. Bassompierre, G. Bohner, J. Ditta, O. Drobychev, M. Forlen, J.P. Guillaud, J. Lecoq, T. Leflour, S. Lieunard, M. Maire, P. Mendiburu, P. Nedelec, L. Oriboni, J.P. Peigneux, M. Schneegans, D. Sillou, J.M. Thenard, J.P. Vialle

DSM/DAPNIA, CEA/Saclay, Gif-sur-Yvette, FRANCE
M. Anfreville, P. Besson, P. Bonamy, E. Bougamont, R. Chipaux, V. Da Ponte, M. De Beer, P. De Girolamo, M. Dejardin, D. Denegri, J.L. Faure, M. Geleoc, F.X. Gentit, A. Givernaud, Y. Lemoigne, E. Locci, J.C. Lottin, Ch. Lyraud, J.P. Pansart, J. Rander, Ph. Rebourgeard, J.M. Reymond, F. Rondeaux, A. Rosowsky, P. Roth, P. Verrecchia, G. Villet

Laboratoire de Physique Nucléaire des Hautes Energies, Ecole Polytechnique, IN2P3-CNRS, Palaiseau, FRANCE
J. Badier, M. Bercher, L. Buiron, A. Busata, Ph. Busson, D. Chamont, C. Charlot, B. Chaurand, A. Debraine, L. Dobrzynski, O. Ferreira, K. Geun Beom, A. Heurtel, H. Hillemanns, A. Karar, L. Kluberg, D. Lecouturier, P. Matricon, G. Milleret, Ph. Miné, P. Paganini, P. Poilleux, A. Romana, R. Tanaka, J.-C. Vanel, C. Violet

Institut de Recherches Subatomiques, IN2P3-CNRS, ULP, UHA, LEPSI, Strasbourg, FRANCE
F. Anstotz, Y. Benhammou, G. Berges, J.D. Berst, J.M. Brom, F. Charles, J. Coffin, J. Croix, F. Drouhin, W. Dulinski, J.C. Fontaine, W. Geist[4], U. Goerlach, J.M. Helleboid, Y. Hu, D. Huss, F. Jeanneau, A. Lounis, J. Michel, A. Pallares[5], Ch. Racca, Y. Riahi, I. Ripp, Ph. Schmitt, J.P. Schunck, B. Schwaller, J.L. Sohler, T. Todorov, R. Turchetta, A. Zghiche

Institut de Physique Nucléaire de Lyon, IN2P3-CNRS, Univ. Lyon I, Villeurbanne, FRANCE
M. Ageron, P. Antilogus, J.E. Augustin, M. Bedjidian, D. Bertini, V. Chorowicz, P. Cluzel, D. Contardo, P. Depasse, N. Djaoshvili, O. Drapier, L. Ducroux, H. El Mamouni, J.-P. Ernenwein, J. Fay, R. Genre, N. Giraud, M. Goyot, R. Haroutounian, B. Ille, G. Jacquet, S. Katsanevas, P. Lebrun, Ch. Lemoine, N. Madjar, F. Martin, J.-P. Martin, H. Mathez, L. Mirabito, S. Muanza, M. Rebouillat, P. Sahuc, G. Smadja, S. Tissot, J.-P. Walder, F. Zach

High Energy Physics Institute, Tbilisi, GEORGIA
N. Amaglobeli, I. Bagaturia, L. Glonti, V. Kartvelishvili, R. Kvatadze, D. Mzavia, T. Sakhelashvili, R. Shanidze

Institute of Physics Academy of Science, Tbilisi, GEORGIA
I. Iashvili[6], A. Kharchilava[7], N. Roinishvili, V. Roinishvili

RWTH, I. Physikalisches Institut, Aachen, GERMANY
Ch. Berger, W. Braunschweig, J. Breibach, W. Gu, K. Gundlfinger, W. Karpinski, Th. Kirn, T. Kubicki, Ch. Kukulies, K. Lübelsmeyer, D. Pandoulas, G. Pierschel, F. Raupach, C. Rente, D. Schmitz, A. Schultz von Dratzig, J. Schwenke, R. Siedling, O. Syben, F. Tenbusch, M. Toporowsky, W. Wallraff, B. Wittmer, W.J. Xiao

RWTH, III. Physikalisches Institut A, Aachen, GERMANY
S. Bethke, O. Biebel, H. Faissner, H. Fesefeldt, D. Rein, H. Reithler[2], H. Schwarthoff, V. Sondermann, V. Tano, H. Teykal, M. Tonutti, J. Tutas, M. Wegner

RWTH, III. Physikalisches Institut B, Aachen, GERMANY

S. Bachmann, F. Beissel, K. Boffin, C. Camps, V. Commichau, G. Flügge, K. Hangarter, R. Ischebeck, J. Kremp, D. Macke, A. Novack, G. Otter, M. Petertill, O. Pooth, P. Schmitz, R. Schulte

Humboldt-Universität zu Berlin, Berlin, GERMANY
Th. Hebbeker, S. Piperov

Institut für Experimentelle Kernphysik, Karlsruhe, GERMANY
M. Ackermann, P. Blüm, W. de Boer, S. Chowdhury, V. Drollinger, M. Feindt, H. Gemmeke, S. Heising, S. Junghans, D. Knoblauch, M. Kraeber, A. Menchikov, R. Metri, Th. Müller, D. Neuberger, M. Reischl, E. Ruoff, A. Sauer, H.J. Simonis, W.H. Thümmel, H. Wenzel, S. Weseler, B. Zittel

University of Athens, Athens, GREECE
L. Resvanis

Institute of Nuclear Physics "Demokritos", Attiki, GREECE
M. Barone, N. Dimitriou, G. Fanourakis, D. Fassouliotis, S. Harissopulos, E. Karvelas, P. Kokkinias, A. Kyriakis, D. Loukas, A. Markou, Ch. Markou, E. Saragas, I. Siotis, M. Spyropoulou-Stassinaki, S. Tzamarias, A. Vayaki, E. Zevgolatakos

University of Ioánnina, Ioánnina, GREECE
A. Assimidis, V. Christofilakis, I. Evangelou, K. Kloukinas, N. Manthos, A. Pagonis, F.A. Triantis

KFKI Research Institute for Particle and Nuclear Physics, Budapest, HUNGARY
G. Bencze[2], A. Csilling, E. Denes, J. Ero[2], C. Hajdu, D. Horvath[8], D. Kiss, I. Manno, G. Odor, G. Pa'sztor, F. Sikler, A. Ster, L. Urban, G. Vesztergombi, P. Zalan, M. Zsenei

Kossuth Lajos University, Debrecen, HUNGARY
T. Bondar, L. Brunel[2], S. Juhasz, G. Marian, S. Nagy, P. Raics, J. Szabo, Z. Szabo, S. Szegedi, Z. Szillasi, T. Sztaricskai, G. Zilizi

Institute of Nuclear Research ATOMKI, Debrecen, HUNGARY
A. Bader, G. Dajko, A. Fenyvesi, J. Molnar, J. Palinkas, D. Sohler, Z. Trocsanyi, J. Vegh

Institute of Physics, Bhubaneswar, INDIA
D.P. Mahapatra, J. Maharana

Panjab University, Chandigarh, INDIA
S. Beri, T.K. Chaterjee, M. Kaur, J.M. Kohli, J.B. Singh

Bhabha Atomic Research Centre, Mumbai, INDIA

R.K. Chaudhury, M.D. Ghodgaonkar, S.B. Jawale, B. John, S.K. Kataria, R.S. Koppikar, A.K. Mohanty, S.V. Sastry, R.V. Srikantiah

Tata Institute of Fundamental Research - EHEP, Mumbai, INDIA
T. Aziz, Sn.Banerjee[2], S.N. Ganguli, S.K. Gupta, A. Gurtu, K. Mazumdar, R. Raghavan, K. Sudhakar, S.C. Tonwar

Tata Institute of Fundamental Research - HECR, Mumbai, INDIA
B.S. Acharya, Sd. Banerjee, S. Dugad, M.R. Krishnaswamy, N.K. Mondal, V. S. Narasimham

University of Delhi South Campus, New Delhi, INDIA
T. Chand, J. Cherian, R.K. Shivpuri, V.K. Verma

Università di Bari e Sezione dell' INFN, Bari, ITALY
M. Abbrescia, M. Angarano, A. Bader, A. Colaleo, D. Creanza, M. De Palma, D. Diacono, L. Fiore, G. Iaselli, F. Loddo, G. Maggi, M. Maggi, B. Marangelli, S. My, S. Natali, S. Nuzzo, G. Pugliese, A. Ranieri, G. Raso, F. Romano, F. Ruggieri, G. Selvaggi, P. Tempesta, G. Zito

Università di Bologna e Sezione dell' INFN, Bologna, ITALY
A. Benvenuti, P. Capiluppi, F. Cavallo, M. Cuffiani, I. D'Antone, G.M. Dallavalle, F. Fabbri, P.L. Frabetti, G. Giacomelli, P. Giacomelli[9], C. Grandi, M. Guerzoni, S. Marcellini, P. Mazzanti, A. Montanari, F.L. Navarria, F. Odorici, A. Perrotta, A.M. Rossi, T. Rovelli, G. Siroli, G. Valenti

Università di Catania e Sezione dell' INFN, Catania, ITALY
S. Albergo, V. Bellini, D. Boemi, Z. Caccia, P. Castorina, S. Costa, L. Lo Monaco, R. Potenza, A. Tricomi, C. Tuve

Università di Firenze e Sezione dell' INFN, Firenze, ITALY
F. Becattini, U. Biggeri, E. Borchi, M. Bruzzi, M. Capaccioli, G. Castellini, E. Catacchini, C. Civinini, R. D'Alessandro, E. Focardi, G. Landi, M. Meschini, G. Parrini, G. Passaleva, M. Pieri, A. Salamone, S. Sciortino

Università di Genova e Sezione dell' INFN, Genova, ITALY
P. Fabbricatore, S. Farinon, R. Musenich, C. Priano

Università di Padova e Sezione dell' INFN, Padova, ITALY
P. Azzi, N. Bacchetta, M. Benettoni, A. Bettini, D. Bisello, G. Busetto, R. Carlin, A. Castro, S. Centro, P. Checchia, E. Conti, M. Da Rold, M. De Giorgi, A. De Min, U. Dosselli, C. Fanin, F. Gasparini, U. Gasparini, P. Guaita, I. Lippi, M. Loreti, R. Martinelli, A.T. Meneguzzo, A. Paccagnella, M. Pegoraro, L. Pescara, P. Ronchese, A. Sancho Daponte, P. Sartori, L. Stanco, I. Stavitski, E. Torassa, L. Ventura, P. Zotto[10], G. Zumerle

Università di Pavia e Sezione dell' INFN, Pavia, ITALY
S. Altieri, V. Arena, G. Belli, G. Bonomi, G. Gianini, M. Merlo, S.P. Ratti, C. Riccardi, L. Viola, P. Vitulo

Università di Perugia e Sezione dell' INFN, Perugia, ITALY
A. Aragona, E. Babucci, P. Bartalini, G.M. Bilei, B. Checcucci, P. Ciampolini, P. Lariccia, G. Mantovani, D. Passeri, P. Placidi, A. Santocchia, L. Servoli, Y. Wang

Università di Pisa e Sezione dell' INFN, Pisa, ITALY
F. Angelini, G. Bagliesi, A. Bardi, A. Basti, F. Bedeschi, S. Belforte, R. Bellazzini, L. Borrello, F. Bosi, C. Bozzi, P.L. Braccini, A. Brez, R. Carosi, R. Castaldi, G. Chiarelli, M. Chiarelli, V. Ciulli, M. D'Alessandro Caprice, M. Dell'Orso, R. Dell'Orso, S. Donati, S. Dutta, A. Frediani, S. Galeotti, A. Giambastiani, P. Giannetti, A. Giassi, G. Iannaccone, M. Incagli, L. Latronico, F. Ligabue, N. Lumb, G. Magazzu, M.M. Massai, E. Meschi, A. Messineo, F. Morsani, M. Oriunno[2], F. Palla, A. Papanestis, G. Punzi, F. Raffaelli, R. Raffo, L. Ristori, G. Sanguinetti, G. Sguazzoni, P. Spagnolo, G. Spandre, F. Spinella, R. Tenchini, G. Tonelli, E. Troiani, C. Vannini, A. Venturi, P.G. Verdini, Z. Xie, F. Zetti

Università di Roma I e Sezione dell' INFN, Roma, ITALY
S. Baccaro[11], L. Barone, B. Borgia, F. Cavallari, I. Dafinei, G. De Canio[11], F. De Notaristefani, M. Diemoz, A. Festinesi[11], E. Leonardi, A. Leone, E. Longo, M. Mattioli, M. Montecchi[11], G. Organtini, M. Puccini[11], E. Valente

Università di Torino e Sezione dell' INFN, Torino, ITALY
M. Arneodo, F. Bertolino, M. Bigi, R. Cirio, M. Costa, F. Daudo, M.I. Ferrero, S. Maselli, E. Migliore, V. Monaco, C. Peroni, M.C. Petrucci, A. Romero, R. Sacchi, A. Solano, A. Staiano

Cheju National University, Cheju, KOREA
Y.J. Kim

Choongbuk National University , Chongju, KOREA
Y.U. Kim

Kangwon National University, Chunchon, KOREA
S.K. Nam

Wonkwang University, Iri, KOREA

S.Y. Bahk

Kangnung National University, Kangnung, KOREA
Y. Ho, K.S. Kang, D.S. Kim, D.W. Kim, S.C. Lee

Chonnam National University, Kwangju, KOREA
H.I. Jang, J.Y. Kim, T.I. Kim, I.T. Lim

Dongshin University, Naju, KOREA
M.Y. Pac

Pohang University of Science and Technology, Pohang, KOREA
G.N. Kim

Kon-Kuk University, Seoul, KOREA
J.T. Rhee

Korea University, Seoul, KOREA
B.S. Hong, S.J. Hong, Y.S. Kim, K.S. Lee, S.K. Park, K.S. Sim

Seoul National University of Education, Seoul, KOREA
D.G. Koo

Kyungpook National University, Taegu, KOREA
H. Jeon, D. Kim, W.Y. Kim, I.H. Park, D. Son

Seonam University, Namwon, KOREA

S.J. Lee

Institute of Electronics and Computer Science, Riga, LATVIA
Y. Bilinskis

Quaid-I-Azam University, Islamabad, PAKISTAN
P. Hoodbhoy, A. Niaz, I.E. Qureshi, K.N. Qureshi

Institute of Experimental Physics, Warsaw, POLAND
M. Cwiok, W. Dominik, A. Fengler, M. Konecki, J. Krolikowski, I. Kudla, P. Majewski, K. Pozniak

Soltan Institute for Nuclear Studies, Warsaw, POLAND
R. Gokieli, M. Górski, P. Zalewski

Laboratório de Instrumentação e Física Experimental de Partículas, Lisboa, PORTUGAL
C. Almeida[12], J. Augusto[12], P. Bordalo, M. Calha[12], A. Chichkov[12], J. Da Silva, O. Dias[12], J. Gomes, J. Martins[12], J. Morgado, R. Nobrega, S. Ramos, H. Sarmento[12], S. Silva, I. Teixeira[12], J. Teixeira[12], G. Varner, I. Videira[12]

Joint Institute for Nuclear Research, Dubna, RUSSIA
S. Afanasiev, I. Anisimov, D. Bandurin, D. Belosludtsev, S. Chatrchyan, A. Cheremukhin, A. Chvyrov, A. Dmitriev, V. Elsha, Y. Erchov, A. Filippov, I. Golutvin, N. Gorbunov, I. Gramenitsky, I. Ivantchenko, V. Kalagin, V. Karjavin, S. Khabarov, V. Khabarov, Y. Kiryushin, V. Kolesnikov, V. Konoplyanikov, V. Korenkov, I. Kossarev, A. Koutov, V. Krasnov, A. Litvinenko, V. Lysiakov, A. Malakhov, G. Mechtcheriakov, I. Melnichenko, P. Moissenz, S. Movchan, V. Palichik, V. Perelygin, Y. Petukhov, M. Popov, D. Pose, R. Pose, A. Samoshkin, M. Savina, S. Selunin, S. Sergeev, S. Shmatov, N. Skachkov, N. Slavin, D. Smolin, E. Tikhonenko, V. Tyukov, V. Uzhinskii, N. Vlasov, A. Volodko, A. Yukaev, N. Zamiatin, A. Zarubin, P. Zarubin, E. Zubarev, C. Zubov

Petersburg Nuclear Physics Institute, Gatchina (St Petersburg), RUSSIA
N. Bondar, G. Gavrilov, A. Golyash, Y. Gusev, O. Kisselev, E. Orichtchine, O. Prokofiev, V. Rasmislovich, V. Sedov, D. Seliverstov, V. Sknar, I. Smirnov, S. Sobolev, V. Soulimov, I. Tkach, G. Velitchko, A. Vorobyov, V.Astashin

P.N. Lebedev Physical Institute, Moscow, RUSSIA
E. Devitsin, A.M. Fomenko, V. Kozlov, A.I. Lebedev, S. Potashov, S.V. Rusakov

Institute for Nuclear Research, Moscow, RUSSIA
G.S. Atoyan V. Bolotov, R. Djilkibaev, S. Gninenko, N. Goloubev, E.V. Gushin, M. Kirsanov, N. Krasnikov, S. Laptev, V.A. Lebedev, V. Matveev, Y. Musienko[13], V. Oustiojanine, A. Pashenkov, A. Polarush, S. Popov, V. Popov, V.E. Postoev, A. Proskouriakov, I. Semeniouk, B. Semenov, V. Shmatkov, A. Skassyrskaia, A. Toropin

Institute for Theoretical and Experimental Physics, Moscow, RUSSIA
S. Abdullin, E. Doroshkevich, V. Gavrilov, Y. Gershtein, I. Gorelov, E. Grigoriev, V. Kaftanov, A. Khanov[2], V. Kolossov, D. Litvintsev, A. Nikitenko[2], A. Papin, O.I. Pogorelko, V. Rusinov, V. Semechkin, Y. Semenov, A. Starodumov[14], N. Stepanov[2], V. Stoline, Y. Trebukhovsky, A. Ulyanov, S. Uzunian, A. Yumashev

Moscow State University, Moscow, RUSSIA
A. Belsky, V Bodyagin, A. Demianov, V. Galkin, A. Gribushin, O.L. Kodolova, V. Korotkikh, N.A. Kruglov, A. Kryukov, I. Lokhtin, V. Mikhailin, L. Sarycheva, A. Snigirev, I. Vardanyan, A. Vasil'ev, A. Yershov

Budker Institute for Nuclear Physics, Novosibirsk, RUSSIA
V. Aulchenko, B. Baiboussinov, A. Bondar, S. Eidelman, V. Nagaslaev, T. Purlatz, L. Shekhtman, V. Sidorov, A. Tatarinov

Institute for High Energy Physics, Protvino, RUSSIA
V. Abramov, I. Azhgirey, S. Bitioukov, A. Dolgopolov, S. Donskov, A. Dyshkant, V. Evdokimov, P. Goncharov, A. Gorin, A. Inyakin, V. Katchanov, V. Khodyrev, A. Kondashov, A. Korablev, Y. Korneev, A. Kostritskii, A. Krinitsyn, V. Kryshkin, A. Kuznetsov, I. Manuilov, V. Medvedev, V. Obraztsov, M. Oukhanov, D. Patalakha, V. Petrov, V.V. Rykalin, P. Semenov, P. Shagin, A. Singovsky, V. Solovianov, V. Sougonyaev, A. Surkov, V. Talanov, S. Tereschenko, L. Turchanovich, N. Tyurin, A. Uzunian, A. Volkov, A. Zaitchenko

Institute of Computing Machines, Zilina, SLOVAK REPUBLIC

V. Sluneckova

Slovak University of Technology, Bratislava, SLOVAK REPUBLIC
P. Ballo, J. Lipka, M. Liska, M. Nagy, V. Necas, J. Safarik, M. Seberini, K. Vitazek

Centro de Investigaciones Energeticas Medioambientales y Tecnologicas, Madrid, SPAIN
M. Aguilar-Benitez, J. Alberdi, J.M. Barcala, J. Berdugo, C. Burgos, M. Cerrada, N. Colino, M. Daniel, M. Fernandez, A. Ferrando, M.C. Fouz, M.I. Josa, P. Ladrón de Guevara, J. Marin, F. Martin Suarez, J. Mocholi, A. Molinero, J. Navarrete, J.C. Oller, J.L. Pablos, L. Romero, J. Salicio, C. Willmott

Universidad Autónoma de Madrid, Madrid, SPAIN
C. Albajar

Universidad de Oviedo, Oviedo, SPAIN

J. Cuevas

Instituto de Fisica de Cantabria (IFCA), CSIC-Universidad de Cantabria, Santander, SPAIN
C.F. Figueroa, N. Garcia, I. Gonzalez, J.M. Lopez, J. Marco, F. Matorras, T. Rodrigo, A. Ruiz, I. Vila

Universität Basel, Basel, SWITZERLAND
L. Tauscher, M. Wadhwa

CERN, European Laboratory for Particle Physics, Geneva, SWITZERLAND
P.A. Aarnio[15], D. Abbaneo, V. Arbet-Engels, P. Aspell, E. Auffray, G. Bagliesi, P. Baillon, R. Barillère, D. Barney, W. Bell, G. Benefice, D. Blechschmidt, Ph. Bloch, M. Bosteels, J. Bourotte[16], M. Bozzo[17], S. Braibant, H. Breuker, A. Calvo, D. Campi, A. Caner, E. Cano, A. Carraro, A. Cattai, G. Cervelli, J. Christiansen, S. Cittolin, B. Curé, C. D'Ambrosio, S. Da Mota Silva, D. Dattola, Th. de Visser, D. Delikaris, M. Della Negra, A. Desirelli, G. Dissertori, A. Elliott-Peisert, L. Feld, H. Foeth, A. Fucci, A. Furtjes, J.C. Gayde, H. Gerwig, K. Gill, W. Glessing, E. Gonzalez Romero[18], J.P. Grillet, J. Gutleber, C.E. Hackl, F. Hahn, R. Hammarstrom, M. Hansen, M. Hansroul, E.H.M. Heijne, A. Hervé, M. Hoch, K. Holtman, M. Huhtinen, V. Innocente, W. Jank, P. Jarron, A. Jusko, Th. Kachelhoffer, K. Kershaw, Z. Kovacs, A. Kruse, T. Ladzinski, Ch. Lasseur, J.M. Le Goff, M. Lebeau, P. Lecoq, N. Lejeune, F. Lemeilleur, M. Letheren, Ch. Ljuslin, B. Lofstedt, R. Loos, R. Mackenzie, R. Malina, M. Mannelli, E. Manola-Poggioli, A. Marchioro, J.M. Maugain, F. Meijers, A. Merlino, Th. Meyer, C. Mommaert, P. Nappey, T. Nyman, A. Onnela, L. Orsini, S. Paoletti, G. Passardi, D. Peach, F. Perriollat, P. Petagna, M. Pimiä, R. Pintus, B. Pirollet, A. Placci, J.P. Porte, H. Postema, J. Pothier, M.J. Price, A. Racz, E. Radermacher, S. Reynaud, R. Ribeiro, J. Roche, P. Rodrigues Simoes Moreira, L. Rolandi, D. Samyn, J.C. Santiard, R. Schmidt, B. Schmitt, M. Schröder, F. Sciacca, P. Siegrist, L. Silvestris[19], N. Sinanis, P. Sphicas[20], G. Stefanini, B. Taylor, A. Tsirou, J. Varela[21], F. Vasey, T.S. Virdee[22], P. Wertelaers, T. Wikberg, M. Wilhelmsson, I.M. Willers, G. Wrochna

Paul Scherrer Institut, Villigen, SWITZERLAND
O. Ayranov, W. Bertl, K. Deiters, P. Dick, A. Dijksmann, M. Fabre, K. Gabathuler, J. Gobrecht, G. Heidenreich, B. Henrich, R. Horisberger, Q. Ingram, D. Kotlinski, M. Lechner, R. Morf, D. Renker, R. Schnyder, H.Ch. Walter, D. Zürcher

Institut für Teilchenphysik, Eidgenössische Technische Hochschule (ETH), Zürich, SWITZERLAND
H. Anderhub, A. Barczyk, F. Behner, B. Betev, A. Biland, D. Bourilkov, V. Brigljevic, M. Campanelli, P. Cannarsa, G. Chevenier[2], R. Della Marina, F. Di Lodovico, M. Dittmar, R. Eichler, G. Faber, M. Felcini, K. Freudenreich, C. Grab, A. Hasan, H. Hofer, I. Horvath, P. Ingenito, K. Lassila-Perini, P. Le Coultre, P. Lecomte, W. Lustermann, P. Marchesini, F. Nessi-Tedaldi, F. Pauss, D. Pitzl, M. Pohl, G. Rahal-Callot, D. Ren, A. Robohm, U. Roeser, H. Rykaczewski, H. Suter, J. Ulbricht, G. Viertel, H. Von Gunten, S. Waldmeier-Wicki, F. Wittgenstein

Universität Zürich, Zürich, SWITZERLAND
C. Amsler, R. Kaufmann, F. Ould-Saada, Ch. Regenfus, P. Robmann, S. Spanier, S. Steiner, P. Truöl

Cukurova University, Adana, TURKEY
I. Dumanoglu, E. Eskut, A. Kayis, A. Kuzucu-Polatöz, G. Önengüt, N. Ozdes Koca, H. Ozturk

Middle East Technical University, Physics Department, Ankara, TURKEY
A.S. Ayan, E. Pesen, M. Serin-Zeyrek, R. Sever, P. Tolun, M. Zeyrek

Inst. of Single Crystals of National Academy of Science, Kharkov, UKRAINE
V.C. Koba, V. Trofimenko

National Scientific Center, Kharkov Institute of Physics and Technology, Kharkov, UKRAINE
L.G. Levchuk, A.A. Nemashkalo, V.E. Popov, A.L. Rubashkin, P.V. Sorokin, A.E. Zatzerklyany

Kharkov State University, Kharkov, UKRAINE
N.A. Kluban, V. Lebedev

University of Bristol, Bristol, UNITED KINGDOM
D.S. Bailey, R.D. Head, G.P. Heath, H.F. Heath, A. Mass, D.M. Newbold, V.J. Smith, R.J. Tapper

Rutherford Appleton Laboratory, Didcot, UNITED KINGDOM
J.E. Bateman, K.W. Bell, R.M. Brown, P. Burch, D.J.A. Cockerill, J.F. Connolly, J.A. Coughlan, L.G. Denton, P.S. Flower, M. French, R. Halsall, W.J. Haynes, F.R. Jacob, P.W. Jeffreys, L. Jones, B.W. Kennedy, A.L. Lintern, G.N. Patrick, B. Smith, M. Sproston, R. Stephenson, M. Torbet

Imperial College, University of London, London, UNITED KINGDOM
G. Barber, J. Batten, R. Beuselinck, D. Britton, W. Cameron, D. Clarke, I. Clark, G. Davies, D. Gentry, G. Hall, J.F. Hassard, A. Jamdagni, K.R. Long, B.C. MacEvoy, N. Marinelli, E.B. Martin, D.G. Miller, D.M. Raymond, J. Reilly, J. Sedgbeer, C. Seez, L. Toudup

Brunel University, Uxbridge, UNITED KINGDOM
B. Camanzi, P.R. Hobson, D. C. Imrie, J. Matheson, C.K. MacKay, A. McKemey, M. Osborne, S.J. Watts

University of Alabama, Tuscaloosa, USA
L. Baksay[23], B. Fenyi, J. Huang, J. Rodin

Boston University, Boston, USA
R. Carey, E. Hazen, U. Heintz, O.C. Johnson, E. Kearns, S.B Kim, E. Machado, J. Miller, D. Osborne, B.L. Roberts, J. Rohlf, J. Salen, L. Sulak, J. Sullivan, W. Worstell

University of California at Davis, Davis, USA
R. Breedon, Y. Fisyak, G. Grim, B. Holbrook, W. Ko, R. Lander, F. Lin, S. Mani, D. Pellett, J. Rowe, J. Smith

University of California at Los Angeles, Los Angeles, USA
K. Arisaka, Y. Bonushkin, F. Chase, D. Cline, S. Erhan, J. Hauser, M. Lindgren, C. Matthey, S. Otwinowski, J. Park, Y. Pischalnikov, P. Schlein, Y. Shi, B. Tannenbaum

University of California, Riverside, USA
D. Chrisman, I. Crotty[2], J.W. Gary, W. Gorn, J.G. Layter, B.C. Shen

University of California San Diego, La Jolla, USA
J.G. Branson, H. Kobrak, G. Masek, M. Mojaver, H. Paar, G. Raven, M. Sivertz, R. Swanson, A. White

California Institute of Technology, Pasadena, USA
L. Borissov, J. Bunn, Q. Deng, G. Denis[2], A. Favara, Ph. Galvez, A. Kirkby, H. Newman, S. Shevchenko, A. Shvorob, R. Wilkinson, R. Zhu

Carnegie Mellon University, Pittsburgh, USA
S. Blyth, A. Engler, Th. Ferguson, H. Hoorani, R. Kraemer, M. Procario, J. Russ, H. Vogel

Fairfield University, Fairfield, USA
C.P. Beetz, V. Podrasky, C. Sanzeni, T. Toohig, D. Winn

Fermi National Accelerator Laboratory, Batavia, USA
M. Atac, E. Barsotti, A. Baumbaugh, U. Baur, A. Beretvas, M. Binkley, M. Bowden, J. Butler, N. Chester, I. Churin, M. Crisler, D. Denisov, M. Diesburg, D.P. Eartly, J.E. Elias, S. Feher, J. Freeman, I. Gaines, H. Glass, D. Green, J. Hanlon, R. Harris, U. Joshi, W. Knopf, S. Kwan, M. Lamm, S. Lammel, K. Maeshima, J. Marraffino, C.S. Mishra, N. Mokhov, J. Ozelis, J. Patrick, A. Pla-Dalmau, R. Raja, M. Reichanadter, A. Ronzhin, M. Shea, R.P. Smith, L.E. Temple, R. Tschirhart, R. Vidal, D. Walsh, R. Wands, W.J. Womersley, W. Wu, A. Yagil, V. Yarba

University of Florida, Gainesville, USA
D. Acosta, P. Avery, R.D. Field, L. Gorn[2], S. Klimenko, J. Konigsberg, A. Korytov, G. Mitselmakher[24], A. Nomerotski, P. Ramond, J. Yelton

Florida State University - HEPG, Tallahassee, USA
H. Baer, M. Bertoldi, S. Hagopian, V. Hagopian, K. Johnson, J. Thomaston

Florida State University - SCRI, Tallahassee, USA
M. Corden, Ch. Georgiopoulos, K. Hays, T. Huehn, S. Youssef

University of Illinois at Chicago, (UIC), Chicago, USA
M. Adams, M. Chung, J. Solomon

The University of Iowa, Iowa City, USA
N. Akchurin, A. Cooper, M. Fountain, E. McCliment, J.P. Merlo, M. Miller, Y. Onel, R. Winsor

Iowa State University, Ames, USA
E.W. Anderson, J. Hauptman, J. Wightman

Johns Hopkins University, Baltimore, USA
T. Anticic, B. Barnett, C.Y. Chien, M. A. Frautschi, D. Gerdes, D. Newman, J. Orndorff, A. Pevsner, X. Xie

Lawrence Livermore National Laboratory, Livermore, USA
L. Bertolini, J. Kerns, D. Klem, M. Kreisler, X. Shi, K. Van Bibber, T. Wenaus, D. Wright, C.R. Wuest

Los Alamos National Laboratory, Los Alamos, USA
R. Barber, Z. Chen, J. Hanlon, B. Michaud, G. Mills, A. Palounek, H.J. Ziock

University of Maryland, College Park, USA
A. Baden, A. Ball, R. Bard, S.C. Eno, D. Fong, M. Garza, N.J. Hadley, R.G. Kellogg[2], Sh. Kunori, M. Murbach, A. Skuja

Massachusetts Institute of Technology, Cambridge, USA
G. Bauer, J. Friedman, E. Hafen, S. Pavlon, L. Rosenson, K.S. Sumorok, S. Tether, J. Tseng

University of Minnesota, Minneapolis, USA
P. Border, P. Cushman, K. Heller, M. Marshak, R. Rusack, Ch. Timmermans

University of Mississippi, Oxford, USA
K. Bhatt, M. Booke, L. Cremaldi, R. Kroeger, J. Reidy, D. Sanders, D. Summers

University of Nebraska-Lincoln, Lincoln, USA
W. Campbell, D.R. Claes, M. Hu, C. Lundstedt, G.R. Snow

State University of New York, Stony Brook, USA
M.M. Baarmand, R. Engelmann, K.K. Ng, J. Steffens, S.Y. Yoon

Northeastern University, Boston, USA
G. Alverson, H. Fenker, J. Moromisato, Th. Paul, S. Reucroft, J. Swain, L. Taylor, E. Von Goeler, T. Yasuda

Northwestern University, Evanston, USA
B. Gobbi, P. Rubinov, R. Tilden

University of Notre Dame, Notre Dame, USA
B. Baumbaugh, J.M. Bishop, N. Biswas, N.M. Cason, R. Ruchti, J. Warchol, M. Wayne

The Ohio State University, Columbus, USA
B. Bylsma, L.S. Durkin, J. Hoftiezer, R. Hughes, M. Johnson, D. Larsen, T.Y. Ling, C.J. Rush, V. Sehgal, B. Winer

Princeton University, Princeton, USA
P. Denes, V. Gupta, D. Marlow, P. Piroué, D. Stickland, H. Stone, Ch. Tully, R. Wixted

Purdue University - Task D, West Lafayette, USA
A. Bujak, D. Carmony, L. Gutay, S. Medved

Purdue University - Task G, West Lafayette, USA
V.E. Barnes, G. Bolla, D. Bortoletto, M. Fahling, A.F. Garfinkel, A.T. Laasanen

Rice University, Houston, USA
D.L. Adams, M. Corcoran, G. Eppley, H.E. Miettinen, B.P. Padley, E. Platner, J. Roberts, P. Yepes

Rutgers, the State University of New Jersey, Piscataway, USA
E. Bartz, J. Conway, T. Devlin, P. Jacques, M. Kalelkar, S. Schnetzer, S. Sherman, S. Somalwar, R. Stone, G. Thomson, T. Watts

University of Rochester, Rochester, USA
A. Bodek, H. Budd, P. De Barbaro, D. Ruggiero, W. Sakumoto, E. Skup, P. Tipton

University of Texas at Dallas, Richardson, USA
R.C. Chaney, E.J. Fenyves, H.D. Hammack, M.R. O'Malley, D.J. Suson, A.V. Vassiliev

Texas Tech University, Lubbock, USA
O. Ganel, V. Papadimitriou, A. Sill, R. Wigmans

Virginia Polytechnic Institute and State University, Blacksburg, USA
H. Meyer, L. Mo, Th.A. Nunamaker

University of Wisconsin, Madison, USA
W. Badgett, D. Carlsmith, S. Dasu, F. Feyzi, C. Foudas, M. Jaworski, J. Lackey, R. Loveless, S. Lusin, D. Reeder, W. Smith

Institute of Nuclear Physics of the Uzbekistan Academy of Sciences, Ulugbek, Tashkent, UZBEKISTAN
A. Avezov, N. Bisenov, A. Gaffarov, E. Gasanov, R. Gulamova, E. Ibragimova, K. Kim, Y. Koblik, D. Mirkarimov, A. Morozov, N. Rakhmatov, I. Rustamov, A. Urkinbaev, B. Yuldashev

1. On leave of absence from Institute of Physics Academy of Science, Tbilisi, Georgia
2. Also at CERN, Geneva, Switzerland
3. Also at Institute Rudjer Boskovic, Zagreb, Croatia
4. Also at M.P.I. Münich, Germany
5. Also at K.F.K. Karlsruhe, Germany
6. Also at Humboldt-Universität, Berlin, Germany
7. Also at DESY, Hamburg, Germany
8. Also at Inst. of Nuclear Research ATOMKI, Debrecen, Hungary
9. Also at University of California, Riverside, USA
10. Also at Dip. di Fisica del Politecnico di Milano, Milano, Italy
11. Also at ENEA, S. Maria di Galeria, Italy
12. Also at INESC, Lisbon, Portugal
13. Also at Northeastern University, Boston, USA
14. Also at Università di Pisa e Sezione dell' INFN, Pisa, Italy
15. Also at Helsinki Institute of Physics, Helsinki, Finland
16. Also at Laboratoire de Physique Nucléaire des Hautes Energies, Ecole Polytechnique, IN2P3-CNRS, Palaiseau, France
17. Also at Università di Genova e Sezione dell' INFN, Genova, Italy
18. Also at Centro de Investigaciones Energeticas Medioambientales y Tecnologicas, Madrid, Spain
19. Also at Università di Bari e Sezione dell' INFN, Bari, Italy
20. Also at Massachusetts Institute of Technology, Cambridge, USA
21. Also at Laboratório de Instrumentação e Física Experimental de Partículas, Lisboa, Portugal
22. On leave of absence from Imperial College, London, United Kingdom
23. Also at Kossuth Lajos University, Debrecen, Hungary
24. Also at Fermi National Laboratory, Batavia, USA

Contents

1. INTRODUCTION **1**

1.1 Structure of the technical design report **1**

1.2 Physics goals **2**

1.3 Performance requirements **5**

1.4 Design considerations **5**
1.4.1 Backgrounds 5
1.4.2 Rates and trigger 6
1.4.3 Detector elements 8

1.5 Detector description **9**
1.5.1 Detector layout 9
1.5.2 Barrel region 9
1.5.3 Endcap cathode strip chambers 10
1.5.4 Resistive plate chambers (RPC) 11
1.5.5 Trigger 12
1.5.6 Alignment 13
1.5.7 Magnetic field 14

1.6 Project organization, schedule, and costs **17**
1.6.1 Organization 17
1.6.2 Responsibilities 17
1.6.3 Costing 18

1.7 Assumptions regarding other CMS detector elements **18**

References **19**

2. SYSTEM PERFORMANCE **21**

2.1 Simulation overview **21**

2.2 Sources and simulation of muon background **21**

2.3 Momentum measurement **24**
2.3.1 Muon momentum resolution 25
2.3.2 Track charge discrimination 28
2.3.3 Momentum dependence of the muon track resolution 29
2.3.4 Muon reconstruction efficiency 30
2.3.5 Matching of muon tracks with the inner tracker 33

2.4 Trigger performance **34**

2.5 Performance for representative physics processes **34**
2.5.1 SM and MSSM Higgs bosons 35
2.5.2 $Z' \rightarrow \mu^+\mu^-$ 36
2.5.3 Top production and decay 38
2.5.4 Muons in b-jets 39
2.5.5 Y production in heavy ion collisions 40

2.6 Summary of detector simulation and performance **42**

Appendix: CMSIM Structure and Track Reconstruction Methodology **44**
A.1 CMSIM 44
A.2 Full track reconstruction 45

References **46**

3. THE BARREL MUON DETECTOR **47**

3.1 General description **47**

3.2 Technical design **50**
3.2.1 Drift cell design 50
3.2.2 Gas mixture 53
3.2.3 Definition of the working point 55
3.2.4 Aging 64
3.2.5 Chamber design 68
3.2.6 Structural analysis of the DT chambers 73
3.2.7 Chamber construction and tools 75
3.2.8 Quality control 86
3.2.9 Detailed station design 88
3.2.10 Integration with RPCs 89
3.2.11 Electrical layout and grounding 90

3.3 Front-end electronics **93**
3.3.1 General 93
3.3.2 Circuit description 93
3.3.3 Bench tests 94
3.3.4 Future developments 95

3.4 Readout and trigger electronics **96**
3.4.1 Readout electronics 96
3.4.2 The trigger electronics 101

3.5 Power and control systems **113**
3.5.1 High voltage 113
3.5.2 Low voltage 114
3.5.3 Cooling 114
3.5.4 Controls 115
3.5.5 Cables and interfaces 115

3.6 Gas system **117**
3.6.1 Gas in the drift chamber 117
3.6.2 Gas distribution on the wheel 119
3.6.3 Mixer and purifier 122
3.7 Installation and maintenance **124**
3.7.1 Installation 124
3.7.2 Maintenance 124
3.8 Production plans **125**
3.9 Performance: tests and simulations **126**
3.9.1 Results of tests in magnetic field 126
3.9.2 Simulations 134
3.9.3 Tests under LHC conditions 134
References **139**

4. ENDCAP CHAMBERS - CATHODE STRIP CHAMBERS **141**

4.1 General description **141**
4.1.1 Overview 141
4.1.2 Special conditions and requirements 146
4.2 Detailed chamber design: ME1/2, ME1/3, ME234/1, ME234/2 **148**
4.2.1 Introduction 148
4.2.2 Panels 149
4.2.3 Strips 151
4.2.4 Gap bars and gas seal 154
4.2.5 Wire fixation bars 156
4.2.6 Wires 157
4.2.7 Winding, gluing and soldering wires 158
4.2.8 Segmentation within a plane 158
4.2.9 Electrical layout 162
4.2.10 Assembly and external frame 163
4.3 Detailed chamber design: ME1/1 **165**
4.3.1 General features of ME1/1 165
4.3.2 ME1/1 chamber design 165
4.4 Front-end readout and trigger electronics **169**
4.4.1 General system requirements 170
4.4.2 Cathode front-end electronics 170
4.4.3 Anode front-end electronics 180
4.4.4 The readout motherboard 185
4.4.5 ME1/1 front-end electronics 186
4.5 Power and control systems **191**
4.5.1 High voltage 191
4.5.2 Low voltage 191
4.5.3 Cooling 192

4.5.4 Controls 195
4.5.5 Cables and interfaces 195
4.5.6 Gas system 196

4.6 Mounting and installation 202
4.6.1 Overview 202
4.6.2 ME1/1 chambers 207
4.6.3 Maintenance 208

4.7 Production plan 209
4.7.1 Production overview 209
4.7.2 Production stations for ME1/23, ME234/1 and ME234/2 chambers 210
4.7.3 Production of ME1/1 chambers 212

4.8 Chamber performance: chamber test results 213
4.8.1 Operating point and overall performance 217
4.8.2 Strips 219
4.8.3 Wires 226
4.8.4 Six-plane CSC performance in the presence of em secondaries 231
4.8.5 CSC performance in a high rate environment 236
4.8.6 Aging 238

4.9 Simulation of CSC detector and electronics response 241
4.9.1 Signal generation 241
4.9.2 CSC precision signal digitization (DAQ path) 241
4.9.3 CSC trigger primitive simulation 242
4.9.4 Cluster hit reconstruction 242

References 244

5. RESISTIVE PLATE CHAMBERS 249

5.1 General description 249
5.1.1 Overview 249
5.1.2 Specific conditions and requirements 251

5.2 Principles of operation 252
5.2.1 Simulation of avalanche growth and signal development 253
5.2.2 Material specification and basic parameters 254
5.2.3 The double-gap design 256
5.2.4 Aging studies 259

5.3 RPC construction and tools 260

5.4 Barrel design 262
5.4.1 Station layout 262
5.4.2 Mechanical assembly and integration 265
5.4.3 Production plans 266

5.5 Endcap design **267**
5.5.1 Layout and assembly of stations ME1 268
5.5.2 Layout of stations ME2, ME3, ME4 270
5.5.3 Production plans 272
5.6 Front-end electronics **272**
5.6.1 Design constraints 272
5.6.2 Electrical schematics 273
5.6.3 The front-end chip 275
5.6.4 The front-end board 277
5.7 Gas system **278**
5.7.1 Mixer 278
5.7.2 Closed circulation loop 279
5.7.3 Purifier 284
5.7.4 Distribution pipework 284
5.7.5 Gas recovery 284
5.8 Control system **285**
5.8.1 Front-end control and monitoring 285
5.8.2 High voltage system 286
5.8.3 RPC low voltage system 286
5.9 RPC Performance **287**
5.9.1 Global performance 288
5.9.2 Studies of rate capability 289
5.9.3 Test at the gamma irradiation facility 292
5.10 Pattern comparator trigger for RPC **295**
5.10.1 The algorithm 295
5.10.2 Segmentation of the PACT trigger 296
5.10.3 Technical description 297
5.10.4 Simulated performance 301
References **308**

6. TRIGGER **311**

6.1 Requirements **311**
6.1.1 General requirements for trigger and DAQ 311
6.1.2 Specific requirements for the first level muon trigger 313
6.2 Technical description **316**
6.2.1 CMS trigger and DAQ 316
6.2.2 First level muon trigger 317
6.2.3 Track finder for DT and CSC 318
6.2.4 Muon sorter 320
6.2.5 Global muon trigger 321

6.3 Trigger performance **325**
6.3.1 Simulation software 325
6.3.2 Geometrical acceptance and low momentum reach 327
6.3.3 Momentum resolution and efficiency curves 330
6.3.4 Performance of the global muon trigger 330
References **334**

7. ALIGNMENT **335**

7.1 Introduction **335**

7.2 Alignment scheme for the barrel **336**
7.2.1 Working principle of the internal barrel monitoring 336
7.2.2 Measurement of the chamber positions with respect to the MABs 337
7.2.3 Measurement of the z positions of the MABs 338
7.2.4 Diagonal connections 338
7.2.5 Elements of the system 338
7.2.6 Quality control, assembly, calibration and installation 342
7.2.7 Simulation of the barrel alignment performance 344
7.2.8 Integration with the barrel resistive plate chambers 346

7.3 Alignment scheme for the endcap **346**
7.3.1 Internal cathode strip chamber knowledge 347
7.3.2 Cathode strip chamber monitoring 350
7.3.3 Integration with the endcap resistive plate chambers 353

7.4 Link between tracker and muon systems **353**
7.4.1 The light path 354
7.4.2 Working principle 357
7.4.3 Elements of the system 358
7.4.4 Expected performance 362

7.5 Experiment tests **363**
7.5.1 Calibration and measurements with camera boxes 363
7.5.2 Multi-point alignment sensors: straight-line monitor test 365
7.5.3 Calibration and tests of laser levels 367

7.6 Validation of the muon alignment performance **368**
7.6.1 Full-scale test of the CMS position monitoring system 368
7.6.2 Performance of the global muon position monitoring system 368
7.6.3 Validation and diagnostics in situ 369

7.7 Alignment with muon tracks **369**
References **371**

8. CONTROLS AND MONITORING **373**

8.1 Overview **373**

8.2 DCS overview **373**
8.2.1 Design principles 373
8.2.2 Controls software system 374

8.3 Data from the drift tubes **375**
8.3.1 Electrical system 375
8.3.2 Gas system 376

8.4 Data from the cathode strip chambers **377**
8.4.1 Electrical systems 377
8.4.2 Gas system 377

8.5 Data from the resistive plate chambers **377**
8.5.1 Electrical systems 377
8.5.2 Gas system 378

8.6 Data from the alignment **379**
8.6.1 Barrel slow control 379
8.6.2 Endcap slow control 380
8.6.3 Link slow control 381

9. SAFETY **383**

9.1 Introduction **383**
9.1.1 Safety objectives 383
9.1.2 General principles 383
9.1.3 Safety documentation 384
9.1.4 Safety responsibilities 384
9.1.5 Full-scale tests 384

9.2 Mechanical aspects **385**
9.2.1 General requirements 385
9.2.2 Applicable design codes and standards 385
9.2.3 Hoists, cranes, transport, and handling 386
9.2.4 Seismic design 386
9.2.5 Magnetic fields in relays 386
9.2.6 Mechanical Safety in specific components 386

9.3 Electricity and electronics **387**
9.3.1 Overview 387
9.3.2 Overcurrent protection 387
9.3.3 Rack and crate protection 388
9.3.4 High voltage protection 388

9.3.5 Cooling systems 388
9.3.6 Specific component safety issues 389
9.4 Gases 389
9.5 Fire protection 389
9.5.1 Prevention 389
9.5.2 Detection and suppression 390
9.6 Lasers 390
9.7 Induced radioactivity 390
9.8 Magnetic fields 392
9.9 Software safety 393
9.10 Access and egress 393
9.10.1 Access 393
9.10.2 Egress 394
References 395

10. RADIATION ENVIRONMENT 397

10.1 LHC parameters 397
10.1.1 Luminosity 397
10.1.2 Assumed operation schedule 397
10.2 General features of the radiation environment 397
10.3 Sources of background in muon stations 398
10.4 Shielding strategies and materials 399
10.4.1 Beam pipe design 400
10.4.2 Shielding at $\eta = 3$ 400
10.4.3 Shielding around the HF 402
10.4.4 The rotating shielding 403
10.4.5 The block house 405
10.4.6 The ME4 wall 405
10.5 Simulation methods 406
10.5.1 Event generators 406
10.5.2 Radiation transport codes 407
10.5.3 General geometry description 407
10.5.4 Energy cuts and transport parameters 408
10.5.5 Estimation of error margins 408
10.6 Particle fluxes in the muon chambers 410
10.7 Machine background 415
10.8 Radiation damage 415

10.9 INDUCED RADIOACTIVITY **416**
10.9.1 Personnel safety 416
10.9.2 Detector background 417
References **418**

11. PROJECT ORGANIZATION AND COSTS **421**

11.1 Participating institutes **421**
11.2 Organiszation **425**
11.2.1 Institution board (IB) 425
11.2.2 Project managers 425
11.2.3 Muon technical board 426
11.3 Construction responsibilities **426**
11.4 Muon schedule and milestones **429**
11.4.1 Prototypes 429
11.4.2 Production of chambers 430
11.4.3 Muon milestones 434
11.5 Estimated costs **435**

GLOSSARY **437**

1. INTRODUCTION

1.1 STRUCTURE OF THE TECHNICAL DESIGN REPORT

Muons are an unmistakable signature of most of the physics LHC is designed to explore. The ability to trigger on and reconstruct muons at the highest luminosities is central to the concept of CMS, the Compact Muon Solenoid. CMS is characterized by simplicity of design, with one magnet whose solenoidal field facilitates precision tracking in the central barrel region and triggering on muons through their bending in the transverse plane. A perspective view of CMS is provided in Fig. 1.1.1(color), while transverse and side views, Figs. 1.1.2 and 1.1.3 (color) show the muon chambers in relation to the rest of the detector. (The color figures will be found at the end of the Report.)

The barrel muon chambers are drift tubes which provide a precise measurement in the bending plane, out to η=1.3. Since most of the return flux of the 4 T magnetic field is contained in the iron yoke, chambers with standard rectangular drift cells perform adequately.

At LHC energies, most events of interest will have one or more muons at higher rapidity, so the muon endcaps are of equal importance. Endcap chambers employ cathode strip chamber technology to provide high precision in the presence of a large and varying magnetic field, while their faster response time and finer segmentation allow them to function in the higher rate environment. A sophisticated alignment system relates the positions of the muon detectors to those of the central tracker elements to provide maximum momentum resolution.

The CMS muon system has a redundant and complementary trigger capability over nearly the entire rapidity range. A dedicated trigger element, the resistive plate chamber, will guarantee a fast, highly segmented trigger with a sharp p_T threshold and make it possible to achieve a very good understanding of trigger systematics.

The first two chapters constitute an “executive summary" of the Muon Technical Design Report and provide a synopsis of the remaining chapters. Chapters 3 through 7 describe in detail the principal hardware elements of the muon system In the first chapter of the TDR we summarize the physics goals of CMS and state the design requirements and special considerations, particularly background rates, which lead to specific choices for the detector parameters of the muon system. Short descriptions of the main detector elements follow.

Chapter 2, System Performance, presents in some detail the results of background studies, with particular emphasis on the impact of the various background sources on the muon detector elements. Studies of the momentum resolution of the full muon system over the entire rapidity range are given, and the salient aspects of the trigger performance are shown. We then put all the elements together in the simulation to show the muon system performance for representative physics processes, to demonstrate that the detector as designed can achieve the physics goals if the signals are there to be found.

Chapters 3 and 4 respectively describe the designs of the barrel Drift Tubes and the endcap Cathode Strip Chambers, giving particular emphasis to the R & D efforts that have led to these designs and describing test beam results that bear out the merits of the choices. System services and installation are also discussed in these chapters, as well as production plans, with emphasis on the tooling that has been developed for production runs.

Chapter 5, Resistive Plate Chambers, presents the status of the dedicated trigger elements, showing the substantial progress that has been made in adapting this technology to

the demands of the hadron collider environment. Preliminary results from the summer beam tests indicate that the baseline RPC design will function with an adequate safety margin in all the rapidity ranges of the detector.

Chapters 3 through 5 also describe the way in which each of these hardware elements generates trigger primitives, i.e., the lowest level pieces of information from each detector station containing position and/or angle information, that must be assembled into a coherent trigger. Chapter 6, Trigger and Data Acquisition, continues this process, showing how the primitives from each station are combined to indicate the presence of a potential track with the requisite qualities, p_T, isolation, etc., so that it can be considered a track candidate. Combining of information from the drift tubes, cathode strip chambers, and resistive plate chambers to form a global muon trigger is also described. Finally, a brief explanation is given of the process of identifying pieces of pipelined information from each detector element and reassembling them into a coherent event when the global trigger, either from the muon system or from another part of the CMS detector, requests that the event be read out.

Chapter 7, Alignment, presents a technological solution to the problem of aligning the barrel and endcap detectors among themselves, and the more complex problem of aligning these elements with respect to the inner tracker, so that the high momentum resolution capabilities of CMS can be realized. The alignment system must be able to cope with the deformation of the iron structure produced by the enormous magnetic forces. The physics solution to the alignment problem, alignment with muon tracks, is discussed as well.

Chapter 8, Control and Monitoring, gives a brief description of the organization of a system to monitor and control all relevant parameters of the muon system. This chapter is purposely generic since the objective is to achieve commonality, not only across detector subsystems, but indeed across the different experiments, to reduce costs and complications of this necessary but straightforward function. We attempt to show here that we have made a complete itemization of the quantities that must be monitored and controlled for each subsystem. Chapter 9, Safety, proceeds with the same philosophy, applying a common viewpoint to the various subsystems, again seeking an exhaustive enumeration of the areas of concern.

Chapter 10, Radiation Environment, presents three different approaches to the modeling of backgrounds, at different levels of sophistication, and the results are compared to give some idea of the level of uncertainty involved in background discussions. More detailed results regarding the background studies are also presented in this chapter. Chapter 11, Project Organization, lists the groups involved in the muon project and their areas of responsibility. Costs and schedules are presented in tabular form.

1.2 PHYSICS GOALS

As the Large Hadron Collider (LHC) pushes both energy and luminosity frontiers to open up discovery potentials, quality muon detection becomes a vital experimental design consideration. From its earliest conceptual stages, robust and precise muon detection has been the central theme (and the middle name) of the Compact Muon Solenoid experiment.

In the tremendously successful Standard Model of elementary particles, the interactions of the fundamental fermions – leptons and quarks – are mediated by gauge bosons obeying SU(3) x SU(2) x U(1) symmetry. More specifically, the electroweak interaction is described by spontaneously broken SU(2) x U(1) gauge symmetry. This leads to the emergence of massive vector bosons, the W and Z, which mediate the weak interaction, while the photon of the

electromagnetic force remains massless. It also leads to the existence of a scalar Higgs field with a non-zero expectation value. The Higgs Boson is virtually the only missing link in the theory, and the currently expected value for its mass is less than about half a TeV. At the LHC center-of-mass energy of 14 TeV, experiments will probe the entire allowed mass range for the SM Higgs boson and either discover it or be able to exclude it.

As experiments probe deeper into matter, exploring ever smaller distances, the corresponding cross-sections become smaller. Given the LHC energy of $\sqrt{s}$=14 TeV, collider luminosity becomes a very important factor in the discovery potential. Unfortunately, high luminosity also means high rates of background. At the LHC luminosity of $10^{34}cm^{-2}s^{-1}$, there are an average of about fifteen hadronic interactions per bunch crossing

Muon detection is the most natural and powerful tool to detect interesting events over the background. A “gold plated" signal of the Higgs Boson is its decay into Z-Z or Z-Z* which in turn decays into four charged leptons. If the leptons are muons, the best 4-particle mass resolution can be achieved, and muons are less affected than electrons by radiative losses in the tracker material. For example, in a 150 GeV Higgs event, Fig. 1.2.1, the muons stand out after the high magnetic field and absorbers filter out the large background of hadrons or non-isolated muons. Such an example underscores the discovery power of muon final states as well as the need for wide angular coverage for muon detection. The four-lepton channel is crucial for the discovery of the SM Higgs boson in the mass range from ~130 GeV up to ~750 GeV.

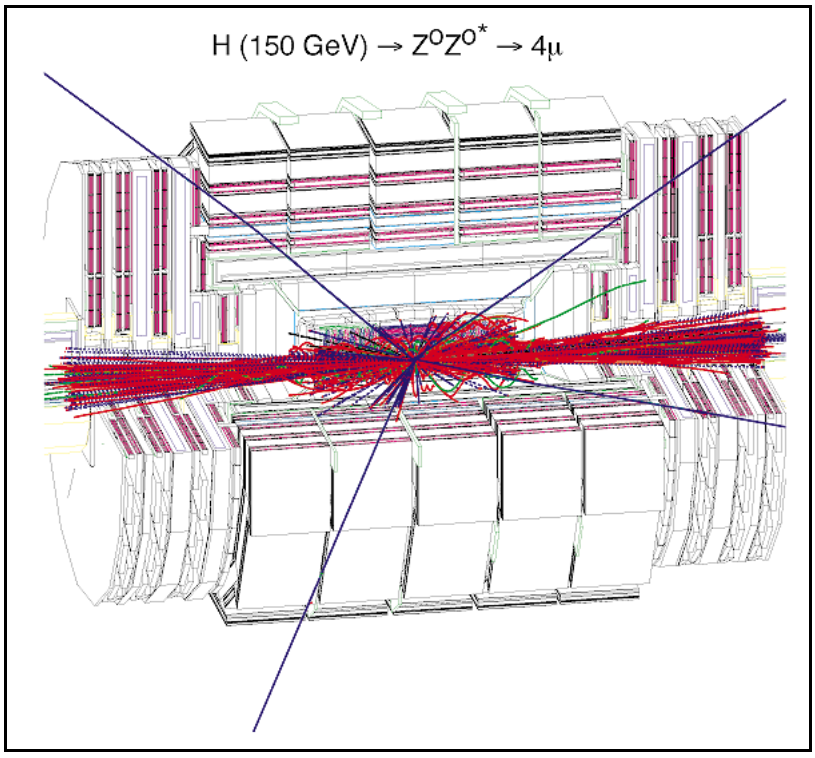


Fig. 1.2.1: A 150 GeV Higgs event decaying into four muons in the CMS detector.

Possible extensions of the Standard Model lead to the existence of other gauge fields. The LHC allows the discovery or exclusion of new gauge bosons with masses below ~4 TeV – more than an order of magnitude heavier than the W and Z. For the highest discovery reach, precision measurements of high energy muons (p_T > 1 TeV) in $Z' \to \mu^+\mu^-$ are important. Furthermore, sign determination for high energy muons is an essential tool to discriminate among various heavy gauge boson models giving different forward-backward asymmetries.

Lepton and photon isolation criteria are essential to extract most of the signals searched for at the LHC. Since muons can be measured within jets, which is generally not the case for electrons and photons, muons make it possible to determine directly the lepton and photon isolation rejection factors. The possibility of measuring muons in jets is also a powerful tool for b-jet tagging, exploiting the $b \to \mu$ decay, which is essential in a number of Higgs studies, top studies, and SUSY searches.

An appealing extension of the Standard Model is Supersymmetry: it allows the unification of the three couplings of the gauge interactions at a very high energy scale. Superpartners for all the presently observed particles are expected at the TeV mass scale. There are also multiple Higgs bosons. In the Minimal Supersymmetric Model for example, these are designated h^0, H^0, A^0, and $H^\pm$. At the LHC, Supersymmetry will be probed over the entire theoretically plausible mass range. Muons are again an essential tool not only for the discovery of these supersymmetric particles, squarks, gluinos, sleptons, etc., but also in determining their properties. An example is the cascade decay of neutralinos to di-muon pairs which yields an extremely well-determined mass difference between the two lowest lying neutralinos, which in turn allows the determination of the lowest supersymmetric particle mass and the reconstruction of $\tilde{q}/\tilde{g}$ masses.

The four-lepton channel is essential in the search for the MSSM Higgs bosons in the reactions $H \to ZZ^*$, $ZZ \to 4l^\pm$ ($4\mu^\pm$) at low tanβ (~2). The search for h, H, $A \to \mu^+\mu^-$ is the best way to explore the high tanβ (~30) region of MSSM parameter space. All these are narrow states (Γ<2 GeV) with expected masses in the ~100-500 GeV range, and detector acceptance and the excellent $2\mu^\pm$ and $4\mu^\pm$ mass resolution is of crucial importance. Large portions of the MSSM parameter space (tanβ, M_A) can also be explored with τ leptons using h, H, $A \to \tau\tau$ or $H^\pm \to \tau^\pm\nu$ modes. The $\tau \to \mu$ decays provide the most appropriate trigger for these channels.

The LHC is a copious source of t-quarks, with ~10^7 $t\bar{t}$ produced per year ($10^5 pb^{-1}$). Top events will largely be triggered through muon triggers ($t \to W \to \mu$) and effectively selected with b-jets tagged again with muons in jets, which is practically impossible with electrons. B hadrons are produced very abundantly as well. In the initial operation period of about 2 years, the integrated luminosity may not exceed ~$10^4 pb^{-1}$, and B-physics may be our main subject of study. Using $B^0_d \to \Psi\, K^0_S \to \mu^+\mu^-\, K^0_S$ or $B^0_d \to \Psi\varphi \to \mu^+\mu^-\, K^+\, K^-$ with μ tag events, significant measurements of CP violation will be possible. Investigation of $B^0_S \to \mu^+\mu^-$ with sensitivities up to BR≈10^{-9} will probe significantly FCNC scenarios. Most of the possible B^0_S oscillation measurements, for example using $B^0_S \to \Psi\, K^* \to \mu^+\mu^-\, K\pi$ with μ tag, rely either on $\Psi \to \mu^+\mu^-$ or more generally on some muon tagging technique.

The capability of the CMS detector to detect and trigger on low momentum muons will allow reconstruction of $\Upsilon, \Upsilon', \Upsilon'' \to \mu^+\mu^-$ in heavy iron collisions and make it possible to compare their relative production rates for various nuclei and in pp collisions. These relative suppression measurements are among the most promising tools to investigate quark-gluon

plasma formation. Detection of $Z \rightarrow \mu^+\mu^-$, even in the most crowded environment, opens up new possibilities in the field of heavy ion collisions.

1.3 PERFORMANCE REQUIREMENTS

The muon system has three purposes: muon identification, muon trigger, and muon (signed) momentum measurement. Performance requirements follow the physics goals, including the maximum reach for unexpected discoveries, and the background environment of LHC at its highest luminosity. A robust 4 T solenoid-based system is the key to the CMS design. Comprehensive simulation studies have indicated that the physics goals can be achieved if the muon detector has the following functionality and performance:

- MUON IDENTIFICATION: at least 16 λ of material is present up to η=2.4 with no acceptance losses.
- MUON TRIGGER: the combination of precise muon chambers and fast dedicated trigger detectors provide unambiguous beam crossing identification and trigger on single and multimuon events with well defined p_T thresholds from a few GeV to 100 GeV up to η=2.1.
- STANDALONE MOMENTUM RESOLUTION from 8 to 15% $\delta p_T/p_T$ at 10 GeV and 20 to 40% at 1 TeV.
- GLOBAL MOMENTUM RESOLUTION after matching with the Central Tracker: from 1.0 to 1.5% at 10 GeV, and from 6 to 17% at 1 TeV. Momentum-dependent spatial position matching at 1 TeV less than 1 mm in the bending plane and less than 10 mm in the non-bending plane.
- CHARGE ASSIGNMENT correct to 99% confidence up to the kinematic limit of 7 TeV.
- CAPABILITY OF WITHSTANDING the high radiation and interaction background expected at the LHC.

1.4 DESIGN CONSIDERATIONS

1.4.1. Backgrounds

As Fig. 1.4.1 shows, the major backgrounds occur at large η. Thus the chambers most affected by backgrounds are in the endcaps. Analysis of background sources has shown that the most critical regions in the background-generating process are the CMS beam pipe and the forward region, i.e., HF and the collimator with their shielding. The first three layers of CSCs see mostly beam-pipe generated background and punchthrough from the calorimeters. The last layer of chambers, ME4, catches particles created inside the forward calorimeter, HE (for ME4/1) and the collimator region (for ME4/2).

Background fluences on the chambers can be classified as follows:

- Low energy radiative electrons following slow neutron capture near or inside the muon chambers. These neutrons originate from hadronic cascades starting somewhere in the detector or in accelerator components.
- Charged hadrons from hadronic cascades: backsplash from HF and albedo, and leakage from HE and the collimator shielding.
- Decay muons coming mostly from the π/K decay inside the central cavity.
- Muons and other particles created in the accelerator tunnel after beam losses.

Various shielding configurations have been simulated for their effect on the baseline chamber design. Background rates of charged hadrons, muons and electrons on the muon chambers are shown in Figure 1.4.1. This figure was calculated using the current baseline design for the shielding at small angles. Further optimization of the local shielding around each muon station and at η~2.4 is in progress and is described in Chapter 10. It may decrease the local background rate of the soft electron component produced by neutrons by a factor of two. The total background rate at the highest pseudorapidity reaches up to 1 kHz/cm^2 at ME1/1 and ME4/1 and 0.4 kHz/cm^2 at ME2/1 and ME3/1.

Rates on other endcap and all barrel chambers are much less, in the range of a few tens of Hz/cm^2. High energy background (charged hadrons and muons) coincides in time with the bunch crossing; low energy background (electrons) is uncorrelated. These results are discussed in greater detail in the following chapter, while specifics of the simulations are the subject of Chapter 10.

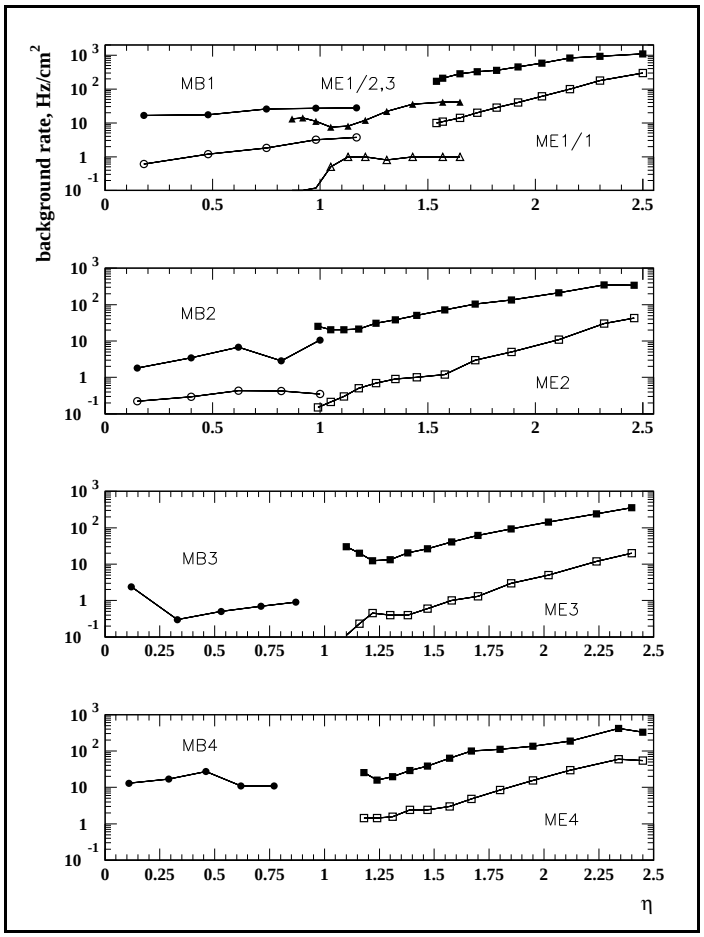


Fig. 1.4.1: Background fluences as a function of pseudorapidity, for each muon station. Solid points are the total fluence, open points are for the charged particle background.

1.4.2 Rates and trigger

With the design LHC luminosity of 10^{34}cm^{-2}s^{-1}, a bunch crossing frequency of 40 MHz and inelastic pp cross section at $\sqrt{s}$=14 TeV of 55 mb, one can expect on average ~15 pp

collisions per bunch crossing. The initial rate of 40 MHz has to be reduced by the First Level Trigger down to 30 kHz by looking for objects like muons, electrons/photons, jets, missing transverse energy and total transverse energy. One can roughly assume an equal sharing of this bandwidth between muon and calorimeter triggers.

Higher level triggers formed by a farm of commercial processors called the Event Filter have to reduce the rate further down to about 100 Hz, in order to match the bandwidth of a mass storage device (e.g. tape). The Event Filter input is designed to be able to accept 100 kHz of events to ensure a safety margin with respect to the expected 30 kHz delivered by the First Level Trigger.

On average, one per several hundred events will contain a muon which can enter the muon system (p_t>2-4 GeV, $|\eta|$<2.4). The resulting rate of 10^7 Hz is far too high for the Second Level Trigger. Therefore the First Level needs not only to recognize a muon but also to apply a momentum cut on single muon candidates. The p_T cut of 20 GeV is enough to reduce the rate to about 1 kHz. However, having in mind the presence of background and uncertainty on the cross sections, one should provide the possibility of raising this threshold to 50-100 GeV in order to maintain the rate at an acceptable value. On the other hand, for the two-muon trigger and in low luminosity runs, one can allow much lower p_T thresholds, down to the ranging-out limit of p_T ~4 GeV. Physics considerations discussed above and some technical limitations lead to the following list of guidelines for the muon trigger design:

1.4.2.1 Flexibility

In order to access all the interesting physics channels and to tune the rate to the level acceptable for the Event Filter, the p_T threshold must be adjustable. In the present design the full range from 2-4 to 100 GeV is covered.

1.4.2.2 Time resolution

The First Level Trigger must be able to assign an event to the proper bunch crossing. Thus the time resolution should be smaller than the bunch crossing interval, i.e. 25 s.

1.4.2.3 Speed

The trigger decision must be available about 3 μs after the collision. This includes propagation time of the signals from the detector to the Control Room (~120 m) and back.

1.4.2.4 High acceptance

Searches for rare events require an acceptance close to 100%. Therefore the muon stations are arranged in such a way that most tracks cross 4 triggering planes but every track crosses at least 3 triggering planes.

1.4.2.5 Redundancy

The trigger system has to deal properly with all possible inefficiencies, noise, accidental pileup and background from muon radiation. Thus it has to have substantial redundancy. In CMS this is ensured by having two complementary subsystems, one based on fast dedicated trigger detectors, namely Resistive Plate Chambers, and the other using precise multilayer muon chambers: Drift Tubes and Cathode Strip Chambers. This complementary is discussed in Chapter 6. For the specific needs of low p_T (~3-5 GeV) muon physics, such as B physics and heavy ion collisions, a double system of RPCs is included in the two innermost muon stations at the barrel.

1.4.3 Detector elements

Before describing the detector elements, we list the principal factors which argue for the choice of technology that has been made for the barrel and endcap muon measuring systems and the dedicated trigger devices.

1.4.3.1 Barrel

The choice of a drift chamber as tracking detector in the barrel was dictated by the low expected rate and by the relatively low intensity of the local magnetic field. A tube as the basic unit was preferred in order to have natural protection against damage from a broken wire and to partially decouple contiguous cells in the presence of electromagnetic debris accompanying the muon itself. Just as the iron thickness decouples two consecutive stations, so the relatively thick walls of the drift tubes, 2 mm, gives an effective decoupling among the several layers of tubes inside the same station. The simplest solution was to assemble together all the tubes in each slot of the barrel iron yoke to form a single rigid structure called a drift tube chamber.

Since the first studies of the drift tube design, it was realized that a group of three consecutive layers of thin tubes, staggered by half a tube, had an excellent time-tagging capability. A time resolution of a few nanoseconds can be obtained using signal processing based on simple meantimer circuits, which in the case of LHC makes it possible to have efficient local standalone bunch crossing identification.

The cell design makes use of four electrodes to shape an effective drift field: two on the side walls of the tube, and two above and below the wires on the ground planes between the layers. With this arrangement the requirement of 250 micron resolution per layer (which guarantees 100 microns per chamber) can be obtained while operating the tubes at atmospheric pressure with a binary Ar/CO_2 gas mixture. The multielectrode design ensures this performance even in the presence of the unavoidable stray magnetic fields present in the chamber region.

1.4.3.2 Endcaps

The cathode strip chamber has been chosen for the endcaps since it is capable of providing precise space and time information in the presence of a high magnetic field and high particle rate. CSC modules containing six layers provide robust pattern recognition for rejection of non-muon backgrounds and efficient matching of external muon tracks to internal track segments.

A strip width wider than the conventional width for CSC was chosen to limit the number of channels. Tests showed that if such strips were properly staggered in the module, a spatial resolution consistent with the multiple scattering limit could be obtained. Similarly, the wire spacing is somewhat larger than what has been used heretofore, but again tests showed that timing resolution was still adequate for bunch crossing identification.

The configuration of a CSC also easily allows chambers to be built to fit into the disk structure of the endcaps. Since the precision of the chambers derives from the strip pattern milled on their surfaces, an external reference can easily be provided to facilitate surveying and alignment.

1.4.3.3 RPCs

Resistive plate chambers have a very fast time response, comparable in fact to scintillators. Consequently they can provide an unambiguous assignment of the bunch crossing. However since they do not demand a costly readout device such as a photomultiplier, they can

be sufficiently highly segmented to make it possible not only to measure transverse momentum, but to do it at trigger time. Thus RPCs constitute a fast dedicated trigger which can identify candidate muon tracks and assign the bunch crossing with high efficiency.

While drift tubes and CSCs protect themselves against backgrounds by requiring coherent track stubs in multilayered modules, RPCs count on their fast response and segmentation to do so. Thus they have a different sensitivity to background. The higher rate capability of the new generation of detectors operating in avalanche mode makes their use at LHC feasible.

1.5 DETECTOR DESCRIPTION

1.5.1 Detector layout

The muon system uses three different technologies to detect and measure the muons; drift tubes (DT) in the barrel region, cathode strip chambers (CSC) in the endcap region, and resistive plate chambers (RPC) in both the barrel and endcap. A muon trigger in the barrel region is generated using a mean-timer to identify patterns. In the endcap the trigger is generated from the cathode readout patterns and the wire timing. For both barrel and endcap the RPCs provide an additional trigger signal which has a different sensitivity to backgrounds. All the muon chambers are aligned roughly perpendicular to the muon trajectories and distributed to provide hermetic coverage over the η range from 0 to 2.4. The barrel DTs cover roughly from $\eta = 0$ to $\eta = 1.3$ while the endcap CSCs cover from $\eta = 0.9$ to $\eta = 2.4$. The RPCs cover the region from $\eta = 0$ to $\eta = 2.1$. Some of the salient facts about these chambers are summarized in Table 1.5.1.

1.5.2 Barrel region

The barrel muon system of the CMS detector consists of four stations integrated in the return yoke of the magnet. Two stations are mounted on the inner and outer face of the yoke; the remaining two are located in slots inside the iron. The segmentation of each station is dictated by the longitudinal segmentation of the iron in five rings, each 2.5 m long, and by the presence of the azimuthal ribs needed to support the coil cryostat and the barrel calorimeter, and to create the slots inside the iron. In total, 60 chambers compose each one of the inner three stations, while 70 chambers are used in the outer station due to the presence of the yoke feet.

The basic sensitive element of the chambers is a drift cell of approximately 400 ns maximum drift time. This choice reduces the total number of wires to less than 200,000, while still keeping the occupancy negligible.

The twelve planes of drift tubes present in every chamber are organized in three independent subunits called Super Layers (SL) made up of four planes with parallel wires. Two SLs measure the coordinate in the bending plane (ϕ SL), the third measures the track coordinate along the beam (z SL). The two ϕ SLs have a separation of about 23 cm, in order to obtain the best angular resolution. This is the maximum allowed by the space available. Between them are the z SL and a thick honeycomb plate used as a spacer.

Within a SL, the four layers are staggered by half a cell, making it possible to use the correlation of the drift times in the different planes to compute the coordinate and the angle of the crossing tracks without any external time tag. The mean timer is fast enough to be used in the first-level trigger.

The obvious redundancy of the system, four stations of twelve planes each, makes it possible to cope with inefficiencies due to the dead zones which are caused by the supporting iron ribs, by the longitudinal space allowed for services, and by the non-negligible probability for a high energy muon to produce electromagnetic showers when exiting the iron slab.

1.5.3 Endcap cathode strip chambers

Each endcap region of CMS has four muon stations (ME1, ME2, ME3, ME4) of Cathode Strip Chambers (CSCs). These chambers have trapezoidal shape and are arranged in a series of concentric rings centered on the beam line. The stations are separated by the iron disks of the flux return yoke, which are thick enough to isolate the electrons in showers. Both YE1 and YE2 are 600 mm thick while YE3 is 250 mm thick. The last station is followed by a 100 mm thick iron disk whose primary purpose is shielding the ME4 station from backsplash backgrounds induced by particles scattered at small angle and interacting with the forward calorimeter, quadrupoles, beam pipe etc.

The ME1 station has three rings of chambers (ME1/1, ME1/2, ME1/3), at increasing radius, while the other three stations are composed of two rings of chambers (MEn/1 and MEn/2). All but the ME1/3 chambers overlap in φ and therefore form rings with no dead area in azimuth. In each of rings 2–4 there are 36 chambers covering 10° in φ at the outer radius, and 18 chambers covering 20° at the inner radius. The radial cracks between the chamber rings are not projective, and thus coverage, defined as at least 3 chambers on a muon path, is close to 100% down to θ=10° or η=2.4. The ME234/2 chambers, at the outer radius, are the largest - about 3.4 m long and 1.5 m wide.

ME1/1 chambers have to operate in an axial magnetic field in excess of 3 tesla, while ME1/2 chambers are in a highly non-uniform magnetic field of up to 1 tesla. The other chambers are generally in much lower magnetic fields. Most muons initially bend through the magnetic field and reach their maximum sagitta slightly in front of the first station. After this the muons are moving through the return flux and the sign of the bending is reversed. Consequently the sagitta measurement in the succeeding stations will be smaller. Therefore, the sagitta measurement at the first station is crucial and leads to more stringent requirements on the resolution and alignment in this station than in the other stations.

Each CSC has six layers of wires sandwiched between cathode panels. Wires run at approximately constant spacing, while cathode panels are milled to make six planes of strips running radially, one plane of strips per gas gap. Therefore, each chamber provides six measurements of the φ-coordinate (strips) and six measurements of the r-coordinate (wires). Strip width varies from 3 to 16 mm for different chambers, or from about 2 to 5 mrad in φ-coordinates. In the endcap geometry, measurement of track coordinates in the r-φ coordinate system is best suited for evaluating muon momentum. The precise φ-coordinate comes from interpolating charges induced by an avalanche on the strips. These charges are digitized and stored by the DAQ. The precision requirement for the endcap chambers is 75 μm for ME1/1 and ME1/2 chambers, and 150 μm for the rest (numbers are per six-plane chamber). Wires are grouped in 16-50 mm wide bunches and provide coarser radial information.

For trigger purposes, the position of hits in φ can be defined with a precision on the order of a tenth of a strip. First, the position of hits on each plane is determined to within a half-strip uncertainty, and then we use a look-up table to extract the most probable track coordinate corresponding to an observed six-plane pattern of the half-strips. The radial coordinate is available with an accuracy corresponding to a wire group width. Wire signals also provide

high-efficiency bunch crossing identification, the formal requirement being 92% per station. By picking the most frequent bunch crossing identification (BXID) out of four track segments from the four muon stations linked to one track, one can obtain better than 99% efficiency for correct bunch-crossing identification.

Overall, the Endcap Muon System consists of 540 six-plane trapezoidal chambers, with about 2.5 million wires, 210,816 anode channels and 273,024 precision cathode channels. A typical chamber has about 1000 readout channels.

1.5.4 Resistive plate chambers (RPC)

CMS has added planes of resistive plate chambers (RPCs) in both the barrel and endcaps to provide an additional, complementary trigger.

RPCs are gaseous parallel-plate chambers that combine a reasonable level of spatial resolution with excellent time resolution, comparable to that of scintillators. In the muon system, these chambers will cover roughly the same area as the DTs and CSCs but will provide a faster timing signal and have a different sensitivity to background. Trigger signals coming from the drift tubes, cathode strip chambers, and the RPCs will proceed in parallel until reaching the level of the global trigger logic. This will provide redundancy for evaluating efficiencies, and result in a higher efficiency and greater rate capability.

A resistive plate chamber is constructed of two parallel plates of material made of phenolic resin, with good surface flatness and a high bulk resistivity. Typically the plate separation is on the order of a few millimeters. The resin material is coated with a conductive graphite paint to form electrodes, and readout is made by means of aluminum strips outside the resin plates, insulated from the electrodes by some plastic material. In normal construction, two such assemblies are placed back to back, with the readout strips in the center. The entire sandwich is gas tight.

In their original concept, for data taking in cosmic ray applications, RPCs were run in streamer mode, in which the resulting pulses were large enough that no amplification stage was required. These large pulses however prevented high rate operation, since the electrode cell involved in the discharge process remained inefficient for the recharge time, which was long enough to limit operation to 100 Hz/cm^2. To use these devices in a high-rate environment, experimenters have begun to run their chambers in avalanche mode, with lower gas amplification and smaller pulses. The consequent drastic reduction of the elementary discharge cell has led to high rate capability, although now a robust signal amplification stage is needed.

Used in this way, RPCs constitute a fast dedicated trigger which can identify candidate muon tracks and assign the bunch crossing with high efficiency. Since they are low-cost devices, they can be sufficiently highly segmented to make it possible to measure the transverse momentum at trigger time. All these functions are ideal for the CMS application, and the higher rate capability of the new generation of detectors makes them feasible at LHC.

A total of six layers of RPCs will be mounted with the barrel chambers, two layers with each of stations MB1 and MB2, and one each in the outer stations. In the endcap region, each of the four layers of CSCs will have a layer of RPCs in conjunction with it, with their shape and method of mounting determined by the η segmentation. The RPCs will extend to η=2.1,

Prototype chambers representing the three technologies described above, drift tubes, cathode strip chambers, and resistive plate chambers, have recently been tested in a high radiation flux environment at the GIF facility at CERN. All three tubes of chamber have

performed according to design specifications in fluxes exceeding those expected at LHC. A photograph of the chambers in the test area is presented in Fig. 1.5.1 (color).

Table 1.5.1
Chamber properties and statistics

Detector	Drift Tubes	Cathode Strip Chambers	Resistive Plate	
Function	Tracking p_T trigger BXID	Tracking p_T trigger BXID	BXID p_T trigger Resolve tracking ambiguities	
η region	0.0 - 1.3	0.9 - 2.4	0.0 - 2.1	
Stations	4	4	Barrel 6	Endcap 4
Layers	RΦ 8, Z 4	6	2	
Chambers	250	540	360	252
Channels	195000	Strips 273024 Wire groups 210816	80640	80642
Spatial resolution (σ)	per wire 250 μm RΦ (6/8 pts) 100 μm Z (3/4 pts) 150 μm	RΦ (6 pts) 75 μm (outer CSCs) 150 μm R(6pts) (15-50)/$\sqrt{72}$ μm	Cell size	
Time resolution	5 ns	6 ns	3 ns	
Within 20 ns window	> 98% (station) no parallel B field	> 92% (station)	98%	

1.5.5 Trigger

The CMS Muon Trigger is based on three kind of detectors: Drift Tubes in the barrel, Cathode Strip Chambers in the endcaps, and Resistive Plate Chambers placed both in the barrel and the endcaps. They are arranged in the four muon stations in such a way that every muon with enough energy to penetrate through the detector material should cross at least three of them. The muon stations are interleaved with iron which serves as a return yoke for the CMS solenoid. Most of the iron is saturated at ~1.8 T, whereas the field inside the coil is 4 T. Bending in the field is used to measure the muon transverse momentum p_T.

RPCs are dedicated trigger detectors. Thanks to their excellent time resolution (σ~3 ns) they ensure precise timing. They are segmented in strips of $\Delta\eta\times\Delta\phi$ = ~0.1 × 5/16° = 20-100 cm × 1-4 cm, which makes possible a p_T measurement up to ~50 GeV. The measurement is done by the *Pattern Comparator Trigger* (PACT) which compares each pattern of hit strips to predefined patterns corresponding to various p_T values.

In the barrel there are 12 Drift Tube layers in each muon station. They are arranged in three quartets, two of them measuring ϕ and one measuring the Z coordinate. DTs can measure muon position (and thus p_T) more precisely than RPCs - 1.25 mm at the trigger level. The drift time is long (~400 ns) but the bunch crossing can be identified using a generalized meantimer technique. The *Bunch and Track Identifier* (BTI) circuit collects the drift time information from four layers of DTs and calculates the track position, angle and time by solving a system of linear equations. Results from two ϕ-layers are combined by a *Correlator*. Together with the Z-layer information they are sent through the *DT Trigger Server* to the *Track Finder*.

Each endcap muon station is equipped with a 6-layer CSC. Each layer contains radial cathode strips and wires perpendicular to them. At the trigger level the muon position is measured in each layer with half-strip precision (2-8 mm). A *Local Charged Track* is formed when a coincidence of ≥4 hit strips in different layers occurs. The strips must belong to a predefined road. A coincidence of ≥4 layers is also required for wires. It was found that the bunch crossing is best defined by the second hit in time. This is accounted for by the large spread of drift times with a maximum of 40–50 ns, by fluctuations in hit times and by accidental overlap with random background hits. As in the case of the drift tubes, a vector from each station is delivered to the *Track Finder*.

The Track Finder (TF) combines vectors received from the DT and CSC stations and forms full tracks with a defined p_T. Then the TF and PACT information is transferred to the Global Level-1 Trigger. Comparing TF and PACT data, the Global Trigger rejects some ghosts and background. Finally, once a track is identified, it applies p_T cuts to the muon candidates.

1.5.6 Alignment

The muon detector spectrometers are instrumented with optical alignment systems to constantly monitor the position and deformations of the muon chambers during detector operation. The aim is to provide position information of the detector elements with an accuracy comparable to the intrinsic chamber resolution, to be used as an off-line correction for track reconstruction.

The muon alignment scheme consist of two local stand-alone subsystems for the internal monitoring of the barrel and endcap muon detectors. To benefit from the highest momentum resolution capabilities of CMS, these subsystems are linked to the inner tracker alignment such that the position in space of the tracker detector and muon stations can be related at any time. The main design parameters are given in Table 1.5.2.

Following the specific detector configurations two different technical approaches have been chosen for the position monitoring of the barrel and endcap detectors.

The scheme for the barrel alignment system is based on the monitoring of the muon chambers position with respect to a network of radial reference structures, mechanically and thermally stable, fixed to the barrel yoke. They are optically connected between themselves, forming a closed reference network. The structures are equipped with video cameras which observe light sources mounted on the muon chamber fiducials.

Table 1.5.2
Alignment design parameters and component statistics.

Intrinsic sensor accuracy	<5 μm
Accuracy of barrel chamber positioning	<150-350 μm
Accuracy of endcap chamber positioning	<75-200 μm
Number of Rasnik systems	12
Number of MPA sensors	546
Number of video-camera detectors	612
Number of proximity measurements	1404

The alignment system of the endcap detectors uses straight-line monitors –Rasnik systems –to monitor the relative position of the four muon stations. The deformations of the CSC chambers are measured as well by optical straightness monitors defined across each layer of chambers.

Opto-mechanical angular and distance measurements and similar straightness monitors as for the endcap alignment are used to relate the inner tracker and muon detector alignment systems.

1.5.7 Magnetic field

The CMS Collaboration has chosen a solenoidal superconducting coil to generate a 4 T magnetic field over the entire tracking region. The inner diameter of the coil is 6.22 m, the coil is 13.48 m long. The tracking and calorimetry subsystems are completely enclosed within the field. The flux of the solenoid is returned by a set of iron disks in the endcaps and concentric twelve-sided cylinders in the barrel. The muon subsystem has four measurement stations in both barrel and endcaps, interleaved in the flux return region with the iron plates. This geometry serves to isolate background showers within one station as well as to provide an effective flux return. Details of the magnet construction are provided in the Magnet Technical Design Report [1.1].

Fig. 1.5.1 (color) shows the CMS magnetic field as calculated with the ANSYS® finite element program using an axisymmetric model. This figure shows a quadrant of the CMS detector with a constant 4 tesla field inside the solenoidal coil. An important advantage of ANSYS is its ability to use the magnetic field as calculated to compute the forces on the iron plates and the resultant deflection. Details of the magnetic modeling and the specific inputs to the calculation are given in a CMS Technical Note [1.2]. Fig. 1.5.2 (color) shows the radial component of the field, and we immediately see the effect of the gaps between the barrel rings as well as the large and rapidly changing radial field at the end of the coils. As a result, chambers in this area (ME1/2 and MB2/1) experience a large field variation.

Large forces on the endcap disks appear as a result of these magnetic fields. The overall magnetic force on the first endcap disk is roughly 7000 metric tons for an object that weighs about 900 metric tons, so the magnetic forces dwarf the gravitational forces even for such heavy disks. The result of the action of these forces is shown in Fig. 1.5.3 (color) where the center region of each endcap disk (including the nose) deflects toward the interaction region by roughly 14 mm.

The high field of the solenoid is the key to the very good momentum resolution of the detector, and at the same time the field confines some fraction of the low momentum particles to the beam pipe region so that they do not confuse the inner tracking. But from the point of view of the muon subsystem, the field sets the environment in which the detectors operate, and the large forces produced by the field mean that the iron structure in which the chambers are mounted cannot be regarded as fixed, so that alignment is an ongoing process.

The full field is present in the region in which the innermost endcap CSCs, the ME1/1 chambers, must operate. However, the field at this position is uniform and almost entirely axial, so that relatively simple measures can compensate for the effect of the field on the drift of the electrons. This is discussed in detail in Sections 4.3 and 4.8.

At the next endcap station going out radially, ME1/2, the field has fallen off to a considerable degree, but it is no longer uniform and no longer axial as shown in Fig. 1.5.4.

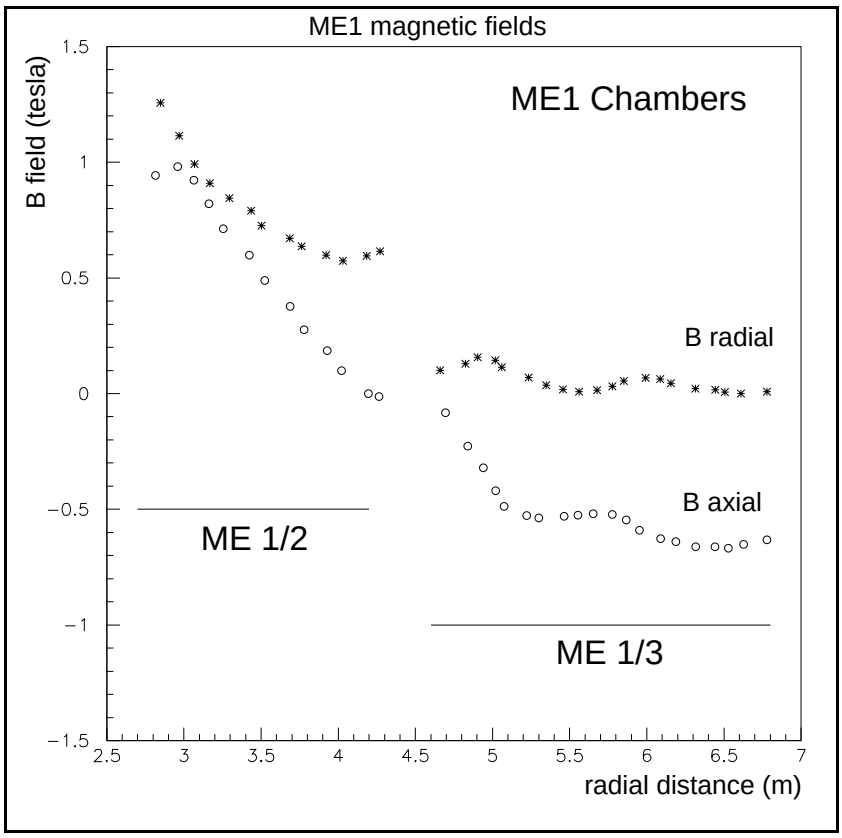


Fig. 1.5.4: Axial and radial components of the magnetic field in the vicinity of the endcap chambers ME1.

The radial component is the same as or greater than the axial component. Due to the large variation across the chamber, simple compensation schemes will not work. However, since the drift space in the CSC is small, the deterioration of resolution from the changing field components is also small, and the resolution of uncompensated chambers is within the requirements of the system.

Ideally the barrel drift tubes should be in a field-free region, since the return flux is largely contained within the iron. However, at the end of the coil and in the iron gaps there are large stray fields in the chamber area, as shown in Fig. 1.5.5. Near the end of MB2/1 the radial component reaches 0.8 tesla. This requires a rather complicated field shaping scheme in the DT cells, and in the worst regions results in a loss of resolution and bunch tagging efficiency. Fortunately, these regions are small with respect to the overall area covered by the DTs.

While most of the magnetic flux is returned via the iron plates, the fringe field outside the detector remains uncomfortably large. In Fig 1.5.6 we show the calculated field outside the solenoid in the z = 0 plane out to a radius of 50 m. In the region of R = 4-7 meters, the three cylindrical rings of iron plates are clearly visible, with a B field near saturation (~1.6 tesla). Outside the detector, at a radius of 8-9 m, where electronics will be located, the field is roughly 0.05 tesla (500 gauss). At larger distances of 35 m (roughly the location of the underground control room) the field is still 0.0005 tesla (5 gauss). Consequently we will require careful shielding of the electronics throughout the CMS underground hall.

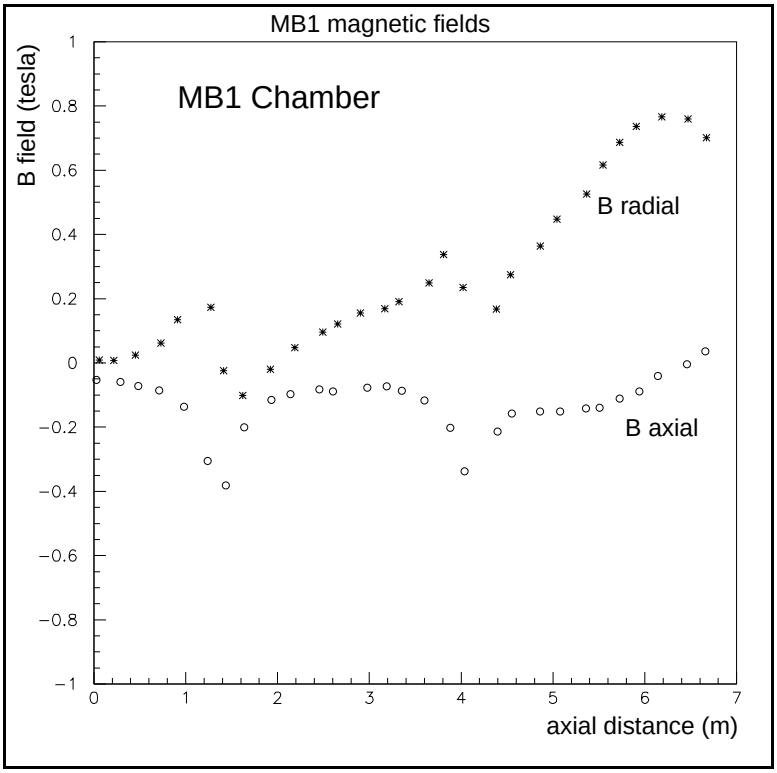


Fig. 1.5.5: Axial and radial components of the magnetic field in the vicinity of the barrel chamber MB1.

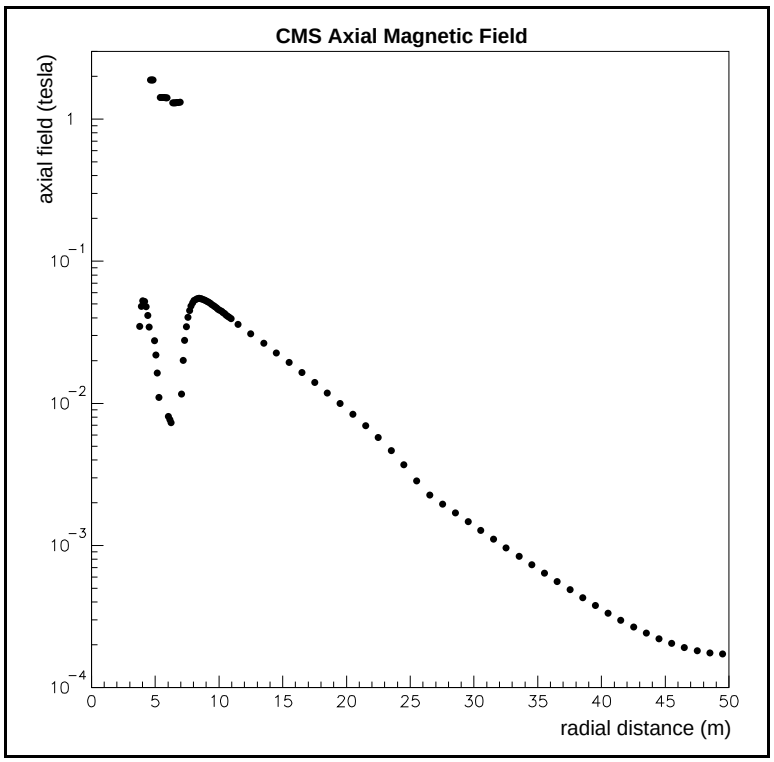


Fig. 1.5.6: Magnetic field moving out radially from the beam line in the z=0 plane. A non-negligible field exists at considerable distance from the detector.

1.6 PROJECT ORGANIZATION, SCHEDULE, AND COSTS

The CMS Muon Group comprises over 400 physicists and engineers from nearly 50 institutes in 13 countries. Its task is to design, construct, and utilize detectors for the identification and measurement of muons in the barrel and endcap regions, and to link those devices to the central tracking instrumentation to form a coherent whole.

1.6.1 Organization

The Muon Group follows the organizational scheme of CMS as a whole. It operates under a constitution which sets up an Institution Board as the highest level decision-making body for the group. This board, headed by a chairman and a deputy chairman, each elected for two-year terms, has as its charge to ratify decisions made by the Technical Board, and to see to it that the resources available to the group are best matched to the demands of the project.

The Technical Board is headed by Project Managers appointed by the CMS Spokesman. Because the barrel and endcap sectors of the detector are in very different regimes of background and operational environment, the Technical Board is divided into two functional units, one for the barrel and one for the endcap. As a consequence of the formation process of CMS, these two units correspond also to a geographical division, the barrel part being largely the responsibility of institutes from CERN member states, and the endcap part the responsibility of US and RDMS institutes. The two Project Managers are members of the CMS Management Board.

Each Project Manager is assisted in his task by a Technical Coordinator in directing the work of subgroups responsible for chamber construction, electronics development, trigger, alignment, integration, software and simulation, and testing. Subsystem Coordinators make up the balance of the Technical Board. The two technical coordinators are members of the CMS Technical Board. Because of the rather independent nature of the barrel and endcap projects, the Technical Boards of each subproject function separately for the most part; they provide a forum for technical discussions and formulate proposals and recommendations for the Muon Institution Board.

1.6.2 Responsibilities

Detailed breakdowns of the responsibilities of the institutions for each subproject are provided in Chapter 11. Because of their global character, questions of software and simulation, alignment, integration, and trigger are to a large degree common, and the subgroups in charge of these areas are formed by individuals from both parts of the overall group.

Detailed planning and scheduling is carried out by the CMS Management Board in consultation with the Muon Technical Board. However, in general terms, the construction phase begins in early 1999 and reaches completion in 2003. Since one endcap must be lowered into the experimental hall before the other, half of the endcap chambers, complete with electronics, must be ready for above-ground installation before 2003. Chapters 3 and 4 discuss in detail the progress of prototypes. Both the barrel and endcap groups are now beginning the construction of "pre-production prototypes" which will be for all practical purposes part of the production sequence.

1.6.3 Costing

Detailed cost estimates have been presented in successive Cost Books, and the current state of these estimates is summarized in Chapter 11. Consistent with the overall cost ceiling on CMS of 475 MCHF, the Muon Project is capped at 61.3 MCHF. Cost estimates developed to this point are consistent with this number, and the available resources are adequate, within the uncertainties, to complete the project. For the endcap sector, the manpower costs are either included in the scope of the project or are counted against the base programs of the institutes involved. For the barrel sector, manpower costs come under the scope of the Memoranda of Understanding. In either case, the Muon Group considers the financial and manpower resources to be sufficient to bring the project to completion.

1.7 ASSUMPTIONS REGARDING OTHER CMS DETECTOR ELEMENTS

Although many assumptions are made in this TDR regarding the performance or characteristics of other element of the CMS detector, e.g., the inner tracker resolution in the calculation of the combined tracking resolution (Fig. 2.3.2), we wish to explicitly mention the assumptions made in the discussion of a) the background levels around the CSCs, and b) the link system of the alignment.

All calculations of background levels and occupancies of the CSCs, in particular of ME4, assume that a 10 cm iron disk, of roughly the same shape as the flux return disks, is installed between ME4 and the forward hadron calorimeter HF and the low-beta quadrupole magnets. The exact location of this disk is shown in Fig. 2.1.1.

The current scheme for the link between tracker and muon detectors, as described in Section 7.3, assumes a tentative baseline design for the inner tracker. Nevertheless the final implementation will follow the design optimization of the tracker detector and will be described in the CMS Tracker Technical Design Report, to be published in early 1998.

References

[1.1] The Magnet Project Technical Design Report, CERN/LHCC 97-10, May 1997.

[1.2] R. Loveless and F. Feyzi, Magnetic and Structural Analysis of the CMS Endcaps, CMS TN/94-293, December 1994.

2. SYSTEM PERFORMANCE

2.1 SIMULATION OVERVIEW

The role of the muon system in pursuit of the physics goals of the CMS experiment and the main features of the design in order to fulfill this role are both covered in Chapter 1. In this chapter we describe the simulated response of these design features to physics signals and background.

The CMS simulation is based upon the GEANT simulation framework providing routines that create detector volumes out of various materials, propagate particles through those volumes taking into account any interactions with the material, and keep track of when and where a particle passes a particular detector boundary. Details of the simulation structure are given in the Appendix. All aspects of the detector design are kept in a common database used for both simulation and event reconstruction. This information includes the geometry, materials, magnetic field map, etc. The following figures illustrate the detector information contained in the database:

- A display of a detector quadrant (Fig. 2.1.1) illustrating the amount of detail available to the simulation that is present in the geometry file;
- The corresponding acceptance curves (Fig. 2.1.2) determined from the geometry file;
- From the geometry and material information entered into the database, the amount of material present before each of the muon stations, measured in absorption and radiation lengths (Fig. 2.1.3);
- From the detailed field map, the field integral $\int \mathbf{B} \cdot \mathbf{dl}$ (Fig. 2.1.4).

Because of the importance of background in determining the design of the muon system and its physics detection capabilities, this chapter begins with a brief overview of backgrounds significant to muon detection at the LHC.

2.2 SOURCES AND SIMULATION OF MUON BACKGROUND

Due to their large detector elements, the chambers of the muon system are very sensitive to background particles in the LHC environment. The muon system receives background hits from secondary muons resulting from pion and kaon decays as well as from punchthrough hadrons and from low energy electrons originating after slow neutron capture by nuclei with subsequent photon emission. These photons have a probability of about 1% to generate electrons by Compton-scattering or photo-electric effect in detector materials and gases that can cause hits in the chambers. Most captures occur in the thermal energy region, but the photons resulting from nuclear de-excitation may have energies in the MeV range. Neutron induced background is likely to be a significant contribution to the occupancy level in the muon detectors.

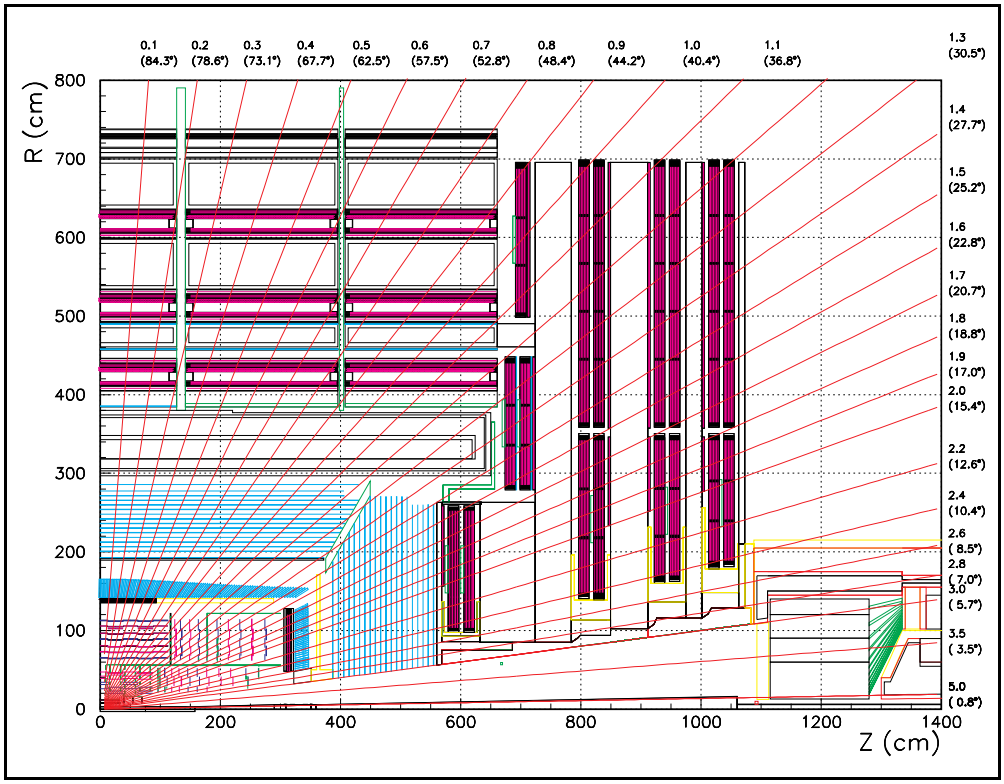


Fig. 2.1.1: Side view of a quadrant of the CMS detector as installed in CMSIM showing details of the implemented geometry.

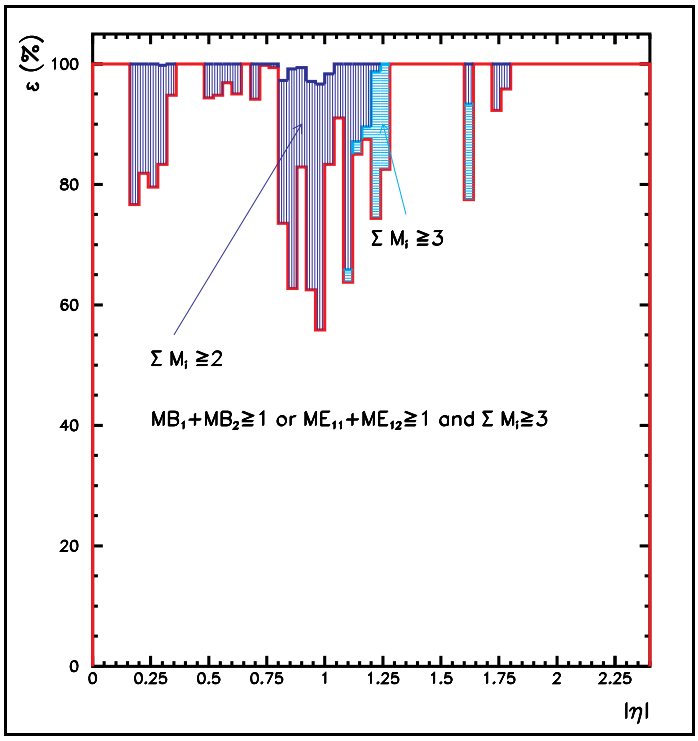


Fig. 2.1.2: Muon system geometrical acceptance shown for the following three requirements: three or more stations, including at least one of the first two barrel stations or the first endcap station; any three stations; and any two stations.

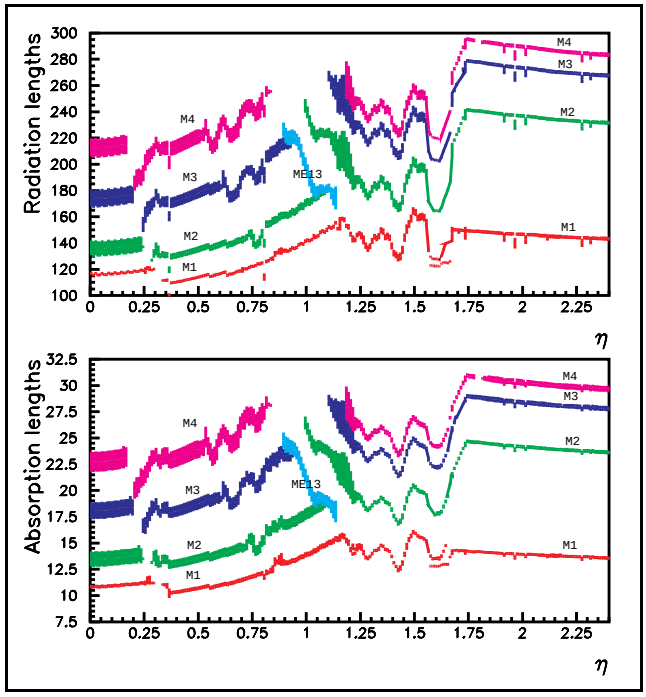


Fig. 2.1.3: Material in front of the muon stations in terms of radiation lengths. (The thickness of the lines reflects the departure from perfect cylindrical symmetry of the CMS detector geometry.)

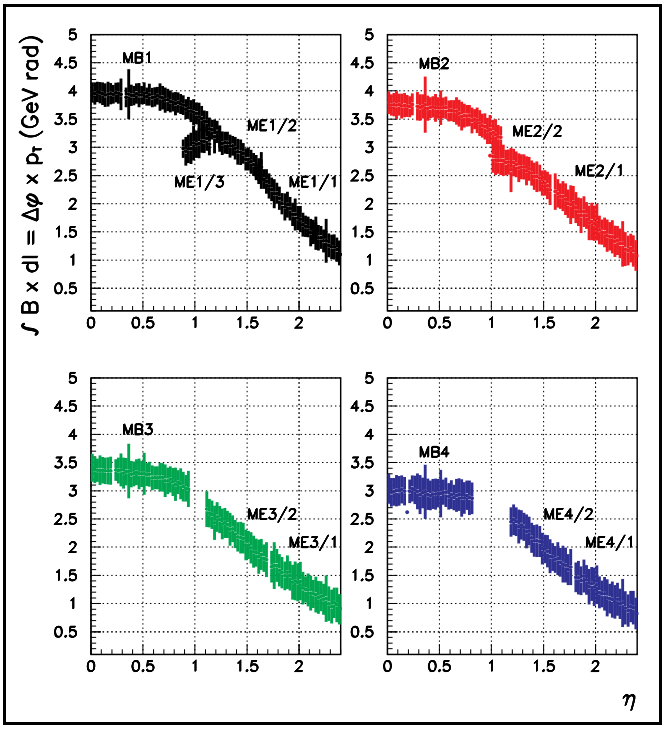


Fig. 2.1.4: Field integrals in the regions of the muon stations.

Analysis shows that the most critical regions for generation of background are the CMS beam pipe and the forward region (very forward calorimeter (HF) and beam collimator and shielding). Sources of background for the muon system can be roughly localized as follows:

- Particles created in primary pp-interactions at the intersection point. These particles have a significant high energy component and represent the main contribution to the punchthrough. The total number of interaction lengths in the barrel and endcap calorimeters through which these particles pass before reaching the muon chambers, as well as the presence of holes and cable passages, are very important for evaluating this background.
- Back-splash from the face of the HF. These background particles have a moderate energy spectrum (in the MeV to GeV range) and mainly affect the part of the muon endcap system lowest in radius. A re-design of the HF employing copper material has led to a reduction in back-splash into the muon stations.
- Particles leaking from the HF and back-splash from the low-beta quadrupole magnet (LBQ) region. These particles also have a moderate energy spectrum, and along with the "gas" of neutrons created by hadrons oozing through shielding into the experimental hall, mainly affect the outer-most chambers such as ME4/2.
- Muons and other particles created from beam losses in the accelerator tunnel. These particles have a rather wide energy spectrum and have the potential to affect all chambers.

Beginning with the TP design [2.1,2.2], various shielding configurations have been tested and the detector geometry has been updated as it has progressed [2.3]. A summary of the expected flux levels in the baseline CMS geometry (Fig. 2.1.1) is presented as a cumulative sum of the respective fluxes due to prompt and decay muons, charged hadrons, and electrons and positrons (Fig. 2.2.1). The plots represent statistics of 2000 "neutron" events and ~200K "punchthrough" events processed with CMSIM. The first two plots give fluxes in terms of Hz/cm^2 versus pseudorapidity. The background rate is quite low in the barrel, being everywhere less than 10 Hz/cm^2. In the endcap, the highest fluxes are in the region of maximum η and approach 1 kHz/cm^2 in the innermost part of ME1/1.

The bottom plot shows the charged particle fluxes in Hz per strip for different types of chambers in the forward region, where background is naturally of greatest concern. The right scale in this plot represents estimates of strip occupancies in percent. These occupancies have been obtained with the assumption that one hit occupies on average 5 strips during 8 x 50 ns time bins (400 ns), where 50 ns is the sampling interval of the SCA (see Section 4.3). The strip occupancies range from a few tenths of a percent in ME1/2 and ME1/3 to almost 4% in ME4/1.

2.3 MOMENTUM MEASUREMENT

There are many factors that limit the ability of the muon system to measure accurately the momentum of a traversing muon:

- Multiple scattering in the calorimeters and in the thick steel plates separating the muon stations;
- The intrinsic resolution of the detectors;
- Energy loss, especially when it is "catastrophic;"
- Extra detector hits generated by muon radiation, δ-rays, and other backgrounds;
- Chamber misalignment;
- Uncertainty of the B field.

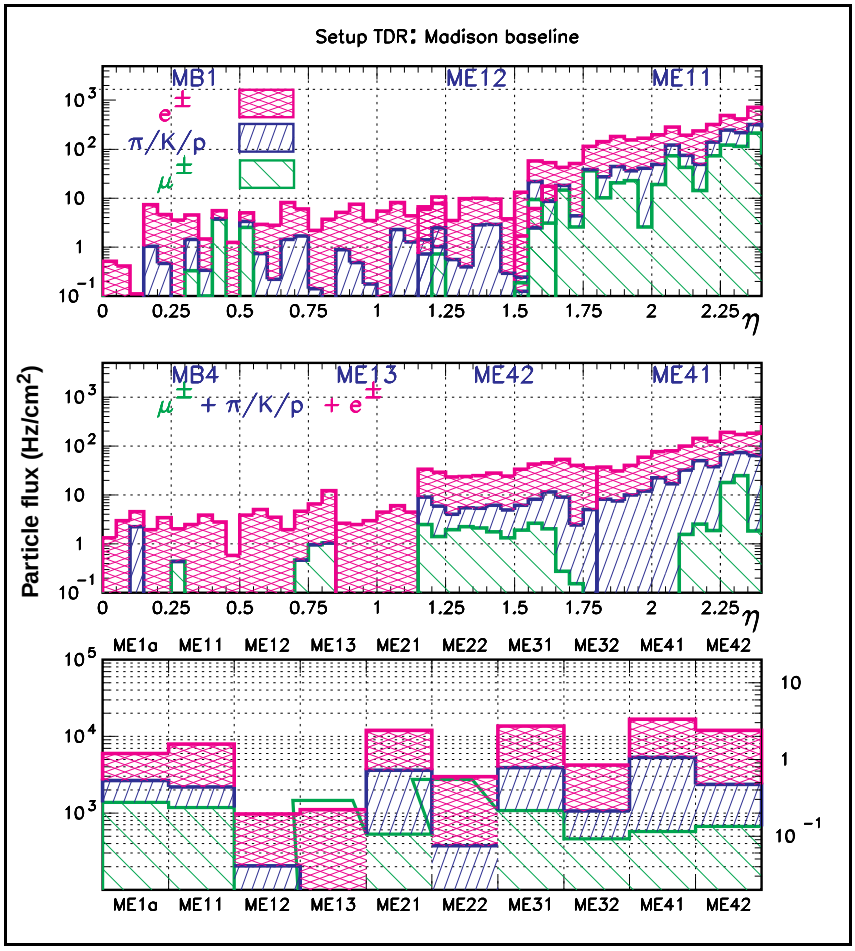


Fig. 2.2.1: Charged particle fluxes in the muon system as a cumulative sum from different sources (prompt and decay muons, hadronic punchthrough, $e^{\pm}$ from neutrons). Top: Fluxes (Hz/cm^2) in the first chamber traversed at a particular h; Middle: Fluxes in the last muon chamber traversed; Bottom: Flux per strip (Hz/strip) and estimated occupancies (%) determined from the fluxes for each type of endcap muon detector. (Occupancies assume 5 affected strips/hit each occupied for 400 ns.) The separate split strip portions of ME1/1 are designated ME1a (inner) and ME11 (outer).

The contributions of many of these effects to the muon momentum resolution measurement have been studied using CMSIM. The muon track reconstruction methodology is described in the Appendix.

2.3.1 Muon momentum resolution

Momentum resolution from the track fit is expressed as $\Delta p_T/p_T$, the percent error in p_T. The fit procedure maintains a covariance matrix of track parameter errors from which this resolution can be estimated. The covariance matrix method always assumes gaussian distributed errors. However, the true error distributions are not likely to be gaussian. Large angle multiple scattering and energy loss in material, for example, are inherently non-gaussian and contribute a tail to an otherwise gaussian error distribution. There is also the possibility of catastrophic muon energy loss (i.e., from hard photon Bremsstrahlung), which can skew the momentum measurement toward lower p_T. These effects are not fully described by the gaussian error

model. A more appropriate error estimate uses the $1/p_T$ residual from the distribution of measured momenta. The residual is defined as

$$\frac{\Delta p_T}{p_T} = \frac{(1/p_T^{meas} - 1/p_T^{gen})}{1/p_T^{gen}}$$

For muons generated at a single transverse momentum, the width of this distribution gives the residual error estimate. The non-gaussian tails should be apparent in the residual distribution, possibly yielding a poorer - yet more realistic - resolution than would the idealized errors in the covariance matrix.

The momentum resolution for muons over the entire CMS η range has been determined for both the muon stand-alone measurement with vertex constraint (Fig. 2.3.1) and the muon system plus tracker (Fig. 2.3.2).

For tracks up to 100 GeV p_T, the resolution is fairly constant in η up to η = 1.5. Tracks in this region have traversed the entire radius of the solenoid, experiencing the full bending power, $\int \mathbf{B}\cdot\mathbf{dl}$, of the magnetic field. Due to multiple scattering and electronic noise, there would be little improvement in the momentum resolutions even if the chamber resolutions were better. For η ≥ 1.5 the tracks exit the end of the solenoid before the entire radius has been reached. There is weaker bending of these tracks, leading to an degradation in the resolution for higher values of η.

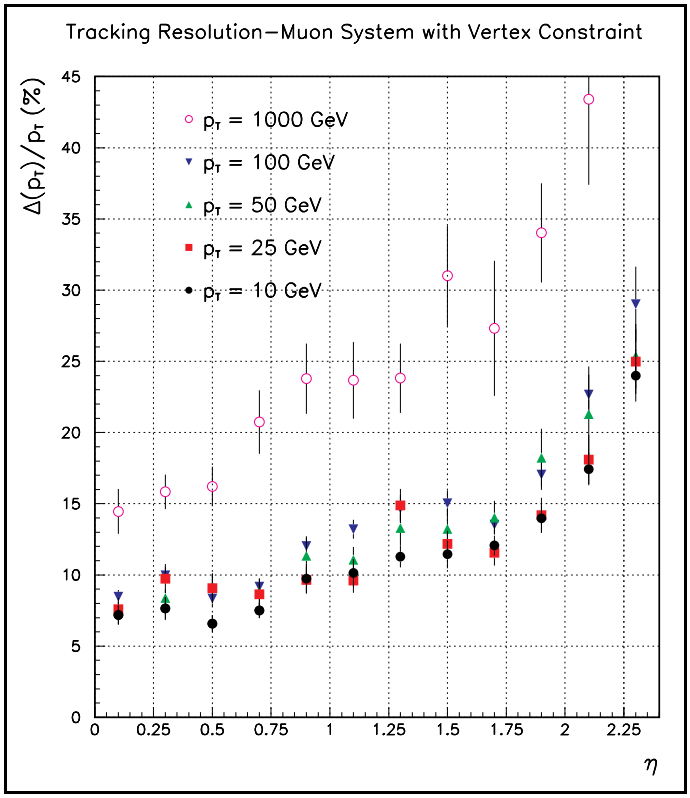


Fig. 2.3.1: Momentum resolution for simulated muon tracks at selected values of transverse momentum using only hits from the muon system with a vertex constraint. Full digitization of the detector response was performed for the endcap chambers.

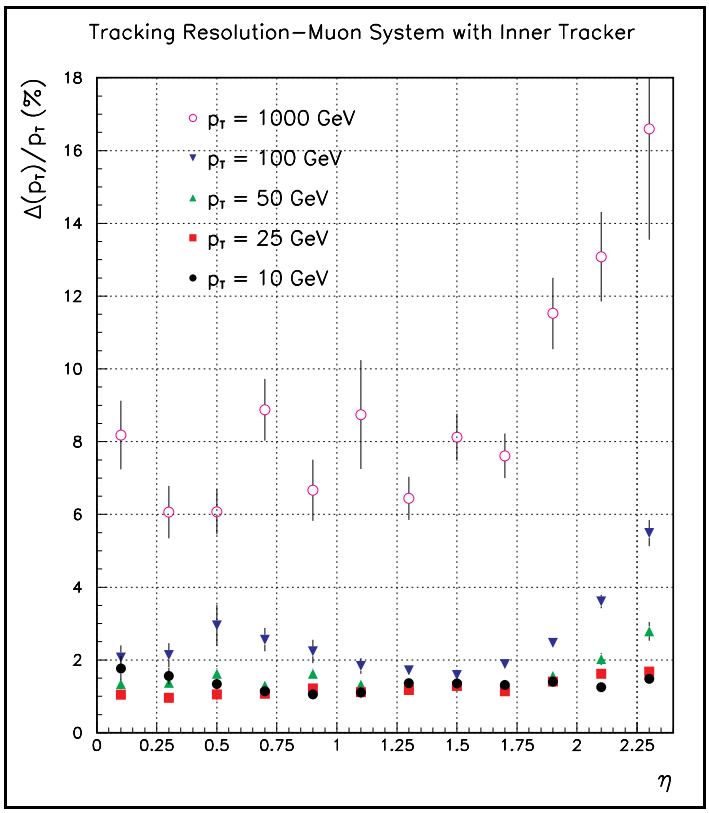


Fig. 2.3.2: Momentum resolution for muon tracks at selected transverse momenta using hits from the muon system combined with hits from the central tracker.

Although the muon system is optimized for measurement of 100 GeV p_T muons, physics demands good measurement over a broad range of p_T. At a lower p_T, a track's curvature in the magnetic field is greater, which should lead to a better estimate of the momentum. However, the mean multiple scattering angle is inversely proportional to momentum, meaning that the deflection of the trajectory as it passes through the absorber becomes larger with smaller p_T. When this error dominates, the momentum error is said to be multiple scattering limited. Muon tracks down to 10 GeV p_T are used to explore this limit.

As track momentum increases above the constant multiple scattering limit, the error becomes measurement limited, increasing linearly with p_T. The momentum resolution as a function of η for 1 TeV muon tracks takes into account all energy losses and includes additional hits from secondary electromagnetic radiation. For the muon stand-alone fit, the error has now risen above the multiple scattering limit and the resolution is significantly worse than for the 10 through 100 GeV p_T range.

Although at high momentum the relative error from multiple scattering is less, the likelihood that a muon loses energy through the production of secondary radiation is increased. This secondary radiation produces additional chamber hits, creating background in the vicinity of the muon hits. These background hits may be incorporated into the reconstructed track, leading to ambiguities. Also, tracks which lose a large amount of energy in this manner will appear to have smaller momenta at a later stage along their trajectories, leading to larger track parameter errors than expected from the position measurement errors and multiple scattering

alone. Fig. 2.3.3 shows the residual distribution for 1 TeV muons reconstructed using the vertex constrained muon stand-alone fit.

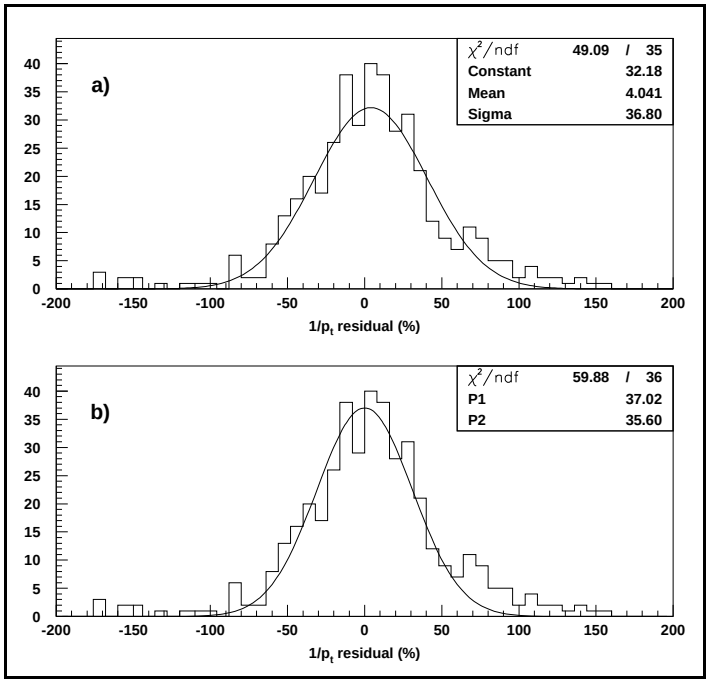


Fig. 2.3.3: $1/p_T$ residual distributions for 1 TeV muons using the muon stand-alone fit with a vertex constraint where a) the distribution is fitted by an unconstrained gaussian, and b) the distribution is fitted with a gaussian constrained to have a mean of zero. The excess of events on the high side of the constrained fit shows that catastrophic energy loss leads to an underestimation of a track's p_T, which is safer when determining its charge.

The top distribution shows the $1/p_T$ residual fitted with an unconstrained gaussian. The mean from this fit is greater than zero, meaning that a larger number of tracks have $1/p_T$ measured higher than their true value. To see this effect more clearly, the lower distribution shows the same residual re-fitted with a gaussian constrained to have zero mean. The excess of events on the high side of the distribution shows the effects of energy loss, especially when it is due to hard photon bremsstrahlung, which makes tracks appear to have smaller momenta (higher $1/p_T$). (Simulation of this effect relies fully on experimental measurements obtained with the RD5 experiment.) This is important when considering the error in the charge assignment. Misassigned charge occurs when a track's curvature, which is proportional to $1/p_T$, is measured lower than its true curvature; so low, in fact, that it crosses zero and acquires the opposite sign. Even though the absolute error on the momentum is larger, it usually appears on the high side of the $1/p_T$ residual, decreasing the danger of charge misassignment. The estimation of the errors is provided by the fit itself through the full covariance matrix of the five fit parameters of the helix in space. Such estimation is performed accurately by the fit procedure and it has been tested by analyzing the distributions of the normalized pulls.

2.3.2 Track charge discrimination

Many physics measurements, such as the $Z' \rightarrow \mu^+\mu^-$ forward-backward asymmetry, depend not only on identifying a track as a muon, but also on whether a particular muon track is

positively or negatively charged. In addition to the accurate measurement of its momentum, it is also important that a high p_T track has the correct charge assignment.

The percentage of tracks with misassigned charge as a function of a track's p_T (Fig. 2.3.4), was determined for comparison purposes for both the muon stand-alone fit with vertex constraint and for the combined muon system and inner tracker fit. Using only the muon system measurements with a vertex constraint, the percentage of misassigned charge is less than 1% for tracks with p_T less than 500 GeV, rising to 4% for 1 TeV tracks. For values of p_T near the 100 GeV optimization point and lower, the muon system alone provides good charge determination. When the inner tracker points are included, no tracks with p_T less than 100 GeV have an incorrect charge assignment due to the additional curvature measurement inside the full magnetic field. The percentage of misassigned charge for 100 GeV p_T is less than 0.1% and remains less than 0.5% up to 1 TeV. The combined fit, therefore, gives good charge discrimination for tracks, even at high p_T.

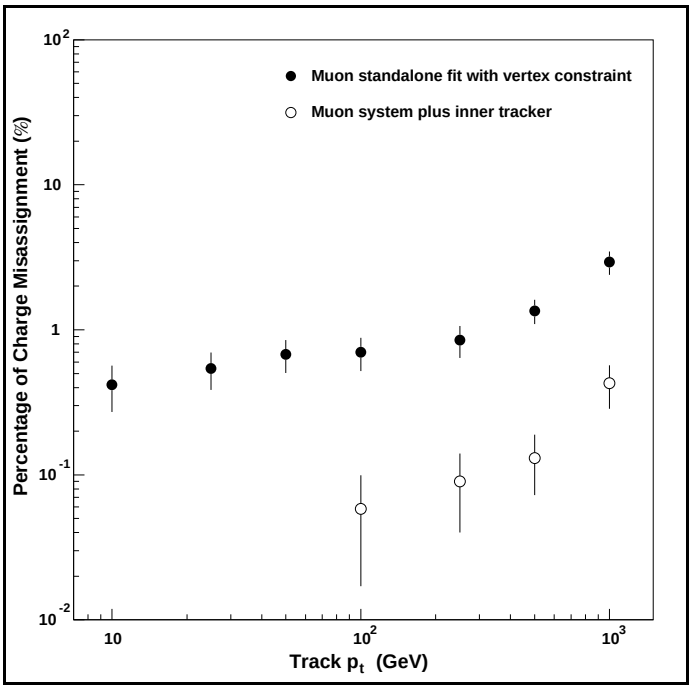


Fig. 2.3.4: Percentage of incorrect charge assignments versus track p_T using both the vertex constrained muon stand-alone track fit and the combined muon system and inner tracker fit. For the combined fit, no misassigned charge is seen for tracks with p_T lower than 100 GeV.

2.3.3 Momentum dependence of the muon track resolution

At low p_T the transverse momentum resolution is determined by the constant multiple scattering error. At sufficiently high p_T, the measurement error, which rises linearly with p_T, begins to dominate, degrading the momentum resolution with increasing p_T. Since p_T is the physical quantity measured, the resolution has been presented at constant p_T or as a function of p_T. However, many physics studies use kinematic quantities, such as invariant mass measurements, that depend upon the total momentum p rather than the transverse momentum. To provide compatible physics measurements in all regions of the chamber it is desirable to have a uniform response for a given total momentum.

Fig. 2.3.5 shows the dependence of the resolution on the total momentum for tracks in the barrel (η=0.5) and in the endcap (η=2.0). Interestingly, when plotted as a function of total momentum, the resolutions for the barrel and for the endcap are very similar for momenta greater than 50 GeV. This suggests that the momentum resolution scales with the total momentum relatively independent of the η value and a simple parameterization is possible. For momenta above 70 GeV, $4\%\sqrt{(p/TeV)}$ provides a good description of the momentum resolution for all η values. This function can be extended below 70 GeV for the barrel measurement, but in the endcap it is limited by multiple scattering in the forward tracker and the endcap measurements assume a constant value of 1.2%.

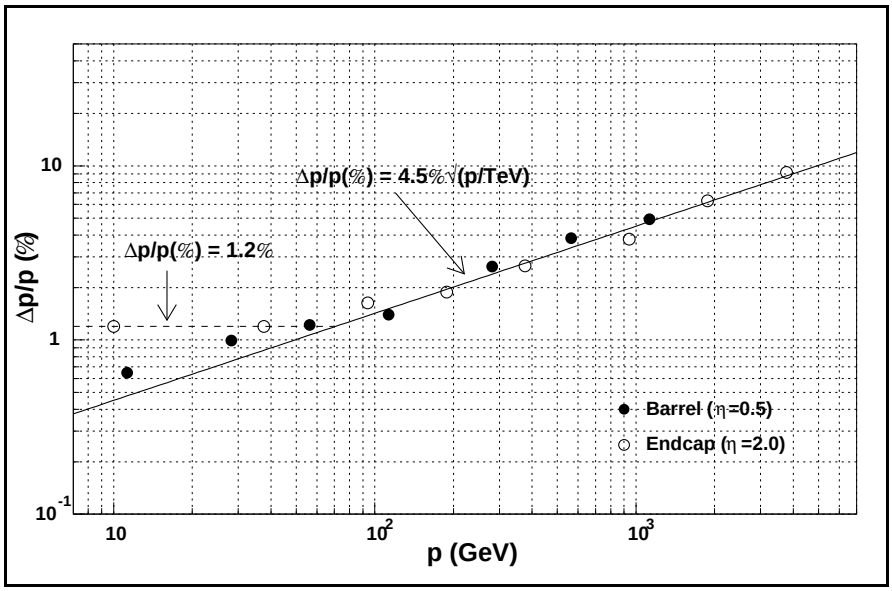


Fig. 2.3.5: Momentum resolution versus total momentum for tracks in the endcap and the barrel reconstructed with the combined muon system and inner tracker fit. Both barrel and endcap can be described by the same function for momenta greater than 70 GeV.

2.3.4 Muon reconstruction efficiency

Using the full track reconstruction techniques described in the Appendix, the ability to find and fit muons with radiation and energy loss was examined. The efficiency of track finding and fitting of the Kalman Filter method as installed in CMSIM was obtained for simulated muon tracks at several values of p_T. Muons were generated uniformly in η and ϕ accompanied by all expected secondary processes including delta-electrons and electromagnetic showers. In the endcap CSCs, hits experienced full digitization including electronic noise at a level to yield an approximate signal/noise ratio of 100 in all chambers, the minimum S/N ratio specified for the CSCs (see Sec 4.4.2.1). In the barrel DTBX chambers, the reconstructed hit position was computed, assuming constant drift velocity, from the measured drift time obtained by a parameterization of the drift cell behavior (see Sec. 3.9.11). The left-right ambiguity with respect to the anode wire was then properly included.

Track segments were formed from hits in individual chambers, with at least two segments required to form a track. It is possible for a track to be associated with more than four segments because of the overlap regions of the muon chambers. (Such tracks passing through chamber

overlap regions leaving two segments in a muon station may be used for inter-chamber alignment.) Efficiencies for finding generated muon tracks in the barrel with 2, 3, or ≥4 segments, respectively, are shown in Table 2.3.1 [2.4].

Table 2.3.1

Efficiencies in the barrel region ($0 \leq |\eta| < 0.8$) for track fitting in the stand-alone muon system with the vertex constraint for several values of p_T by the number of track segments successfully used.

	Track losses (%)		Successful track fits in barrel (%)				Resolution
p_T (GeV)	Fewer than 2 segments	Failure of fit	Number of track segments 2	3	≥4	Total	$\Delta p_T/p_T$ (%)
1000	6.2%	20.4%	27.6%	32.5%	13.3%	73.4%	18.6%
500	3.8%	12.8%	29.4%	34.2%	19.8%	83.4%	15.2%
300	3.2%	7.2%	28.5%	38.6%	22.7%	89.9%	12.3%
100	1.5%	1.1%	31.0%	39.5%	26.9%	97.4%	9.3%
10	5.0%	11.6%	33.4%	32.6%	17.4%	83.4%	8.9%

There are two categories of losses: propagated tracks for which fewer than the necessary two segments could be reconstructed in the muon stations, and those for which a successful fit could not be formed in spite of the reconstruction of two or more track segments. The former category combines geometrical acceptance and track segments lost due to muon radiation and energy loss disturbing the hits. (This loss is greater for higher p_T muons as the probability for catastrophic muon radiation increases.) The latter reflects the performance of the present track fitting algorithm; thus there is the possibility that some of these losses could in fact be recovered. The p_T resolutions are the averages over the given regions for all successful fits.

The momentum resolutions of the stand-alone barrel muon system (averages in Table 2.3.1) are slightly dependent on the number of track segments used in the fit. As an example, Fig. 2.3.6 shows the fitted $1/p_T$ distributions for the three different fit topologies at $p_T = 100$ GeV in the barrel, together with the reconstruction efficiency as a function of η.

The respective percentages of the original simulated muon tracks for which tracks were successfully fitted to points in the muon system with the vertex constraint by the Kalman filter utilizing 2, 3, 4 or more than 4 segments are shown in Table 2.3.2 averaged over the endcap region [2.5].

It is worthwhile to stress that the difficult "overlap" region ($0.8 < |\eta| \leq 1.2$) is still under study with further development of the reconstruction code underway to recover difficult topologies, such as cases in which only one super-layer in a barrel station delivers an r-ϕ measurement with no measurement in r-z.

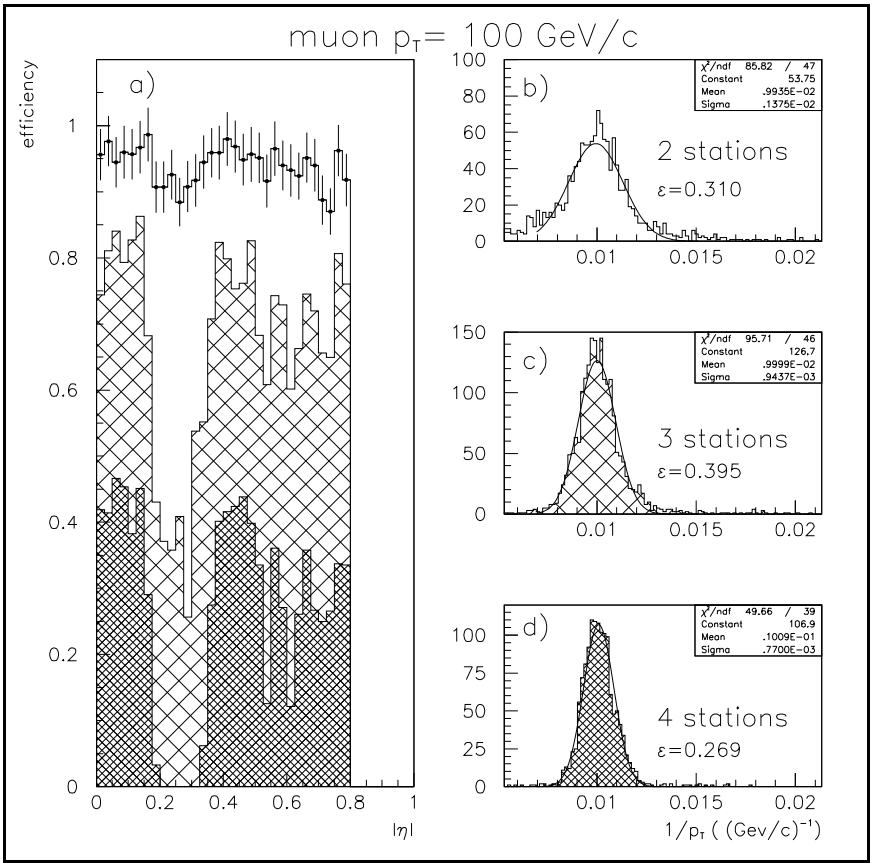


Fig. 2.3.6: a) Muon barrel system efficiency to reconstruct a muon track candidate with a successful fit, constrained to the primary interaction region (σ_{xy} = 15 μm in the plane transverse to the beam orbit), as a function of the generated muon η (dots). The efficiencies to have 2 (white area), 3 (wide cross-hatched) or ≥4 (small cross-hatched) track segments in the fit are also shown. b-d) Fit results for the $1/p_T$ track parameter in the cases of 2, 3 or ≥4 segments contributing to the momentum measurement.

Table 2.3.2

Efficiencies in the endcap region ($1.2 < |\eta| \leq 2.4$) for track finding and fitting in the stand-alone muon system with the vertex constraint (σ_{xy} = 25 μm and σ_z = 5.3 cm) by the number of track segments successfully used. The total efficiencies include the acceptance of the muon stations. Resolutions (for p_T in %) are for the average of all successful fits.

	Track losses (%)		Successful endcap track fits (%)					Resolution
p_T (GeV)	Fewer than 2 segments	Failure of fit	Number of track segments 2	3	4	>4	Total	$\Delta p_T/p_T$ (%)
1000	15.4%	13.4%	35.3%	21.9%	11.4%	2.7%	71.2%	37.9%
100	2.8%	4.3%	19.7%	27.3%	34.9%	11.0%	92.9%	19.4%
10	0.8%	1.6%	12.3%	25.4%	43.3%	16.6%	97.6%	15.2%

2.3.5 Matching of muon tracks with the inner tracker

We have shown the advantage of using both the muon chambers and the inner tracker as a combined system in achieving the best momentum resolution. This requires that track segments in the muon system be matched to the correct track segment in the inner tracker in the presence of several accompanying tracks.

Tracks were reconstructed via a Kalman filter using a tracking model with five parameters at each reference surface: momentum, precise and coarse spatial coordinates, and precise and coarse tangent angles (see Appendix). Tracks in the muon system were filtered, smoothed and propagated to the inner tracker where additional hit points were included for the combined fit. These tracks may be used to investigate track-matching ability. A comparison of the extrapolated muon track parameters to the inner tracker candidates provides the matching criteria: The momentum parameter provides the best match to low p_T tracks while the spatial coordinate gives the best match to the high p_T candidates.

The muon's extrapolated spatial coordinate determines the position and the extrapolated covariance matrix determines the range of allowed positions that are accepted in the matching. To accomplish this, a single muon is reconstructed using only the muon system measurements including a vertex constraint. The track parameters from this muon stand-alone fit and their errors are propagated to the outer measurement planes of the inner tracker. This extrapolation takes the full magnetic field and multiple scattering into account. The extrapolation of the covariance matrix requires the derivatives of the transport matrix and is accomplished using a Runge-Kutta numerical approximation. The error matrix projected onto the inner tracker planes has both precise and coarse spatial coordinate elements that form error ellipses on the extrapolated inner tracker measurement surface. The sizes of the error ellipses are shown in Fig. 2.3.7 for barrel and endcap muons and for transverse momentum in the range $10\ \mathrm{GeV} \le p_T \le 1\ \mathrm{TeV}$. At $p_T = 10$ GeV, multiple scattering dominates the errors and the precise spatial coordinate error is not significantly better than the coarse error. As the muon p_T increases, the effect of multiple scattering becomes smaller and the error ellipses are reduced accordingly.

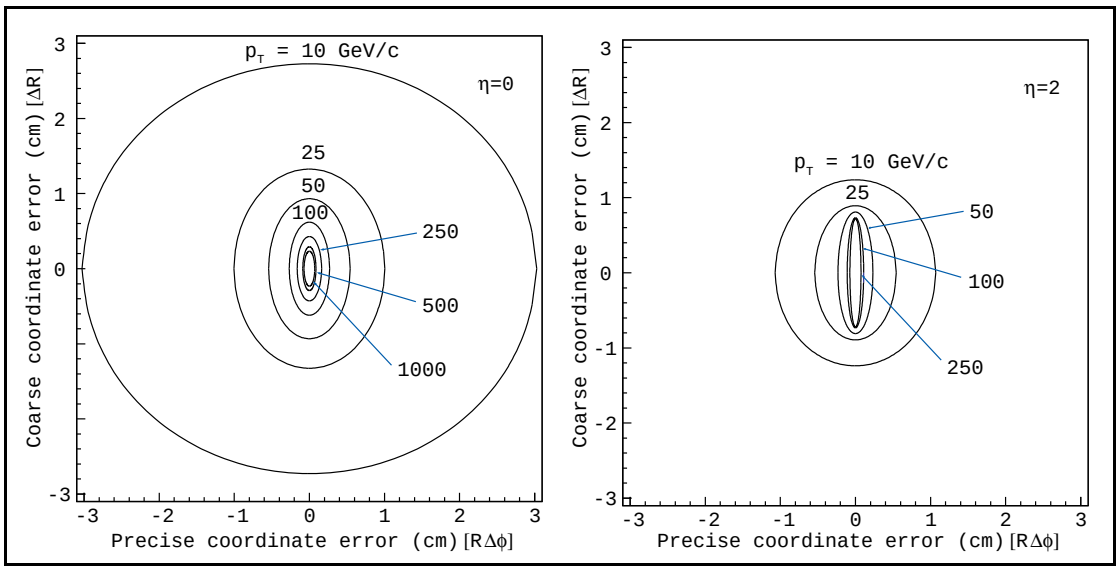


Fig. 2.3.7: Extrapolated position error ellipse for muons at η=0 and η=2.

Tracks that match in space may still have different momenta. The accuracy of spatial matching for high p_T tracks with less curvature and multiple scattering is greater than for tracks with low p_T. The opposite occurs, however, with the momentum matching. The momentum of low p_T tracks, with greater curvature, is measured more accurately than for straighter high p_T tracks. The low p_T tracks are matched best in terms of the momentum parameter.

2.4 TRIGGER PERFORMANCE

The CMS 2nd Level Trigger is designed to receive an event rate up to 100 kHz. The 1st Level is assumed to deliver not more than 30 kHz in order to ensure a safety margin. This bandwidth must be divided among muon, calorimeter and combined triggers. Rates of calorimeter triggers, i.e. one or two electrons or photons; electron from a b-quark decay; 1, 2, 3 or 4 jets; electron/photon + jet; missing transverse energy E_t^{miss} and total transverse energy ΣE_t, have been shown to sum up to 15 kHz [2.6]. Below we discuss the muon triggers (1μ, 2μ) and combined muon/calorimeter triggers, namely μ-e/γ, μ-jet, μ-E_t^{miss}, and μ-ΣE_t.

Combined muon-calorimetric triggers have a great importance for many processes to be studied at the LHC. The presence of a highly energetic muon gives a very good event signature mainly due to the significant improvement in the signal/noise ratio. In the case of the CMS detector, for many processes it is sufficient to use a muon trigger alone; but there are processes where only the combined muon-calorimetric signature makes their study feasible. There are also several processes for which the combined signature is expected to improve the efficiency significantly since the muon requirement should allow the lowering of calorimeter threshold values – extending in this way the physics potential.

In the case of two-object triggers, at low luminosity we can afford the lowest possible muon p_t cut, which is determined by the muon energy loss in the calorimeters and thus varies with η. In the barrel it is ~4 GeV. In the endcaps it decreases to ~2 GeV at $|\eta|=2.4$. More precisely, one can define the thresholds as

$$p_T > 4.0 \text{ GeV} \quad \text{for} \quad |\eta| < 1.5$$

$$p_T > 2.5 \text{ GeV} \quad \text{for} \quad 1.5 < |\eta| < 1.9$$

$$p_T > 2.0 \text{ GeV} \quad \text{for} \quad 1.9 < |\eta| < 2.4.$$

At high luminosity it is convenient to set the muon threshold for two-object triggers at 4 GeV over the entire η range.

Results of the simulation are given in Table 2.4.1. In the columns headed “Individual” are listed the rates for particular trigger types. Under “Cumulative” is the total trigger rate for a logical OR of the given trigger type with all the types listed above it. We have chosen the thresholds to keep the total trigger rate at 30 kHz.

2.5 PERFORMANCE FOR REPRESENTATIVE PHYSICS PROCESSES

The performance of the muon system for representative physics processes has been studied, covering muon p_T range from a few GeV to a few TeV. Muon acceptance, matching

with the inner tracker, charge determination and multiple-muon mass resolution are important in all these processes.

Table 2.4.1
Expected trigger rates for selected cuts.

	$L = 10^{33}\ cm^{-2}s^{-1}$				$L = 10^{34}\ cm^{-2}s^{-1}$			
Trigger type	Threshold (GeV)		Rate (kHz)		Threshold (GeV)		Rate (kHz)	
	Muon	Calo	Individual	Cumulative	Muon	Calo	Individual	Cumulative
μ	7		7.0	7.0	20		7.8	7.8
$\mu\mu$	2-4		0.5	7.3	4		1.6	9.2
μ-e	2-4	7	2.4	9.2	4	8	5.5	14.4
μ-e_b	2-4	4	5.2	12.8				
μ-j	2-4	10	4.2	14.4	4	40	0.3	14.4
μ-E_t^{miss}	2-4	40	0.2	14.4	4	60	1.0	15.3
μ-ΣE_t	2-4	100	0.7	14.4	4	250	0.2	15.3

2.5.1 SM and MSSM Higgs bosons

The Standard Model Higgs decay to four muons is a benchmark process for evaluating the performance of the muon system. The Standard Model Higgs measurement is studied with Pythia with LO cross sections dominated by the gluon fusion production mechanism $gg \rightarrow H^0$, followed in importance by the vector boson fusion process. The background includes LO cross sections of di-boson production with both quark-anti-quark scattering and the gluon-gluon box diagram as well as $t\bar{t}$, $Z^0b\bar{b}$ contributions. The reconstructed mass distribution for a 150 GeV Standard Model H^0 decay is shown in Fig. 2.5.1 for an integrated luminosity of 10^{-5} pb^{-1}, including all expected backgrounds ($t\bar{t}$, $Z^0b\bar{b}$, ZZ^*, etc.) as well as effects of internal bremsstralung. The four-muon mass resolution is 0.96 GeV. Further details regarding the expected performance of CMS in $H^0 \rightarrow ZZ^* \rightarrow 4l^{\pm}$ searches may be found in Ref. [2.7]. For the SM Higgs with $m_H \geq 230$ GeV the natural width overtakes the instrumental resolution. Nonetheless, the muon system, thanks to its acceptance and the robustness of muon measurements at high luminosity, is of central importance for Higgs detection throughout the expected mass range, with $H^0 \rightarrow ZZ \rightarrow 4\ \mu^{\pm}$, $H^0 \rightarrow ZZ \rightarrow \mu^+\mu^-\nu\nu$ and $H^0 \rightarrow WW \rightarrow \mu\nu jj$ channels, as well as in mixed electron and muon e^+e^- channels, e.g. $H^0 \rightarrow ZZ \rightarrow \mu^+\mu^-\ e^+e^-$.

The excellent multiple lepton mass resolution is essential in the search for MSSM Higgs bosons. These are narrow objects ($\Gamma \leq 1.5$ GeV) which can be searched in the channel $h^0(H^0,A^0) \rightarrow ZZ^* \rightarrow 4l^{\pm}$ at low tanβ (tan$\beta \leq 2$) up to $m_H \approx 2m_{top}$. Searches may also be made for $h^0(H^0,A^0) \rightarrow \mu^+\mu^-$ modes to which CMS is sensitive at high tanβ (tan$\beta \geq 10$)[2.8].

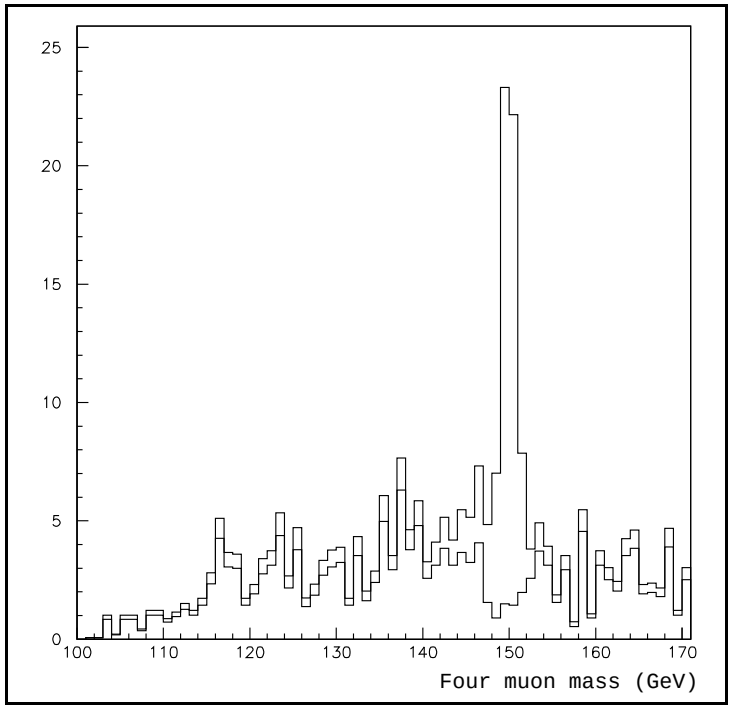


Fig. 2.5.1: Reconstructed mass distribution with background of H^0 (150 GeV) $\rightarrow$ ZZ*, ZZ* $\rightarrow \mu^+\mu^-\mu^+\mu^-$ for L = 10^{-5} pb^{-1}.

2.5.2 $Z' \rightarrow \mu^+\mu^-$

A common feature of many extensions of the Standard Model is the existence of additional vector gauge bosons. Grand unified theories (GUTs), Left-Right symmetric models and superstring theories all extend the Standard Model through additional gauge symmetries. The observation of an additional neutral gauge boson *Z′* depends upon the *Z′* mass and its coupling to the observed final state muons. The accuracy with which the track parameters of muons are measured must be sufficient for good S/B and to reconstruct the kinematics of the original *Z′* interaction. Choosing among models requires the study of other event characteristics, in particular the forward-backward asymmetry. The asymmetry measurement depends upon accurate reconstruction of the momentum and production angles, and the correct charge assignment, in particular at large rapidities i.e. in the endcaps.

2.5.2.1 Z′ Invariant Mass

The sharpness of the measured invariant mass peak depends on the width of the *Z′* and on the muon momentum resolution. A large $M_{Z'}$ produces final state muons with higher transverse momenta, which have large measurement errors, contributing to the spread in the invariant mass. To obtain the measured *Z′* mass and width, the background subtracted *Z′* distribution is fitted to a gaussian - the mean providing the measured *Z′* mass and the sigma providing the width. Fig. 2.5.2 shows an example fitted for a 3 TeV *Z′* generated according to the Alternative Left-Right model.

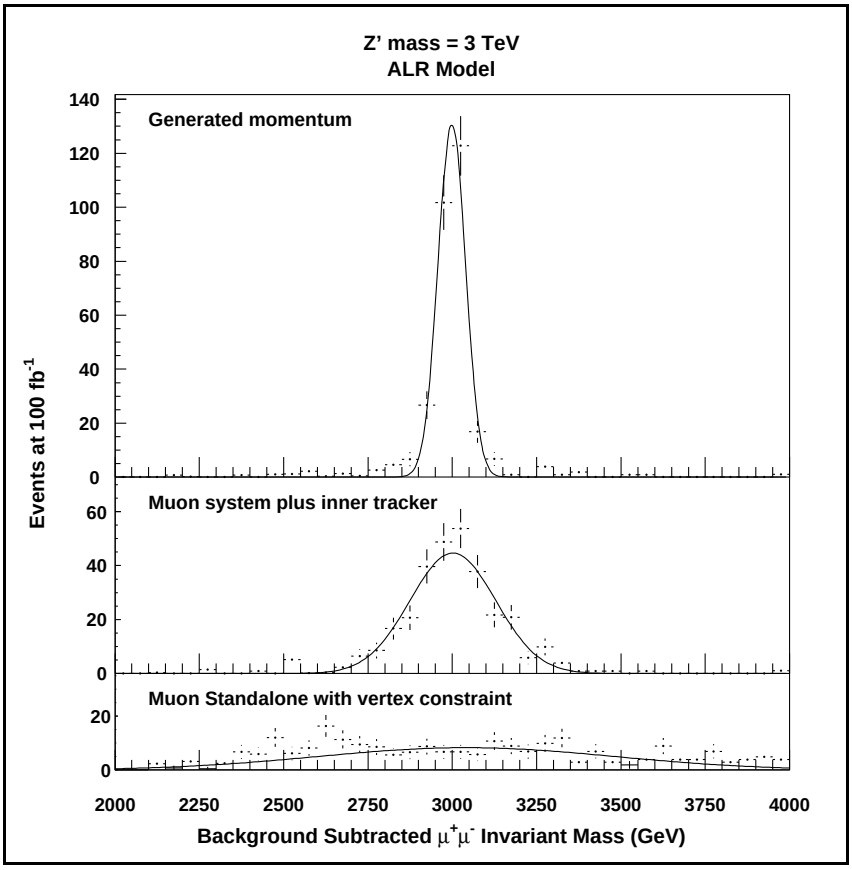


Fig. 2.5.2: Background subtracted invariant mass distributions for a 3 TeV Z' produced via the Alternative Left-Right model. The parameters of the gaussian fit are used as the measured Z' mass and width.

2.5.2.2 Forward backward asymmetry of the Z'

The presence of a resonance peak in the di-muon invariant mass distribution is enough to verify the existence of an additional *Z'* boson. The total number of events in this peak could be used to select among possible candidate models on the basis of expected theoretical cross sections. The true nature of the Standard Model extension may still remain undetermined, however, since several of the theoretical models have similar crossections. To discriminate further among the models, the forward-backward asymmetry can be used.

The asymmetry is calculated in the center of mass of the final state muons. Muons are first boosted to the center of mass of the *Z'*, then the angle between the boosted μ^- and the Z' direction is used as the scattering angle θ^*. In addition, the events are classified into rapidity, regions. When the *Z'* is heavier, the lower cross section will introduce a larger statistical error into the asymmetry measurement. Also, the poorer momentum resolution for the higher p_T final state muons adds an additional error. Fig. 2.5.3 shows the measured asymmetry points from a 3 TeV *Z'* generated with Alternative Left-Right model couplings superimposed on five theoretical asymmetry curves. When the more precise momentum from the combined muon system and inner tracker fit it used, the measured asymmetry eliminates three possible candidate models (see Ref. [2.10]).

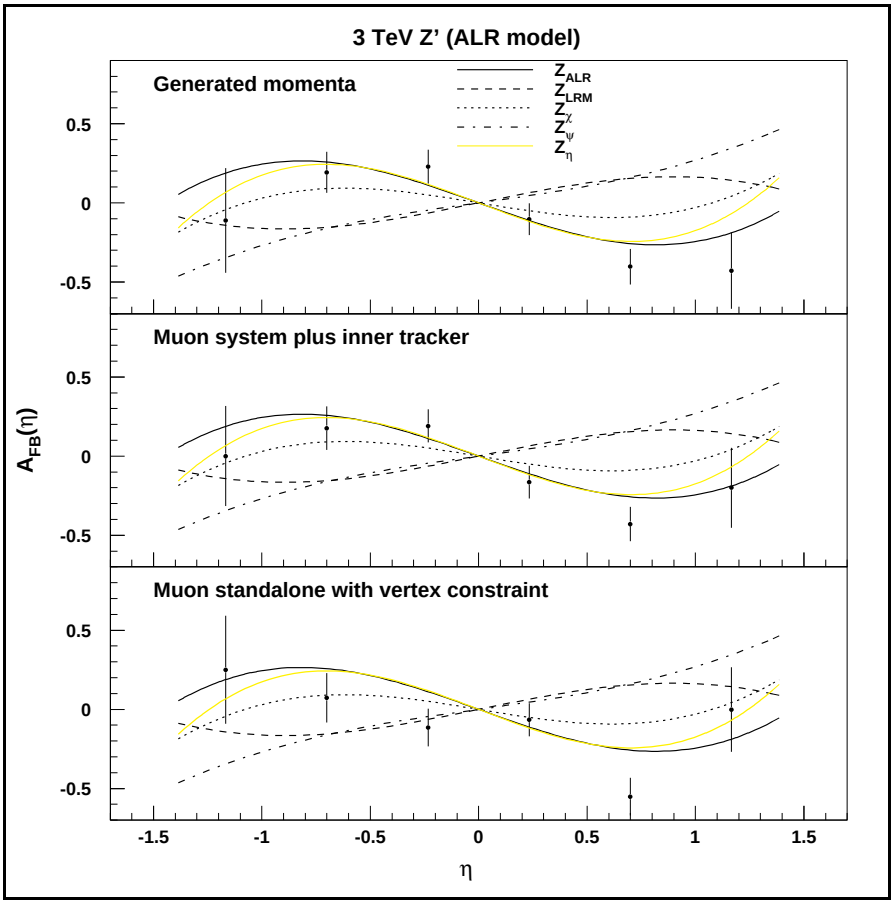


Fig. 2.5.3: Measured forward-backward asymmetry from a 3 TeV Z' generated according to the ALR model, plotted versus the η of the boosted center of mass. The theoretical asymmetry curves for all five models are superimposed for comparison.

2.5.3 Top production and decay

The efficiency to identify prompt muons from semi-leptonic top decays was studied by generating a sample of 1000 $t\bar{t}$ events (with the top quarks forced to the muonic decay $t \rightarrow b\mu\nu$) using the Pythia 5.7 generator and propagating all the generated particles through the full CMS detector simulation. Fig. 2.5.4 shows such an event, in which also one of the b quarks decayed semi-leptonically in the barrel muon detector. The muon candidates resulting from the muon system stand-alone fit described in Sec. 2.3.1 were extrapolated back to the outer surface of the inner tracker and matched to the tracker candidates according to the criteria used in Sec. 2.3.5. Backgrounds from electronic noise and event pile-up were not included, nor was any effect from muon chamber misalignment. The study was performed in the region $-0.8 < \eta < 0.8$. Fig. 2.5.5 shows the generated and reconstructed (by the standalone muon system) muon momentum spectra, together with the efficiency to have successfully matched muon candidates.

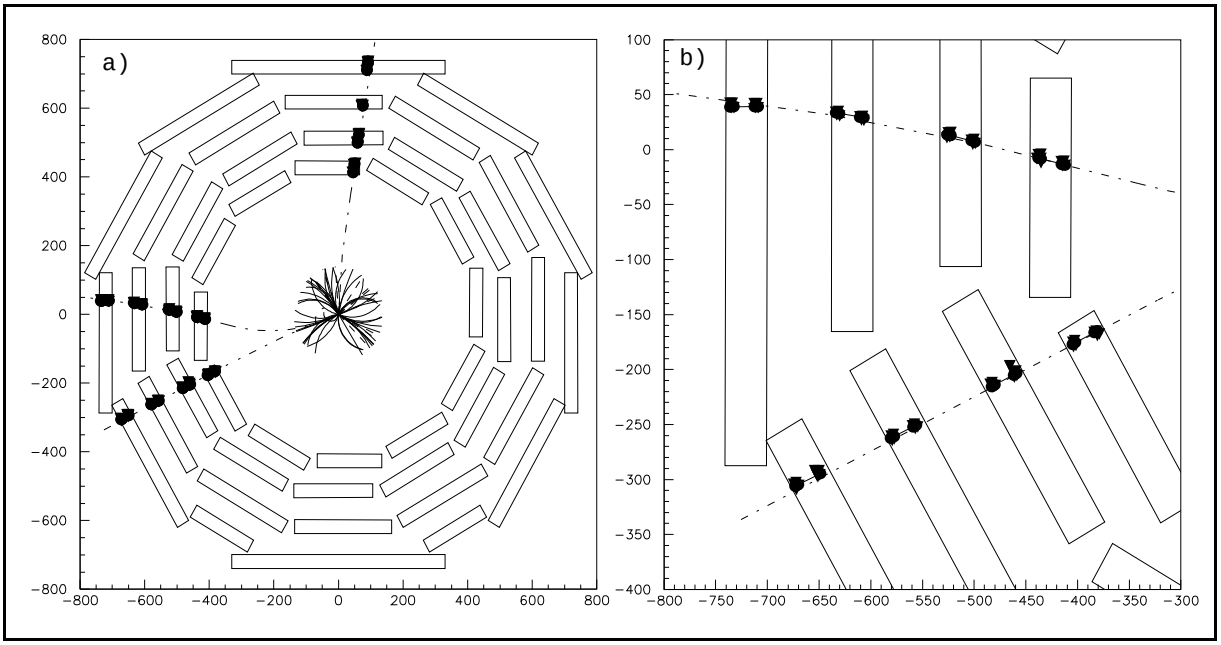


Fig. 2.5.4: a) Side view of a $t\bar{t}$ event generated by Pythia, with both top quarks forced to decay semi-leptonically. Dashed-dotted lines show the extrapolated track from the muon system to the inner tracker. b) Enlarged view: full line segments show track elements in the barrel muon chambers; dots show hits in the chamber super-layers associated with the track candidate.

2.5.4 Muons in b-jets

An important way to identify a b-jet is by using muons in the jet and applying isolation or secondary-vertex criteria. To study the feasibility of matching muon tracks in the presence of multiple inner tracker candidates, Pythia 5.7 was used to generate b-jets at p_T values of 100, 500 and 1000 GeV with 400 events each. B-hadrons were forced to decay into muons, resulting in events with a single muon track surrounded by multiple stable mesons, all of which are propagated by the simulation through the full CMS geometry, including all radiation and energy loss processes. Backgrounds from electronic noise, neutrons and event pile-up are not included, nor are any chamber miscalibration and misalignment errors.

The track parameters from the muon stand-alone fit with the vertex constraint are extrapolated to the outer measurement planes of the inner tracker. The hit coordinates in these outer planes of each track candidate in the inner tracker are compared to the extrapolated muon hit position. The track candidate with hit position closest to the extrapolated muon position is kept as a possible matching track. Including the p_T of the track in the matching criteria further reduces the number of fake candidates. Both the precise coordinate and p_T are used simultaneously in the χ^2 fit and the inner tracker candidate with the smallest χ^2 is accepted as a possible match, where

$$\chi^2 = \frac{(r\phi^{muon} - r\phi^{tracker})^2}{\sigma^2_{r\phi}} + \frac{(1/p_T^{muon} - 1/p_T^{tracker})^2}{\sigma^2_{1/p_T}}.$$

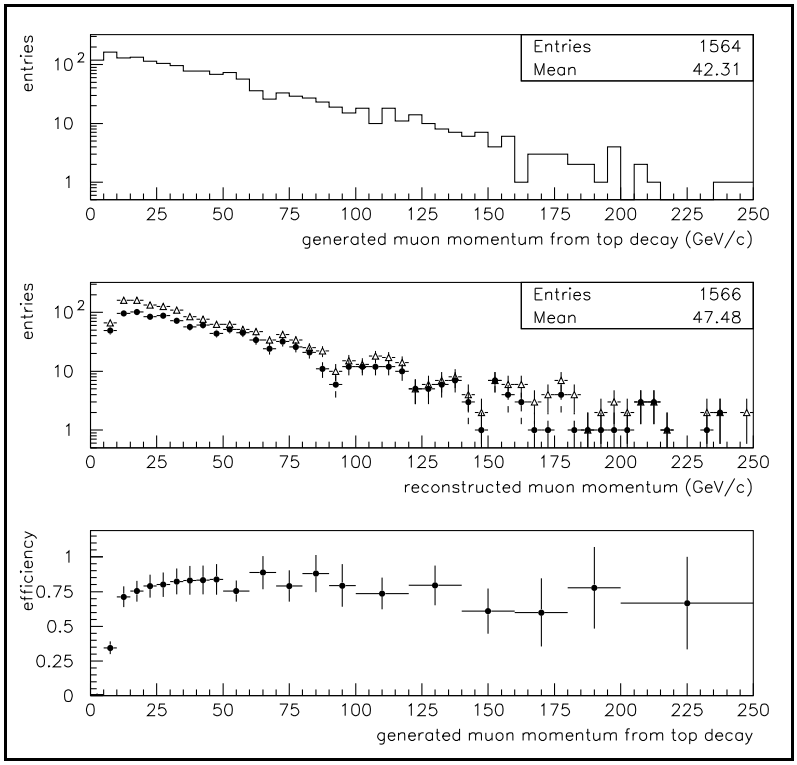


Fig. 2.5.5: a) Generated momentum spectrum of the muons originating by semileptonic top decay; b) fitted momentum of reconstructed muons (triangles) and of muons successfully matched (dots) to the inner tracker candidate coming from the generated muon; c) efficiency for muon reconstruction and matching as a function of the generated muon momentum. misalignment.

The distribution of $1/p_T$ residuals as a function of p_T is shown in Fig. 2.5.6 for inner tracker candidates that have been previously matched using the precise spatial coordinate alone. The residuals for muon tracks show a broadening at low p_T since multiple scattering limits the covariance matrix in this regime giving a larger extrapolation error. Fortunately the spatial matching has already filtered out all the fakes in that region. The combination of both the precise coordinate and the track p_T gives an even greater reduction in the percentage of matched muon fakes: at η=2 only 0.45% of the muon system tracks are matched to fake inner tracker candidates when both p_T and the extrapolated precise coordinate are used.

In practice, several track parameters are used simultaneously in muon matching. Table 2.3.2 shows muon track matching purities when combinations of the track parameters are used in the matching criteria. Except at the highest η, the purity for correctly matched muons is higher than 98% when both the track p_T and the precise hit coordinate are used to select matched inner tracker candidates. At η=2.4 this purity is 96% since the p_T resolution is poorer and the b-jets more collimated, leading to a difficult precise coordinate match.

2.5.5 Υ Production in heavy ion collisions

Although CMS is optimized for the study of p-p collisions, it is proposed to take advantage of the large acceptance and excellent mass resolution of the muon system and central tracker to detect cc and bb resonant states from heavy ion beams through their muon decay channel. With not only the J/ψ and ψ' but also the Υ family resonances accessible to

observation, it is of great interest to look for their possible suppression as is foreseen to be one of the measurable effects if the quark-gluon plasma is formed.

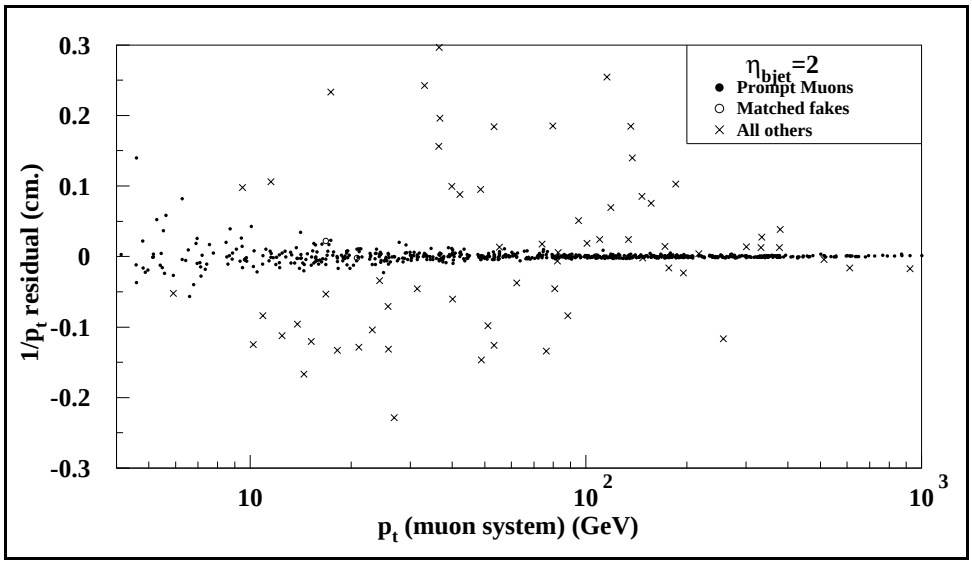


Fig. 2.5.6: Residual of the inverse p_T for the track and the muon momentum as a function of p_T. Only candidates that were previously passed the precise coordinate spatial matching are shown.

Table 2.3.2
Purities of matched muon tracks from b-jets.

ηb-jet	0.9	1.0	1.2	1.4	1.6	1.8	2.0	2.2	2.4
Matching Criteria	*Purity of matched muons (%)*								
pT	94.3	94.3	92.3	89.7	92.5	92.7	90.5	88.9	81.3
precise coordinate	75.5	75.6	75.2	68.1	80.9	84.9	82.9	81.9	79.8
coarse coordinate	52.5	49.7	49.0	32.0	39.4	47.1	39.7	47.8	37.7
pT + precise	99.2	98.9	98.2	97.7	98.7	99.1	99.4	99.3	96.0
pT + coarse	98.0	98.4	96.6	93.4	97.1	96.8	94.4	94.0	97.7
precise + coarse	92.2	90.6	90.4	84.2	90.8	92.7	90.8	90.0	86.0
pT + precise + coarse	99.5	99.7	99.4	98.3	99.3	99.6	99.7	100.	97.1

For the estimate of the detection efficiency of $\Upsilon \rightarrow \mu^+\mu^-$ (Fig. 2.5.7), 2000 generated particles were forced to decay into muons using the Pythia Monte Carlo program processed through the complete CMSIM simulation and reconstruction apparatus. The Υ particles were generated based on a quark-gluon plasma model for $b\bar{b} \rightarrow \Upsilon$ production in pp collisions [2.9]. Trigger efficiency was simulated by requiring that for both muons at least two muon stations each register at least 8 hits in the barrel or 4 hits in the endcap.

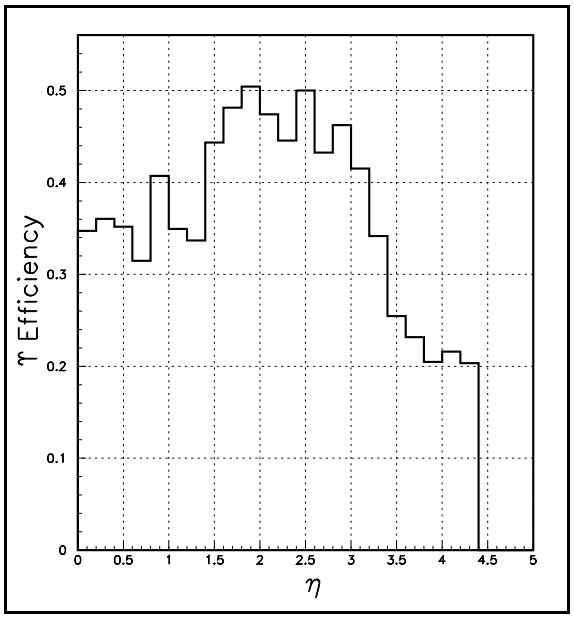


Fig. 2.5.7: Efficiency of reconstructing an $\Upsilon \rightarrow \mu^+\mu^-$ in the CMS detector by η of the generated Υ. Both muons must traverse at least two muon stations and create at least 8 hits in each barrel station or 4 hits in each endcap station.

After generation, Υ particles were forced to decay into $\mu^+\mu^-$ and each muon momentum was smeared based on the fast CMS simulation program [2.11]. The top portion of Fig. 2.5.8 indicates the Υ mass resolution obtained by using only information from the muon system alone. The bottom plot illustrates the improvement in mass resolution obtained when the central tracker information is folded into the mass determination. Besides Υ acceptance and mass resolution, another important issue is the main background of secondary particles, mainly pions and kaons, copiously produced in the collisions . For the discussion of expected signal to background ratios see Ref. [2.12].

2.6 SUMMARY OF DETECTOR SIMULATION AND PERFORMANCE

The behavior of the muon detector has been extensively studied using the full CMS simulation (CMSIM) based on GEANT code, including detailed geometrical description of all the parts of the apparatus and complete simulation of the digitization process. Emphasis was made on the study of background conditions (particularly severe in some regions of the forward chambers) and on the capability of the detectors to reconstruct and identify muons over a broad momentum range from a few GeV to the TeV region. The effect of multiple scattering and hard photon bremsstrahlung in the apparatus on momentum resolution and reconstruction efficiency was carefully studied. Extensive trigger simulation was performed to define the first level

trigger decision, showing that a momentum cut as low as 20 (4) GeV for single (double) muon candidates guarantees a tolerable first level trigger rate at the highest LHC luminosity.

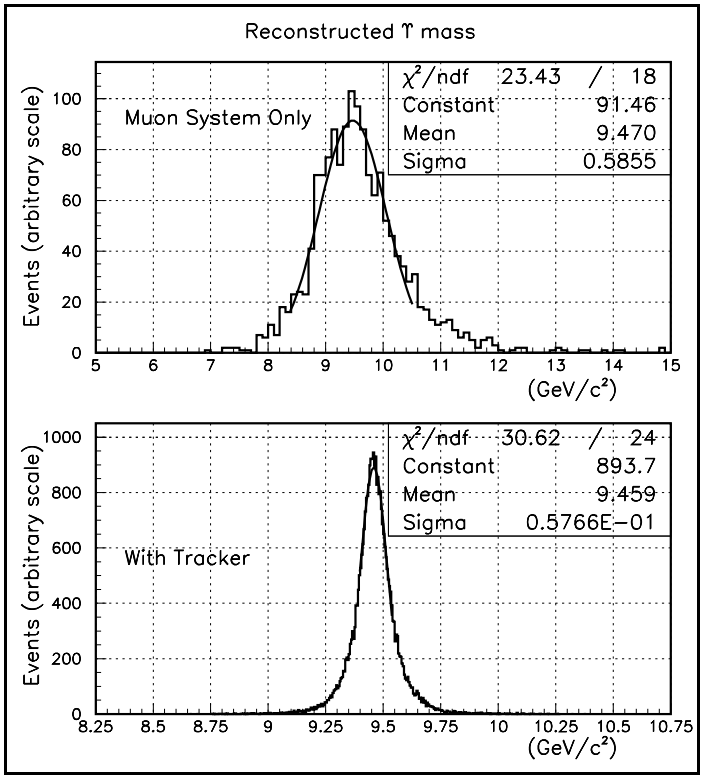


Fig. 2.5.8: The fast Monte Carlo simulation program was used to smear muons from the decay of the Y. Top: Y mass resolution using only muon system information. Bottom: Mass resolution with central tracker points included.

The stand-alone muon system was proven to be able to reconstruct muons for $|\eta| < 2$ with a momentum resolution of 6-20% below p_T = 100 GeV and 15-35% at p_T = 1 TeV, depending on the angular position. Global efficiency is more than 90% for track momenta below 100 GeV everywhere in the detector, and remains above 70% up to the highest momenta allowed by the kinematical range of the LHC. Muon charge identification is accomplished by the muon system alone with a probability of charge missasignment less than 1% below 500 GeV, rising to 4% at 1 TeV.

The matching of the reconstructed muon with inner tracker candidate tracks provides a correct association of the muon track produced in b-jets in more than 96% of the cases in the full η range covered by the muon detector. Samples of a few "benchmark" channels of physical interest were generated and followed through the complete simulation and reconstruction chain, showing a quite adequate performance of the overall system. It must be stressed that many of the results quoted here have to be considered conservative, since they were obtained with a reconstruction code not yet optimized, and that further developments in both pattern recognition of the stand-alone muon system and matching algorithms with the inner tracker are foreseen.

APPENDIX

CMSIM Structure and Track Reconstruction Methodology

A.1 CMSIM

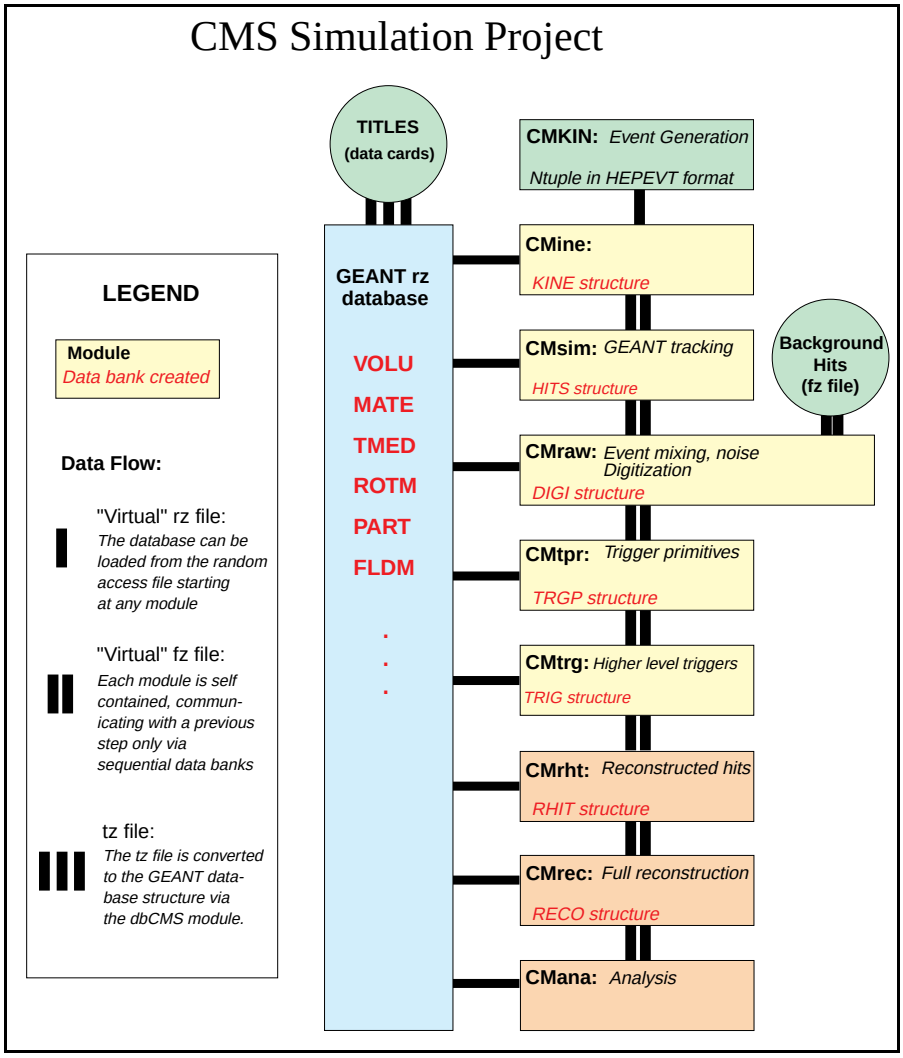


Fig. A.1.1: Flow diagram of CMSIM.

The CMS simulation and reconstruction package CMSIM is based upon the GEANT simulation framework. It includes the following major features (Fig. A.1.1):

- common database for simulation, reconstruction, calibration, analysis, and event-display;
- modular flow, so that sub-tasks may be performed independently by reading the output data structure of the previous task in the chain;
- background integrated into the simulation to produce “Raw Data” that resemble real data in every way;
- common reconstruction program for simulated and real data.

The flow in CMSIM can serve as the road map for our description of the details of simulation studies of the muon system performance.

A.2 Full track reconstruction

Track hit positions are determined in CMSIM for simulated data in the barrel and endcap muon chambers as described in their respective chapters. Track parameters are then obtained from a given collection of cluster hit positions in the tracking chambers by the Kalman Filter method. There are two aspects of this problem that must be addressed. First is track finding: It must be recognized which hit positions actually belong to a single track. High-energy muons will radiate electrons and photons as they pass through the absorber, leading to extraneous chamber hits close to the track position. Second is track fitting: The track parameters must be determined from the recognized hit positions.

The Kalman Filter accomplishes both of these tasks simultaneously. In the first stage, pattern recognition is performed locally on the hits of each chamber to construct "track segments." If at least two segments can be connected, track parameters are then calculated recursively at each measurement surface, with the parameter estimates updated along the way. Additional measurements from adjacent surfaces are incorporated into the candidate track if their positions fall within the extrapolation of the previous measurements. In this way the combinatorial background is considerably reduced.

The initial track parameters used to start the filter are estimated using hits in the measurement surfaces farthest from the interaction point. A vector of five true track parameters - the inverse transverse momentum $1/p_T$, the precise and coarse measurement positions x and y, and their two angles (dx/dz) and (dy/dz) - at measurement surface i is propagated to the surface $i+1$ transformed to "measurement space." This combines with the measurement at surface $i+1$ into a "least squares" expression, the minimum of which provides the best estimate of the track parameters there.

Once the track parameter extrapolation to surface $i+1$ is complete and its measurements have been incorporated into the fit, the new parameter estimate at $i+1$ can be propagated to the next measurement surface using the same scheme. In this manner, all measurements are recursively incorporated into the estimate of the track parameters.

After all possible measurement surfaces have been included into the track parameter estimate, a smoothing algorithm is used to incorporate the full information into each measurement and remove possible background hits. The final fit procedure gives estimates based on three different sets of hit position measurements. The first estimate includes only the set of positions measured by the muon system. This is called the *Muon stand-alone measurement*. The second includes the first with the addition of a constraint of the vertex point and is called the *Muon stand-alone with vertex constraint* fit. Finally, the third measurement adds all hit positions from the inner tracker for the combined *Muon system plus inner tracker* fit.

References

[2.1] "The Compact Muon Solenoid: Technical Proposal," CERN/LHCC 94-38, LHCC/P1, December 15, 1994.

[2.2] R. Breedon, Yu. Fisyak, "Muon system background simulation of the CMS TP-baseline design," CMS TN/96-035.

[2.3] Yu. Fisyak, "Evaluation of the CMS Muon Endcap Shielding," CMS TN/96-076. Additional results are in http://ucdcms.ucdavis.edu/~fisyak/cms/background.

[2.4] CMS Note in preparation.

[2.5] R. Breedon, Presentation at the CMS Collaboration Meeting, Sept. 15-19, 1997, Madison, Wis.

[2.6] S. Dasu, J. Lackey, W.H. Smith, W. Temple, "CMS Level 1 Calorimeter Trigger Performance on Technical Proposal Physics," CMS TN/95-183.

[2.7] I. Iashavili, R. Kinnunen, A. Nikitenko, D. Denegri, "Study of the $H \rightarrow ZZ^* \rightarrow 4l^{\pm}$ channel in CMS," CMS TN/95-059; D. Bomestar, "SM Higgs search at the LHC," CMS TN/95-156.

[2.8] R. Kinnunen, "Investigation of $H_{SUSY} \rightarrow ZZ,ZZ^* \rightarrow 4l^{\pm}$ in CMS," CMS TN/96-096;
R. Kinnunen, D. Denegri, "Expected SM/SUSY Higgs observability in CMS," CMS CN/97-057.

[2.9] R.V. Gavik, D. Kharzeev, H. Satz, G.A. Schuler, K. Sridhar, R. Vogt, Intl. J. Mod. Phys. A10 (1995) 3043; R. Vogt, "Y suppression in Pb+Pb collisions at the LHC?" CMS TN/96-041; J.F. Gunion, R. Vogt, Nucl. Phys. B492 (1997) 301.

[2.10] J. Rowe, "Muon measurement in high field solenoid detectors," Chap. 8, Ph.D. dissertation, Univ. of Calif., Davis (1996).

[2.11] J. Rowe, ibid., Sec. 7.3.3.

[2.12] M. Bedjidian, "($b\bar{b}$) and ($c\bar{c}$) resonances in Pb-Pb collisions at CMS," CMS CR/97-008; R. Kvatadze, "Heavy ion physics at LHC with CMS detector," CMS CR/97-015.

3. THE BARREL MUON DETECTOR

3.1 GENERAL DESCRIPTION

The CMS barrel muon detector is made of four stations forming concentric cylinders around the beam line: three of them consist of 60 drift chambers each, the fourth, the most outer, of 70. The total number of sensitive wires is about 195,000.

The choice of a drift chamber as the tracking detector for the barrel muon system was possible due to the low expected rate and the relatively low intensity of the local magnetic field.

The principal wire length, around 2.5 m, is constrained by the longitudinal segmentation of the iron barrel yoke. The transverse dimension of the drift cell, i.e. the maximum path and time of drift was chosen to be 2 cm or 350-400 ns, depending on the gas mixture. This value is small enough to produce a negligible occupancy and avoid the need for multihit electronics, and large enough to limit the number of active channels to an affordable value. The final dimension will probably be fixed by matching the number of wires per plane to the multiplicity of readout channels in the electronics boards. The choice of a tube as the basic drift unit was made in order to obtain protection against the damage from a broken wire and to partially decouple contiguous cells from the electromagnetic debris accompanying the muon itself.

The amount of iron in the return yoke is dictated by the basic choice of having a large and intense solenoidal magnetic field at the core of CMS. Two stations are not enough for a reliable identification and measurement of a muon at the LHC. Therefore, further stations are embedded within the yoke: with reference to Fig. 3.1.1 the twelve sides of the yoke define twelve thin pockets physically separated by the yoke's iron ribs. The ribs result in twelve unavoidable dead zones in the Φ coverage of each station. Their effect is partially mitigated by avoiding the overlap in Φ of the iron ribs.

The tubes of each pocket are assembled into a rigid body, named hereafter a drift tube chamber. In this scenario, there still exist limited regions of η in which the combined effect of the Φ and Z discontinuities limits to only two, out of four, the number of stations crossed by a muon.

At momenta larger than 40 GeV, the probability of electromagnetic cascades accompanying the parent muon becomes relevant (see table chapter 2). The only safe way to cope with this effect in the regions where only two stations are available is to have a good tracking efficiency in each station even in the presence of electromagnetic debris. Redundancy is also needed to cope with uncorrelated hit background generated by neutrons and gammas whose rate is from 10 to 100 times larger than the one from prompt muons.

Redundancy of information is obtained by having several layers of separated drift cells per station: the separation, i.e. the thickness of the tube walls, should be large enough to decouple the basic units against low energy electrons. The relatively thick wall for the drift tubes, 2 mm, gives an effective decoupling among the several layers of tubes inside the same station. With this design, the efficiency to reconstruct a high p_T muon track with a momentum measurement delivered by the barrel muon system alone is better than 95% in the rapidity range covered by 4 stations, i.e. $|\eta|<0.8$ (see chap. 2 and references quoted therein for details).

The constraints of the mechanical stability, the limited available space and the requirement of redundancy pushed us toward a tube cross section of 13 by 40 mm^2 pitch. Many layers of

"heavy" tubes require a robust and light mechanical frame to avoid significant deformations due to gravity in the chambers, especially in those which lie in a nearly horizontal plane.

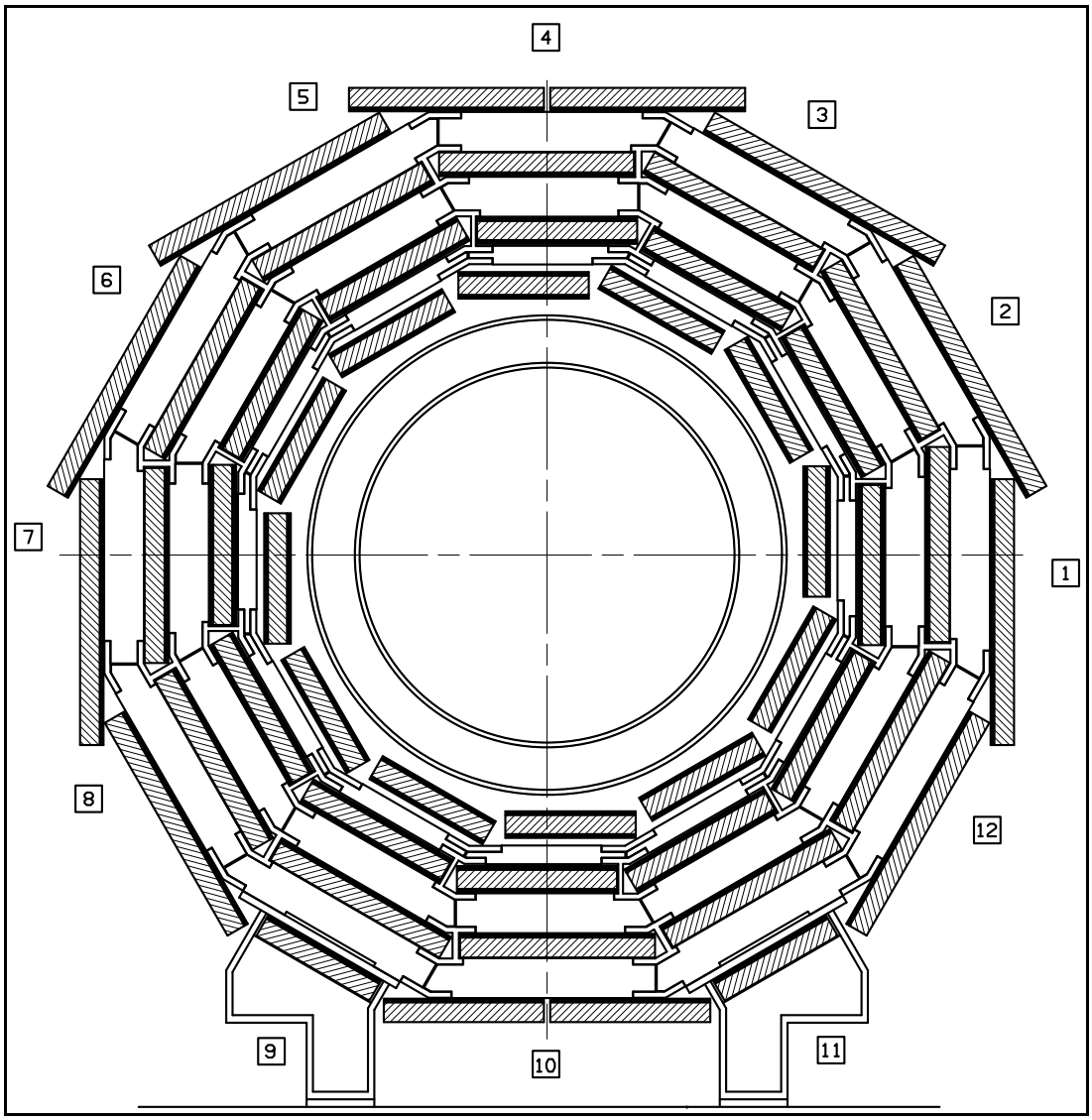


Fig. 3.1.1: Layout of the CMS barrel muon DT chambers in one of the 5 wheels; in all of them the chambers are identical with the exceptions of wheels -1 and +1 where the presence of the cryogenic chimneys shortens the chambers in two sectors; note that in sectors 4 and 10 the MB4 chambers are cut in half in order not to have wires longer than 4 meters. Also shown, not to scale, as bold lines are the RPC chambers, 2 layers for the MB1 and MB2 chambers and 1 layer for MB3 and MB4.

In order to create a solid and light frame, an aluminum honeycomb plate, 128 mm thick, separates the sensitive layers of the two groups. The two groups are glued to the outer faces of the honeycomb. In this design, the honeycomb plays the role of a very light, ideally massless, spacer, the rigidity being given by the outer planes of tubes. A thick spacer also has the advantage of providing good angular resolution within a station.

A group of four consecutive layers of thin tubes, staggered by half a tube, provides excellent time-tagging capability. A time resolution of a few nanoseconds was obtained in a test beam using common signal processing techniques based on meantimer circuits.

In the case of the LHC, this capability provides local, standalone and efficient bunch-crossing identification. The time tagging is delayed by a constant amount of time equal to the maximum possible drift-time which is determined by the size of the tube and by the gas mixture. The time resolution was shown, within the angular range of interest, to be largely independent of the track angle, but this requires the cell optics to maintain a linear relationship between the distance from the wire of the crossing track and the drift-time of the electrons, along the entire drift path.

The tracking and timing performance of a chamber was optimized with a design using twelve layers of drift tubes divided into three groups of four consecutive layers, hereafter named Super Layers (SL). Inside each SL, the tubes are staggered by half a tube. Two SLs measure the (R,Φ) coordinate, i.e. have wires parallel to the beam line, and the third measures Z, the coordinate running parallel to the beam line. A muon coming from the interaction point encounters a Φ SL first, passes through the honeycomb plate, then crosses the Z SL and the second Φ SL. The bunch-crossing tagging is performed independently in each of the three SLs by fast pattern-recognition circuitry. This circuit delivers, together with the bunch-crossing assignment, the position of the center of gravity of the track segment and its angle in the SL reference system. The precision is 1.5 mm and 20 mrad, respectively. This information is used by the first-level muon trigger for the time and transverse momentum assignment. It is shown later that the SL is, from all points of view, the smallest independent unit of the design. The mechanical precision in the construction of a chamber is dictated by the CMS requirement of achieving a global track resolution of 100 μm without any local correction to the primary information.

The mechanical precision of the construction of a chamber is dictated by the aim to achieve the global resolution in (R,Φ) of 100 μm. This figure makes the MB1 chamber precision comparable to the multiple scattering contribution up to p_t= 200 GeV. At higher momenta, where the global fit of muon and tracker information gives the best performance, the muon detector contribution to the error is of the same order as the one from the tracker.

The 100 μm target chamber resolution may be achieved by the 8 track points measured in the two (R,Φ) SL, if the single wire resolution is better than 250 μm.

In order to avoid corrections to the primary TDC data, the deviation from linearity of the space-time relation in each drift cell must be less than 100-150 μm. This figure coincides well with the requirements of linearity from the Bunch-Crossing identifier. The wire pitch tolerance inside one layer and the misalignment between layers in the same Super Layers has to stay within 100 μm. Misalignment between Super Layers of the same chamber should be less than 500 μm and be measured, during assembly, with 100 μm resolution.

The proposed cell design makes use of five electrodes to shape a homogeneous drift field: the wire, the two I-beams enclosing a tube and, in addition, the two central electrode strips. With this arrangement the requirement of 250 μm resolution and 150 μm nonlinearity can be obtained by operating the tubes at atmospheric pressure with Ar/CO_2 gas mixture and keeping the CO_2 concentration in the range from 10 to 20%. The multi-electrode design also ensures this performance in the presence of the stray magnetic field present in some regions of the chambers. It is worth noting that, in order to reach this performance of a single tube the precision requirement on the position of the field-shaping electrodes, including the wires, is about 300 μm, i.e. considerably less demanding than the 100 μm on the mechanical construction.

For the construction of the SLs, which are, by themselves, fully independent detectors, a full layer of cells is built at the same time by gluing together two aluminum plates separated by an array of parallel aluminum I-beams. The pitch of the I-beams determines the larger dimension of the cell, their height the smaller. Five aluminum plates, 2 mm thick, and four I-Beams arrays are glued together to make a Super Layer.

The SL has an independent gas and electronics enclosure; each SL is assembled and tested individually before being glued to the honeycomb plate and/or to the other SL to form a chamber.

The space for the chamber supports and attachments, the passages for alignment and the local readout and trigger electronics is provided by a channel running around the border of the honeycomb plate. The channel is approximately as wide and deep as the honeycomb plate thickness, that is about 13 cm. The two channels parallel to the beam line and to the iron ribs house the kinematic fixations to the ribs themselves, and the longitudinal alignment passages. We are studying the possibility of using one of the two remaining sides for the readout and trigger electronics collecting the information of the full chamber and the other for the high voltage and test pulse distribution.

Each of the five wheels of the barrel iron yoke contains 50 chambers. All the general services of these chambers, like high and low voltage supplies, slow controls, terminal and collecting boards of readout and trigger, the higher stages of the CMS trigger and DAQ, the cooling and gas distribution, etc. are located around the wheel on 4 balconies on which space for racks and crates is foreseen. This makes each wheel an independent, large subsystem.

Table 3.1.1 gives the inventory of the barrel muon DT system. As shown in Fig. 3.1.1 all MB1, MB2 and MB3 chambers are identical for all sectors while the MB4 chambers are different from sector to sector. Furthermore, in wheels -1 and +1 the presence of cryogenic chimneys forces, in two sectors, the shortening of the corresponding MB1 to MB4 chambers. The numbering of the sectors refers to Fig. 3.1.1.

3.2 TECHNICAL DESIGN

3.2.1 Drift cell design

The baseline cell design, shown in Fig. 3.2.1, has a pitch of 40 mm by 13 mm. At the center is the anode wire, made out of 50 μm diameter stainless steel type 304L. The cathodes defining the cell width are aluminum I-beams 1.2 mm thick and 9.6 mm high. A plastic profile, made of 0.5 mm thick extruded polycarbonate plastic (Lexan), is glued to the upper and lower parts of the I-beams in order to electrically insulate the cathodes from the aluminum plates.

These plates, which are kept at ground potential, form the two remaining sides of the cell. All the prototypes built so far have cells with these dimensions. The final design might show small changes to obtain the best geometrical coverage. With this geometry, the drift field is formed by putting the wires at positive voltage and the cathode at negative.

Table 3.1.1
Barrel Muon System - Inventory of the Drift Tubes Chambers.

		Dimensions					**# of channels**		
Station	Sector	X (mm)	Y (mm)	Z (mm)	Area (m2)	Weight (kg)	F	Z	Total
MB1	all	1990	290	2536	5.05	780	376	244	608
MB2	all	2450	290	2536	6.22	970	472	244	704
MB3	all	3030	290	2536	7.68	1190	584	244	816
MB4	1,2,3,5,6,7	4190	290	2536	10.63	1650	816	244	1014
“	8,12	3880	290	2536	9.84	1530	760	244	1048
“	9,11	1990	290	2536	5.05	780	376	244	992
“	4 (*)	5350	290	2536	13.57	2100	1048	244	608
“	10(*)	5966	290	2536	15.13	2350	1176	244	1408
TOTAL (1 wheel)					350		26576	11712	38288
Grand Total					1750		132880	58560	191440

(*) The MB4 chambers in sectors 4 and 10 are split in two.

A pair of positively-biased strips is placed at the center of the cell and has the effect of “squeezing” the drift lines, improving, as will be shown in later sections, the linearity of the space-time relationship and the resolution of the cell. These electrodes are custom-made strips of 0.1 mm thick and 20 mm wide mylar tape on which a 14 mm wide and 70 μm thick copper strip is glued. The 3 mm of mylar on each side of the copper strip prevents sparking from the copper to the Al plates. The mylar strip is made self-adhesive with an acrylic glue so the bonding of the strip to the aluminum plate can withstand years of safe operation in a zero-humidity environment. The electric field obtained with this geometry and with the HV settings: V_{wire}= +3600 V, $V_{cath.}$= -1800 V and V_{strip}= +1800 V is shown in Fig. 3.2.1.

The wire length varies, from the smallest to the largest chamber, from about 2 m to 4 m; no intermediate wire support is used. The wires are pulled at a tension equal to 70% of the rupture value corresponding to 2.9 N (about 90% of the elastic limit). The resulting wire sags are 35 μm and 135 μm respectively for 2 m and 4 m wires.

The wire is crimped on a solid copper-tellurium block 4 mm on a side (see Fig. 3.2.2), in which a 0.1 mm wide, 0.3 mm deep groove is machined (this 3D figure, like all others shown in this chapter, is the output of a CAD solid modeling computer package where all mechanical details are present; the technical drawings necessary for the various machining are obtained from these solid models).

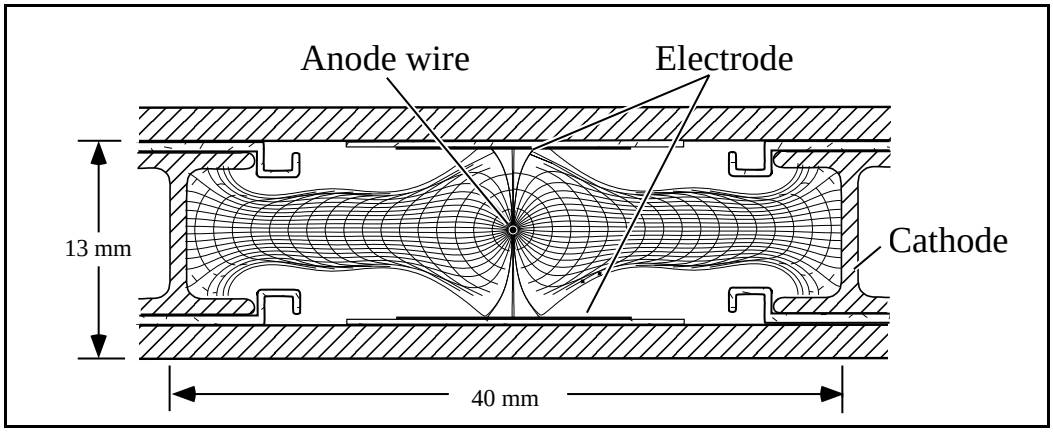


Fig. 3.2.1: Transverse view of the baseline cell; also shown are drift lines and isochrones, for a typical voltage configuration of the electrodes.

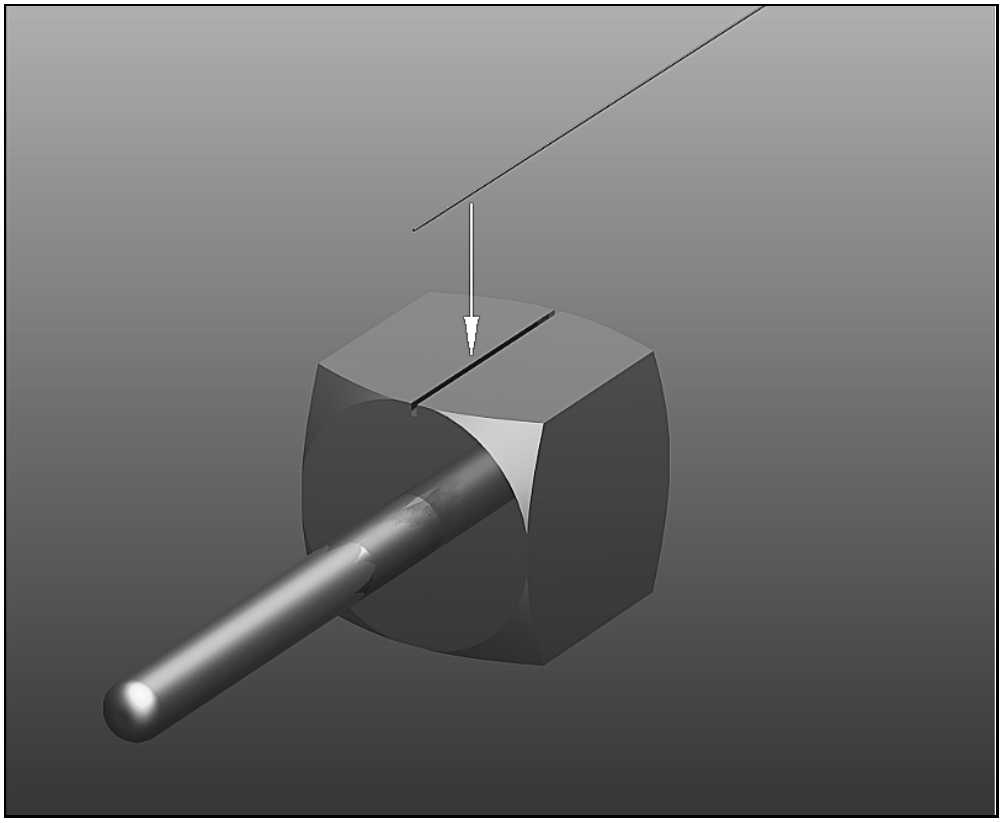


Fig. 3.2.2: 3D model of the crimping block; also indicated is the 50 μm thick steel wire that must be located (as indicated by the arrow) inside the cut in order to be crimped.

The wire with 50 μm diameter is placed in this groove and kept under the nominal tension defined by a weight. Crimping is achieved by pressing the block from the top with a small piston covering about 70% of the groove length. This deforms a small region of the block and causes the groove to close; the material fully envelops the wire, without deforming it. This crimping technique, used in the past for the L3 muon chambers, proved to be a reliable way of terminating the wires. No slipping was observed over a few thousand cells and many years of operation. The wire positioning is defined by means of plastic end-plugs that glue to the aluminum plates at the ends of each cell. Between two adjacent end-plugs, a wire-holding piece is inserted which houses the crimping block. The complete set up is shown in figure 3.2.3 a),b),c) and d). Within this set up, all plastic pieces of one layer of cells will be glued and mounted in one single operation. The wires can be crimped in advance and stored in an appropriate place, such that they are easily available for rapid assembly.

The plastic end-plugs also house the necessary HV contacts for the strips, cathodes and wires; 3-D computer models of the I-beam contacts, strip contacts and central end-plug are shown in Fig. 3.2.3 b), c) and d), respectively.

3.2.2 Gas Mixture

The muon detector is a large-volume detector and will operate underground, which raises possible safety concerns. Therefore the gas needs to be a non-flammable mixture. Also, its cost should be as low as possible and organic components should be avoided as possible sources of aging. In addition, the gas should have a saturated drift velocity, since the algorithm used in the trigger processor assumes a linear space-time relationship.

Mixtures of Ar/CO_2 satisfy all these requirements, as demonstrated by extensive studies done in the past. These studies showed that our constraints are satisfied by mixtures with a CO_2 fraction varying from 10% to 20%. Below 10%, the quenching properties of the mixture are quite bad, resulting in a short efficiency plateau, before discharges in the gas occur, while the drift velocity is not saturated above a 20% CO_2 concentration.

The linearity of the space-time relationship was measured in a test beam using different CO_2 concentrations. Figs.3.2.4 a) and b) show, for two of the mixtures, the correlation between the drift-times for two consecutive planes. A linear correlation is expected for the case of a saturated drift velocity; no sizable deviation from linearity is observed in varying the CO_2 content up to 18%. The data were taken at V_{eff} = 2100 V (cf. 3.2.3.1).

The chambers will operate inside the iron yoke and therefore will be immersed in a stray magnetic field region. In the acceptable range of CO_2 concentrations (10 to 20 %), the variation of the Lorentz angle is small, the average value being:

$$\alpha \cong 44^0 \cdot \frac{B(T)}{E(kV/cm)}$$ (for E ~ 2 kV/cm and B< 1 T).

Most of the data collected so far with prototypes were taken with carbon dioxide concentrations within the acceptable range; the final choice will be made at a later stage.

Simulation studies were done to optimize the cell optics in order to fulfill all the requirements while using an Ar/CO_2 mixture. Figure 3.2.5 shows that, for the final cell configuration, the requirement of a well-saturated drift velocity along the entire drift path of the

electrons to the anode is obtained. Simulations of the cell response using GARFIELD [3.1] provide reliable predictions which were confirmed by previous measurements.

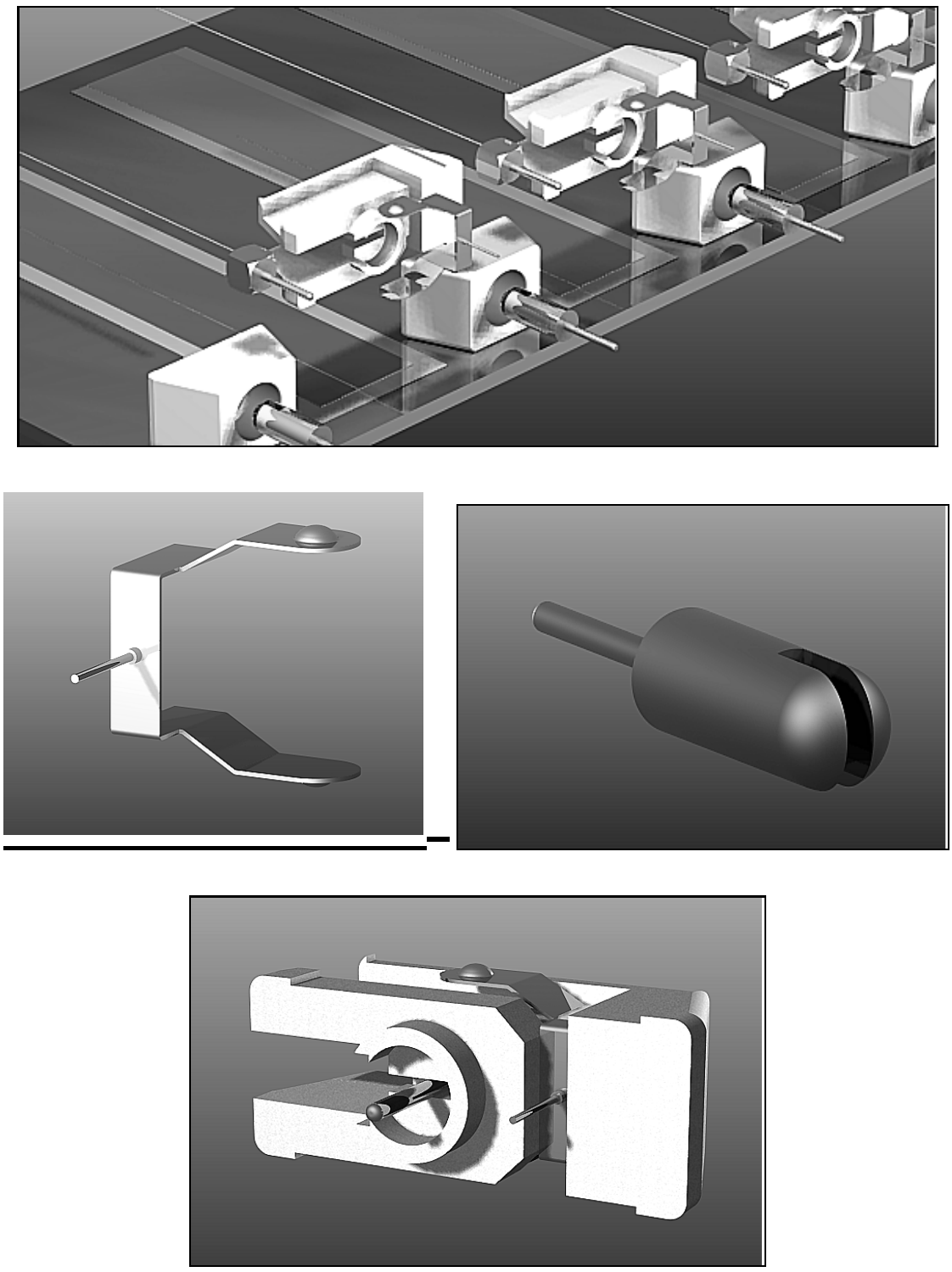


Fig.3.2.3: Details of the various parts used to position the wires and to power the various contacts; in **a)** (top) the exploded view of the end part of few cells is shown; **b)** (middle left) spring-like metal contact used to connect the strips of each cell to HV; **c)** (middle right) the contact for I shaped cathodes and finally **d)** (bottom) the plastic end-plug containing the wire and the strips contacts.

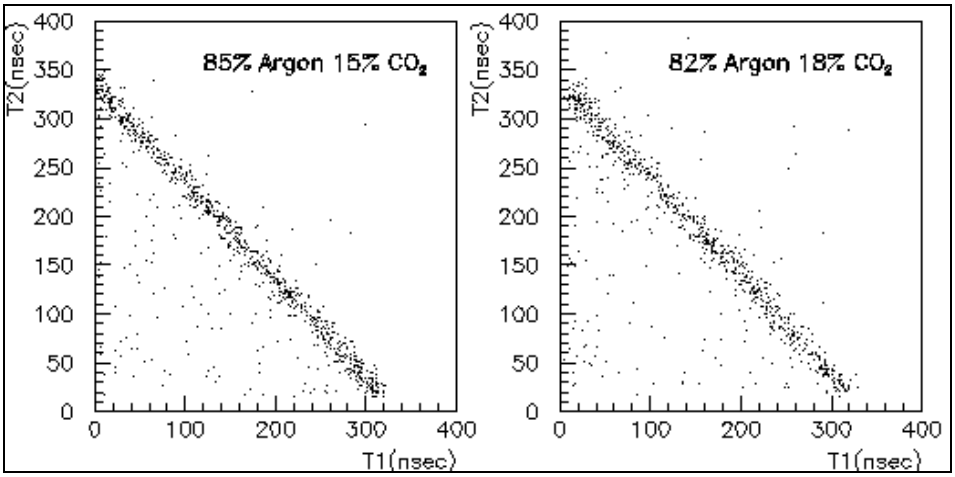


Fig. 3.2.4: Correlation of the drift-time in two consecutive planes for two different gas mixtures: **a)** (left) Ar/CO_2 85/15 and **b)** (right) Ar/CO_2 82/18; it can be seen that in both gas mixtures the correlation stays linear.

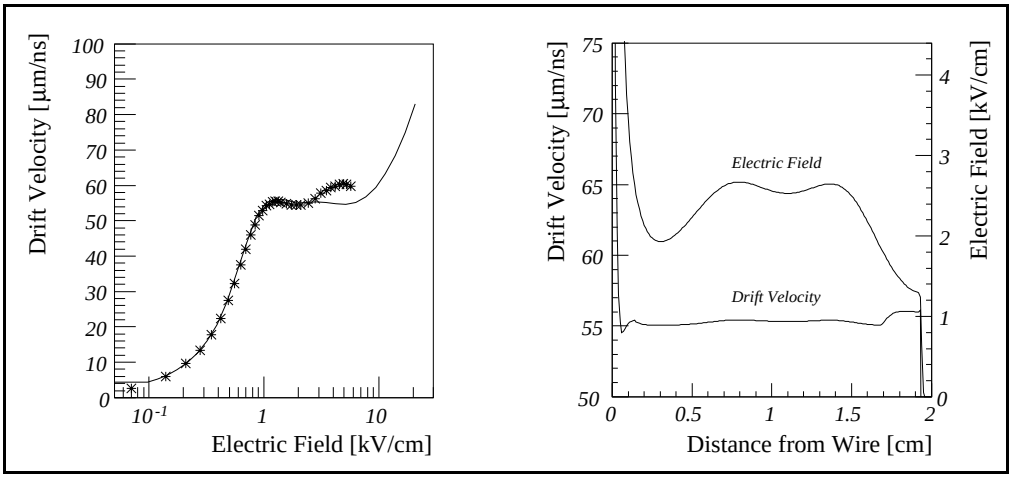


Fig. 3.2.5: a) (left) drift velocity vs. electric field for simulations and measurement with the final gas choice (Ar/CO_2 85/15); b) (right) drift velocity across the drift cell; it can be seen that a good linearity is present in the entire cell.

Several measurements were also done in a test beam to verify that the expected behavior was indeed obtained. In particular, a prototype trigger device was used to collect data and we verified that any remaining non-linearity had a small impact on the trigger efficiency, at least for the geometric and magnetic configurations expected in CMS.

3.2.3 Definition of the working point

In order to assess the working point and the main features of this detector, extensive tests were performed at the CERN CMS test beam facility. We present here results of relevant studies of the efficiency, drift velocity, linearity and spatial resolution.

The prototypes were operated with an Ar (85%) CO_2 (15%) gas mixture and at different V_{wire}, V_{strip} and $V_{cathode}$ voltages. Since we always kept $V_{strip} = -V_{cathode}$ the working point will be identified by the two voltages:

$$V_{ampl} = V_{wire} - V_{strip},$$

$$V_{drift} = V_{strip} - V_{cathode}.$$

3.2.3.1 Gas gain

The gain of the prototype cells has been measured using both cosmic rays and a radioactive source (Am^{241}). Since the electric field close to the wire surface, on which the gain of the drift cell depends exponentially, is proportional to a linear combination (V_{eff}) of the three voltages applied to the cell, the gas gain can be parametrized in the following way:

$$1)\quad G = e^{k+\alpha V_{eff}}, \text{ where } V_{eff} = \left(V_{wire} - V_{strip}\right) + b \cdot V_{strip} + c \cdot V_{cathode}$$

Several sets of measurements were made. Fits to the data give the following values for the constants in the expression above:

$$2)\quad \begin{aligned} k &= -6.4 \pm 1.0; \quad \alpha = (8.5 \pm 0.5) \cdot 10^{-3}\ V^{-1} \\ b &= 0.16 \pm 0.1; \quad c = -0.037 \pm 0.002 \end{aligned}$$

Fig 3.2.6 is a summary of all the measurements as a function of the effective voltage V_{eff}; for further details see Ref [3.2].

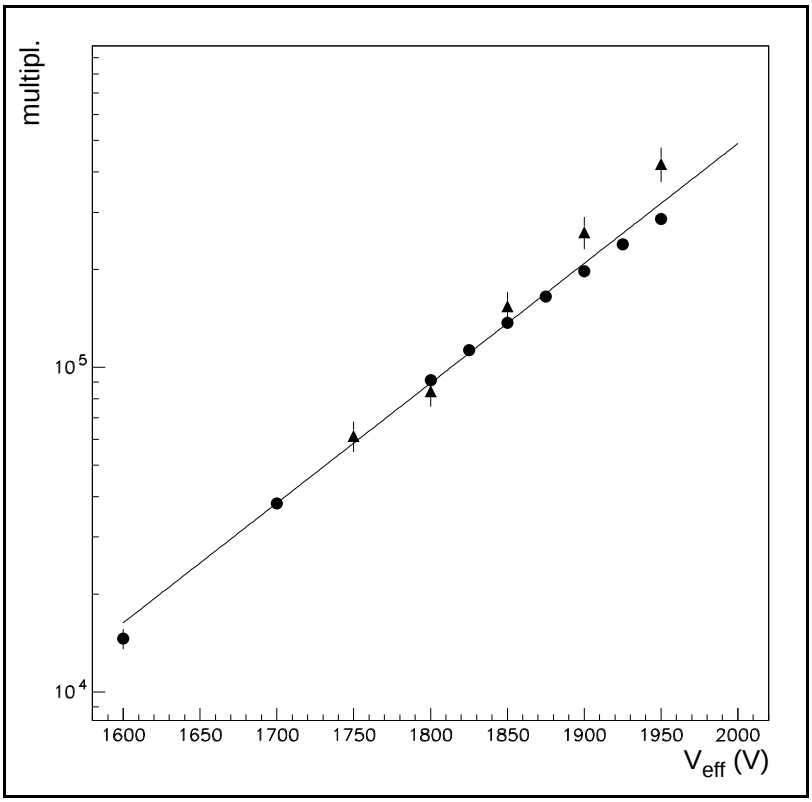


Fig. 3.2.6: Gas gain as a function of V_{eff}; dots are measurements performed with an ^{241}Am radioactive source while the triangles are obtained with cosmic rays; the fit is described in the text.

3.2.3.2 Efficiency

The efficiency was measured for each half-cell using data taken with orthogonally incident tracks. In Fig. 3.2.7 the average cell efficiency, neglecting dead areas caused by the cathodes, obtained at different voltage settings is given as a function of the effective voltage V_{eff}, computed by eq. 1) using the fitted b, c values given in 2).

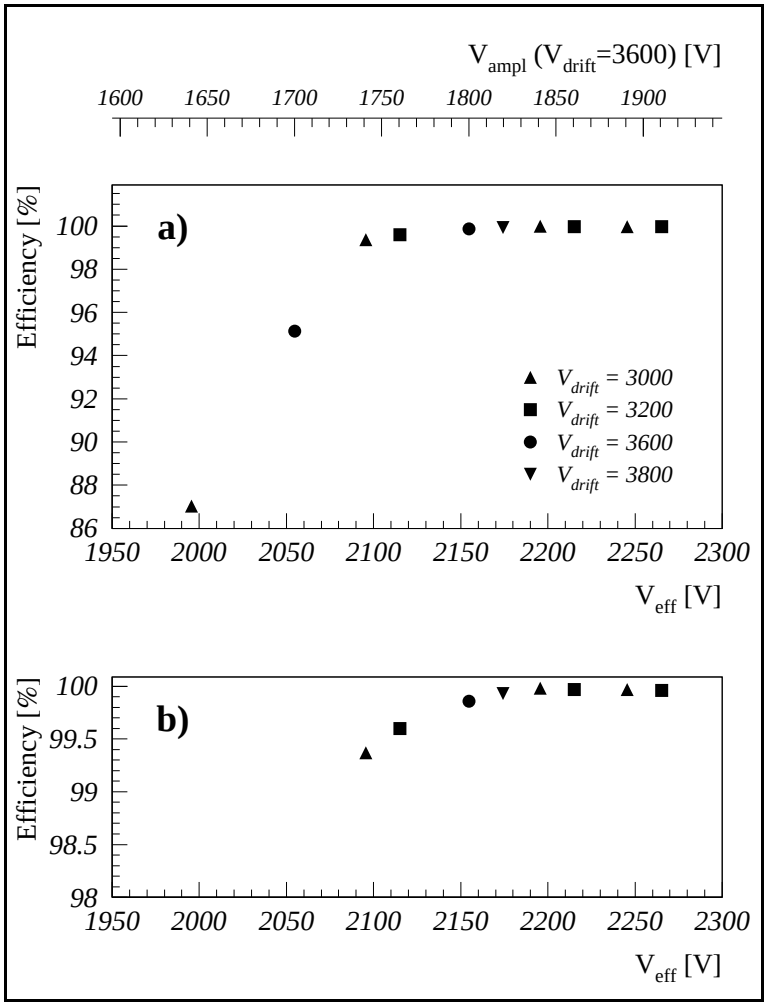


Fig. 3.2.7: Cell efficiency as a function of the effective voltage V_{eff} , proportional to the electric field on the wire **(a)**; expanded scale **(b)**.

Efficiency measurements made at different voltage settings lie on the same curve, confirming that the gas amplification is the significant parameter affecting the value of the efficiency.

The data show that the efficiency plateau is reached above V_{eff} = 2100 V, corresponding to a gas gain G= 10^5. The inefficiency is very low, 0.2%, when the chamber is operated at the reference voltages: V_{ampl}= 1800 V and V_{drift}= 3600 V.

The dependence of the efficiency on the threshold applied to the signal was studied using the ASD8 electronics [3.3]. No significant drop of the efficiency was observed when varying the threshold from 1 to 6 fC.

The data show that the efficiency plateau is reached above V_{eff} = 2100 V, corresponding to a gas gain G= 10^5. The inefficiency is very low, 0.2%, when the chamber is operated at the reference voltages: V_{ampl}= 1800 V and V_{drift}= 3600 V.

The dependence of the efficiency on the threshold applied to the signal was studied using the ASD8 electronics [3.3]. No significant drop of the efficiency was observed when varying the threshold from 1 to 6 fC.

Data were also collected with another chamber prototype using different front-end electronics with a wider range of discriminator thresholds and with V_{drift} = 3000 V. The results indicate that no significant efficiency loss occurs for thresholds smaller than 9 fC.

The onset of the efficiency in proximity to the plastic end plugs was measured in a test beam with a scintillator hodoscope with a resolution of ± 2 mm.

As can be seen in Fig. 3.2.8 where the efficiency is plotted against the coordinate along the wire, the cell already reaches full efficiency at 5-8 mm from the point where the wire emerges from the plastic endplug.

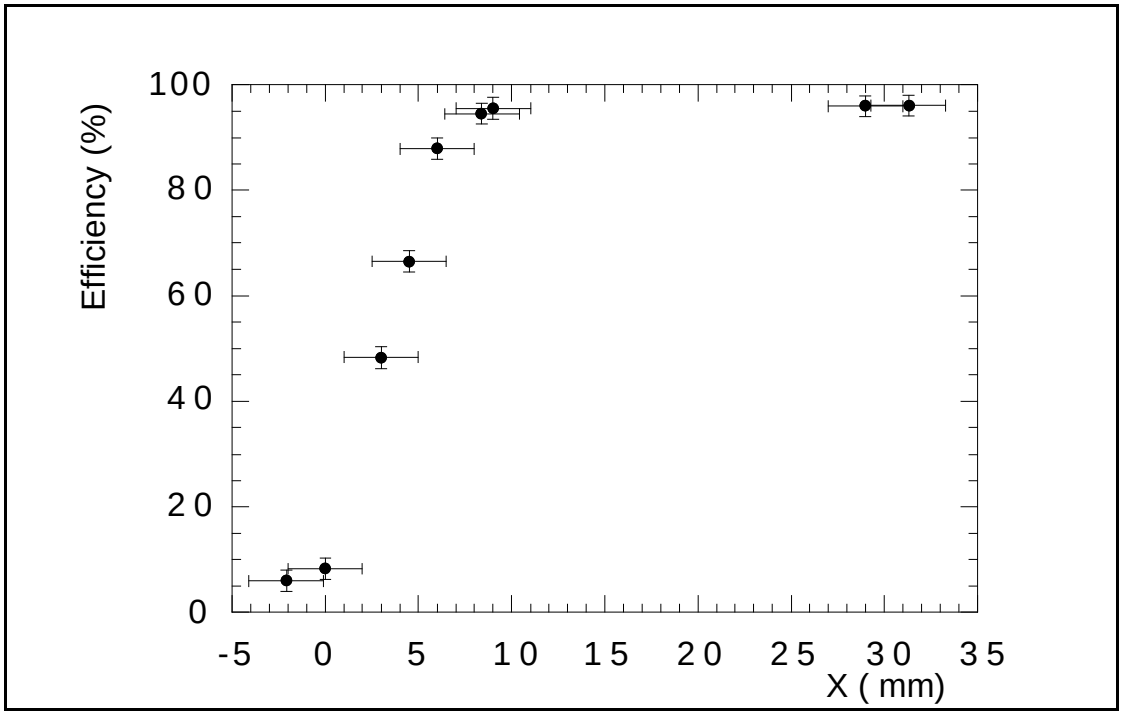


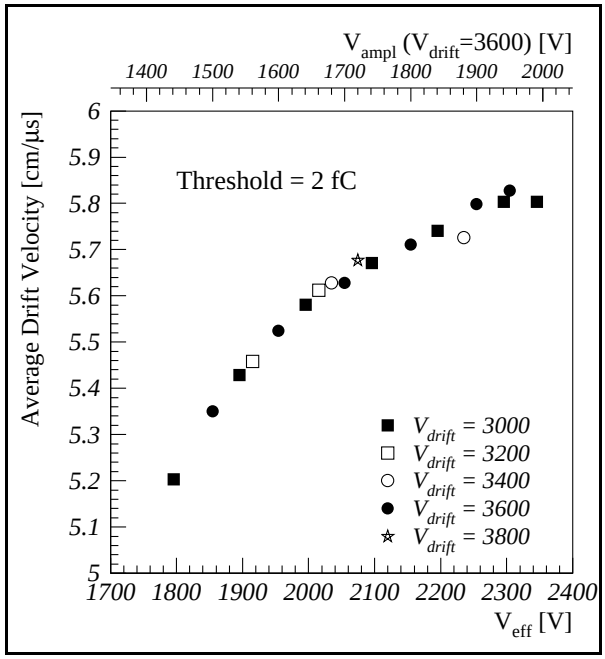
Fig. 3.2.8: Efficiency as a function of the coordinate along the wire; x = 0 is where the wire emerges from the plastic end-plug, whereas the I-beam cathodes start at x = +5 mm; it can be seen that the efficiency rapidly reaches full value. The errors on the x coordinate correspond to the size of the impinging beam that was defined by a set of scintillators.

3.2.3.3 Drift velocity

In order to study the drift velocity we make use of the presence of staggered planes in our chambers. For orthogonally incident tracks the sum of the drift-time of two consecutive layers (for a linear space-time relation) is a constant called t_{max}; in the case of inclined tracks the same quantity can be obtained from the drift-time of three consecutive layers by:

$$t_{\max} = \frac{1}{2}\left[t(j) + t(j+2) + 2t(j+1)\right]$$

The drift velocity averaged along the total drift length is obtained from the relation $v_{drift} = d/t_{max}$ where d is the wire pitch minus the wire diameter. Fig. 3.2.9 shows the results from data taken at various voltages and threshold settings.



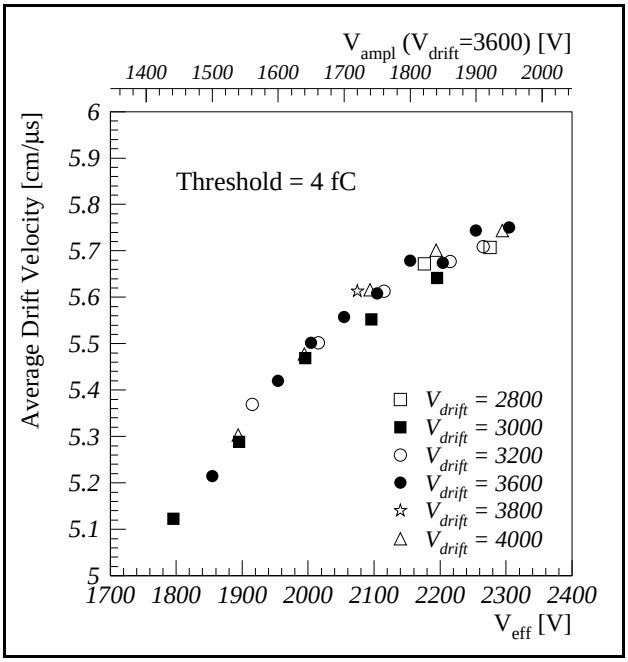


Fig. 3.2.9: a) (left) Average drift velocity at different voltage settings vs V_{eff} at 2 fC threshold; b) (right) same as (a) but 4 fC threshold.

For a given threshold value the average drift velocities measured for different settings of V_{drift} lie on the same curve, when plotted as a function of the effective voltage, V_{eff} proportional to the electric field close to the wire. The decrease of t_{max} as V_{eff}, i.e. the gain, increases indicates that fewer and fewer electrons are needed to trigger the detector. The independence of t_{max} on V_{drift} at constant gain indicates that v_{drift} is saturated over a wide interval of drift field values.

For a given threshold value the average drift velocities measured for different settings of V_{drift} lie on the same curve, when plotted as a function of the effective voltage, V_{eff} proportional to the electric field close to the wire. The decrease of t_{max} as V_{eff}, i.e. the gain, increases indicates that fewer and fewer electrons are needed to trigger the detector. The independence of t_{max} on V_{drift} at constant gain indicates that V_{drift} is saturated over a wide interval of drift field values.

The dependence of the maximum drift time t_{max} on the threshold value and on V_{eff}, and thus on the gas amplification, indicates that the signal from the first arriving electron is not always detected. This effect must vanish at high amplification values.

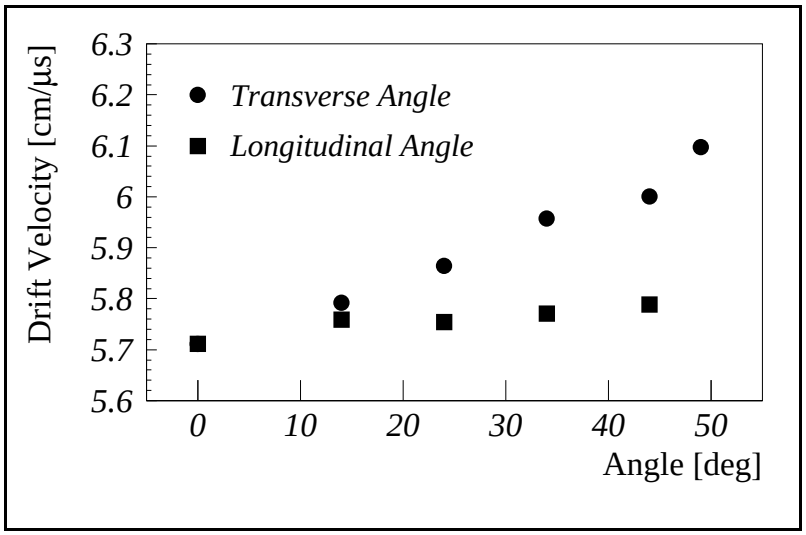


Fig. 3.2.10: Effective drift velocities for different orthogonal incident angles.

The variation of the effective drift velocity with the angle of incidence of the tracks was studied by taking data with the chamber rotated about an axis parallel to the electric field (longitudinal angle) and an axis parallel to the wires (transverse angle). The results, shown in Fig. 3.2.10, confirm the expectation that the average drift velocity should be independent of the longitudinal angle and should increase with the transverse angle. In the CMS setup, the incidence angle of high energy tracks will always be smaller than 20^0 in the bending plane, and in this angular region no large effects are observed. Only low momentum muons could enter the chambers with a larger angle, but in this case even a poor resolution is sufficient for the p_t measurement.

The dependence of the apparent drift velocity on the incidence angle can be corrected at the track measurement stage, but can generate systematic effects on the trigger efficiency, since the trigger algorithm expects the correct alignment of the hits to occur after the fixed delay t_{max} after the bunch-crossing. A preliminary study of this subject has been reported in [3.4].

3.2.3.4 Linearity

A linear space-time relationship across the full drift space is essential for the Mean Timer method at the trigger level, as we shall see later.

The linearity of the space-time relation was verified with the following formula:

$$\int_0^{\tau} \frac{dt}{\rho(t)} \cdot \frac{dN}{dt} = x(\tau) - x(0),$$

where t is the drift-time, ρ(t) is the density function of the incoming tracks, which can be extracted from the beam profile (Fig. 3.2.11 a)) and dN/dt is the drift-time distribution in a cell (Fig. 3.2.11 b)).

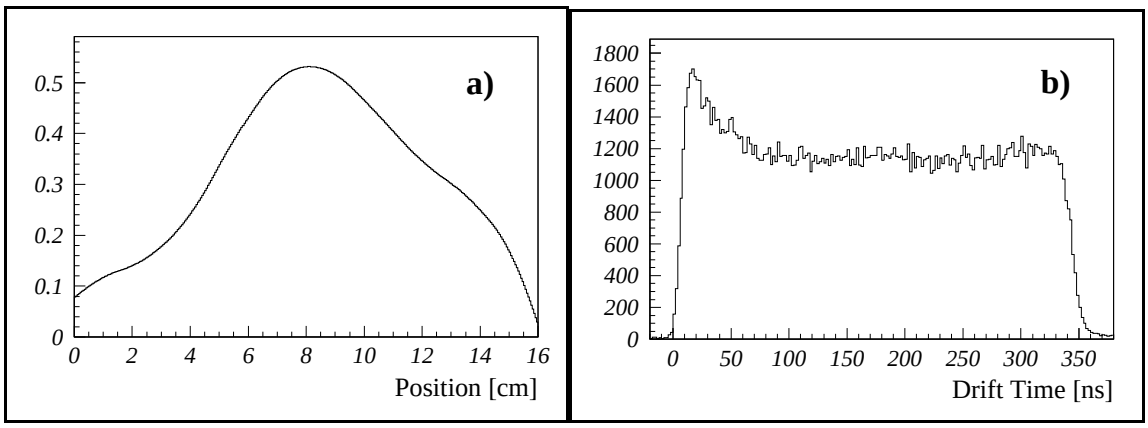


Fig. 3.2.11: (a) Beam profile distribution; (b) Typical drift-time distribution of a cell.

The integral of the drift-time distribution, weighted by the density function ρ(t), was calculated for each half cell. The resulting integral distribution x(τ) was then fitted to a straight line and the deviation from linearity at a given value of τ, converted to a length assuming a constant drift velocity, was plotted as a function of the corresponding distance from the wire along the half cell axis. Figure 3.2.12 shows this deviation averaged among the half cells illuminated by the beam. The non-linearity is within 0.1 mm everywhere, well below the intrinsic cell resolution. The drift-time distribution of all cells will be continuously monitored during the data taking to check for possible local variations. The method allows one to check the drift velocity along a single wire by coupling data from Z and Φ SL.

3.2.3.5 Resolution

The cell spatial resolution after corrections for non-linearities, measured at several amplification voltages and discriminator threshold settings, is shown in Fig. 3.2.13. The values at the plateau are well within the specifications required for the single-cell resolution and give some safety margin for the overall track resolution.

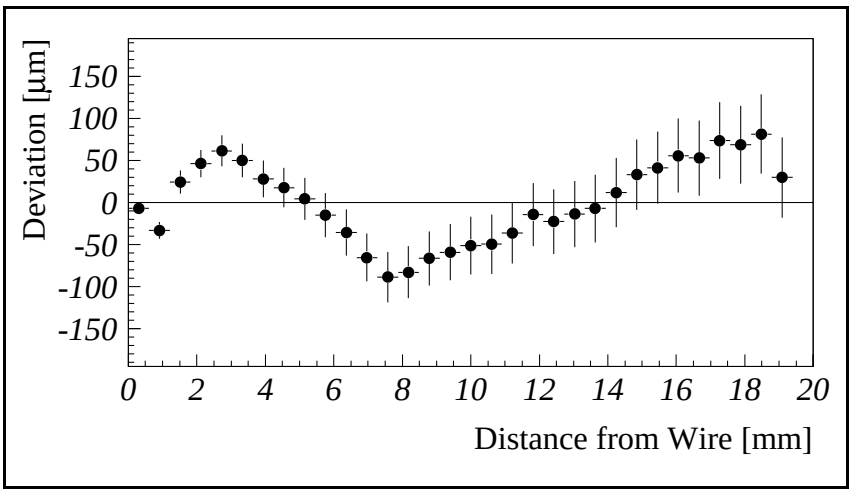


Fig. 3.2.12: Deviation from a linear space-time relationship.

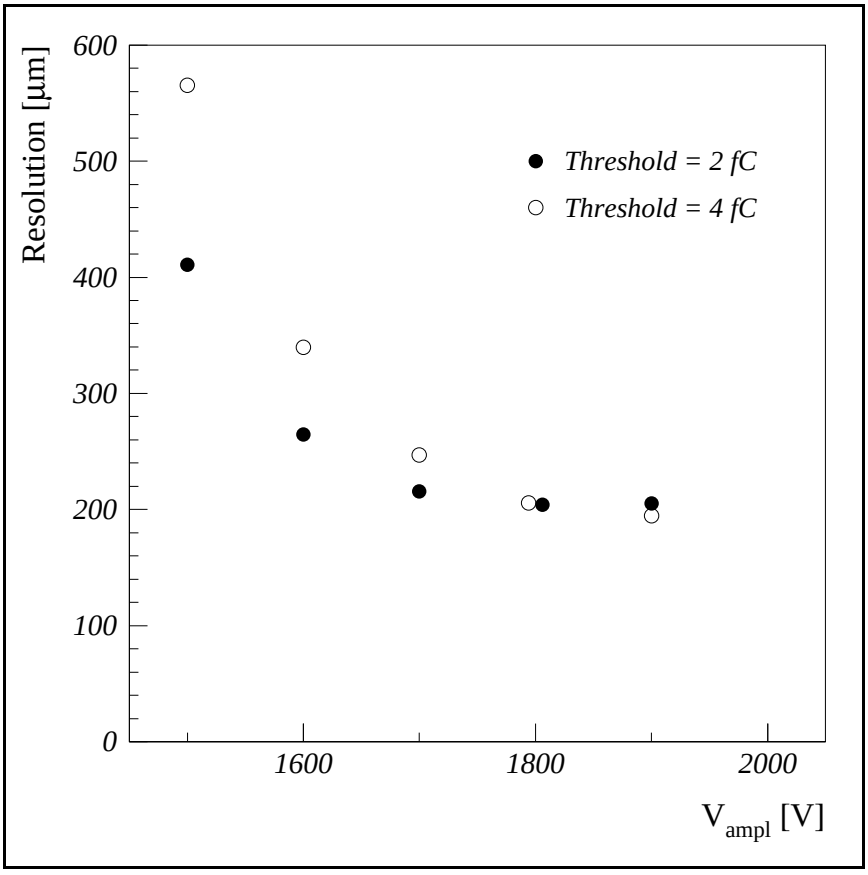


Fig. 3.2.13: Single cell spatial resolution evaluated at different voltage and threshold settings for orthogonally incident tracks.

The dependence of the resolution, measured along the middle plane of the drift cell, on the track incidence angle and position in the cell is shown in Fig. 3.2.14. The values are uniform and within the specifications along the full drift space for a wide range of transverse incidence angles, while a substantial deterioration can be observed for very large angles. However, their influence on the track position error is also reduced by the cosine of the angle, e.g. by 66% at the largest angle.

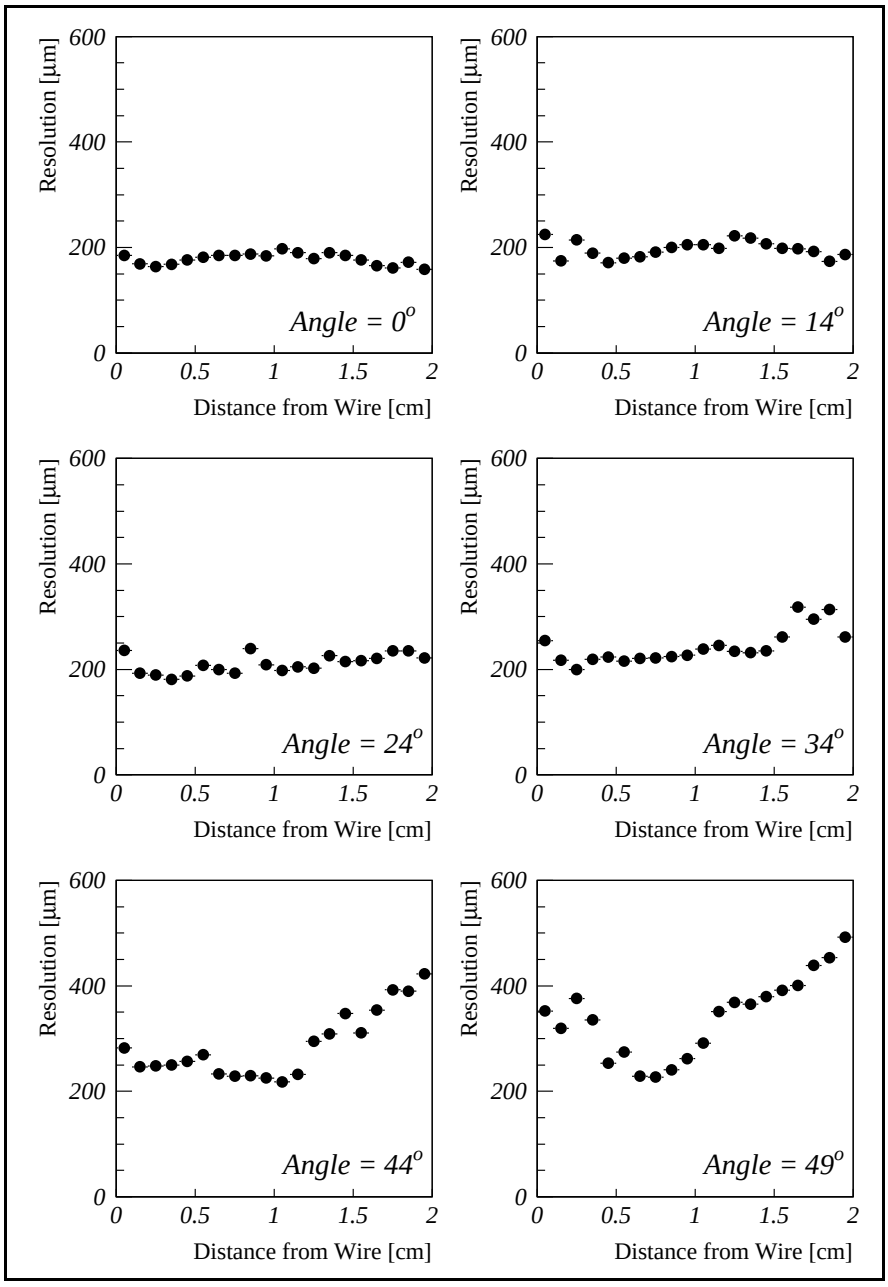


Fig. 3.2.14: Single-point resolution calculated from the residuals of a track fit at different positions along the cell and for different incident angles.

In order to study the impact of the central electrodes on the cell performance, a prototype was constructed where 50% of the drift cells were not equipped with strip electrodes. The comparison of the resolution obtained for the two types of drift cells as a function of discriminator thresholds and for orthogonally incident tracks is shown in Fig. 3.2.15. In all cases, the resolution is considerably better for cells with the central electrodes.

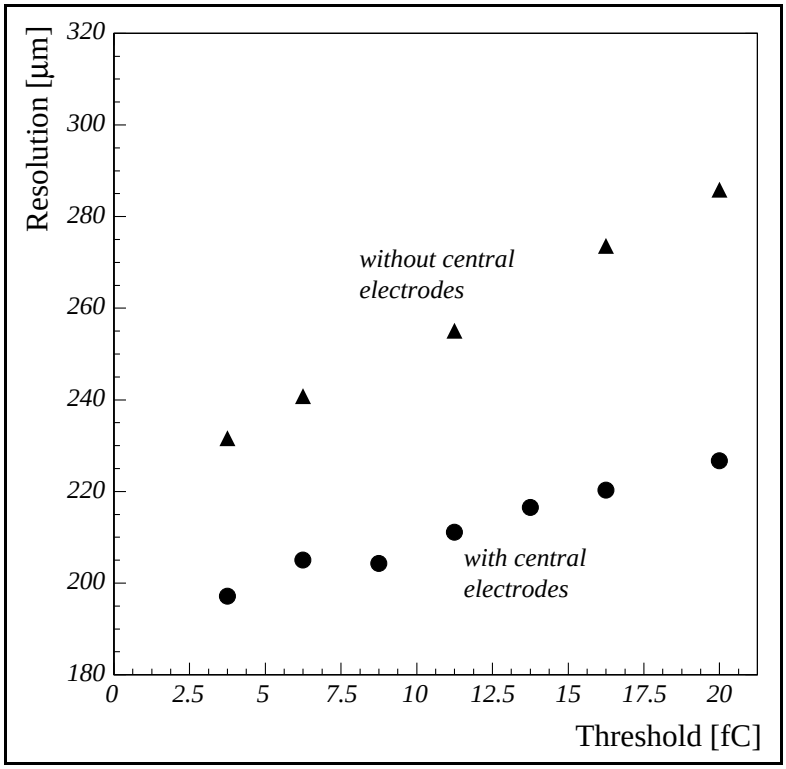


Fig. 3.2.15: Single cell resolution as a function of the threshold applied to the front end electronics; as it can be seen the addition of the central strip electrodes results in a uniform improvement at all threshold values.

Tests were performed also with the 3 m long chamber prototype in a muon beam at CERN. Measurements at points close to the wire ends and at the center of the chamber demostrate a uniform performance along the drift cells.

3.2.4 Aging

3.2.4.1 Introduction

Under the term “aging” a vast area of effects are grouped whose good understanding is important for the safe and reliable operation of the chambers. Amongst the many, some of the most relevant aspects are:

1) long term HV behavior of the insulators
2) aging of wires due to pollutants in the gas itself (from, e.g., outgassing of electronics boards) or due to accumulated charge during running.

3.2.4.2 Insulators

The breakdown of insulators in a high electric field is a stochastic process. The failure probability depends on the field intensity E and time t, and can be parametrized as

$$F(E,t) = 1 - e^{-\left(\frac{E}{E_0}\right)^{\gamma}\left(\frac{t}{\tau}\right)^{\beta}}$$

At an electric field strength $E = E_0$ 63% of the samples will fail in a time $t = \tau$. The behavior over long time intervals can be simulated by increasing the applied field, once the constants γ and β have been measured. Figure 3.2.16 shows the scaling law for a mylar sheet of 75 μm thickness. From the fit we extrapolate a failure probability for the field-shaping electrodes of 10^{-10} in 10 years. This figure appears to be safe enough, even taking into account the uncertainties associated with the large extrapolation needed to compute it.

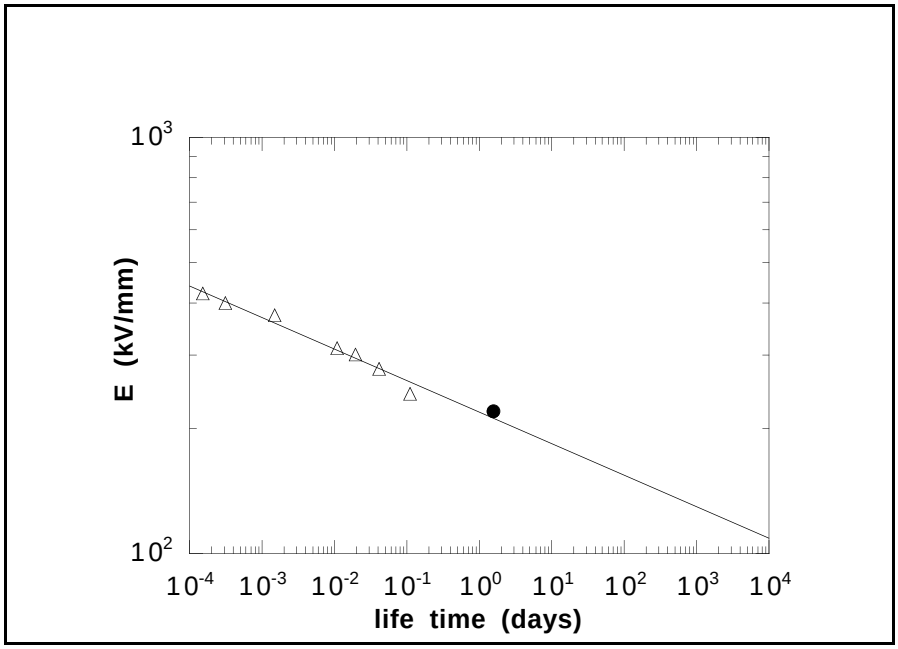


Fig. 3.2.16 Average time between HV breakdowns as a function of the applied electric field; the black point is our measurement, triangles from ref. [3.5].

We did not find similar data for polycarbonate. During tests made with 0.25 mm thick sheets, we did not observe a breakdown after applying an electric field as high as 180 kV/mm for up to several hours. Since we will apply a field of about 4 kV/mm, we do not foresee breakdown problems.

3.2.4.3 Aging of wires

The aging effects in a wire chamber typically fall into two general categories:

1) loss of gain or of gain uniformity. This effect is due to deposition of material on the anode wire surface. The parameter which measures the aging rate in terms of loss of gas gain is:

$$R = -\frac{1}{G} \cdot \frac{dG}{dQ} \qquad [\text{ in \%/(C/cm)}]$$

where G is the wire gain and Q is the charge per unit length deposited on the wire. A value R < 10 is usually taken as a good aging rate, while 10 < R < 30 is moderate and R > 30 means rapid deterioration.

2) electrical breakdown usually results in self-sustained discharges or dark current. This is due to a coating on the cathode ("Malter effect" [3.6]). Because of this effect, the dark currents of the electrodes must be monitored.

We estimate the total charge produced per unit length in the barrel DT during 10 years of LHC operation as follows. The total rate of charged particles, including accelerator related background (mainly $n \rightarrow \gamma \rightarrow e$), is less than 100 Hz/cm^2 [3.7]. For each hit a total charge of about 1 pC is generated (assuming a wire gain $\approx (0.5–1)\cdot 10^5$). So the total charge density will be

$$10 \text{ y} \cdot 3\cdot 10^7 \text{ s/y} \cdot 100 \text{ Hz/cm}^2 \cdot 4 \text{ cm} \cdot 1 \text{ pC} = 0.12 \text{ C/cm}.$$

This shows that even for a large R value (i.e. R= 30%/C/cm), after 10 years of LHC operation the gas gain would be reduced by only 4%. A direct test of these effects is planned.

Setup of a material aging test

Material to be tested for outgassing effects is contained in a clean tank while the Ar/CO_2 mixture flows through it. The dirty gas then flows through a wire chamber cell which is irradiated and whose gain is monitored at the same time. The performance of the "dirty" cell is then compared to a clean reference wire cell which is free of aging effects.

The set up is shown schematically in Fig.3.2.17. It consists of a two-arm apparatus, one with the reference cell and the other with the "aging" cell. The same Ar/CO_2 gas mixture, purified by a filter (Oxisorb cartridge [3.8]) to a level of a few tens ppb of oxygen, flows through both arms. Two identical wire chamber cells are placed in the two arms and operate under the same conditions (electric field on the wire, gas flow, temperature, pressure). A low intensity X-ray source (for example, a Fe^{55} source which emits 5.9 keV photons) is used to monitor the gain of the two cells. The electrode currents are also monitored.

In the "aging" arm, before the wirechamber cell, is a clean, stainless steel tank which contains the material under test. The tank can be heated and/or irradiated to accelerate the outgassing while the gas is flowing. The tank can be replaced by a DT module to investigate its overall outgassing features.

The "aging" cell is irradiated by a Cs^{137} γ source (E_γ = 662 keV) with 15 mCi intensity. The gas from the output of the cell can be analyzed by gas chromatography and/or other techniques.

The reference wire cells must be intrinsically safe from the point of view of aging. The two-arm apparatus must be completely metallic (stainless steel, copper and aluminum) without any plastic components and the vacuum tightness must be insured. The inner surfaces must be cleaned to avoid contamination from outgassing. Such a cell is shown in Fig. 3.2.18. It is a stainless steel cylinder, 35 cm long and with a 35 mm internal diameter. A 50 μm diameter stainless steel wire is clamped by two specially shaped Macor [3.9] pieces. Macor is a ceramic which is known to be safe as far as aging [3.10]. The window for the passage of the soft X-

rays is a mylar or kapton foil. They are also known to be safe for aging [3.10]. The gas tightness is insured by an indium O-ring pressed against the flange.

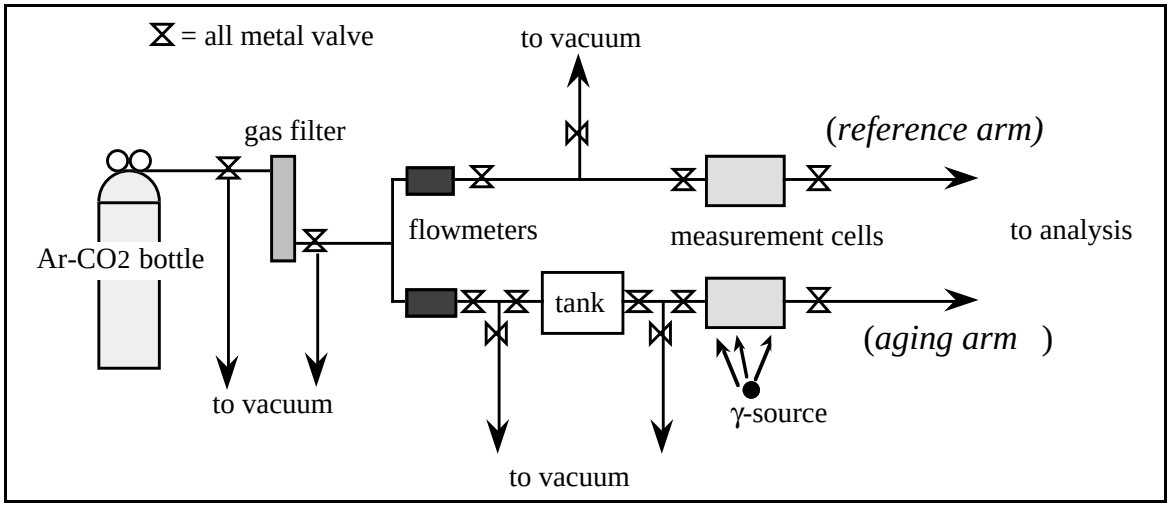


Fig. 3.2.17: A schematic of the experimental set up for aging tests.

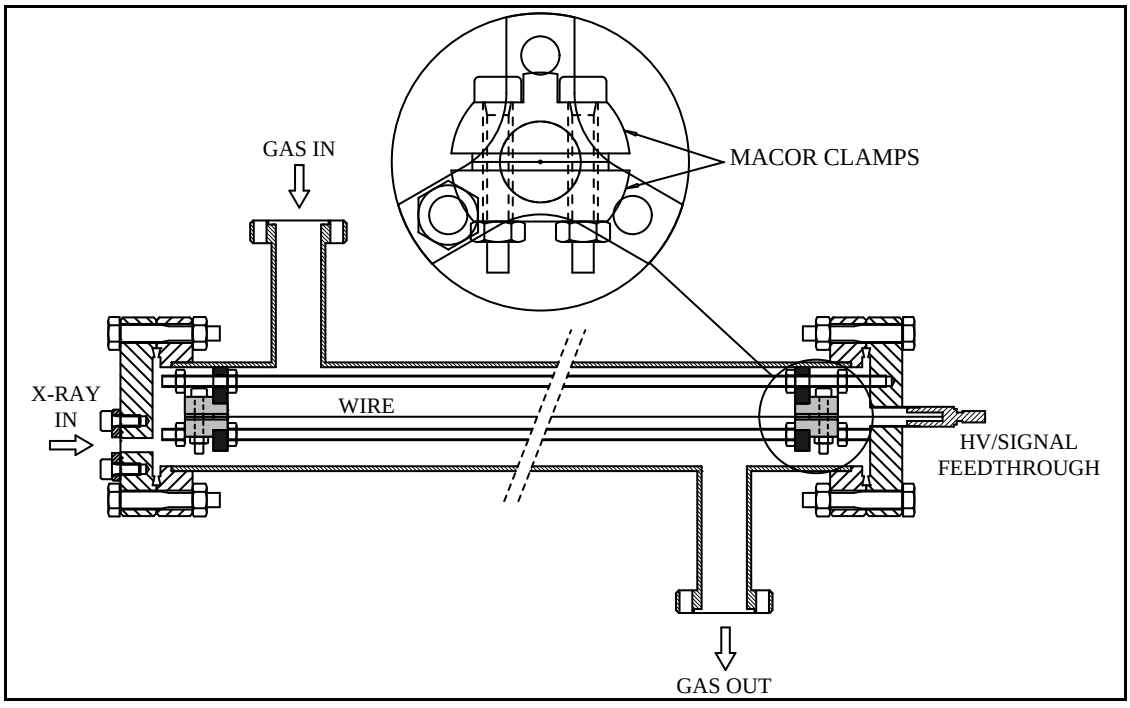


Fig.3.2.18: A schematic of a wire chamber cell for aging studies.

3.2.4.4 Aging and chamber performance

At high-luminosity LHC operation, the DTs are exposed to hit rates in the range 1-10 Hz/cm^2, which are dominated by random hits from low-energy neutrons via $n \rightarrow \gamma \rightarrow e$. A direct test of the muon reconstruction performance with a full-size DT under such conditions, before and after aging, is needed.

There is no muon beam matching the required (a) illumination of large areas (> 10 m^2), (b) high rate, and (c) sustained rate. An LHC-like environment for the test of muon detectors was recently built at CERN using two independent beams. The continuous main load on the detectors is generated by a radioactive source; here 20 Ci of Cs^{137} which deliver 662 keV photons in a 74°x74° solid angle. Depending on the distance from the source and on the conversion probability in the detector (about 2% for the DT cell), hit rates of several kHz/cm^2 are obtained. The test beam is called the Gamma Irradiation Facility, "GIF". The detector performance is directly measured with the help of a usual (narrow, low-intensity, pulsed) high-energy muon beam. The detector is moved transversely to expose different points to the muon beam, while still being irradiated over its entire area by the photon source.

Aging tests are done at a rate higher than the nominal one. For aging tests under operational conditions, a 10- to 50-fold increase in rate is envisaged, while the calibration measurements are performed regularly at the nominal maximum rate. It must thus be possible to change the photon rate. For this purpose a set of movable lead filters (in three planes) has been constructed, allowing us to vary the photon intensity in 17 steps, with a dynamic range of 10,000. Furthermore, a thin filter ensures a uniform photon rate over a flat detector, rather than over a spherical surface. When testing detectors designed for lower rates, like the DT, a further filter is installed to limit the maximum intensity; the full dynamic range remains thus available.

This facility has first been used to make performance tests at different rates of a large DT prototype, see Sec. 3.9. Aging tests will be carried out in the near future.

3.2.4.5 Other aging tests

The obvious question of whether aging effects, partly enhanced by irradiation, can compromise the electrical and mechanical properties of the insulators and the glues used in the DT, must also be answered by tests. Here, small material samples are sufficient. Exposure to heat, photons and neutrons are adequate to rapidly simulate aging.

3.2.5 Chamber design

A drift tube chamber is made of three Super Layers (SL) (Fig. 3.2.19) each made by four layers of rectangular drift cells staggered by half a cell. The wires in the two outer quadruplets are parallel to the beam line and provide the track measurement in the magnetic bending plane. In the inner quadruplet, the wires are orthogonal to the beam line and measure the track position along the beam. A chamber is assembled by gluing the SL to an aluminum honeycomb plate to ensure the required stiffness.

Each SL is made of five aluminum sheets, 2 mm thick, separated by insulated, 9.6 mm high 1.2 mm thick aluminum I-beams, as described in Sect. 3.2.1 The cell pitch is 40 mm, while the layer pitch is 13 mm. As will be described later, the HV connections to the cells and the front-end electronics are located at opposite ends of the wires.

The gas enclosures are consequently different: on the HV side they contain only the HV and test pulse distribution systems and the gas outlet, whereas on the front-end sides there will

be the HV decoupling capacitors, the front-end circuitry, the gas inlet distribution and the necessary cooling for the electronics. This difference means that the resulting dead areas will not be the same at the two ends of the chamber. In the current prototypes, counting as dead space the distance between the position where the wire enters the end plug and the outer face of the gas enclosure, there are 70 mm on the HV side and 75 mm on the front-end side. Closer views of these crowded areas are shown in Fig. 3.6.1. These are critical parts of the chambers and a robust R&D effort is ongoing to minimize these dead areas.

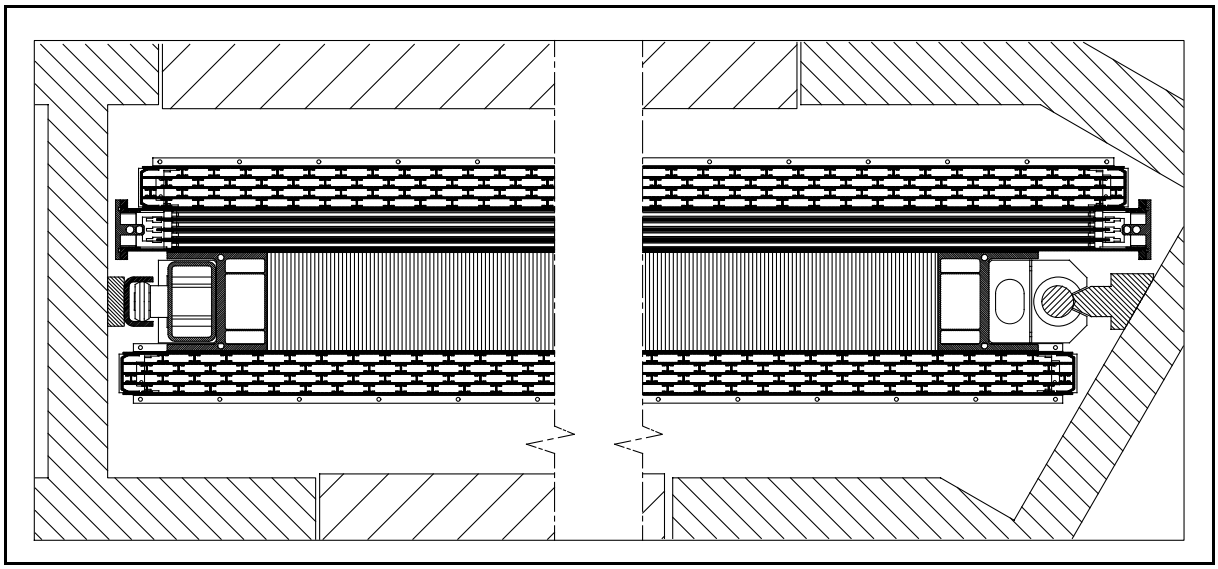


Fig. 3.2.19: Drift Tubes Chamber in its final position inside the iron yoke; the cut is in the (R,Φ) plane. One can see the two SLs with wires along the beam direction and the crossed one. In between is the honeycomb plate with the supports to the iron.

The gas distribution inside the Super Layer is in parallel through all the cells with the input at the front-end side. In order to equalize the impedance seen by the gas entering all the cells and to minimize the pressure drop that would be inevitable for the case of a simple inlet, we envisage having the gas distribution as sketched in Figs. 3.2.20 a and b

There are two gas inlets at the sides of the chamber; these supplies feed a distribution bar that is placed inside the enclosure and has many small holes from which the gas enters the chamber. The total impedance of the holes matches the inlet impedance. The same structure is present at the outlet. In order to ensure fast filling, a procedure using moderate vacuum in order to remove the air from inside the chambers is also foreseen.

It is very important that the individual Super Layers of the DT chambers are gas tight because contamination by nitrogen (from air) changes the drift velocity by a sizable amount. Figure 3.2.21 shows the variation of the maximum drift velocity inside a cell as a function of the oxygen contamination in the gas. The data obtained with the DT chamber prototypes are compared with simulations based on the Garfield package. A contamination of air giving 1000 ppm of O_2 changes the maximum drift time by about 10 ns with respect to zero contamination. Since, as will be explained in sect. 3.4.2, the trigger electronics is preset to a well defined t_{max} , chambers with varying oxygen concentration could result in a wrong bunch-crossing tag.

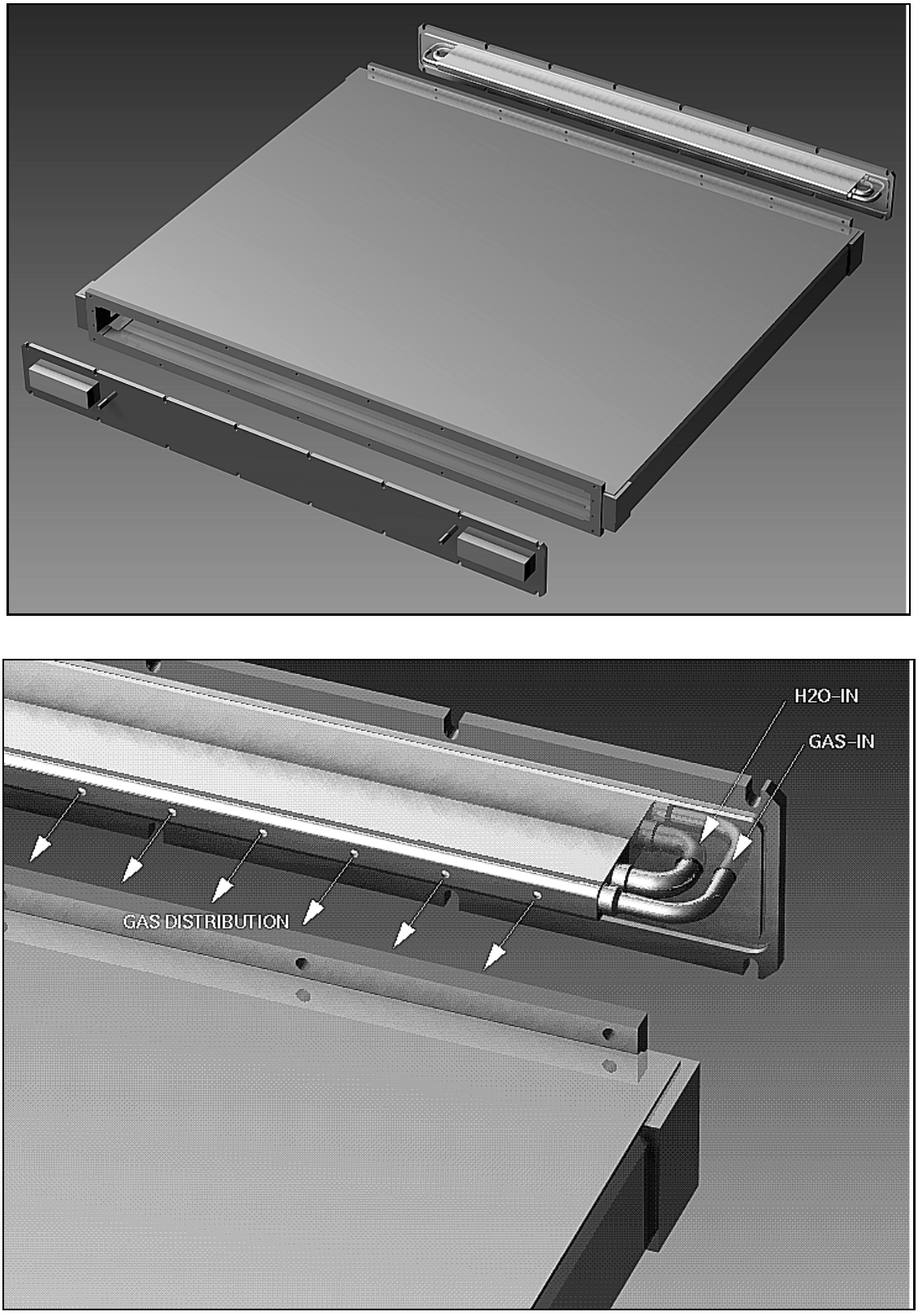


Fig. 3.2.20: 3D computer model of the gas enclosure of a Super Layer; a) (top) for the entire SL, b) (bottom) enlarged part of one end where the details of the gas distribution can be seen.

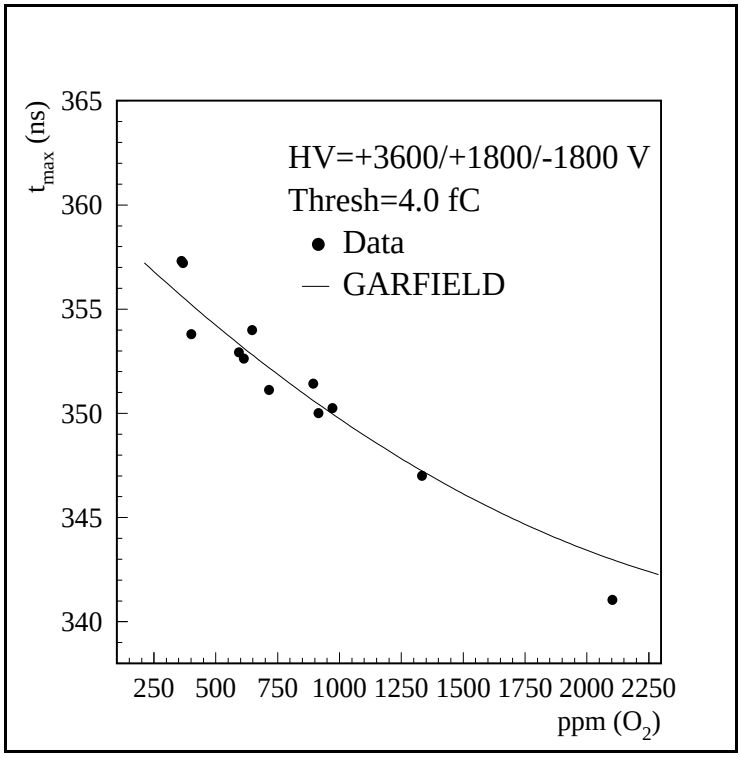


Fig. 3.2.21: Maximum drift time versus oxygen concentration.

As a consequence, 500 ppm of oxygen contamination was defined to be an acceptable limit for each SL. It is worth noting that in the presence of 2000 ppm of O_2 no drop in efficiency was detected.

In the DT chambers, the gas tightness of the quadruplets is obtained by gluing profiles to the outer aluminum skins. Along two sides of the Super Layer, the ends of these profiles are glued to reference blocks (see Fig. 3.2.22), forming the corners of the Super Layer box. The front and back of the box is then closed with plates, containing all necessary gas connectors, HV connectors and signal outputs, equipped with O-rings that seal the structure. The 3-D computer model of the gas enclosure for one SL, where the outer aluminum plates have been removed in order to see all details of the gas enclosure, is shown in Fig. 3.2.23.

With this type of gas enclosure and a full-scale prototype (called MB96), we have obtained a level of oxygen contamination of 10-20 ppm, downstream of the three Super Layers flushed in series with ~ 1 volume change per day.

At the assembly phase of the SLs, before the fifth aluminum plate is glued closing the structure, the reference blocks are glued such that their positions with respect to the wires are precisely known. Thus it is always possible, when the chamber is completed, to determine the wire positions just by measuring the reference marks on the blocks.

Pressure and temperature probes to monitor chambers, ground straps that short-circuit all aluminum planes in order to have a unique ground reference for the signals, front-end electronics and HV distribution complete the equipment that is in the gas enclosures of each SL.

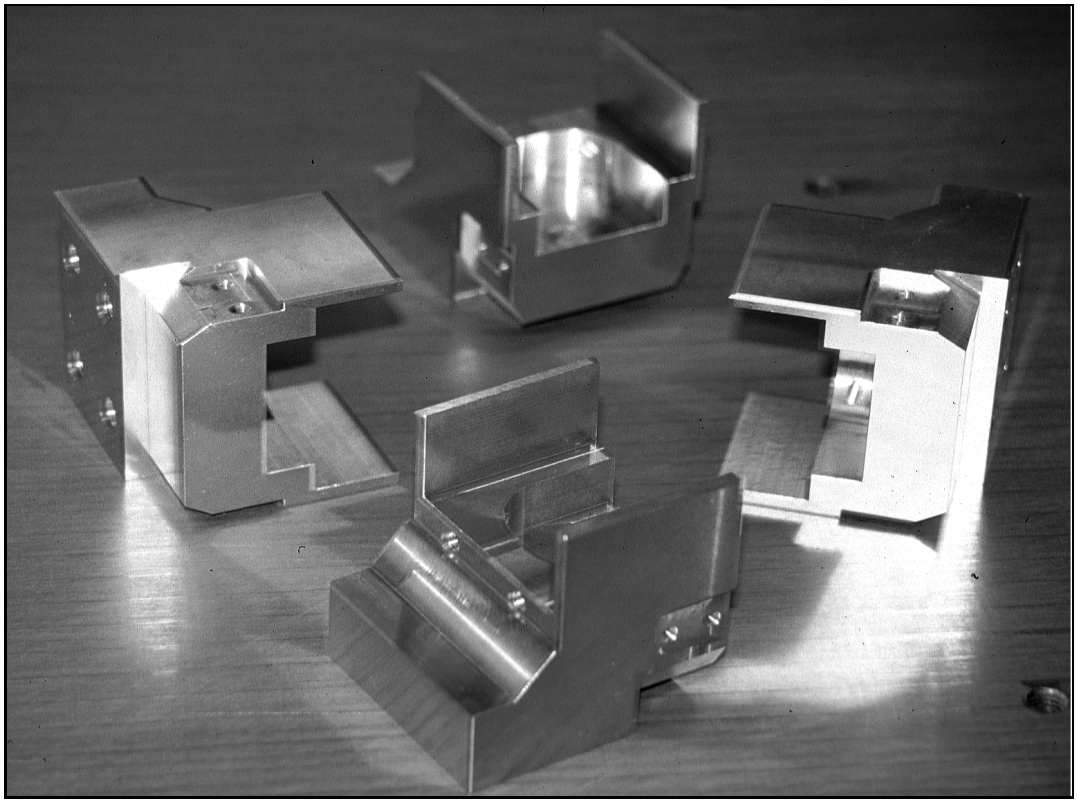


Fig. 3.2.22: Picture of the corner blocks of a Super Layer; these pieces also carry the reference marks with respect to which the wire positions are measured.

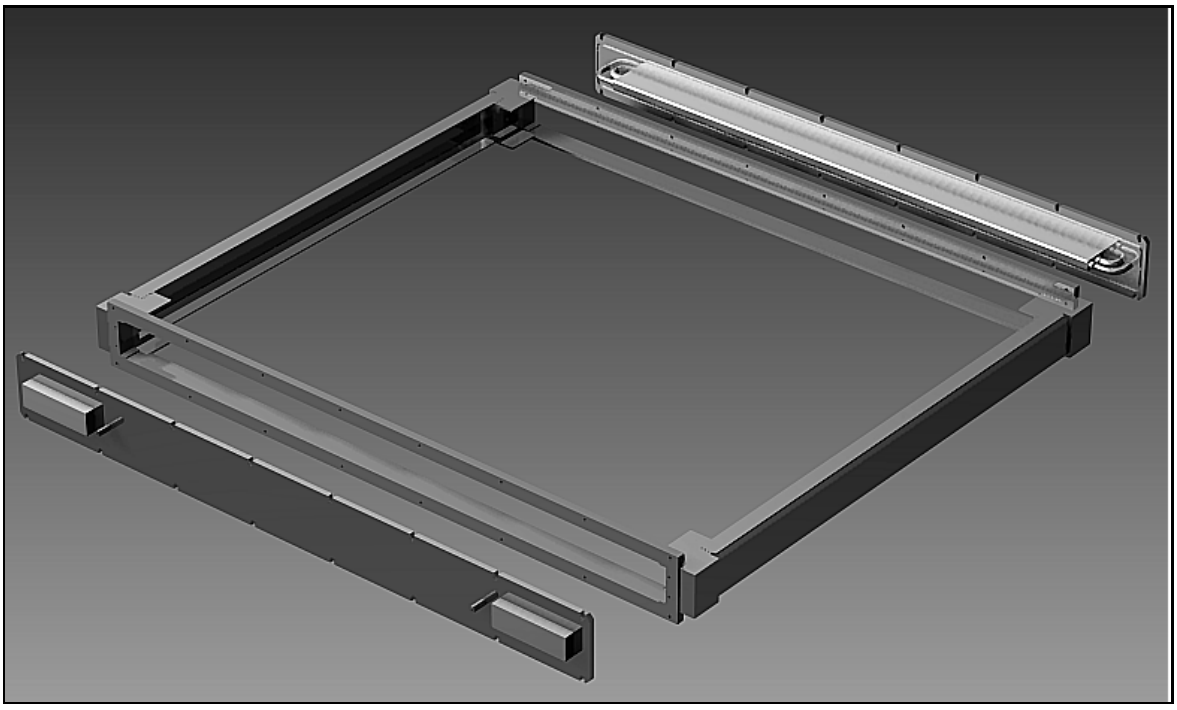


Fig. 3.2.23: A three-dimensional computer model of the gas enclosure of the Super Layers; to improve the comprehension of this picture, the two aluminum plates that complete the box have been removed.

Each quadruplet is an independent chamber as far as gas tightness, HV and front-end electronics are concerned, and hence it can be fully tested before it is glued to form a DT chamber.

Finally, it is worth mentioning that industry will supply the raw materials (e.g. wires, Al plates, I-beams, etc.) and more complex items including the honeycomb structures. The latter will be delivered with the correct dimensions and equipped with the C-shaped profile at the periphery that will be used for the supports and for housing part of the electronics. This was already done for the full-scale prototype and Fig. 3.2.24 shows the equipped honeycomb plate that was received from the company and used in the chamber.

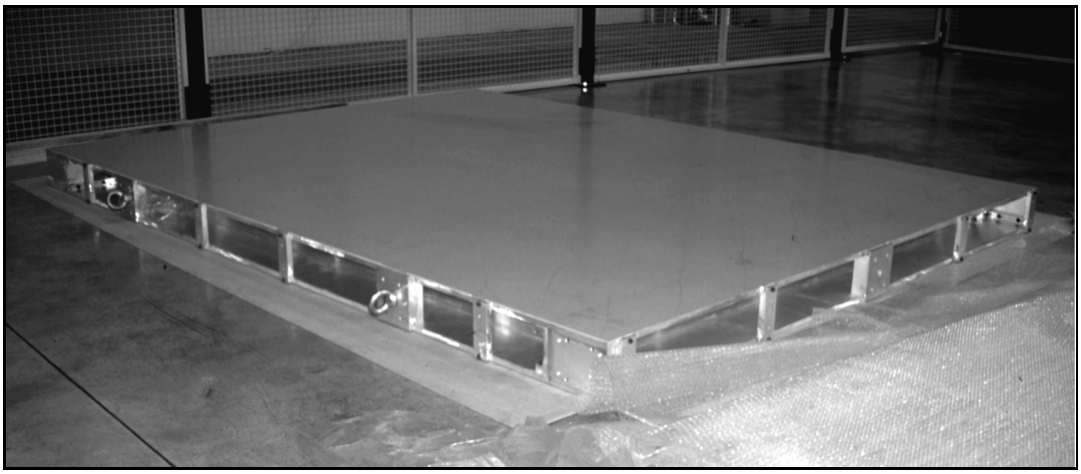


Fig. 3.2.24: A honeycomb plate, complete with C-shaped profiles, ready to be glued to the three SLs of a chamber.

3.2.6 Structural analysis of the DT chambers

3.2.6.1 Introduction

The DT chamber is a complex structure composed of three detection units and a structural skeleton. The width of the chambers ranges from 1800 mm to 4000 mm, whereas the depth is fixed at 2500 mm. The maximum sagitta allowed is 100 μm. To attain this very high flatness, we use aluminum aeronautical honeycomb as the structural skeleton. Moreover, since the positioning of the supports was recognized as the most relevant factor for chamber deformations, we heavily exploited simulations to find the best possible solution. The analysis was performed with the ANSYS ® package.

3.2.6.2 Measurements on a mockup

Measurements of the deformations were performed on a prototype consisting of three Super Layers, 3 m long, glued together in the same configuration as a DT chamber with the two crossed SLs only 0.2 m long; no honeycomb plate was present. The deformation of the structure, supported at the two ends, was 0.404 ± 0.062 mm.

Loading the center of the structure with additional weight, an effective Young's modulus of 0.083×10^{11} N/m^{2,} with a 2% error, was measured, corresponding to a sagitta of 0.361 ± 0.008 mm without additional weight. This scales to less than 0.07 mm when a 120 mm thick honeycomb spacer is present.

Measurements were repeated on the same 3 m long and 0.2 m wide prototype after about 2.5 years. They showed an increase in effective rigidity, with sagittae reduced to about 40% of the original measurements, probably related to further long-term hardening of the glue. The onset of non-linearities in the sagitta versus point-load relation was at an added point load of 240 kg, which corresponds to four times the prototype's weight as a point load, or six times as distributed load. The structure did break after 30 minutes with a 550 kg point load, corresponding to about 14 times its own weight as distributed load. It should be remembered that this structure had no honeycomb plate

3.2.6.3 Simulation inputs: limits and model reduction

It was clear from the initial simulations that local deformations were the largest contribution to the overall deformation. A dedicated effort has been made to improve the local structural solution for the supports. The second problem in order of importance was the need for a three-dimensional simulation.

On the other hand, the need to keep the number of elements and nodes below about 20000, above which the CPU at our disposal for these calculations was no longer adequate, required a two-step modeling. At the beginning, we analyzed in two dimensions the properties of each SL in two section planes. These results were used as input to a new "Super-Layer equivalent" element for the three dimensional large model. A serious difficulty was the impossibility of obtaining structural properties of the glue used in the chamber assembly. It has been assumed that the 100 μm thickness could mask, or even completely hide, the typical non-linear behavior of the glue. With this assumption, constant Young's and shear moduli were used as a first rough approximation. This assumption has been tested with prototypes.

3.2.6.4 Analysis

First, a new layered three-dimensional element describing the honeycomb was tested. Results from an exact algebraic method and the discrete analysis were in agreement to within 5%. Then, the discrete simulation was applied to only the skeleton consisting of the honeycomb and its "C" beam enclosures. The simulations showed that it was impossible to reach the deformation goal with a simple three points isostatic fixture. We have thus introduced an auxiliary balancing beam to perform an internal four-point supporting scheme with an isostatic interface to the iron. This auxiliary beam is housed inside one of the perimeter "C" profiles. This is also the designed space for supports and services such as electronics, gas, cooling, alignment devices, etc.

As a first step, two-dimensional simulations of the super-layers were performed using the geometric models which were accurate down to the smallest detail (Fig. 3.2.25) including thin glue layers. Figure 3.2.25 shows also the resulting stresses which reach their maximum value in the vertical portions of the I-beams because the bending deformation induces shear stresses on them. In this case, "layered" elements were used to better simulate the glue, plastic insulator and metallic base of the beams. A large number of runs have been dedicated to find the correct thickness of aluminum plates and the inner I-beams, having as a goal the maximum rigidity with the minimum weight.

Finally, the 3D model was assembled, using as input the intermediate results obtained from the analysis of the SL. Figure 3.2.26 shows the deformation of a MB3 chamber in horizontal position, with a maximal sagitta of 67 μm.

3.2.6.5 Simulations results

Two main results confirmed our expectations. The first result was that the contribution of the Super Layer to the global stiffness of the chamber is not negligible. The second was that supports are the most dangerous point for stresses and hence for deformations. In fact, as can be seen in Fig. 3.2.27, the maximum of the stresses occurs near the supports where, in this simulation, the Von Mises stress value has a maximum of 4.1 N/mm^2.

Another model with larger elements was used to calculate the stresses on the chamber as a whole. The results, shown in fig. 3.2.28, show another area of large stresses, namely the interface between the single SL and the honeycomb plate, at the center of the chamber.

The poor description of the glue characteristics suggests that we should not blindly believe in the numerical stress results. Therefore, three prototype chambers for a destructive test are preparation in order to cross-check the simulations. For the time being, the soundness of the simulations has only been verified by comparing the predicted deformations with the measured ones. The agreement is within 25%.

The flatness predicted from the simulation of the full chambers is below 0.1 mm for all chambers.

3.2.7 Chamber construction and tools

3.2.7.1 Introduction

Several prototypes of increasing size and number of layers were built in the last three years. Two of them were four-layer systems, 150 x 64 cm^2 in size. One consisted of four Super Layer chambers 50 x 50 cm^2 in area. Two large chambers were also built.One was 1 x 3 m^2 with twelve layers, and the second, named MB96, was a real MB1 “final” chamber.

The prototypes were also used to study, develop and improve the tools and the procedures that were successfully used for the production of MB96 and that are described in the following. These procedures are assumed to be “final” in the sense that in the construction of this chamber we followed, step by step, the procedure envisaged for the chamber mass production. Aluminum I-beams and aluminum plates were prepared in advance with tools suitable for mass production. Then the assembly was done on a precision table as it will be done in one of the future assembly lines. In the real mass production of the chambers, in order to achieve a safe construction rate, several of the elementary operations described in the following will be done by the same more refined tool or at the same time. Nevertheless the chamber design and the individual assembly operations will be the same as for this prototype.

3.2.7.2 Gluing Lexan profiles on aluminum I-beams

The insulated I-beams are a crucial item in the chamber construction because they guarantee the structural integrity of the chamber and also constitute one of the electrodes that shape the field in the cell.

They are assembled by attaching 500 μm thick extruded Lexan profiles on the top and bottom of the I-beams (see Fig. 3.2.29). Tiny ridges on the profile allow a better control of the glue thickness. The edges are shaped like eaves both to increase the path from the electrode to the ground plane and to collect any excess glue during the bonding to the aluminum plane.

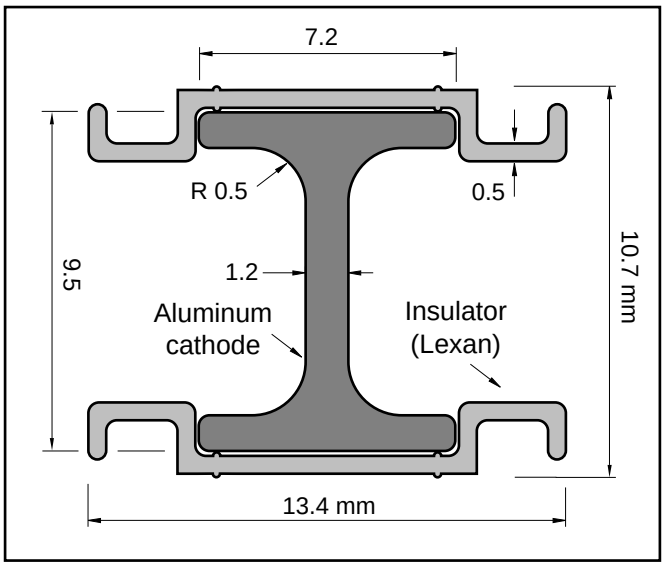


Fig. 3.2.29: Drawing of an I-beam and a Lexan strip.

Several commercial glues were tested to determine the best bonding agent for gluing the aluminum to the Lexan strip. The choice was made to use slow-curing Araldite (AW106) which gave the best results in rupture tests and also has been widely used for chamber construction in previous experiments.

The main requirements for the isolated I-beams are:

- overall thickness within 100 μm of design value
- overall length within 500 μm of design value
- a Lexan strip extending 5 mm beyond the I-beam at each end.

To meet these requirements, the gluing operation is done using the following procedure:

1) the Lexan strips are put in precisely-machined grooves on an aluminum plate and attached to a 5 cm thick honeycomb plane with profiles that define channels in which vacuum holds the Lexan against the aluminum.
2) the glue is deposited at the center of the Lexan strip with an automatic dispenser, beginning and ending 5 mm from the ends of the strip
3) the I-beams are inserted in the Lexan strips and are positioned with precision reference pieces with respect to the Lexan strips.
4) the aluminum plate, with thick rubber tubing attached corresponding to the positions of the I-beams, is bolted onto the plate holding the Lexan and I-beams.
5) a pressure of 2 bars is applied inside the rubber tubing during the curing of the glue.

After 12 hours of curing time at room temperature, the operation is repeated to attach the second Lexan strip to the I-beam.

The equipment used to produce the I-beams for MB96, illustrated in Fig. 3.2.30, allowed the gluing of 23 I-beams at a time, but for the final production it will be extended to 33 I-beams. This number is defined primarily by the time needed to distribute the glue and to put the I-beams on the Lexan.

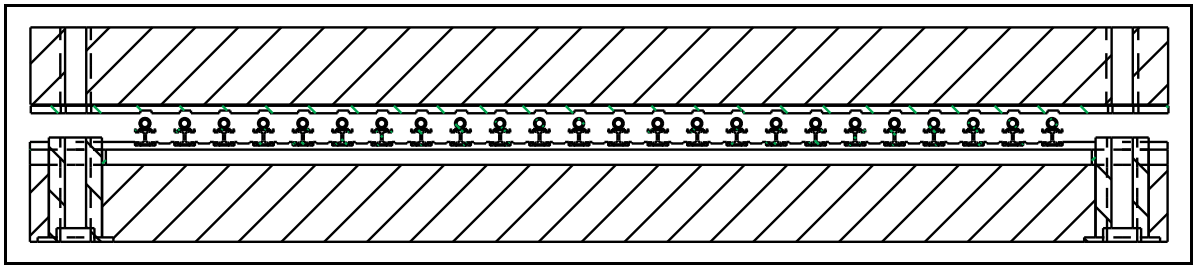


Fig. 3.2.30: Drawing of the equipment used to glue the I-beams and Lexan.

The quality control of the finished I-beams is done with the following procedure:

- visual inspection of the glue joints
- measurement of the thickness at three points along the I-beam
- isolation test at 5000 V in air.

The results of the thickness measurements for the MB96 I-beams, shown in Fig. 3.2.31, have an rms of 50 μm, which is well within the design specifications.

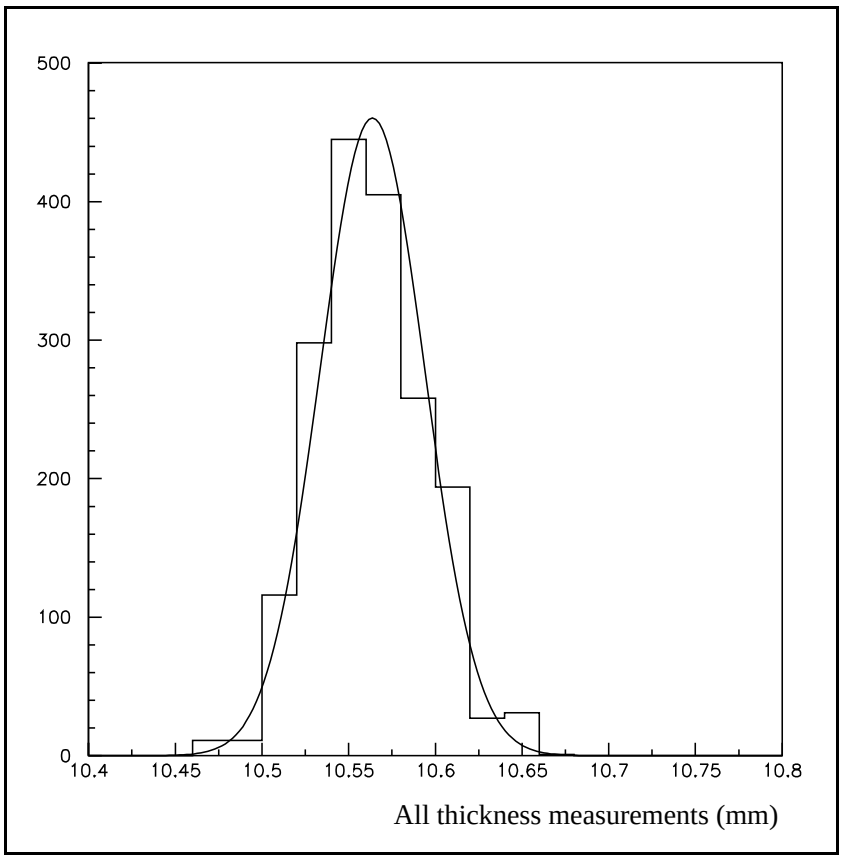


Fig. 3.2.31: Distribution of thickness measurements for the MB96 I-beams.

3.2.7.3 Crimping the wires

All wires needed for a layer are prepared in advance, with the two ends crimped to the small blocks and tensioned to 3.2 N. They are then placed on a storage jig where all wires remain under tension until needed for chamber assembly.

3.2.7.4 Gluing the strip electrodes onto the aluminum plates

As explained in Sect. 3.2.1, in the middle of each drift cell there are, above and below the wire, field-shaping electrodes consisting of copper strips on a self-adhesive mylar backing. These strips are put on the aluminum plates before starting the assembly procedure. This operation is performed on the assembly table by means of the same machine used later for gluing the I-beams. It consists of a head that can move on a frame mounted on the precision table. The head carries the roll of strips, the roll on which the paper protection is wound and a knife to cut each strip to the desired length.

The machine is computer controlled and the operator can specify how many strips of which length the machine lays down for that particular layer. At the start, the machine will automatically position itself at the initial coordinate of strip number one and will then process the complete layer. Human intervention is possible in case the end of a roll of strips is reached, or a replacement strip needs to be laid down to correct a HV problem found in the following tests. The entire operation takes about half an hour for a plane with 60 strips of 2 m length. At its end, every strip must be insulated with respect to ground; for the time being this process is done manually by encapsulating the strip end inside a mylar tape pocket. This method is labor intensive and is not yet considered as the final choice. The approximate time needed for the insulation of a complete layer is half an hour for each end.

The strips must be positioned with a precision of about $\pm$ 0.5 mm; the result obtained for the MB96 prototype is shown in Fig. 3.2.32. As can be seen, most of the strips are well within the limits, but there is still room for improvement.

Before storing each Al plate equipped with strips a HV test is performed; details will be given in the paragraph devoted to quality controls.

3.2.7.5 Super Layer assembly

All assembly procedures are performed on a precision table equipped with all references for the different tools that are needed for chamber assembly. The table is flat to $\pm$ 0.1 mm in order to ensure the quality of the final planes.

The first aluminum plate, equipped with the field-shaping strips, is transported to the assembly table and fixed to it using reference pins. All transports are performed with a jig equipped with suction disks that allow plates to be moved without bending. The total lifting power is adequate for the movement of an entire quadruplet. The next operation is the gluing of the I-beams (already prepared with the Lexan insulator) onto the aluminum plate. All I-beams necessary for one layer are placed over the tool (see Fig. 3.2.33) where movable pins, pneumatically controlled, block them at their nominal position. The tool is then lifted with a crane near the assembly table. Before placing the I-beams, one has to put the glue lines at their correct position. The chosen glue is Araldite AW106. In order to have a uniform glue layer after curing of about 0.1 mm thickness, one has to lay down a line roughly 1 mm in diameter. The glue dispensing phase is done using the same movable equipment used for laying the strips after changing the head. In this case, one uses a dynamical mixer where the two glue components arrive from the supply and are mixed inside the nozzle. The procedure is shown in Fig. 3.2.34

where a few glue lines are being laid down. The speed at which the head could be moved was such that one layer was completed in about half an hour.

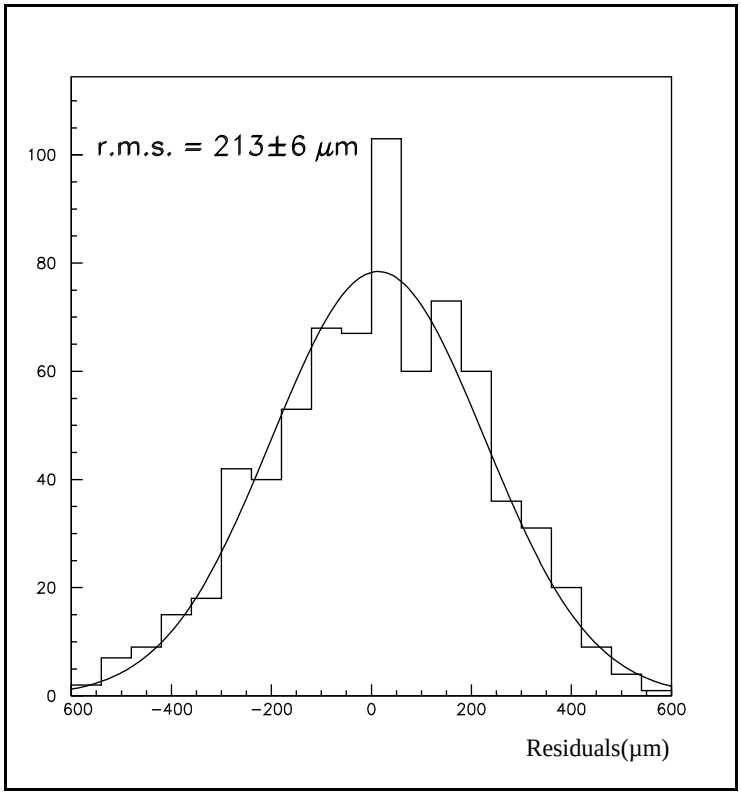


Fig. 3.2.32: Distribution of the distance of the measured strip position from the nominal coordinate.

When the glue dispensing is complete, one brings the I-beam tool to the table and, using the same references as all other tools, places them on the Al plate. The last operation needed is to remove the upper part of the I-beam tooling in order to leave necessary space for the weights which will ensure uniform contact between the parts that must be glued together. (One relies on the uniformity of the glue layer thickness in order to meet the specifications on the total Super Layer thickness.) The necessary pressure is applied with a frame loaded with iron weights, which is brought into position with the crane. The total weight applied to the glue is 600 kg corresponding to an average pressure of 1.3 N/mm^2.

After a time sufficient for the glue to polymerize, the weights and the jig are removed and one can then glue the small plastic end-plugs that define the wire pitch with the required precision of 0.1 mm. The end-plugs themselves are loaded into the tool (Fig. 3.2.35) by inserting them into an aluminum bar. The “cells” inside the bar were made by precision milling and verified with a 3D high-precision measuring device. This is shown in Fig. 3.2.36, where one can see the machined profile resting on a precision table and the measuring head which is being moved by computer control onto it.



Fig. 3.2.33: Tool for the I-beam transport and gluing.

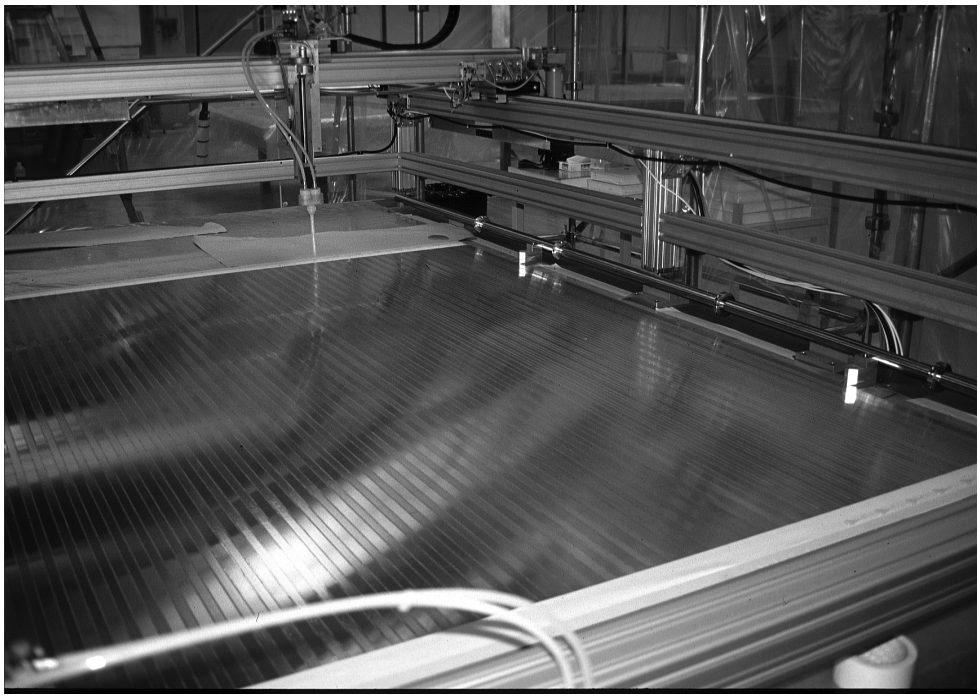


Fig. 3.2.34: Laying of glue lines prior to gluing the I-beams.



Fig. 3.2.35: Insertion of the end-plugs into the tool before gluing.



Fig. 3.2.36: 3D precision measurement of the tool for the end-plug gluing.

Once all the end-plugs of a row are inserted into the tool, it is moved by the crane onto the assembly table and positioned with respect to the “standard” reference points. The bar is then lowered until the end-plugs are in contact with the fast drying Araldite glue that was previously placed on the aluminum plate. The choice of using fast Araldite for this part is probably valid only for this prototype since during the mass production the end plugs will be glued most likely at the same time as the I-beams and hence with the same glue. After a few minutes, the glue is cured and the jig can be removed, leaving a side of one layer completely equipped with end-plugs. This procedure is repeated on the opposite side of the plate and then the layer is ready for the mounting of the wires. The time needed for the end-plug gluing for one MB96 layer is about one hour using the same tooling for both ends.

The wiring of the layer is done manually by two operators. Each of them inserts the crimping block (that has the wire already crimped in it) inside the second plastic end-plug (wire holder) that is then placed between two adjacent glued end-plugs. The operation is very fast and after about half an hour one MB96 layer is wired. At this point, before closing the layer with the second Al plate, a few steps still must be taken, namely:

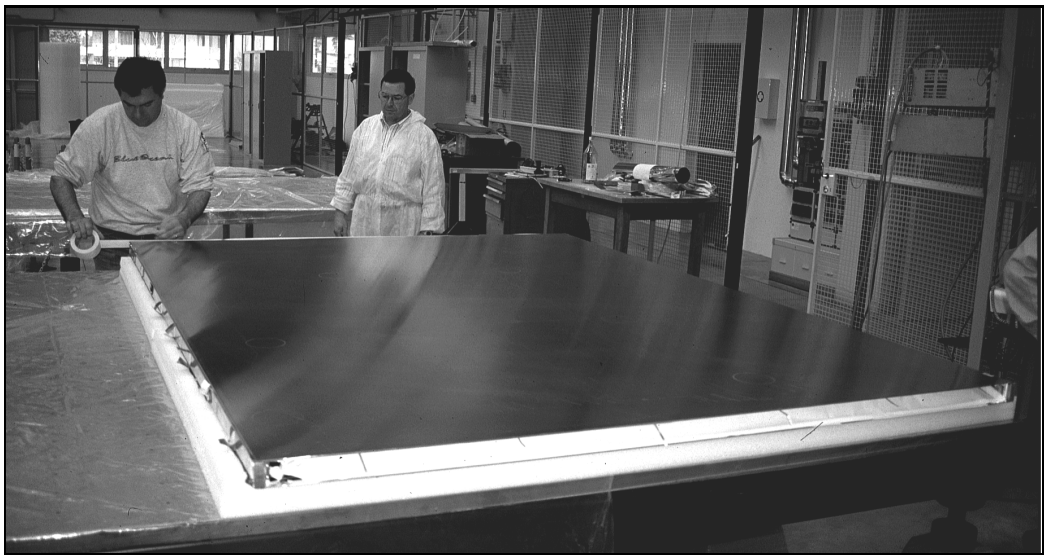


Fig. 3.2.37: Finished Super Layer ready to be equipped with electronics.

1) insertion of the HV contact for the I-beam through the glued end-plugs;
2) checking the mechanical tension of the wire;
3) checking the HV contact of the field-shaping strips;
4) measuring the wire position;
5) point-welding the ground straps.

Having performed all the steps described so far, one has finished one complete layer. At this point, one can close it by gluing (with the same procedure described above) the next Al plate that will be the cover for the first layer and the beginning of the second one. The procedure is then repeated until all the aluminum plates are glued except one.

Before gluing the last Al plate and hence closing the Super Layer, one must glue on some machined aluminum pieces that will be the corner blocks for the gas-tight box, and that are

positioned at known coordinates with respect to the wires. These will be the reference marks for any external measurement of the wire position. Together with the corner blocks the profiles closing laterally the gas volume are also glued on.

After this, the last aluminum plate can be glued and the Super Layer is mechanically ready (Fig. 3.2.37) to be moved to a different table where the necessary work to finish it starts. At the same time on the assembly table the construction of a new Super Layer can begin. The transport of the complete Super Layer from one table to another is done, as can be seen in Fig. 3.2.38, with the same tool used to transport the individual aluminum plates.

The last part of the assembly work for a quadruplet consists first in gluing on the front cover frame, then installing the boards housing the HV and test pulse distribution systems, the HV decoupling capacitors and the front-end amplifiers plus discriminators and finally making the last ground connections. Once this is done, the SL can be closed with the front plate which is equipped with feedthroughs for HV connection, gas inlet and outlet and digital signal output. At this point, the Super Layer is a self-standing chamber and can be fully tested under HV before being integrated into the final chamber body.

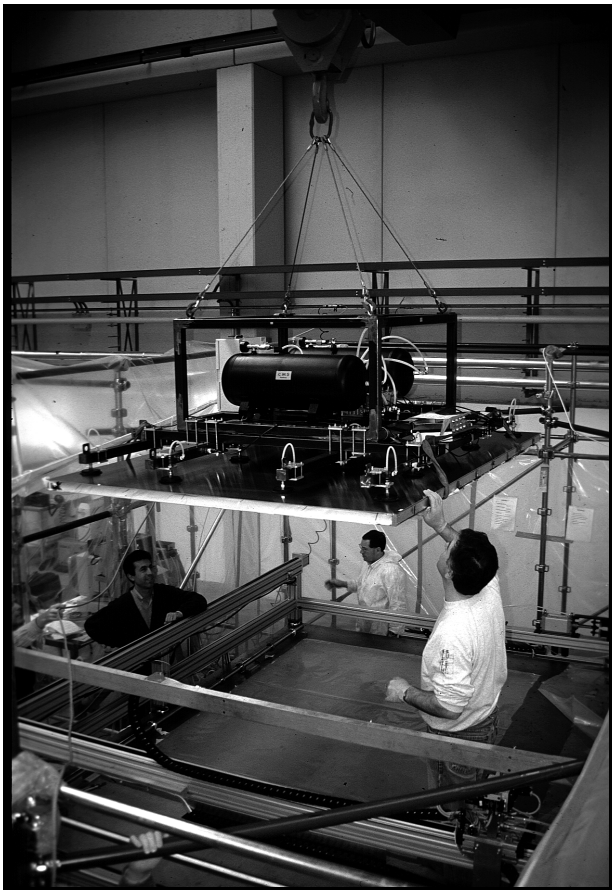


Fig. 3.2.38: Transportation of a finished SL from the assembly table.

3.2.7.6 Chamber assembly

The final part of a chamber construction consists of the assembly of the three SL and the honeycomb backbone to form a single body. As we have seen, the SL must be glued together to within ± 0.5 mm of their nominal position.

The procedure used to assemble the chamber is similar to the construction of the individual SL, namely:

1) the first SL is brought to the assembly table and fixed with respect to the reference points. The flatness of the SL is guaranteed by the precision of the table;
2) glue is laid, by means of the same moving head, to form many lines. These are spaced in such a way as to result, after being pressed, in a continuous layer of glue 0.1 ± 0.05 mm thick;
3) the second SL is brought with the crane and lowered onto the first one. During this operation, the SL is guided by rollers in order to be in the correct position;
4) sequence 1 to 3 is repeated until the chamber is finished.

The completed chamber MB96 is shown in Fig. 3.2.39.

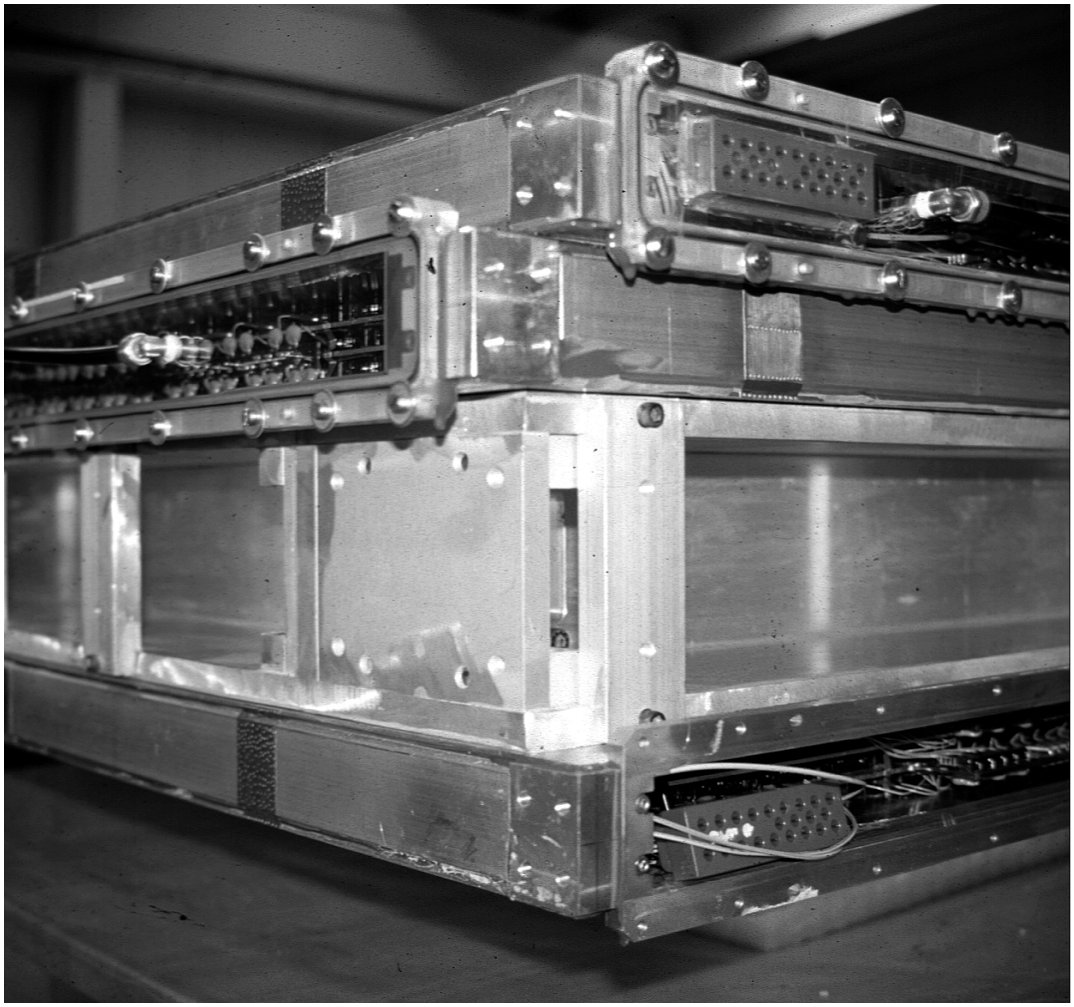


Fig. 3.2.39: Full-size prototype showing details of the three assembled SL's.

3.2.7.7 Mechanical tolerances achieved

The procedure described above was used, as we have seen, to build the first "final" MB1 prototype in order to check whether the most important mechanical tolerances required by the design were kept, namely:

1) wire positioning within ± 0.1 mm horizontally;
2) the thickness of a complete SL within ± 0.2 mm and ± 0.45 mm for the entire chamber;
3) hardware positioning of the three SL one with respect to the other to ± 0.5 mm;
4) gas tightness resulting in an oxygen concentration below 500 ppm at the chamber outlet with a flow corresponding to one volume change per day.

These requirements were checked during and after the MB96 construction. The wire positioning was measured with a tool (see Fig. 3.2.40) that can be positioned on the assembly table in defined positions with respect to the references and that holds a CCD camera. By reading the position of the computer-controlled camera one could measure the coordinate across a layer by means of an optical bar (resolution around 0.01 mm) and the vertical coordinate from the readout of a stepping motor (resolution about 0.1 mm). The wire position for all cells of the MB96 chamber with respect to their nominal position is shown in Fig. 3.2.41, after applying corrections for temperature difference between measurements. About 95% are within the desired tolerance. The measured position can also be used in later event reconstruction.

The thicknesses of the three SL were measured by means of comparators and found to be within ± 0.2 mm. Even more satisfactory was the fact that the complete chamber thickness, after about 50 superimposed glue joints, was measured to be within ± 0.45 mm of the nominal thickness.

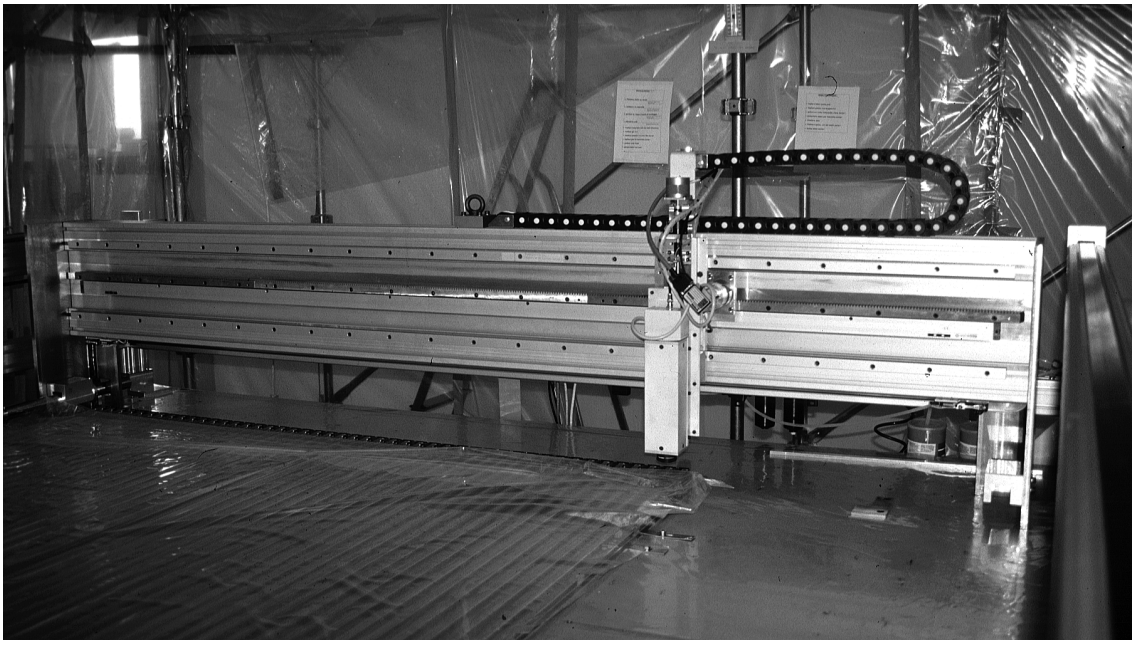


Fig. 3.2.40: Wire-measuring tool.

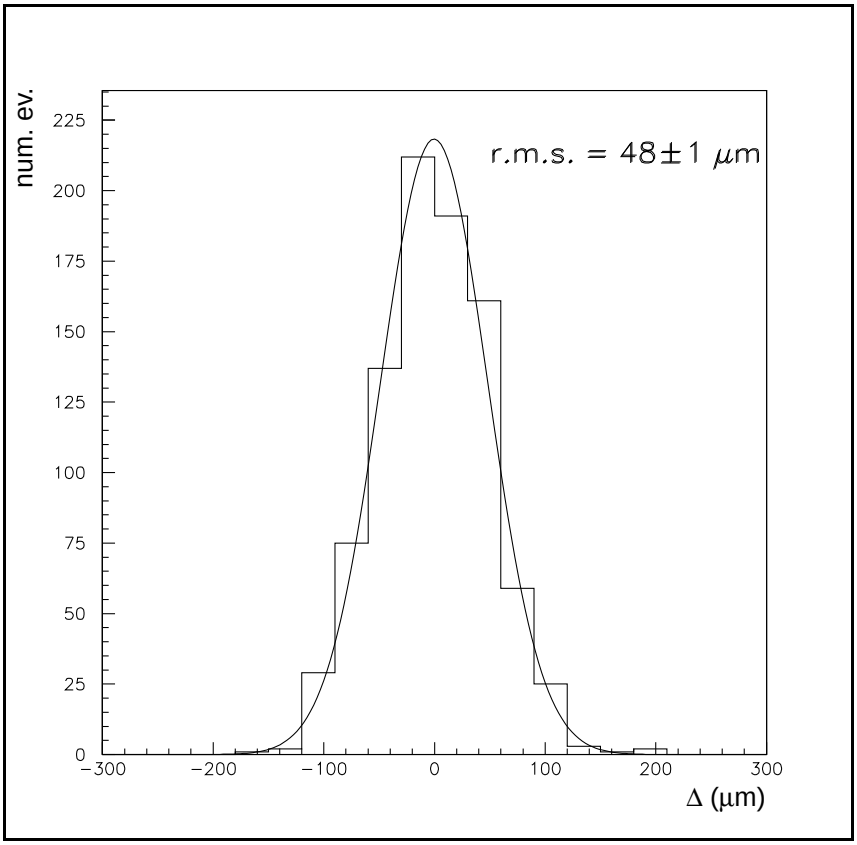


Fig. 3.2.41: Measured wire positions with respect to their nominal coordinate.

The SL were glued one with respect to the other to within 0.1 mm of their nominal positions by using the relatively simple tool described earlier.

Finally, by flushing the chamber with a flow corresponding to a volume change every two days (i.e. about a factor two smaller than what is planned for the experiment), the oxygen contamination was measured to be about 30 ppm downstream of the three SL which were serially connected to the gas supply.

3.2.8 Quality control

As for all detectors used in particle physics, the production of the chambers described in this document will be done in institutions where the manpower might have vastly different work experiences.

Moreover, the chambers, as we have seen, will be assembled by successive gluings and hence inner parts of them will very rapidly become inaccessible. Finally, once installed, the access for maintenance and repair will be at best problematic.

All these considerations, which are quite standard for present-day detectors, call for a well thought-out effort of quality control at each stage of the construction in order to have a product quality that is constant and acceptable, be able to spot possible problems at the earliest moment and save precious work and materials.

We will give here a complete list of the checks that will be performed at various stages in order to guarantee that the final product is within specs. They are :

- ∑ I-beams - Lexan preparation: the sandwich consisting of Lexan -I beam - Lexan is a structural element of the chamber and half of the glue joints contributing to the total thickness of the chamber are in these pieces. It is therefore very important that the gluing is checked by measuring, for each finished piece, the total thickness. Since these pieces are not only structural but also electrical elements of the cells, they must be tested with HV in order to spot possible defects in the Lexan insulator. This test is very important since the presence of a sparking I-beam in a layer will result in at least two adjacent dead cells with no possibility of recovery. For the time being, the test is performed in air at twice the nominal voltage, to account for the different electrical strength in air and in the Ar - CO_2 gas mixture.
- ∑ gluing of field shaping strips: as in the previous case, the quality checks performed verify two different aspects: the mechanical and the HV behavior. For the first, the position of each strip is measured in order to correct possible mistakes. After this and having properly terminated the ends of each strip, a HV test (again in air at a voltage roughly twice the working one) is performed. It must be stressed again that the purpose is to spot a problem prior to the use of the plates since a sparking strip inside a finished layer will result in at least one dead cell, with no possibility of repair.
- ∑ wires: the position of each wire is measured with the tool already described. Then, the mechanical tension of each wire is measured by applying a varying HV which excites a resonance mode. The method works well and has the advantage that one can at any time check whether or not a wire is loose. The results obtained for the MB96 prototype are shown in Fig.3.2.42 for the first 250 wires; the jump in wire tension coincides with a small change in the mechanics of the crimping machine which resulted in a slightly higher tension. We did not check the HV behavior of each wire during the production phase, but it is still not clear whether such a test should be incorporated in the final list of checks. For instance, in the production of the 3 x 1 m^2 chamber, we set the covering aluminum plate in place (without glue) and made a HV test. This still allows for an intervention in case of problems.
- ∑ strip contacts: the field-shaping strips are connected to the HV by means of a metallic strip inserted inside the plastic end-plug holding the wire. The plug touches the upper and the lower strip of each cell at the same time. In order to minimize the probability that this spring-like contact does not touch one of the strips, both end-plugs in the same cell are equipped with the contact, even though the HV is connected only at one end. Nevertheless, it could be that a cell has one strip which is not connected to HV. In order to spot this, the capacitance with respect to ground of all strips is measured. The method is very fast and capable of spotting the problem. In Fig. 3.2.43, the result for a sample of strips is shown; the distribution is very narrow and the presence of a value roughly half of the standard one would be easily recognized, as demonstrated in the same figure where for cell 41 one of the two strips was insulated on purpose before the check.
- ∑ general checks: finally checks more related to the chamber mechanics are performed such as verifying the various thicknesses and that the gas tightness is within acceptable limits.

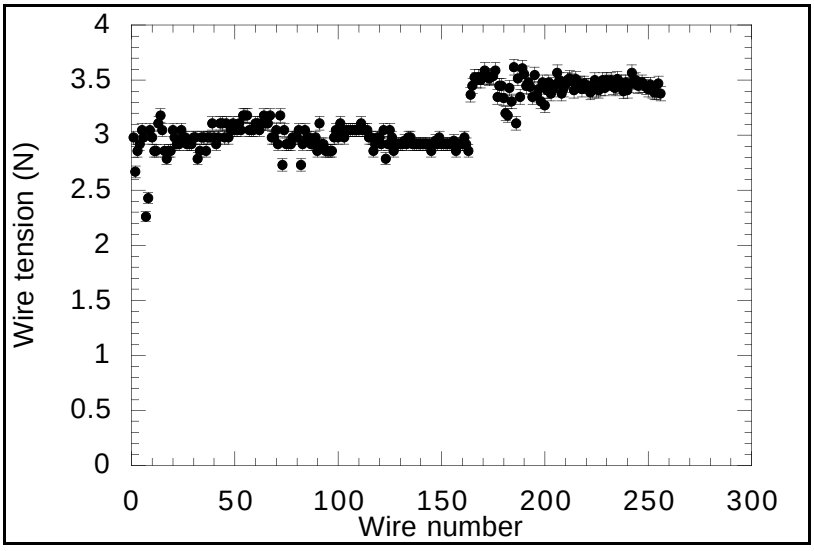


Fig. 3.2.42: Measured wire tension for some of the wires installed in the full-size prototype. The nominal value is 3 N.

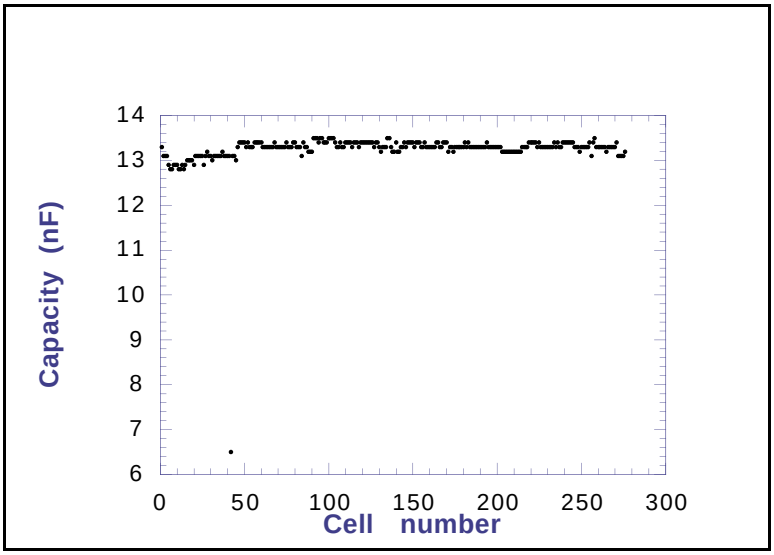


Fig. 3.2.43: Measured strip capacitance. One of the two strips of cell 41 was insulated on purpose to verify the procedure.

3.2.9 Detailed station design

The barrel chambers are distributed inside the five wheels of the barrel yoke. The wheels are movable along the beam line direction for detector access and maintenance. This requires that there not be any electrical or service connections from wheel to wheel. The wheels and not the stations, as in the endcaps, are the functionally-independent sub units of the barrel muon detector. With reference to Fig. 1.1.3, the wheels are numbered as 0, +-1, +-2 following their position along the CMS Z axis. Each wheel houses four concentric layers of DT chambers (Fig.3.1.1). Starting from the innermost one, they are named MB1, MB2, MB3 and MB4. Two RPC chambers sandwich each DT chamber in layers 1 and 2, one RPC chamber is

coupled to the inner side of each DT chamber of layers 3 and 4. The MB2 and MB3 chambers are supported by precision rails bolted to the iron ribs that separate the three iron rings of the wheels. To support the MB1 and MB4 chambers, special ribs are soldered to the inner face of the first iron ring and to the outer face of the third. The ribs are staggered in F to avoid an overlap of dead regions. Three special sliding blocks connect the chamber to the rails: two of them slide on one rail and the third on the other in order to have the chamber isostatically fixed to the iron at three points. A 1 cm clearance separates the detectors' outer surfaces from the wheel plates after insertion. This requires the positioning of the supporting rails to the iron to be within 1 mm of their nominal position. No adjustment in this positioning is planned.

The DT and RPC chambers are inserted as a single body during the detector assembly in the surface hall and can be extracted for maintenance during breaks in the detector operation. Once in position, the RPC will be fixed independently of the DT chambers. The insertion/extraction operation will be done only from the outer faces, the ones at larger Z, for wheels 1 and 2. In the central wheel, the insertion direction is different for the different sectors. Insertion is along the positive Z direction for sectors: 1, 4, 5, 8, 9, 12 and along the opposite direction for sectors: 2, 3, 6, 7, 10, 11. The insertion face must be kept clear of non-movable cables and services for which room is allotted on the opposite face. The side of the chamber housing the F front-end electronics (and the full readout and trigger electronics in the onboard option) will be visible on the insertion face of the wheel. This facilitates the access for maintenance and, being at larger Z, offers the possibility of partial compensation of the different times of flight of particles due to the propagation time of the signal along the wire toward the front-end amplifier.

Each wheel will have an independent cooling circuit and gas system, the main distribution point being probably on one of the two wheel feet. The readout and trigger electronics, the HV and LV supplies and the local Slow Control system for the chambers of each wheel are housed inside crates inserted in four pairs of racks fixed to the four balconies (visible in Fig.3.6.3 a) and b)) and movable with the wheel itself. Each balcony houses the services of three consecutive sectors of the wheel. For alignment purposes, fiducial marks and LEDs are fixed to the chambers and viewed by CCD cameras sitting on special rigid, radial structures (MABs) which are isostatically fixed to the iron wheels 1 and 2 (see Sec. 7.2). The appropriate MAB fixed to the insertion face of a wheel must be removed to access the front-end electronics or to extract a chamber.

3.2.10 Integration with RPCs

The DT chambers will be inserted in the experiment inside "pockets" in the iron structure. The same pockets will also house the RPC chambers which are described in detail in chapter 5 of this TDR. It is evident that there could be interference between these two detectors and a strategy for their mechanical integration must be worked out.

The current working hypothesis considers the DT chamber body as not sufficiently robust enough to support the extra weight of the RPC chambers without being appreciably deformed. The assumption here is that the RPC chamber body is a mechanically rigid body and it is hence sufficient to connect its side supports to the DT chamber borders near the chamber supporting rails.

It is planned that before installation the DT chamber is also equipped with the RPC (one RPC layer in stations 3 and 4 and two, on both sides of the corresponding DT chamber, in stations 1 and 2) and this body is then inserted as a whole into the apparatus. This plan must still be verified in terms of possible losses in the DT chamber's acceptance, and the mechanical rigidity of the entire structure must be verified both with prototypes and with FEA calculations. It is nevertheless the simplest and most natural solution that reduces the need for rails and other installation structures.

It is evident that this scheme forces the production schedules of the DT chambers and RPC to be well matched so that the chambers which must be connected together for the installation are ready at the same time.

Finally, the thermal interference between the two detectors sitting very closely together coming from any internal sources which are not well cooled must be carefully studied. In the final location of the detectors, the thermal dissipation to air is very limited and hence heat-producing element which are not properly cooled will heat up the detectors, giving rise to undesired losses in position accuracy (due to thermal distortions) and stresses on the mechanical structure.

3.2.11 Electrical layout and grounding

Our experience in equipping previous chamber prototypes led to some conclusions: a) the location of the front-end electronics inside the gas enclosure results in a reduction in connection complexity, dead space, noise and crosstalk; b) the internal HV distribution system and the front-end electronics should be separated in the two opposite enclosures of the SL in order to separate insulation problems, resulting in better use of space and dead space reduction; c) the chamber body acts as a unique ground reference for signals and the HV; d) the tolerances in the position of the pin-connections of the cell electrodes are not compatible with a monolithic plug-in structure for both the HV distribution and F.E. circuits. They are therefore connected to the electrodes via short wires.

3.2.11.1 High voltage enclosure layout

The HV distribution is based on six-layer PCBs, each one servicing 16 DT cells: 2x8 in two adjacent planes of a SL. Each PCB layer feeds the HV to one type of electrode (cathodes, strips or wires) of the eight cells of a plane. The voltages are distributed via 50 MΩ hybrid resistors: one resistor per wire and one resistor per two strip pairs or cathodes. Each layer of the PCB is powered by a separate input line so that any fault will affect only the cells of one plane of a SL. A distributed ground surrounds all connections in the different layers, which are also staggered to avoid crosstalk among the various electrode connections. The connections to the cell electrodes are made, in the present prototypes, with short wires (3.5 cm) terminating at the appropriate contact. These wires are carefully positioned in front of their respective cell electrodes to avoid criss crosses and cabling mistakes. The PCB is positioned and fixed to the aluminum plate between layers by means of three strong spring-contacts which act as mechanical support and ground connection at the same time. Each PCB is isolated with an appropriate HV insulating varnish; tests are planned to check for possible outgassing. HV inputs of the PCBs can be daisy-chained and the actual number of cells powered by a single primary line will depend on the segmentation in the HV distribution tree. The segmentation implemented in the MB96 chamber has one primary strip or cathode line per half plane of a SL and a primary line for every eight wires (two per PCB). Figure 3.2.44 a) shows the connection

of the HV PCBs, while Fig. 3.2.44 b) depicts the cross section of the two PCBs connected to the aluminum plates and to the cell electrodes.

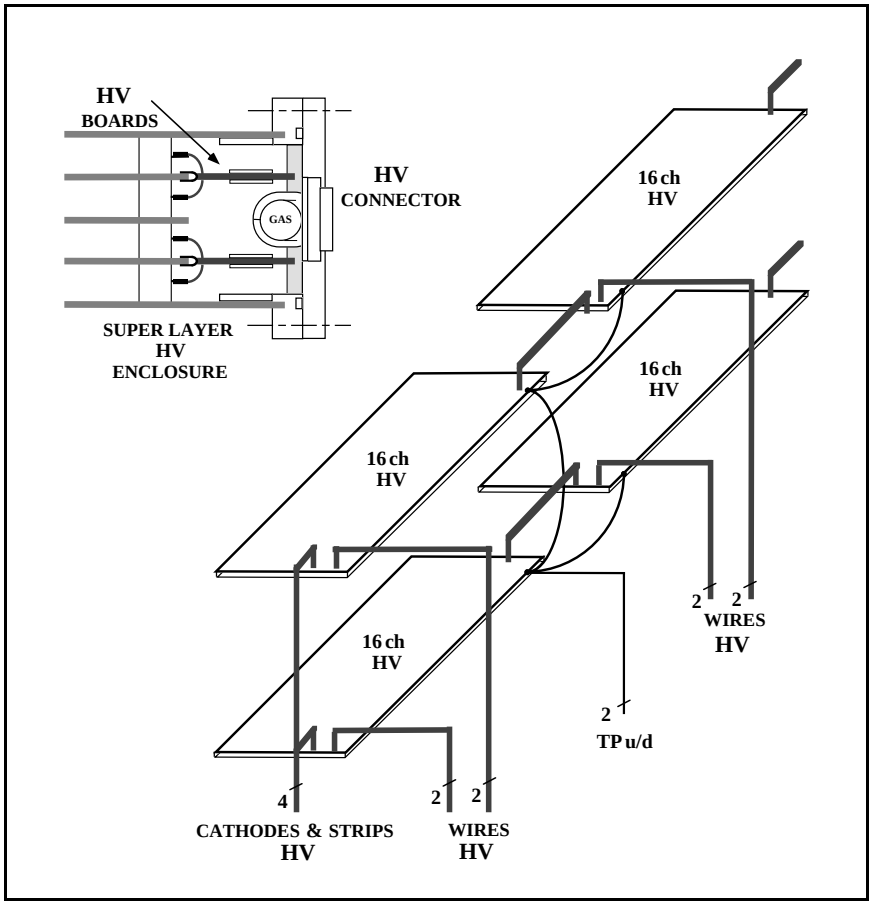


Fig. 3.2.44 a): Layout of the gas enclosure of a Super Layer at the HV side.

An additional important feature of the HV PCBs is the Test-Pulse system: on each board, two strip-lines are embedded and AC coupled to the wire connections of one cell plane (TP up to the eight upper cells, TP down to the lower eight ones). The coupling is realized via one pad per wire with a capacitance of 1pF. The two strips can be operated independently by injecting voltages of variable amplitude. As shown in Fig. 3.2.44 a), four PCBs are connected to several TP lines: an external fan-out circuit is needed to operate the TP lines of all the PCBs. The cover of the enclosure supports two HV input connectors and the gas collector pipe. All I/O connections to the enclosure pass through gas-tight connectors in the cover.

3.2.11.2 Front end enclosure layout

With reference to Fig. 3.2.44 a) and b), in each SL the Front End circuitry is located in the opposite side enclosure of each SL from the HV distribution. FEs are grouped in PCBs servicing 16 channels (four channels by four layers of the SL). Simple boards supporting HV decoupling capacitors interface the wire pins to the FE boards. These decoupling boards are connected to the anode wires via short connections (3.5 cm) terminated with 1 mm diameter insulated contacts, and are positioned and fixed to the central aluminum plate by means of two strong spring-contacts acting as both mechanical support and ground connection. FE PCBs

connect to the decoupling board via strips of contacts guided by slightly longer leads. The FE board is a multilayer PCB where input and output lines are kept on different layers separated by a ground plane in order to avoid any input/output crosstalk. The crosstalk among input lines is kept under control by the distributed ground. The differential outputs of each PCB are fed via a short flat cable to a gas-tight connector on the cover of the enclosure. Besides the Front End chips the PCBs will also accommodate a temperature sensor and trimming circuits for the threshold. A common threshold line is daisy chained to all the FE PCBs in a SL. Independent threshold values can be assigned to the SL of a chamber; equalization among channels may be adjusted with four-channel granularity (four chips) at installation time. Two lines, CK and R/W, are common to all the PCBs in a SL and are dedicated to control the programming of the internal masks of the Front Ends. Four T lines collect temperature information from four PCBs along the enclosure.

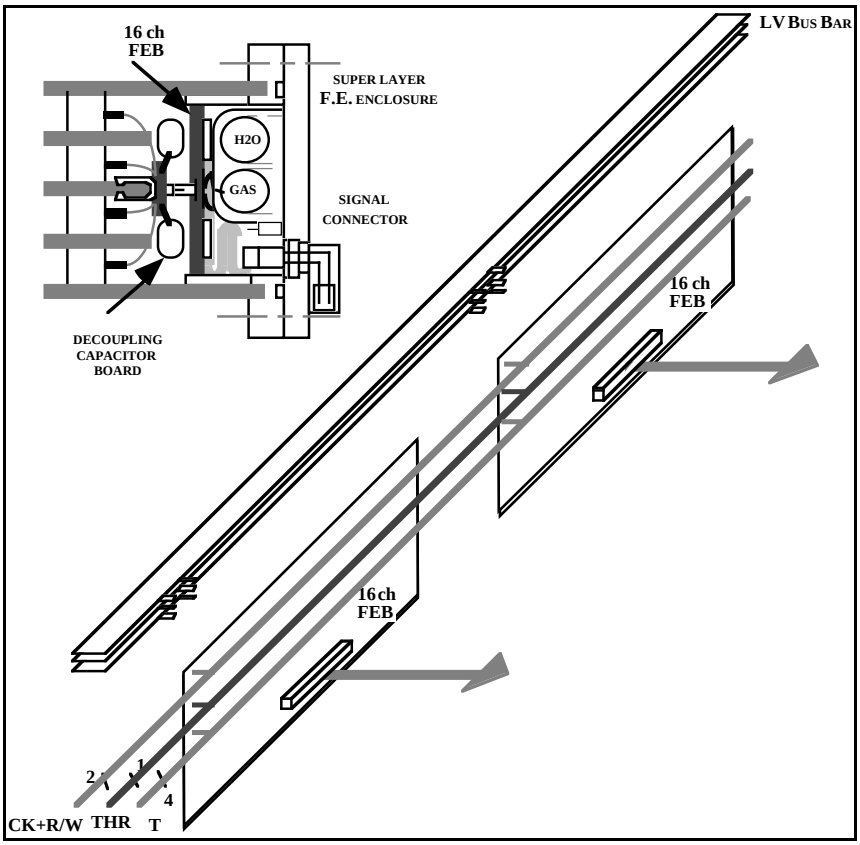


Fig. 3.2.44 b): Layout of the gas enclosure of a Super Layer at the front-end side.

The power dissipation of the FEs is less than 50 mW per channel, i.e. 0.8 W per PCB. In order to dissipate the heat produced on the board and prevent it from flowing towards the cells, a copper spring is soldered to the ground plane along the central axis of the PCB just on the opposite side and in correspondence to the pinstrip connection for the decoupling board. The copper spring touches the cover of the enclosure when this is closed, thus conveying the heat towards the outside. The aluminum cover will contain two pipes: one for the cooling water (thermally connected with the gas enclosure) and the other one conveying the gas mixture through tiny holes pierced along the length of the pipe.

Each PCB will be protected by a fuse on the incoming LV power lines. A bus bar distributes the +5 V, +2.5 V and GND to the PCBs. All control and monitor lines like CK, R/W, THR (Threshold) and T (Temperature) are connected to the Chamber Control Board. All I/O connections to the enclosure pass through gas-tight connectors in the cover.

3.2.11.3 Grounding

The reference potential of all the signals and power lines should be the chamber body itself. The chamber must be properly connected to the iron yoke to which it is mechanically attached. All the glued elements of the chamber, like the aluminum plates, frames and covers, are connected to each other by means of point-welded copper strips at distances no longer than ~30 cm so that the chamber body is as much as possible a true ground cage.

3.3 FRONT END ELECTRONICS

3.3.1 General

The front-end electronics for the barrel muon detector must satisfy many stringent requirements. Its basic functions are to amplify the signals coming from the detector, compare them in the fastest way with a threshold and send the result as a logic signal to the trigger and readout chains using twisted-pair cables.

The analog part (the amplifier) must exhibit low noise in order to allow operation of the drift tubes at low gain, which is advisable for reasons of reliability and chamber lifetime, together with a fast shaping time to avoid degradation in spatial resolution.

The comparator has to be very fast and precise in order to have a time response independent of the amplitude of the signals and to keep good uniformity among the channels, especially at the low threshold values where it is supposed to operate. The cable driver should not reduce the overall performance.

The possibility to mask off single channels has to be implemented in order to preserve downstream electronics from undesirable noise. All of the above characteristics are subject to the main constraints of little space, minimum power consumption and affordable cost.

A prototype two channel ASIC has been produced using AMS 1.2 μm BiCMOS technology. Each channel consists of a charge preamplifier followed by a precision discriminator and a pulse stretcher capable of driving long twisted-pair cables. The block diagram of the chip is shown in Figure 3.3.1. The chip was used in the test beam and some results have been shown in sect. 3.2.3.

Two other types of front end circuits [3.11] have been used in tests. Each one partially fulfilled the above requirements. To entirely meet our specifications, the BiCMOS ASIC was chosen as the baseline.

3.3.2 Circuit description

The preamplifier is of the charge sensitive input type with a designed decay time constant of 50 ns and a sensitivity of 2 mV/fC (δ-function input). Simulations give a noise of about 1000 electrons r.m.s. at zero detector capacitance with a slope of 50 electrons/pF (BW=500 MHz). It employs a mixed folded-unfolded cascode circuit with GBW=1 GHz (simulation), followed by an emitter-follower that drives the output pad for a total of 4 mW

occurs with 1 pC signals, while the input impedance of 180 Ω is close to the drift tube characteristic impedance of about 300 Ω.

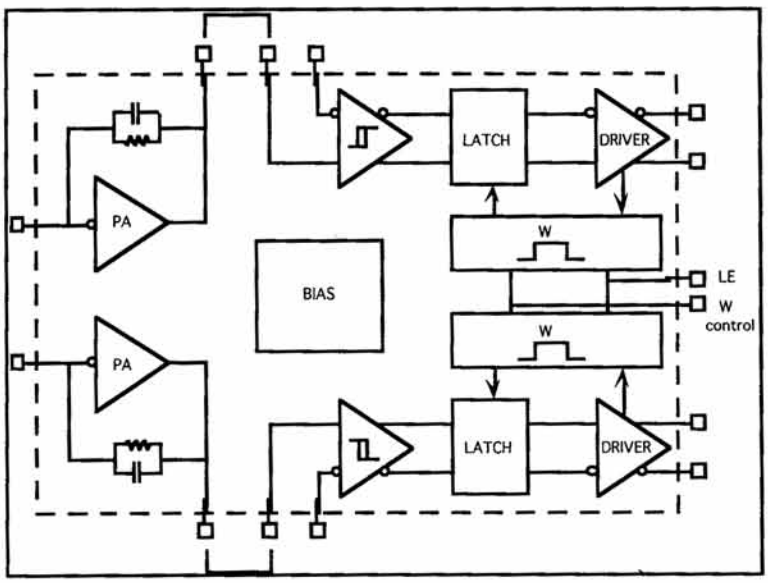


Fig. 3.3.1: Block diagram of the ASIC prototype

The discriminator design includes a latch and a hysteresis network to prevent noise retriggering. The output is level-translated to feed the cable driver which is a low-power, differential one: it works from a 2.5 V supply and drives a 50+50 Ω ground-referenced load to a level of 300+300 mV, while consuming less than 20 mW. One tap in the driver triggers a one-shot that, when active, enables the latch in order to detect short pulses from the discriminator when the input is just over threshold. The circuit then stretches the output in such a way as to overcome the bandwidth limitation of the long cables. This "capture" function is externally enabled by a voltage level applied to one pin, and the duration of the one-shot pulse is programmable in the range 20-150 ns by means of an external analog level.

3.3.3. Bench Tests

A total of 80 prototype ASIC's have been produced in two different Multi Project Wafer runs with resistor values differing by a factor of two, much more than the maximum process tolerance, resulting in a power consumption of 30 and 40 mW per channel. The yield was higher than 80%. We ordered untested chips and all working parts have been tested in detail: the results are shown in Table 3.3.1.

The preamplifier performance agrees very well with the simulations. The sensitivity was measured to be 2.1 mV/fC on average at zero detector capacitance and the slewing rate about 400 V/μs. Input impedance in the range 3 MHz - 300 MHz is adequate for our purposes since the drift tubes are connected via 470 pF capacitors whose reactance dominates at lower frequencies.

The rest of the chain, the discriminator, the one-shot and the output driver have also been tested with respect to supply and temperature variations and have shown very good

performance in their DC and AC characteristics. The most important results are listed in Table 3.3.1.

Table 3.3.1
Main characteristics of the ASIC prototype.

CHIP VERSION		30 mW	40 mW	Units
preamp.	ENC	1000+40·C_D(pF)	1150+34·C_D(pF)	e^-
preamp.	rise time	3.5 +0.3·C_D(pF)	3.0 + 0.2·C_D(pF)	ns
preamp.	Z_{in}	180	130	Ω
discrim.	offset	0 ± 0.9 max	0 ± 0.9 max	mV
discrim.	hysteresis	2.4 ± 0.4 max	2.4 ± 0.4 max	mV
discrim.	V_{cm}	1 - 3.8	1 - 3.8	V
discrim.	t_{pd}	3.3 ± 0.4 max	3.0 ± 0.4 max	ns
discrim. t_r (in=1mV/μs)		3.0 ± 0.3 max	2.7 ± 0.2 max	ns
discrim. t_r (in=10mV/ns)		2.8 ± 0.3 max	2.5 ± 0.2 max	ns
discrim. bandwidth		150	190	MHz
discrim. min input width		4	3	ns
one-shot dead time		15	12	ns

From data on the discriminator offset and hysteresis, threshold variation among different channels can be calculated. The maximum variation is ±0.6 fC when the preamplifier is AC coupled to the input of the discriminator. This connection has been used with the 30 mW ASIC version equipping a small prototype muon chamber, which was exposed to a test beam and successfully worked at a threshold of 2.5 fC.

Another important characteristic of the entire chain is the time walk or the difference in time response to different input levels. We have measured less than 2 ns difference when varying the input charge in the range 2.5 fC to 1 pC, while keeping a constant threshold of 2 fC. Such a value is not expected to change appreciably if the threshold is raised by a factor ~ 2.

3.3.4 Future developments

Tests performed on this chip confirm that our basic requirements are already satisfied, while also suggesting the most useful improvements one can implement in the next version. The next generation chip has been already designed and ordered using 0.8 μm BiCMOS technology. The smaller scale technology will increase the performance/power ratio and will also improve the matching of components critical for the offset. In this way, it has been possible to include a baseline restorer without significant degradation in precision and noise, thus allowing a DC connection between the discriminator and the amplification sections. The amplifier could also include the cancellation of the signal tail produced by the slow ion drift and of some kind of shaping, although the particle rate foreseen in the experiment does not make this mandatory.

Another improvement in the design has been to make the output driver compatible with the LVDS standard so as to use a commercial component or a standard cell at the receiving end of the cable. This could also reduce the power consumption for this stage.

The next step will be to integrate four channels into one chip, a number that better suits the detector geometry, and include in the chip a mask register to suppress noisy channels.

3.4 READOUT AND TRIGGER ELECTRONICS

The trigger and readout electronics are integrated in a complex system, sharing wire chamber signals, Timing and Trigger Control (TTC), power supplies, cooling and mechanics. The block structure of the chamber electronics is shown in Figure 3.4.1.

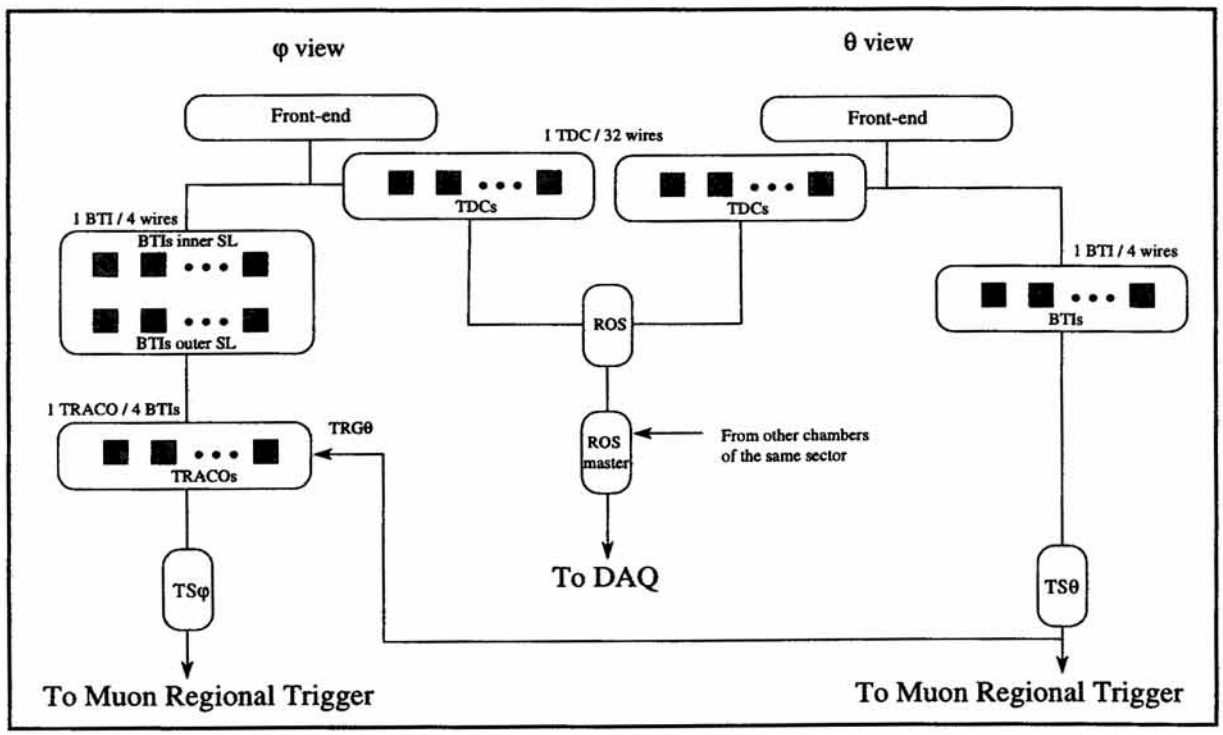


Fig. 3.4.1: Block scheme of the DT chamber electronics.

3.4.1 Readout electronics

3.4.1.1 Overview

The system is basically composed of readout boards (ROB) and readout servers (ROS and ROS Master). All these units are housed in crates which are placed in racks on the balconies. A block diagram of the system is shown in Fig. 3.4.2.

3.4.1.2 Front-end signals and cables

The front-end electronics, placed inside the gas volume, will provide discriminated differential signals at a feed-through connector grouping 16 channels together. These signals will be taken to the Read Out Boards (ROBs) by a 25 m twisted-pair cable.

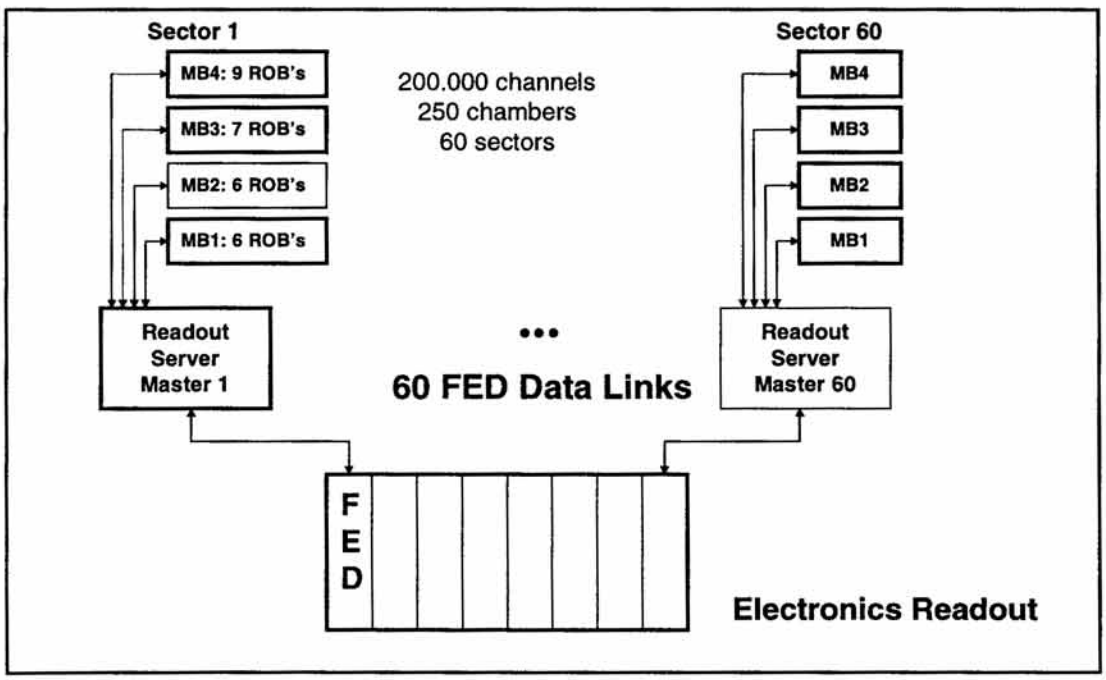


Fig. 3.4.2: Block diagram of the readout electronics.

3.4.1.3 ROB

Each ROB will have four 32-channel TDC circuits and will receive up to 128 differential signals from the FE. (Fig. 3.4.3). These signals, presumably LVDS, will be converted by 32 4-channel differential line receivers and sent to the TDCs.

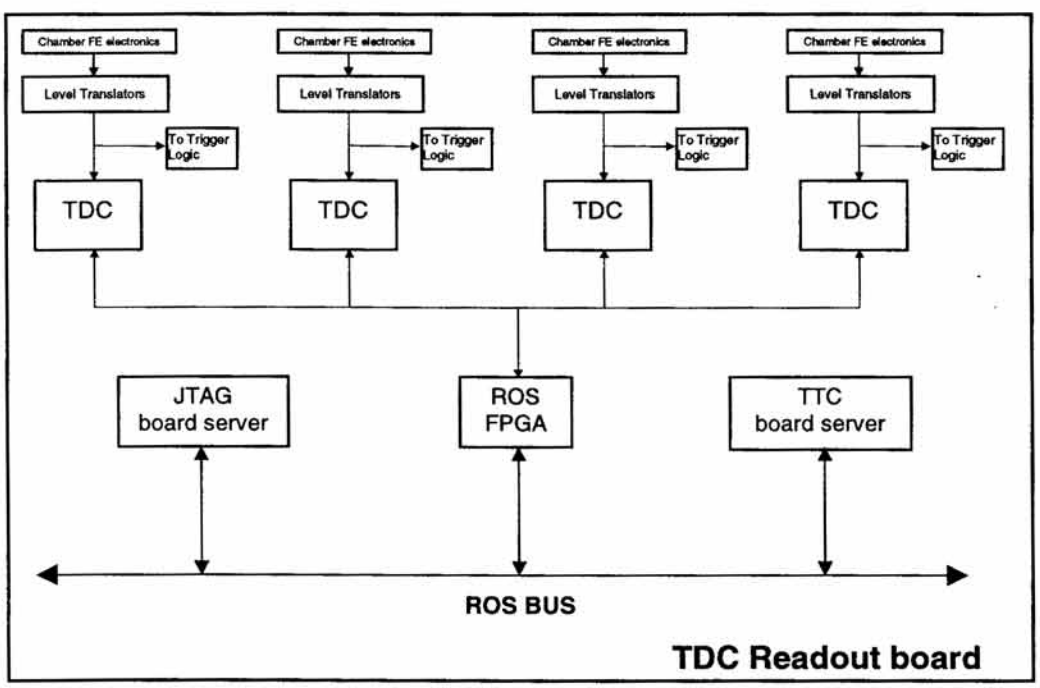


Fig. 3.4.3: Block diagram of the TDC readout board.

In order to simplify the overall electronics design and minimize the number of components, converted signals are also sent to the trigger logic which is placed nearby.

At present, our interest is focused on the "32-channel general purpose TDC" developed by the CERN-Microelectronics Group. It is a good candidate to populate the 1680 ROBs required for the readout system.

This a highly programmable 32 channel TDC based on the Delay Locked Loop (DLL) principle. It has a time bin of 0.78 ns at 40 MHz, with a dynamic range of 21 bits. Each channel consists of two time registers where measurements are stored until they can be written into a common on-chip 256-word deep event buffer. With this mechanism, the two-pulse resolution is 15 ns. A trigger-matching function selects hits related to a given trigger, i.e. hits located within a time window, which is programmable to accommodate the maximum drift time. Overlapping trigger are also supported. As a hit may belong to several closely spaced triggers (it falls inside several trigger windows), a fast and efficient search mechanism, which takes this fact into consideration, has been implemented as two search pointers and two programmable pointer windows. After trigger matching, data are passed to a 32 words deep readout FIFO. In this way one event can be read out while another is being processed by the trigger matching. Readout of data is performed via a synchronous bus, which can be shared by several TDCs [3.12].

In addition, ROBs will receive signals from the TTC (clock, trigger, BC counter reset, etc.), and from the control (TDC configuration, channel masks, status query, etc.).

3.4.1.4 ROS

After digitization, data are collected by one dedicated ROS per chamber, and sent to its corresponding ROS Master in one data block per trigger.

3.4.1.5 ROS master

Each ROS master receives data from the ROS servers corresponding to one sector (four chambers). Data belonging to one event will be packed in one data block and sent to a FED. An optical data link connects each ROS master to its corresponding FED. The required bandwidth of this link is 80 Mbytes/s.

3.4.1.6 TDC measurements

Several tests have been performed on the 32 channel TDCs, namely:

- time resolution
- linearity
- cross talk
- double hit resolution
- radiation tolerance

Also a set of necessary capabilities have been checked:

- overlapping triggers
- programmable trigger window
- programmable trigger latency
- raw data readout
- multi chip readout
- JTAG programmability
- channel masking.

For all time measurements a pattern generator has been used (Tektronix DG2020, clock jitter ≤ 50 ps). An example of this test is presented in Fig. 3.4.4, in which a hit is delayed in steps of 100 ps. The time measured, the time error and the corresponding histogram are shown.

3.4.1.7 Operation

The design parameters of the readout system are:

- trigger rate ≅ 100 KHz
- track rate ≅ 1 track / cm^2 / s.

Since each track can produce up to 48 hits (i.e. one per layer), and each hit needs 3 bytes, an estimated event size of the order of 4 kbytes is expected, corresponding to 30 tracks per event with a sector cross section of 5 m^2.

A TDC channel will provide a datum whenever there is a hit on its corresponding wire within the trigger window. At the reception of a trigger, all data available from the four TDC devices placed in every ROB will be sent to the corresponding chamber server (ROS). At each ROS, data will be packed in one data block and sent to the corresponding ROS Master (one per sector).

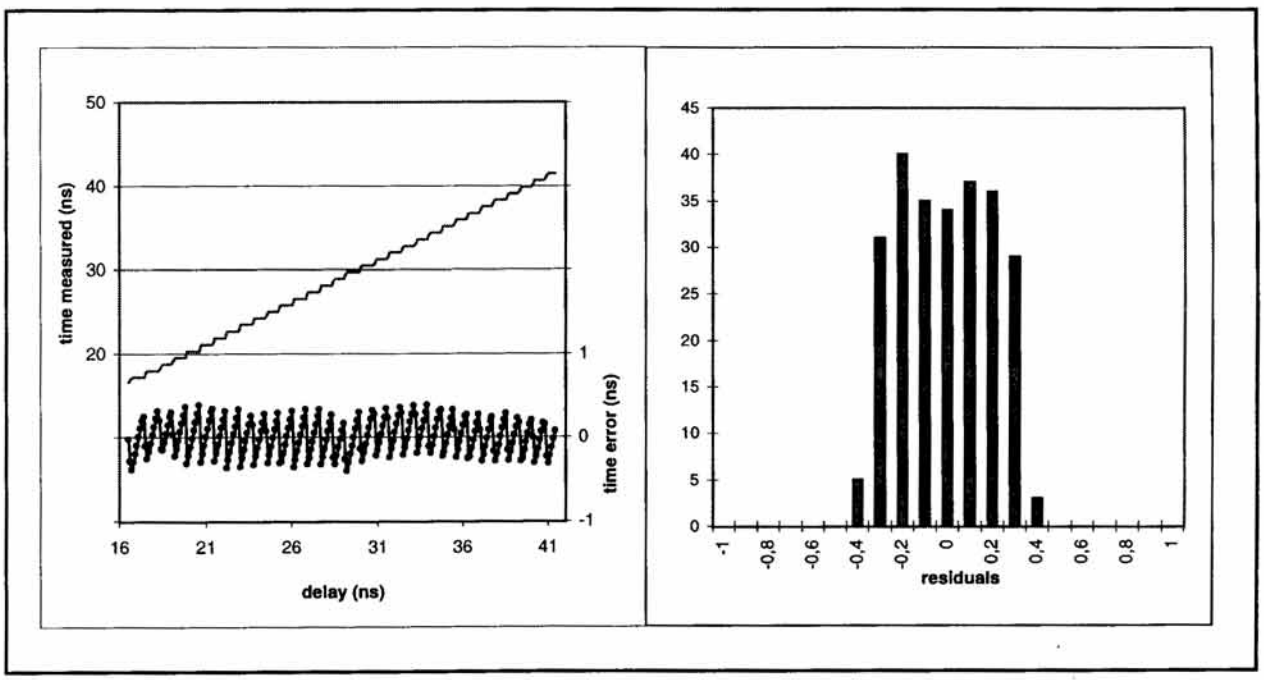


Fig. 3.4.4: Test of the TDC chip: linearity and resolution measurements in small dynamic range. Left hand side picture shows a 100 ps time sweep over 25 ns (top graph) and the corresponding deviations from the expected values (bottom graph). On the right is shown the histogram of the residuals.

The expected distribution is flat, with maximum deviations of ± 0.39 ns. The Table 3.4.1 summarizes the main test results:

In the ROS Master, data blocks corresponding to the four chambers of one sector will be merged into one single block and sent to the corresponding FED. Summing over the whole detector, the DAQ will receive 60 blocks of data for every trigger, one from each sector.

Table 3.4.1
TDC prototype test results

Time resolution	< 0.5 ns
Cross talk (influence on resolution)	< 0.2 ns
Two hit resolution	15 ns
Three tracks resolution (8 hits per track)	275 ns
Radiation tolerance (tests not completed)	> 8000 rads

Table 3.4.2 shows the sequence of events from the arrival of a trigger at a TDC to the arrival of data at the FED. The estimated delays are minimum values. As a time-scale reference, the mean time between triggers is 400 bx.

Table 3.4.2
Readout delay estimates (units are in bunch-crossings).

Event	Delay	Cumulative time
Arrival of trigger to TDC	0	0
TDC data ready (1)	10	10
ROB data sent (2)	38	48
Transmission to ROS (3)	3	51
ROS data sent (4)	64	115
Transmission to ROS Master (5)	7	122
ROS Master data sent (6)	100	222
Transmission to FED (7)	26	248

Notes:
1) Mean time required for the trigger matching mechanism;
2) Time required to fetch data from TDCs common bus and serialize data into the transmitter;
3) transmission time for the last serialized byte;
4) time required to fetch data from each ROB of a chamber and serialize data into the transmitter;
5) transmission time of the last serialized byte over 25 meters of cable;
6) time required to fetch data from four chambers and serialize data into the transmitter;
7) transmission time of the last serialized byte over 120 m of optical fiber.

3.4.1.8 On-chamber electronics

The placement of the trigger and readout electronics on the periphery of the iron yoke, in a position accessible without opening the detector, has clear advantages for the commissioning

and the long-term maintenance of the detector. Therefore this has been chosen as the base line solution since the Technical Proposal.

However, space is available around the honeycomb plate to house large parts of the electronics if sufficient miniaturization can be reached. Recent studies on the reliability of the electronics do not appear to exclude its use in positions of difficult access. This option has a big advantage in terms of the overall cost. To allow a complete study of important aspects of this solution, such as the reliability, effectiveness of cooling and integration in the chamber, it has been agreed that in the realization of the electronics prototypes, "the prototypes will be compatible with a chamber on-board installation".

3.4.2 The trigger electronics

3.4.2.1 Overview

The aim of the trigger electronics of each drift chamber is to select trigger candidate segments, to measure their position and direction and to provide bunch-crossing identification.

Trigger candidates are ordered in quality, with priority to segments with small bending angle. The data are forwarded to the Muon Regional Trigger which looks for tracks correlating segments in different stations.

Each muon station is composed of two Super Layers (SLs) in the φ-view and by one SL in the θ-view. Each SL is made of four layers of drift tubes.

Candidates are selected independently in the φ-view, perpendicular to the beam-line, and in the θ-view.

The trigger front-end devices are called Bunch and Track Identifiers (BTI). For each SL, the BTIs generate a trigger when at least three hits are aligned along a valid track pattern, and measure the position and direction of trigger candidate segments. The trigger is generated after a fixed number of bunch-crossings (bx), thus enabling bx identification. Triggers generated by the alignment of four hits have top quality.

In the φ-view the BTI data undergo two further steps of processing. In the first step, Track Correlator (TRACO) devices are used to correlate segments of the inner and outer SLs, thus reducing the noise and improving the angular resolution. Correlated high quality segments are assigned top quality. Every TRACO selects up to two trigger candidates, looking for the two *best* segments, i.e. with the higher quality and with the smaller bending angle. In the second step the Trigger Server of the φ-view (TSφ) looks at all segments transmitted by the TRACOs and selects the two *best* segments in the chamber.

In the θ view the BTIs select only tracks pointing to the interaction region. Through the Trigger Server of the θ view (TSθ) the OR of the BTI outputs is transmitted to the TRACOs of the corresponding φ-view, where it is used for additional noise reduction. The trigger information is transmitted synchronously from each TS via optical links to the Muon Regional Trigger.

3.4.2.2 The BTI

The Bunch and Track Identifier (BTI) has been studied for groups of four layers of staggered drift tubes (i.e. a Super Layer) with the aim of identifying tracks which give a signal in at least three of the SL planes. We present the basic description of the device; more details can be found in [3.13].

Each BTI is connected to nine wires of four layers allocated as shown in Fig. 3.4.5. The BTI collects the signals from the wires and injects them in one (or more) shift registers where they propagate at a speed corresponding to the drift velocity of electrons in the DTs. After a number of clocks equal to the maximum drift time divided by the clock frequency the position of the hits in the register reproduce the positions where the track crossed the layers. The time, i.e. the clock number, at which at least three hits "align" inside three shift registers belonging to three different layers is recognized by the BTI comparing at each clock the relative positions of the hits running in the shift registers. This is done using the positions as input data to a number of equations.

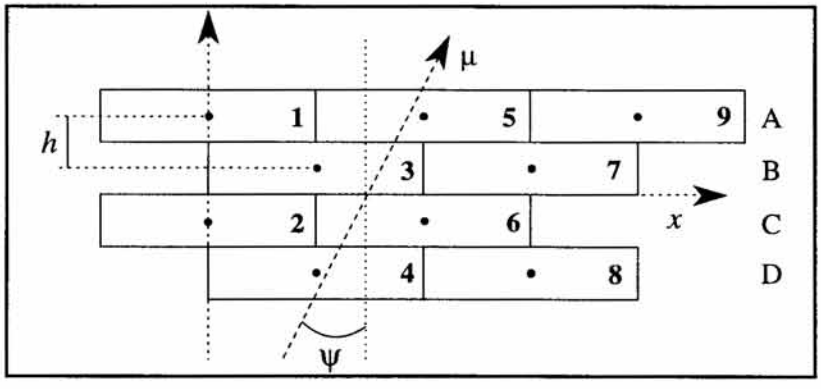


Fig. 3.4.5: Layout of the group of cells connected to a single BTI chip. The computed parameters are also shown.

The parameters computed from the BTI are the coordinate x, computed in the SL central plane, and the angular k-parameter, $k = h \tan \psi$, where ψ is the angle of the track in the plane normal to the wires and $h = 13$ *mm* is the distance between the wire planes.

The track information is flagged by a strobe signal (TRG) and is transmitted with fixed delay equal to the maximum drift-time, t_{max}, plus four clock cycles needed for input-signal synchronization and BTI calculations. Then, the nominal delay of the TRG signal with respect to the particle crossing of 20 bunch-crossings takes place. The BTI operation is summarized in Fig. 3.4.6.

The BTI algorithm to find candidate track segments computes in parallel several track pattern hypotheses: a pattern is identified from a sequence of wire numbers and labels stating whether the track crossed the tube on the right (R) or left (L) of the given wire (e.g. in Fig. 3.4.5 the track corresponds to the pattern 5L3R6L4R). Any given pattern includes six pairs of planes (AB, BC, CD, AC, BD, AD), each one providing a measurement of the position (through an *x-equation*) and the k-parameter (through a *k-equation*) of the track. The definition and the full list of the preloaded patterns is available in [3.12].

The value of k is proportional to the distance between the pair of hits inside the shift register at any clock cycle and corresponds to a rough measurement of the track direction at that cycle. Since the hits are shifted inside the register, this value is time dependent. Therefore, each pair included in a pattern gives its own measurement of the track direction: the hits are aligned when, after applying the pair-dependent proportionality factor, the values of the k-parameter of each pair are equal within the tolerance defined below.

At every clock cycle all *k-equations* are computed and a BTI trigger is generated if at least three of the six k-parameters associated with any of the patterns are in coincidence. The tolerance on the coincidence of the *k-parameters* is defined according to the resolution of each pair, which in turn depends on the distance between the wires and was chosen to allow a maximum cell linearity error equivalent to 25 ns. This coincidence allows the bunch-crossing identification, owing to the time-dependence of the k value.

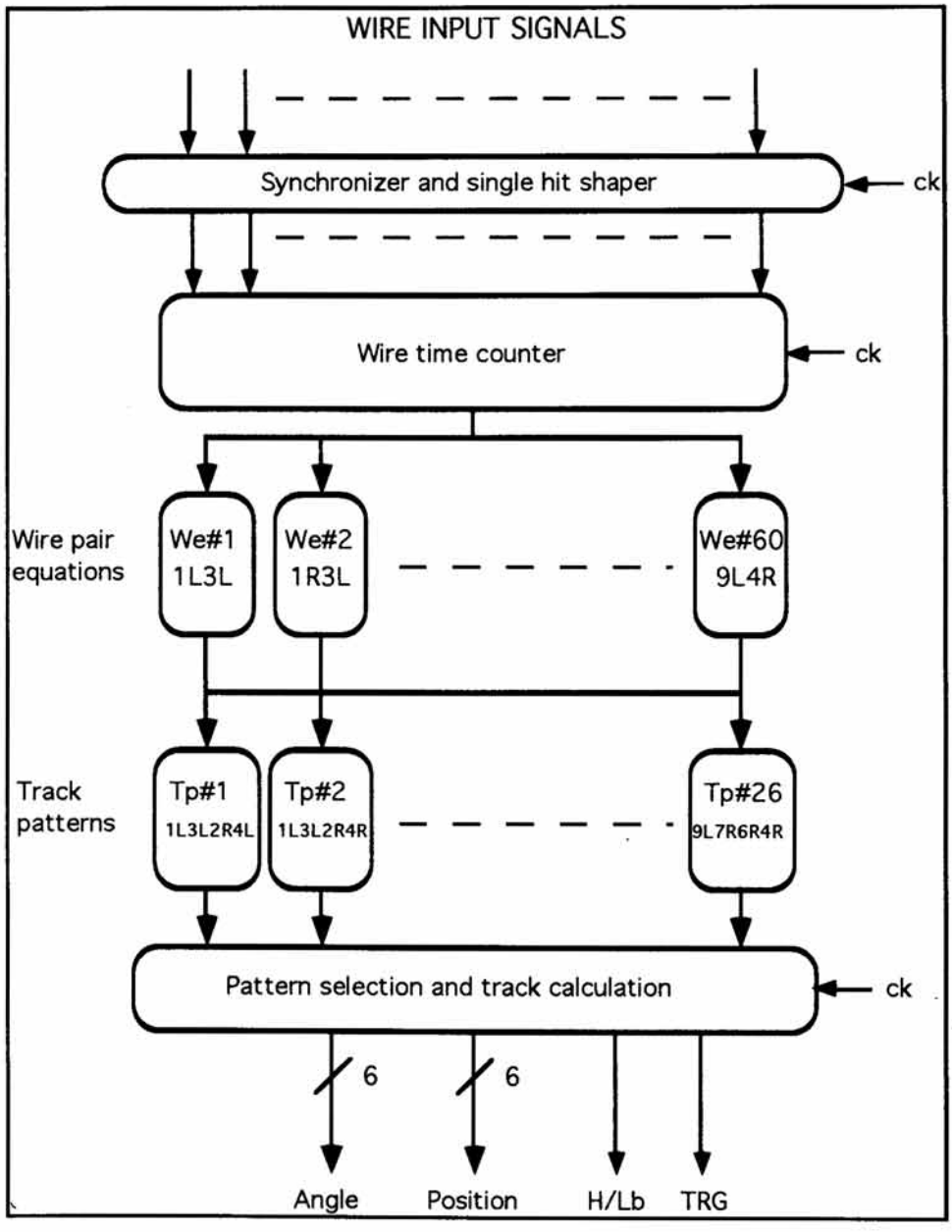


Fig. 3.4.6: Block diagram of the BTI functional operation

If there is a coincidence of all six k-parameters, the trigger corresponds to the alignment of four hits and is marked as a High Quality Trigger (HTRG). In any other case, with a minimum of three coincident k-parameters, due to the alignment of only three hits, it is marked

as a Low Quality Trigger (LTRG). The angular resolution of LTRGs is track pattern dependent and is generally worse than the one for HTRGs. If in a cycle several track patterns give a response, the HTRG is chosen as the triggering track pattern. If there is more than one HTRG or the triggers are all LTRGs, the first one, in an arbitrarily defined order, is selected.

Given the high (~5%) probability for a hit to have the wrong timing due to the presence of δ-rays, to have a high efficiency it is mandatory to accept also LTRGs. This is however a substantial source of background, since two effects can create false triggers. First there is a large probability that the alignment of four hits at some clock step produces the alignment of just three of them at the step just before or after the HTRG signal, thus generating "ghost" LTRG candidate tracks. Second there is some probability that a random LTRG could happen with some pathological k-parameter due to the left-right ambiguity, that is duplicating the possible choices for every hit. The noise reduction of the former kind of "ghosts" is obtained by issuing the LTRG signal only if at the neighboring steps there is no HTRG generated: this mechanism is called Low Trigger Suppression (LTS). The frequency of the latter kind of "ghosts" is only reduced in filters applied in the next trigger stage.

The impact position of the muon does not enter the track-selection algorithm. It is computed only for the selected triggering pattern. The position and angular resolution of the device depend on the drift velocity and on the sampling frequency. For a nominal drift velocity of 50 μm/ns and a sampling frequency of 80 MHz, the angle is measured with a resolution better than 60 mrad, while the position is measured with a resolution of 1.25 mm (for HTRG).

With the present geometric parameters of the chamber, the angular range is nominally $\psi_{MAX} = \pm 55°$, although the acceptance falls rapidly beyond 45°. This is adequate for a full acceptance down to $p_t = 4$ GeV/c.

A single BTI is connected to nine wires. Since neighboring BTIs are overlapped by five cells to guarantee full angular coverage for all impact positions of the tracks, each SL is in fact equipped with one BTI every four cells.

The k-parameter and the position of the track, coded in six bits, plus one trigger quality bit, marking HTRG or LTRG (H/L), are transmitted to the TRACO on the BTI track-data bus. Only one track per bunch-crossing per BTI is forwarded to the TRACO.

BTI ASIC prototypes were produced and tested. Their response to a sequence of 20000 tracks generated with a Montecarlo program in the interval ± 60° and fed to the chips with a pattern generator completely matched expectations. The BTI efficiency as a function of the track angle is shown in Fig 3.4.7 a). The upper curve gives the triggering probability at the expected bunch crossing, whereas the lower one gives the probability to get only wrong HTRGs. Figures 3.4.7 b) and 3.4.7 c) are the time distributions respectively of the high quality and low quality triggers. The correct output time corresponds to bin 22. No LTS algorithm was active during this test.

3.4.2.3 The TRACO

The TRACO processor receives the information from a group of BTI devices and tries to find the pair of BTI track candidates from the two φ SL that fits the *best* track, linking the inner Super Layer track segments to the outer Super Layer track segments.

The chip now being developed connects four BTIs of the inner Super Layer to twelve BTIs of the outer Super Layer, allocated as shown in Fig. 3.4.8. The block diagram of Fig. 3.4.9 describes the TRACO functional operation.

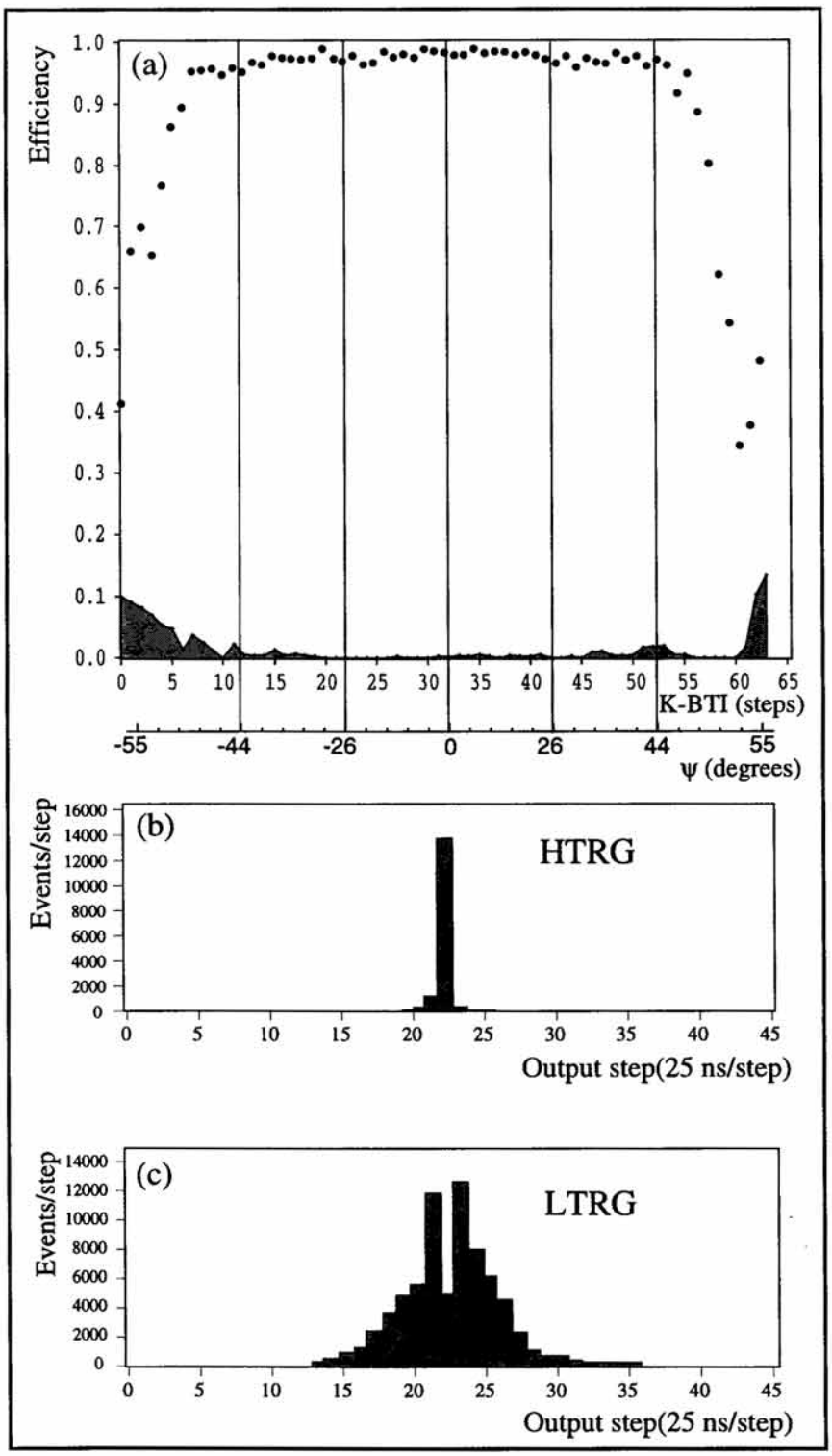


Fig. 3.4.7: a) BTI efficiency and high quality noise versus track angle; b) High quality trigger time distribution; c) Low quality trigger time distribution.

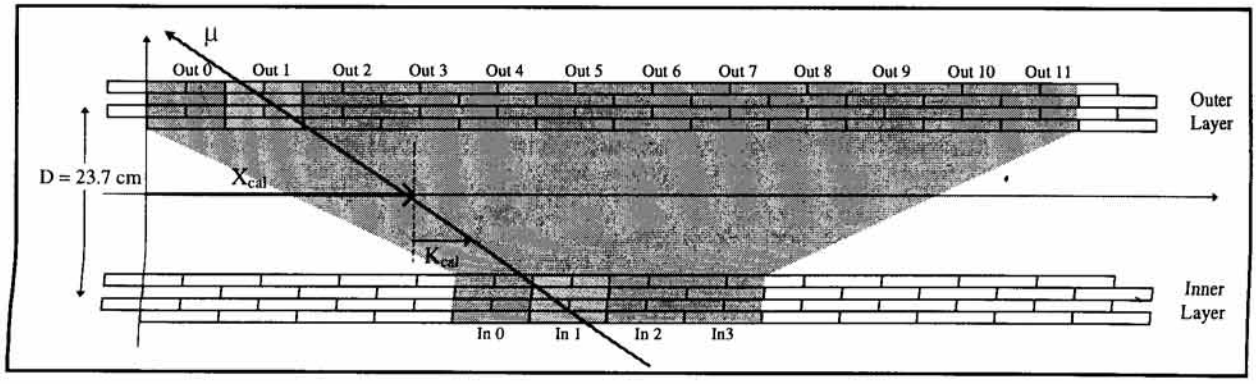


Fig. 3.4.8: Layout of one TRACO in a chamber. The computed parameters are also shown.

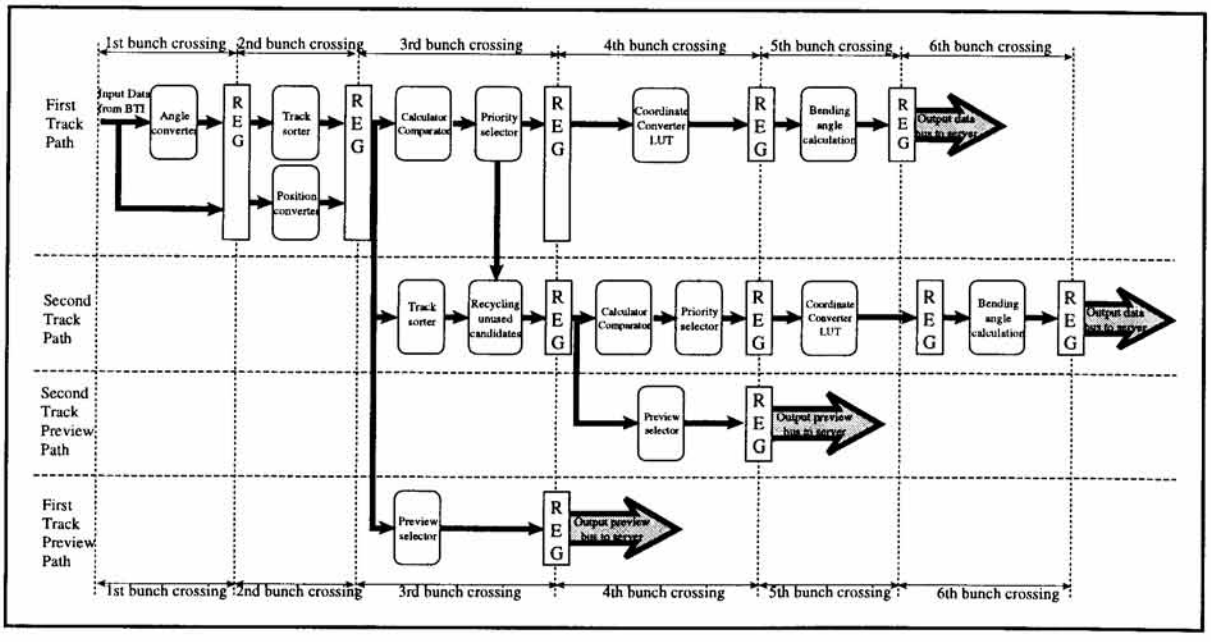


Fig. 3.4.9: Block scheme of the TRACO functional operation.

The algorithm first selects independently the *best* segment among all the candidates in the inner Super Layer and the outer Super Layer by means of a sorting operation. The selection criteria are programmable and take into account the proximity of the candidate to the radial direction to the vertex, in order to give priority to the higher p_T tracks, and the trigger quality (H/L). Then, after converting the positions and k-parameters of the two track candidates into the correlator reference system, it computes the position and the k-parameter of the correlated segment. The k-parameter of the correlated segment is compared with the k-parameters of the track candidates selected in the inner and outer Super Layers. If these track-segments match within a programmable tolerance, the correlated track is forwarded to the TSφ for further selection. If the matching fails, the correlator forwards one of the two segments as an uncorrelated track depending on a preference list that includes the parent Super Layer (IN/OUT) and the quality bit (H/L) of the two candidate tracks. If only one Super Layer triggers, no correlation is possible, and the available track segment is forwarded as an uncorrelated track.

The parameters computed for the correlated tracks are:

$$\begin{cases} k_{COR} = \dfrac{D}{2}\tan\psi = x_{inner} - x_{outer} \\ x_{COR} = \dfrac{(x_{inner} + x_{outer})}{2} \end{cases}$$

The angular resolution of the k-parameter for a correlated track is 10 mrad for the nominal drift velocity, i.e. a factor of six improvement with respect to the BTI calculations, while the resolution of the position remains unchanged.

Therefore, the correlator can output tracks falling in the following categories:

HH	correlated track with HTRG in both SLs
HL+LH	correlated track with HTRG in one SL and LTRG in the other one
LL	correlated track with LTRG in both SLs
H_i	uncorrelated track with HTRG in inner SL
H_o	uncorrelated track with HTRG in outer SL
L_i	uncorrelated track with LTRG in inner SL
L_o	uncorrelated track with LTRG in outer SL

The track output values are converted to an angle via a LUT and sent to the Trigger Server on a data bus using 9 bits for the angle corresponding to the k-parameter and 12 bits for the angle corresponding to the position. They are accompanied by three quality bits identifying HH, HL+LH, LL, H_i, H_o, L_i, L_o track candidates.

As remarked earlier, uncorrelated LTRGs are contaminated by a large amount of noise. To reduce this noise, a programmable coincidence with the time of the triggers given by the BTI in the Θ SL is planned.

In order to allow the identification of two muons inside the same correlator, the same procedure is applied a second time to the unused track segments. Therefore, sometimes a second track is forwarded to the TSφ. The programmability of the preferences for the choice of the first track and the second track is completely independent, although in principle we believe that the same criteria should apply. Since more than one TRACO inside a chamber can give a trigger, a further level of selection is provided in the TSφ.

In order to optimize the processing time in the whole trigger chain, a copy of the angular information of the two *best* BTI segments in each TRACO is sent to the TSφ. While the TRACOs continue processing these segments and exploit the correlation information, the TSφ selects which TRACOs contain the most interesting data to be shipped to the regional trigger. Again priority is given to the highest quality tracks with the smallest bending angles.

The BTI and TRACO algorithms were implemented in the standard CMS software. Using the GEANT simulation of the full detector, several studies were done on trigger efficiency when changing the programmable parameters in order to choose their default values.

In the following we will refer to a sample of single muons generated for $\eta < 1.5$ and full φ range and the quoted efficiencies are computed only for tracks crossing the sensitive area covered by the TRACO. All the electromagnetic processes associated with the muon interaction with matter were included in the simulation.

From Table 3.4.3 we see that the efficiency for finding HTRGs in the BTI and the efficiency for having a correlated candidate (HH, HL+LH or LL) in the TRACO is a function of the muon momentum, since the inefficiency is proportional to the probability of secondary electromagnetic processes. The same effect is present in the global efficiency which decreases slowly with momentum, since the probability of a degradation of the information is larger at higher momenta. Since the TRACO can output two tracks per bunch-crossing, the sum of the fractions split in different categories exceeds 100% .

Figure 3.4.10 shows the response of the combined BTI+TRACO algorithms as a function of the incident angle at the TRACO output. We see that the TRACO efficiency is flat until 35°, as expected from the design parameters, and that beyond that limit the reconstructed tracks are mainly uncorrelated due to the acceptance limit of the device.

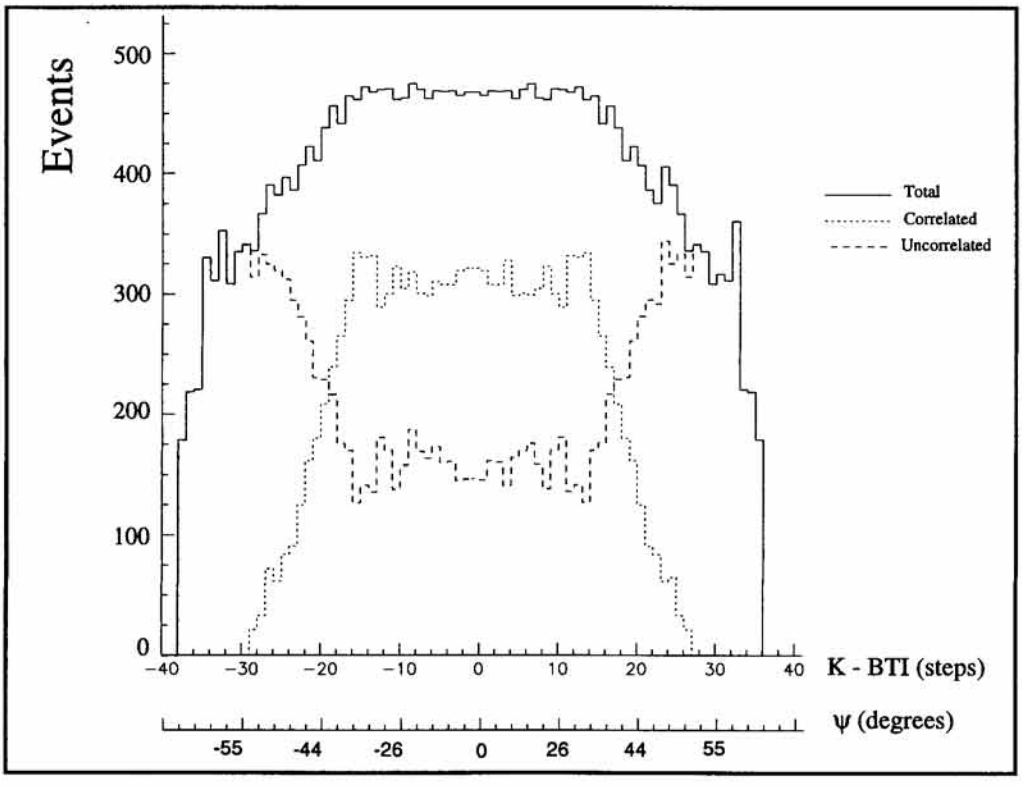


Fig. 3.4.10: Response of the BTI+TRACO combined algorithms as a function of the incident track angle. Muons were generated flat in angle.

The efficiency as a function of transverse momentum in muon station 1 is given in Fig. 3.4.11. It is shown for three different trigger conditions that act on the noise level. In practice, we use the θ-view trigger information to filter the LTRG single triggers. In the normal flow, this type of trigger is accepted only if there is a trigger of any type (HTRG or LTRG) in the θ-view. In case the noise level is still too high, we have the possibility of accepting them only if the trigger in the θ-view is a HTRG one, or even to just reject all these triggers. The effect of these filters is shown in the figure.

Table 3.4.3

Probability for finding a certain trigger quality and efficiency at BTI and TRACO output. Due to the possibility of selecting two tracks per event, the TRACO fractions add up to more than 100%. The efficiency includes the identification of the correct bx.

P_T (GeV/c)	20	50	100	200	300	1000
	%	%	%	%	%	%
H from BTI	79.4	77.3	78.1	76.3	76.3	74.1
L from BTI	15.7	17.3	17.1	18.4	17.1	18.3
BTI efficiency	95.2	94.6	95.2	94.7	93.4	92.4
HH from TRACO	44.3	42.9	41.1	40.8	40.3	39.0
HL+LH from TRACO	23.3	22.9	23.7	23.9	24.2	23.2
LL from TRACO	3.3	3.4	3.8	3.4	3.5	3.7
H from TRACO	46.6	46.6	46.4	47.1	47.0	48.9
L from TRACO	13.8	15.2	15.6	15.9	15.8	16.6
TRACO efficiency	97.2	97.3	97.0	97.1	96.6	95.7

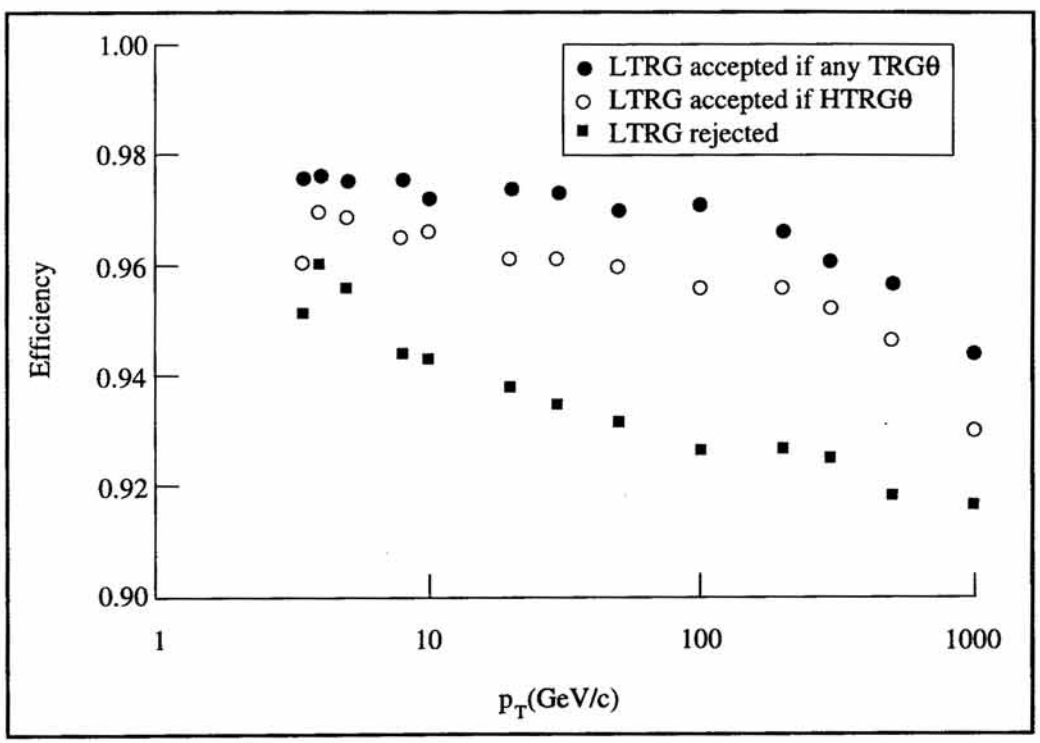


Fig. 3.4.11: TRACO efficiency for finding a track at station 1 as a function of transverse momentum.

3.4.2.4 The TSφ

Among the trigger candidates selected by all TRACOs in a chamber the TSφ has to select the two best track segments and transmit them to the Muon Regional Trigger. The TSφ block diagram is shown in Figure 3.4.12. The functional requirements on the selection mechanism have been studied in [3.14] both for physics issues and technical aspects, and a dedicated algorithm has been designed. The main features of the algorithm have been implemented on FPGA and ASIC prototypes. The successful performance of the prototypes gives confidence in the proposed design.

The number of TRACOs for a station can be quite large; as much as 24. Each TRACO transmits to the TSφ two best tracks serially in two consecutive bunch-crossings (bx), ordered in quality. No dead time is introduced by this operation. In fact, each TRACO sends in advance to the TSφ a rough measurement (PREVIEW) of the $\Delta\psi$ angle (with respect to the radial direction) of a track being checked for correlation. We define BUNCH1 and BUNCH2, respectively, as the first and second group of tracks arriving from the TRACOs connected to the TSφ at two consecutive bxs. For selecting the first-best (FBT) and second-best (SBT) tracks, the TSφ has to:

- sort out the best track of BUNCH1, thus determining the FBT, and sort out and store the next-to-best track (CARRY);
- search for the best track of BUNCH2 and compare it with the CARRY, in order to determine the SBT.

Notice that even TSφ with two muons in the same φ sector are likely to produce two high-quality (HTRG) track segments in BUNCH1 from different TRACOs in the same station, which are correctly picked up by the TSφ carry algorithm.

In an ideal situation, when all non-null tracks in BUNCH1 are HTRGs with correlated segment TSφ in the inner and outer Super Layers, selection of the best track means a search for the track closest to the radial direction (minimum $\Delta\psi$), i.e. the highest transverse momentum track. In the general case, three bits accompanying the PREVIEW angles define priorities among the input TRACO segments: a HTRG/LTRG bit, a BUNCH1/BUNCH2 bit, and an inner/outer Super Layer bit. The BUNCH1/BUNCH2 bit is useful for handling the pile-up of two triggers one bx apart in different TRACOs: the TSφ is able to provide to the Regional Trigger at least the FBT data resulting from the sorting of BUNCH1 for both triggers. The priority rules are programmable in order to optimize the selection locally, according to the local BTI-TRACO efficiency and the background conditions. The quality of the SBT selection was studied when different priority assignments are applied in the CMSIM TSφ simulation. The results are displayed in Table 3.4.4.

The TSφ logic block diagram is shown in Figure 3.4.12. The selection algorithm uses a two-layer cascade of processing units, all having the same functionality. This architecture has been chosen in order to minimize the number of logic cells within a unit and the amount of I/O cabling around the detector. In each unit, a parallel minimum and next-to-minimum search is performed over a small group of input data words. The full parallel approach guarantees a fixed-time response, independent of the number of TRACOs in a chamber. Each unit of the first layer (TSS: Track Sorter Slave) processes up to four data words, while the second-layer unit (TSM: Track Sorter Master) processes up to six data words. It is planned to duplicate the TSM chip with a "shadow" chip, which takes over in case of failure.

Table 3.4.4
Expected performance of the First-Best (FBT) and Second-Best (SBT) selection with different priority assignments.

	No carry	with Carry and No Fake Rejection	with Carry and Fake Rejection
Efficiency for 2nd track	11%	98%	80%
Efficiency for 2nd track in open pairs	11%	98%	98%
Prob. of correct id for both tracks	45%	70%	86%
Prob. of correct id for both tracks in open pairs	50%	75%	95%
Prob. of generating a fake 2nd track	4%	34%	5%

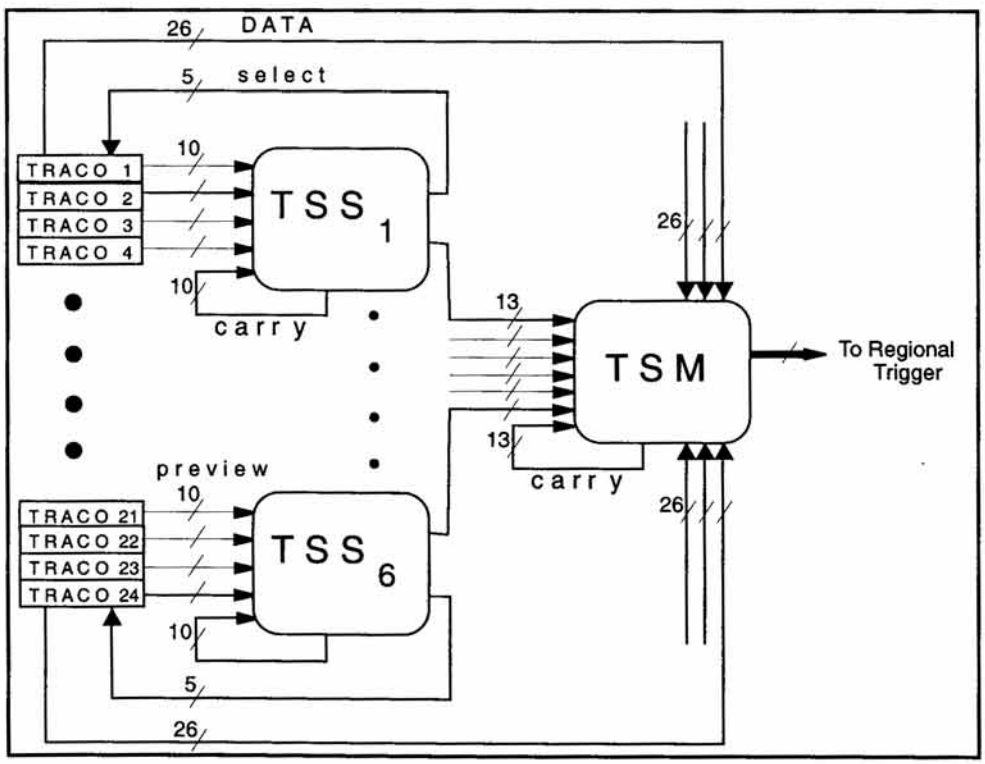


Fig. 3.4.12: Trigger Server logic block diagram.

The functionality of each unit is performed in two consecutive cycles (one cycle per bx), called SORT1 and SORT2. The SORT1 processing status is recognized when at least one TRACO gives a non-null track of BUNCH1 type, while the SORT2 status simply corresponds to the cycle following SORT1. The SORT2 status can be aborted in case of pile-up triggers. In the SORT1 cycle, each TSS unit analyzes four PREVIEW data words and transmits the minimum to the TSM unit in the second layer, while the next-to-minimum is stored locally and carried over to the SORT2 cycle. At the same time a local select is given in output to enable transmission of the full data from the selected TRACO to the TSM. In the SORT2 cycle, each TSS unit analyzes the four input words of BUNCH2 together with the carry word of the SORT1 cycle.

The TSM unit in the second layer analyzes the six PREVIEW words from the TSSs. It behaves similarly to a TSS unit of the first processing layer, but its processing begins two bxs later. The timing diagram of the TRACO-TSS-TSM system is displayed in Fig. 3.4.13. The information handshake between the TSφ system and the TRACO devices allows data from up to twelve tracks to be stored in the TSM unit. The selected output signals from the TSM, corresponding to the FBT in the first processing cycle and to the SBT in the second cycle, are used to enable the transmission of full track data to the Regional Trigger for two out of the twelve possible candidates stored in the TSM unit.

In 1996, a first TSS prototype using a XILINX FPGA was built to thoroughly check the logic with all possible input patterns. The I/O rate of the chip was 40 MHz, but the whole sorting algorithm was executed in a pipeline with six clock cycles. Then in 1997, a TSS prototype on an ASIC chip (1 μm CMOS) was designed and tested with input patterns at 40 MHz. In Fig. 3.4.14, the time response of the real chip is compared to the expectation of the CAD simulation. Although the real response time is already compatible with the constraint of the 25 ns between bunch-crossings, use of ASIC chips in 0.5 μm technology will reduce the time response of each processing unit even further, to well within one bx.

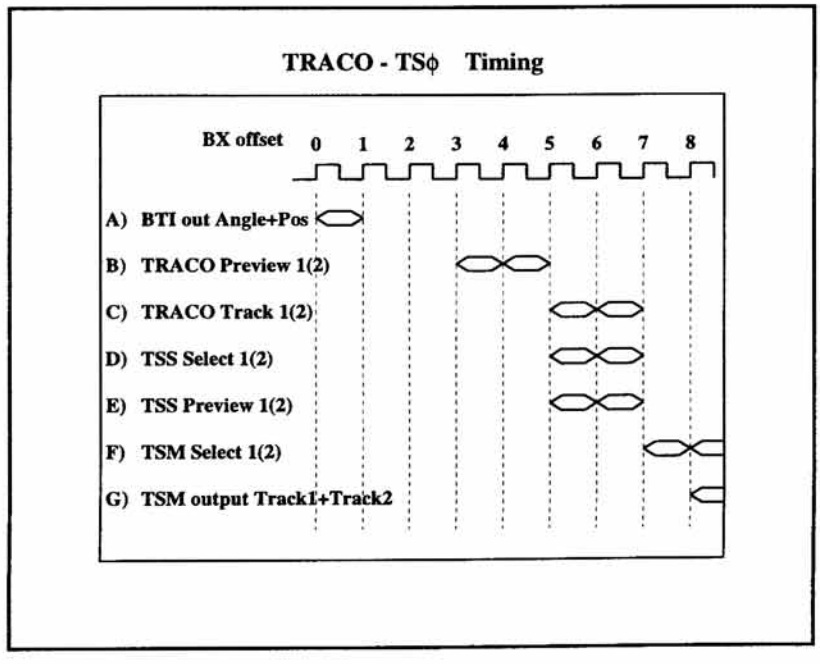


Fig. 3.4.13: TRACO-TSφ timing diagram.

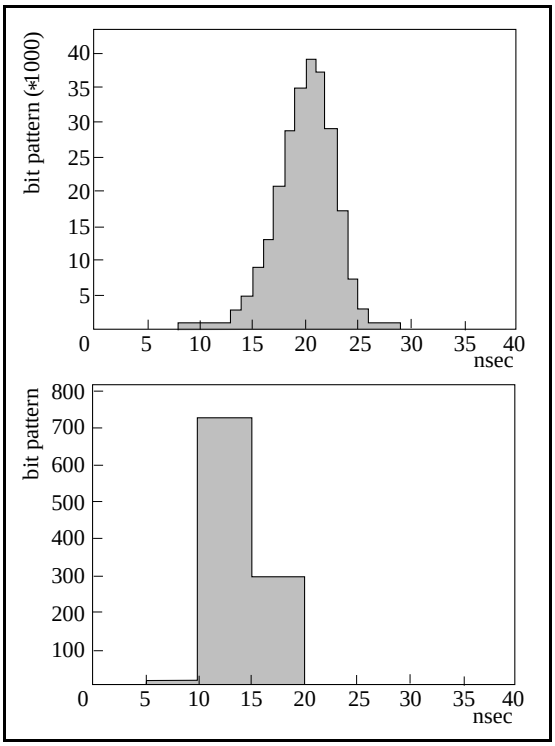


Fig. 3.4.14: Time response of TSS prototype (lower) compared with expectations from CAD simulations (upper).

3.5 POWER AND CONTROL SYSTEMS

3.5.1 High voltage

The high voltage segmentation will have the maximum affordable granularity for the wires, whereas a much coarser distribution is used for the cathodes and strips. In the baseline design there is a primary HV source, fully monitored and protected against overcurrent, roughly every 25 wires. The cathodes of an entire SL will be connected to one HV channel and the same granularity applies to the strips. In this way, the total number of HV channels is about 7400.

The high voltage system for the DT chambers is now the object of a development program set up in collaboration with a selected firm which specializes in the field. The design has a tree structure based on: a) a multicrate mainframe residing in balcony racks, capable of handling a wide variety of dedicated modules in a highly flexible way with a multimaster high-speed communication protocol on a standard RS232 interface; b) dedicated primary modules residing in the system crates, generating +4 kV for anode wires, +2 kV for strip electrodes and -2 kV for cathodes, with control of all the sensitive parameters like voltage, current, ramp-up and ramp-down rates, and on and off switching; c) dedicated secondary modules (either residing in the system crates or on the chambers), with adjustable current limit, on and off switching, and monitoring of voltage and current. The control will be performed via opto-couplers to prevent ground loops.

All the controls will be permanently active in a static way on the secondary modules: while the hardware response to any malfunction will be immediate, the detailed status of the

channels has to be requested by the central control, in order to keep to a minimum the EMI due to control-data traffic.

While the general features of the main system are fairly well defined, being part of a development program already started by the firm, the actual specifications of the dedicated modules are to be defined in the next few months. One important aspect is the segmentation attainable in relation to the cost/performance ratio that the actual design of the secondary modules will allow, given the fixed budget limits. Of course, the actual cost/performance figure also has to take into account the number of HV cables and their length, which could be strongly affected by the possibility of locating secondary modules close to the chambers. Other important aspects to settle are the magnetic field and radiation level in which the HV system should work.

3.5.2 Low voltage

The low voltage system has to supply the chamber front ends with +2.7 V at 10 mA and +5 V at 5 mA for the output driver and preamp/discriminator circuits, respectively. This will lead to average currents of 10A and 5A respectively per chamber

Since the mainframe described in the HV paragraph is designed to handle any kind of DC voltage, it can also be used to host the LV dedicated modules that are yet to be developed. The actual number of chambers powered by a single LV module will depend on the optimization of its cost/performance ratio, but will be at least four chambers per module (one sector) and at most 12 chambers per module (one quadrant).

3.5.3 Cooling

As we have seen, the chambers will have “on board” front-end electronics located inside the gas enclosures of each Super Layer, and possibly the trigger and read-out electronics located in the outer C-shaped profiles.

In order to evaluate the need for cooling of such chambers, we must examine the anticipated power consumption. The front-end electronics need 50 mW per channel and this practically doubles if one considers all the rest of the electronics. Taking into account that the largest chambers have about 1000 channels, we see that the cooling needs for the internal heat sources are relatively modest.

To calculate what is needed to cool the produced 100 W with water the following assumptions are made:
1) the piping length inside the chamber in order to reach all the electronics: L=10 m;
2) the pipe cross-section: 100 mm^2.

To remove 100 W with a 1 l/s flow of water per chamber will result in a temperature rise of the water itself of $\Delta T = 0.024\ ^0C$ and a factor of 10 higher with a flow that is correspondingly reduced. In this last hypothesis, the pressure difference between the input and output pipes is 12.5 Pa corresponding to 0.12 mbar; even putting more chambers in series will not limit the effectiveness of the cooling.

The most delicate part is to have a very high efficiency in removing the heat produced inside the chamber. The fraction not removed in fact accumulates with time and produces a general increase of the chamber temperature.

It is felt that water cooling is needed because heat is generated in areas where the thermal dissipation in air is not easy. On the other hand, the heat sources are very weak, and to first

order any type of water cooling would be sufficient. It is then natural to use small pipes, put more chambers in series and, since there is no need for extreme conditions, stay away from water temperatures so low that condensation is a concern. Input temperatures of the order of 16 - 18 ^{0}C are adequate.

The statements above are valid for self-generated heat; of course, the chambers must be protected against heat produced by any external source that is near the chambers. As a final remark, it is worth noting that forced ventilation will also be used in every gap between iron slabs in order to remove possible pockets of hot air.

3.5.4 Controls

In order to assure the continuous and reliable operation of the system, a set of parameters has to be controlled and monitored by a slow control system. These include:

- temperature and gas pressure measured on the chamber,
- high voltage and low voltage values and currents,
- readout of the strain gauges inserted in critical points of the chamber's mechanical structure,
- oxygen contamination in the input and output of the gas system,
- measured drift times obtained by the drift velocity monitors,
- input and output temperatures and flow rates of the cooling water,
- programming and monitoring of the front end, trigger and readout electronics.

3.5.5 Cables and interfaces

The Read Out and Trigger units and the Power and Control System modules will be outside the iron yoke. The modules are foreseen to be housed in VME crates, placed in racks, on four balconies of a service structure surrounding each wheel (Fig. 3.5.1 and Tab. 3.5.1 and 3.5.2).

Each platform has a place for two racks which will hold a total of 10 crates to instrument 12 Drift Tube Chambers (1 quadrant).

The estimated power dissipation of the crates is around 1.5 kW per balcony (a total of 35 kW for the entire barrel DT system).

The cables coming from the chamber patch panels are channelled radially for each sector on the wheel faces and distributed to the racks through cable trays installed on the service structure. The estimated cross section per sector is less than 400 cm^2, including cooling and gas piping. This cross section is shared with the cables and services needed for the RPCs.

The cables for the chambers which are installed in the external wheels (wheels +/-2 and +/-1) run over the outer faces of the rings. For the central wheel (wheel 0), the services are on both faces of the ring, alternating every two sectors with the services coming from the inner CMS detectors. This distribution ensures access to all of the muon chambers. From the balconies, cables leaving the racks will be guided to flexible cable chains located at each side of the CMS detector and from there to the counting room cavern.

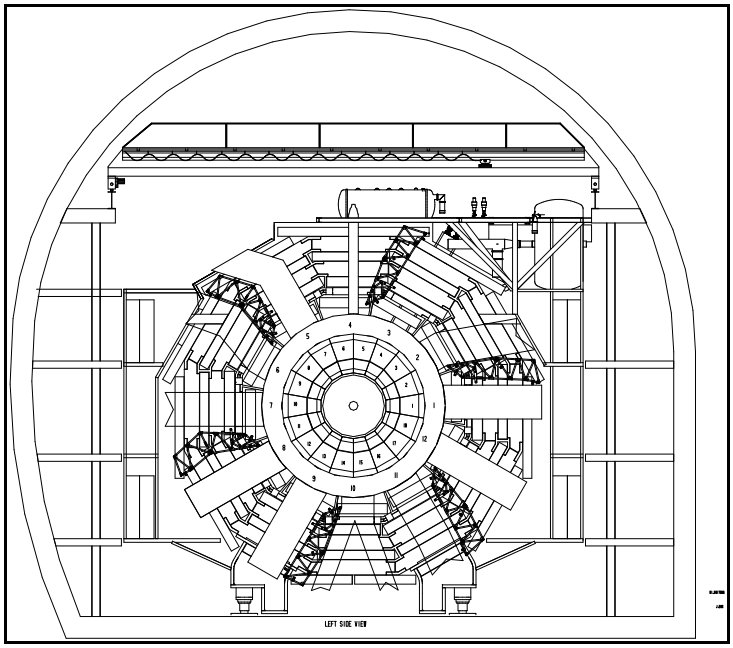


Fig. 3.5.1: Layout of cable trays and balconies for one wheel.

Table 3.5.1
Crates and racks per quadrant and total number of racks.

	#crates/quad.	Type	Total crates
Readout	6	9+2 VME U	120
FE LV	1	6+2 VME U	20
HV	2	6+2 VME U	40
Other serv.	1	6+2 VME U	20
Total	10		200

Table 3.5.2
Services cross section per sector

		units/sector	Cross Sect.	Type of cable
Cables	R-Out	106	306 cm^2	32 tp round shielded cable (Φ = 17 mm)
	HV	12	27 cm^2	12 cores round shielded cable (Φ = 10 mm)
	LV	24	15 cm^2	multiwire (Φ = 8 mm)
Gas piping	DT	8	14 cm^2	12 mm diameter supply - 14 mm diameter return
Cooling	DT + RPC	8	14 cm^2	12 mm diameter supply - 14 mm diameter return
Total			376 cm^2	

3.6 GAS SYSTEM

In this chapter, we describe the requirements for the gas system for the drift chambers (DT) and the implementation of the system, starting from the elementary building block which is the single drift cell.

A non-flammable and low-cost gas mixture of argon and carbon dioxide with 85% and 15% volume, respectively, is used. The task of the gas system is to flush, with controlled pressure, temperature, flow and purity, every drift tube. There are about 200,000 drift tubes of 11 mm x 39 mm cross section and 200 to 400 cm length to be flushed. A gas flow corresponding to a few volume exchanges per day is foreseen.

The actual flow is mainly dictated by considerations of flow control and purity. The drift chambers are rigid enough to not notice changes in atmospheric pressure. This could allow us to work at constant absolute pressure inside the DT, to maintain a constant drift velocity.

An overview of the global parameters of the gas system is given in Table 3.6.1.

Table 3.6.1
General parameters of the gas system for the DT chambers.

	Value	Comment
Gas mixture	Ar/CO2 85%/15%	Non flammable; low cost
Pressure stability	±10 mbar	
Purity	< 500 ppm O2	
Closed circuit	Yes	Add some fresh gas
Number of purifiers	2	
Number of drift cells	~200 000	
Number of chambers	250	
Volume of one chamber	~ 1m3	Average
Gas flow per chamber	50 l/h	150 l/h to purge

3.6.1 Gas in the drift chamber

Groups of 200 to 400 drift tubes, distributed over four layers (see Fig. 3.6.1), have a common gas enclosure and are called a Super Layer (SL). The drift tube has small openings at the ends, which allow the passage of gas. Within an SL, the drift tubes are flushed in parallel. The total cross section of these ~300 drift tubes (or of their openings) is very large in comparison with the cross section of the gas tube for the supply/exhaust line. Flow non-uniformity due to this mismatch of impedance is overcome with a manifold inside the gas enclosure: the gas enters via a 2-4 m long tube having an outlet hole in front of each drift tube, with a diameter over 4.5 (this is $400^{1/4}$) times smaller than the diameter of the supply line. At the other end of the drift tubes, a similar manifold collects the gas and is connected to the exhaust line.

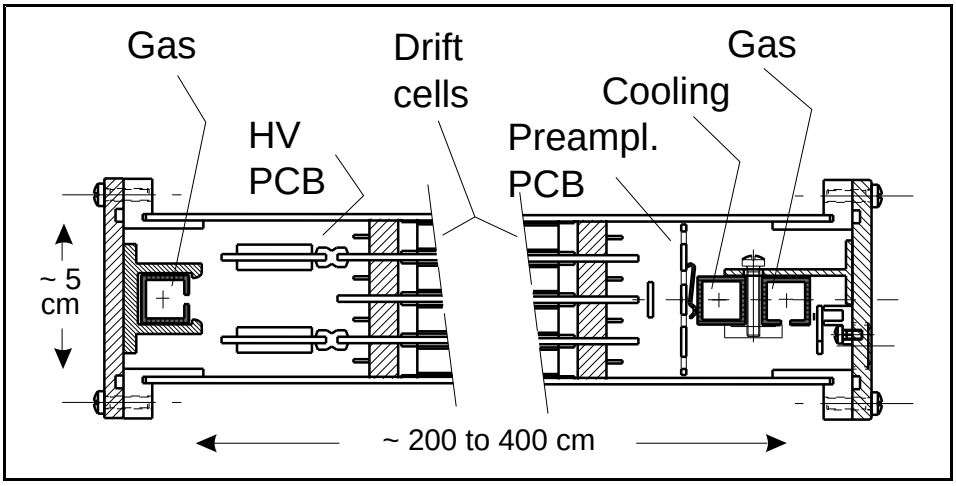


Fig. 3.6.1: Gas distribution inside a Super Layer (SL) of a barrel muon chamber (here the prototype MB96). A tube, inside the chamber, has one small outlet hole in front of each drift cell, and serves as a manifold. It feeds all the drift cells of the four layers in parallel. At the other end of the chamber, a similar manifold collects the gas.

To better equalize the pressure drop along the internal manifold, there is a gas connection at each end of the manifold. The gas temperature and pressure are monitored by sensors on every chamber.

The barrel muon chamber system, consisting of three SLs, has thus 12 gas connection points available (see Fig. 3.6.2) in total. In order to ensure an effective removal of air from the whole chamber at small gas flow, the inlet of the denser Ar/CO_2 mixture is always at the lowest point of the chamber, the outlet at the highest.

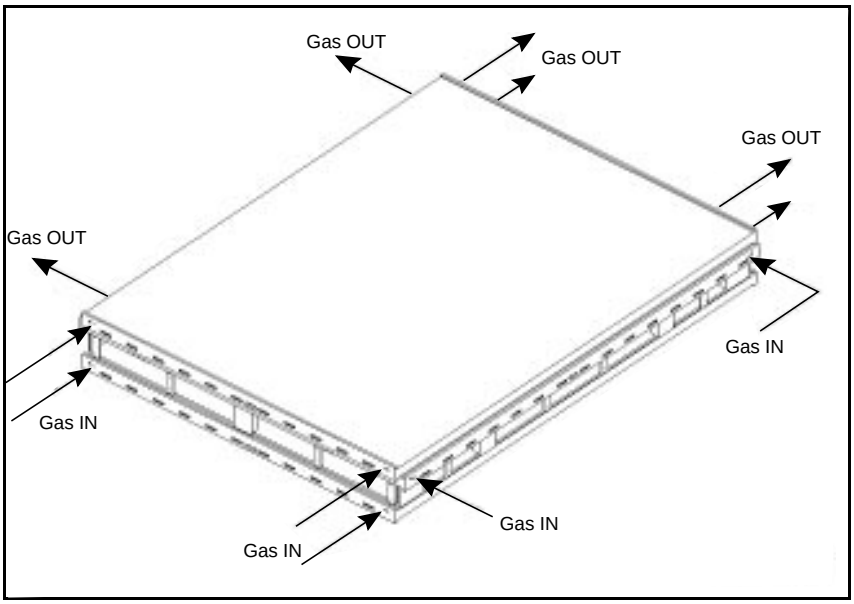


Fig. 3.6.2: The three Super Layers (SL) of each barrel muon chamber have independent gas circuits and thus in- and outlets. Connecting them to the common line in parallel ensures equal pressure in each SL. The gas line inlet is connected to the lowest point and the outlet to the highest point of the SL in its actual position.

3.6.2 Gas distribution on the wheel

Four of the five wheels housing the barrel muon chambers are movable. To simplify the gas distribution and to ensure equal pressure in the SLs, the three SLs forming each chamber are connected in parallel to one common gas tube.

Each of the 50 drift chambers on one wheel has its own gas supply and exhaust line linking it to a distribution panel located on the side of the wheel (Fig. 3.6.3 a). The panel on one side will be used for the DT chambers, while the panel on the other side will serve the RPCs. Copper tubes run from the chamber radially along the surface of the wheel to its perimeter, where they run on trays to the panel. The tube length varies from 3 to 30 m. An effort was made to pass the tubes along the dead space between the chambers, to allow free access to the chambers.

Due to the presence of alignment equipment, the gas tubes can only be placed on every second sector; the other sectors are then equipped on the opposite wheel face. At the level of the outer chambers MB4, which have no dead zone between them, it is important to pass the gas tubes through a gap between the chambers (Fig. 3.6.3a). Otherwise, (Fig. 3.6.3b) the requirement of extracting all chambers through the same face of the wheel could not be fulfilled. A short piece (~50 cm) of flexible tubing connects the end of the copper tube to the chamber.

The gas panel on the wheel has only one connection to the outside world. A flexible section allows the wheel to be moved without disconnecting the chambers, which are thus kept operational. For an exceptionally large displacement this section can be disconnected, then reconnected at the new position and cleaned before reflushing the chambers.

The same arguments, and hence the same type of solutions, are valid for the four sets of distribution of fluids on the wheels, namely (a) gas for the DT chambers, (b) gas for the RPCs, (c) cooling liquid for the DT chambers and RPCs, and (d) the ventilation of the DT chambers and RPCs.

On the wheels, copper tubes with an inner diameter of 10 (12) mm will be used for supply (exhaust); for the maximum length of 30 m and a flow of 50 l/h this implies a pressure drop of 0.4 (0.2) mbar. This is small in comparison with the 2.7 mbar barometric difference between the top and bottom chambers (15 m apart), and with atmospheric variations of 25 mbar. With the system at constant absolute pressure - as regulated at the gas panel on the wheel, only the barometric pressure variation with height will distinguish the chambers. Simulations show that a 25 mbar increase in pressure induces ~20% loss in pulse amplitude, which is comparable with variations along a wire. The individual chamber senses at most a height difference of 4 m, out of the wheel height of 15 m, and could have its high voltage tuned to its gas pressure. However, for the small total barometric difference of 2.7 mbar this is not required.

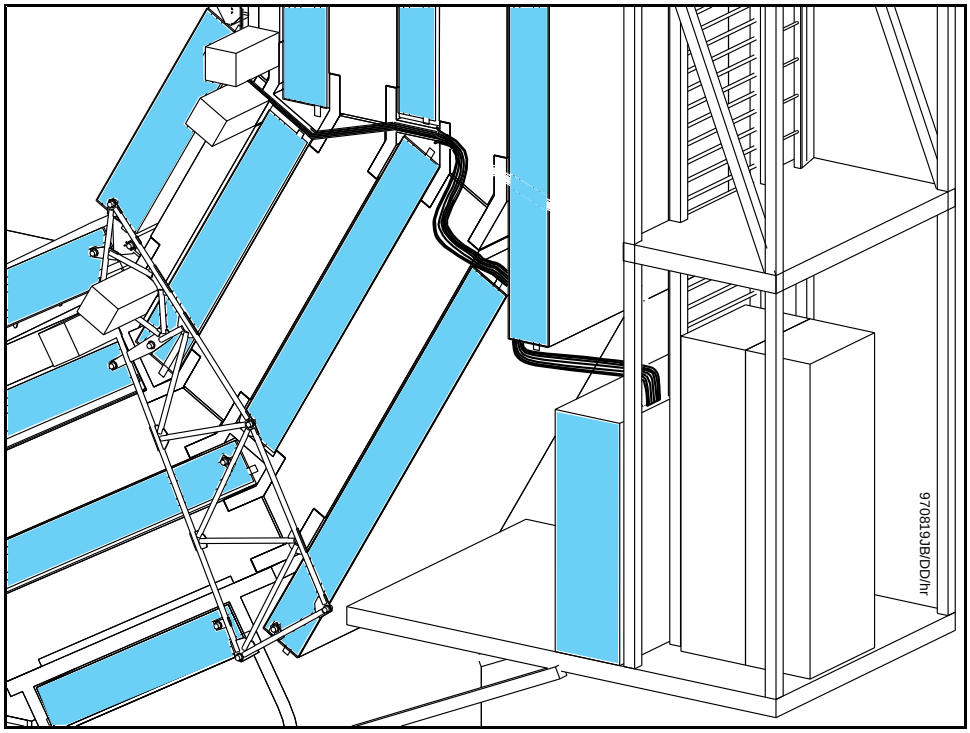


Fig. 3.6.3a: View of the gas tubing between the barrel muon chambers (marked in gray) and the distribution panel on one wheel. The detail shows the passage of the gas tubes on the face of the wheel: even at the outer chamber MB4 the gas tubes leave free access to all barrel chambers.

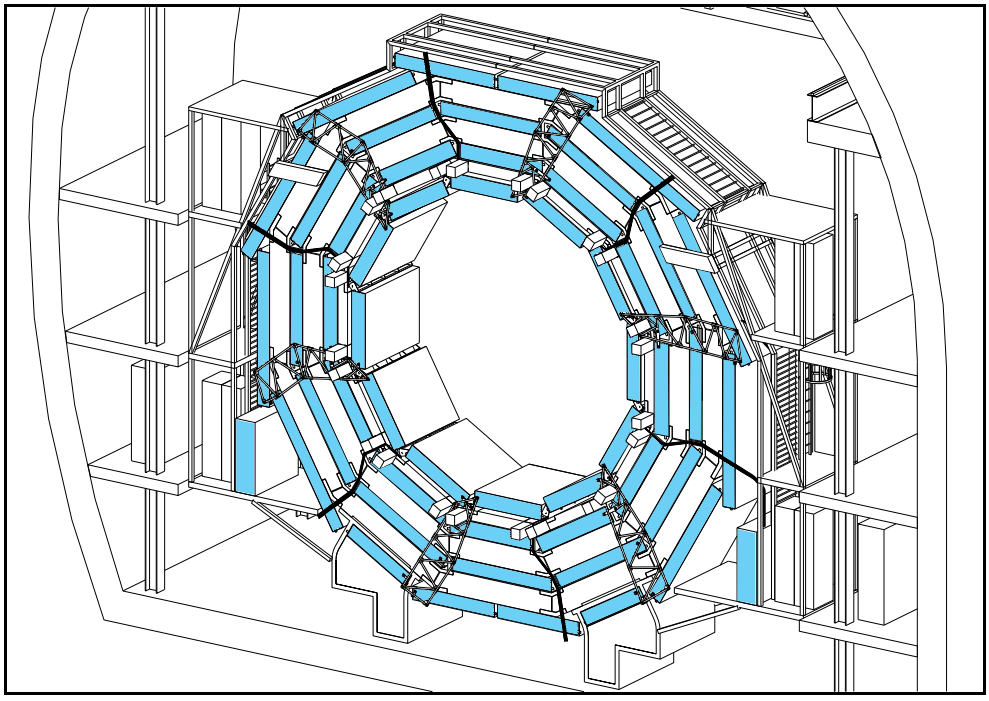


Fig. 3.6.3b: View of the gas tubing between the barrel muon chambers and the distribution panel on one wheel. Here, the overview is shown. The radial tubes are placed every second sector, on both faces of the wheel, and staggered by one sector. There is an individual in- and outlet tube for each of the 50 chambers on the wheel, but only one line connecting the distribution panel to the outside world.

The elements of the gas circuit in the cavern are shown schematically in Fig. 3.6.4. A single gas supply line arrives from the surface building. At the accessible area US, a manifold distributes the gas to the five wheels. The flow is adjusted for each wheel individually. At the gas panel on the wheel, flow, pressure and temperature are monitored. A manifold distributes the gas to the 50 individual chambers, and has a spare channel and a 100 mbar overpressure security valve. Every line is equipped with a remotely controlled shut-off valve, a needle valve for manual flow adjustment, and a mass flow meter. This is connected to the long copper tube via a self-sealing quick connector and a short flexible tube, allowing us to disconnect by hand, to exchange channels for testing, etc.

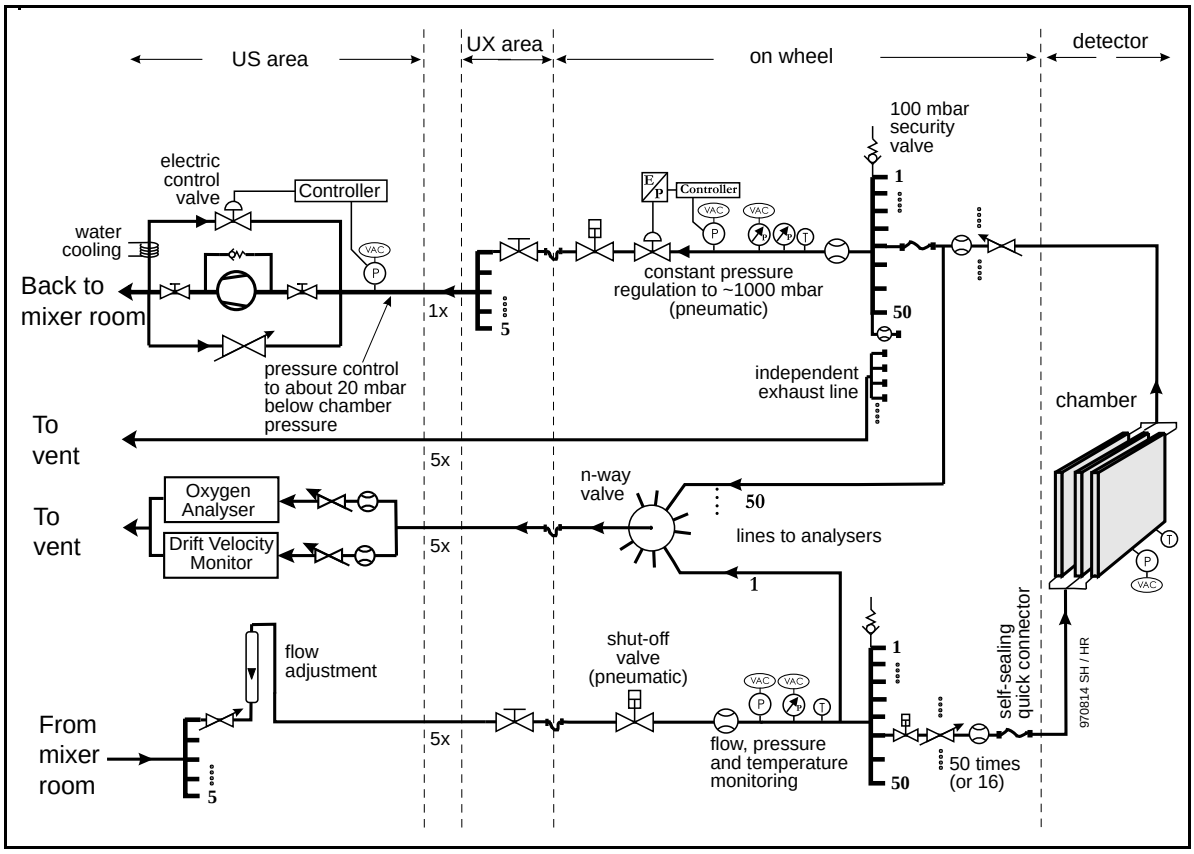


Fig. 3.6.4: Schematic circuit of the gas distribution in the caverns, for the barrel muon chambers. The elements on the left are in the accessible gas room in the cavern US, while the others are in the actual detector cavern (UX).

The exhaust lines are equipped similarly. Downstream in the manifold which collects the gas from the 50 chambers, the absolute gas pressure is regulated to about 1 bar, with a precision of 10 mbar. This ensures that the maximum drift time in the chamber varies by less than 1%. An independent manifold with an unregulated exhaust line allows us to purge single chamber(s) without disturbing the closed circuit of clean gas from the other chambers. A compressor then forwards the exhaust gas from the five wheels to the mixer room at the surface hall.

The following gas parameters are monitored for the individual chamber:

- Flow at the supply and exhaust lines,
- Pressure and temperature at the chamber,
- Oxygen content,
- Drift velocity.

For economy, there is one oxygen analyzer and one drift-velocity monitor per wheel. They are located at a common place in the US area, and sequentially sample gas from every exhaust line and from the common supply line. For tests, or in the case of a failure, these two monitors can be connected to a different wheel.

Temperature variations affect the drift velocity. With both electric field and gas pressure kept constant, the drift velocity and hence the maximum drift time will vary with the density of the gas and thus with temperature, as $\Delta t_{max}/t_{max} = -\Delta v_d / v_d = -\Delta(\rho^{-1/2}) / \rho^{-1/2} = \Delta\rho / 2\rho = \Delta T / 2T$. A 1% change in t_{max}, tolerable for the hardware trigger, corresponds thus to a $\Delta T = 6\ ^oC$ temperature variation. The gas temperature will be constant to 1 ^oC at the supply line. The cavern is also kept at constant temperature, but with a gradient of up to 7 ^oC along its height. This means that the temperature (after some running-in time) will be very constant, although it is slightly different for each chamber. Monitoring of the chamber temperature is therefore sufficient during the runs, while a further correction for any temperature effect can be performed during the offline reconstruction.

3.6.3 Mixer and purifier

Gas storage, mixer, purifiers and further analyzers (Fig. 3.6.5) are located in a gas building at the surface (Fig. 3.6.6). The gas is purified and recirculated. Gas samples are analyzed, and a small fraction of the gas is replaced by fresh gas.

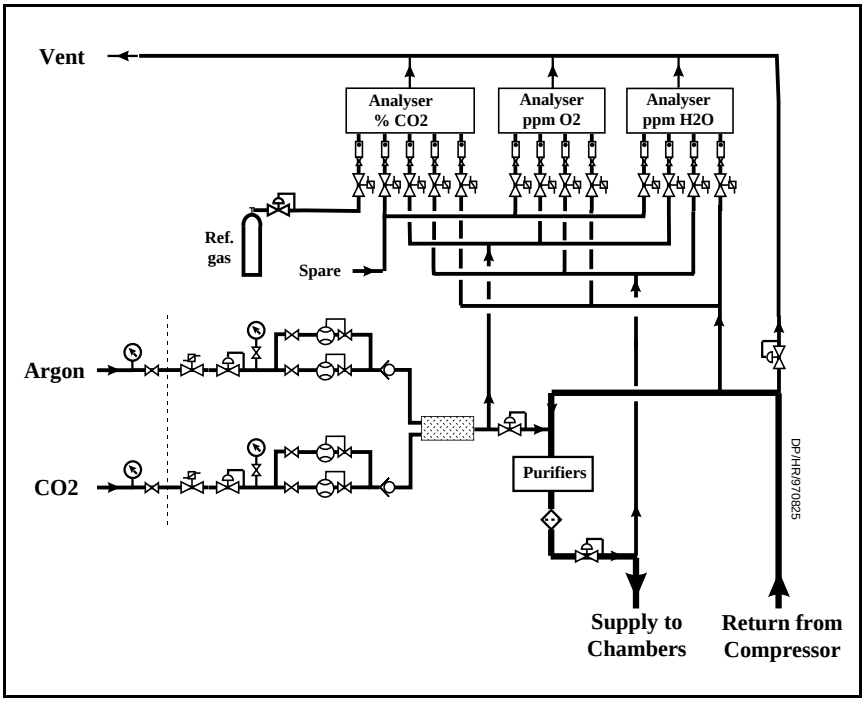


Fig. 3.6.5: Schematic circuit of the gas mixing and purifying station, located in the surface building.

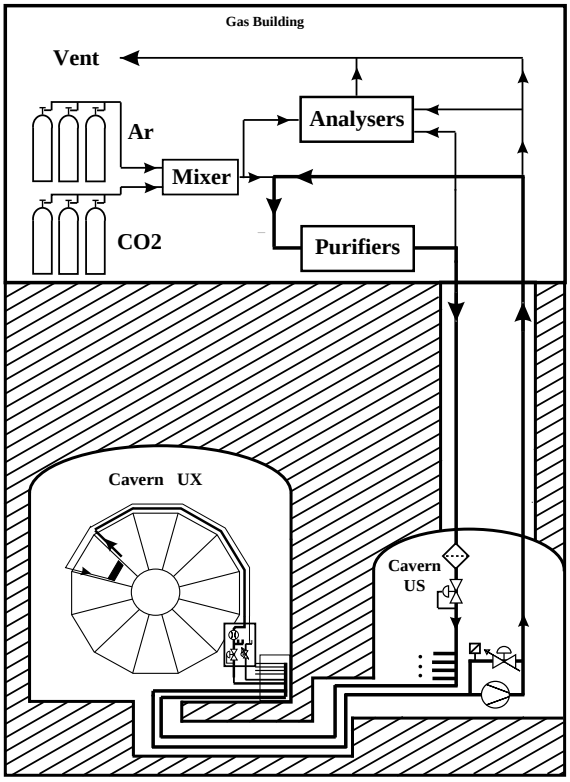


Fig. 3.6.6: General view of the gas system, showing schematically the location of the main components. Gas storage, mixing and purifying are done in the surface hall. Main gas flux regulation and gas analyzer for each wheel are in the cavern US. Each of the five barrel wheels has one connection to the cavern US. The elements to distribute the gas to the 50 chambers are located on the wheel.

3.6.3.1 Mixer

The flows of component gases are metered by mass-flow controllers, which have an absolute precision of ~1% over a year, and have a medium term stability of ~ 0.3% under constant conditions. Flows are monitored by a process control computer, which continually calculates the mixture percentages supplied to the system. The process control computer compares the running mixture with the required mixture: this required mixture may be a constant ratio, or alternatively may be derived from comparison of the running mixture with a reference gas mixture in the infrared analyzer.

3.6.3.2 Purifier

Most close-loop circulation systems need gas purification in the return line in order to achieve high regeneration rates (usually 90%). The most relevant impurities which may harm the detectors are air, water vapor, halogens and silicones.

The proposed purifier cartridges have uniform sizes and gas connections throughout all CMS gas systems. The purifying agents inside the cartridges are chosen individually depending on the specific cleaning requirements for that gas. In this way, the set-ups for the regeneration can be standardized and remain interchangeable. Three different cartridge sizes are available to adapt the individual purifier to the required gas flow and the needed cleaning capacity.

For the barrel muon system the oxygen level will remain below 500 ppm. Two cartridges are filled with a reducing agent; e.g. activated copper, which is oxidized by free oxygen in the gas stream forming a metal oxide and thus leaving the gas oxygen-free. If necessary, the gas may be dried in an independent twin column packed with a molecular sieve upstream of the oxygen cartridges. The advantage of having two parallel cylinders for each purifying stage is that one can run the gas mixture through one of them while the other one is regenerating. The molecular sieve is regenerated by heating to 180 ^{o}C under argon flow, the copper oxide is reduced from oxygen at 220 ^{o}C using a counterflow of Ar + 7%H_2. The entire process of operation and regeneration is supervised by a process controller and can run without human intervention.

The gas purity at the output of the purifier is likely to be better than required, thus one may divert only a fraction of the total flow through the purifier in order to lengthen its running time. Humidity and oxygen meters are available in the surface building to measure the impurity concentrations before and after the purifier.

3.7 INSTALLATION AND MAINTENANCE

3.7.1 Installation

As we have seen, the barrel DT chambers are connected to the iron by a three-point support scheme in which rollers are connected to the chambers and rails are attached to the iron structure. The chambers will be installed on the wheels in the surface hall. After the construction of each of the five wheels composing the CMS barrel structure, the relevant 48 chambers (i.e. 4 chambers per sector, 12 sectors per wheel) are inserted inside the “muon pockets” in the iron by sliding them on the rails. For installation purposes the DT and RPC chambers pertaining to a particular slot will be joined to form a single body.

Since the installation is not particularly difficult, no special equipment has been designed yet, but some tower-like structure equipped with extension rails in which the chambers will be placed during the installation phase is foreseen.

3.7.2 Maintenance

In the baseline design each DT chamber will have “on chamber” the following equipment:

- inside the gas volume:
  1) HV-decoupling boards,
  2) temperature and pressure sensors,
  3) HV distribution boards.
- outside the gas volume
  4) trigger boards (option under study),
  5) readout boards (option under study),
  6) gas, LV and HV patch panels,
  7) HV, LV and gas connections.

Most of the equipment mentioned above is located on the faces of the chamber which are visible from the outside of the iron structure. Studies are in progress and prototypes are being built in order to prove that this is also true for all trigger and readout boards. Of course, for the crossed Super Layer (i.e. with the wires parallel to the beam line) the gas enclosures that are at the end of the wires are inside the iron structure.

With all this in mind, we can divide the maintenance needs for the installed detector into three main categories that call for different scales of intervention:

- routine access to accessible hardware

This category contains interventions in order to replace a faulty card, isolate a sparking wire or change gas connections. For this it is "only" necessary to get to the chamber and it is hence required that no permanent installation, including the cables of the DT chambers themselves, be in front of the chamber and that the iron wheels are sufficiently open such that a convenient scaffolding can be installed. Unfortunately, due to the necessity of bringing out cables from the inner detectors, the chambers are blocked in the central wheel on one side (alternating every sector) by permanent structures. In this case, it might also be necessary, depending on which side of the chamber must be accessed, to install the necessary extension rails that allow us to pull the chamber completely out for maintenance. Repair work could then be done in place, but the wheel's opening must give the necessary space.

- routine access to hidden hardware

This class is an extension of the previous one and should be required only to access a crossed Super Layer in case of problems with a wire, front-end card or the HV distribution. For these interventions one must extract the chamber and hence we have the same requirements stated above in the case of a chamber blocked on one side.

- special access

It might be necessary, in hopefully rare instances, to remove a chamber from the iron structure and bring it to a dedicated hall where sophisticated checks and/or repairs can be carried out. In this emergency, one must be able to open the iron wheels wide enough to bring in the installation device (as above). It is also required that there be available a sufficiently equipped hall to carry out these kinds of interventions on defective chambers. The necessary equipment is a gas distribution system and a crane facility in a semi-cleanroom environment.

3.8 PRODUCTION PLANS

Six institutions will take part in the DT chambers construction: Bologna, CIEMAT (Madrid), Padova, RWTH (Aachen), Torino and Wien. Chambers will be assembled at three sites: CIEMAT (Madrid, Spain), INFN LNL (Padova, Italy) and RWTH (Aachen, Germany). In these sites, separated production lines will assemble and briefly test the DT chambers before shipping them to CERN. The Italian site will be built and manned by the three involved Italian institutions.

The availability of three fully equipped and independent assembly sites gives some protection against possible local problems, which might appear in such a long running project.

In the present definition of the project there are items that should be provided to the production sites by other sources or by other collaborating laboratories: the most important are the aluminum plates equipped with strips and the aluminum I-beams already glued to the LEXAN profiles; both should have passed the HV test. INFN Torino is planning to take over the aluminum plates equipment.

A possible chamber construction share amongst the three sites takes into account the number of wired tubes, to be supplied in the ratio 50%, 25% and 25% by Italy, Germany and Spain. This would imply that the 110 large MB3 and MB4 type chambers are assembled in Italy while the MB1 and MB2 types, some of which equip also the fourth station, are shared by

Germany and Spain, which should produce 70 chambers each. Spare chambers are to be added to these numbers.

The production plan foresees the assembly of the lines in fall 1998 in order to start the production during 1999. The anticipated time required for the production of the full set is 4.5 years. After the production, the chambers will be shipped to CERN where they will be stored and tested before installation. The installation phase will start in mid 2001 and will be completed by the beginning of 2004.

In conclusion, the barrel muon groups are moving in the direction of defining the final tools and starting the assembly of the production lines in the allocated halls. As an example the one in Legnaro is shown, as it stands waiting to be filled by assembly tables, in Fig. 3.8.1.



Fig.3.8.1: The hall in the Legnaro INFN National Lab. near Padova ready for the installation of the DT chamber production lines; at the far left the equipped table used for the assembly of MB96.

3.9 PERFORMANCE: TESTS AND SIMULATIONS

3.9.1 Results of tests in magnetic field

Stray magnetic field is present in the barrel chambers. In the chamber pockets inside and outside the CMS return barrel yoke, the field is inhomogeneous in direction and intensity, and the latter can reach locally non-negligible values. It has, however, on average a good symmetry around the beam line axis. As a result, we can consider it as having only two main components. One, B_r, is radial and perpendicular to the chamber plane, and the other B_Z, is axial and lies in the chamber plane, parallel to the Φ SL wires and perpendicular to the Z SL wires.

The expected value of the two components, computed by a two-dimensional program (ANSYS), is shown in Fig. 3.9.1. It is worth noting that the axial component reaches a small value (less than 0.2 T) which is constant with z. Large variations occur only in the dead spaces between the wheels. On the other hand, the radial component reaches rather significant values in some chambers (e.g. in MB1 near the Endcaps). In addition, it is not constant and may even invert its sign in some cases (e.g. MB4).

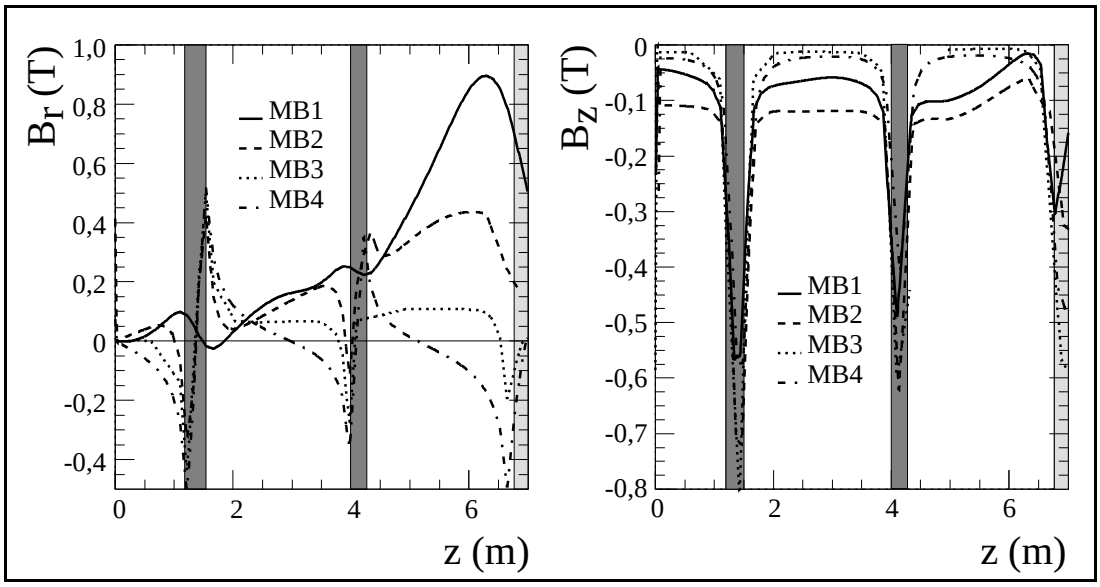


Fig. 3.9.1: The magnetic field components parallel (B_Z) and perpendicular (B_r) to the proton beam axis inside the barrel muon chambers of the CMS detector. The shaded areas are the gaps between the detector rings.

The main source of concern is the absolute value of the radial component and its variation along the chamber wires. The presence of an axial field affects the symmetry of the tube behavior with respect to the track angle (see Fig. 3.9.2).

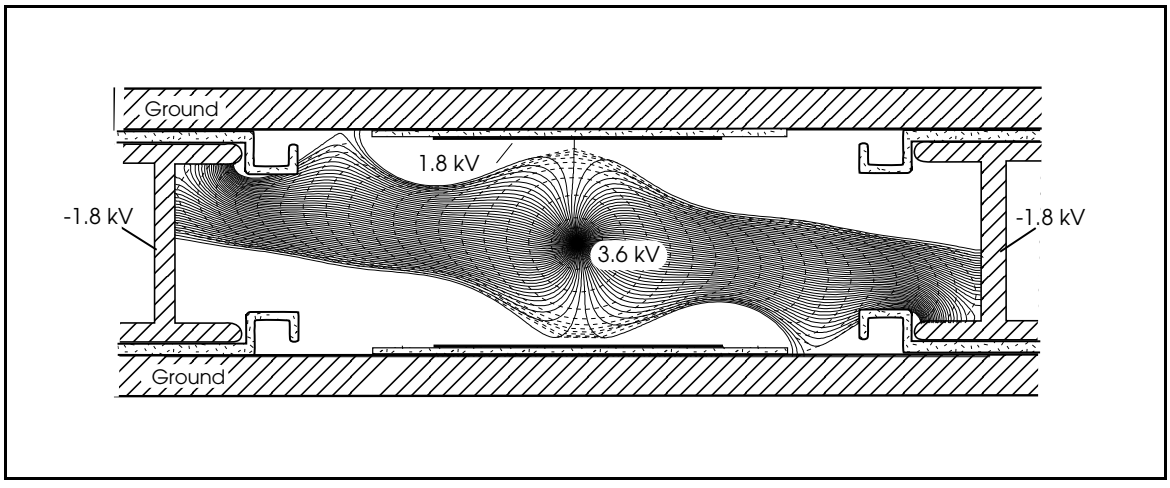


Fig. 3.9.2: The drift cell of the CMS barrel muon detector under the influence of a magnetic field of 0.45 T parallel to the anode wires. The drift gas is Ar (85%) CO_2(15%).

The magnetic field affects drift chamber performance because the electron paths are modified by the non-vanishing value of the *v x B* component of the magnetic force. The amount of the deviation is proportional to the cosine of the so-called Lorentz angle. This angle depends on the gas mixture and on the electrical field shaping inside the cell.

Table 3.9.1 shows measurements of the Lorentz angle and the effective drift velocity in the CMS DT in the presence of a radial magnetic field. The reported values are deduced from data collected with a small DT chamber in a configuration in which the magnetic field was perpendicular to the chamber plane, simulating the CMS radial field, and parallel to the impinging beam of particles . The Ar/CO_2 ratio was 85/15 and the drift field was around 2 kV/cm. These data are included in the results presented later in this section.

Table 3.9.1

The drift velocity and corresponding maximal drift time and the Lorentz angle (α_L) for different voltage and magnetic field settings.

U (kV)	B_N(T)	t_{drift}^{max} (ns)	$<v_{drift}>$ (μm/ns)	α_L (deg)
	0	351±2	55.6±0.2	
3.3/1.5/-1.5	0.5	356±2	54.7±0.2	10.4 ± 2
	1.0	394±1	49.5±0.2	26.4 ± 2
	0	346±2	56.4±0.2	
3.6/1.8/-1.8	0.5	351±2	55.7±0.2	9.7 ± 3
	1.0	373±1	52.3±0.2	22.4 ± 1

The radial component is not expected to introduce important local distortions in the x-t relation. The drift path will be longer, the net result being an increase of the drift time proportional to the distance from the wire. The effect can be accounted for by a reduced drift velocity.

The axial component affects the Z and Φ cells in different ways. In the Z cells, the axial component is perpendicular to the wires and parallel to the midplane electrostatic field. The effect is expected to be small or negligible. In the Φ tubes the axial field is parallel to the wires. It generates a rotation of the field path pattern around the wire axis, as shown in Figure 3.9.2. The distortions depend on the field intensity and affect the x-t linearity, the value of the effective drift velocity and also the cell geometrical acceptance in the region enclosed in the C-shaped profile of the aluminum I-beam.

The effects of the magnetic field on the performance of a DT Super Layer have been studied in the CERN H2 beam by putting DT Super Layer prototypes in a uniform field generated by the M1 magnet. The muon beam, from 100 to 300 GeV/c in momentum, was parallel or perpendicular to the direction of the magnetic field. The change of direction of the magnetic field required the physical rotation of the huge M1 magnet and only these two orientations were possible. The chamber was installed perpendicular to the beam line, with either vertical or horizontal wires. The supporting frame allowed its rotation around a horizontal and a vertical axis.

Data were taken with the B-field perpendicular to the chamber, and also with B parallel to the chamber plane and perpendicular or parallel to the wires. Data were taken also at various angles by tilting the chamber. Keeping the orientation of the magnetic field fixed and tilting the chamber generates the simultaneous presence of the two magnetic field components. Drift velocity effects due to having tracks with different angles of incidence sum up too. The results of these measurements are shown in Figures 3.9.3 to 3.9.10. Figure 3.9.3 shows the effect of the CMS radial magnetic field component in the range from 0 to 1 Tesla. The B-field is parallel to the beam line, the normal to the chamber plane was parallel to B.

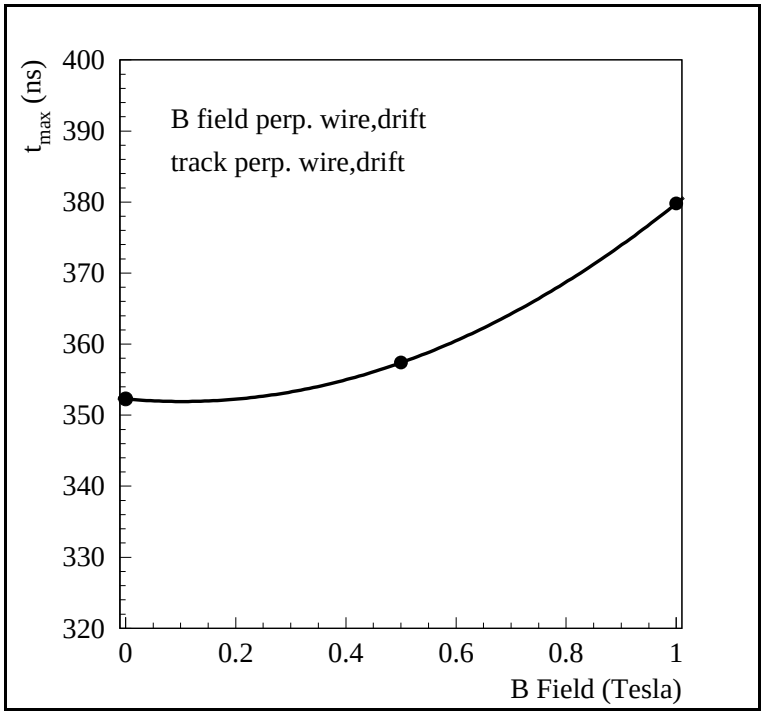


Fig. 3.9.3: Maximum drift time versus the radial component of the magnetic field.

The maximum drift time, from which the average drift velocity is deduced, is computed under the assumption of a linear space-time relation taking the average mean time

$$t_{MT} = \frac{1}{2} \cdot \left[t(j) + t(j+2) + 2t(j+1) \right] = t_{drift}^{\max} \ ,$$

using the arrival time of the drifting electrons in three successive layers (j,j+1,j+2) staggered by half a cell.

Figure 3.9.4 shows that for fields up to 1T the maximum error in the track coordinate measurement due to local non-linearities is 250 μm (t_{MT} is always inside a ± 5 ns window), which is acceptable.

Figure 3.9.5 shows that once the proper effective drift velocity is taken into account there is no sizable degradation of the average spatial resolution.

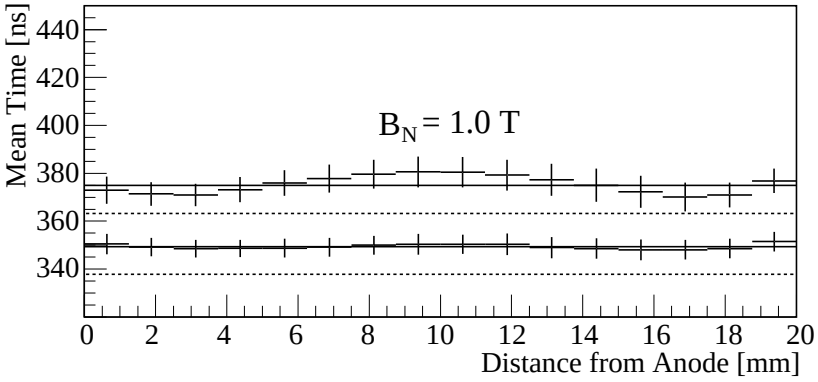


Fig. 3.9.4: The average maximum drift time, calculated from the equation illustrated in the text, for a triplet of drift cells versus the drift distance in the intermediate cell. The vertical bars are the widths of a Gaussian fit, hence the mean time resolution. The dotted lines indicate the beam inter-bunch spacing of 25 ns.

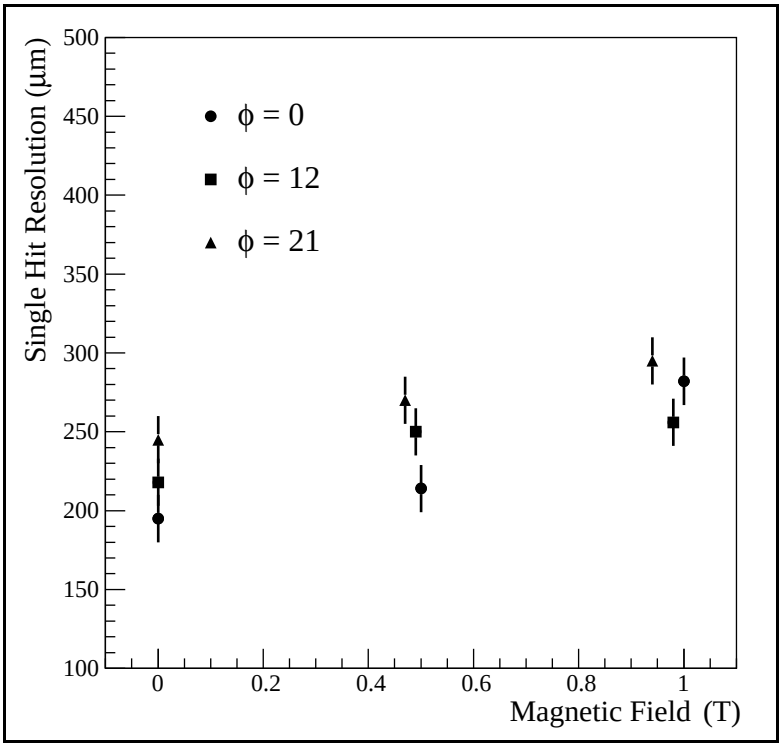


Fig. 3.9.5: Single-cell spatial resolution as a function of the magnetic field component B_N and the measured angle **Φ**.

The effects on the apparent drift velocity and on the resolution of the field components lying in the chamber plane are shown in Figures 3.9.6 and 3.9.7. In this case, B was horizontal and parallel to the chamber plane.

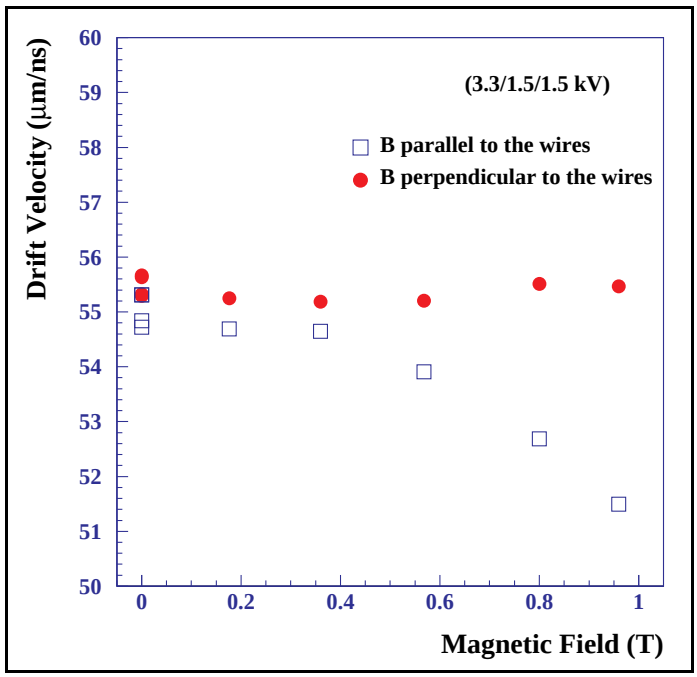


Fig. 3.9.6: Drift velocity as a function of the magnetic field B for vertical and horizontal anode wires.

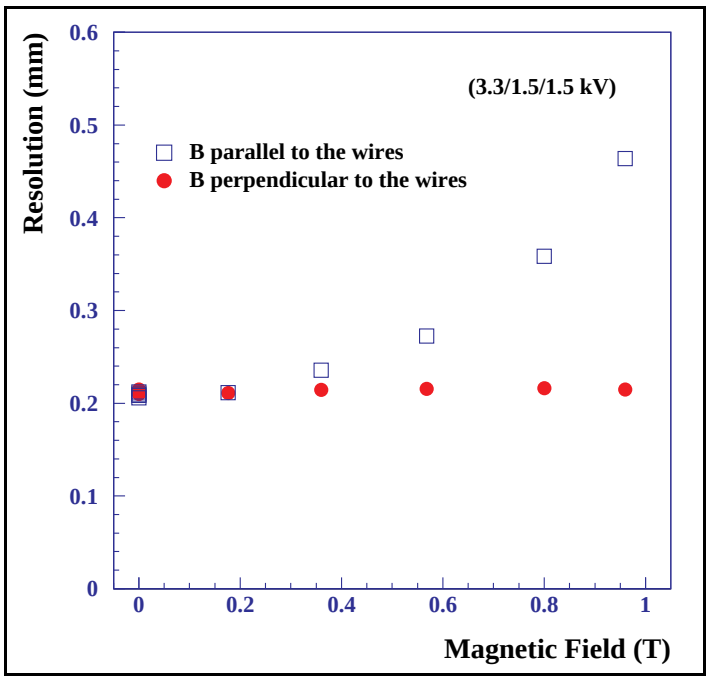


Fig. 3.9.7: Single-wire spatial resolution as a function of the magnetic field B for vertical and horizontal anode wires.

No effect is detected when B is parallel to the drift field. A sizable change in the apparent average drift velocity is found when B is parallel to the wires and larger than 0.6 T. The change is related to the distortion of drift lines which produces longer paths and also non-linearities concentrated in the region near the I-beams (this is clearly seen by looking at Figure 3.9.8). From Fig. 3.9.7 it can be deduced that the degradation of the resolution is not recoverable beyond 0.6 T, at least if a linear space-time relation is assumed. Figure 3.9.8 displays the combined effect of a radial component of 0.9 T and an axial component of 0.45 T parallel to the wires.

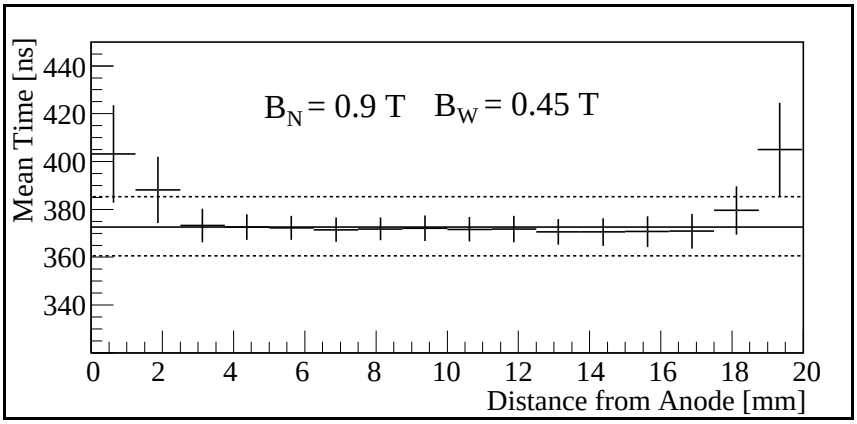


Fig. 3.9.8: The average maximum drift time for a triplet of drift cells versus the drift distance in the intermediate cell for B_N = 0.9 T and B_W =0.45 T. The vertical bars are the widths of a Gaussian fit. The dotted lines indicate the beam inter-bunch spacing of 25 ns.

In Figure 3.9.9, the measured effect of the axial field on the efficiency is reported: a significant drop is observed for field values larger that 0.4 T. This is due to the reduction of the useful cell width with the increasing field (see Fig. 3.9.2).

The above results show that the target values of resolution and efficiency can be reached assuming a linear space-time relation if the radial magnetic field does not exceed 1.0 T and the axial field is below 0.4 T. We expect that these figures will not be exceeded in the space where the DT chambers are located. Field variation along the wire length requires a local correction taking into account the local field value. A radial field uncertainty of 5% at 1 T would introduce a maximum error comparable to the layer resolution and a negligible error below 0.5 T.

The conclusion is, however, different for the trigger capability, where the bunch crossing identification is mandatory. Each BTI, the local track finder circuit, looks over the full length of the drift cell, i.e. of the wire, and the correct effective drift velocity can be set inside each circuit. This puts a constraint on the acceptable maximum drift time variation along the wire and therefore on the magnetic field uniformity. Basically, the variation in the maximum drift time along the wire should never exceed the 25 ns, i.e. the interbunch time. However the bx identification is obtained by looking at the same time at the four layers of the same SL, and the staggered layers smooth out the effect of a possible time error in one of them. As a result, a 25 ns increase of the maximum possible drift time is the limit beyond which the trigger algorithm might start to show some inefficiency. With reference to the BTI description, this inefficiency will start to show itself as an increased rate of LTRG cases.

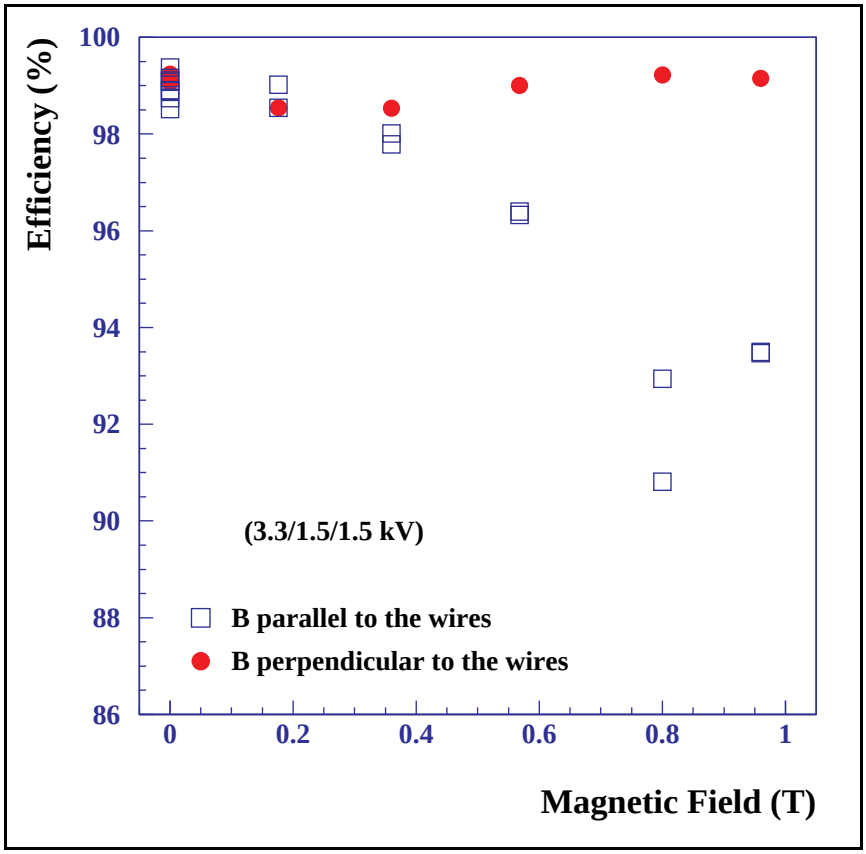


Fig. 3.9.9: Efficiency as a function of the magnetic field B for vertical and horizontal anode wires.

Looking at Table 3.9.1 and Figures 3.9.1 and 3.9.4, it can be deduced that the limit of a 25 ns variation along the wire might be reached only in the MB1 chambers at the border between the barrel and forward yoke. In those chambers, the radial component variation along the Φ cells is 0.7 T, from 0.2 to 0.9 T the value of 0.9 T being reached in a small region of the chamber 50 cm from the end. The axial component exceeds the harmless value of 0.1 T only in very limited regions. Figure 3.9.2 indicates that the presence of an axial field can be roughly simulated by a rotation of the cell around its wire. Being an "internal" rotation, it affects the symmetry of the behavior of a layer with respect to its normal. This can be seen in Fig. 3.9.10, where it can be seen that the limit of 25 ns is exceeded for an angle variation from -24 to +24 degrees, in the presence of an axial field of 0.3 T, a factor of three larger than the expected 0.1 T.

In conclusion, the electrical design of the CMS DTs, the choice of gas mixture and the local track finding algorithm should make the chamber performance insensitive to the stray magnetic field inside the barrel yoke.

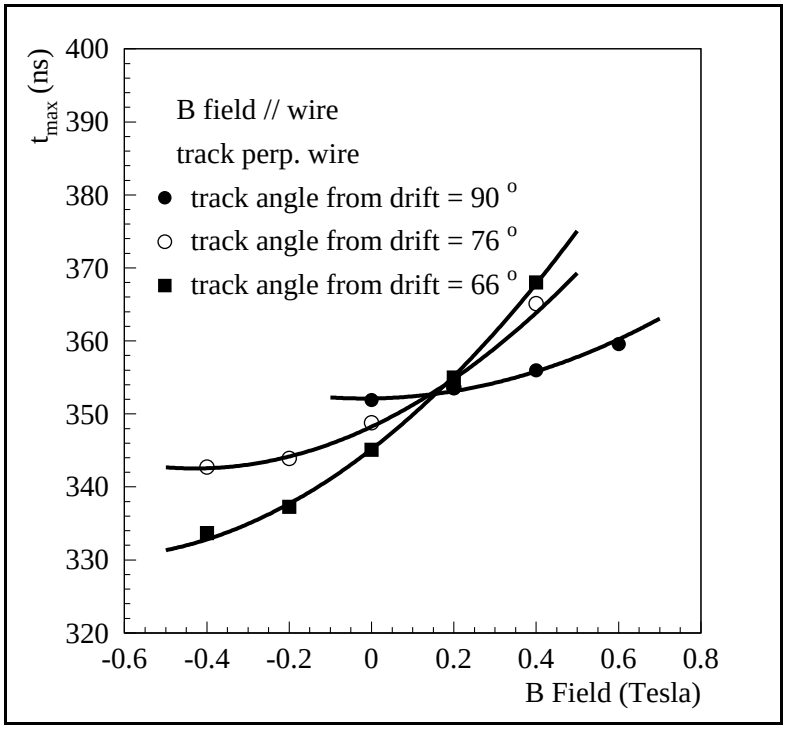


Fig. 3.9.10: The maximum drift time t_{max} versus the magnetic field at different values of the incident angle.

3.9.2 Simulations

Extensive simulations of the cell and chamber behavior were done during the DT chambers design and in subsequent improvements [3.15]. They include electrostatic field computations, using Garfield, and a combination of Garfield and Poisson computer packages, and the Garfield and ANSYS programs to take into account the effects of the dielectric polarization, and the chamber behavior in a magnetic field.

Many details and examples have already been mentioned or shown in previous paragraphs and chapters. We present below a few other examples in Figs. 3.9.11 to 3.9.13. Starting from the computation of the gas gain, compared in Fig. 3.9.11 to the actually measured values, and including the transfer function of the front-end amplifier and shaper, Figs. 3.9.12 and 3.9.13 show a satisfactory reproduction of the basic behavior of the chambers.

3.9.3 Tests under LHC conditions

A large-size drift chamber prototype has been tested under LHC conditions at the CERN GIF facility, as described in section 3.2.4.

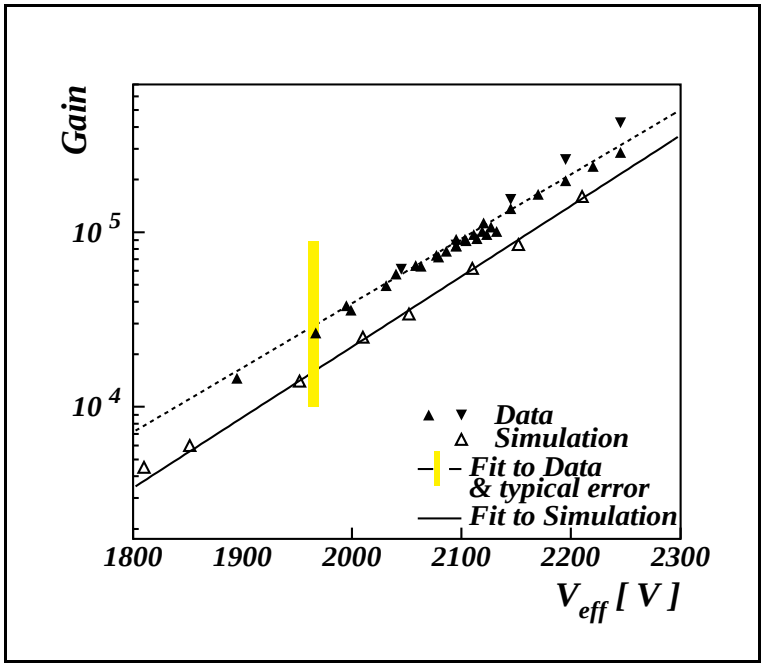


Fig. 3.9.11: Gas gain versus V_{eff} for data and simulation.

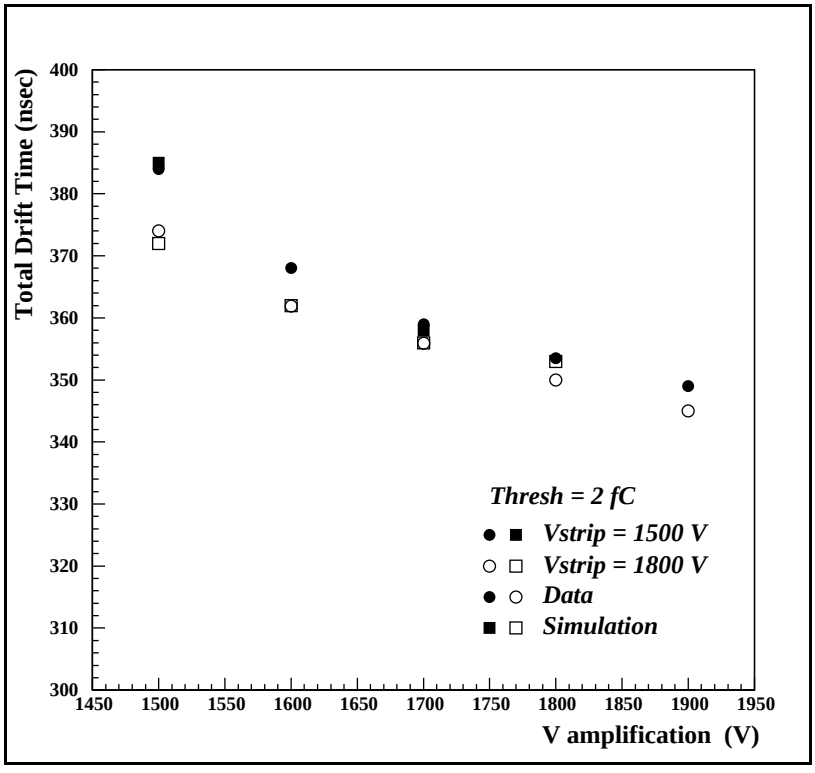


Fig. 3.9.12: Total drift time vs. $V_{ampl.}$ for data and simulation.

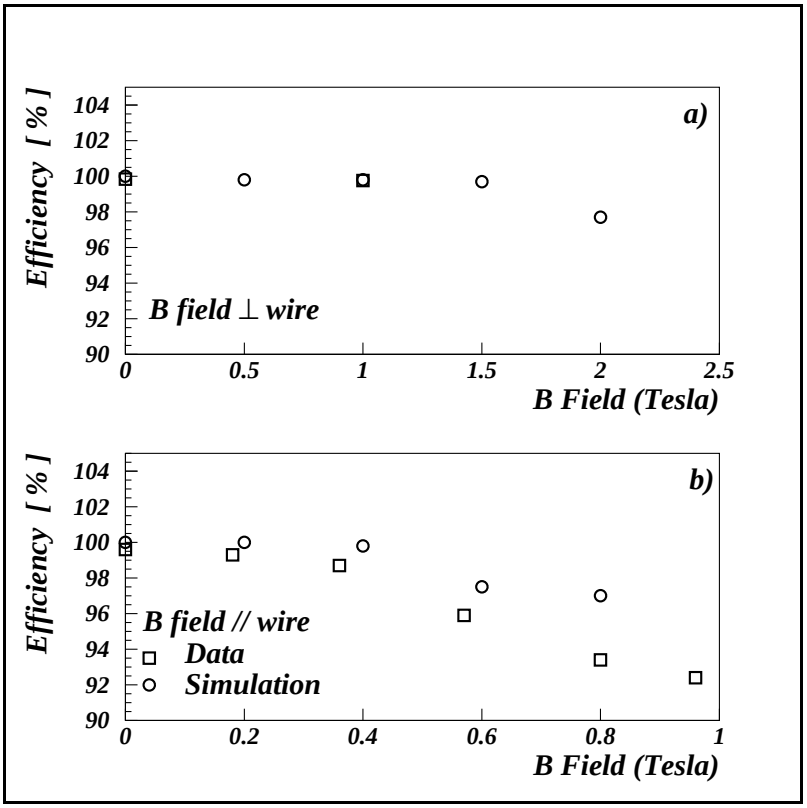


Fig. 3.9.13: Single layer efficiency as a function of the magnetic field intensity; comparison of test beam data and simulation.

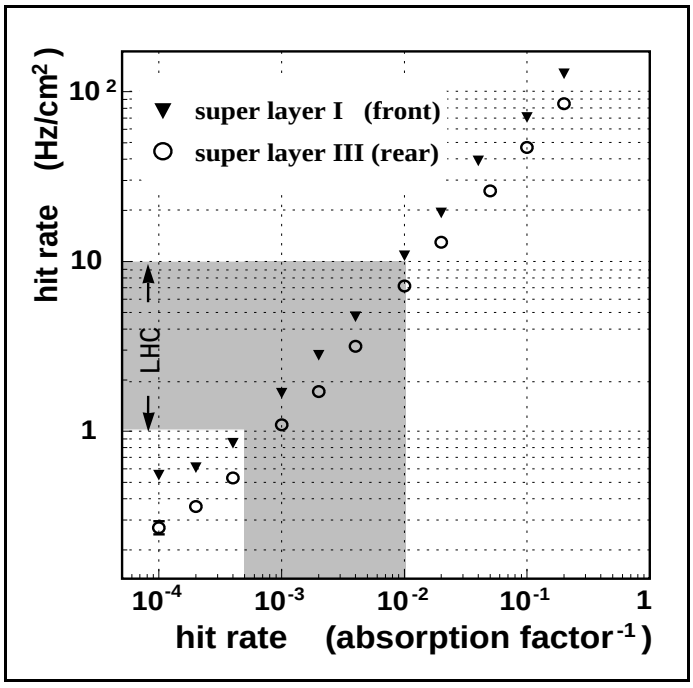


Fig. 3.9.14: Rates of random hits measured in a 12-layer, 3 m x 1 m drift chamber prototype, as a function of the rate of impinging photons from a Cs source. The rate is uniform over the whole chamber area, but is less attenuated at the front Super Layer (SL I). The photon rate is set with lead filters in front of the source.

The chamber has the full 12 layers of drift tubes, is 3 m x 1 m in size, has 480 cells and operated at the standard HV values, i.e. V_{ampl}= 1800 V and V_{drift}= 3600 V. The projections with four and eight layers have one and three meter long drift tubes, respectively.

A wide range of sustained rates of random hits uniformly distributed over the whole chamber was used for the tests. The measured relation between the rate of impinging photons from the Cesium source and the observed hit rate in every drift cell is shown in Fig. 3.9.14. At the LHC, the barrel muon chambers will be exposed to rates in the range of 1 to 10 Hz/cm^2. From Fig. 3.9.14 one can read which filter settings correspond to these rates. The chamber was operated at HV currents reaching the unusually high value of 200 μA at the highest rate tested. It is also visible that at rates significantly higher than the LHC rates there is no saturation in the chamber.In order to measure the performance of the chamber, it was simultaneously exposed to a narrow muon beam of about 150 GeV/c. As evidenced in Fig. 3.9.15, the single-cell efficiency stays very high over the full range of rates corresponding to those at the LHC. The small drop in efficiency at a rate ten times the LHC rate is to some extent explained by the overlap of the muon pulse with the pulse from an earlier random hit. The leading edge is then shifted in time, falls outside the time window used to measure the efficiency, and causes an apparent loss of efficiency. This depends on the total rate, and thus requires a three times larger rate to produce in the short cells the same effect as in the long cells. The data corroborate this interpretation.

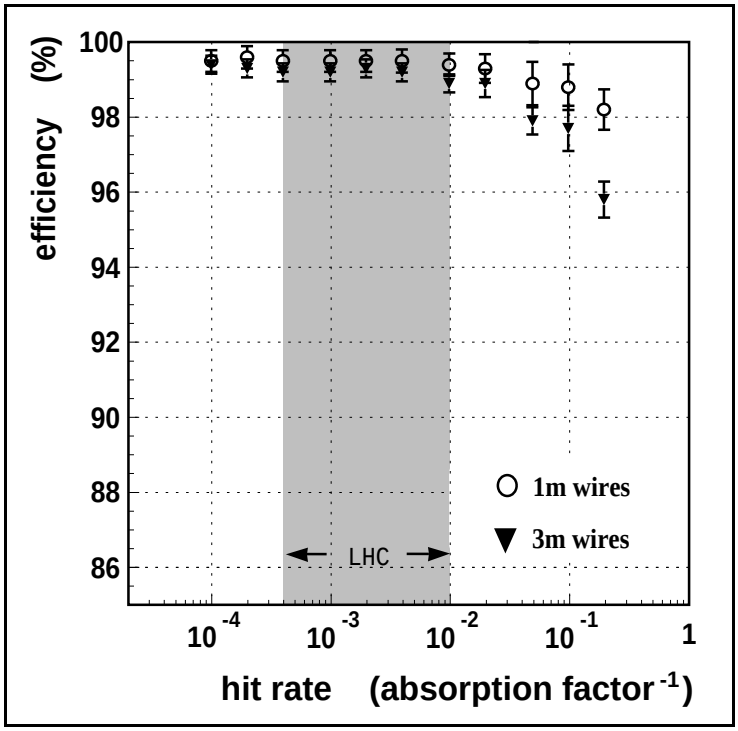


Fig. 3.9.15: Efficiency of a single drift cell, as measured with the help of a narrow muon beam operated simultaneously with the wide photon beam.

The single-cell resolution was obtained from the reconstruction of the track segment in each Super Layer. Random hits close to the muon track disturb the reconstruction, and are visible as a second, wider pedestal on the resolution peak. Also, hits from electromagnetic

secondaries produced by the high-energy muon contribute to this pedestal [3.16]. The standard deviation of the Gaussian is shown in Fig. 3.9.16 for a wide range of hit rates. For rates up to the highest LHC rate about 15% and 25% of the hits contributed to the pedestal for the 1 m and 3 m long drift cells, respectively. The observed width of the Gaussian peak, i.e. the cell resolution, does not vary over the LHC range of rates.

To conclude, tests done with a large prototype demonstrated, for rates as high as ten times the highest rate expected at the LHC, that there is no degradation of the drift tube performance.

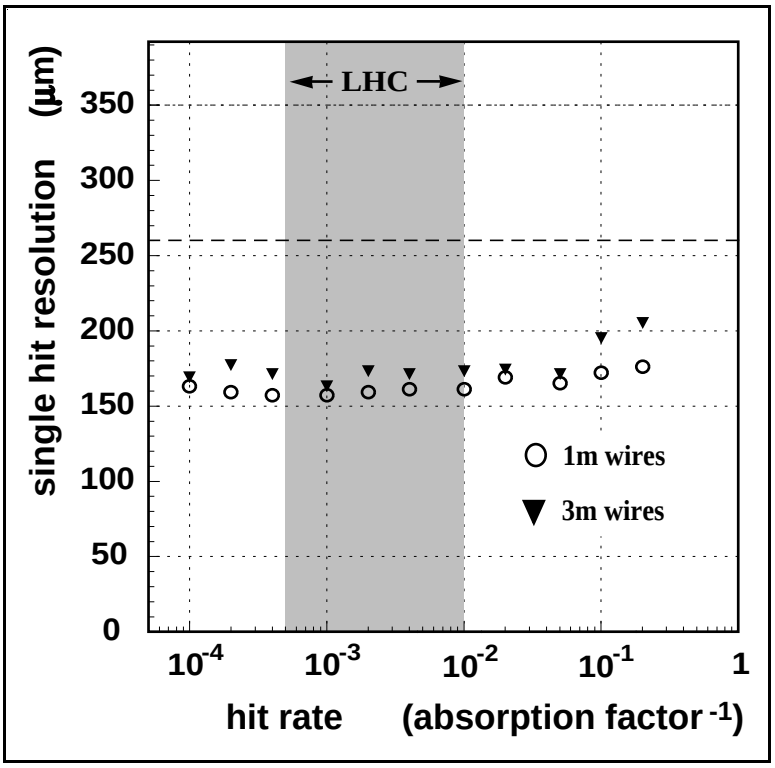


Fig. 3.9.16: Single hit resolution, from muon tracks reconstruction in every group of four drift cell layers. Overlap of muon hits with pulses from muon e.m. secondaries and from the photon irradiation add a pedestal to the gaussian distributions.

References

[3.1] R. Veenhof, "GARFIELD: a Drift Chamber Simulation Program User's Guide", Version 5.13, CERN Program Library W5050, 1995.

[3.2] E. Conti et al., "Experimental Test of the Q2 Drift Tubes Prototype Chamber for the CMS Muon Barrel", CMS Note/97-019.

[3.3] F.M. Newcomer et al., IEEE Trans. Nucl. Sci.40 (1993) 630.

[3.4] M. De Giorgi et al., Proceedings of the 1st Workshop on Electronics for LHC Experiments, CERN/LHCC 95-56, p. 222.

[3.5] G. Kalkanis and E. Rosso, "The inverse power law model for the lifetime of a mylar-polyurethane laminated DC-HV insulating structure", DELPHI 88-58

G. Kalkanis et al., Nucl. Instr. and Meth. A283 (1989)37-42.

[3.6] L. Malter, Phys. Rev. 50 (1936), 48.

[3.7] R. Breedon, Yu. Fisyak, CMS TN/96-035.

[3.8] Oxisorb by Messer Griesheim GmbH, Düsseldorf, Germany.

[3.9] Macor is a machinable ceramic by Corning, USA.

[3.10] J.A. Kadyk, Nucl. Instr. and Meth. A300 (1991), 436.

[3.11] J. Vandenhirtz, "Studien zum Bau von Driftkammern fuer den Myonnachweis am LHC", Diploma Thesis RWTH Aachen 1996; J. Tutas, private communication.

[3.12] J. Christiansen, "32-Channel General Purpose Time to Digital Converter", CERN/ECP-MIC.

[3.13] M. De Giorgi et al., "Design and simulations of the trigger electronics for the CMS Muon Barrel Chambers", CMS TN/95-01.

[3.14] CMS TN/96-078.

[3.15] A. Benvenuti et al., "Simulations in the development of the Barrel Muon Chambers for the CMS detector at LHC", Nucl. Instr. and Meth. A, in print.

[3.16] C. Albajar et al., Nucl. Instr. and Meth. A364, 473 (1995).

4. ENDCAP CHAMBERS — CATHODE STRIP CHAMBERS

4.1 GENERAL DESCRIPTION

4.1.1 Overview

An overall view of the CMS Endcap Muon (EMU) system is shown in Fig. 4.1.1. There are 540 endcap chambers of trapezoidal shape placed between the iron disks, which return the magnetic flux of the central solenoid and also shield the chambers. The chambers are arranged to form four disks, called stations (ME1, ME2, ME3, ME4). The station ME1 has three rings of chambers (ME1/1, ME1/2, ME1/3), while the other three stations are composed from two rings of chambers (MEn/1 and MEn/2). All but the ME1/3 chambers overlap in φ and therefore form rings seamless in azimuth. There are 18 or 36 chambers in every ring. The cracks between the chamber rings are not projective, and thus coverage, defined as at least 3 chambers on a muon path, is close to 100% - see Fig. 2.1.2.

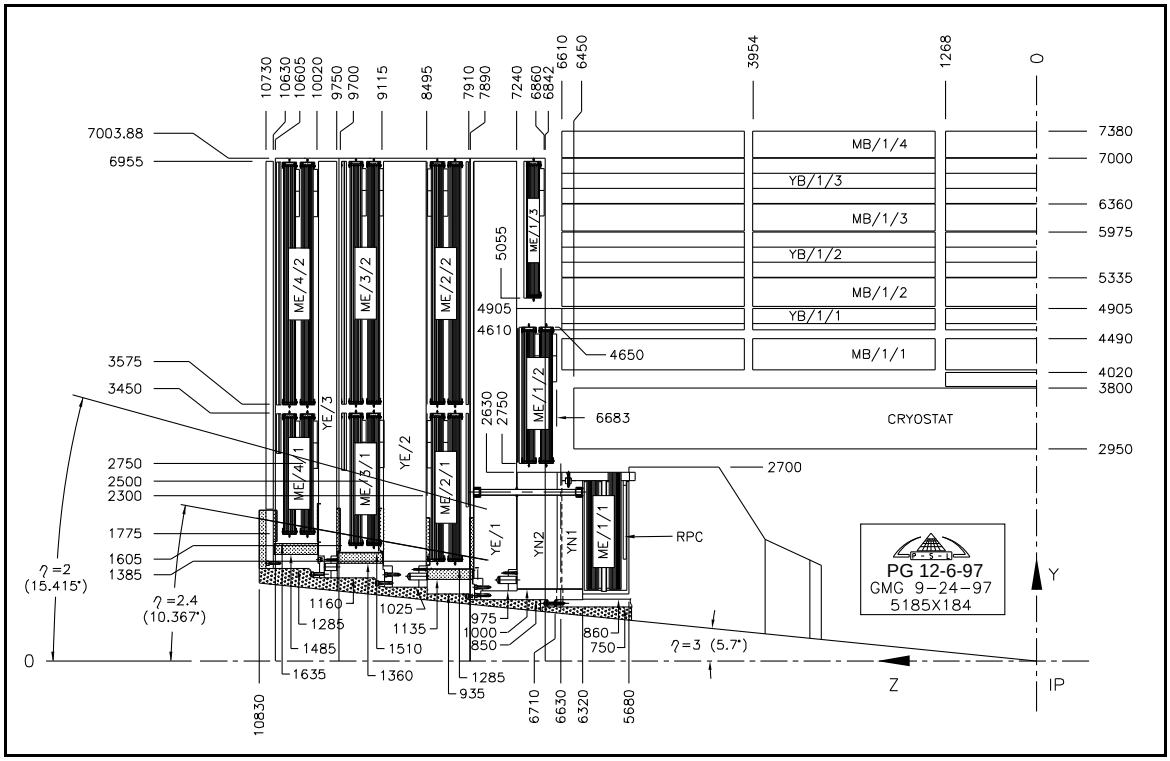


Fig. 4.1.1: Side view of the CMS Endcap Muon system

In the endcap geometry, an r-φ view of the bending of a fixed p_T muon track is η-dependent (Fig. 4.1.2). Results of the direct simulation (Fig. 4.1.3(a)) show that the sagitta, if expressed in linear (cm) coordinates, changes by a factor of 5 from η=1.6 to 2.4 for fixed p_T muons. If the same sagitta is measured in φ-coordinates it is substantially less η-dependent (changes by a factor 2 in the same range of pseudo-rapidity). Thus, φ-coordinates are more natural for measuring p_T and therefore the chambers have trapezoidal shape and readout is arrange in the way to provide φ- and r-coordinates.

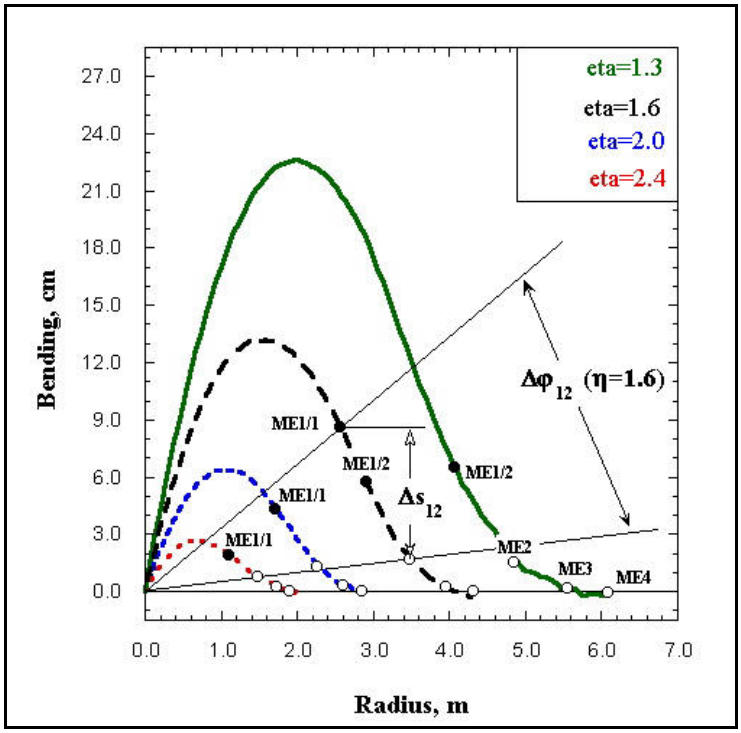


Fig. 4.1.2: Muon tracks of fixed p_T =10 GeV as seen in the r-φ view. The points at which muons cross the chambers are marked (filled circles for ME1 stations, open circles for ME2, ME3, ME4). The sagitta, for example, as measured between IP, ME1 and ME2 Δs12 (expressed in cm) for fixed p_T muons, is clearly η-dependent.

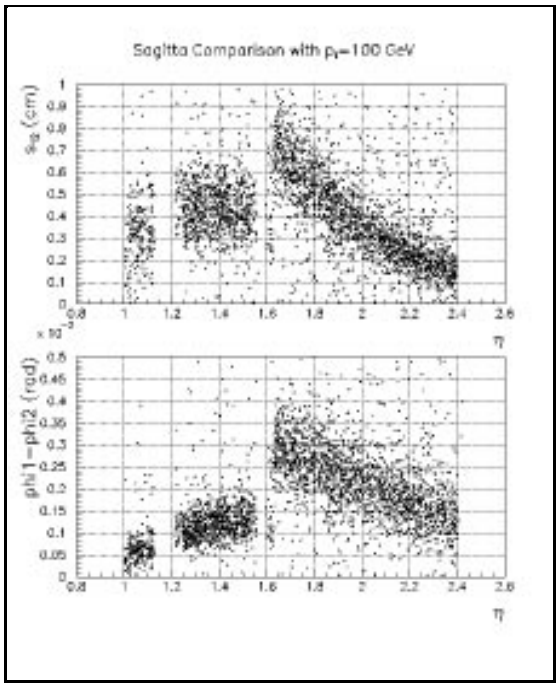


Fig. 4.1.3: Sagitta as measured between IP, ME1 and ME2 stations vs. η: (a) expressed in cm for fixed p_T muons; (b) expressed in φ-coordinates for fixed p_T muons.

The detector technology chosen for the Endcap Muon System is the Cathode Strip Chamber (CSC), a multiwire proportional chamber in which one cathode plane is segmented into strips running across wires. An avalanche developed on a wire induces on the cathode plane a distributed charge of a well known shape which is defined by electrostatics [4.1]:

$$\Gamma(\lambda) = K_1 \frac{1 - \tanh^2 K_2 \lambda}{1 + K_3 \tanh^2 K_2 \lambda},$$

where $\lambda = x/h$ (x - coordinate, h - cathode anode spacing), $K_3 \approx 0.45$ for ME1/1 and ≈ 0.33 for the other chambers, where

$$K_2 = \frac{\pi}{2}\left(1 - \frac{1}{2} K_3^{1/2}\right) \quad \text{and} \quad K_1 = \frac{1}{4} K_2 \cdot K_3^{1/2} \,/\, \operatorname{atan} K_3^{1/2}$$

Charpak et al. [4.3] showed that by interpolating fractions of charge picked up by these strips, one can reconstruct the track position along a wire with a precision of 50 μm or better (for normal track incidence, the precision is almost entirely determined by the ratio of signal to electronic noise). The principle of operation is shown schematically in Fig. 4.1.4.

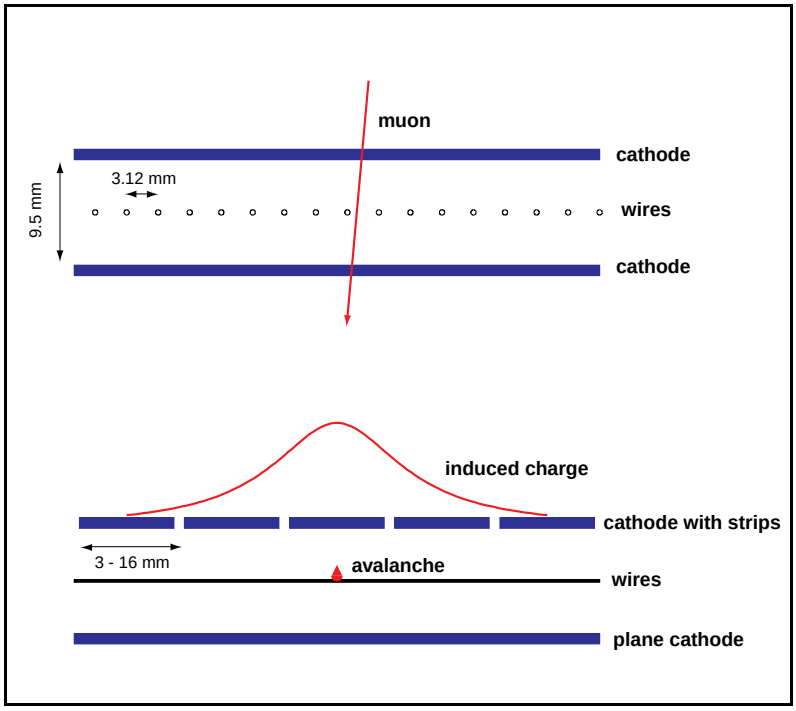


Fig. 4.1.4: Principle of coordinate measurement with a cathode strip chamber: cross-section across wires (top) and across cathode strips (bottom). Close wire spacing allows for fast chamber response, while a track coordinate along the wires can be measured by interpolating strip charges.

The major advantages of CSCs are:

- their intrinsic spatial resolution, being basically defined by signal-to-noise ratio, can be as good as 50 μm,
- closely spaced wires make the CSC a fast detector,

- by measuring signals from strips and wires, one easily obtains two coordinates from a single detector plane (the precise coordinate comes from interpolation of charges induced on strips),
- strips can be fan-shaped to measure the φ-coordinate in a natural way,
- CSCs can operate in large and non-uniform magnetic field without significant deterioration in their performance,
- gas mixture composition, temperature, and pressure do not directly affect CSC precision and thus stringent control of these variables is not required,
- detector mechanical precision is defined by strips which can be etched or milled with the required accuracy and can be easily extended outside the gas volume, thus making survey of plane-to-plane alignment very simple.

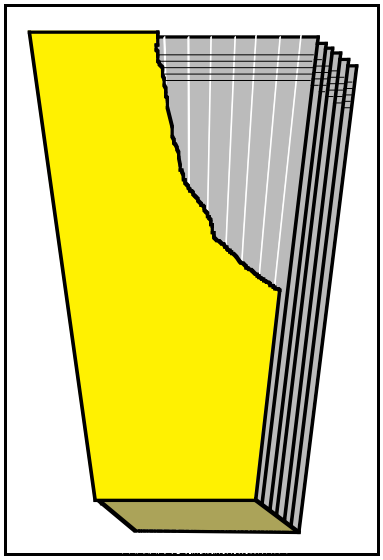


Fig. 4.1.5: Schematic view of an endcap muon CSC: a six-plane chamber of a trapezoidal shape with strips running radially (strips have constant Δφ width) and wires running across.

A typical EMU CSC is a six-plane chamber of trapezoidal shape with a maximum length of 3.4 m and with a maximum width of 1.5 m. A schematic view of a CSC is provided in Fig. 4.1.5. The large chambers cover 10° sectors, while the smaller chambers cover 20° sectors. (see Table 4.1.1). Cathode planes are formed by honeycomb panels with copper clad FR4 skins. Gas gaps defined by the panels are either 6 mm thick, for the ME1/1 chambers, or 9.5 mm thick, for all other chambers. Strips are fan shaped, i.e., they run radially in the endcap geometry and thus provide the phi-coordinate of muon hits. The strip configurations are milled in the FR4, and the strip width ranges from 3 to 16 mm for different chambers. Wires are stretched across strips without intermediate supports and, for readout purposes, are grouped in bunches from 5 to 16. They provide the radial coordinate of muon hits with a few cm precision. For the ME1/1 chamber, which is in a 3T B_z-field, the wires are strung at a 25° angle to a perpendicular to the chamber centerline to compensate for the skewed drift of electrons.

The most important parameters for all chambers are given in Table 4.1.1. Detailed discussions of the chambers are given in Sections 4.2 and 4.3. Overall, the Endcap Muon System consists of 540 six-plane trapezoidal chambers, with about 2.5 million wires, 210,816 anode channels and 273,024 precision cathode channels. A typical chamber has about 1000 readout channels.

Table 4.1.1
Chamber parameters.

Parameter	ME1/1	ME1/2	ME1/3	ME2/1	ME3/1	ME4/1	ME234/2
Basic single plane parameters							
full gas gap (2h), mm	6	9.5					
wire diameter, μm	30	50					
wire spacing, mm	2.5	3.16	3.16	3.12	3.12	3.12	3.16
Active area							
width (top), mm	487	819	933	1254	1254	1254	1270
width (bottom), mm	201	511	630	534	617	685	666
length, mm	1505	1635	1735	1900	1680	1500	3215
Wires							
wire tilt	25°	0°					
wires per plane	600	528	560	620	550	492	1028
wires per wire group	11-12	11	12	5, 6	5, 6	5	16
wire group width, mm	27.5-30	35	38	16, 19	16, 19	16	51
wire group cap., pF	60-150	40-70	50-80	20-60	20-60	25-45	80-150
wire channels per plane	48	48	48	112	96	96	64
Strips							
$\Delta\varphi$(single strip), mrad	2.96	2.33	2.16	4.65	4.65	4.65	2.33
width (top), mm	7.6	10.4	14.9	15.6	15.6	15.6	16.0
width (bottom), mm	3.15	6.6	11.1	6.8	7.8	8.6	8.5
gap between strips, mm	0.35	0.5					
strip capacitance, pF	90-140	110	145	145	130	120	250
radial split of strips	@η=2.0	none					
strip channels per plane	2x64	80	64	80	80	80	80
HV							
Operating HV [kV]	~3.0	4.1					
HV segments per plane	1 or 2	2	3	3	3	3	5
Overall chamber parameters							
Number of chambers	72	72	72	36	36	36	216
Planes/chamber	6						
φ-coverage, degrees	10°	10°	10°	20°	20°	20°	10°
φ-overlap, strips	5	5	none	5	5	5	5
η-coverage	1.5-2.4	1.2-1.6	0.9-1.1	1.6-2.4	1.75-2.4	1.85-2.4	varies
η-overlap	none						
Length, mm	1680	1800	1900	2065	1845	1665	3380
Width (top), mm	613	1078	1192	1534	1534	1534	1530
Width (bottom), mm	311	740	859	751	835	903	895
Chamber thickness, mm	148	250					
Chamber weight, kg	~60	150	160	190	180	160	276

4.1.2 Special conditions and requirements

4.1.2.1 Reliability

Given the scale of the system, the primary concern is obviously its reliability. The system must be designed so that, once commissioned, it will require a minimum of maintenance and repairs. We have paid particular attention to wire strength and fixation, HV segmentation, gas tightness, and chamber rigidity and stability.

4.1.2.2 Off-line spatial resolution: φ-coordinate

Detailed Monte Carlo studies have been performed to identify the required CSC spatial resolution [4.4]. The optimization was done by requiring that the chamber spatial resolution contribution to the precision of muon momentum measurement (standalone muon system) be less or comparable to the contribution of multiple scattering. Muons with p_T<100 GeV were chosen as a reference since this range of momenta covers most of the plausible physics processes. The outcome of the analysis is the 75 μm requirement for the ME1/1 and ME1/2 chambers and 150 μm for the others (both numbers refer to resolution per six-plane package). Prototype results show that this goal is well within reach (see subsection 4.8.2.1).

4.1.2.3 Off-line spatial resolution: r-coordinate

To reconstruct the muon p_T or p, one needs to know the radial position of hits. High background rates impose an additional requirement on the maximum width of the anode wire groups. Radial resolution also affects efficiency of finding a muon track in the tracker by tracing it backward from the muon system. An additional constraint is wire group capacitance, which should remain sufficiently small to ensure high precision of time measurements. Optimization among all of the above requirements leads to the choice of wire group segmentation as specified in Table 4.1.1. Wire group hits are read out in yes/no mode every 25 ns, and thus the radial spatial resolution per plane is defined by the wire group width.

4.1.2.4 Magnetic field

The map of magnetic field shows that the ME1/1 chambers will have to operate in an axial magnetic field ranging from 2.7 to 3.1 T. The effect of such a field cannot be fully compensated by tilting the wires but can be minimized to an acceptable level. The ME1/2 chambers, on the other hand, will be placed in a highly non-uniform field of up to 1.2 T which will inevitably affect their resolution. However, their performance remains within our specifications despite this deterioration. Some of the other chambers will also experience quite noticeable magnetic fields. Discussion of how the B-field affects the CSC spatial resolution, and results of prototype tests and simulation, can be found in subsection 4.8.2.2 and 4.9.

4.1.2.5 Background rates

Backgrounds and shielding issues are discussed in section 1.4. There are four major sources of background hits:

- random hits induced by neutrons/gammas,
- punchthrough and pi/K in-flight decays,
- tunnel muons,
- e/m debris associated with energetic muons going through matter, e.g., calorimeter, iron disks, etc.

The rate of random hits is largest and goes as high as 1000 Hz/cm^2 in the bottom area of the ME1/1 chambers. Although the rate per plane is very high, hits rarely penetrate more than a few planes [4.5], so that this background can be suppressed by having multilayer chambers.

Experimental results and simulation have shown that six-plane chambers with a requirement of having 4 out of 6 planes hit will provide sufficiently robust performance (see sections 4.8.4 and 4.8.5).

The rate of punchthrough background reaches about 300 Hz/cm^2 in the worst spots. The danger of punchthrough is that the charged particles will get through the entire six-plane chamber.

The rate of tunnel muons is in the range of a few Hz/cm^2. Although this is relatively low, the hits induced by these muons in the φ-coordinate view appear as if they were produced by muons coming from the IP with infinite momentum. Thus this background is a primary concern for the trigger. The capability of the chamber of pointing back to the IP (θ-angle) is of critical importance for suppressing these fake triggers.

The last source of background (muon Bremsstrahlung) will compromise track measurements with a few percent probability per station. If one requires high precision measurement, this can reach almost 10% (for details see subsection 4.8.4). It is worthwhile mentioning that this background is associated with real muons themselves and is therefore luminosity independent.

4.1.2.6 Aging

High hit rates up to 1000 Hz/cm^2 raise a question of chamber aging due to gas polymerization on wires or cathodes. The baseline operational point corresponds to a charge per avalanche of about 100 fC, as seen by the fast cathode pre-amplifiers, which have a shaping time of 100 ns. This corresponds to about 1 pC total charge released in an avalanche. Assuming that one year of LHC operation corresponds to $3 \cdot 10^7$ seconds, one immediately estimates that the total accumulated charge on wires in 10 years of operation at the full LHC luminosity will be 0.1 C/cm. The results of aging tests (see subsection 4.8) show that this number results in a very good safety margin, provided that CF_4 gas is present in the mixture.

4.1.2.7 Trigger: r-coordinate and timing

A track stub in the wire readout side of a CSC is recognised when at least 4 planes have hit wire groups which line up in a pattern consistent with a track pointing back to the IP. The time measurement from a single plane has a spread exceeding the 25 ns window and, therefore, a single plane cannot provide a reliable bunch crossing identification. However, one can take advantage of multiple planes in a chamber: prototype tests show that by taking the second or third earliest hit out of six hits in a pattern, one can achieve a very high efficiency in tagging the bunch crossing (see subsection 4.8.5). The earliest hit out of six also has a very narrow distribution, but this scheme would be very vulnerable to random hit backgrounds. Once all four local track stubs found in chambers are linked to form a muon track, one can take the most frequent bunch crossing ID (out of the four linked stubs) as the bunch crossing ID for the track. In this scheme, one obtains the correct bunch crossing assignment more than 99% of the time, if the individual chambers provide the correct identification with 92% probability or better. This goal is well within the CSC reach (see subsection 4.8.3 and 4.8.5).

4.1.2.8 Trigger: φ-coordinate precision

Trigger rates simulation shows that one needs to have about 30% momentum resolution at the L1 trigger up to p_T of around 50 GeV. This ensures sufficient sharpness of the trigger turn-on curves and thus makes it possible to control the trigger rate, should the background

problems turn out to be worse than anticipated. To achieve 30% momentum resolution, one would need to localize muon hits within about a half-strip width per chamber plane. Hardware implementation to provide half-strip digitization at the trigger level will be discussed in subsection 4.4. Prototype tests proved the capabilities of this approach (see subsections 4.8.2.3 and 4.8.3.2). Using muon hits localized to within a half-strip per plane, special trigger logic will look for patterns of hits consistent with the passage of muons of interest.

4.2 DETAILED CHAMBER DESIGN: ME1/2, ME1/3, ME234/1, ME234/2

4.2.1 Introduction

This section covers the design of the seven types of EMU CSCs, ME1/2, ME1/3, ME2/1, ME3/1, ME4/1, ME234/2, the total number of which is 468. Although being very different in terms of size, number of readout channels and resolution requirements, the basic design grounds for all these chambers are essentially the same. An exploded side view of a CMS Endcap Cathode Strip Chamber, identifying all the major chamber components, is shown in Fig. 4.2.1. Seven panels are stacked together to form six gas gaps. Six out of the seven panels carry strip artwork on one side (strips face up in the drawing), the other side being a smooth uninterrupted ground.

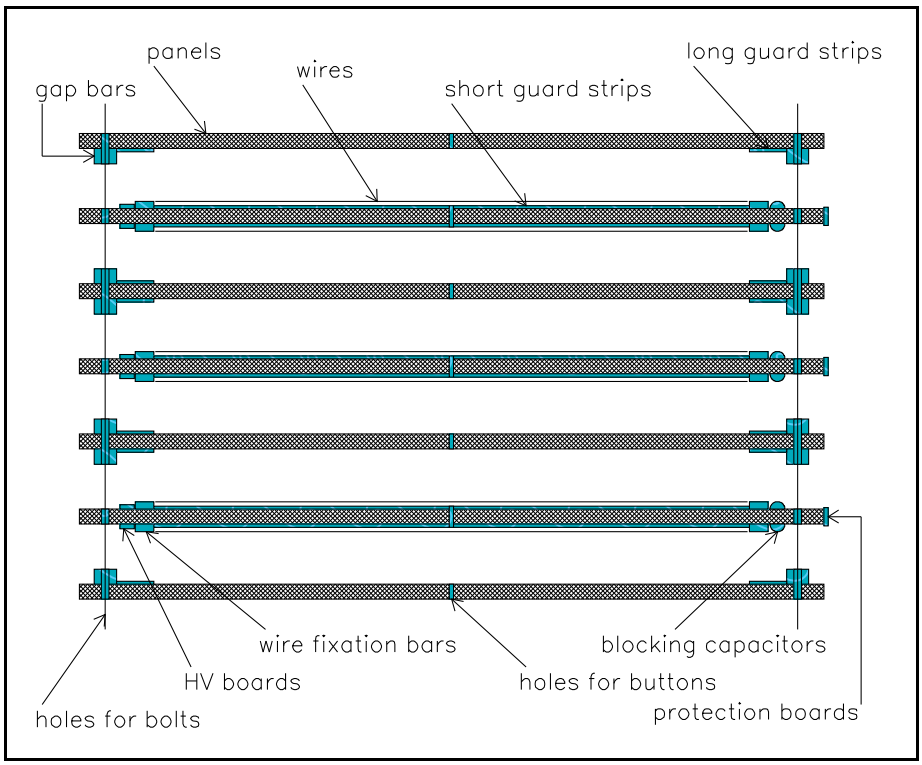


Fig. 4.2.1: Exploded view of a cathode strip chamber (not to scale) showing its main components and the way the chamber is assembled.

Anode wires are wound onto both sides of the three panels called *anode panels*. Naturally, these panels also carry artwork for taking anode signals out at one side of the panels and for feeding high voltage in at the opposite side (HV is applied to the wires). The wires are

soldered and glued to the *wire fixation bars*. Each wire plane will be connected to an independent HV power supply channel. Within a plane, the HV is split between up to 5 segments which can be disconnected from outside of the chamber should HV or wire noise problem persist in any of these segments.

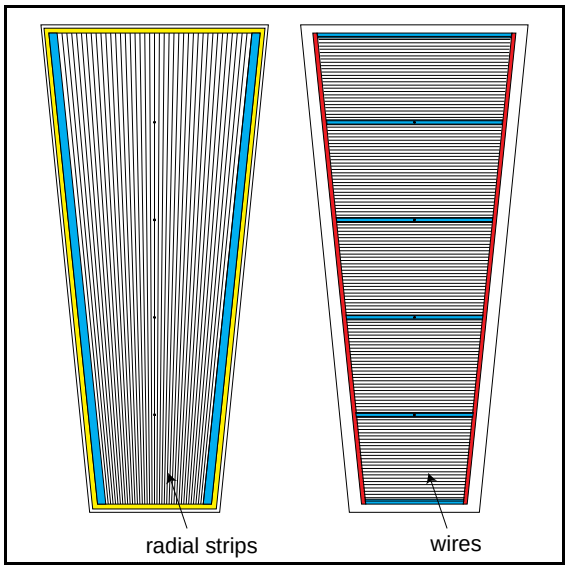


Fig. 4.2.2: Face of a cathode panel showing the arrangement of strips (left) and face of an anode panel showing subdivision of wires into five independent HV segments.

Schematic views of the strip and wire planes are given in Fig. 4.2.2. *Insulating guard strips* are glued to the panels under the first and last wires of each of the HV segments. By charging up, the strips decrease the electric field on the edge wires, which otherwise would be too high. The other four panels, the ones which are free of wires and of referred to as *cathode panels*, have *gap bars* glued to them. These bars define the full gas gap between cathodes. These panels also have long guard strips, or insulation strips, which go over the anode wire ends and insulate them from being exposed to the ground. The entire stack of panels is bolted along the chamber perimeter with the bolts going through the gap bars. When the chamber is assembled, the panels are also tightened down at a few intermediate points, and the cathode-to-cathode distance, or panel-to-panel spacing, at these points is defined by special spacers, referred to as *buttons*. This is done to relax tolerances on panel flatness and to prevent bulging due to gas over-pressure inside a chamber when the working gas mixture is flushed through the chamber.

Not shown in Fig. 4.2.1 is a *global frame* which runs around the chamber perimeter: it stiffens the stack of panels, distributes the compressive force of the assembly bolts, carries all the chamber mounts, and provides RF shielding along the chamber sides.

4.2.2 Panels

The panels are the basis of the chamber mechanical structure: they carry the stress of the wire tension, and a strip pattern is milled on their surface and determines chamber precision. Panel flatness is of critical importance for gas gain uniformity and consequently for the width of a chamber's operational plateau. In addition, the cost of panels amounts to almost half of the

cost of all chamber materials. Therefore, we have conducted a thorough panel R&D program, which included quality tests of panels produced by a few of the most promising vendors. The detailed report of the results can be found elsewhere [4.6]. Described below are the baseline panels.

A panel consists of two copper clad FR4 (fire-resistant fiberglass epoxy) skins interleaved with a honeycomb core made of polycarbonate -a material known for its high structural stability and strength. FR4 skins of 1.6 mm thickness with 34 μm copper are a standard commercial product. The core of our choice has 3.2 mm cells, 80 kg/m^3 density and a crush strength of 140 kPa. Its thickness is 12.7 mm (1/2 inch). Both the core fabrication and the entire process of bonding the skins is done at Plascore [4.7]. Edge filling is not envisioned in our design since the compressive force of the through-bolts is broadly distributed along the panel perimeter by means of aluminum extrusions forming part of the external frame. The ratio of the buckling strength of the panels to the wire tension stress is 9, i.e. there is a sufficient safety factor in the panels to carry this stress. The panels have passed the CERN requirements on flammability and toxic fumes [4.8].

Panel flatness is one of the most crucial characteristics, since the variations in the full gas gap will change the electric field on the anode wire surface and, thus, will result in gas gain variations. Large variations in gas gain will inevitably shrink the operational HV range. Typical sensitivity of gas gain to the electric field on the wire surface is

$$\frac{\Delta G}{G_0} \sim \exp\left(20\frac{\Delta E}{E_0}\right)$$

We set a goal of keeping gas gain variations within a factor of two, which is comparable to the charge spread due to unavoidable Landau fluctuations and would roughly correspond to about a 100 V variation in operating HV. Garfield-based electrostatic calculations [4.9] show that, to satisfy this specification, one needs to ensure that panels do not sag by more than 250 μm on a span between points of support, which does not exceed 60 cm for our chamber design. Plascore-made panels satisfy this criterion. (an example is shown in Fig. 4.2.3). Direct measurements of gas gain variations in the full scale prototypes show that gas gain is indeed uniform within our requirements (see section 4.8).

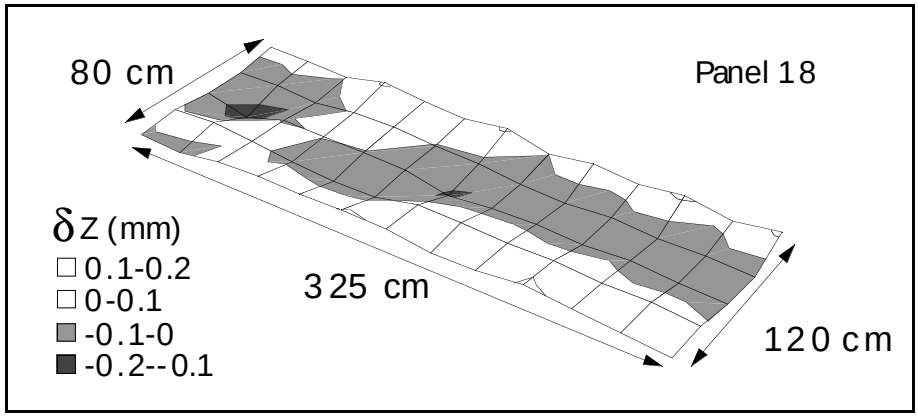


Fig. 4.2.3: Panel flatness as obtained in direct optical measurements. The panel flatness over 60 cm spans is well within the 250 μm specification.

4.2.3 Strips

The pattern of strips and connector artwork is milled directly on the panels by computer controlled machines available at Fermilab: the Gerber, a 2D plotter fitted with a milling head (Fig. 4.2.4), and the Axxiom machine, a 3D router (Fig. 4.2.5). A specially developed cutter tilted at 45 degrees to the panel plane (see insert in Fig. 4.2.4) makes a smooth groove virtually free of burrs which otherwise could cause electrical discharges. Fig. 4.2.6 shows an artwork for an anode panel (i.e. the panel which carries wires and, therefore, in addition to strips, also has an artwork associated with anode signals and HV. Strips are milled radially, i.e. they have constant width in φ as specified in Table 4.1.1. The gap between strips formed by the cutter is about 0.5 mm wide and about 0.2 mm deep. Strips end with traces routed directly to the top panel edge (wide side of a trapezoid) in groups of 16, where 34-pin connectors are later soldered. Mechanical precision of milling has been verified by direct measurements: errors in absolute strip position did not have any accumulative systematics (less than 15 μm over $\pm$60 cm range from a symmetry line of a chamber) and had a local spread of 30 μm (RMS). Strips were also checked for straightness and were found to be straight to the same precision (22 μm RMS). As a consequence of wearing of the cutter (one cutter is used per plane), the gaps between strips do widen slightly from one side of the panel to another, the change being less than 0.1 mm. Beam tests of the P0' prototype, which had strips milled with both 1 mm and 0.5 mm gaps, showed that the difference in gaps had hardly any affect on the induced charge shape and chamber spatial resolution.



Fig. 4.2.4: A photograph of the Gerber machine. It is capable of milling over a 1.5x3.6 m^2 area. The insert shows a specially developed cutter which is tilted at 45° to the panel plane and can follow panel thickness variations so that the groove comes out to be very uniform in thickness and depth and is virtually free of any burrs.



Fig. 4.2.5: A photograph of the Axxiom machine, a 3D-router. This machine is used for cutting trapezoidal panels, drilling all holes, and non-precision milling.

However, the width of the gap between strips does effect strip capacitive coupling and therefore strip-to-strip cross-talk. (Cross-talk is defined by the interplay of the following parameters: strip-to-strip and strip-to-ground capacitances, preamplifier input impedance, and shaper wavefunction response). Direct measurements on the full length prototypes equipped with cathode electronics of essentially the final design showed about 12% signal cross-talk. These levels of cross-talk can be calibrated and taken out in the offline analysis. However, at the trigger level, they are irreducible and their asymmetry (cross-talk to the left vs cross-talk to the right) may affect the comparator-based 1/2-strip resolution. This cross-talk asymmetry was measured on the large prototypes and was found to be less than 0.25% (RMS) and, as simulation has shown, its effect on the trigger is negligible [4.10].

Each plane of a chamber has either 64 or 80 fan-shaped strips to measure the φ-coordinate of tracks when the chamber is placed in the system. Patterns of strips in all six planes are essentially identical, except that odd and even strip planes are rotated with respect to each other to make a half-strip staggering. All but the ME1/3 chambers overlap in φ, and there are five strips in the overlapping region. In addition, each plane has one extra strip of constant width running next to the set of readout strips. This strip, when pulsed from outside the chamber, induces signals on the wire groups which allows for calibration and gives a quick check of the anode electronics readout.

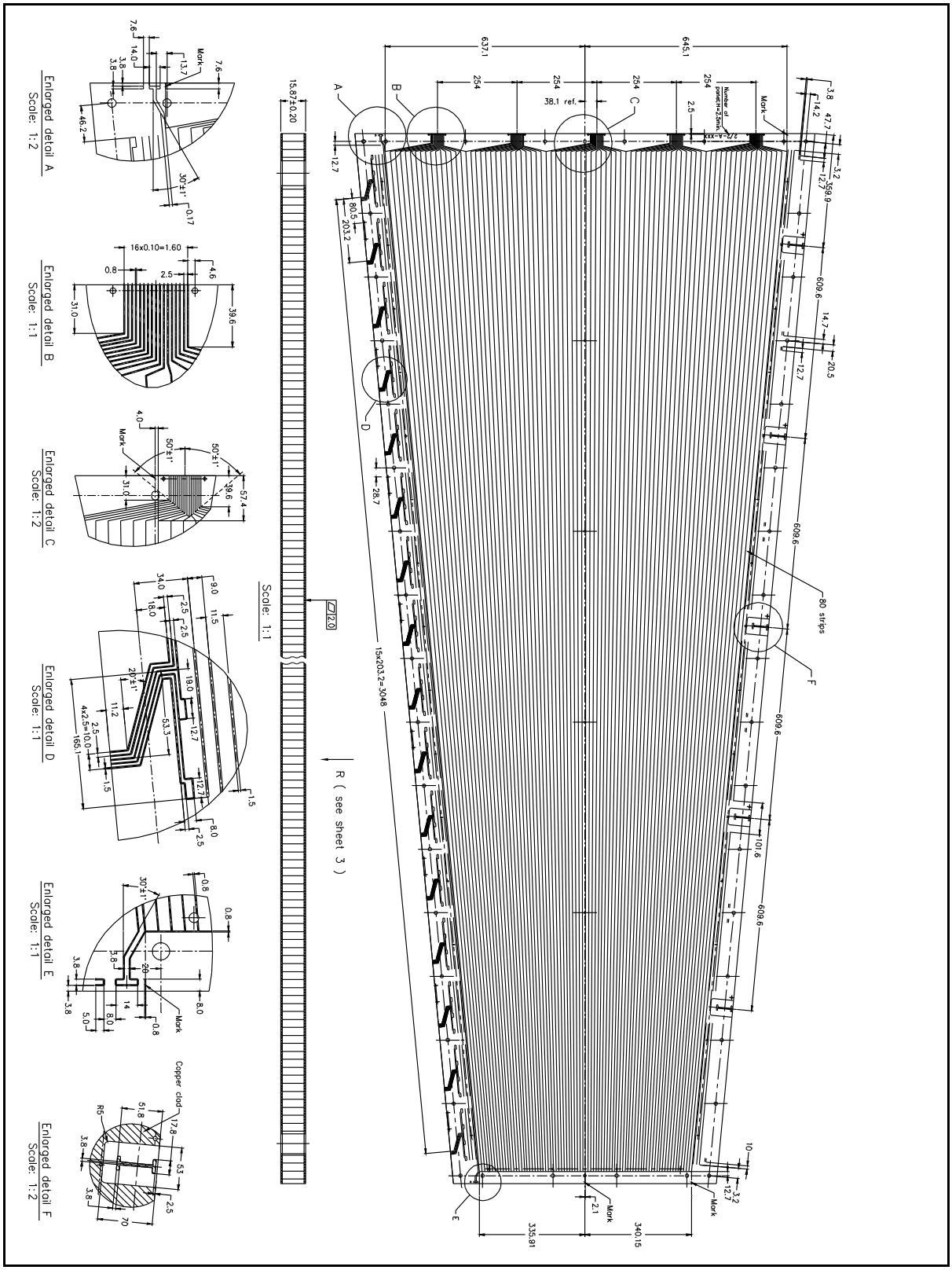


Fig. 4.2.6: Milling an anode panel, i.e. a panel which carries anode wires. In addition to strips, it also has traces associated with anode signals and HV to be applied to the wires.

4.2.4 Gap bars and gas seal

The spacing between panels in a chamber is defined by gap bars (Fig. 4.2.7), one bar along each side of a trapezoidal cathode panel (the four panels free of anode wires - see Fig.s 4.1.1 and 4.1.2). The bars are saw-cut from FR4 sheets and have a width of 25.4 mm (1 inch). Then the bars are sanded to the required thickness of 9.525 ± 0.050 mm (the only dimension of high tolerance). This is a very efficient process and yields relatively inexpensive bars.

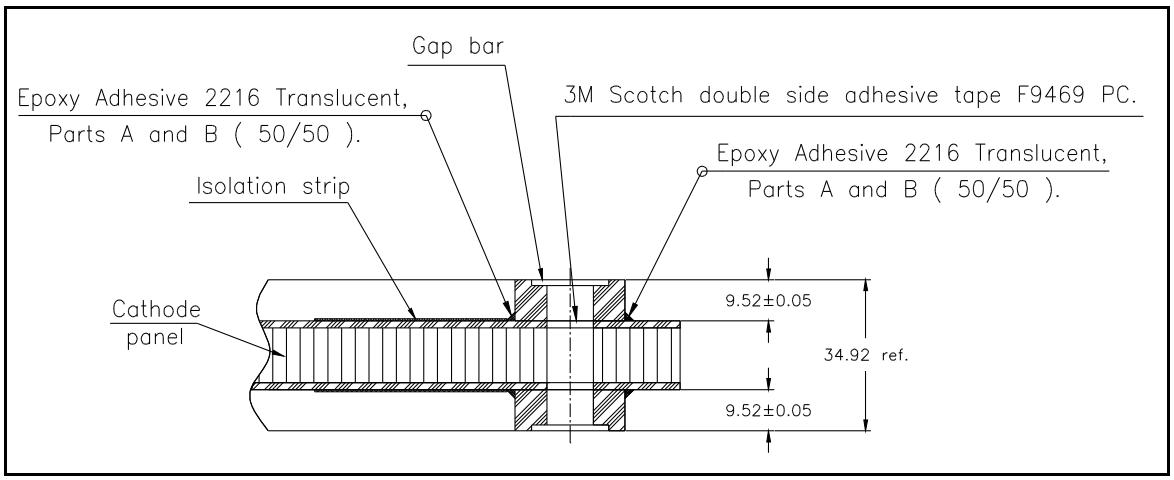


Fig. 4.2.7: Gap bars attached to a cathode panel.

Holes of 10.7 mm diameter for assembly bolts are drilled in the bars with a spacing not exceeding 25 cm, and 2 mm deep counterbores are machined on one side of the holes. During chamber assembly, O-rings will be inserted in the space provided by the counterbores to prevent gas leaks through the bolts.

The gap bars, commercially made, will be inspected on arrival and subsequently glued to the cathode panels. First, the bars are attached to their proper position by means of double-sided scotch tape, which itself makes a very strong bond, and then a continuous bead of epoxy is applied along each side of the bars to insure even stronger bonding and a reliable gas seal (an automated glue dispensing head mounted on a 3D-machine will be used for this operation - see Fig. 4.2.8). A photograph of a complete set of panels with gap bars is shown in Fig. 4.2.9.Gas inlets are inserted in the gap bar of the top plane while outlets are placed symmetrically in the bottom plane (these two bars have specially milled grooves for more uniform dispensing and collecting of the gas over the 1.5 m width of the chambers - Fig. 4.2.10). Gas flows through all six gaps in series in zigzag manner through the holes made in the panels.

When the chamber is assembled and the bolts are tightened down, RTV is applied from outside along the contact line between gap bars and panels, which provides a gas-tight seal. This scheme of gas sealing, while simple, has proved to be very efficient. Measurements with the two-gap large scale prototype, where the technique was implemented, showed that the leak did not exceed 0.5 cc/min at 12.7 mm H_2O over-pressure, which corresponds to a less than 0.5% per day leak at the nominal gas volume exchange (1 CSC volume per day).



Fig. 4.2.8: A photograph of an automated glue dispensing machine being set up and tuned for applying a continuous bead of epoxy in the corner line between a gap bar and a panel.



Fig. 4.2.9: A photograph of a complete set of cathode panels for the US P1 prototype, with gap bars fixed and glued. The top panel will be turned over, and three anode panels with wires will be placed between this set of four cathode panels.

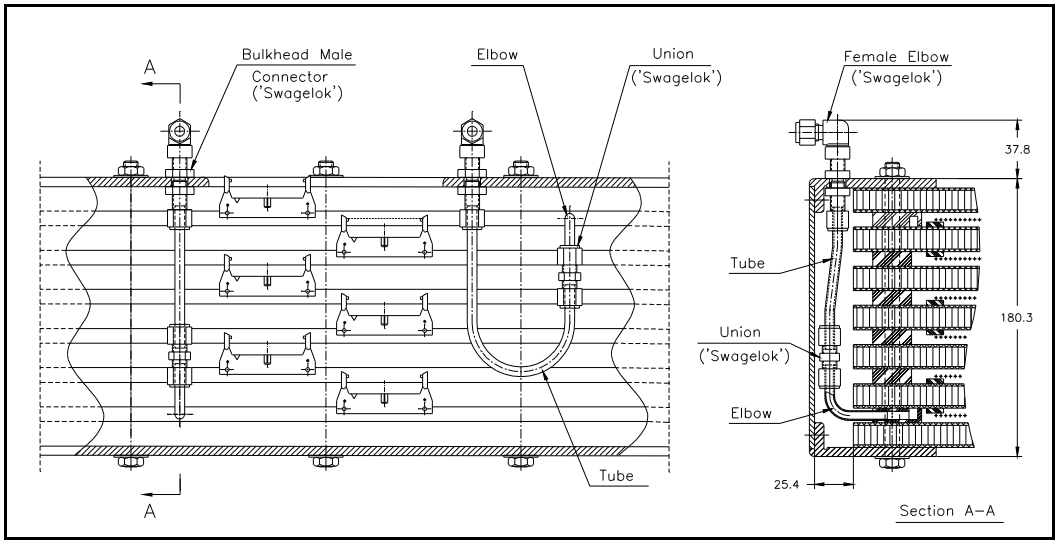


Fig. 4.2.10: The gas connection goes through the gap bars in the top and bottom planes. Gas flows in a zigzag path from the first plane to the last one through holes made in the panels.

4.2.5 Wire fixation bars

As was mentioned in the previous section, four of the seven panels have gap bars. The other three panels carry anode wires. On both faces of the panels along their long sides, a set of wire fixation bars are glued. These bars have a thickness of half a gas gap (4.76 mm) and a length corresponding to a single HV segment (typically around 60 cm). They are made according to standard printed circuit board technology out of one-sided copper-clad FR4.

A pattern of finger-tip pads is etched on the bars, and these pads will be used for soldering wires. They are interconnected in groups (anode wire groups), and each group has a special pad made for soldering a blocking capacitance (on the side of the chamber where the signals come out) or a HV resistor (on the other side where HV is distributed to the wires). The artwork is gold-plated to ensure high quality soldering. A drawing of a typical wire fixation bar is shown in Fig. 4.2.11.

Wire fixation bars are glued to the panels with epoxy under the pressure provided by a special clamping tool (Fig. 4.2.12). The pressure is needed to insure a strong and reliable bond as well as an uniform height of the bars over the panel surface. Their position on a panel is defined by small FR4 pins going through the pre-drilled holes.

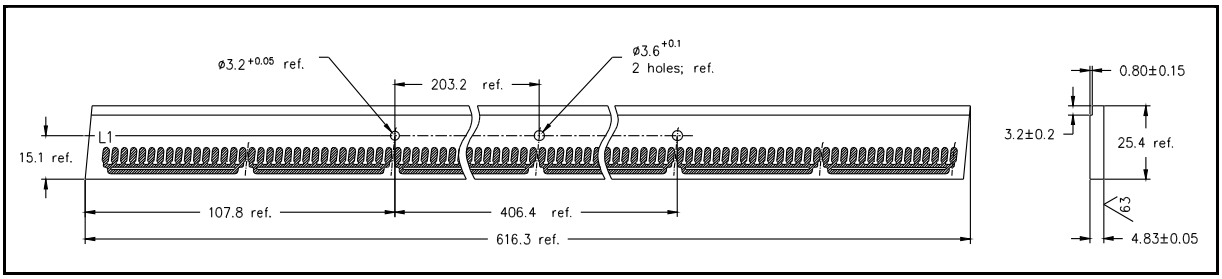


Fig. 4.2.11: A drawing of a typical wire fixation bar.

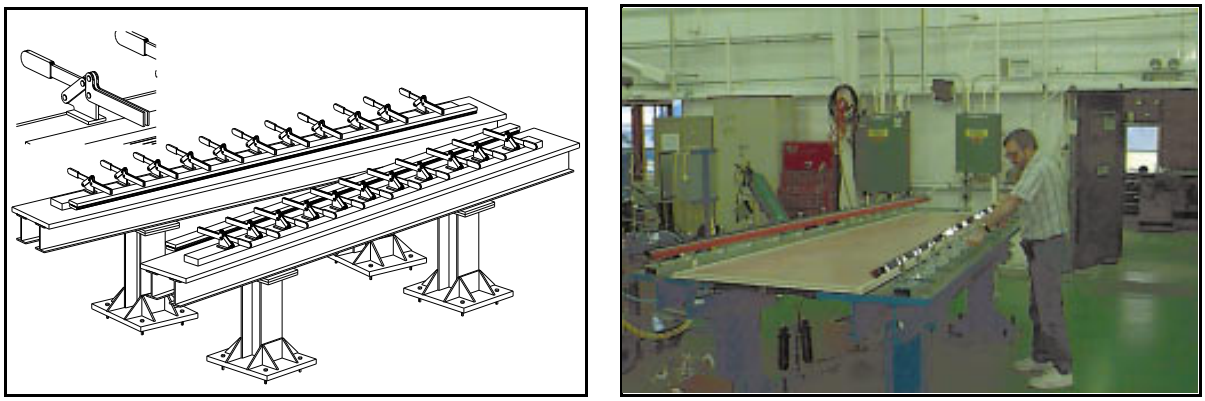


Fig. 4.2.12: Clamping setup to provide a pressure during gluing wire fixation bars: (a) design and (b) the actual setup.

4.2.6 Wires

The total number of wires in the chambers under consideration sums up to about 2.5 million. This fact alone made us to conduct an extensive R&D effort to address the two major issues: an efficient and reliable scheme of winding and attaching wires, and, once the wires are in place, the operational reliability of the chamber.

We chose to use 50 μm gold-plated tungsten wires produced by Sylvania [4.11]. Tungsten wire of 50 μm diameter or thicker is known to be very reliable in long term operation (i.e., it does not break) when properly attached. (See the discussion in the next subsection).

Our tests show that the elastic limit of these wires is around 350 g and that breaking occurs at around 450 g. At the baseline wire spacing (3.12 mm) and nominal operational HV (4.1 kV), the wires of maximum length (1.3 m) will become electrostatically unstable if their tension is below 150 g. The chosen baseline wire tension and its spread of 250 ± 25 g precludes these problems. It is worth mentioning that no intermediate wire supports are needed.

We have tested a good number of wires in sparking conditions to see how many discharges they can withstand before breaking. Tests revealed that when the value of the blocking capacitor was larger than 1 nF, it had a strong impact on wire breakage. On the other hand, if its value is less than 1 nF (but still larger than 0.1 nF), the breakage rate is fairly stable: it takes from a few hundred thousand to a million sparks to break a wire at HV=4.5 kV fed to the wire via a 5 MΩ resistor. (The higher the wire tension, the smaller the number of sparks required for breakage.)

The exact electrical layout for the wire planes will be discussed in subsection 4.2.9. The wire connections in the tests briefly described here were exactly the same, i.e. the HV was fed to the wire via 1 MΩ and 5 MΩ resistors with a 1 nF filtering capacitor, and on the other end the wire was connected via a blocking capacitor to a 25 Ω resistor going to the ground (this resistor was a mockup of an anode amplifier input impedance). Details on this study are reported elsewhere [4.12].

4.2.7 Winding, gluing and soldering wires

A special winding machine has been designed to wind wires directly on panels (Fig. 4.2.13). In this process, precision threaded rods, or *combs*, are first fastened to the panels along their long edges. The combs have longitudinal slots which fit over the edges of the panels. Then, the panel is set to rotate about its symmetry axis on special spindles fixed at its top and bottom while wire is fed synchronously through a standard wire tensioner. This machine is capable of winding two thousand wires (one thousand per panel face) in less than four hours.

Wire tension uniformity was measured to be within ±5% and wire spacing variations never exceeded ±100 μm. Both numbers are well within our formal specifications: ±10% and ± 200 μm. (The wire tension specification is important to ensure wire electrostatic stability, while the wire spacing specification is needed to guarantee the gas gain uniformity).

After the winding operation, a continuous bead of epoxy is applied to the wire fixation bars, and one day is allowed to let the glue set. Many years of experience with multiwire chambers show that wire gold-plating tends to defuse into solder, and the tungsten core of a wire occasionally snaps out from a solder joint. Having wires glued in addition to soldering has proved to be a very efficient measure to prevent this from happening.

At the next step the panel, still fixed on the same cart used for winding (Fig. 4.2.14), is moved to a soldering station which we have developed, based on the automated Panasonic soldering head [4.13] - see Fig. 4.2.15. A focused high-intensity light and solder feeding mechanism are synchronized and move along the chamber edge, making one soldering joint every 3.5 seconds. (It takes about one hour to solder 1000 wires on one side of a panel.) In addition to speed, one obtains a much better control of soldering quality.

After all wires have been soldered, they are cut right next to the solder point (sharp wire ends are varnished to prevent discharges), and the combs are removed. The last step is to hand solder blocking capacitors (which will connect wire groups to the traces on the panel leading to the anode connectors) and, on the other side, to fix small PC boards carrying HV resistors and filtering capacitors.

4.2.8 Segmentation within a plane

Assuming 20 noisy wires per every 100,000 (a number quoted by the NA4 experiment with a 113,000-wire MWPC system [4.14]), and also that a single noisy wire destroys the strip readout in the plane, simple combinatoric calculations show that 8% of an area covered by 6-plane chambers will be dead. This calculation assumes 1000 wires per plane without any segmentation, and that a chamber is defined to be dead if three or more planes are not operational (such chamber will not provide a local charged track trigger which requires at least four hits). If one breaks up a plane into five independent sectors, so that a sector containing a noisy wire can be disconnected without affecting the other four, the dead area immediately reduces to 0.1%. This simple exercise shows the importance of HV segmentation.

However, electrostatic calculations show that one cannot just disconnect a group of wires from the high voltage: this would result in a substantial increase of the electric field on the wires adjacent to the disconnected ones, thus putting them in the danger of sparking. After analysis of different solutions, we have adopted a scheme which appears to be the simplest and has proved to be very effective in the tests of both small and full scale prototypes: on the boundary between

plane segments two wires are removed and an insulating (FR4) strip of 16 mm width and 3.2 mm thickness is glued under the wires on one of the two cathodes (see Figs. 4.2.1 and 4.2.2).

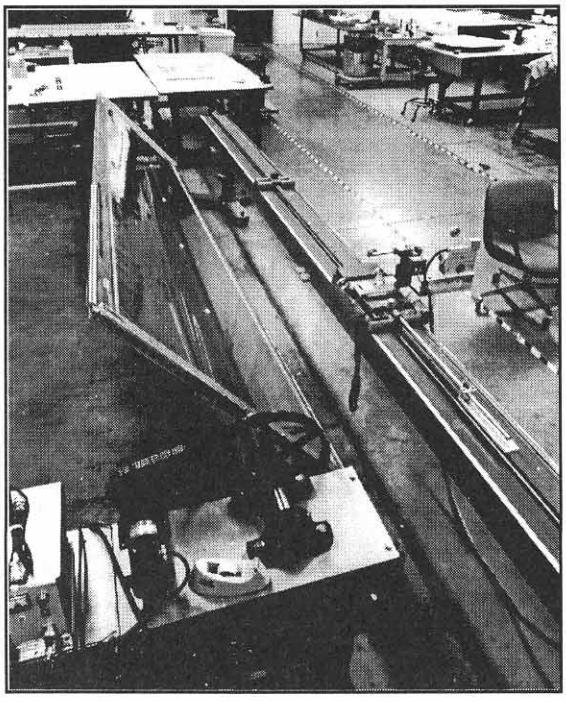


Fig. 4.2.13: The winding machine used for building large CSC prototypes.

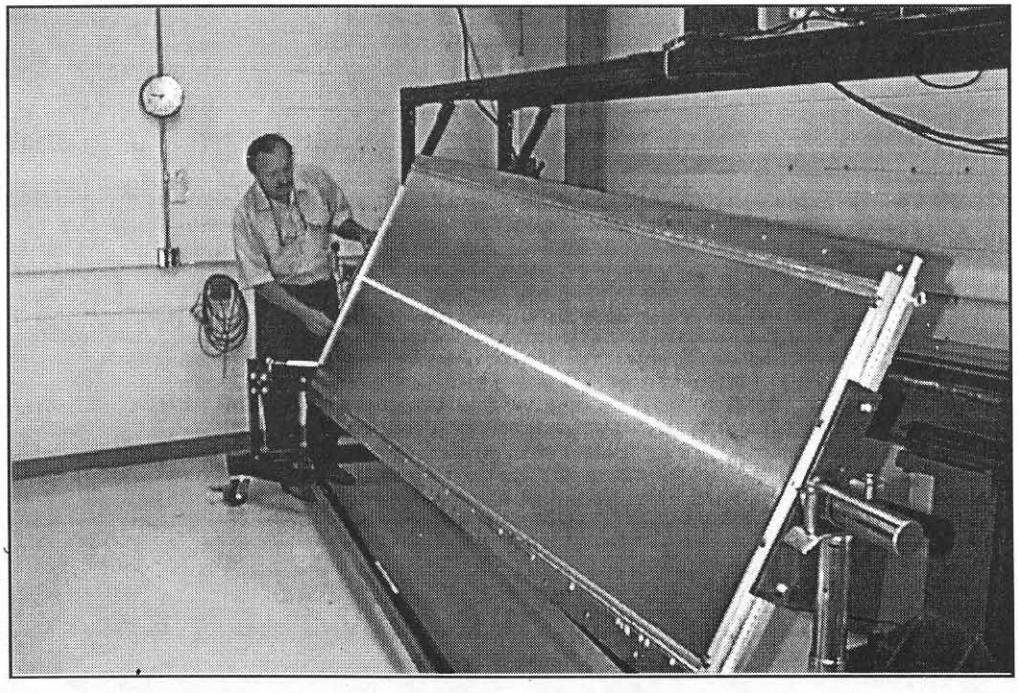


Fig. 4.2.14: A panel stays on the same cart from the beginning of winding until the end of soldering. The cart allows the operator to move the panel from one machine to another and to rotate it about its long axis.

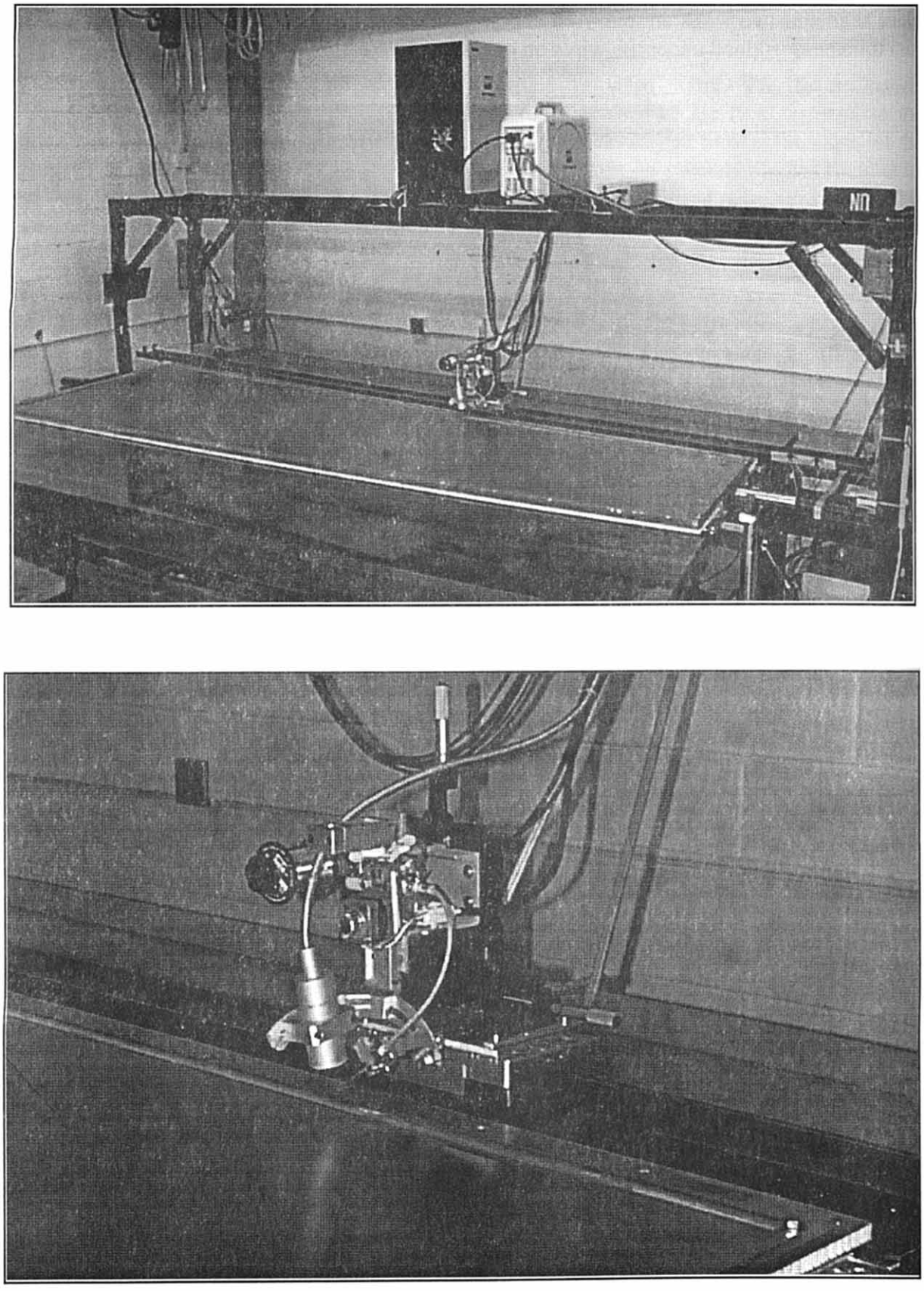


Fig. 4.2.15: The automated soldering machine (top) and close-up view of the soldering head (bottom).

Of course, the guard strip is glued before winding begins. When HV is on, this insulating guard strip charges up positively and substantially reduces the electric field on the edge wires. The dead zone induced by its presence is less than 25 mm wide. Very similar guard strips run under the first two and last two wires in the plane and solve the same problem of the increased field on the edge wires. Independent HV segments are of the order of 60 cm wide in all chambers.

As was mentioned above, to ensure constant gas gain one needs to keep cathode-to-cathode spacing fairly constant (±250 μm). To insure this specification we introduce a few intermediate spacers. Their purpose is twofold: first, they maintain panel flatness (the span between support points becomes a factor of two smaller: 60 cm instead of 120 cm), and, also, they prevent bulging of panels due to gas overpressure inside the chambers during gas flushing. Having removed a couple of wires between HV segments, we open plenty of space (about 9.5 mm) where these spacers or buttons can be placed (Fig. 4.2.16). Panels will be pre-drilled in these spots and after winding and attaching the wires, the buttons are inserted and glued. Then, after completion of chamber assembly, the entire stack of panels is tightened down at the locations of the buttons with through-going tie-rods. As a result, the panel flatness requirement becomes substantially looser, and, as calculations show, bulging reduces from 0.1 mm to 0.01 mm at the nominal 1 cm of H_2O overpressure [4.15].

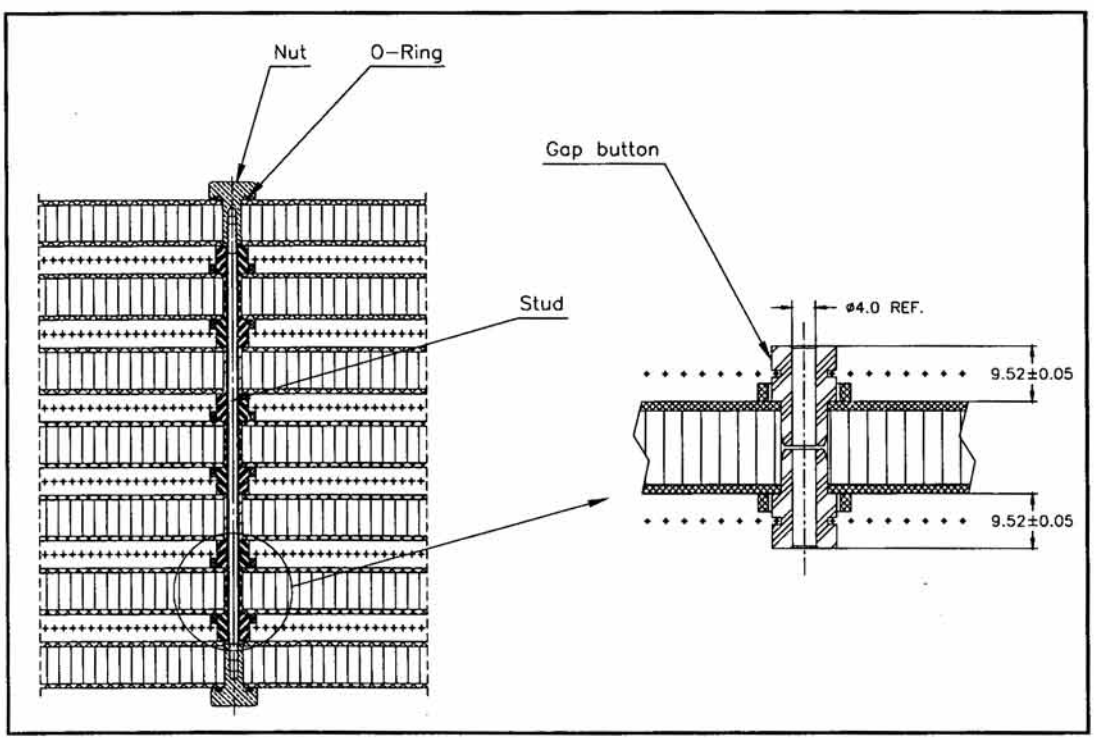


Fig. 4.2.16: From one to four special spacers, or buttons, will be placed in every chamber gap and panels will be tightened down in these points. These considerably relax requirements on panel flatness and prevent excessive bulging due to gas overpressure.

4.2.9 Electrical layout

A schematic drawing showing how HV is brought to the chamber wires and how signals from wires and strips are taken out is given in Fig. 4.2.17 (for chambers ME234/2). Each chamber plane has a plane of wires between two cathode planes, one of which has the strip pattern milled into it. The smooth cathode plane free of strips is a clean ground for both anode and cathode electronics readout. The two outermost copper-clad panel surfaces, together with the aluminum side frame, form an external ground and constitute RF-shielding for the entire chamber.

HV is brought to the chamber via a shielded multi-lead HV cable. This cable is a few meters long and comes from one of the HV distribution boxes sitting on the outer rim of the iron disks. At the point where the HV cable is connected to the chamber there is a primary RC-filter which blocks the main part of possible pickup in the cable. Its shield is connected to the chamber ground via 1 kΩ resistor. From the main connector, the HV is distributed to the corresponding segments via seven-lead HV cables of the same type (one out of seven is spare) which have banana-plugs at their ends.

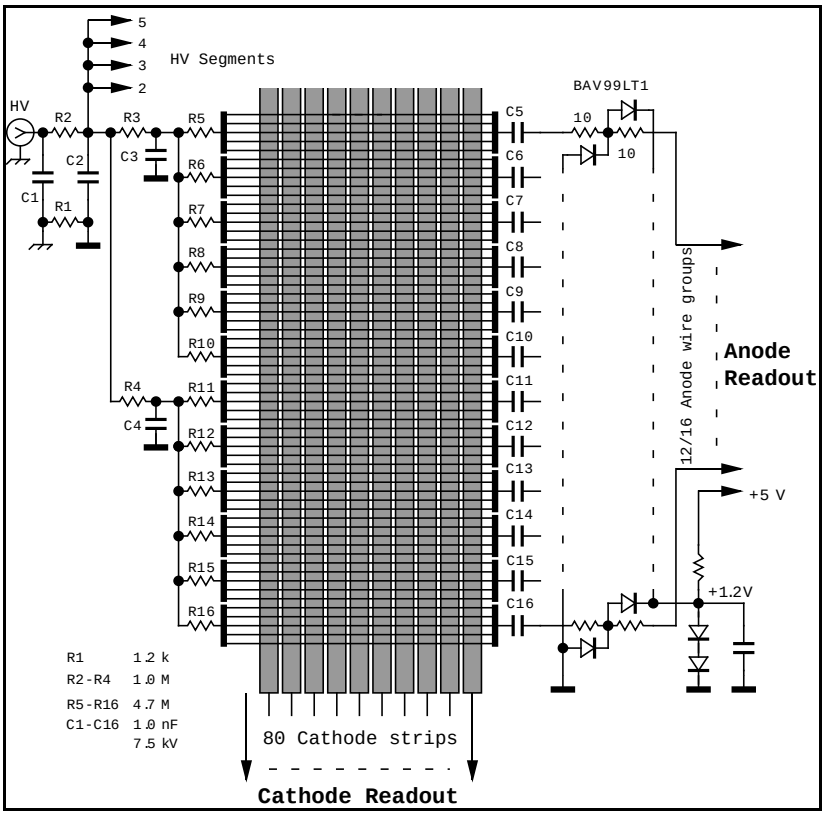


Fig. 4.2.17: Electrical layout of signal grounding and HV connection.

These allow for manual disconnection of any of the segments should the need arise. The plugs are soldered to the panels where HV traces come out from under the gap bars. RC-filters, formed by a combination of 1 MΩ and 5 MΩ resistors and 1 nF capacitors, which are placed inside the chamber de-couple signals from different wire groups (they also provide additional filtering of the HV).

On the other side of the chamber, wire group pads are interconnected with traces going to the edge of the panel via 1 nF blocking capacitance (the largest wire group capacitance is 135 pF). The traces come to the edge in groups of 4. Special protection boards are mounted on the panel edges, and each board takes 8 signals from one side of a panel and 8 signals from the other side and brings them to a 34 pin connector where the 16-channel input cable for the anode electronics plugs in. These boards have 10 Ω resistors and diodes which are intended to protect electronics should a spark occur in the chamber. Also, they provide a small leakage current so that blocking capacitors do not charge up if the anode electronics is disconnected. Cathode strips in groups of 16 are brought directly to 34-pin connectors mounted on the panel edge.

All panels are interconnected by means of copper braid jumpers soldered directly to them on each side of the anode and cathode 16-channel connectors. Thus, all grounds have one L-shaped continuous line of interconnection and no ground loops are formed. Preamplifier input twisted-pair flat cables are shielded, and the shield is also soldered to the ground. Our experience with the large prototypes showed that this grounding scheme provides a very good and consistent result.

4.2.10 Assembly and external frame

After the seven panels have been stacked and sandwiched between 3.2 mm thick aluminium extrusions going along the perimeter under the bottom and above the top panels, the assembly bolts are tightened. The extrusions distribute the compressive force of the bolts over a larger area and allow a greater torque to be applied. Then, when the 3.2 mm side plates are fixed to the extrusions, the overall package gains a good deal of stiffness, and the entire chamber can be treated as a single block and can be easily handled. A drawing showing the chamber embedded in the frame is shown in Fig. 4.2.18. We measured that the chamber sags by less than 1 mm over the full 3.4 m length under its own weight when it is simply supported at the opposite ends [4.16]. In addition to distributing the compressive force of the bolts and providing essential rigidity, the frame interconnects the copper faces of the top and bottom panels and encloses the rest of the chamber in the Faraday cage. It should be mentioned that there are two important procedures which precede the attachment of the side plates. First, RTV is applied along the perimeter of all six gaps and gas tightness is checked. Second, relative plane alignment is surveyed: each plane of strips has a few milled alignment marks extending outside of the gap bars so that they are visible from outside.

A photograph of the assembled chamber is shown in Fig. 4.2.19. The photograph shows the US P1 prototype being tested in the cosmic rays. One can see the frame going around the chamber perimeter, cathode electronics on the top of the chamber on its wide (closest) side, and anode electronics, covering the middle third of the chamber in this photograph and placed on the top of the chamber along its left side. Two rectangular fixtures near the corners (the wide side of the trapezoid) are the two out of three kinematic mounts to hold the chamber on the vertical walls on the iron disks of the return yoke. Swivel rings on the chamber corners are intended for handling the chamber with a crane. More details of the chamber mounts, its frame, and handling fixtures as well as installation procedures can be found in subsection 4.6.

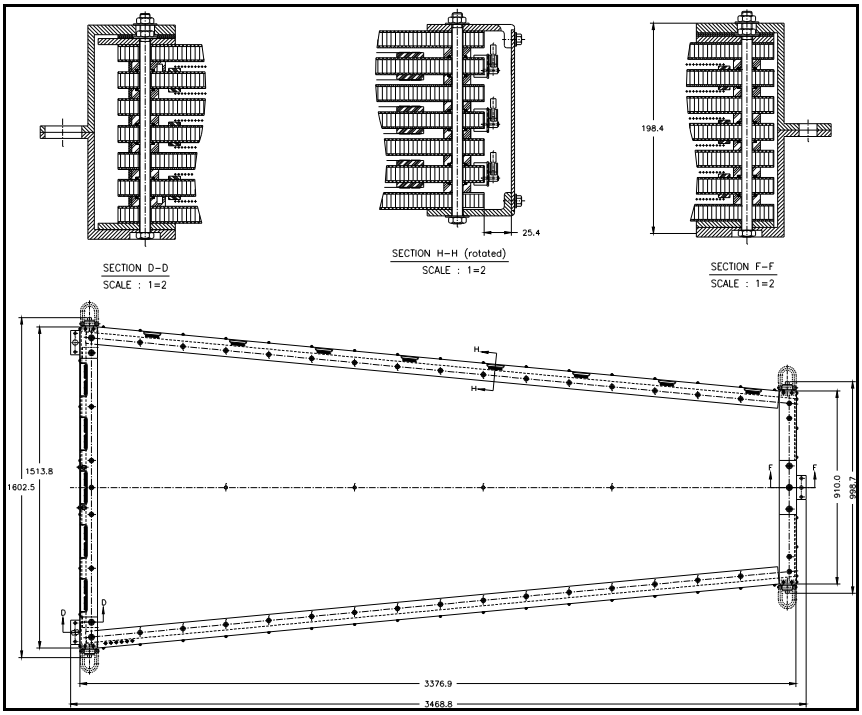


Fig. 4.2.18: Assembled large scale P1-prototype (3.4×1.2 m^2 in size).

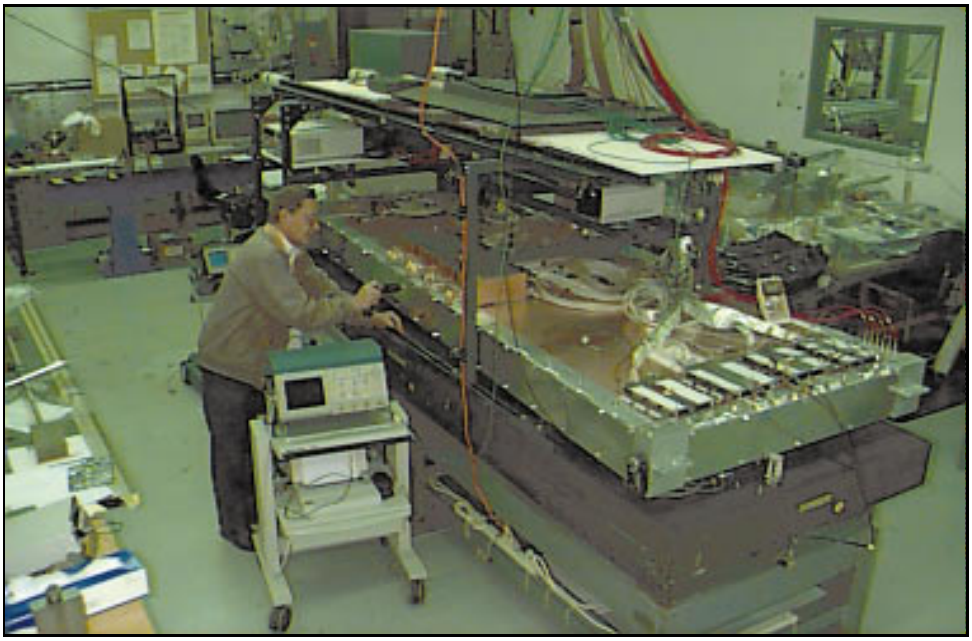


Fig. 4.2.19: The large scale US P1-prototype, 3.4×1.2 m^2 in size, is under the tests at the cosmic ray stand (details on the different prototypes and the results obtained with them can be found is Section 4.8).

4.3 DETAILED CHAMBER DESIGN: ME1/1

4.3.1 General features of ME1/1

The innermost ME1/1 station should provide very good spatial resolution of 75 μm per station in order to achieve the required momentum resolution in the endcap muon system. The chambers must provide efficient pattern recognition and matching with the inner tracker. This spatial resolution should be delivered in the presence of a strong axial magnetic field in excess of 3 Tesla. The chambers should be very fast in order to identify the bunch-crossing. Their recovery time should be fast because the chambers will operate in the presence of the highest particle background rate in the CMS Muon System, up to 1 kHz/cm^2, which corresponds to a rate of 100 kHz per cathode readout channel.

4.3.2 ME1/1 chamber design

The design parameters of the ME1/1 CSCs are optimized to meet the specified requirements. A general view of the chamber is shown in Fig. 4.3.1.

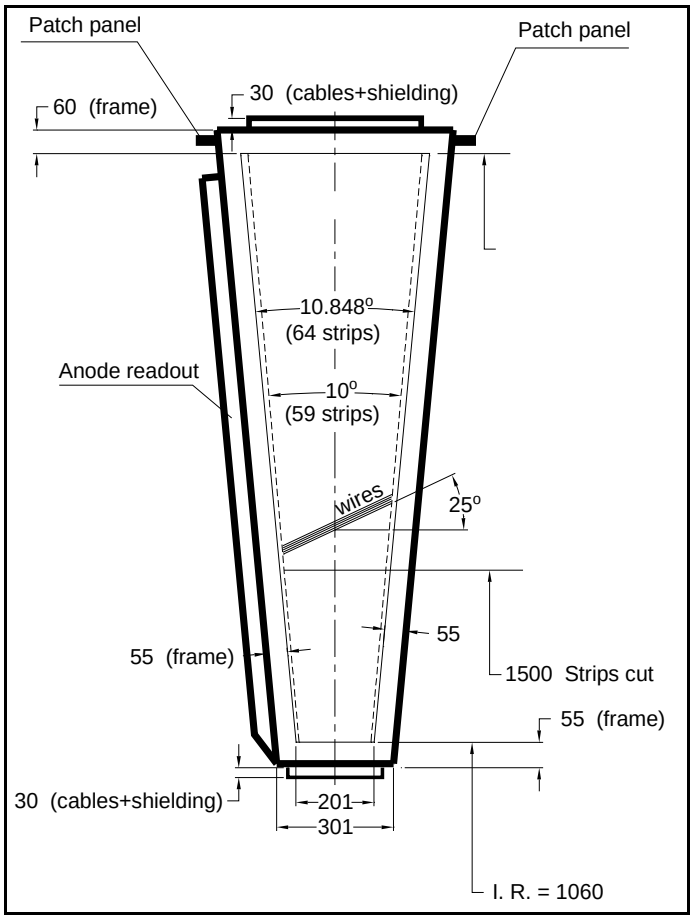


Fig. 4.3.1: A general view of the ME1/1 chamber.

The inner radius of the chamber sensitive area is set by the required acceptance at η=2.4, and the outer radius by the gap between the endcap and barrel detectors. The ϕ-dimensions of the chamber correspond to the baseline segmentation of 10°. Cross-section views of all four chamber sides are presented in Fig. 4.3.2.

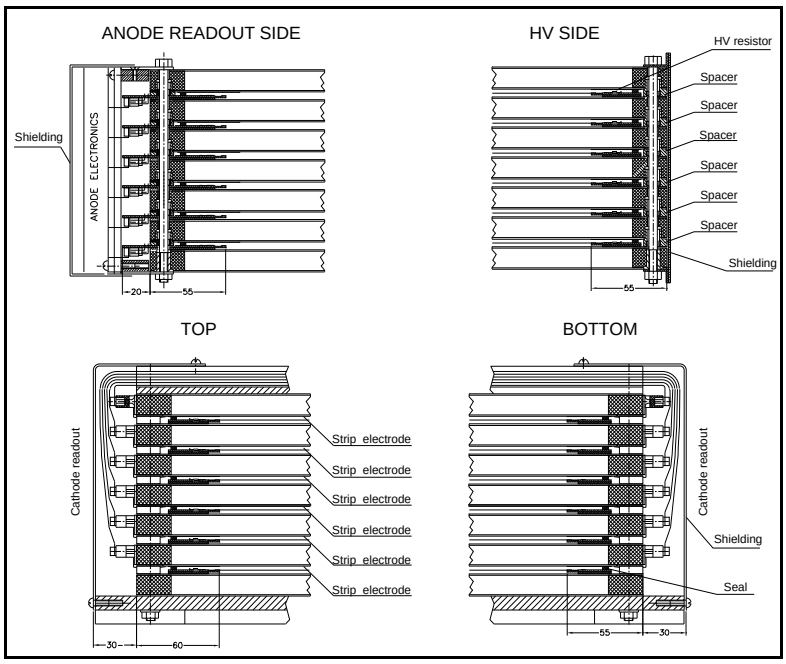


Fig. 4.3.2: Chamber cross-sections along the wire plane.

A general overview of a CSC is described in section 4.2. Seven panels are stacked together to form six gas gaps. The width of each gas gap (cathode-to-cathode, approximately 6 mm) is set by 32 precise spacers with a tolerance on height of ±25 μm. The main mechanical construction element of a CSC, a “honeycomb” self-supporting panel, is shown in Fig. 4.3.3.

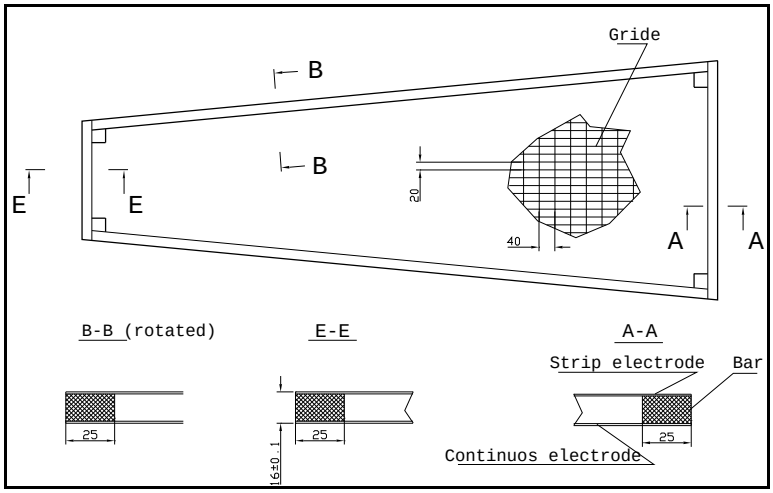


Fig. 4.3.3: Self-supporting “honeycomb” panel.

The main requirements for the ME1/1 panel are flatness and rigidity. Such panels have been designed, and prototypes produced. A first set of panels was used for the P3 prototype fabrication. The panel consists of a "honeycomb-like" structure sandwiched between two electrodes, one with a continuous copper surface and the other with a milled strip pattern. The "honeycomb-like" filler of a rectangular shape grid is made out of 0.5 mm G10 strips. The size of a cell is 20×40 mm^2. The honeycomb has edge-reinforcing 25 mm wide bars running along its perimeter and between the electrode sheets. Electrodes are made out of 0.8 mm single-sided copper clad FR4 sheets. The thickness of the copper lamination is 18 μm.

Six out of the seven panels carry strip artwork on one side. For strip electrode production a milling machine has been designed and assembled (Fig. 4.3.4).

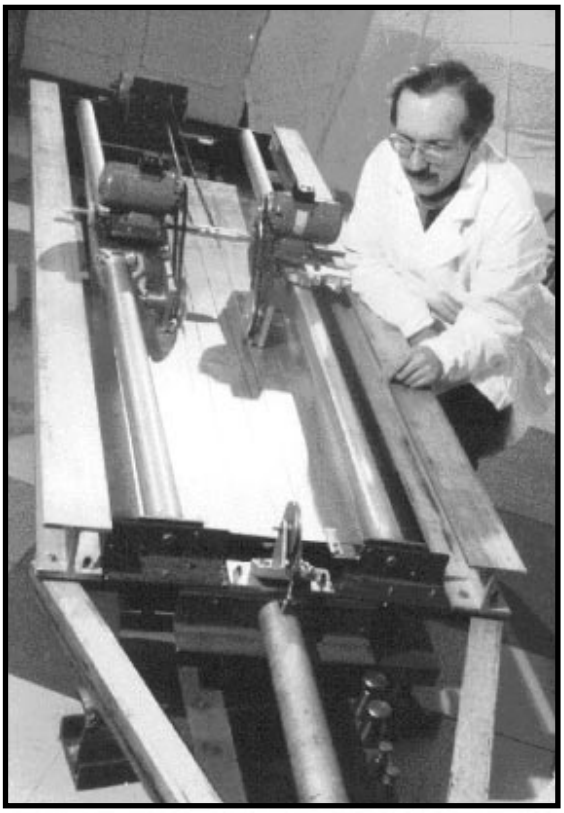


Fig. 4.3.4: Photo of the strip milling machine.

The radial shape of the strips is made by a 0.35 mm thick rotating diamond disk. The strips cover the ϕ-angle range of ±5.42° to provide an overlap with the neighboring CSCs. A cross cut of the strips provides a radial split of the strips into two groups in order to minimize background rate per cathode channel. After milling, the strip electrodes are polished.

The anode-to-cathode distance is defined by wire fixation bars with a tolerance of ±25 μm. A special technology for making precision bars (G10 sandwich) was developed.

Anode planes consist of 30 μm wires produced by the Luma [4.17]. The elastic limit of these wires is 125 g while the breaking tension is around 160 g. Wire tension is chosen as 80 g and is delivered with an accuracy of ±5 g by the wire stretching machine which is shown in Fig. 4.3.5.

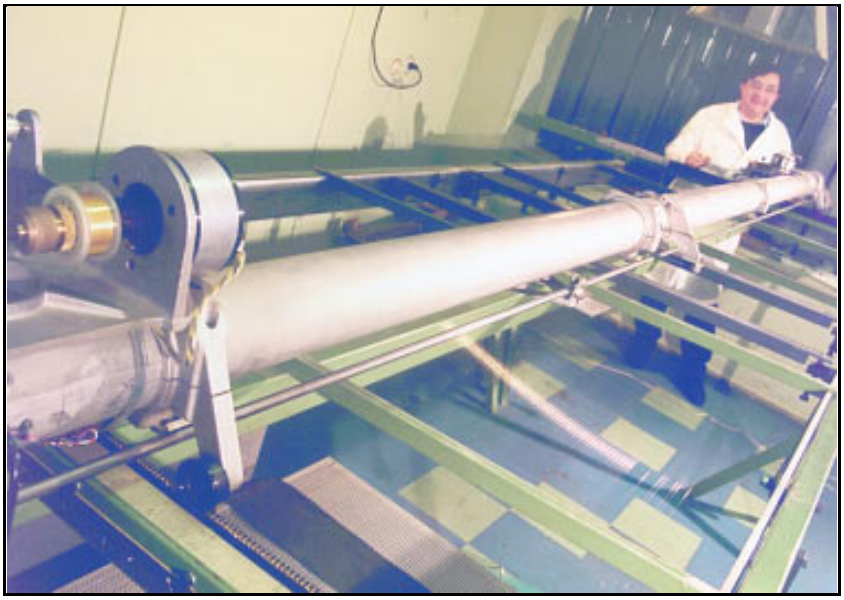


Fig. 4.3.5: Photo of the wire stretching machine.

A wire plane is transferred from the winding machine by using transfer frames and soldered on the wire fixation bars with precision combs which ensure 2.5 mm wire spacing with an accuracy of ±25 μm. To compensate for the Lorentz effect of the axial magnetic field at a nominal value of 3.5 Tesla, the anode wires are positioned at an inclination angle of 25° with respect to and perpendicular to the central strip axis, as shown in Fig. 4.3.6.

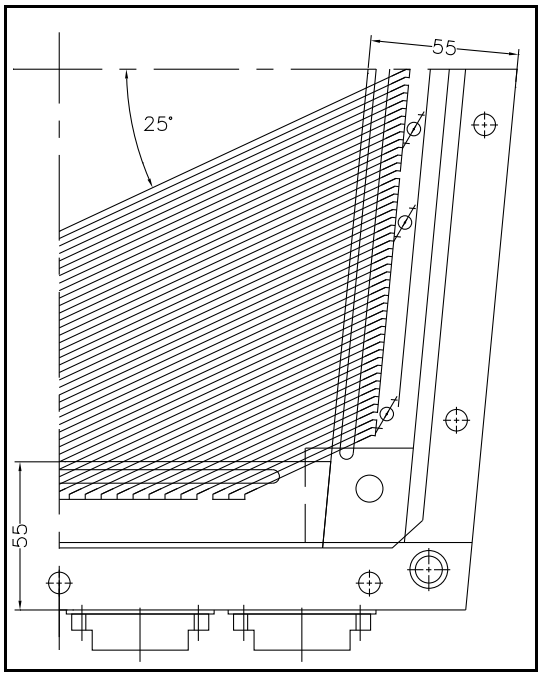


Fig. 4.3.6: Detail of lower corner of the ME1/1 chamber, showing how slanted wires are soldered.

Each anode wire readout channel corresponds to a group of 11-12 wires. Here we mention that the design of the readout electronics cards (taking into account a small strip width and tilted wires) should also be matched to the limited space of the chamber surface.

4.4 FRONT-END READOUT AND TRIGGER ELECTRONICS

The front-end electronics for the CMS Endcap Muon System has two main purposes:
1) to acquire precise muon position and timing information for offline analysis;
2) to generate muon trigger primitives for the Lev-1 trigger system.

In a CSC layer, the anode wires are in the azimuthal direction and the cathode strips are in the radial direction. The bending of charged tracks by the magnetic field in the endcap region is in the azimuthal direction, and the precise measurement of the azimuthal coordinate of a hit is achieved by interpolation of charges induced on neighboring cathode strips. The anode wires provide precise timing measurement of a hit as well as a coarse measurement of its radial position.

The organization of the front-end electronics is schematically shown in Fig.4.4.1.

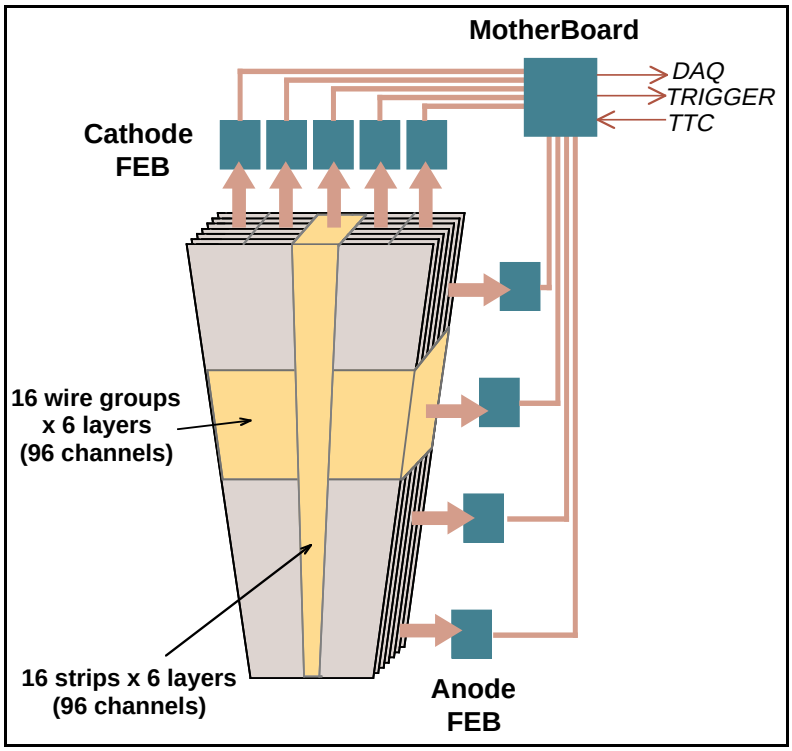


Fig. 4.4.1: Organization of the CSC front-end electronics.

Cathode and anode front-end boards (FEB) are mounted directly on the CSC modules. The data from the FEBs are sent by cables to a readout motherboard (MB), also mounted on the chamber. The MB serves as the link between the FEBs and the rest of the detector. It sends the readout and trigger data to the central DAQ system and the Lev-1 trigger system. It receives trigger, timing and control (TTC) signals and distributes them to the FEBs.

4.4.1 General system requirements

The general requirements of the front-end readout and trigger electronics are:

1) to perform without dead-time;
2) to be able to function with high strip and wire singles rate;
3) to identify and reject random background hits due to neutrons or photons;
4) to be compact and be suitable for chamber mounting;
5) to be inexpensive on a per channel basis;
6) to generate as little heat as possible;
7) to be able to withstand the radiation level in the endcap muon region.

Requirements 4),5) and 6) are related and are consequences of the large channel count of the electronics system. In particular, they mean that the electronics must make extensive use of ASICs (application specific integrated circuits). The per channel power consumption is required to be less than 200 mW. In order to use the less expensive non-rad-hard ASIC processes, the total radiation dosage integrated over 10 LHC years in the endcap chamber region must be kept below 1 krad for ionizing particles and below 10^{12} neutrons per cm^2. Background simulation shows that this condition will be met.

4.4.2 Cathode front-end electronics

The cathode FEB consists of 96 input channels per board. Each front-end board is designed to read out a tower consisting of 16 neighbouring strips per layer by 6 layers deep. The functional diagram for the cathode FEB is shown in Fig. 4.4.2.

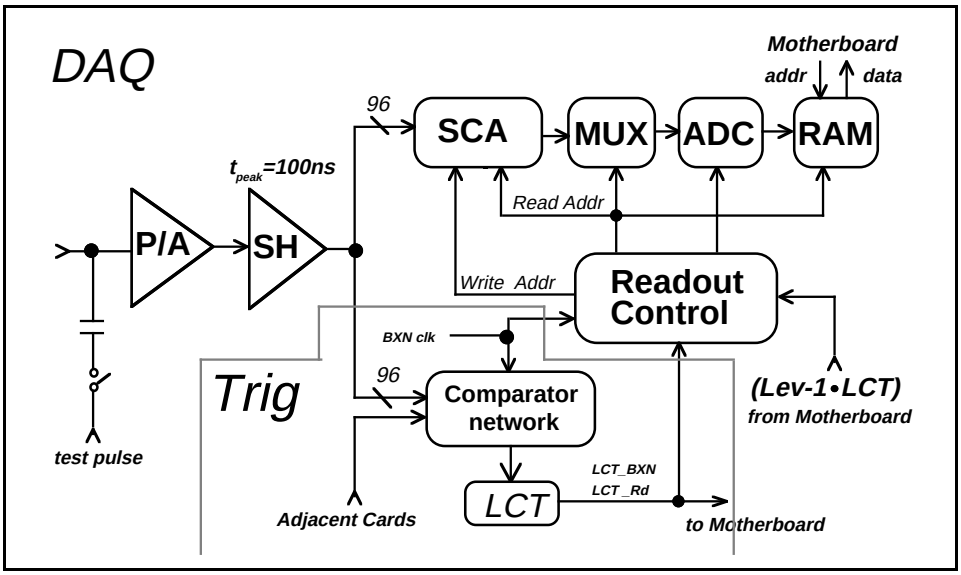


Fig. 4.4.2: Functional diagram of the cathode front-end board.

The input signals from each of the strips are sent into 16-channel amplifier-shaper ASICs (There are 6 such ASICs per FEB). Each input signal is amplified and shaped into voltage pulses. The output pulse shape is semi-Gaussian and the shaper peaking time is 100 ns. To minimize pile-up effects in high rate environment, circuits to cancel the long tail of the chamber

pulse due to ion drift are integrated into the shaper. Channel-by-channel calibration will be done using a set of precisely matched capacitors that couple a test pulse to each channel's input.

One output of the shaper is connected to the trigger path whose main components are a Comparator Network and a Local Charge Track (LCT) processor. The comparator network locates the centroids of the strip charge clusters in each chamber layers to an accuracy of half the strip width and marks its time. The resulting information is fed into the LCT trigger processor which look for coincidence of cluster centroids from a minimum number of chamber layers which form a “road”. The time, location and angle of the LCT are used to determine trigger primitive parameters for the Lev-1 muon trigger.

The other output of the shaper is connected to the DAQ readout path. The voltage is sampled every 50 ns and held in a Switch Capacitor Array (SCA) during the Lev-1 latency. The readout of the stored samples is data-driven: they are digitized and read out only when an LCT trigger associated with the sampled pulses occurs and that the LCT is time correlated with a Lev-1 Accept. This requirement significantly suppresses random background hits induced by neutrons and photons. The digitized data is saved in memory and transmitted to the main DAQ system upon request by the MB. The IC’s on the cathode FEB are listed in Table 4.4.1.

Table 4.4.1

ICs on the cathode front end board.

ASIC Type	No. Channels per ASIC	No. of ASICs per Board
Preamp-Shaper	16	6
SCA	16	6
Readout Control (FPGA)	96	1
Comparator	16	6
LCT Demux/Controller	96	2
LCT Selector	96	2
Trigger RAM (32 kByte)	6	16
ADC (12 bits, 20 MHz)	96	1

4.4.2.1 Cathode preamp-shaper

For the CMS endcap chambers, the cathode strips are in the radial direction and they provide the measurement of the bending (azimuthal) coordinate. This measurement relies on the interpolation of charges induced by the avalanche process on several (4-5) neighboring cathode strips (hereafter referred to as a cluster). The resulting position resolution is proportional to the percentage error of the cluster charge measurement. For chambers with strip width equal to the gas gap (twice the anode to cathode distance), this resolution is approximately equal to $w\Delta Q/Q$, where w is the strip width, Q and ΔQ are the total cluster charge and its error. For a cluster with N strips, where Δq is the noise of each strip channel. In the absence of RF pickup noise, Δq is dominated by the electronics noise of the input FET in the preamp ASIC.

The required resolution per station is 75 μm for ME1/1 and ME1/2 chambers (<w>~0.5 cm) and 150 μm for rest of the endcap chambers (<w>~1.0 cm), which includes electronics noise and all other contributions. To achieve these resolutions, the strip charge q must be measured with an accuracy of $\Delta q/Q$~1% for all chambers. The design goal is to achieve <1% in $\Delta q/Q$ for the entire endcap muon system. This calls for a state-of-the-art low noise amplifier.

Table 4.4.2

Cathode preamp-shaper specifications.

Equivalent Input Noise (rms):	Cstrip x 25e/pF + 700 e
Shaper Peaking Time:	100 ns
Peaking Time of Amplified and Shape Chamber Signal:	170 ns
Shaped Waveform:	5 pole semi-gaussian with tail cancellation
Nominal Input Charge[i,ii]	112 fC (=7000 x 100 (S/N))
Preamp-Shaper DAQ Gain:	0.9 mV/fC
Preamp-Shaper LCT Gain:	3.6 mV/fC
Non-Linearity:	<1%; 0 - 1.5 volt
Dynamic Range:	12 bits
Overall System Gain:	0.5 fC/ADC count
Two Track Time Resolution:	125 ns
Gain Variation:	<4% channel-to-channel <10% chip-to-chip
Calibration Precision:	0.5% over full range

i) Corresponding to the average ionization deposition (Landau peak) for a normally incident minimum ionization particle. The operating voltage or the chamber gas gain corresponding to this input charge should be determined empirically.

ii) The gas gain required is $100 \times 7000 \times N_{ion} \times f_{att} \times f_{ind} \times f_{sh}$, where N_{ion} is the number of ion pairs generated by the traversing particle; f_{att} is fraction of drift electrons lost due to attachment to chamber gas molecules; f_{ind} is fraction of the anode charge induced on either cathode; and f_{sh} is fraction of avalanche charge collected by anode for a given shaping time. Simulation [4.18] of CSC response gives N_{ion} = 180 (for 10 mm gas gap); F_{att} = 0.5; f_{ind} = 0.41; f_{sh} (100ns shaper peaking time) = 0.19. Based on these numbers, the gas gain is estimated to be about 10^5.

The intrinsic noise for the preamp-shaper depends primarily on three parameters: the input (strip) capacitance, the size (width and length) of the preamp FET and the shaper peaking time. Anticipating the high rate environment at the LHC – the estimated neutron and charged particle hit rate can be as high as 1 kHz/cm^2 at the design luminosity of 10^{34}/cm^2 s – the shaper peaking time is chosen to be 100 ns for fast recovery and for good two-pulse time resolution. These

considerations together with practical choices for the FET size lead to the requirement that the rms equivalent input noise be less than 7000 electronics for the strip with the highest capacitance in the system (250 pF).

The required minimum signal to noise ratio of 100 can be met by operating the chamber with a gas gain such that the induced cathode charge by a normally incident minimum ionizing particle is about 7×10^5 electrons, or 112 fC. The overall system gain is 0.5 fC per ADC count. The electronics noise from the largest chambers will result in an ADC pedestal rms width of 2.2 counts and the peak of the Landau distribution will be located at around 250 counts (8 bits). The dynamic range is 4000 (12 bit ADC), which is necessary to accommodate the tail of the Landau distribution and variations due to chamber and amplifier gains. The gain of the trigger output of the preamp/shaper may be set higher in order to minimize any effects due to comparator offsets. These specifications are listed in Table 4.4.2.

A charge sensitive preamp-shaper ASIC, named the BUCKEYE chip, has been developed based on the above requirements for all endcap chambers, except ME1/1. The BUCKEYE chip has gone through five submissions. Each of the submissions is a four channel prototype ASIC. The foundry used is MOSIS-HP and the process is 1.2 μm CMOS with linear capacitors. The block circuit diagram for the BUCKEYE chip is shown in Fig. 4.4.3.

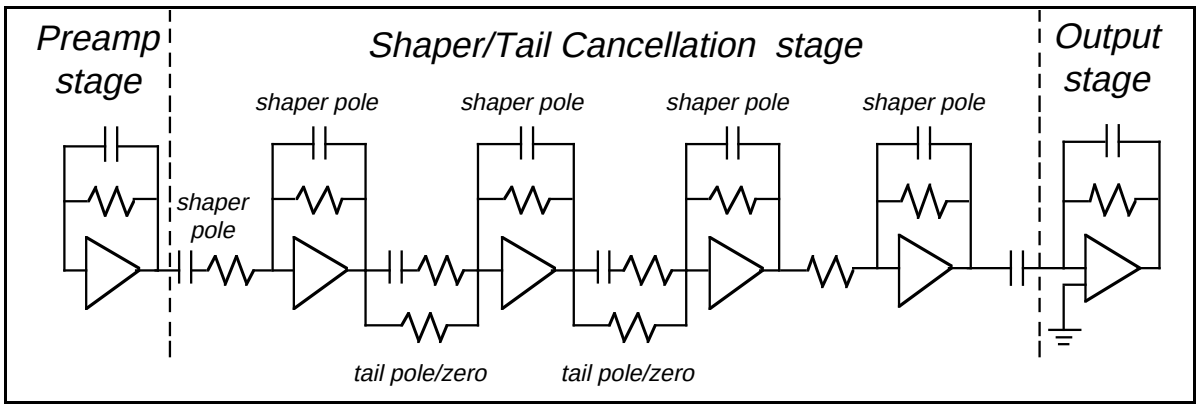


Fig 4.4.3: Circuit block diagram of the BUCKEYE ASIC.

The test result of the latest submission shows that the BUCKEYE chip has met all the key design requirements. Fig. 4.4.4(a) shows the output pulses of the BUCKEYE chip in response to impulse input charges of magnitude ranging from 1 to 20 mips (1 mip is equivalent to a charge of 110 fC). No change in the peaking time versus amplitude is observed. The output pulse height is 93 mV per mip, which corresponds to a gain of 0.85 mV/fC. Channel-to-channel gain variation (based on a total of 60 channels) is measured to be less than 4%.

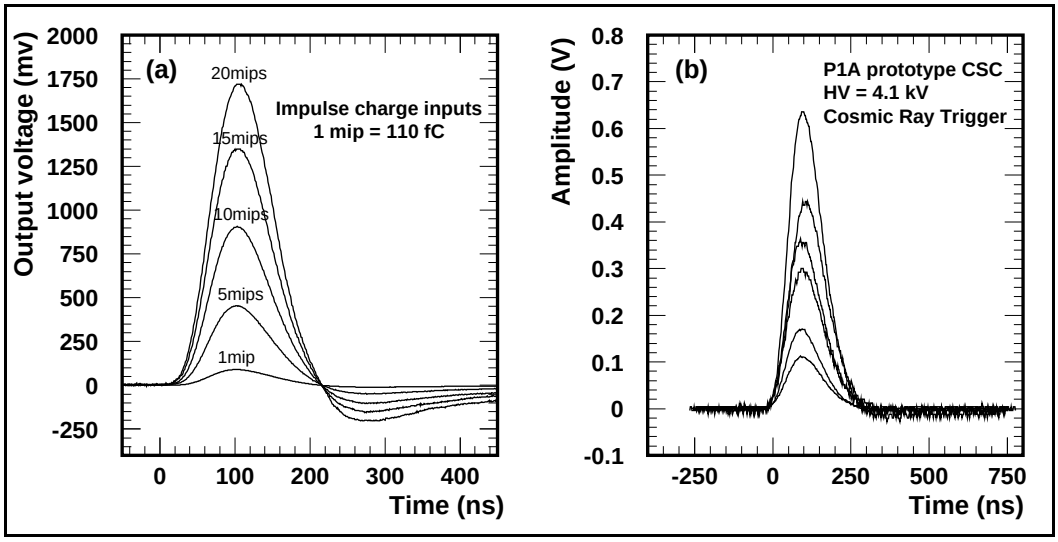


Fig. 4.4.4: a) Output of the BUCKEYE chip in response to impulse charge inputs; b) Output of the chip in response to chamber signals due to cosmic rays in PIA, a full-scale prototype CSC with 3.3 m strip length.

The BUCKEYE chip was also tested on a full size prototype CSC chamber (P1A). Fig. 4.4.4b) shows the response of the chip to chamber signals generated by cosmic rays. The shaped pulses are observed to come back down to baseline after 300 ns as a result of tail cancellation. The output pulse height versus input charge is plotted in Fig. 4.4.5 (a), which shows that deviation from linearity is less than 1% from 0 to 1.4 volts, corresponding to the range from 0 to 15 mips.

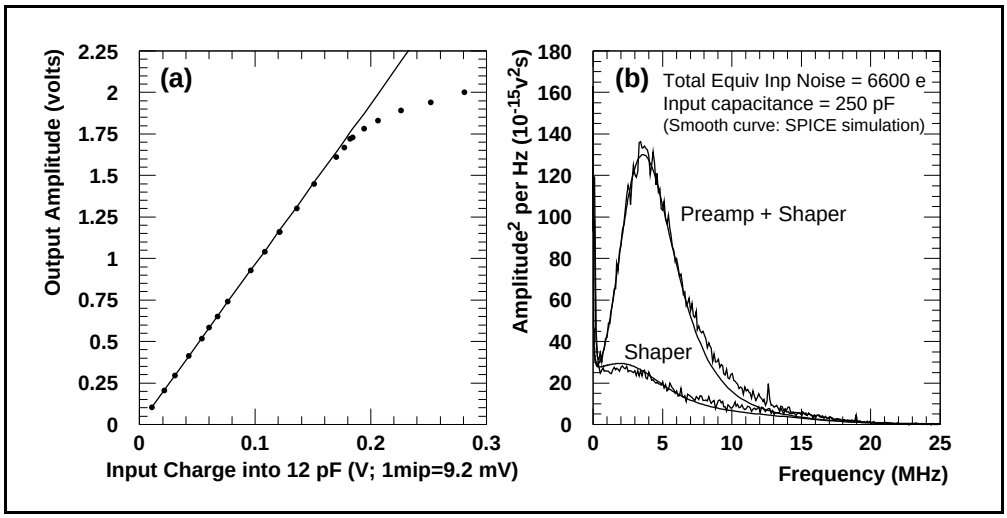


Fig. 4.4.5: a): Measured linearity of the BUCKEYE chip; b) measured noise spectrum of the BUCKEYE chip.

Fig. 4.4.5 (b) shows the measured noise spectrum of the BUCKEYE chip, which is in excellent agreement with SPICE simulations. The total measured noise is 6600 electrons for an input capacitance of 250 pF, well within the design specification.

4.4.2.2 Analog storage and control

The output pulse of the preamp/shaper ASIC will be sampled at 20 MHz rate and the voltages stored in an SCA channel. There are 6 SCA ASICs on an FEB and each ASIC contains 16 channels for a total of 96 channels per FEB. Each SCA channel contains 96 capacitors. Note the nominal number of capacitors per channel is 60, corresponding to the Lev-1 latency of 120 beam crossings. The additional capacitors provide extra buffer which ensures deadtime-free sampling during the readout and digitization processes.

The development of the SCA ASIC is nearing completion. First 16 channel prototype ASIC has been produced and tested. There are 96 capacitor cells per channel. The chip was tested in simultaneous write/read mode with the required speeds. The cell-to-cell pedestal variations were measured. The rms deviation of cell pedestal values from the the channel mean (average of 96 cells) for different channels is found to lie within 0.5-1.0 mV, comparable to the amplifier noise level of 1 mV. This variation will be further reduced in the next iteration, making pedestal subtraction unnecessary. The measured linearity and the uniformity of cell-to-cell transfer functions are also within the specification.

The main consideration for choosing full-wave sampling over the Track-and-Hold method is to ensure that pulse height and timing measurements be not affected by pileup effects. (At the designed luminosity of 10^{34}, the charged particle plus neutron hit rate could reach 1 kHz/cm^2 and the singles rate on the longest strip can be as high as 300 kHz.) Eight samples for each pulse will be saved. The eight samples include 2 to 3 samples of the baseline voltage for pile-up correction and 5 to 6 samples of the signal pulse for offline reconstruction of the pulse timing and pulse height. The digitization and readout of the samples is managed by the Readout Controller on the FEB.

Fig. 4.4.6 shows the schematic diagram of the readout controller logic. The controller's main function is to generate write (every 50 ns), and read addresses of the SCA. To minimize noise generated in the SCA chip, the addresses of the 96 capacitors of a given SCA channel are kept in a Gray code sequence instead of a numerically ordered one. In a Gray code, the neighboring addresses differ only by 1 bit in binary. The capacitors of an SCA channel will be identified by 96 7-bit address words. These addresses are organized into 16 blocks, the higher 4 bits of each address represent the block address of a cell. Within a block the lower 3 bits of the cell address represent the sub-address. Both the block addresses and sub-addresses are generated in Gray code sequences.

The sampling (at the rate of 20 MHz) of the preamp-shaper output voltage is a non-stopping process, and the capacitor cell used to store the voltage is taken from a pool whose content is contantly updated. When a voltage sample is stored on a capacitor, its address is tagged so that it is taken out of the available capacitor pool. The tag is reset and the capacitor put back into the pool when either of the following conditions are satisfied: 1) no LCT associated with the stored voltage is found; 2) an LCT is found but there is no Lev-1 Accept after 120 beam crossings. Otherwise, the addresses remain tagged. When the Readout controller receives a Lev-1·LCT signal, these tagged addresses are issued as SCA read and the multiplexing and digitization of the stored voltages on these capacitors are initiated. As soon as the digitization process is finished, the tags on these capacitors are reset and digitized data stored in the RAM. This bookkeeping scheme is common to all channels of the SCA ASICs on the FEB. The readout controller logic has been implemented and tested using a XILINX 4005 field programmable gate array (FPGA).

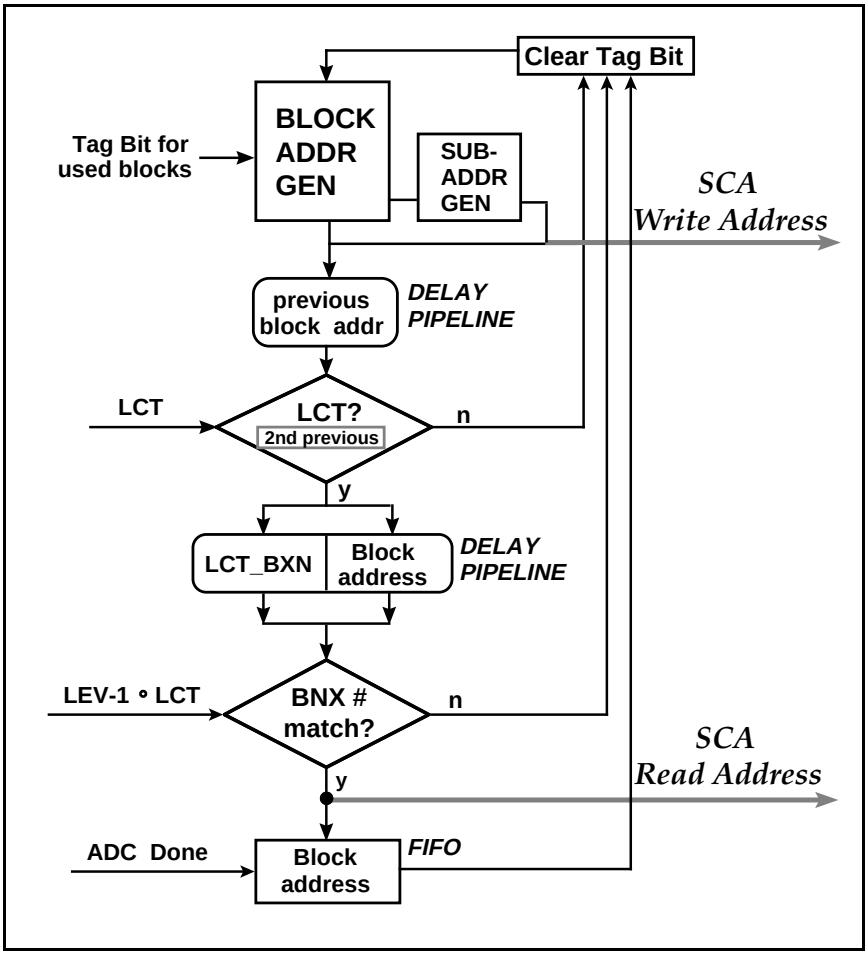


Fig. 4.4.6: Schematic diagram of the Readout Controller.

4.4.2.3 Cathode FEB prototype test

A prototype PC board was made which houses the BUCKEYE preamp-shaper chip, the SCA chip, the XILINX chip, a 12 bit ADC and an oscillator. The board was tested on a full size CSC prototype (P1A) with 3.3 m long cathode strips. Raw chamber pulses from neighbouring strips are sent into the BUCKEYE chip. The output of which is sampled and stored in the SCA. The stored voltage samples are read out upon request, digitized and read into computer. Fig. 4.4.7 shows the digitized data for several adjacent strips. Also shown are the scope traces of the output pulses of the BUCKEYE chip. As can be seen the agreement between analog input and digital output is excellent. The total noise is measured to be 1.7 mV rms. The contribution from the preamp-shaper ASIC is 1.1 mV and the rest comes mainly from the ADC (0.5 mV) and the pedistal variation from cell to cell in the SCA (1.0 mV).

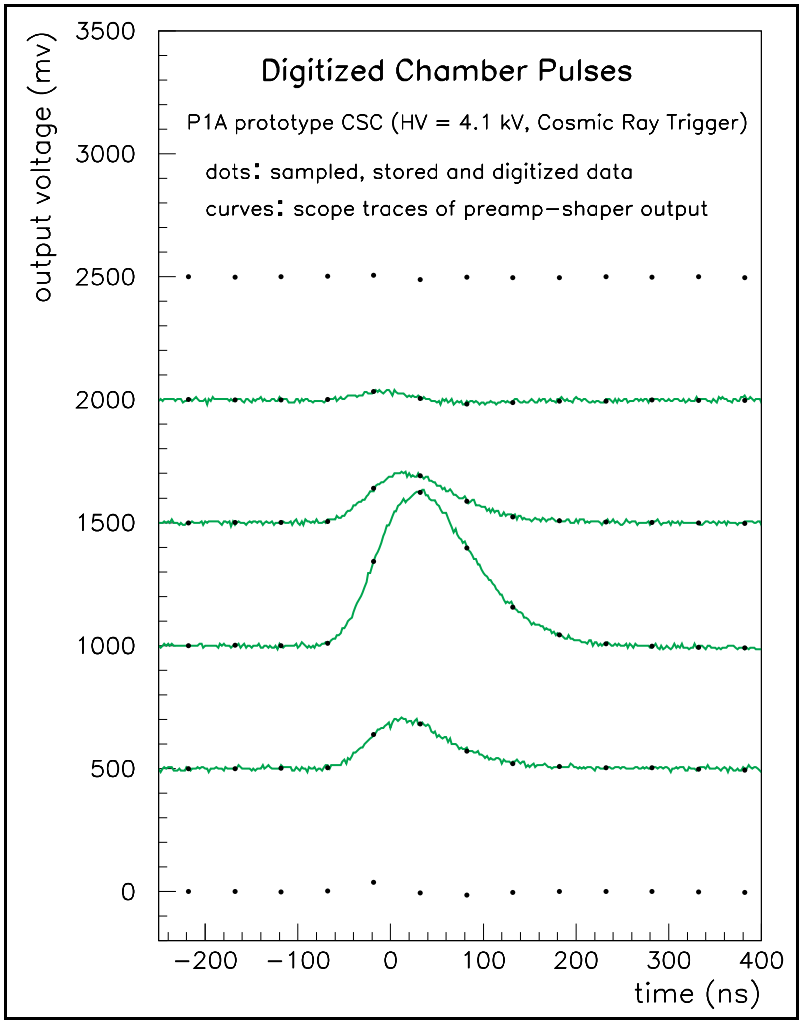


Fig. 4.4.7: Digitized chamber pulses amplified by the BUCKEYE chip and sampled and stored in SCA.

4.4.2.3 Cathode trigger comparator

The CMS Lev-1 trigger system is designed for a maximum output rate of 100 kHz and single muon trigger rate is capped at few kHz. Studies [4.19]showed that, for p_T thresholds of 20-40 GeV/c, a 30% momentum resolution is required to achieve this limit. For $\eta = 2.4$, Monte Carlo calculation demonstrates that 30% momentum resolution is achievable if track hits can be localized to within half the strip width. Two methods are considered.

The first method adopted in the EMU baseline design to realize this resolution involves the comparator network scheme [4.20]. The basic building block of the comparator network is shown in Fig. 4.4.8. Four comparators are used for every input channel. The pulse from the fast shaper for strip n is compared with a pre-set threshold level and also with pulses from neighboring strips (strip n-1 and strip n+1). Strip n has the peak charge if its pulse is larger than the neighboring strips. At the same time, the track hit position is localized to either right or left half of strip-n by a fourth comparator which compares pulses from strip n-1 and strip n+1. The output levels from the comparators are latched synchronously with the bunch crossing frequency and fed into AND gates to produce two digital signals, L_n and R_n. The L_n and R_n signals are used for high p_T (10-100 GeV) trigger where good spatial resolution is important.

Additionally, these signals are ganged 4:1 into 2-strip wide bits for use by a low p_T (2.5-10 GeV) trigger. Since the analog signals are slow compared to the bunch crossing interval, the five comparator network output signals (four half-strip plus one ganged output) are time-multiplexed into three consecutive bunch crossings for output from the comparator chip. In the first bunch crossing, an output bit represents a hit on either of the strips, while during the following two crossings the output contains encoded information as to the half-strip location of the hit.

The second method is a digital one [4.21]. The aim of this algorithm is to define the geometrical center of a cluster. Fig. 4.4.9 shows the functional diagram of the "digital" algorithm.

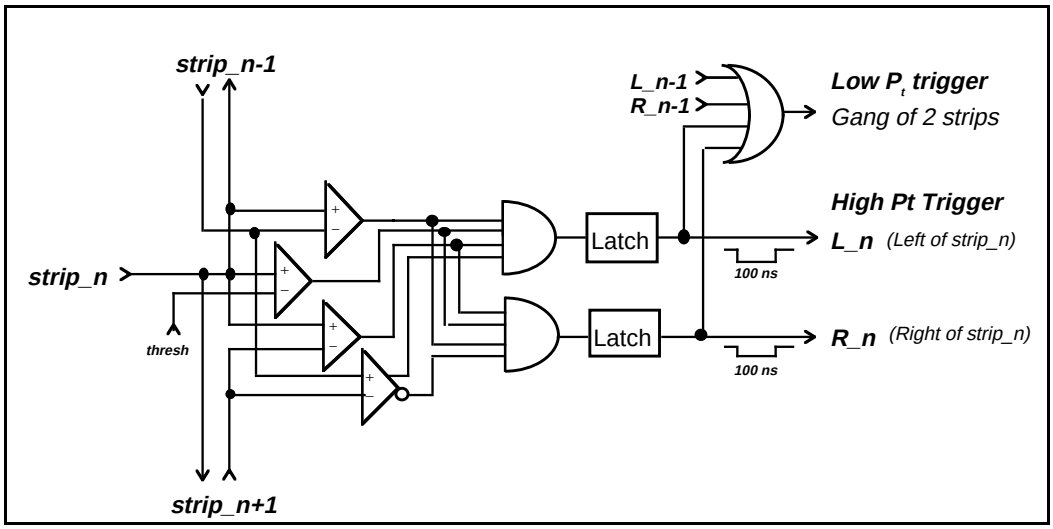


Fig. 4.4.8: Functional diagram of one channel of the comparator ASIC.

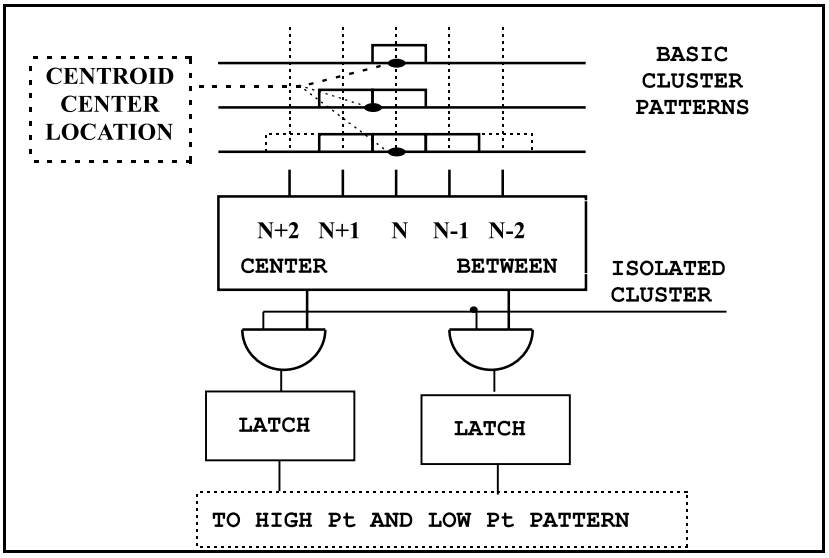


Fig 4.4.9: Base cell schematic diagram for each strip.

Basic cluster patterns (1 or 2 or 3 strips in the cluster) represent experimental data obtained with the Dubna X-ray prototype exposed to cosmic rays in December [4.22]. The main logical unit (basic cell), implemented in standard logic gates, is connected to the discriminated fast shaper outputs from 5 adjacent strips. If the cluster width is odd, the bit appears on the output "center". In the case of even cluster width, the bit appears on the output "between". The absence of signals on N+2 and N-2 inputs indicates that the cluster is isolated. If the cluster is wider than 3 adjacent strips, one suspects that it was caused by more than one particle. It is possible to extend the algorithm to set more than 1 bit on output in such a case [4.23]. The algorithm could be adjusted (e.g. number of inputs to one basic cell might be changed) to the actual chamber geometry and parameters of the fast cathode electronics which may change the average cluster size. The outputs of the basic cell are latched synchronously with BX clocks. The interface to the pattern processor is the same as for the comparator ASIC. For compatibility with the pattern processor, the pin layout and output data encoding have to be the same as the comparator ASIC.

4.4.2.4 Cathode trigger processor

The digital signals generated by the comparator network are brought into the cathode LCT processor which finds track "roads" through the 6 cathode layers within in a time interval of 75 ns [4.24]. The magnetic field in the endcap causes bending of charged tracks in the direction transverse to the strips (azimuthal direction). High pt (>10 GeV/c) tracks bend a maximum of 1.8 strips in the 15 cm between the first and sixth layer in the chamber. Low pt (2.5-10 GeV) tracks will bend as much as 7.2 strips in the chamber module.

The cathode LCT processor cycles through six phases at 40 MHz. The processor normally cycles in the first phase, in which the circuitry finds patterns among the 2-strip wide bits. There are 48 such bits per card, plus an additional 16 bits input from adjacent cards in order to handle all cases of bending tracks. If any "pretrigger" pattern is found in the first phase, then the processor continues through the following phases sequentially. Before the second phase, there is a short delay to allow signals from all layers to arrive, then all signals are latched until the end of the processor cycle. During the second phase, the 2-strip wide bits are interrogated again, to find in this case the "best" possible such pattern (either low- p_T or high-p_T). In the following four phases, additional high- p_T patterns are found among the half-strip bits in time-multiplexed fashion. In case more than one pattern is found, priority encoding circuitry selects the single best pattern per card for output.

The cathode LCT processor consists logically of four pipelined data sections, coordinated by an LCT controller state machine. A simplified diagram of the cathode LCT processor is shown Fig. 4.4.10. The input signal demultiplexor receives comparator network output signals, stretches them to persist for approximately 75ns to allow for the variation in drift times from the different chamber layers, and outputs the bits to pattern look-up circuitry in a particular time-sequenced order. Upon receiving a pretrigger signal, the controller instructs the signal multiplexor to latch the signals for a somewhat longer period of time to allow the LCT to be found precisely. The signal demultiplexor and LCT controller are ideally implemented in an FPGA for prototyping and converted to an ASIC design for cost savings in final implementation.

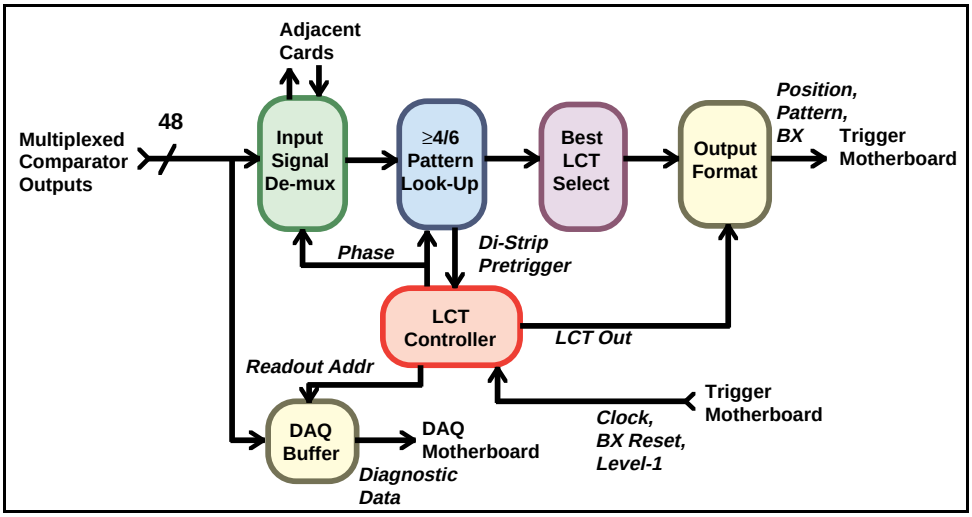


Fig. 4.4.10: Schematic diagram of the cathode LCT processor.

The pattern look-up section of the cathode LCT processor simply inputs patterns of hits and outputs pattern ID numbers for all found patterns. The set of patterns allows for missing hits, i.e. 4 out of 6 layers or 5 out of 6 layers, in addition to 6 out of 6 layers. This section must be programmable in order to handle the various types of chambers and to maintain flexibility of triggering. While the pattern look-up could in principle be implemented as AND gates in an FPGA, at present a more cost-effective solution is an array of sixteen 32-kByte static RAM chips.

Since the pattern look-up circuitry can find more than one valid pattern within a given set of input bits, additional circuitry is included to select the most desirable pattern found. This is done by priority encoding: for each track pattern, there is a unique associated 8-bit pattern ID. The pattern ID is assigned according to the desirability of the pattern. For instance, a 6/6 pattern which goes straight through the chamber corresponding to an infinite momentum track will have the highest possible pattern number, 255. At the end of the cathode LCT processor cycle, LCT data is presented at the output and sent by cable to the motherboards. The LCT output includes the best pattern ID number, as well as the bunch crossing number. The pattern ID=20 represents the full knowledge of the strip pattern found, and can be used as input to a look-up table to find the number of hits and the best estimates of position and angle. The bunch crossing number gives a cross check of system timing. Since the functionality is fixed, the LCT selector can be implemented in ASICs with minimal or no programmability.

Provision is also included in the cathode LCT processor for downloading the pattern lookup tables, and for optional readout of the raw bit patterns from the comparator chips for debugging. The clocking of the comparator and LCT processor chips is done by the motherboard, and is programmable adjustable within the bunch crossing interval.

4.4.3 Anode front-end electronics

The anode readout is similar to that of the cathode except that the emphasis is on the accuracy of timing instead of pulse height. Each input channel of the anode FEB is a ganged group of wires (10 to 20) from a layer.

Fig. 4.4.11 shows the functional diagram for the anode FEB. The input signals go into 16-channel preamplifier-shaper ASICs (6 per FEB).

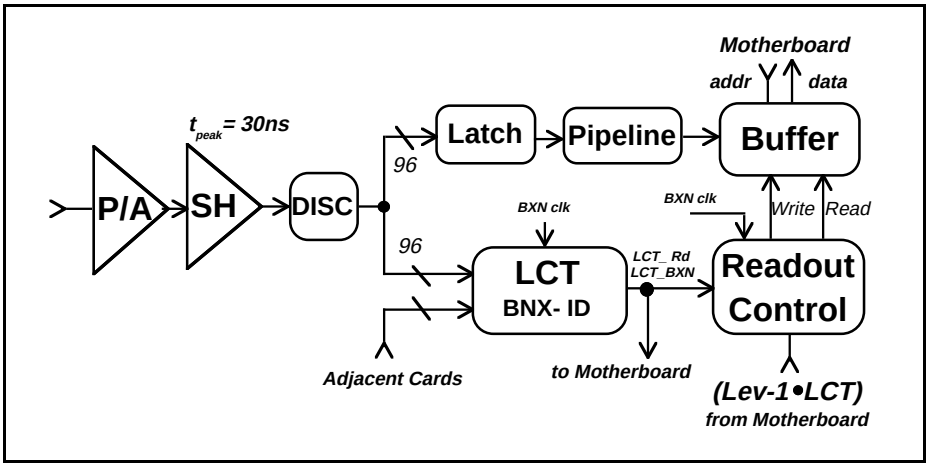


Fig. 4.4.11: Functional diagram of the anode front-end board.

The amplifiers are similar to the ones on the cathode FEB, but optimized for the summed anode input capacitance. The signals are shaped with shaper peaking time of 30ns and sent into discriminators. The logic pulses from the discriminators are used to form the LCT and to determine the bunch crossing time of the track segment. The discriminator output pulses are also latched and pipelined for readout into the DAQ network via the motherboard, providing hit/no-hit information for each of the wire groups. Table 4.4.3 lists the ICs housed on the anode front-end board.

Table 4.4.3
ICs on the anode front end board.

ASIC Type	No. Channels per ASIC	No. of ASICs Per board
Preamp-Shaper	16	6
Discriminator	16	6
Readout Control (FPGA)	96	1
LCT Pretrigger/Controller	96	2
LCT Selector	96	2

4.4.3.1 Anode preamp-shaper and discriminator

The primary function of the anode electronics is to determine the timing of the track hit with an accuracy of better than 1 bunch crossing (25ns). Therefore the anode preamp-shaper requires fast shaping. Good timing resolution can be obtained by sensing the first few electrons from the initial ionization in the CSC. However, shorter shaping time results in higher intrinsic electronics noise. For shaping time of 30 ns and for nominal chamber gas gain, the CSC signal arise from the avalanche produced by a single electron is comparable to the equivalent input noise of the amplifier. To stay safely above this noise level, discriminator threshold needs to be

set at 7 to 10 initial electrons, which can result in large time jitter. These considerations lead us to adopt the scheme of a two-threshold discriminator which is triggered above the noise level while at the same time achieve precision timing.

In this scheme, a high-threshold discriminator is driven by the initial signal from the amplifier. The threshold level is adjustable from 10% to 70% of a nominal MIP signal. The resulting pulse serves as the enable for the precision-time discriminator. The precision time discriminator consists of a constant-fraction shaper and a low-level discriminator. The constant-fraction shaping is done by adding the differentiated amplifier signal and the corresponding delayed and inverted signal. The resulting pulse is further amplified and delivered to the input of a low level zero-crossing discriminator. The zero crossing point corresponds to approximately half the rise time of the input signal. The threshold of the low-level discriminator is used for adjusting the start time of the output pulse. Table 4.4.4 lists the design specifications for the anode preamp-shaper and discriminator circuits.

Table 4.4.4
Anode preamp-shaper specifications.

Equivalent Input Noise (rms):	fC at 0 pF (1.7 fC at 200 pF)
Shaper Peaking Time:	30 ns
Shaped Waveform:	Semi-gaussian with Two-exponent tail cancellation
Nominal Input Charge[i]	142 fC (8.8 x 10^5 es)
Transfer Function (gain)	5 mV/fC (differential output)
Non-Linearity:	<10%; 0 - 1.5 volt
Two-threshold Discriminator:	High threshold disc used as ENABLE; Low threshold zero crossing disc Driven by const-frac shaped pulse.
High-level Threshold:	Adjustable from 20 – 500 mV
Discriminator Slewing Time:	2 ns

I) Corresponding to the average ionization deposition (Landau peak) for a normal incident minimum ionization particle. For a gas gain of 10^5, this input charge is equal to $(N_{ion})(f_{att})(f_{aval})(f_{sh}) \times 10^5$, where faval is the fraction of the avalanche charge collected by the anode and all other factors are defined the same way as in footnotes *i* and *ii* of Table 4.4.2. Simulation [4.18] gives N_{ion} = 180 (for 10 mm gas gap); f_{att} =0.5; f_{aval} = 0.82; f_{sh} (30ns shaper peaking time) = 0.12.

A combined preamp-shaper-discriminator ASICs based on the above specifications are being developed using the ORBIT process through MOSIS for all the endcap chambers except those in the ME1/1. Fig. 4.4.12 shows the circuit block diagram for this ASIC.

Bench and on-chamber test results with third generation ASIC prototypes have been obtained shortly before this document is finalized. The results show that the key design requirements have been met. Using this chip on the full size CSC prototype P1, the measured arrival time distribution (shown in Fig. 4.4.13) of cosmic ray hits in a single layer has an RMS width of 9.8 ns and full width of about 70 ns.

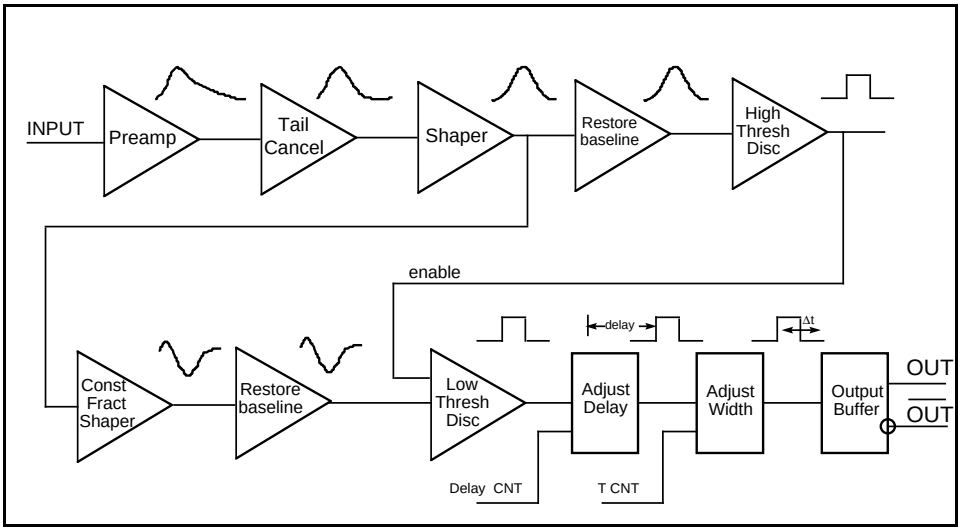


Fig. 4.4.12: Circuit block diagram for the anode preamp-shaper-discriminator ASIC.

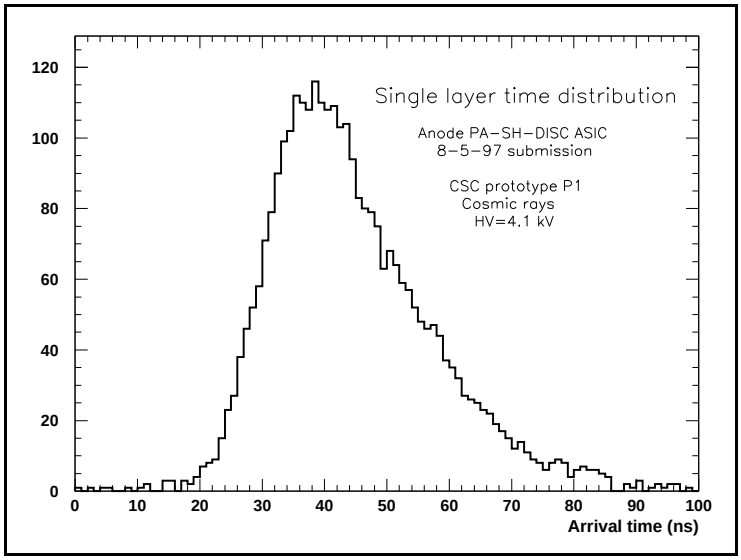


Fig. 4.4.13: Anode arrival time distribution with Aug 97 submission of PA/SH/DISC ASIC.

4.4.3.2 Anode LCT processor

The anode LCT trigger processor finds track "roads" through the 6 anode layers just as the cathode LCT trigger circuitry does. There are, however, several differences. The anode segmentation is much coarser and the roads are straight lines to the interaction region, independent of p_T. The roads also may differ in different chips and boards due to the changing polar angle. More importantly, though, the anode timing is preferred over the cathode timing to identify the correct bunch crossing. This is because the analog circuitry on the anodes is optimized for timing rather than pulse height measurement. A diagram of the anode LCT processor is given in Fig. 4.4.14.

First, the discriminator outputs are latched at the bunch crossing frequency. Whereas the maximum drift time is as large as 50-70ns, tests using beam muons (see Section 4.8.3) have

shown that the earliest signals out of the six layers arrive with about 97% probability within the 25 ns bunch crossing interval. If the background neutron hit rate is high, it will be safer to use the timing of the second earliest hit in preference to the very earliest. Therefore, a pretrigger finds a coincidence of hits on two or more layers within a single bunch crossing in order to establish the proper bunch crossing. In order to establish optimal timing, the phase of the latch clock relative to the actual bunch crossing time is controlled by the motherboard and is adjustable to 2ns accuracy. The anode LCT pretrigger/con troller functions can be implemented in one or two ASICs, but must maintain limited programmability to allow for flexibility in the bunch ID algorithm.Discriminator outputs are also latched for a longer time interval and presented to pattern look-up tables, which find roads with up to six hits. Pattern look-up circuitry for the anode LCT is similar to that for the cathode LCT, i.e. patterns of hits are input and pattern ID numbers for all found patterns are output. The set of patterns allows for missing hits, i.e. 4 out of 6 layers or 5 out of 6 layers, in addition to 6 out of 6 layers. The look-up tables are programmable in order to handle the various types of chambers and to maintain flexibility of triggering. While the pattern look-up could in principle be implemented as AND gates in an FPGA, at present a more cost-effective solution is an array of sixteen 32kByte static RAM chips.

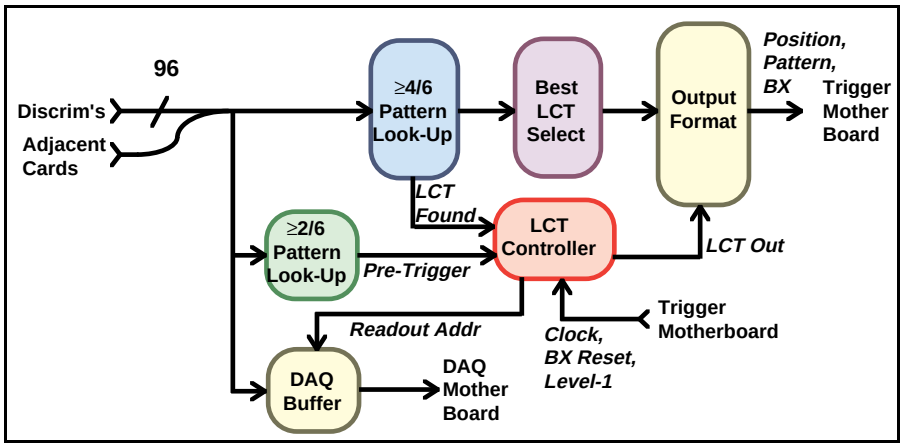


Fig. 4.4.14: Functional diagram of the anode LCT processor.

Since the anode pattern look-up circuitry can find more than one valid pattern within a given set of input bits, addition al circuitry is included to select the best LCT. This is done by priority encoding: for each LCT pattern, there is a unique associated 7-bit pattern ID. The pattern ID is assigned according to the desirability of the pattern. If an LCT pattern is found, then a bunch crossing ID from the pretrigger requirement is assigned and anode LCT data is sent onto cables to the motherboards. The anode LCT output data includes the best pattern ID number and the wire number, as well the bunch crossing number. The pattern ID represents full knowledge of the strip pattern found, and can be used as input to a lookup table to find the number of hits and the best estimates of position and angle. The bunch crossing number gives a cross-check on the system timing. The LCT selector and output formatting can be implemented in ASICs with limited or no programmability, due to their fixed functionality.

Provision is also included in the anode LCT processor for downloading the pattern lookup tables, and for readout of the raw bit patterns from the discriminators.

4.4.4 The readout motherboard

The readout motherboard serves as the link to the Lev-1 muon trigger and to the DAQ network of the experiment. Several other functions vital to the operation of the front-end electronics are also located on the MB. These include bunch crossing clock fanout to the FEBs; interface to the Run Control; calibration input; slow control; and low voltage distribution. There is one motherboard for each CSC module. Above Fig. 4.4.15 shows the schematic diagram of the trigger and DAQ interface on the motherboard.

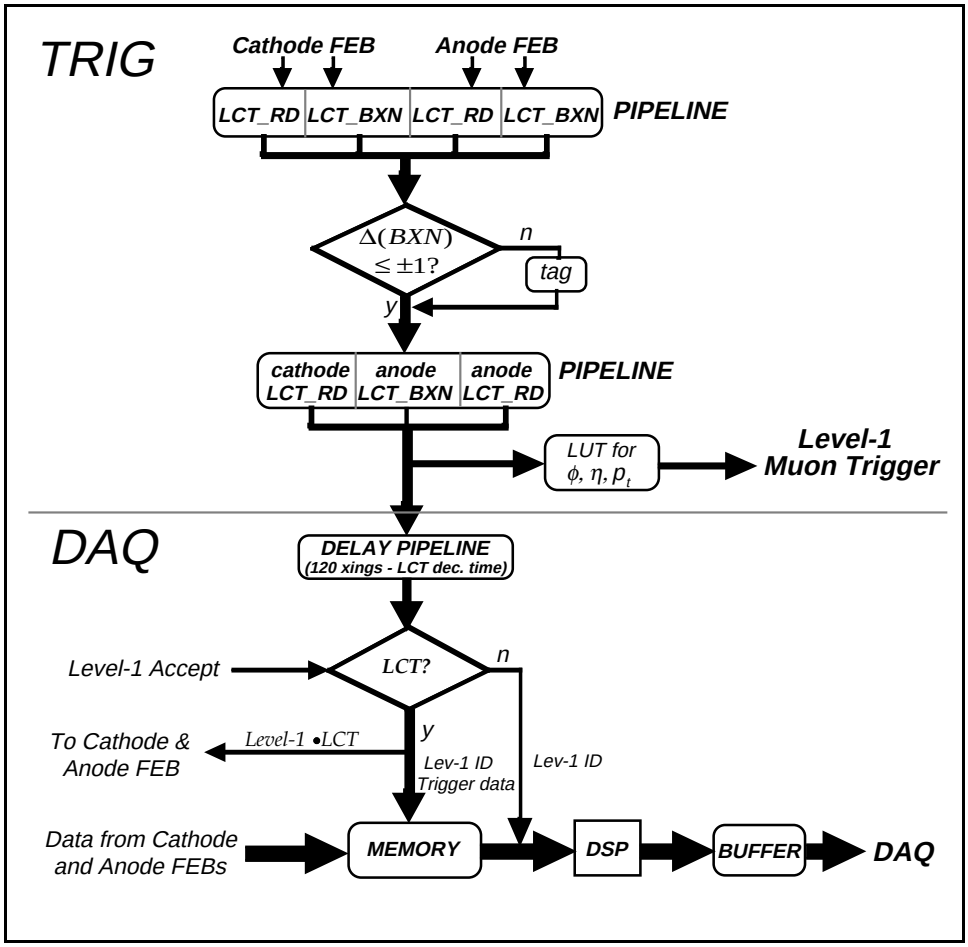


Fig. 4.4.15: Functional diagram of the Trigger and DAQ interfaces on the motherboard

4.4.4.1 Trigger interface

The information associated with LCT's generated on cathode and anode FEBs are sent to the motherboard. This information includes the bunch crossing time and the location and angle of each LCT as well as a programmable quality factor. The LCT location and its angle are coded in the LCT-road (LCT_Rd) number issued by the LCT chip.

When the timing between cathode and anode LCT's is found to agree within 1 bunch crossing, the LCT is kept and the η, f and p_T of the track segment is computed from the LCT_Rd numbers. When more than one valid LCT is found by the motherboard, only the best two, as determined by the quality factors, are retained. These are then passed on to the port

cards along with the (anode) LCT bunch crossing number (LCT_BXN). Each port card spans a 30° sector of an endcap layer. It will in turn pick the best 3 LCT's originating in a 30° sector and pass them on to the sector processor of the muon Lev-1 trigger (See Chapter 6). The trigger interface is fully pipelined and synchronous with the beam crossing clock.

4.4.4.2 DAQ interface

The readout of the data from each FEB is coordinated by the motherboard so that readout across FEB card boundaries will be seamless. As shown in Fig. 4.4.15 digitization of the stored voltage samples is initiated by the arrival on the MB of a Lev-1 accept which has a bunch crossing number (BXN) matching that of an LCT. When this occurs, the readout controllers on the FEBs are notified with an Lev-1•LCT "true" signal.

Upon the reception of the Lev-1•LCT "true" signal from the motherboard, the readout controller on each FEB checks for the occurrence of time correlated LCT in that part of the chamber. If an LCT is found, data within the corresponding sampling time window from all channels of that FEB will be digitized and readout.

To estimate the amount of readout data, we assume that whenever an Lev-1·LCT occurs, all 96 channels from 1 or 2 (if the LCT crosses board boundary) FEB(s) would be digitized and readout out. Sixteen capacitor cells (2 blocks × 8 cells per block) per channel must be digitized to guarantee 8 useful samples per pulse. The amount of digitized data per LCT is 16 samples × 96 channels × 1(2) or about 1600(3200) 16-bit words. The digitization time using one 20 MHz ADC per FEB is 16 samples × 96 channels × 50 ns = 76.8 usec.

This data is transmitted by digital optical link (one per MB) to the FED card in the central DAQ crate. The Monte Carlo simulated average LCT rate per chamber is on the order of 300 kHz [4.25]. Assuming the designed Lev-1 rate to be 100 kHz and the coincidence time window between Lev-1 accept and LCT to be 100ns, the Lev-1·LCT rate per chamber is 100 kHz × 300 kHz × 100ns = 3 kHz. Therefore the required bandwidth per link is 3 kHz × 3200 words × 16 bits/word = 154 Mbits/s.

The readout of the anode information, i.e. addresses of the wire hits and the bunch crossing number corresponding to the hits, will also be driven by the coincidence of the anode LCT with an incoming Lev-1 accept. The process is similar to the one used for the cathode readout. The volume of the anode data per track segment is much smaller (<10%) than that of the cathode data.

4.4.5 ME1/1 front-end electronics

4.4.5.1 General features

The design parameters of the ME1/1 chambers such as gas gap, wire diameter, strip width and pitch are optimized to deliver a space resolution of order of 75 μm and timing resolution of 2 - 3 ns for BX identification, in strong magnetic field of 3 Tesla at background rates exceeding 100 kHz per strip readout channel. To achieve the required chamber performance, the ME1/1 front-end electronics has been separately designed in order to be matched to the chamber design parameters. Since 1992 many prototypes of front-end CSC readout were designed using various concepts and technologies. They have been thoroughly studied and tested in beams and cosmic rays. As a result of this development, three ASICs were designed and produced in Minsk by the Integral company:

- 16 channel preamplifier-shaper for the readout pass;
- 16 channel fast shaper-discriminator for trigger;

- 8 channel anode wire readout chip.

An optimized version of the analog memory is being investigated to achieve the maximum possible rate capability for the ME1/1. The front-end ASICs will be implemented in the standard CSC readout scheme described in subsections 4.4.1 - 4.4.4. The layout and size of the PC board will be matched to the available space in the ME1/1 chambers.

4.4.5.2 16-channel preamplifier-shaper ASIC for DAQ

The cathode preamplifier-shaper ASIC comprises 16 identical cathode strip readout channels. Layout of this ASIC is shown in Fig. 4.4.16.

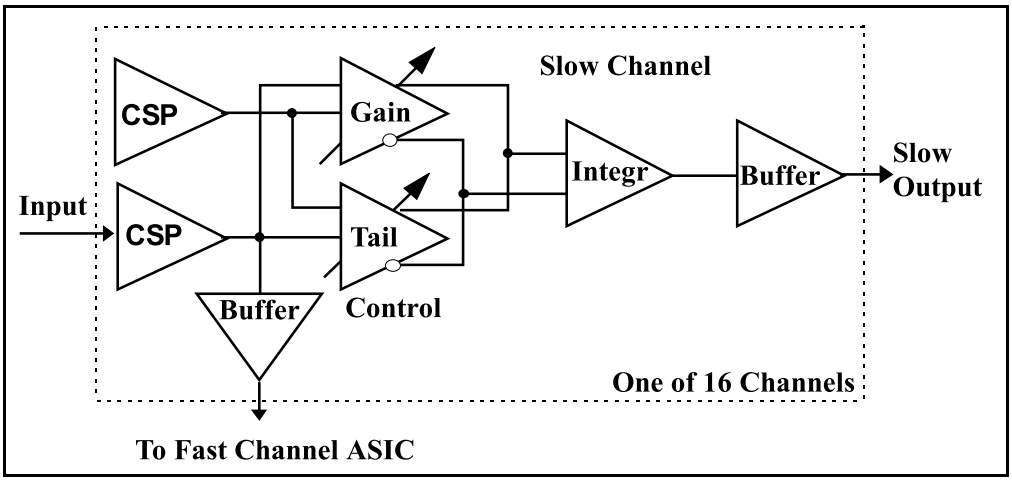


Fig. 4.4.16: Layout of cathode preamplifier -shaper ASIC

Each channel of the ASIC consists of a CSP pair, enhanced preamplifier output for trigger channel, and shaper with gain and tail cancellation control. The shaper is composed of five stages: four integrators and an output booster, which have to drive a relatively high capacitive load. A pseudo-differential configuration was chosen to avoid undesirable self-oscillations and to minimize cross-talk. The shaping time is about 100 ns. The precise value will be defined in a later iteration of the ASIC. The results of ASIC testing shown in Table 4.4.5 agree well with simulation.

Table 4.4.5
Parameters of the cathode preamplifier shaper ASIC

gain	(1÷5) mV/fC
noise	2400+11.7 e/pF
shaper peaking time	~100 ns
cross-talk	< 1 %, adjacent channels
nonlinearity	1 %; (0 ÷1.5) V

4.4.5.3 16-channel fast shaper-discriminator ASIC for trigger

A 16-channel shaper-discriminator ASIC (shaping time 30 ns) with threshold and output pulse width control for cathode readout has been designed. The layout of this ASIC is shown in Fig. 4.4.17. Each of 16 channels consists a of 3-stage shaper with a two-exponent tail cancellation circuit, a comparator and latch circuit with output pulse width and magnitude control, and an output buffer. A differential configuration was used. First bench tests of the ASIC show good agreement between simulation and test results. Measured parameters of the ASIC are shown in Table 4.4.6.

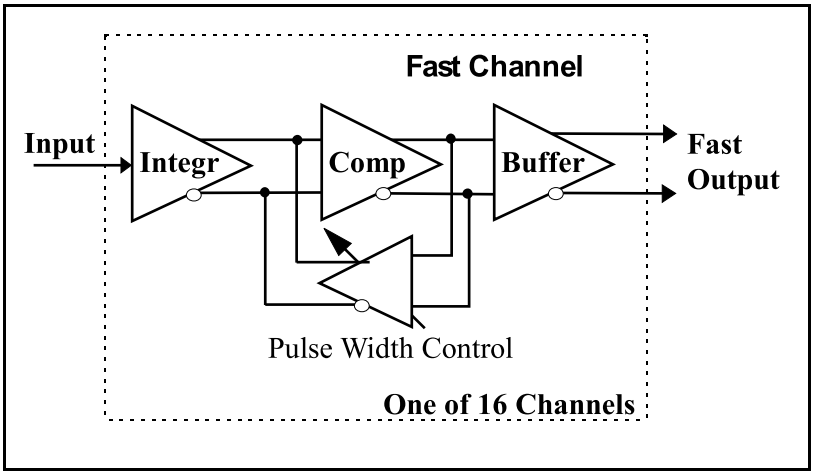


Fig. 4.4.17: Layout of shaper-discriminator ASIC.

Table 4.4.6
Parameters of the cathode fast channel ASIC

gain (differential)	5 mV/fC
max. amplitude of the output signal (differential)	300 mV
noise	2400+25 e/pF
shaper peaking time	25 ns
output pulse width	(40÷100) ns

4.4.5.4 8-channel anode front-end ASIC

An eight-channel charge sensitive preamplifier-shaper-discriminator ASIC (shaping time 15 ns) with threshold control has been designed for anode wire readout. The layout of ASIC is shown in Fig. 4.4.18. Each channel consists of a two-stage shaper, a comparator and latch circuit with output pulse width control, and an output buffer. The shaper has nonlinear response in order to minimize negative overshoot for large signals. Bench tests of the first submission anode ASIC show good agreement with simulation. The recovery time for a 1 m.i.p. is 100 ns.

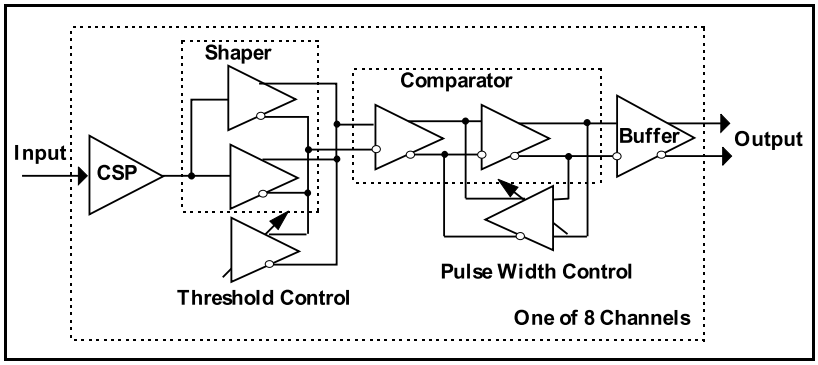


Fig. 4.4.18: Layout of anode front -end ASIC.

Table 4.4.7
Parameters of the anode ASIC

gain (differential)	5 mV/fC
noise	1600+20 e/pF
shaper peaking time	15 ns
max. amplitude of the output signal (differential)	(0÷0.5) V
discriminator threshold, adjustable	(0÷250) mV
output pulse width	(40÷200) ns

4.4.5.5 Beam test results

The cathode preamplifier-shaper ASIC has been tested on the P3 ME1/1 prototype with cosmic rays, and in the H2 and GIF beams at CERN. Preliminary results show a signal to noise ratio of order 200 and a pulse recovery time of less than 500 ns which agrees well with the simulation. Typical response of the cathode preamplifier-shaper for 225 GeV muons is shown in Fig. 4.4.19.

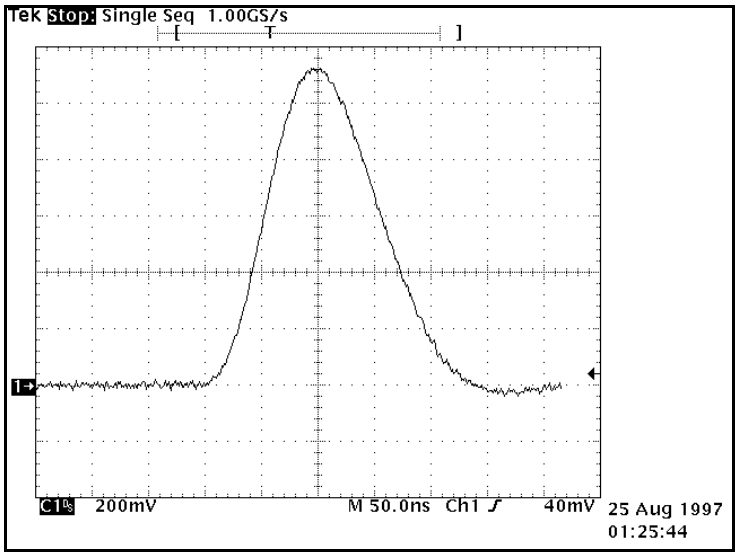


Fig. 4.4.19: Preamplifier-shaper response for 225 GeV muons.

The 96 channel prototype of the cathode readout was tested with the P3 ME1/1 prototype. Typical anode and cathode fast channel single layer time spectra are shown in Fig. 4.4.20. The TDC scale is 0.1 ns per count. The full width of both spectra is about 30 ns. The delay of the fast channel time spectrum with respect to the anode one is about 10 ns.

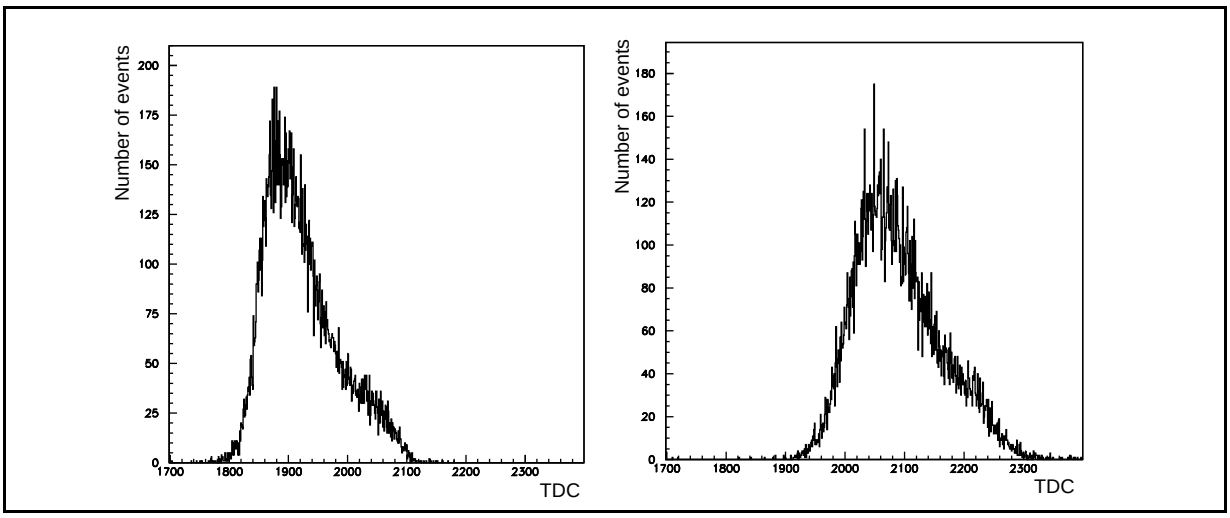


Fig. 4.4.20: Typical single layer time spectra for (left) anode and (right) cathode fast channel

Shown in Fig. 4.4.21 is the residual distribution between track coordinates reconstructed with fast trigger and readout channels. Sigma of the distribution is 0.54 mm, in line with expectations from the simulations.

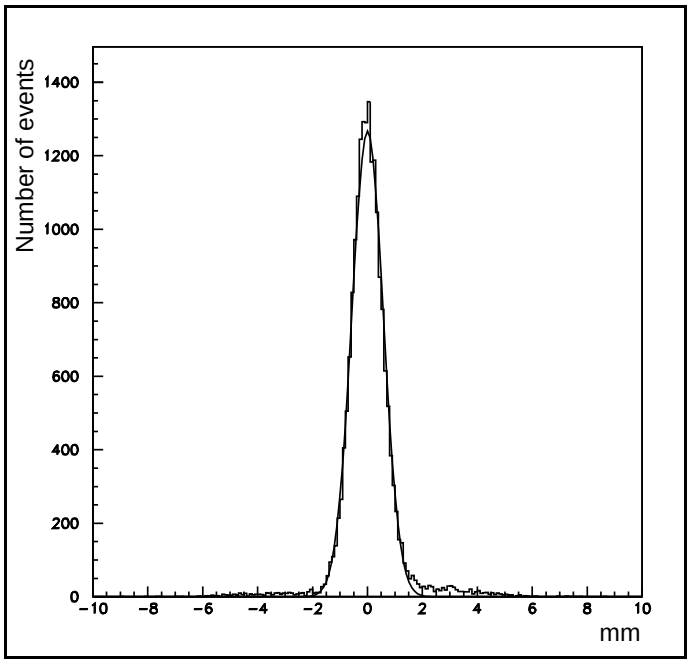


Fig. 4.4.21: Residual distribution between track coordinates reconstructed with fast trigger and readout channels.

4.5 POWER AND CONTROL SYSTEMS

4.5.1 High voltage

Each of the 540 chambers will have 6 channels of HV so that the total system must provide 3240 channels. The system will be based on a commercial multi-channel HV main frame, such as the ones currently available from CAEN (Model SY 527 in combination with A-832P HV cards) or from LeCroy (Model 1458 with 1471 HV cards). Both systems will accommodate all HV channels in 30 crates where each channel is fully computer-controlled and capable of delivering a current of 200 μA at the maximum of 6 kV. These HV chassis will be mounted in the control room.

This main frame HV system is going to be connected to fanout terminals located on the outer edge of the endcap disks by 12-conductor flexible cables. The maximum distance for this connection is approximately 100 m. At the fanout terminals each channel, which corresponds to a single plane of one of the CSC chambers, is fanned out into two to five HV segments depending on the size of the chamber (see Table 4.1.1). At the fanout terminal it is possible to disconnect manually any of the segments of a single plane if that segment is drawing excessive current (current monitoring for each of the segments will be available at the fanout terminals). Several multi-conductor cables (depending on chamber size) connect the fanout terminal to each chamber.

This design of the HV system allows us the option of turning off a single chamber plane under computer control should any HV problem or excessive noise occur during a run. The chamber remains operational and no hole opens in the muon system since the local chamber trigger requires 4 planes out of 6. Then during a short access shutdown one can identify the malfunctioning segments, disconnect them mechanically at the distribution terminals, and recover the remaining part of the plane for further runs without moving the endcap disks or dismounting the chambers.

At nominal running conditions, the total charge in an avalanche is of about 1 pC. At the expected average background rates of up to 20-40 kHz/strip this translates into roughly 5 μA per plane. Adding safety factors to cover uncertainties in background calculations, local splashes in backgrounds and the option of operating the chambers at a higher gas gain, we arrive at a requirement for the HV system to be capable of supplying at least 100 μA of current per plane, a requirement easily met by either of the commercial systems. The chamber operational HV is expected to be between 4.0 and 5.0 kV, depending on the final choice of the gas mixture.

4.5.2 Low voltage

The low voltage supplies must deliver a large amount of current at 5 and 3.3 volts to each of the 540 CSC chambers. Ideally this would require power supplies located close to the chambers to decrease the power (and heat) loss in the cabling. However, these CSC chambers operate in a high magnetic field of up to 700-800 gauss where power supply operation will be difficult.

The present plan calls for the large power supplies to be located remotely at a distance of roughly 60m on the hall balconies. In this region the magnetic field is expected to be less than XXX Gauss. The required power will be delivered over large cables at higher voltage (75 V) to reduce the heating losses. These large cables pass through the endcap cable chain to fan-out

terminals located on each of the endcap disks. From these terminals the large cables fan out around the outer edge of each endcap disk. Along this path they connect with Vicor DC-to-DC convertors which convert the power from approximately 70 volts (less than the original 75 volts due to losses in the cables) to the required 5 and 3.3 volts.

There are 2 Vicor DC-to-DC convertors for each chamber to provide the +5 and +3.3 volt power. Each DC-to-DC convertor is housed in a soft iron box mounted on the outer edge of the endcap to shield it from the large magnetic fields (approximately 600-800 gauss) in this region. The Vicor +5V and +3.3V outputs are connected to their respective chambers through flexible AWG4 cables. AWG2 cables are used for +5V on ME2, 3, 4/1 chambers.

4.5.3 Cooling

A large portion of the endcap electronics is attached to the face of the CSC chambers as cathode front-end boards, anode front-end boards, and motherboards. The electronics on each of these boards need to be cooled.

Table 4.5.1
Estimate of heat load for the largest chamber ME234/2.

Electronic Board	Heat/Board(w)	Boards/Chamber	Heat/Chamber(w)
cathode 96-channel FE	4.3	5	21
cathode 96-channel trigger	8.7	5	43
anode 96-channel FE	11.0	4	44
anode 96-channel trigger	7.6	4	27
motherboard (trigger)	25.0	1	25
motherboard (DAQ)	7.0	1	7

The estimated heat load for the CSC systems is 80 kW, which is about 170 W per chamber. Table 4.5.1 shows an estimate of the heat load for the largest chambers (ME2/2, ME3/2, and ME4/2). The most efficient method for removing this heat is to mount each of the boards on a metallic pad which has good thermal contact with the heat production on the board. Then the pads are cooled using a connection to a pressurized water system. The overall height of the CMS detector is 14 m so the water pressure differential over this height will vary by roughly 1.4 bar. The return pressure should be higher than this differential and the supply pressure should be at least 2 bar above the return.

On the outer face of the chamber copper pads are mounted under each electronic board. All the pads on a chamber face are connected by a “continuous” 1/4” copper tube which is brazed to each pad (see Fig. 4.5.1). A flexible 1/4” hose is connected to the water inputs and outputs of each chamber. This flexible hose connects to the manifold laterals via O-ring fittings. An aluminum faraday shield (for both RF and cooling) is mounted on each copper pad to cover the electronic board.

The present plan for stations 2, 3, and 4 is to connect three chambers in series (2 10° and 1 20°- CSCs) covering a sector of 20° as shown in Fig. 4.5.2 for station 4. For station 1, which has no 20° chambers, we will connect only two 10° chambers in series.

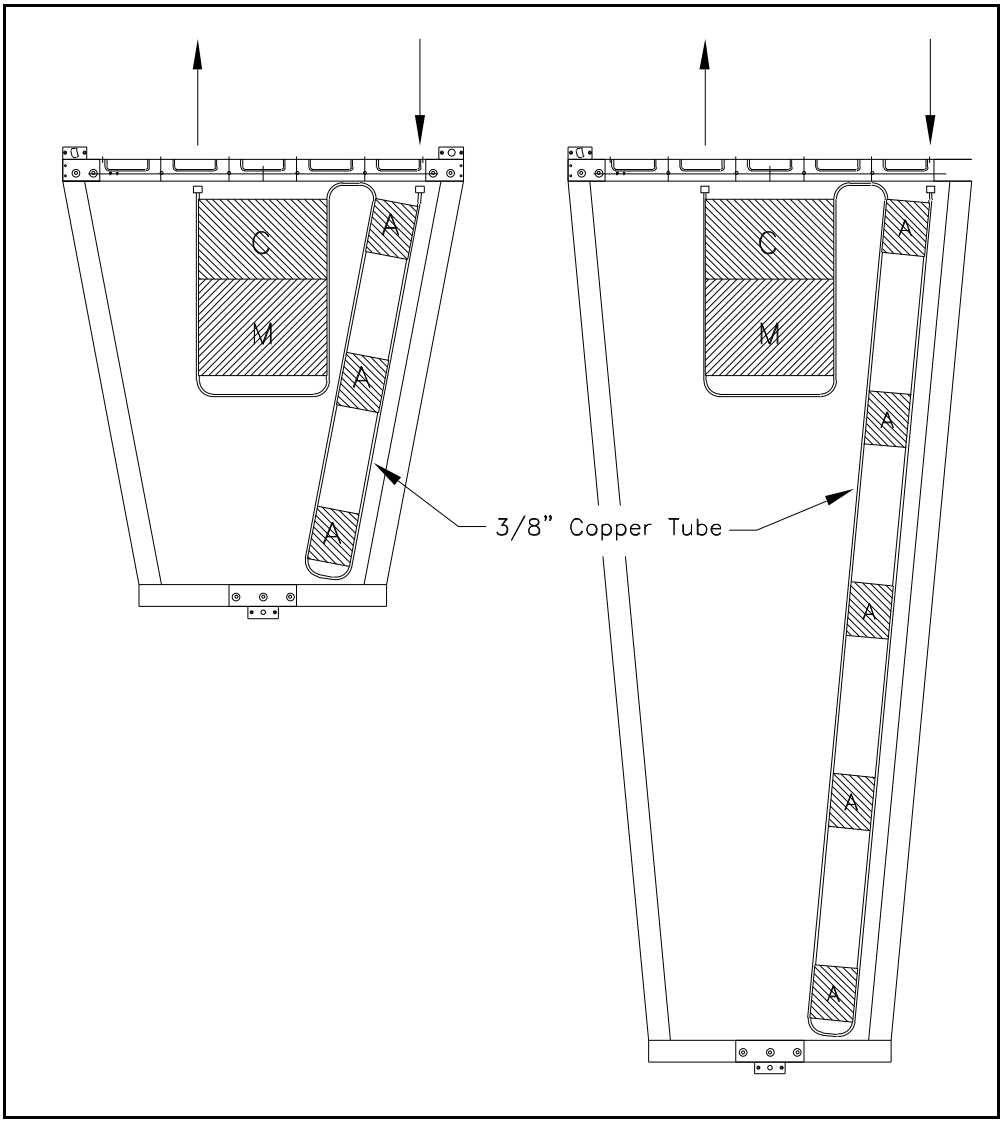


Fig. 4.5.1: Copper pads and tubing mounted on the face of a ME1/3 chamber (left) and a ME2/2 chamber (right).

The cooling manifolds, supply and return, located on the outer edge of each disk as shown in Fig. 4.5.2 for disk YE3. These manifolds are 1.25" stainless steel pipes with lateral connections to each group of CSC chambers. Each face of the 12-sided endcap disks contains one section of the manifolds; sections are connected by O-ring seals on flanged ends. In order to accommodate installation tolerances we add a short flexible section for each connection. Along the manifold holes are drilled for local connections and 1/4" stainless steel half couplings are welded. Each lateral connection has a 1/4" ball valve; the return connection also has a flow restrictor (2.8l/m or .75GPM). Flexible 1/4" hoses carry the water to the chambers. Each hose connection is made with O-ring fittings which are robust and reliable.

Fig. 4.5.3 shows a close-up view of the water manifolds and the cable trays on the outer edge of the endcap disk. A top view shows the layout of lateral connections to either side of the disk. Also shown is a cut view of the edge of the disk with manifolds for water, gas, and hydraulics.

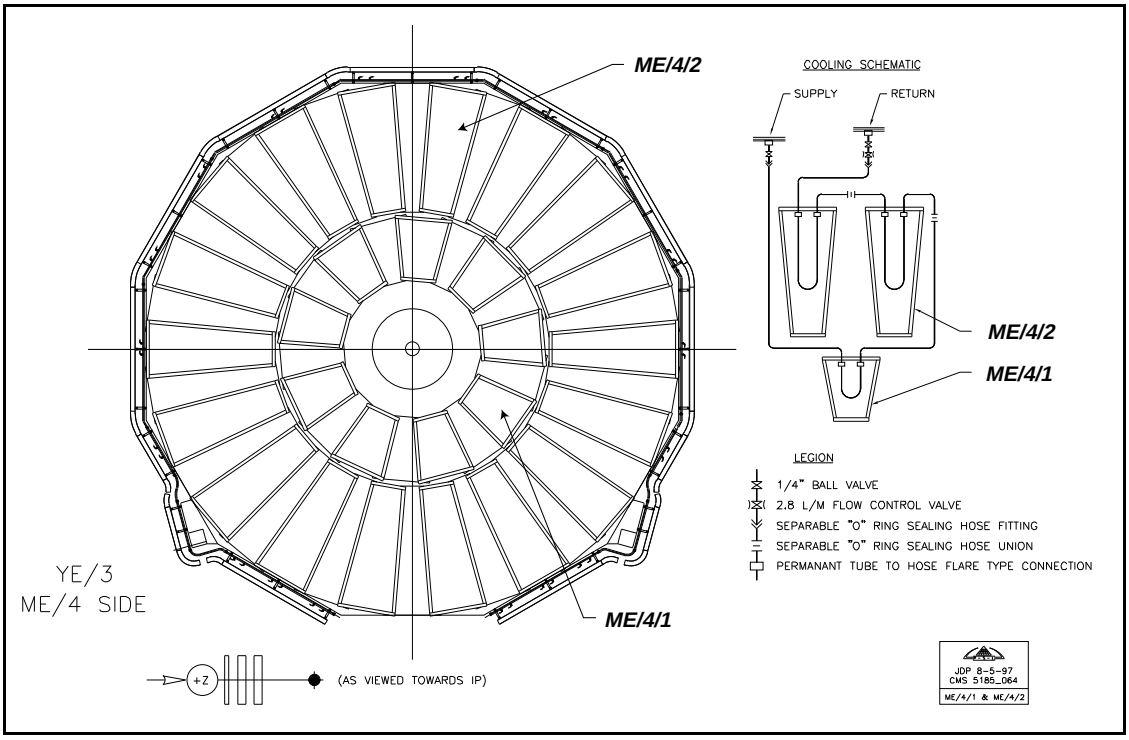


Fig. 4.5.2: An axial view of the layout of water manifolds and cable trays on a typical endcap disk. Also shown is the series connection of individual chambers

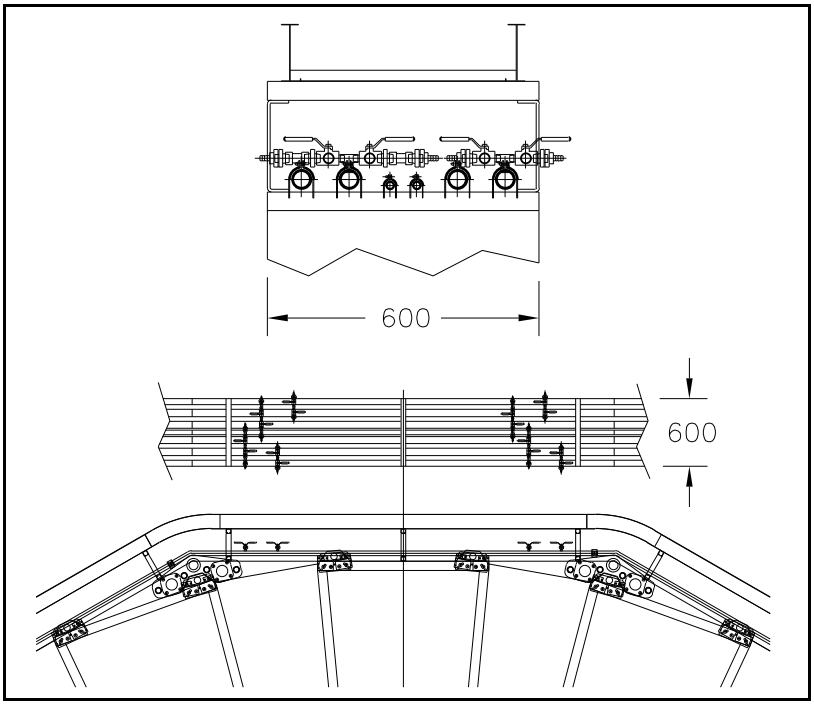


Fig. 4.5.3: Layout of the gas, water, and hydraulic manifolds on the top edge of an endcap disk.

The input water temperature will be 18-20°C (about 5° above the dew point). The sizing of the system has been made to insure that the temperature rise per connection remains less than 2°C.

4.5.4 Controls

In order to ensure continuous and reliable operation of the CSC detector a set of parameters has to be controlled and monitored by the central CMS Slow Control system:

- High Voltage and Low Voltage values and currents
- Gas pressure and flow as measured on the chambers
- Input and output temperature and flux values of the water used in the cooling system
- Oxygen and Nitrogen contamination at the input and output of the gas system
- Low Voltages of the electronics crates

4.5.5 Cables and interfaces

The primary endcap cables are: (1) signal (both trigger and readout); (2) power (high and low voltage); and (3) monitoring (alignment). These cables generally run from the control room to each chamber via the cable trays on each endcap disk. The following table lists the cables that will be located in the cable chain and/or the cable trays running on the outer edge of each disk.

Table 4.5.2
Cable list for endcap systems

cable	number	description	upstream end	downstream end
signal-trig	672	optical: 7 fibers per port card	port card	control room
signal-DAQ	540	optical: 1 fiber per motherboard	CSC motherboard	control room
TTC	96	optical: clock & control	control room	port card
low voltage input	16	75 V bus	balcony supply	dc-dc converter
low voltage output	1872	+5V &+3.3V busses	dc-dc converter	CSC power distrib.
high voltage	270	12-conductor HV cable	power supply	fanout box
high voltage	1, 2, 3, 5 per CSC	7-conductor HV cable	fanout box	CSC
configuration	540	send trigger config	control room	CSC motherboard
alignment laser sensors	24	50-conductor flat cable	disk face	control room
alignment laser power	24	LV power cable	disk face	control room
alignment z sensors	12	50-conductor flat cable	disk edge	control room
alignment z power	12	LV power cable	disk edge	control room
temperature sensors	24	50-conductor flat cable	disk face	control room

4.5.6 Gas system

The CSC chambers in the endcaps of CMS comprise a gas volume of ~76 m^3 and operate with a gas mixture of Ar-CO_2-CF_4 (30%-50%-20%). As an alternative a four component mixture with an additional C_4H_{10} component is also considered.

The basic function of the gas system is to mix the three components in appropriate proportions and to distribute the clean gas mixture into the individual chambers at a pressure of 1 mbar above atmospheric pressure. For a detector system of this size a closed loop circulation system is recommended. Moreover the baseline gas mixture contains an important fraction of expensive Tetraflouromethane (CF_4) which may justify economically a recovery plant for the recuperation of that component in the exhaust gas.

The system proposed will consist of functional modules, which are designed as far as possible uniformly for all CMS gas systems. The component sizes and ranges are adapted to meet the specific requirements of the CSC system. The CSC gas system will consist of the modules as shown in Table 4.5.3.

Table 4.5.3
Major CSC gas system modules.

Module	Situated in
Primary Gas Supplies	SGX Building
Mixer	SGX Building
Inside closed circulation loop:	
Chamber Distribution Systems	UX Cavern
Purifier	SGX Building
Pump and Return Gas Analysis	US Area
CF4 Recovery Plant	SGX Area

4.5.6.1 Mixer

The flows of component gases are metered by mass flow controllers, which have an absolute precision of ± 1% over a year, and have a medium term stability of ± 0.3% in constant conditions. Flows are monitored by a process control computer, which continually calculates the mixture percentages supplied to the system. The process control computer compares the running mixture with respect to the required mixture: this required mixture may either be a constant ratio, or alternatively may be derived from comparison of the running mixture with a reference gas mixture in an analysis instrument. In either case the process control computer calculates the correction required to bring the running gas mixture to the required values; this is then fed back to the mass flow controllers as an adjustment of their ‘set value’. The medium term stability in constant flow conditions is better than 0.1%: absolute stability will depend on the absolute precision of the analysing instrument.

At a regeneration rate of 95% the expected fresh gas flow at operating conditions is about 0.35 m^3/h. That rate is adjusted to 30-40% of full scale of the instruments allowing variations of the fresh gas flow by nearly a factor three up or down. For filling the detector with the mixture a second set of mass flow controllers is used to increase the flow range by a factor 10.

This flow meter change will allow a full volume exchange with fresh gas only in less than 12h. To obtain operating conditions one needs 3-4 full volume changes with fresh gas leading to a start-up time of 2-3 days. It may be less expensive to fill first the two cheap components (Ar - CO_2) in their right proportions and toping up that mixture afterwards with the appropriate CF_4 fraction. This process could be done under automatic control based on an infrared gas mixture analysis. A schematic layout of the gas mixer for the CSC detectors is shown in Fig. 4.5.4.

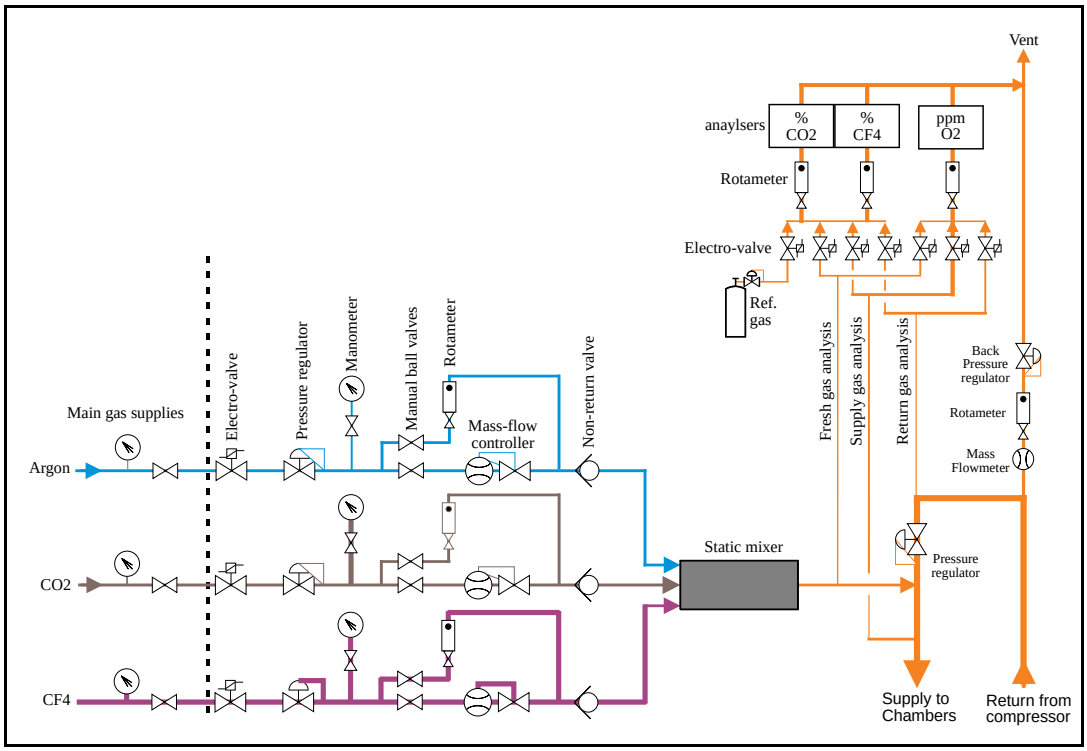


Fig. 4.5.4: Layout of the gas mixer

4.5.6.2 Closed Circulation Loop

The CSC chamber gas is circulated in a closed loop with an expected regeneration rate of 90 to 95% using inline gas purification. A volume exchange rate of one volume every 12 hours leads to a circulation flow rate of 6.3 m^3/h and one complete volume renewal every 10 days.

As shown in Fig. 4.5.5 the circulation loop is distributed over three different areas:

- the mixer room in the SGX building housing the input from the mixer, the purifier and the exhaust gas recovery plant.
- the US- service area which is permanently accessible where the chamber pressure regulation, the flow regulation for individual wheels, the compressor and the analysis instruments are placed.
- the experimental cavern (UX) containing the individual chamber gas distribution, channel flow meters and gas sampling connections at the chamber outlets.

4.5.6.3 The gas distribution

The CSC detector consist of 4 stations per endcap which are supplied independently from the US area allowing to control global flow or pressure adjustments for one stations from the

permanently accessible zone. In the UX cavern a gas rack is mounted on each of the 8 detector stations for the gas distribution to the individual chambers (see Fig. 4.5.6).

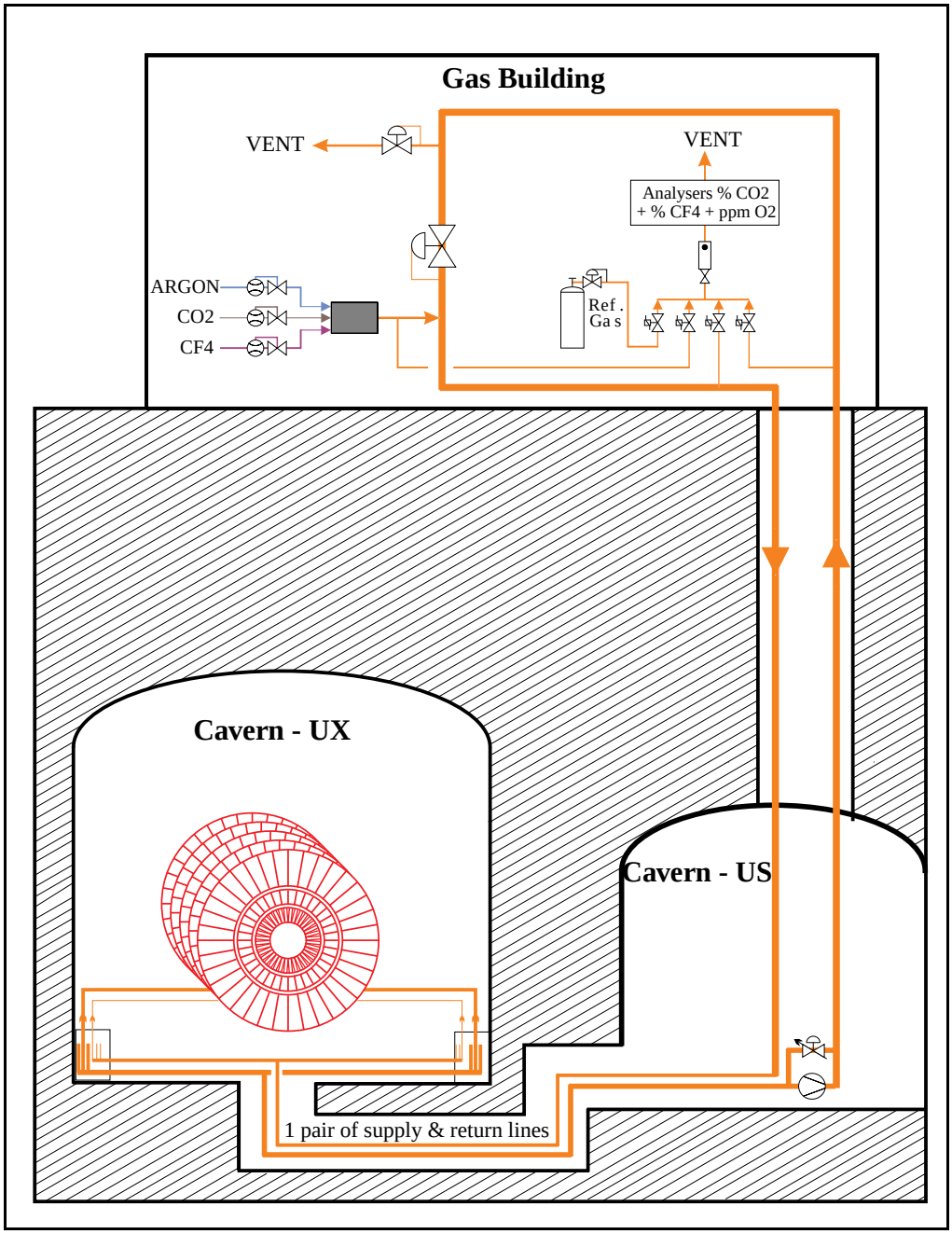
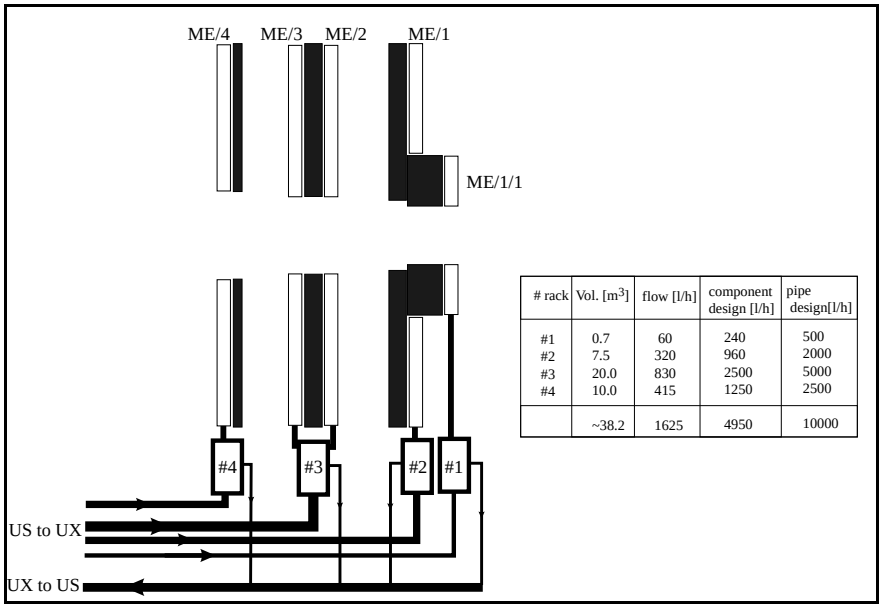


Fig. 4.5.5: Gas circulation loop.

The CSC detector consist of 54 chamber modules on each of the stations ME2 to ME 4 and of 72 modules in the most inner station ME1. For stations ME2 to ME 4 all chambers in a 20° Phi section are grouped together on one single gas line. For the inner station the gas supplies are separated radially keeping the chambers of the inner ring ME1/1 independent (see Fig. 4.5.7). This arrangement results in 90 independent gas channels on each endcap.



# rack	Vol. [m^3]	flow [l/h]	component design [l/h]	pipe design[l/h]
#1	0.7	60	240	500
#2	7.5	320	960	2000
#3	20.0	830	2500	5000
#4	10.0	415	1250	2500
	~38.2	1625	4950	10000

Fig. 4.5.6: Gas connections to the individual CSC detectors.

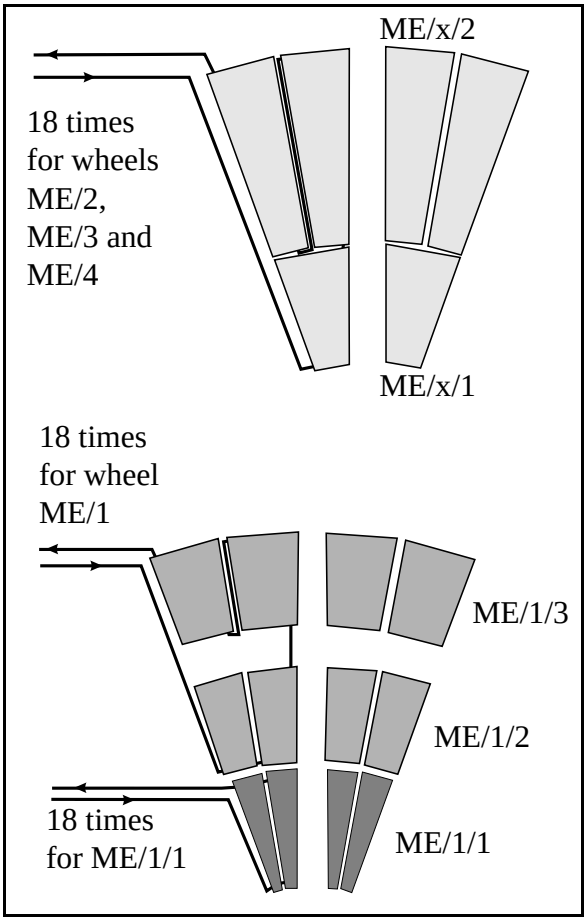


Fig. 4.5.7: Gas connections to the different forward muon stations.

4.5.6.4 Pressure regulation and the compressor

The inlet pressure regulation is done for each individual wheel in the US area allowing flow adjustments on individual Stations even during physics periods. One can also purge one single Station manually with neutral gas from this place which might be useful during a short shutdown. Four output pipes return the gas from the detector to the US area. A turbine blower pump allows to compress the gas to approximately 100 mbar for return to the surface and recycling through the purifiers. In the output line a back-pressure regulator in parallel with the pump controls the pressure to -0.5 mbar below atmospheric pressure. The pressure drop in the chamber return pipe is 1-2 mbar leading to a chamber operational pressure near 1 mbar at nominal flow rate. A lower chamber operation pressures can be obtained by reducing the pressure at the pump below the atmospheric level.

4.5.6.5 The gas distribution within one station

The distribution systems, shown in Fig. 4.5.8, contains a distribution manifold supplying gas to all chambers in that Station. Every channel has a short flexible pipe with a self-sealing quick-connector at the inlet and at the outlet line. This permits gas channels to be individually disconnected from the circulation loop for flushing with inert gas and exhausting to direct vent. This facility is also very useful for leak tests of individual gas channels. Every supply and return gas line has remotely read flowmeters allowing a direct comparison between inlet and outlet flow as well as a simple adjustment of individual channel flows using the needle valve at the inlet. Seeing the number of gas channels, and the fact that the channel flow meters are in a normally non-accessible zone, the flow metering technology must be simple, reliable and inexpensive. Currently two measurement principles are considered to meet this requirements: (a) hot wire anemometers (similar to LEP -type channel flowmeters) and (b) ultra-sonic time of flight meters.

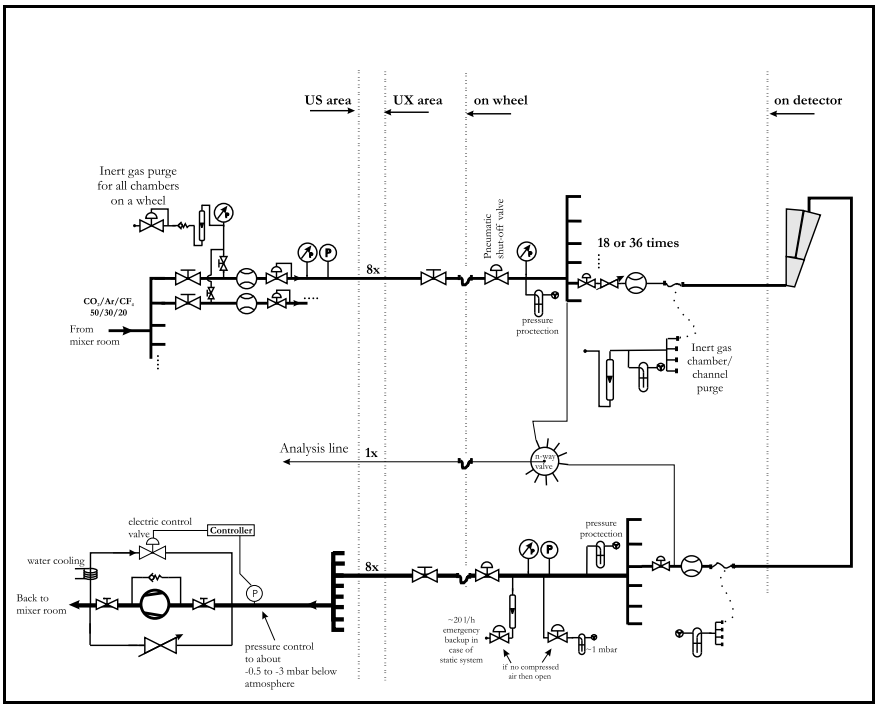


Fig. 4.5.8: Layout of the gas distribution within one station.

A sensitive indication of gas leaks in a chamber system is an O_2 measurement in the return gas. It is foreseen to sample the chamber output gas in the distribution systems. The modularity can be the channel level or a group of channels. The sampled gas is sucked back to the US area with a little pump. Thus gas analysis instruments are accessible at any time and can be shared also by several detector groups.

The distribution systems on the detector are situated in a high magnetic field (up to 1 T) region which excludes the use of electro-magnetic valves. Pneumatic or manual valves have to be installed instead. The mounting of the racks on the detector itself allows to accommodate easily for movements of the individual stations during the shut-down work by simply disconnecting the main supply and return pipes. Pipes for compressed air to drive the pneumatic valve will need long flexible plastic pipes to accommodate for the movement (2-5 m depending on the wheel) of the wheels.

4.5.6.6 Distribution pipework

There will be one supply and one return pipe between the SGX building and US area. Eight supply and return pipes connect the US area with the experimental zone where the pipes enter from underneath the detector. Gas racks on either side of the endcap-stations distribute the gas to the individual gas channels. The fixed piping in the vertical and horizontal sections in the underground will be all stainless steel with welded connections while the internal detector piping is foreseen in copper and screwed fittings in order to reduce installation costs.

4.5.6.7 Gas purification

Most close loop circulation systems need gas purification in the return line in order to achieve high regeneration rates (usually 90 - 95%). The principle impurities which may harm the detectors are oxygen, water vapour, halogens, silicones or N_2 in higher concentrations. For the CSC system the purity requirements are not very strict:

$$O_2 \langle 1000 ppm$$
$$N_2 \langle 3000 ppm$$
$$H_2O \langle 1000 ppm$$

The purifier cartridges proposed have uniform sizes and gas connections through out all CMS gas systems The purifying agents filled inside the cartridges are chosen individually depending on the specific cleaning requirements for that gas. In this way the set-ups for the regeneration can be standardised too and remain interchangeable. Three different cartridge sizes are available to adapt the individual purifier to the required gas flow and the needed cleaning capacity.

A first set of twin cartridges filled with e.g. 3Å molecular sieves can be used to remove water vapour. In a second stage of twin columns patched with a reducing agent, e.g. activated copper, for oxygen removal. The advantage of having two parallel cylinders in each cleaning stage is to run the gas mixture through one of them while the other one is regenerating. The molecular sieve and the activated copper can be regenerated at the same time by heating up the columns to 180^0C and flushing with an Ar/H_2 (93% - 7%) mixture. The operating chamber gas of the CSC contains CF_4 which must be separated in all circumstances from the regeneration gas containing H_2 to prevent the formation of hydrogen fluoride. To avoid mistakes while regenerating the columns manually it is proposed to automate this process so that no human intervention is necessary.

The gas purity at the output of the purifier is likely to be better than required, hence one may consider to deviate only a fraction of the total flow through the purifier in order to lengthen its running time. A humidity and an oxygen meter must be available to measure the impurity concentrations before and after the purifier.

4.5.6.8 CF_4 recovery plant

Two stage recovery plant (first, clean mixture from CO_2 and then freeze out the CF_4) will be studied when gas mixture is final.

4.6 MOUNTING AND INSTALLATION

4.6.1 Overview

There are two distinctive schemes of mounting and installation to be used for the endcap muon stations. One scheme is designated for ME1/1 chambers which have to be lowered into the slot between the endcap iron nose and endcap hadron calorimeter. The other scheme deals with the rest of the chambers which are to be pasted on the endcap iron disks.4.6.1 ME1/2, ME1/3, ME2/1, ME3/1, ME4/1, ME234/2 chambers

4.6.1.1 Overall layout

The layouts of the these chambers are shown in axial views in Fig. 4.6.1 (ME1/2 and ME1/3) and in Fig. 4.6.2 (ME2/1 and ME2/2, the other stations being very similar). All of these stations (except for ME1/3) have overlapped chambers as shown by the hatching in these figures. As a result of this overlapping some chambers (shown by cross-hatching) will be mounted close to the iron (inner chambers). Others (no cross-hatching) will be mounted farther from the iron (outer chambers). Fig. 4.6.1 also shows z-supports which insure spacing between the endcap and barrel.

Fig. 4.6.3 shows an expanded view of the endcap disks and identifies which CSC chamber stations mount onto which disk faces. The ME1/2 and ME1/3 chambers are fixed to the front face of disk YE1. The ME2/1 and ME2/2 chambers are fixed to the front face of disk YE2, while the ME3/1 and ME3/2 chambers are fixed to the back face of disk YE2. Finally the ME4/1 and ME4/2 chambers are mounted on the back face of disk YE3. Each of the iron disks is self-supporting and mounted on air pads so the disks can be moved apart for access to the CSCs during installation or maintenance (details on the iron design, carts, etc. can be found the CMS Magnet TDR).

The φ orientation of the CSCs was chosen such that the y-axis (vertical line) passes through the center of the top chamber. This provides reasonable matching with the ME1/1 chambers as well as the barrel drift chambers, which are located on the 12 flats of the barrel return yoke.

Each chamber is mounted on 3D quasi-kinematic mounts, which can accommodate chamber tolerances and any possible expansion or contraction. The chambers are individually mounted to posts fixed on the iron endcap disks. As a result, it is easy to replace any of the outer chambers. To replace one of the inner chambers, it is necessary first to remove both of the outer chambers blocking it.

The frame is composed of aluminum extrusions which attach to the top and bottom edges of the chamber. A 1.6 mm thick aluminum plate is screwed to the upper and lower extrusions to

connect the edges and provide good longitudinal stability. The chamber panels are held together by threaded rods which are bolted on the outside face of each extrusion.

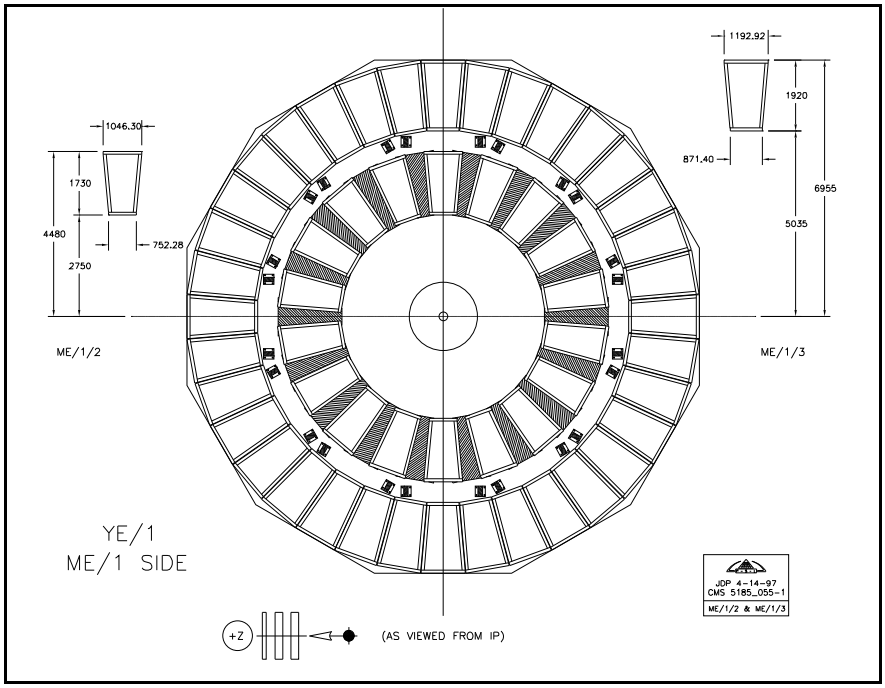


Fig. 4.6.1: Layout of ME1/2 and ME1/3 chambers.

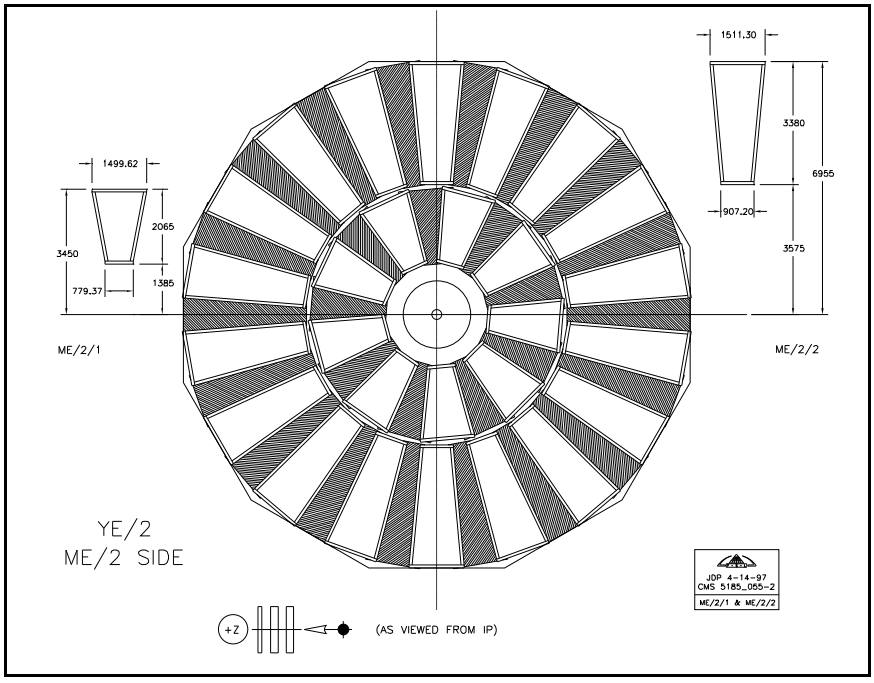


Fig. 4.6.2: Layout of ME2/2 and ME2/3 chambers.

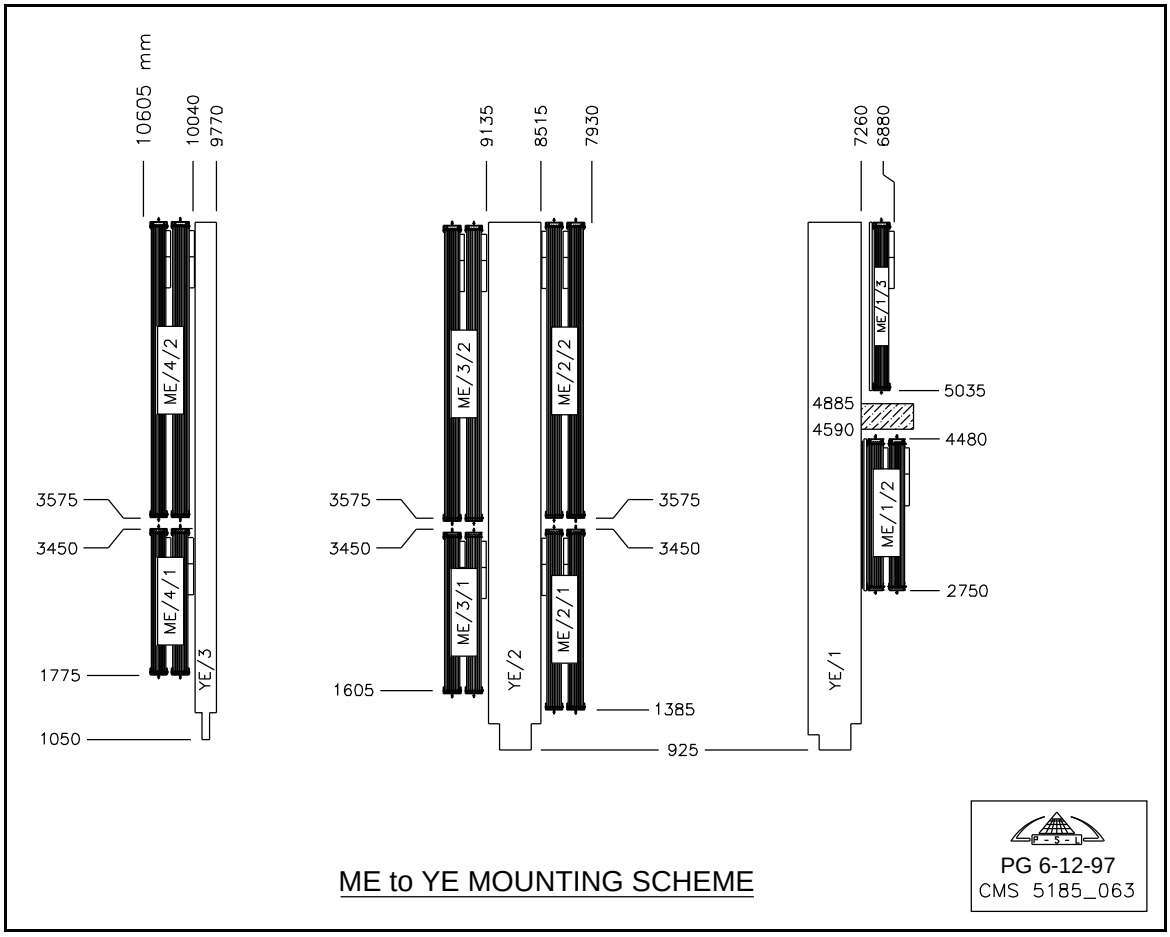


Fig. 4.6.3: An expanded view of the endcap showing where each of the CSC stations is attached to the iron disks.

The mounting tabs are also formed from aluminum extrusions. The top and bottom pieces are identical, and they are bolted over the frame pieces so the tab pieces line up (Fig. 4.6.5). To provide a quasi-kinematic mount, the mounting tab on the inner edge of the trapezoid (narrow side) fixes the chamber in 3D, but allows for rotations. The mounting tab at the left corner of the outer edge (wide side) of a CSC chamber has a slot which allows motion in the R direction but fixes both φ and z locations. The mounting tab at the right outer edge has a large hole which only fixes the z location of the chamber. At each corner of a CSC chamber aluminum blocks are attached to the frame pieces to provide a stable location for threaded holes which can accept rigging hooks.

Measurements made on the full-size 6-layer prototype have confirmed that the chamber with the frame sags less than 1mm and can be handled as a single block.

4.6.1.3 Mounting posts

Mounting posts for the CSC chambers are bolted to the surface of the iron disks as shown in Fig. 4.6.6, which gives both a 3D view of the posts and an axial view of the region between the ring of smaller 20° chambers (ME234/1) and the ring of large 10° chambers (ME234/2). Most of the posts contain both a lower tab (for attaching the inner chambers) and an upper tab (for the outer chambers). However, the posts located at the inner edge of the chambers support either an inner or an outer chamber, but not both.

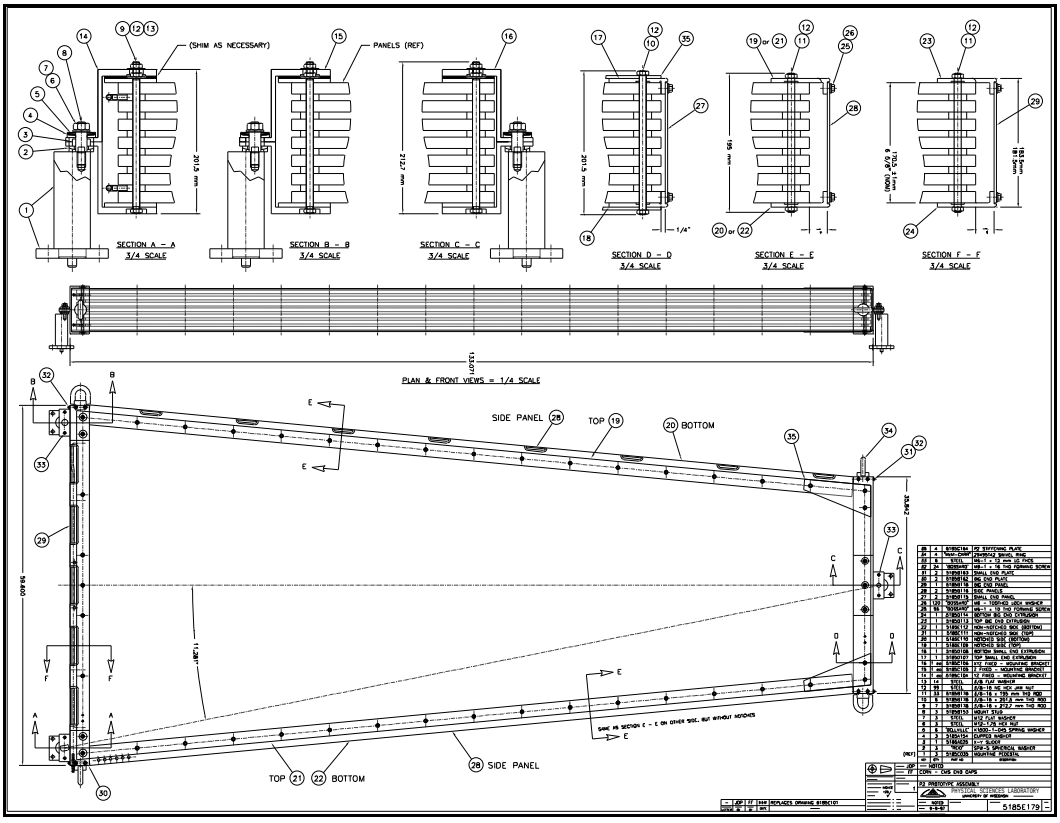


Fig. 4.6.4: Typical CSC with the frame, three mounting tabs (two in the corners of the wide side and one in the middle of the narrow side of the trapezoid) and four swivel rings in the chamber corners.

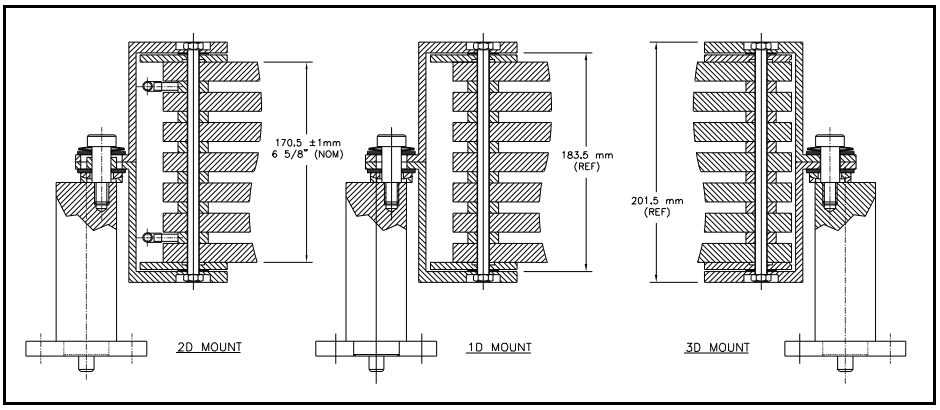


Fig. 4.6.5: Close-up view of all three kinematic mounts.

The diameter of the posts is 60mm, determined from a requirement that the post bend less than 0.5mm if the full weight of the largest CSC (about 300 kg) were carried by one of these posts. Each mounting post has a locating hole in the iron disks plus smaller threaded holes for bolting the posts onto the iron disks. If possible, we will locate and drill these holes during the machining of the yoke pieces. The major concern here is the tolerance which we have on the

assembly of the yoke pieces into a complete disk. If the tolerance for this assembly is not sufficiently good, we will have to drill these holes after the disk assembly has been completed.

At the center of each post is a threaded hole which accepts the photogrammetry reflective targets that will be used to measure the locations of the posts during and after installation. Once the posts have been installed and the alignment targets are fixed on the top of each post we can survey the assembly using photogrammetry and make any required adjustments. The design of mounting posts and tabs described above allows for the required positioning tolerance of ± 2mm on the chamber location.

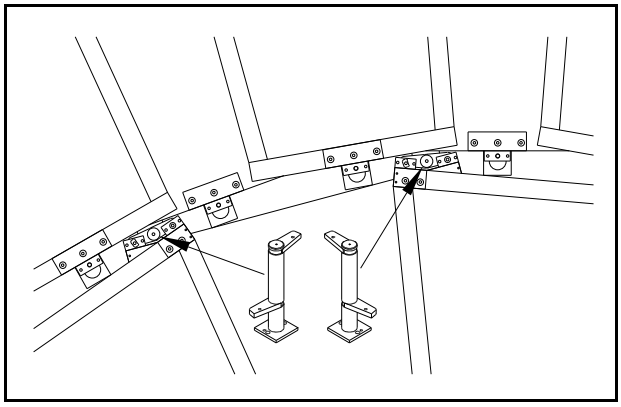


Fig. 4.6.6: Mounting posts are bolted to the face of the iron disk. Each post has welded wings to attach both overlapped CSC chambers.

4.6.1.4 Installation

The chambers are installed one at a time using a small overhead crane (Fig. 4.6.7). The chamber is lifted using the rigging connections at the corners of the frame (see previous section). Once in the air, the angle of the chamber is adjusted and the chamber is bolted into place on the correct posts.

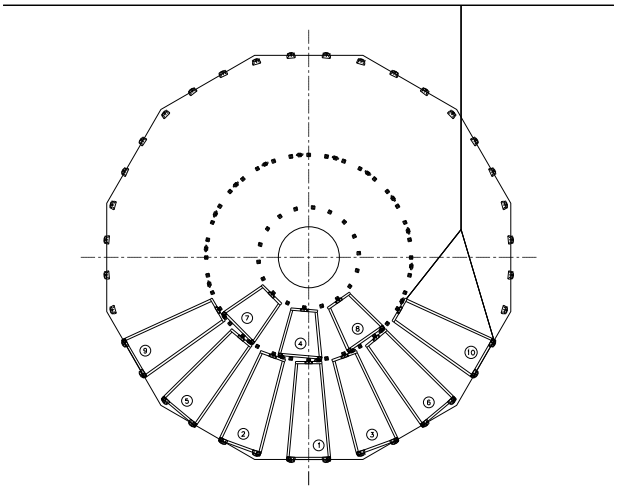


Fig. 4.6.7: Axial view of CSC installation.

4.6.2 ME1/1 chambers

The location of the ME1/1 station in the slot between the HE hadron calorimeter and the return yoke nose, where all cables and services of the endcap detectors pass over the station, implies strict constraints on the design of chamber supports. Also, a non-trivial design of cable trays is required in order to allow for access to the on-chamber electronics. As was mentioned above, the chamber electronics is placed on the chamber surface and covers its full area. Thus, the electronics can be reached only when the endcaps are moved out and a chamber is extracted from the slot.

The baseline layout of passages for endcap cables and services over the ME1/1 station is shown in Fig. 4.6.8. Endcap cables and services are distributed in φ in a thin layer over the SE, EE and HE in order to minimize the gap between endcap and barrel detectors. Then they are bunched at the end of the HE. The ME1/1 chambers are arranged in two disks and the free space between chamber disks is used for the passages of cable bunches. Z-shaped cable trays between the iron nose and the HE flange are mounted and form individual gateways for extraction and installation of each chamber.

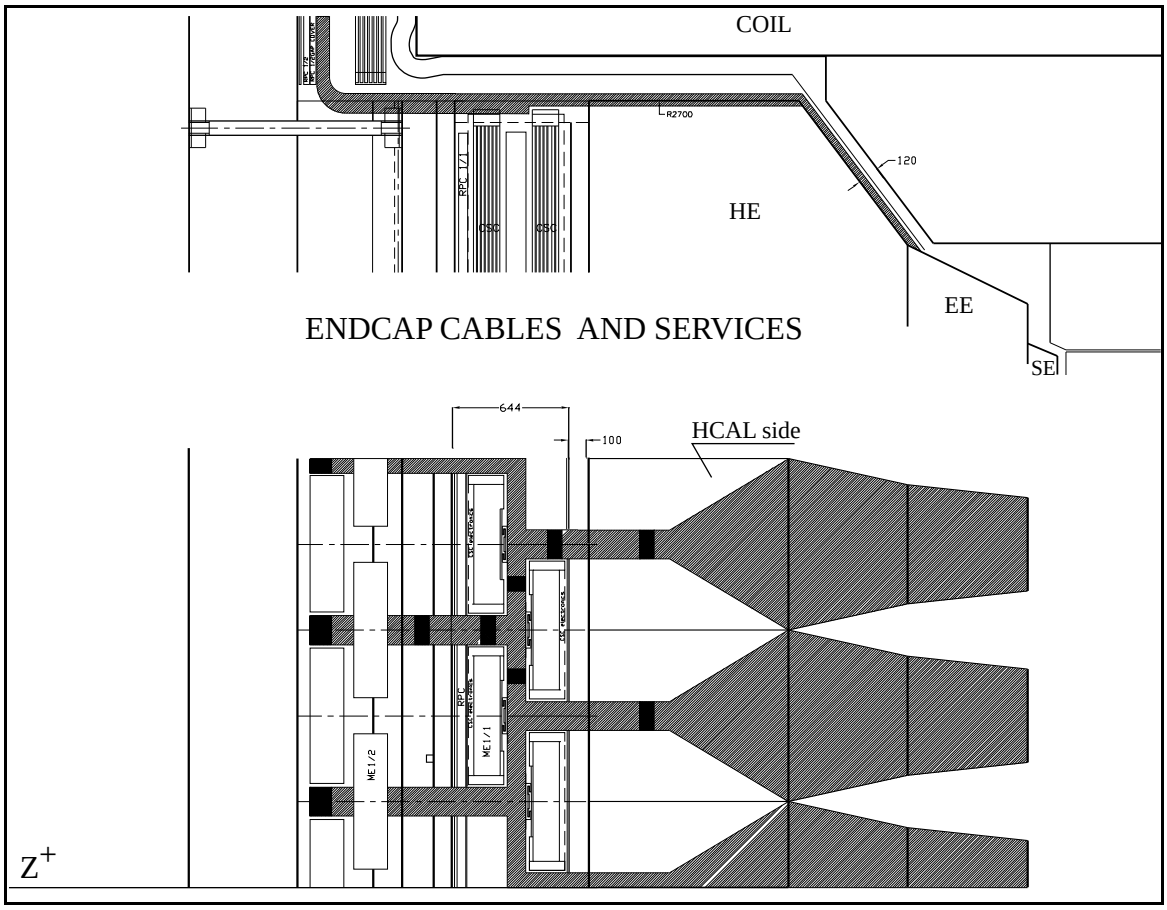


Fig. 4.6.8: Baseline layout of passages for endcap cables and services over the ME1/1 station.

The top view of the ME1/1 station layout in the slot between the HE and the return yoke nose is shown in Fig. 4.6.9. The inner surfaces of the gap are covered with shielding of 20 mm thickness. The RPCs are mounted and installed on the iron nose. A space under the cable trays is used for chamber support. The chamber support system is fixed in the bottom of the slot on the cylindrical tube of the HE suspension system without connection to the HE flange and the iron nose in order to minimize the influence of their mechanical deformations under gravitatonal and magnetic forces. The CSCs will be mounted in a way which can accommodate the mechanical tolerance of the chamber. The rails and mounting devices are installed on the CSC surfaces which are free from electronics.

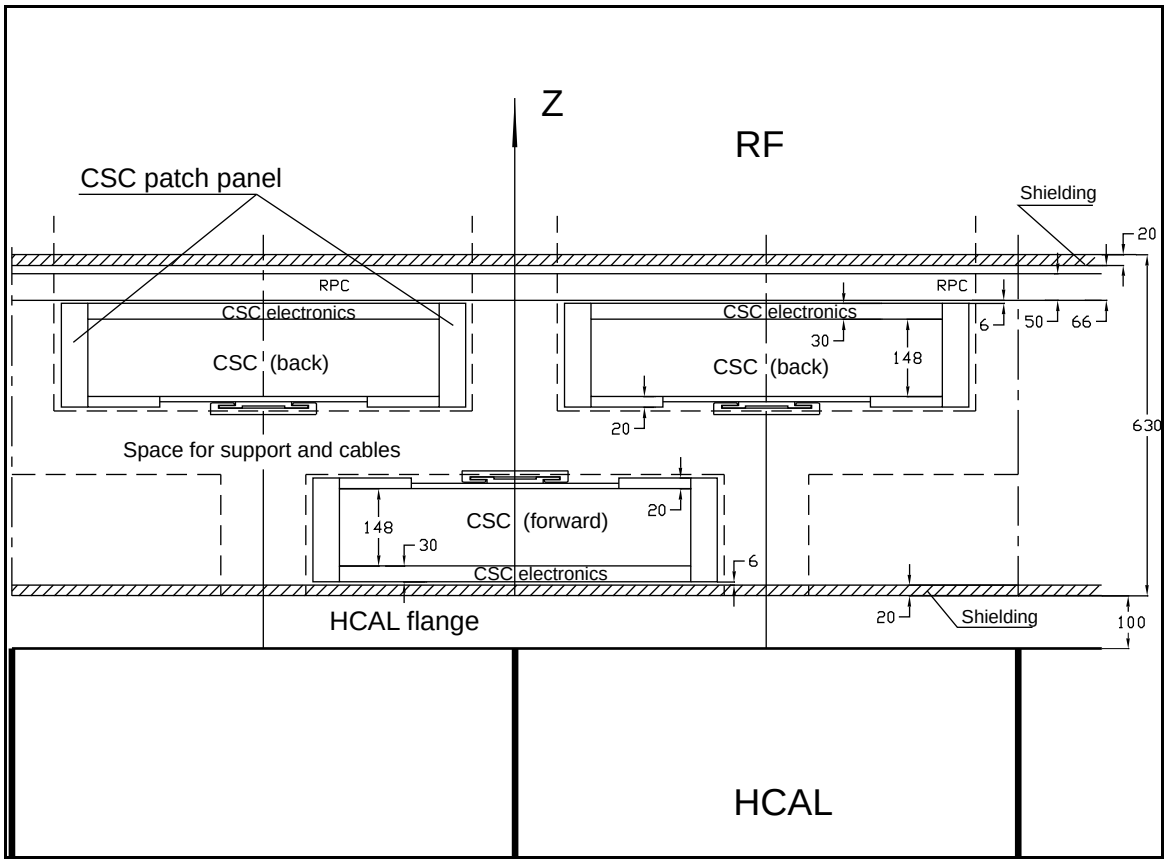


Fig. 4.6.9: The top view of the ME1/1 station layout in a slot between the HE and the nose of the return yoke.

4.6.3 Maintenance

The endcap must be removed for any access to the interior of CMS, which contains all the tracking and calorimetry. Thus most maintenance periods will have the endcaps opened.

In a brief access the endcap is removed. This requires first lowering the 300-ton HF calorimeter down to the floor level and rolling it back into the HF garage. Then the endcap can be rolled back to the garage allowing access to the inner parts of the detector. At this stage there will be good access to chambers ME1/2, ME1/3, ME4/1, and ME4/2. ME1/1 chambers are not readily accessible as they are inserted in the slots between the endcap nose and endcap calorimeter, but they are not blocked by anything else and can be extracted if time permits. If an

access to the chambers in stations 2 and 3 is needed, the iron disks will be decoupled and moved apart. This type of access will require a longer period of time.

The major on-chamber electronics (cathode boards, anode boards, motherboards) are located on the face of each chamber. Electronics maintenance of ME1/1 chambers requires extracting those chambers. One half of the other chambers (outer chambers, i.e. those which are farther from the surface of the iron disks) have electronics immediately accessible without dismounting any of the chambers, while the remaining half is only partly accessible and, to gain an access to these boards, two outer neighboring chambers need to be removed.

4.7 PRODUCTION PLAN

4.7.1 Production overview

There are 540 six-gap chambers to be built for the endcap muon system. To accomplish this task within the given time and budget constraints, one needs to make maximum possible use of resources available at different laboratories and universities. The plan adopted for the CSC production calls for multiple sites as presented in Table 4.7.1. The production interplay between the different sites is as follows.

Table 4.7.1
Production sites for various CSCs to be built for the endcap muon system.
(The total does not include spares.)

Chamber Type	Number	Production Site
ME1/1	72	JINR-Dubna
ME1/2, ME1/3	144	FNAL, IHEP-Beijing
ME2/1, ME3/1, ME4/1	108	FNAL, PNPI-St. Petersburg
ME2/2, ME3/2, ME4/2	216	FNAL, UC, UF

ME1/1 chambers (for design see section 4.3), 72 in total, will be made and tested at the JINR, Dubna site. The production is scheduled to begin in 1999 and finish in 2003.

ME1/23, ME234/1, ME234/2 chambers, 468 in total, the largest ones being about 3.4x1.5 m^2 in size, have a common underlying design (see section 4.2 for details on chamber design and tooling to be used in the production). They will be assembled and tested at five sites: Fermilab, UCLA, UF, PNPI and IHEP. All critical assembly tooling and equipment, as well as testing procedures, are common to all sites. Sub-division of the work between the sites is as follows (for enumeration of stations and their functions see the next sub-section 4.7.2).

All chamber materials and parts are purchased from commercial vendors via one procurement center and undergo quality assurance check upon arrival. Panel milling (Station 1) is done at Fermilab for all the chambers. Then, materials for the ME234/1 and ME1/23 chambers are sent to PNPI and IHEP respectively, where the rest of the chamber production and testing is done. The larger chambers ME234/2 are assembled at Fermilab (Stations 2 through 6) and then sent to the UCLA and UF sites for final assembly and system tests (Station 7). Sites responsible for the tests also carry the primary responsibility for installation and maintenance of the chambers. The tooling, chain of assembly steps, and testing procedures are designed to yield one chamber per three working days at the peak of the chamber production. The production is planned to begin in 1999 and end in mid-2003.

4.7.2 Production stations for ME1/23, ME234/1 and ME234/2 chambers.

1) Panel Production Station:
   - Newly arrived commercially made panels are removed from protective covers and their flatness is certified. Flatness measurements are made on the Axxiom machine.
   - While remaining on the Axxiom machine bed, panels are cut to size and assembly and service holes are drilled.
   - Then the panels are moved to the Gerber machine where strips, signal traces and other details are milled. The quality of strip milling is verified with an automated strip-to-strip capacitance meter.

2) Gluing Station:
   - Gap bars defining the cathode-to-cathode gas gap spacing are glued to the four panels to be called cathode panels (panel 1 has bars on the top face, panels 3 and 5 on both faces, panel 7 on the bottom face). First, double-sided adhesive tape is stretched over the bars (tape covering assembly holes is punched out with a special tool). Then the bars are fixed in their positions along the panel perimeter and the 3-D gluing machine applies a continuous bead of epoxy along the bar-panel corner lines.
   - Insulation strips (long thin guard strips) are glued along the long sides of these four panels.
   - Anode wire fixation bars are glued on both sides of the other three panels, to be called anode panels (panel numbers 2, 4 and 6). Gluing is done under the pressure provided by specially designed clamps. The position of the wire fixation bars is defined by small pins going through the pre-drilled holes in the panels.
   - Short guard strips are glued to both sides of the same panels. No clamping is needed.

3) Wire Winding and Soldering Station:
   - Each anode panel is mounted on a cart. The long panel axis is horizontal and the panel can be rotated around this axis. Full length precision combs are attached along the panel's long sides.
   - Wire is wound directly on the panels at a speed of 5 turns per minute (3h20m per 1000 turns, each turn giving one wire on one panel side and another wire on the other side).
   - After finishing the winding, a continuous bead of epoxy is applied on long pieces of adhesive tape, which are then flipped and placed onto the wire fixation bars across the wires. The panel is left overnight to allow the epoxy to set. (Note that the tape allows the glue to set without contact with humidity in the air, which strengthens the bonding considerably). Next day the tape is easily removed. Now the panel is flipped around, and the operation of gluing the wires is repeated.
   - The panel, still remaining on the same cart, is now placed along side the automated soldering machine which has a Panasonic soldering head mounted on a 1-D linear motor. Wires are soldered at a rate of 3.5 s/joint (1h per 1000 soldering joints). The operation is repeated four times (both ends of the wires, both sides of a panel).
   - Now pairs of wires between HV segments are removed (they were glued, but not soldered); buttons are fixed and glued in the holes between the segments (two or four buttons depending on chamber type); wire segments going around the panel edges are cut; and the combs are removed.
   - Wire tension and wire spacing are checked selectively.

4) Pre-Assembly Station:
   - At this stage the following chamber elements are fixed and soldered: blocking capacitors; HV boards; protection boards with anode connectors; cathode connectors.
   - HV is applied to verify the quality of the wiring. An automated capacitance measuring device is used to make sure that all connectors are properly connected to strips and wire groups.

5) Assembly Station:
   - By this stage of production all seven panels are ready for stacking to form a six-gap chamber. Before stacking all panels are cleaned on both sides with an ionized air jet. Alignment is defined by two pins on opposite sides of the panels going through alignment holes. One of them is a round hole of a diameter just slightly larger than a pin. The other one is actually a slot aligning relative rotation between panels. Assembly bolts are larger than the bolts and do not determine the alignment.
   - O-rings are inserted in counterbores in the gap bars, and all panels are stacked together. Extruded Al bars are placed along the chamber perimeter on both sides. Tie-rods going through buttons and assembly bolts along the chamber perimeter are tightened.
   - One more quick HV test is done. Then continuous beads of RTV are applied along the perimeter of all six gaps to seal the chamber. The chamber is allowed to stand overnight.
   - The next day gas tightness is checked with a specially designed leak detector with a sensitivity of 0.1 cc/min at 1 cm over-pressure. By making use of alignment marks milled on the panels at the same time as the strips and extending to the edge of panels, one measures relative plane shifts, if any.
   - HV connectors and fixtures are attached and HV wiring is done.

6) HV Training Station:
   - At this stage gas is flushed through the chamber and the HV is slowly raised. A HV of 300 V above the operating point must be reached without drawing significant current ($<0.5\ \mu A$). The chamber is expected to be conditioned under this HV for about one day.

7) Final Assembly and System Tests Station:
   - External elements of the chamber are attached at this stage. Among them are cooling pads and plumbing, cathode electronics, anode electronics, motherboard, electronics enclosures, inter-cabling of all electronics elements, temperature and pressure sensors.
   - The operation of the chamber-plus-electronics system is tested, tuned and calibrated as necessary. The list of tests includes:
     - disentangling connection mix-ups, misconnections, dead channels, etc.
     - fixing noisy channels (either chamber or electronics problems);
     - verification of low noise operation of the system (proper grounding and shielding);
     - on-chamber calibration of cathode electronics;
     - on-chamber calibration of anode electronics; tuning of delays for proper Bx-tagging;
     - testing the LCT trigger performance with test pulses;

- testing the full system performance in cosmic rays (resolution, trigger, efficiency).

4.7.3 Production of ME1/1 chambers

The quality of all chamber materials and parts purchased from commercial firms is checked on arrival.

1) Chamber Mechanical Assembly
   - Strip electrodes are made on copper- clad FR4 sheet material with the required precision using a diamond disk. The quality of the strip electrodes is verified by an optical technique.
   - Flatness and overall dimensions of the 'honeycomb-like' panels are checked by an optical measuring device.
   - Standard CSC jigs are designed for precise assembly of the modules. Reference and other service holes are drilled in the panels using these jigs.
   - Anode PC-boards with wire fixation artwork are glued on a common bar and are sanded to the required thickness. Anode bars with PC-boards are glued to the panel with the smooth cathode. Position of the bars are defined by the jig. The cathode-cathode gap is defined by precise spacers.
   - The panels are cleaned and stored in a clean storage area.

2) Wire Plane Assembly
   - A wire plane is produced with the required wire tension by the wire tensioning machine.
   - Wires are soldered on the transfer frames with precision combs. Wire tension is kept within the limits 80 ± 5 g.
   - Transfer frames are fixed on the anode bars using precision combs and adjusting devices. Wires are soldered and then glued.
   - Wires tension is checked.

3) Chamber Pre-Assembly
   - At this stage all resistors, blocking capacitors, anode and cathode connectors, etc. are fixed and soldered
   - All electrical connections to strips and wire groups are checked.
   - Wires, strips and chamber gas volume are cleaned.

4) Chamber Assembly
   - At this stage of production all seven panels are ready for stacking to form the six-gap chamber. Seals and gas outlets are installed.
   - Patch panels with HV and LV connectors are attached.
   - All panels are stacked together and tightened down.
   - Gas flow is turned on. CSC gas leakage is checked.
   - HV dark current is checked.
   - Noisy channels are found usng the anode and cathode read-out electronics and fixed.
   - The chamber is trained under HV until the dark current is less than 0.1 μA at 3000 volts.

5) Final Assembly and Test Operations
   - are similar to those described in subsection 4.7.2.

4.8 CHAMBER PERFORMANCE: CHAMBER TEST RESULTS

Before discussing the chamber R&D results, it is appropriate to list briefly the CMS CSC prototypes along with the major tasks addressed in their construction and tests. The Dubna-line chambers were designed with the goal of converging on the final ME1/1 chamber to operate in a very difficult environment (high rates, large B-field). The US-line prototypes were addressing the challenges of designing the very large CSCs to be produced in mass quantities (some of them will operate in difficult environments as well). The most important performance results will follow this short introduction.

Dubna P0 prototype (September - November 1993)

This is a small four layer prototype with $0.5\times0.5 m^2$ dimensions, 2.5 mm anode-cathode gap, 2.5 mm wire spacing, 30 μm wire diameter and 5.08 mm cathode readout pitch. It was instrumented with electronics designed at Dubna. The P0 prototype design incorporated the know-how gained in testing two previous chambers: two-layer 1.5×1 m^2 and four-layer 3×0.3 m^2 prototypes with 2.5 mm and 4 mm anode-cathode gap, respectively. It was tested at the RD5 high energy muon beam at CERN and demonstrated position resolution of 50 μm with a good uniformity across the strips. The Lorentz angle dependence on the magnetic field up to 3 Tesla parallel to the strips was measured in the RD5 magnet with cosmic rays. Results obtained with the prototype can be found elsewhere [4.26].

Dubna P1 prototype (May 1994)

Based on the P0 results, a new P1 prototype, the first of a new generation of large size ME1/1 prototypes with six layers and radial strips, was constructed. The chamber was instrumented with cathode electronics based on the analog signal processor, GASPLEX, designed at CERN. The P1 prototype with anode wires orthogonal to the central strip was tested in a 200 GeV muon beam in the absence of magnetic field. The spatial resolution for muons at normal incidence was 50 μm. Analysis details can be found elsewhere [4.27].

Dubna P2 prototype (May 1994, April 1995, Integrated Test in June 1995)

The P2 prototype was tested in a 3 Tesla magnetic field with horizontal cosmic rays. The anode wires were rotated by 24.8° with respect to the central strip to compensate for the effect of the magnetic field. An average spatial resolution over the full sensitive chamber area of 63 μm was obtained with the cathode plane perpendicular to the field.

One year later, in April 1995, this prototype was fully instrumented with GASPLEX cathode electronics and new LABEN anode front-end Dubna-designed electronics. Precise timing and spatial resolution were simultaneously measured in a high energy beam. Studies of the Lorentz angle in an axial magnetic field parallel to the muon beam were performed.

CSC performance in conditions close to those expected in the CMS detector were studied in the Integrated Test. The endcap configuration prototypes of the preshower, PWO crystal electromagnetic calorimeter, hadron calorimeter and ME1/1 (P2) were mounted in the RD5 magnet with the magnetic field parallel to the beam. The chamber performance in the presence of the electromagnetic secondaries associated with high energy muons passing through the upstream material of the calorimeters was studied, namely: spatial resolution, chamber capability to tag the right bunch crossing, and spatial resolution achievable at the level-one trigger with different fast algorithms for finding local charged tracks. A variety of results can be found elsewhere [4.28].

Dubna X-ray prototype (summer 1996)

A small prototype, similar to P0, was constructed to study the effects of high rates on CSC performance [4.29]. One layer was irradiated by 8 keV X-rays through a thin window with a background rate of up to 500 kHz/strip while the other three layers were used for track reconstruction of the cosmic rays. Although GASPLEX electronics, being too slow, is not appropriate for high rate tests, the results nevertheless gave us the first insights into the problems associated with a high rate environment (spatial resolution deterioration, efficiency of the LCT finding algorithms and their accuracy). This was important for the optimization of new prototypes of the cathode front-end ASICs designed in Minsk for the Dubna P3 prototype.

Dubna P3 Prototype (December 1996)

The P3 prototype represents a six-layer full-scale CSC of a 10° sector of the ME1/1 muon station. For the summer 1997 beam tests, P3 was instrumented with new cathode strip front-end electronics based on the 16-channel Minsk ASICs. It was tested at the H2 beam at CERN in the presence of both axial and radial components of the magnetic field and high beam intensity up to 500 kHz/strip. Another test was performed at the CERN Gamma Irradiation Facility, GIF, under a very high gamma background up to 2×10^6 γ/cm^2s. The tests demonstrated efficient and precise track reconstruction and bunch-crossing identification with the new front-end electronics at background rates corresponding to LHC conditions. Preliminary results have been summarized elsewhere [4.30].

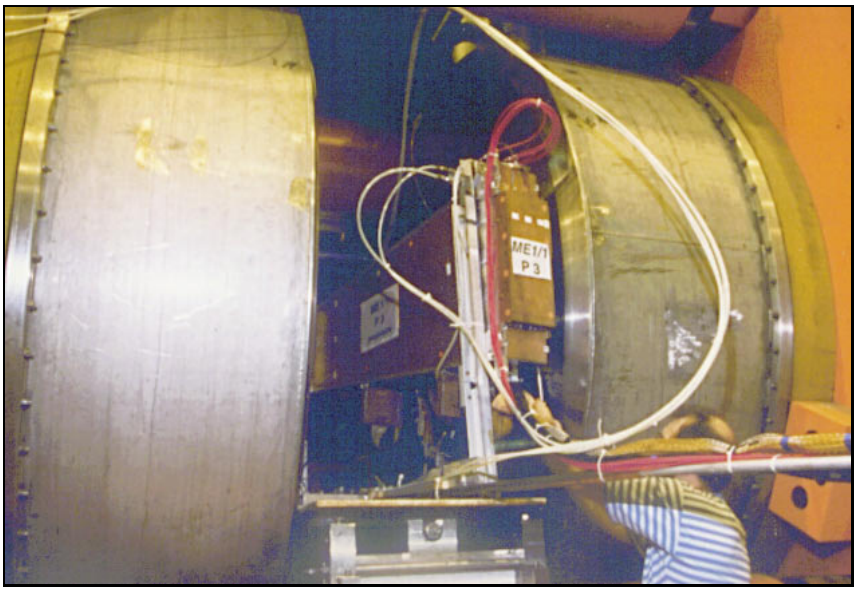


Fig. 4.8.1: The Dubna P3 prototype installed in the 3 tesla magnet at the CERN H2 beam line.

Dubna P4 Prototype (December 1997)

This is a preseries sample of the ME1/1 chambers to be fabricated in Dubna by the end of 1997 [4.31]. Essential tooling being designed for the mass-production of these chambers will be used in the P4 construction.

US T0 prototype (December 1994)

The major goal of this prototype was to optimize chamber design from an engineering standpoint, i.e. to make it simple, reliable and cost-effective, both in terms of material and labor. It was a 0.7×1.44 m^2 two-layer chamber. We tested wire groups of full length and width envisioned for the largest chambers in the endcap muon system, and wires obtained from different vendors. Very importantly, we verified the operational reliability of planes with milled cathode strips (one plane had strips, another did not). This is the only cost effective scheme for producing the large chambers in mass quantities. The chamber showed very reliable basic performance [4.32].

US P0 (summer 1995)

The P0 prototype was a 0.6×0.6 m^2 six-plane chamber, with 9.5 mm full gas gap (h=4.76 mm for the anode-cathode gap), and 30 μm wires spaced 2.5 mm apart. The design of this chamber was driven by the effort to minimize the future costs of building the large system of CSCs. To reduce tolerances on panel flatness and to allow for wider strips we built a chamber with a large gas gap and unconventionally wide strips (w/h~3.4, while the usual ratio is between 1 and 2). Our simulations showed that, while resolution was expected to vary substantially across a strip, the six-plane chamber with half-strip staggering between planes should have an adequately good overall spatial resolution. The beam tests in the RD5 area at CERN confirmed that about 50 μm resolution (per six-plane chamber) is indeed attainable in a chamber of this design [4.33]. Timing efficiency for the large gas gap was also found to be quite adequate.

US T1A and T1B prototypes (1995)

Again, these two prototypes were built to test a set of new engineering solutions. With the previous T0 prototype, they both were 0.7×1.44 m^2 two-layer chambers. The T1-prototypes were made of commercially fabricated panels - a very important breakthrough in the design. Also, they had gap frames of a new design, not requiring expensive milling. To enhance future chamber reliability, we decided to use wires of 50 μm in diameter and spaced at about 3.2 mm. The design for segmenting a plane of wires into HV-independent parts so that one could turn off a part of a plane without affecting the rest of the wires was implemented in these prototypes. Insulating guard strips were also tested on these prototypes. The optimal scheme of grounding and shielding has emerged from the studies with these prototypes. The very good results obtained with the T1s made them the basis for the rest of the US-line chambers [4.34].

US P1A prototype (February 1996)

This prototype was almost the size of the largest CMS chamber, but had only two gaps. It was made as a trial run before building the large scale prototype P1. Commercial shipping survival has also been verified. (Accelerations in excess of 10g were detected.) Results [4.35] showed that the design was free of flaws and allowed us to quickly proceed with construction of the full scale P1 prototype in the same year.

US P0' (summer 1996) prototype

From outside, the P0' prototype looked like the US P0 chamber, i.e. it was a 0.6×0.6 m^2 six-plane chamber, with 9.5 mm full gas gap. However, the strip pitch was now 6.4 mm - the

narrowest strip in chambers of the Endcap, other than ME1/1. Also, reflecting the evolution of the chamber design optimization process, the wires were now 50 μm in diameter and spaced 3.4 mm apart. This time during the muon beam tests at RD5, we made use of the Si beam telescope detectors to do detailed trigger studies (both on strip and wire sides). Half-strip comparator electronics was tested on this prototype (92% probability to detect correct half-strips, 99% probability to find valid half-strip based LCTs, spatial resolution for LCTs thus found was measured to be 0.11×w). Timing behavior of the detector with much larger wire spacing was of special interest in these tests (99.5% probability of finding valid wire group based LCTs with >98% probability of correct bunch tagging). Spatial resolution with the narrow strips was expected to be good and uniform across a strip (60 μm per plane as measured). All the results confirmed the right choice of the basic chamber design parameters [4.33].

US P1 prototype (October 1996)

This prototype of 3.3 m length and 1.2 m width and with all six planes in place represents the largest CMS Cathode Strip Chamber. Its width is somewhat smaller than the full width of the largest planned chamber (1.5 m) as the panel material of the full width is available from the manufacturer only in substantial quantities. All engineering and design solutions as envisioned for the final chambers have been implemented in this prototype. A picture of the prototype is shown in Fig. 4.8.2. Its performance is being thoroughly tested during this (1997) year with cosmic rays. The chamber has an operational plateau where it meets all the required specifications on spatial (150 μm resolution per chamber) and timing (92% correct bunch tagging efficiency) performance from 4.0 to 4.5 kV, 4.1 kV being defined as the nominal operational point for this gas [4.36]. It has been constantly under HV since November of 1996 and has not shown any problems.

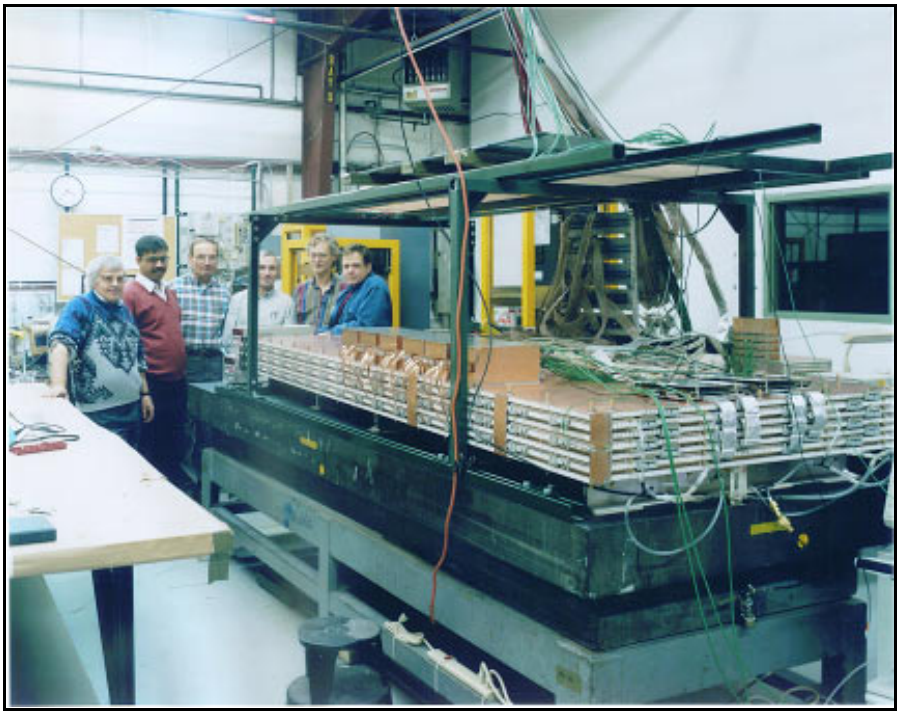


Fig. 4.8.2: A photograph of the US P1 prototype.

US P2 prototype (December 1997)

This is exactly the full scale chamber (3.3×1.5 m^2) and will be assembled by the end of this year [4.37]. Its design is essentially final. It will be instrumented with prototype electronics and will be tested in the high rate background environment at the GIF at CERN in the summer of 1998.

4.8.1 Operating point and overall performance

The high voltage at which the total cathode charge in a cluster of strip signals equals 100 fC is defined as the *nominal operating point*. The induced cathode charge depends on the total charge released in an avalanche, the ion drift velocity, the front-end electronics shaping time, and the charge fraction induced on one cathode plane. The detailed analysis of these processes can be found elsewhere. Results presented in this section show that all CMS CSC performance requirements are met at this operating point.

Fig. 4.8.3 shows the cathode charge (Landau peak) as a function of HV for the US P1 large prototype. One can see that the nominal operating point (100 fC at about 4.1 kV) is well below the maximum voltage HV_{max}=4.5 kV (at 4.6 kV we observed excessive dark currents and the operation became unstable). Gas gain variations within a plane of all the large prototypes were measured to be within a factor of 2 (Fig. 4.8.4), which meets our requirements.

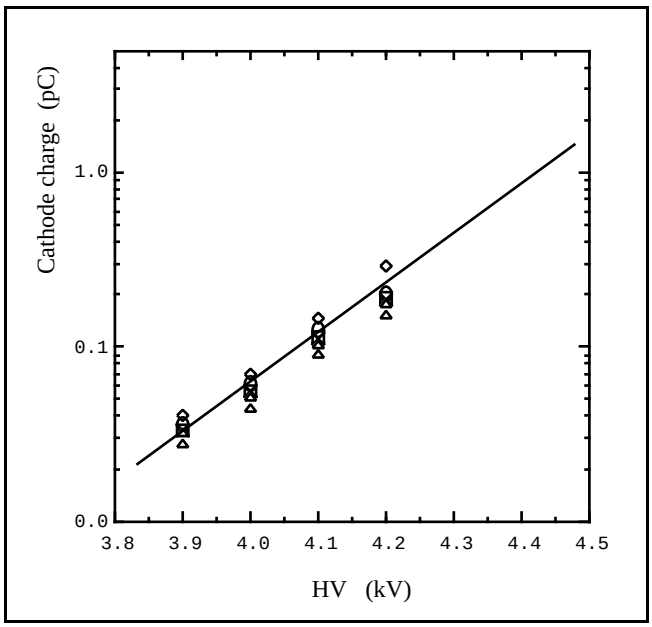


Fig. 4.8.3: Cathode charge vs. high voltage for the US P1 prototype. The nominal operating point is defined to be $Q_{cathode}$=100 fC. The maximum HV at which the chamber operated without abnormalities was 4.5 kV. (Cathode electronics saturated at 200 fC (~4.2kV) - thus the line is drawn only to guide the eye).

Fig. 4.8.5 shows single plane strip and wire efficiencies. To determine the efficiency, muon track coordinates were reconstructed in two dimensions making use of Si microstrip detectors in the muon beam (US P0' prototype). Strip hits were counted if the predicted strip or

either of its neighbors had a charge above 6 fC, while wire hits were counted if the predicted wire group or the nearest neighboring wire group had been hit within a 100 ns wide window. One can see that the prototype was at its full efficiency at the nominal operating point (100 fC cathode charge).

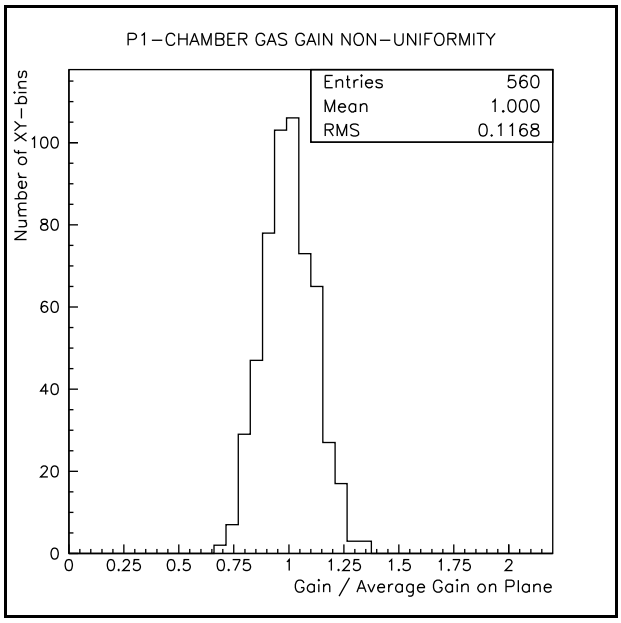


Fig. 4.8.4: Spread of gas gains over the area of all six planes. The data are for the large US P1 prototype (3.3×1.2 m^2) and explicitly show that the goal of keeping gas gain variations in a chamber plane within a factor of two is achieved.

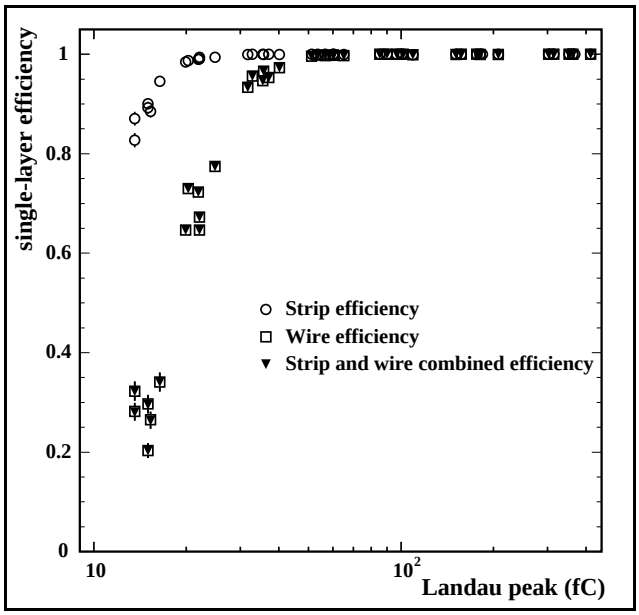


Fig. 4.8.5: Cathode and wire channel efficiencies vs. charge measured on the cathode plane (see text for definitions). Combined efficiency represents events when both anode and cathode signals are present. The chamber is at its full efficiency at the nominal operating point (100 fC cathode charge). The data are obtained in the muon beam for the US P0' prototype.

Another important consideration in designing large chambers with many channels of very sensitive and fast electronics is the issue of pick-up noise and oscillations. We have put a good deal of effort into laying out proper grounding for the readout electronics and HV power supplies, as well as in devising a scheme of HV filtering and overall shielding (for details see section 4.3). As a result, the large prototypes showed no excessive noise or instabilities from the very first turn-on.

4.8.2 Strips

As was mentioned in Section 4.1, the precision muon coordinate comes from fitting strip charges. Two chambers, ME1/1 and ME1/2, are required to have 75 μm resolution, while the other chambers must provide 150 μm resolution (numbers refer to the full 6-plane package).

4.8.2.1 Stand alone chamber resolution

Spatial resolution results for precise chamber prototypes (ME1/1 and ME1/2) are presented in Figs. 4.8.6 and 4.8.7. Fig. 4.8.6 shows residuals (per plane) as measured with the Dubna P1 prototype operated at the nominal HV. One can see that, given this per-plane resolution, a six-plane chamber will meet the spatial resolution requirement with a good margin, which is needed to accommodate other contributions to the resolution: misalignment, track inclination, non-perpendicularity of strips and wires, B-field non-uniformity, etc. The bottom part of a ME1/2 chamber was represented by the US P0' prototype: its per-plane spatial resolution (sigma of a Gaussian fit) vs. HV is presented in Fig. 4.8.7. Again, adequate performance is achieved at the nominal point. In the same data sample, we specially investigated the residual tails and found that about 5% of hits per plane were significantly (>3σ) compromised, which is acceptable.

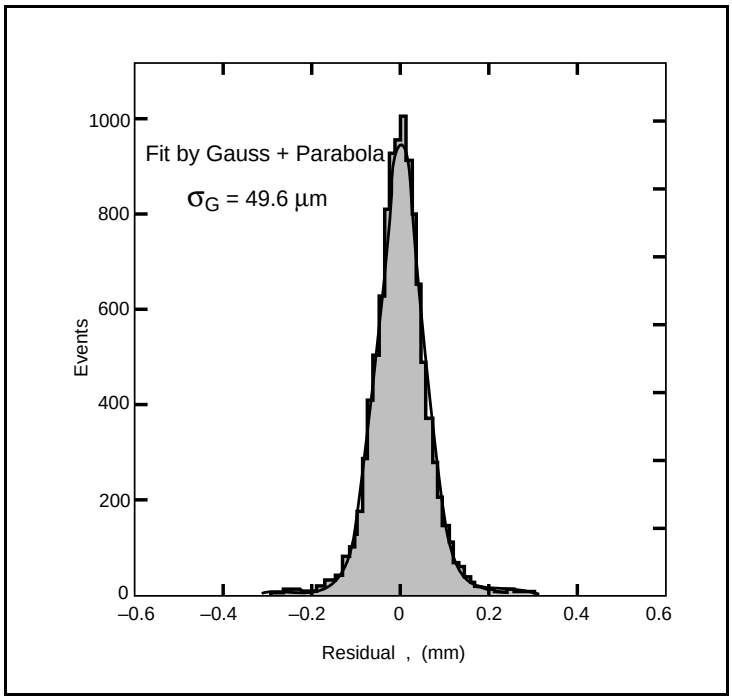


Fig. 4.8.6: Single plane resolution of the Dubna P1 chamber prototype as measured in the muon beam tests at normal incidence for muons.

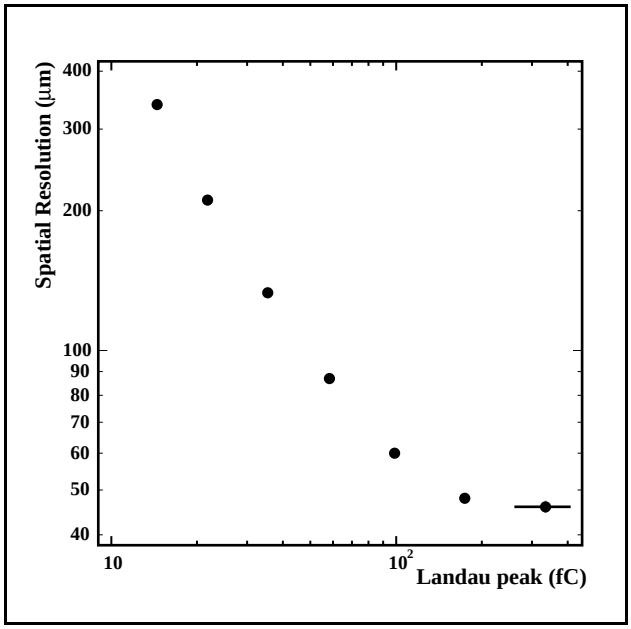


Fig. 4.8.7: Single plane resolution of the US P0' prototype, representing a part of the ME1/2 chamber vs. $Q_{cathode}$.

The rest of the chambers will have much wider strips, and the US P0 prototype was made to represent the widest (16 mm) strips of the ME234/2 chambers. With strips this wide, the spatial resolution depends on the hit position across a strip: it is worst when the hit occurs at the center of a strip since there is almost no charge sharing, while on the contrary it is very good between strips. Resolutions at different hit positions across a strip, presented in Fig. 4.8.8, show this effect explicitly.

To compensate for this effect, odd and even chamber planes are staggered by half a strip width, which ensures that 3 out of 6 hits will be in the area of very good spatial resolution. By taking the individual plane residuals as measured in the beam tests (i.e., including shape of the distribution core and its tails), we can simulate the overall six-plane chamber resolution, which turns out to be better than 50 μm. This strategy of using wide and staggered strips obviously allowed us to reduce the number of strip channels.

The largest chamber prototype (US P1) is currently being tested in cosmic rays. Preliminary results obtained with this prototype are shown in Fig. 4.8.9. The P1 data includes all contributions of multiple scattering of soft cosmic ray particles, effects of track inclination and non-perpendicularity of strips and wires, etc. It should be pointed out that the default geometry as of the P1-drawings have been used in the analysis and no local adjustments (except for global plane shifts) have been done. Given this resolution per plane and taking into account staggering, the overall expected spatial resolution for the six-plane chamber is expected to be about 80 μm, i.e. safely better than the required 150 μm. Further and more detailed data analysis is in progress.

For tracks which are inclined with respect to wires, the primary ionization spreads along a wire. Primary ionization fluctuations (spatial spread of cluster as well as number of electrons per cluster) and the gas gain fluctuations result in variations of the induced charge shape. As the result, the CSC resolution worsens. This has been studied experimentally and the results are shown in Fig. 4.8.10, where it can be seen that the scale of the deterioration is tolerable.

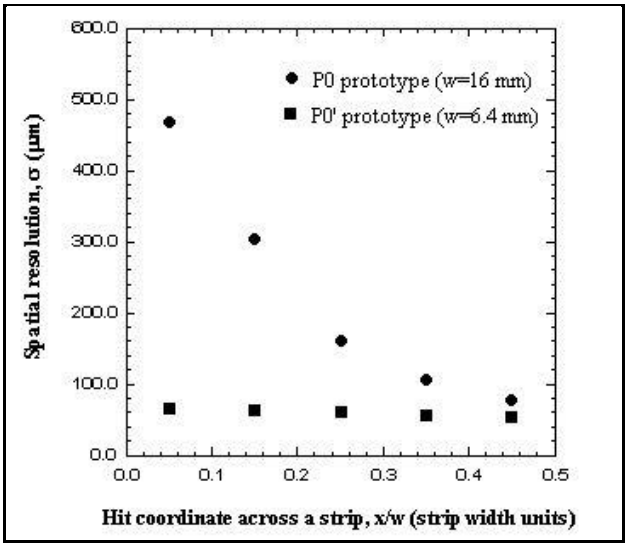


Fig. 4.8.8: Single plane spatial resolution of a CSC with 16 mm wide strips (US P0 prototype) and with 6.4 mm wide strips (US P0' prototype) vs. track position across a strip, x/w, i.e. in units of strip width. The resolution is best for tracks going between strips. A drastic dependence of the resolution on x/w is obvious for very wide strips. (Data obtained in the muon beam.)

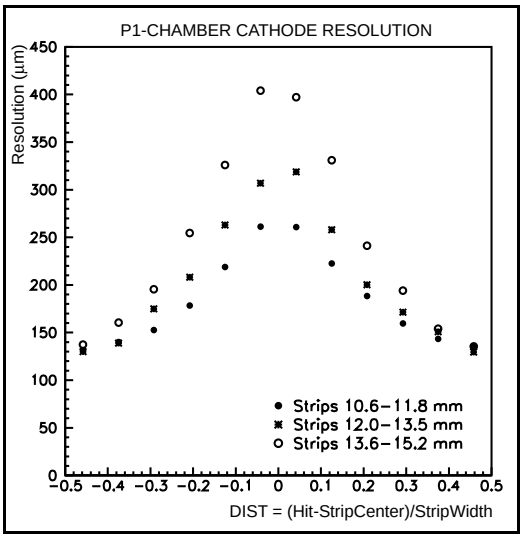


Fig. 4.8.9: Single plane spatial resolution of the largest CSC prototype (US P1), as measured with cosmic rays. Given this resolution per plane and taking into account staggering, the overall spatial resolution for the six-plane chamber is expected to be around 80 μm, i.e. safely better than the required 150 μm.

Another subtle effect comes from the fact that strips, being radial, are not always perpendicular to wires. Ionization electrons drift perpendicular to the wires and therefore will produce avalanches which can be shifted with respect to the strip coordinate system. This contribution cannot exceed 90 μm per plane for 20° chambers. In fact, track inclinations in θ-angle of muons make this contribution even smaller. Thus, at the scale of our requirements, this contribution is insignificant.

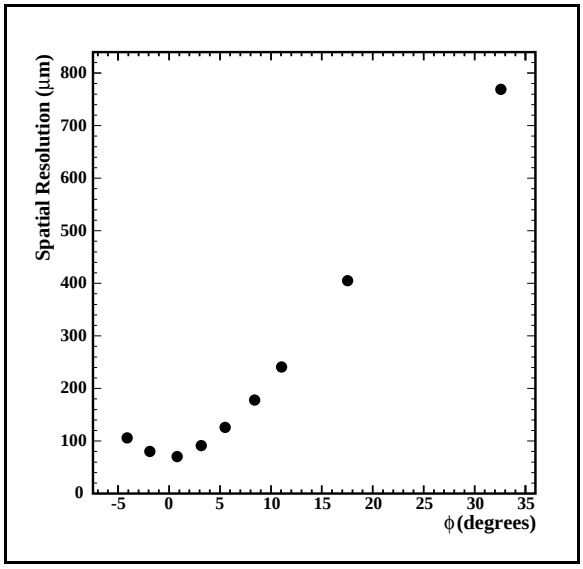


Fig. 4.8.10: Deterioration of the spatial resolution vs. track inclination with respect to the wires. The range of ϕ-angles in the EMU CSCs due to their size and placement is less than $\pm 5°$ (or $\pm 6°$ for muons with p_T >30 GeV), meaning that the resolution deterioration due to track inclinations is not significant. (Data obtained with the US P0' prototype in the muon beam.)

4.8.2.2 Chamber in a magnetic field

As was pointed out earlier, the ME1/1 and ME1/2 chambers have to operate in substantial magnetic fields. The presence of a B-field (both B_z and B_r components) results in skewed drift of electrons towards the wires.

The radial component of the B-field, being as large as about 1 T in the ME1/2 chambers, substantially affects their spatial resolution. The mechanism is shown schematically in Fig. 4.8.11. The spread of ionization clusters along the wires is very much similar to that occurring when tracks have inclinations in ϕ-angle. This effect can be compensated only by chamber rotation abuot the radial axis which clearly would make the system very awkward. Thus, the chamber resolution is inevitably deteriorated, but still remains within the required one (75 μm per chamber, or approximately 150 μm per plane).

The observation that B_r has the same effect on the resolution as that due to track inclinations allowed us to measure the Lorentz angle in the RD5 magnet with cosmic rays. Fig. 4.8.12 presents the data taken with the Dubna P0 prototype in this field configuration. The Lorentz angle as measured for several values of the radial field has an obvious linear dependence on the field (see Fig. 4.8.12 inset).

The effect of the z-component of the field is very strong for the ME1/1 chambers (the field is as large as 3 T in these CSCs). Fig. 4.8.13 illustrates the effect of the z-component of the B-field (i.e. field normal to the chamber). When electrons drift towards the plane of the wires, i.e. along the B_z-field, they do not experience any deflection. However, when they turn to drift in the radial direction toward one or another wire, they shift towards left or right, the amount and sign of the shift depending on where between wires the ionization has been deposited (the maximum shift can be estimated as $\pm s/2 \cdot \tan\alpha_L$, where s is the wire spacing and α_L is the Lorentz angle). From the same figure, one can immediately see that tilting the wires at

the Lorentz angle eliminates the spread of ionization across the strips. Direct measurements with prototypes in a magnetic field show these effects explicitly.

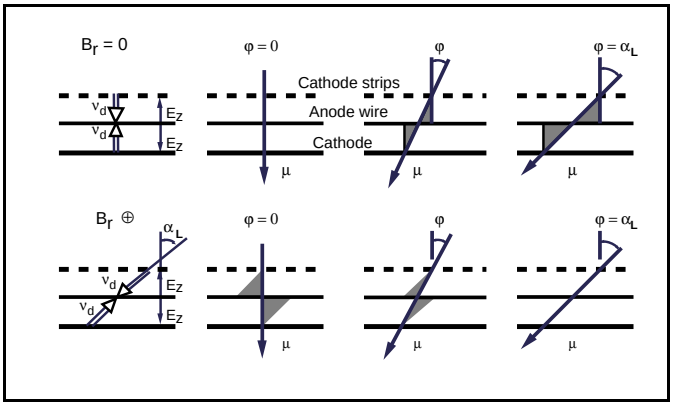


Fig. 4.8.11: Different clusters of the primary ionization in the presence of a B-field going along the strips (radial component of the CMS EMU field) drift to different places along the chamber wires. Thus, the effect of this cluster spreading is similar to the effect of track inclinations in ϕ-angle.

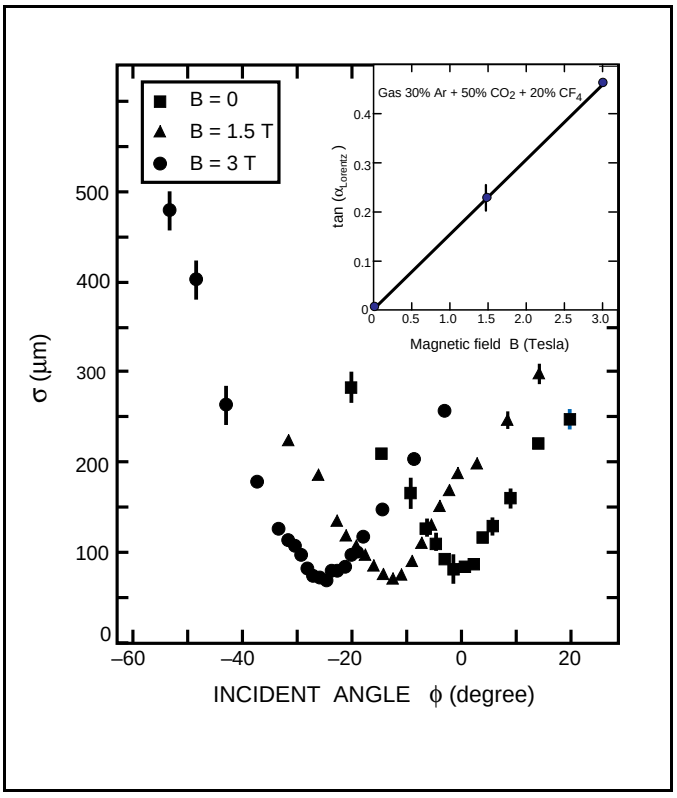


Fig. 4.8.12: Chamber resolution deterioration due to the B_r-field vs. track inclinations as measured with the Dubna P0 prototype. The position of the minimum for each field value corresponds to the Lorentz angle. The inset shows the linear variation of $\tan\alpha_L$ with the magnetic field.

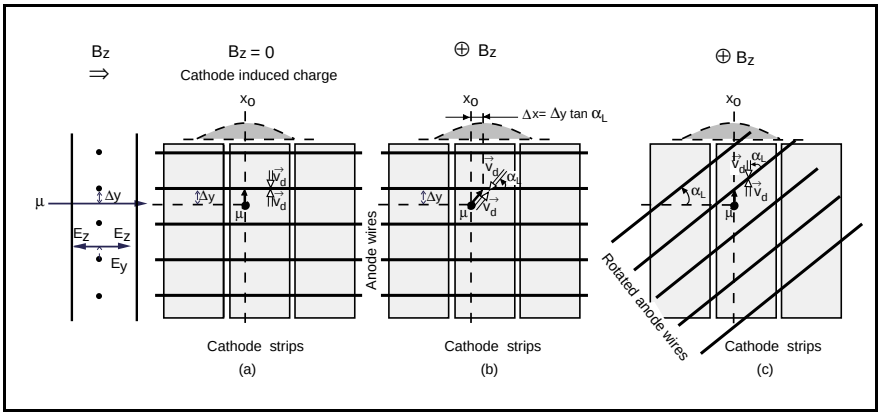


Fig. 4.8.13: Z-component of the B-field (i.e. field normal to the chamber in the CMS Endcap System) causes ionization clusters to spread along the chamber wires, which results in chamber spatial resolution deterioration. The effect can be compensated by rotating the wires at the corresponding Lorentz angle.

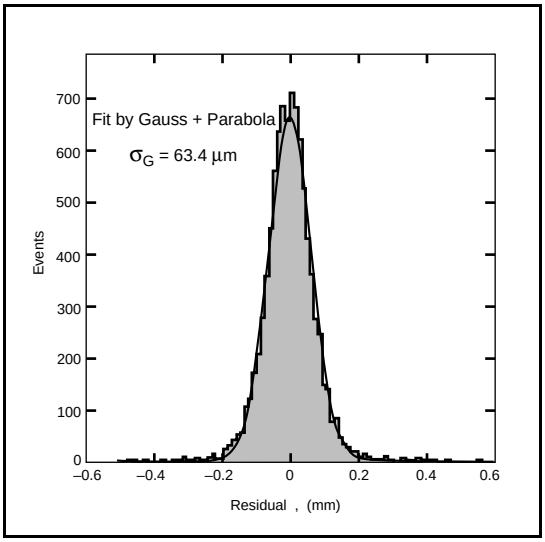


Fig. 4.8.14: By rotating the wires with respect to the strips, one can compensate for the Lorentz angle effect. The beam test results with Dubna P2 prototype confirm this explicitly.

Fig. 4.8.14 shows test results obtained in a magnetic field with the Dubna P2 prototype which had a proper wire tilt chosen from the previous Lorentz angle measurements. Clearly, the chamber resolution is almost completely restored. An average spatial resolution of 63 μm over the full sensitive chamber area was obtained.

However, due to the difference in the average electric field values between the wires and the rest of the gas volume, the Lorentz angle for the B-field oriented parallel to the strips is different from the one for the field normal to the chamber plane. Further beam tests with the same prototype in the endcap orientation of the magnetic field confirmed this observation. Fig. 4.8.15 shows deterioration of the spatial resolution with B_z-field. The resolution minimum occurs at the field such that the Lorentz angle corresponding to this field is the same as the wire tilt angle in this prototype.

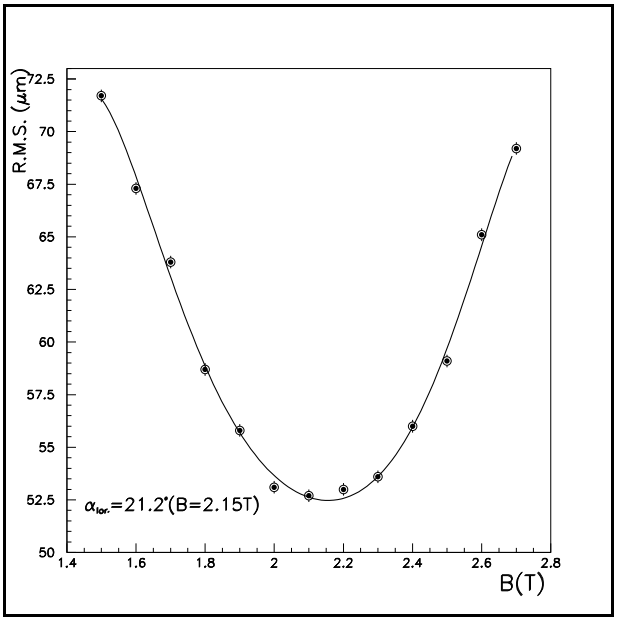


Fig. 4.8.15: Chamber resolution deterioration due to the Bz-field as measured with Dubna P2 prototype.

The Dubna P3 prototype was tested at the H2 beam line at CERN in presence of both components (axial and radial) of the magnetic field and demonstrated that the ME1/1 spatial resolution will meet the CMS requirement.

4.8.2.3 Local charged track

Apart from the off-line resolution requirements, the EMU CSCs are required to localize hits to within a half strip at the trigger level. Two different hardware solutions have been suggested and investigated. The 'comparator' algorithm [4.20] uses a set of comparators for each cathode strip to look at the charge differences in three adjacent strips (see section 4.4 for details). It gives hit coordinates known to half a strip. The 'digital' algorithm proposed for RPCs [4.23] calculates a center of gravity of strips in a cluster with charges above a threshold. This also gives hit coordinates with half-strip stepping, but the actual boundary defining which of the two neighboring half-strips the hit is assigned to depends on the strip width and signal/threshold ratio for this hit. This feature together with higher sensitivity to tails is the drawback of the digital scheme. A more complicated circuitry is the drawback of the comparator scheme.

The intrinsic capabilities of the two algorithms to handle good hits, i.e. the ones which are not dramatically compromised by secondaries or δ-electrons, were first evaluated by using the preselected Dubna P2-prototype experimental data. First, only good events with all six hits along a track within a narrow road of 350 μm were extracted. Then, the differences between the hit coordinate calculated from strip charge interpolation and the coordinate found by applying either the digital or comparator algorithms were plotted. In this analysis, we did not attempt to simulate possible trigger electronics imperfections. The comparator algorithm gave an essentially half-strip wide flat distribution, while the digital result was slightly wider. Fig. 4.8.16 shows the probability to get a difference within a $\pm\Delta x/w$ window for the two algorithms. For a $|\Delta x/w| \leq 0.25$ window, the comparator algorithm was ~100% efficient, and the digital one was ~92% efficient. Both algorithms were about 100% efficient for $|\Delta x/w| \leq 0.5$.

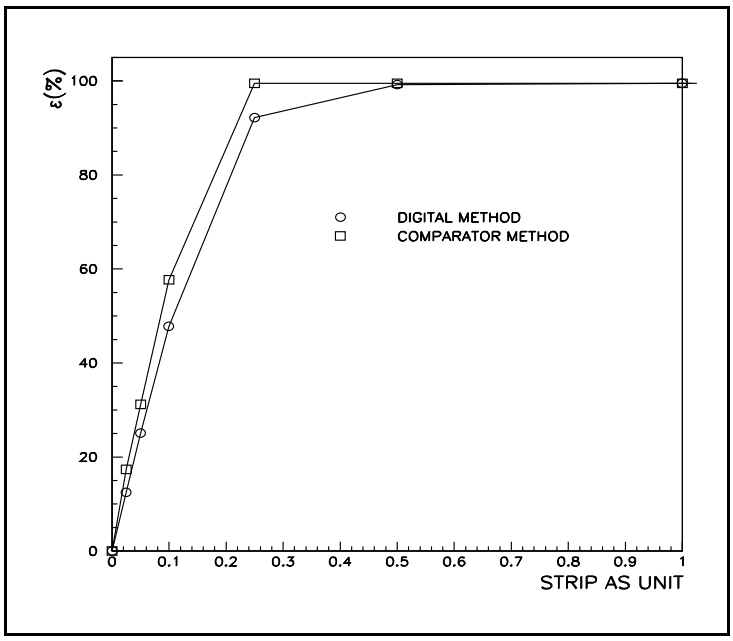


Fig. 4.8.16: Probability to measure a muon hit in a plane at the level-one trigger with a residual within a $|\Delta x/w|$ window. The result is obtained for muon tracks not compromised by secondaries or δ-electrons (Dubna P2 prototype result).

The comparator-based circuitry has been prototyped in hardware and tested in the muon beam with the US P0' Prototype. The differential efficiency of detecting the correct half-strip (efficiency vs. track coordinate across the strip) is presented in Fig. 4.8.17. No suppression of bad hits was done, and the track position in the plane under study was obtained by fitting the track with the other five chamber planes. One can see natural efficiency losses at the edges of a half strip, which are mostly due to electronic noise and channel-to-channel gain variations, and some small coordinate-independent losses, which are presumably due to δ-electrons. The overall efficiency was found to be 92% and almost independent of HV, as soon as one operates above the knee of the plateau (Fig. 4.8.18). The probability of obtaining the correct half-strip or the next nearest half-strip is 98%.

Trigger electronics imperfection was simulated and applied to the off-line data as well as to the MC-generated data which did not have δ-electrons. This allowed us to explicitly analyze contributions of different factors.

Finding hit positions to within a half-strip is the first step towards finding an LCT (local charged track segment), which is based on searching patterns of half-strip hits in six planes consistent with a muon track. Even in the presence of electromagnetic debris accompanying high energy muons after passing the iron filter or calorimeter, this is achieved with the 99% probability (more details are given in sub-section 4.8.3).

4.8.3 Wires

As was discussed earlier, the CSC wires serve a dual purpose. First, they define muon track stubs, or LCTs (local charged tracks), in the radial view: an LCT pattern must be consistent with a track originating from the IP. Second, the anode signals, being faster than

those from the cathode (smaller channel capacitance, larger signal amplitude and no requirements on precise measurement of amplitudes allows for much faster electronics), will be used to identify at the Lev-1 trigger the bunch crossing number associated with a registered muon.

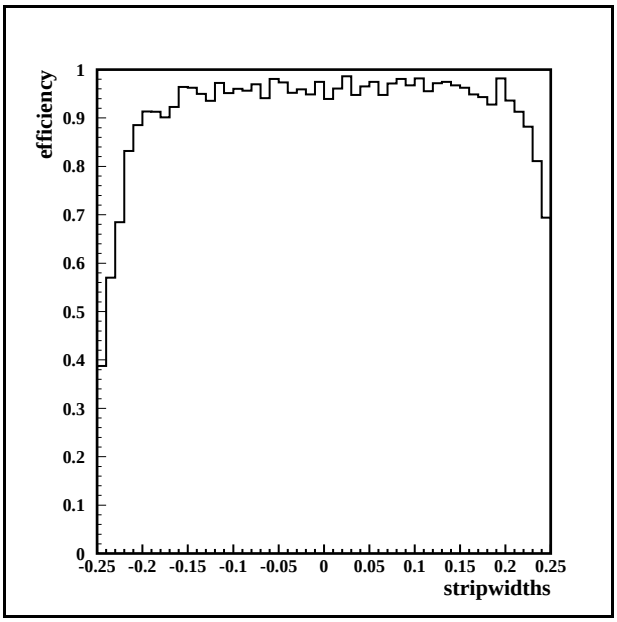


Fig. 4.8.17: Efficiency of detecting the correct half-strip vs track coordinate across the strip (US P0' prototype results).

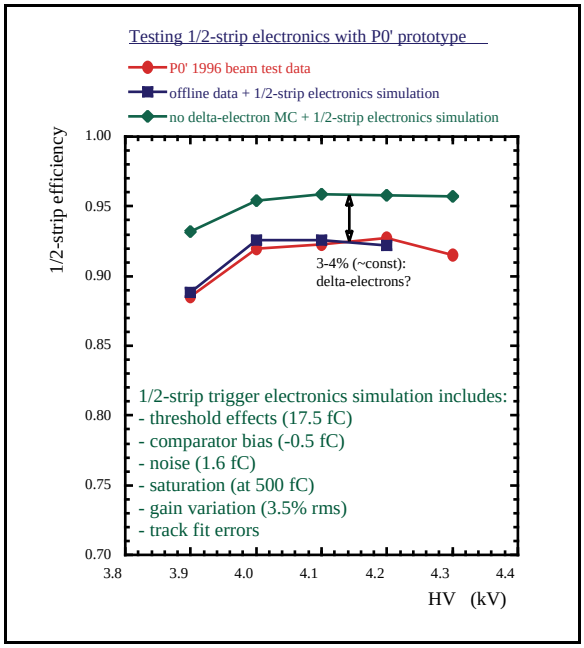


Fig. 4.8.18: Overall efficiency (per plane) of measuring the correct half-strip vs. high voltage (US P0' prototype results).

Due to finite drift velocity in the gas, even for the ME1/1 chambers which have the smallest wire spacing (2.5 mm), the single plane timing is not good enough to allow for reliable bunch-crossing identification. The time spectrum of anode signals from a single plane is shown in Fig. 4.8.19: one can see that a noticeable fraction of signals falls out of any given 25 ns window.

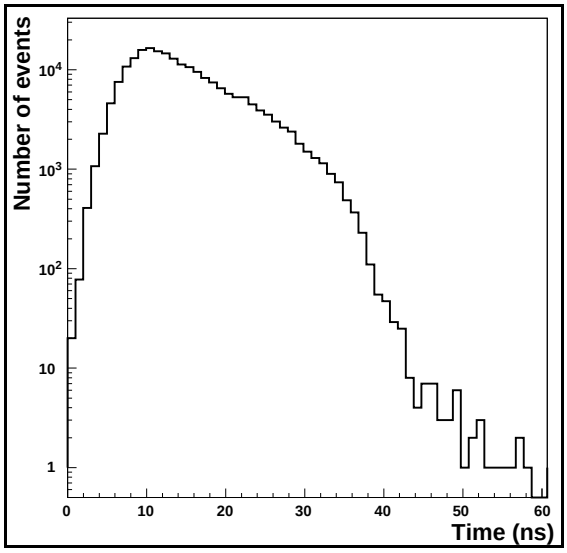


Fig. 4.8.19: Time distribution of anode signals from a single plane for the inclined muon tracks in the θ-angle range from 10° to 24°. The spectrum width is 34 ns at the level of 99%. Data are taken in a muon beam with the Dubna P2 prototype.

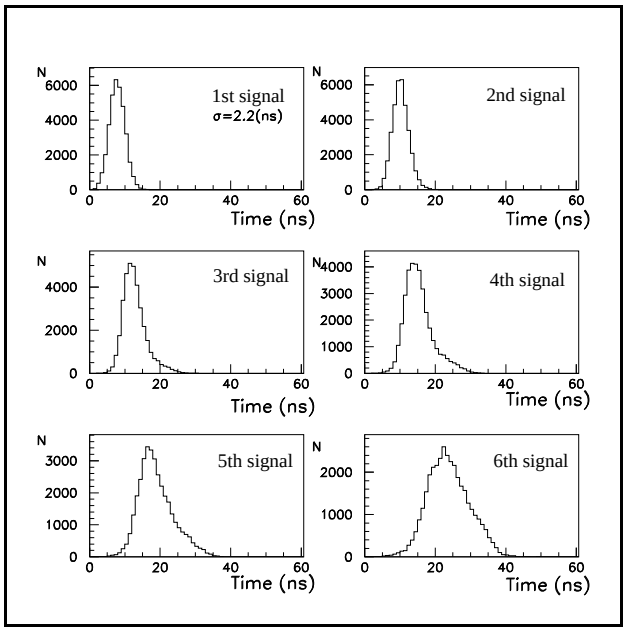


Fig. 4.8.20: Time distributions of the 1st, 2nd, etc. signals out of the six planes. Spectra for the 1st and 2nd signals are substantially narrower than a single plane time distribution and provide a reliable bunch-crossing identification. Data are taken in a muon beam with the Dubna P2 prototype.

However, we take advantage of having multiple plane chambers: time distributions for the earliest, second, third and fourth signals out of the six planes are substantially narrower as shown in Fig. 4.8.20. One can see that the earliest, second and even the third signal can be used for bunch crossing identification with efficiency more than 99%.

In operation, the anode trigger electronics logic will be searching for hits in six planes lining up to make a pattern (at least 4 hits in 6 planes) consistent with a muon track coming from the IP, as described in the electronics subsection 4.4. For charged particle identification the majority coincidence can be used. Efficiency of the majority coincidence vs. strobe width is shown in Fig. 4.8.21 (zero corresponds to the time when the muon passes through the chamber). Measurements with the Dubna P2 prototype show that a charged particle can be identified in a time strobe less than two bunch crossings (50 ns) with efficiency close to 100%.

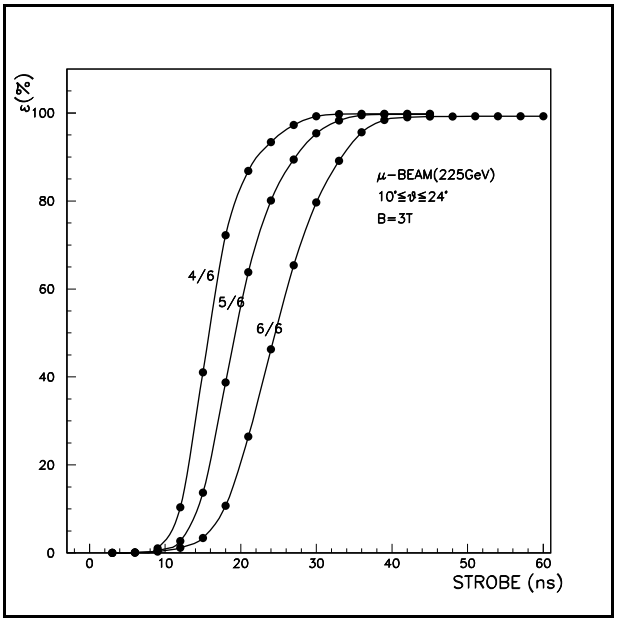


Fig. 4.8.21: Efficiency of the majority coincidence vs. strobe width. Majority coincidence of at least four out of six signals provides a reliable charged particle identification within a gate shorter than two bunch crossings. Data are taken in a muon beam with the Dubna P2 prototype.

The efficiency of finding a muon generated pattern or LCT was measured in beam tests with the US P0' prototype and found to be around 99.5% above the knee of the operating range plateau as shown in Fig. 4.8.22. The same figure shows the probabilities of the correct bunch crossing identification by using the earliest, second, third and fourth hit from the found LCT pattern. The results are obtained with the US P0' prototype (large 3.4 mm wire spacing). As was discussed in subsection 4.1, the requirement for correct tagging of a bunch crossing associated with an LCT in one station is 92% (then, the 4-station based global muon track trigger will be more than 99% efficient by selecting the most frequent bunch crossing among the 4 LCTs linked in a track). One can see that the chamber performance at the nominal operation point (100 fC cathode charge) is safely better than this requirement. The tests of the large US P1 prototype in cosmic rays showed the same high bunch tagging efficiency (Fig. 4.8.23).

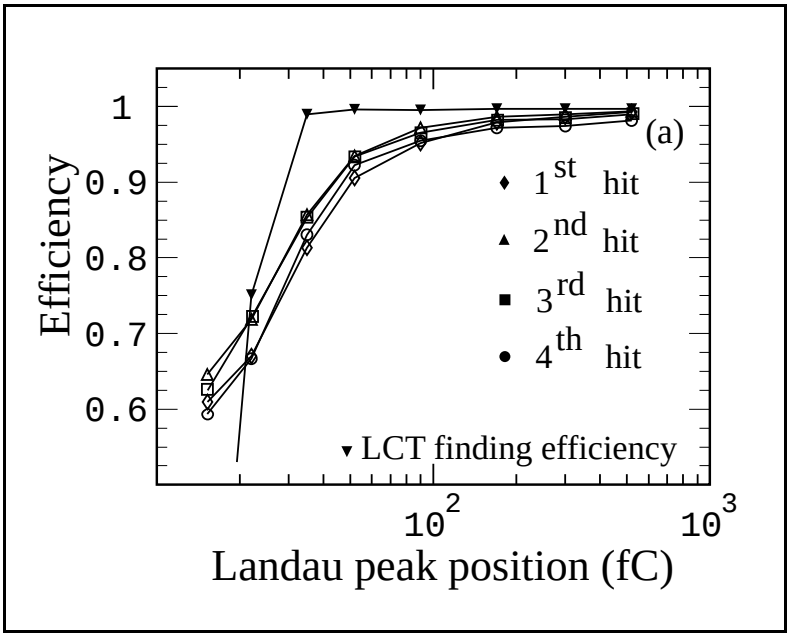


Fig. 4.8.22: Efficiency for finding a "4 out of 6" wire LCT (inverted triangles) and efficiency for tagging the correct bunch crossing by triggering on the first, second, third, or fourth hit in the found LCT. The results are obtained in the offline analysis of data taken in a muon beam with the US P0' prototype (3.4 mm wire spacing). The chamber performance at the nominal operation point (100 fC cathode charge) is safely better than the 92% requirement.

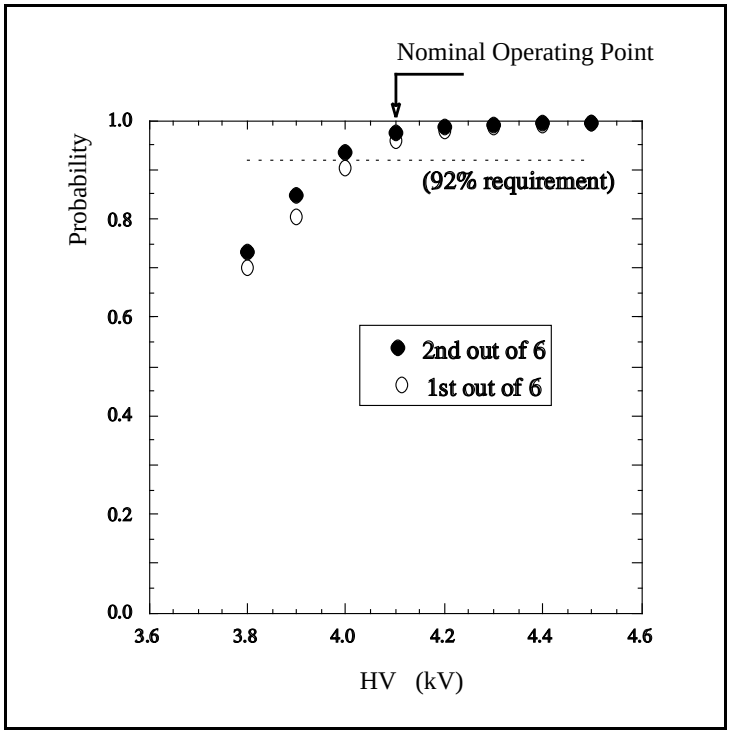


Fig. 4.8.23: Probability of tagging the correct bunch crossing vs. high voltage, as measured with the full scale US P1 prototype in cosmic rays. The probability at the nominal high voltage of 4.1 kV is safely above the 92% requirement.

The sensitivity of the bunch tagging efficiency to various factors has been studied in the beam. Fig. 4.8.24 shows that the probability does not depend on the track inclination for the range of angles expected in the Endcap Muon System. The effect of the B-field on the timing was also found to be negligible.

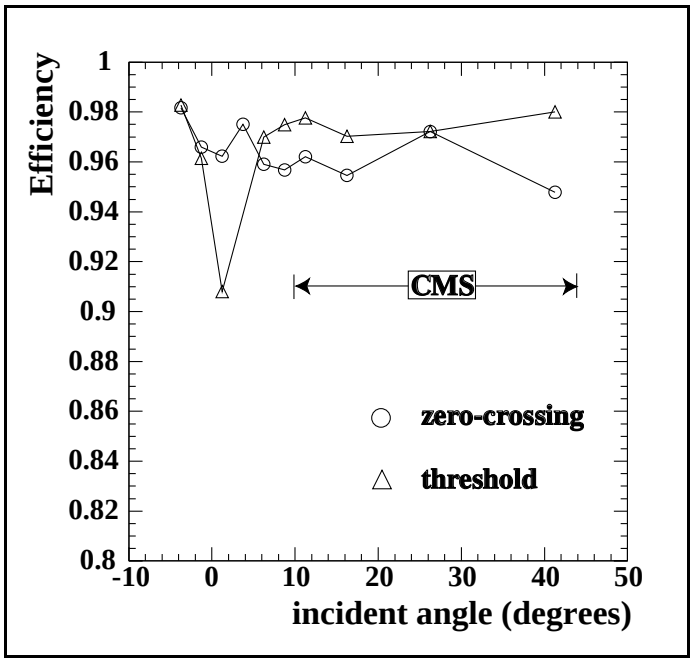


Fig. 4.8.24: Independence of bunch tagging efficiency on track inclination for the range of angles expected in the Endcap Muon System (US P0' prototype in a muon beam).

It may be appropriate to recall that bunch crossing tagging based on the second earliest hit is the baseline. A simple consideration of backgrounds shows that one cannot use the earliest hit, even if it were the best time estimator (as in the case for the small wire spacing of the ME1/1 chambers). Indeed, a random hit overlapping with a muon pattern and preceding the muon by a few bunch crossings would clearly compromise such a measurement (given the signal duration, two hits must be separated by more than 200 ns to be resolved). To compromise the second earliest hit, one needs to have more than one random hit overlapping with an LCT within the 200 ns window. Therefore, the second hit should give much more robust time tags in terms of tolerating random hit backgrounds (see subsections 4.8.4 and 4.8.5)

4.8.4 Six-plane CSC performance in the presence of electromagnetic secondaries

4.8.4.1 Track finding in off-line

The influence of electromagnetic (em) secondaries on muon track reconstruction was studied with the Dubna P2 prototype with and without the calorimeters in front of it in the Integrated Test of CMS endcap prototypes.

Without any material upstream, a fraction of high energy muon tracks with fatal distortion of clusters in three or more layers due to δ-electron production was measured to be around 5%.

This value is in agreement with our previous measurements in cosmic rays with the Dubna P0 prototype.

In the Integrated Test configuration, high energy muons passing through the calorimeter matter produce a significant number of em secondaries which make muon track reconstruction more difficult. The Integrated Test setup at the H2 beam line of the CERN SPS is shown in Fig. 4.8.25. Note that the variation of the magnetic field in the chamber was in the range of 2.5–3.0 Tesla for different layers, similar to the realistic B-field.

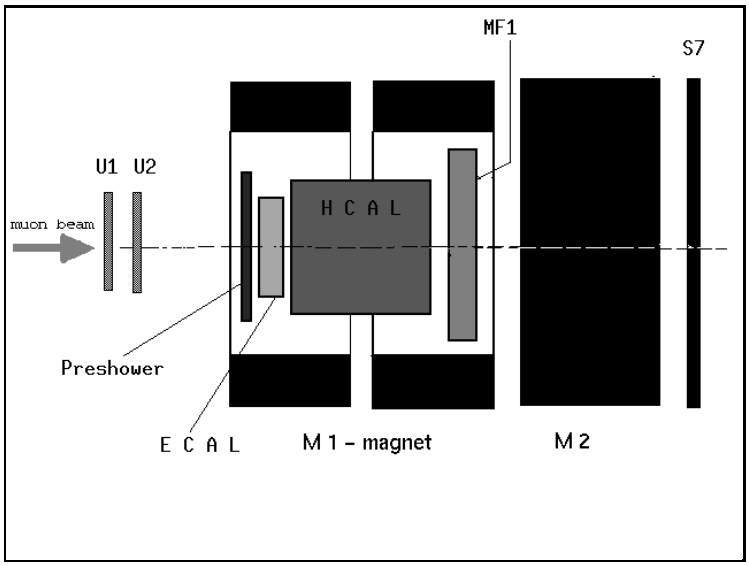


Fig. 4.8.25: Endcap Integrated test setup. The Dubna P2 prototype is behind the HCal+ECal and the entire set of the detectors is within a magnetic field corresponding to that of the Muon Endcap System.

The experimental data have shown that the high energy muons (100 - 300 GeV) produce up to 20-25 % of events with em secondaries hitting the CSC. The track finding algorithm was as follows. First, all wide (overlapped) clusters were split into sub-clusters and hit positions for all clusters and sub-clusters were calculated. Second, we searched for at least four hits within a 1 mm wide road (at the angle consistent the muon beam direction within ±2°) and required that at least four out of a possible six hits line up to make a decent track fit (χ^2/dof<7). If these criteria were satisfied, the event was called a class A event. Among the remaining events, we searched again for at least four hits lining up with much looser cuts (6 mm wide road, ±4° angle, no χ^2 cut). If found, the events were tagged class B. What was left after the two iterations were called class C events. Typical events representing all the three classes are shown in Fig. 4.8.26.

For 300 GeV muons, the fraction of events in class A was 92% and tracks were reconstructed with almost the ultimate precision of 45 μm (Fig. 4.8.27(a)), 6% of events were assigned to class B and they had track fit residuals of the order of 1 mm (Fig. 4.8.27(b)). The remaining 2% of class C events represent irrecoverable losses. Fig. 4.8.28 shows how the fraction of class A events changes for different numbers of planes in a chamber.

We also studied how often muon induced secondaries can generate fake tracks. The probability of such fake tracks (at least 3 hits per track) was measured to be around 3% (10%) for 100 GeV (300 GeV) muons.

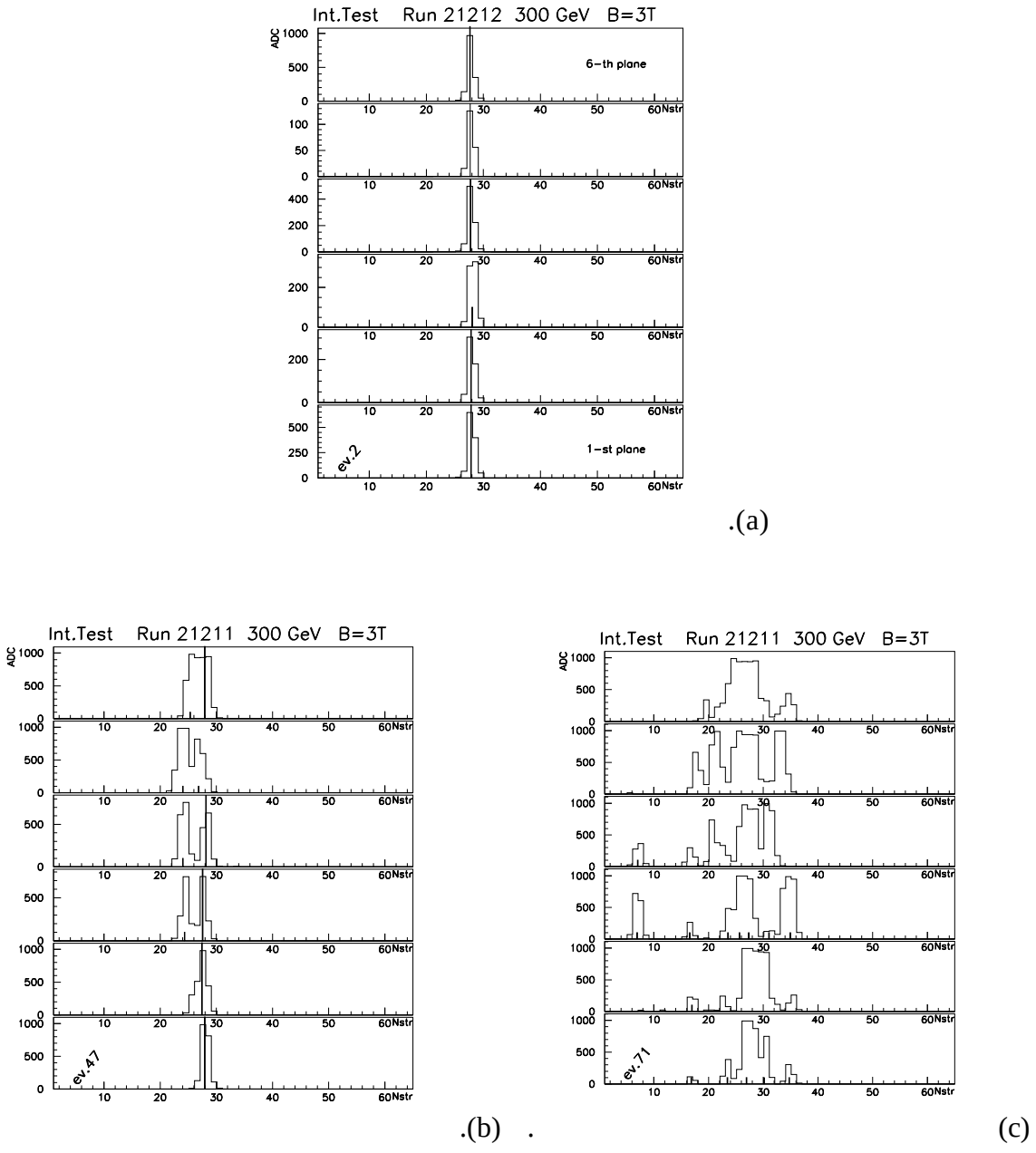


Fig. 4.8.26: All events observed in the integrated tests (Dubna P2 prototype) at 300 GeV could be sub-divided in the three classes A, B, C: (a) events with good muon tracks with no muon background hit or well separated from muon background hits (reconstructed with the full 45 μm precision, 92% of all events); (b) events with compromised, but still reconstructable muon tracks (precision deteriorated to about 1 mm, 6% of all events); (c) events where the track finding algorithm failed (less than 2% of all events).

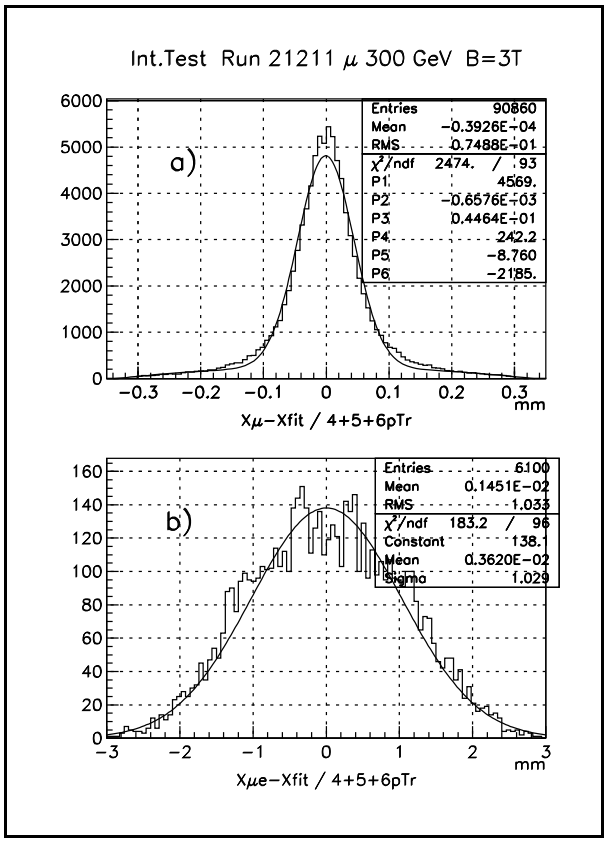


Fig. 4.8.27: Residuals for tracks from class A events (a) and from class B events (b). Data is for the Dubna P2 prototype.

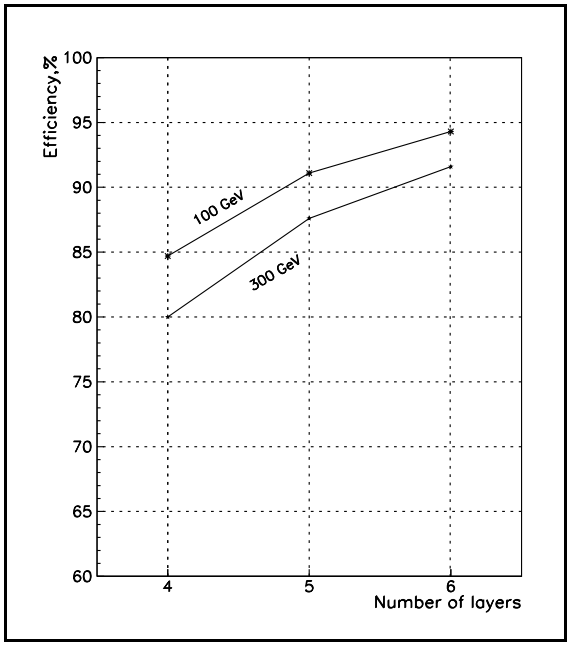


Fig. 4.8.28: Efficiency for class A events (events with a muon track reconstructed with the ultimate chamber resolution) as a function of the number of chamber layers (Dubna P2 prototype). Two sets of data correspond to muons of different energies: 100 and 300 GeV.

4.8.4.2 Strip LCT

To verify the robustness of the strip LCT trigger, the US P0' data taken in a 300 GeV muon beam with the prototype placed behind a 30 cm thick iron slab were analyzed. The Si beam telescope placed upstream from the iron was used to confirm muon triggers and to predict the coordinates where a muon should hit the chamber (projected precision was about 100 μm). The off-line chamber data were fed into the routine which was simulating half-strip comparator and digital algorithm performance (the simulation routine was consistent with the results obtained with the actual comparator network hardware - see Figs. 4.8.17 and 4.8.18). A list of all valid strip LCT patterns was generated with an independent MC and a fixed (most probable) coordinate was assigned to each of the generated patterns. Each pattern was also given a priority code based on the relative frequency of appearance. As was discussed in section 4.4.2.3, we envision using two sets of patterns: one based on the half-strips for high p_T muons and another one based on double-strips for low momentum muons. Then the valid strip LCT patterns in the order of their priorities (see discussion in section 4.4.2.3) were searched for in all the events. The results are as follows:

- For comparators: about 98.9% of events had valid half-strip LCTs and the Gaussian sigma of the distances between predicted track position and a coordinate assigned for the found patterns was 0.107×(strip width) - see Fig. 4.8.29(a). For the digital scheme: 94% and 0.147×(strip width).
- For comparators: about 1.1% of events did not have valid half-strip patterns, but they did have valid double-strip LCTs, and the spatial resolution for those few LCTs was 0.732×(strip width) - see Fig. 4.8.29(b). For the digital scheme: 6% and 0.907×w.
- Less than 0.1% (0.2%) events had no patterns in the comparator (digital) schemes.

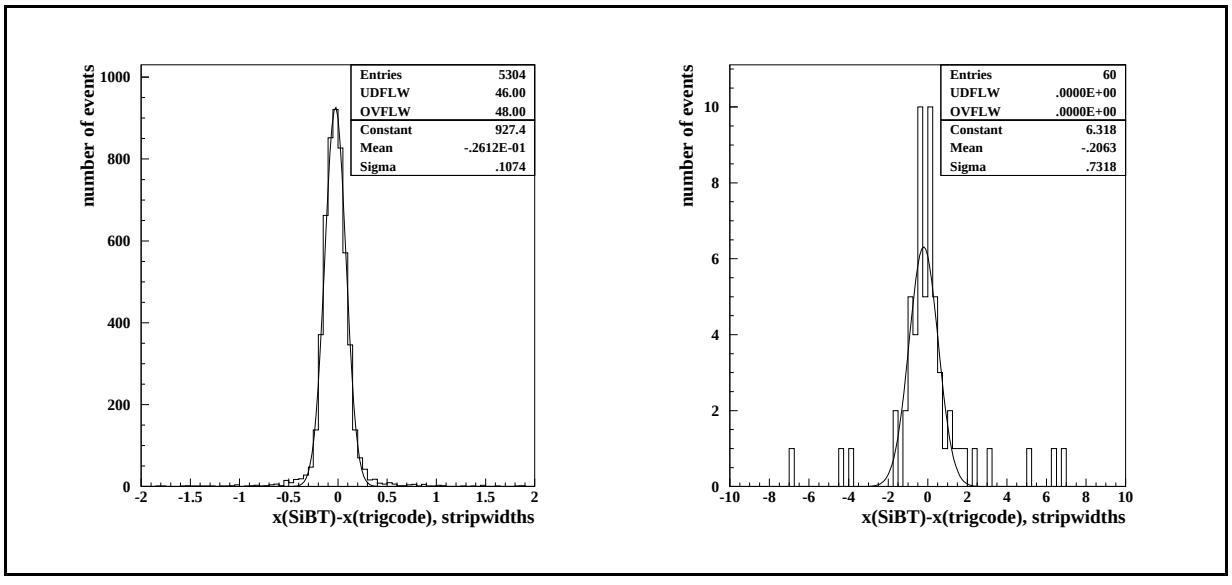


Fig. 4.8.29: Distances between predicted muon track positions in the CSC and coordinates assigned for the highest priority LCT: (a) 98.9% of events had valid half-strip patterns; (b) remaining 1.1% of events had no half-strip based LCTs, but had valid double-strip LCTs. Data are taken with the US P0' prototype in a 300 GeV muon beam behind a 30 cm iron block.

4.8.5 CSC performance in a high rate environment

For the 1997 beam tests the Dubna P3 ME1/1 was instrumented with new cathode front-end electronics based on 16 channel Minsk ASICs (charge sensitive preamplifier-shapers with 100 ns shaping time and fast shapers with 30 ns shaping time). A total of 96 channels (6 planes × 16 channels/plane) were used for precise muon position measuring and for triggering. The anode readout was equipped with Laben front-end electronics and MVL discriminators. The test was performed at the H2 beam line in a strong magnetic field corresponding to CMS endcap experimental conditions. The first results showed a high track reconstruction efficiency and good spatial resolution. Timing resolution for both anode and cathode readouts was also measured to be very good.

New fast cathode electronics make it possible to operate a CSC in a pion beam with a rate up to 500 kHz/strip. Fig. 4.8.31 shows deterioration of track reconstruction efficiency vs. pion rate. Efficiency in this figure is normalized to be 100% at zero rate. For chambers behind the calorimeters or iron, the absolute efficiency of reconstructing a muon track was measured to be 92% (see subsection 4.8.3.1). As mentioned above, the expected background hit rates can be as high as 1 kHz/cm^2 (at the bottom of ME1/1) and the total signal rate per strip may reach about 100 kHz. One can see that at this rate the losses in the track reconstruction efficiency are negligible and the chamber spatial resolution per layer remains acceptable (Fig. 4.8.31).

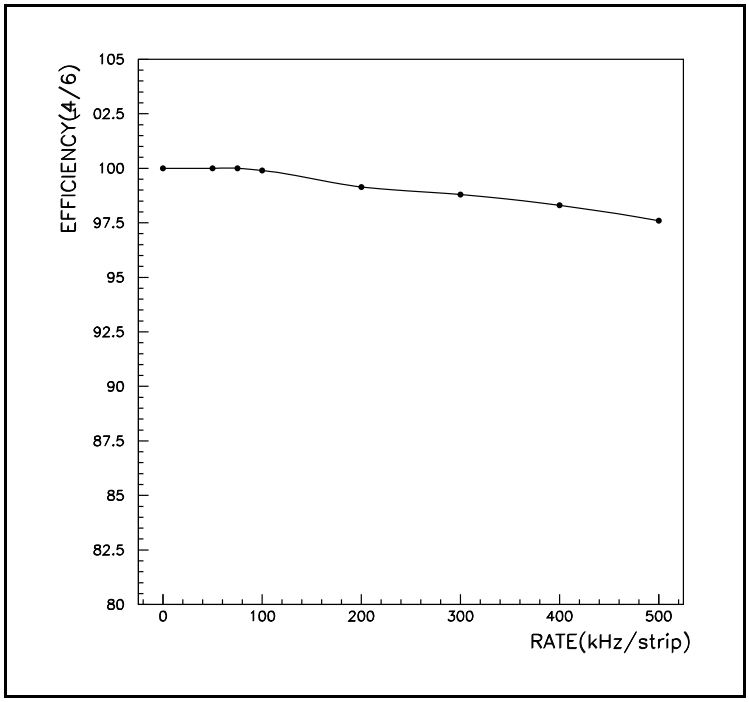


Fig. 4.8.30: Relative efficiency of reconstructing a muon with at least 4 out of 6 residuals within a ±300 μm window as a function of particle rate in kHz/strip. Data are taken with the Dubna P3 prototype in a high rate pion beam (preliminary results).

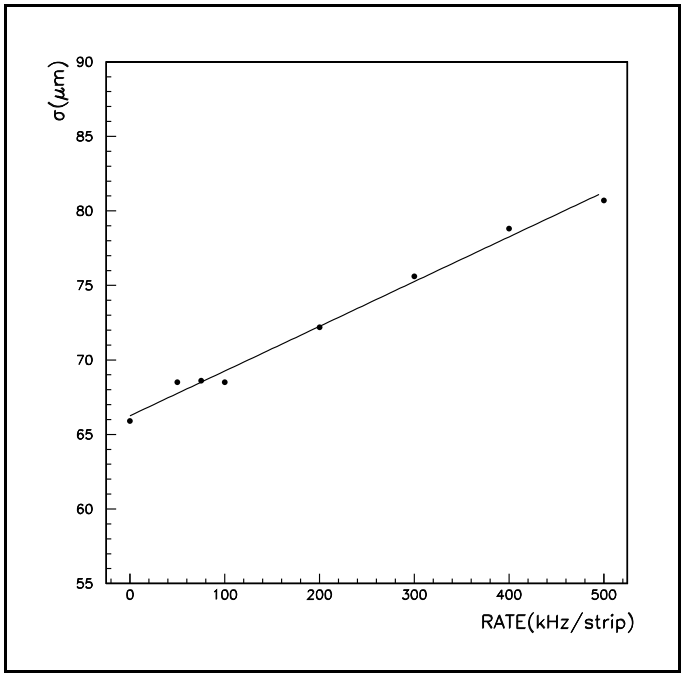


Fig. 4.8.31: Deterioration of a single plane resolution with the rate in kHz/strip.

Another test was performed with the Dubna P3 prototype in the CERN West Area with a muon beam at the Gamma Irradiation Facility (GIF). The GIF provides a muon beam in combination with a superimposed very high rate gamma background, up to 2 MHz/cm^2. A photo of the chamber being installed at the GIF is shown in Fig. 4.8.32.

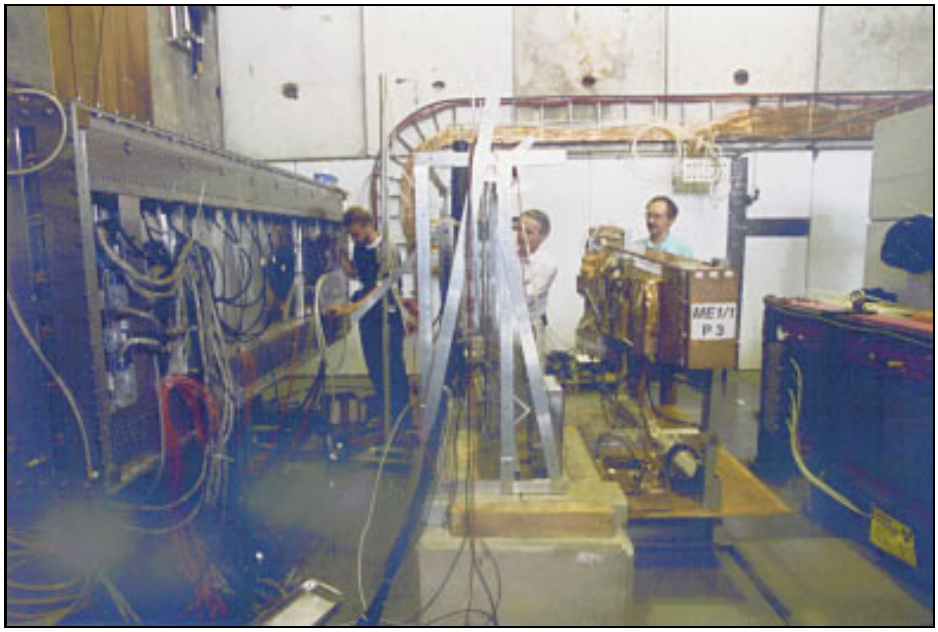


Fig. 4.8.32: The Dubna P3 prototype being set up for tests at the GIF facility at CERN, i.e. in a muon beam with superimposed flux of photons from a high intensity gamma source.

The estimates of background gamma rates at the bottom (top) areas of the ME1/1chambers at the full LHC luminosity is around 70 (7) kHz/cm^2. These rates correspond to an absorption factor of the GIF source filter of 35. (The unattenuated GIF gamma flux is about 2.3×10^6 γ/cm^2/s.) Preliminary result shows adequate efficiency of bunch crossing identification and a high timing resolution of the first-out-of-six and second-out-of-six hits as a function of random hit rate as illustrated in Fig. 8.3.33. Data analysis is in progress.

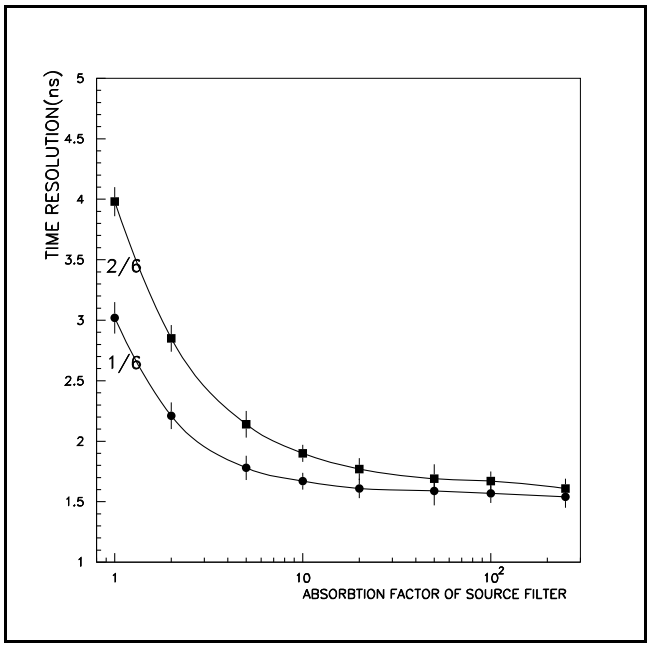


Fig. 4.8.33: Broadening of the time distribution of the first-out-of-six and second-out-of-six hits. Data are taken with the Dubna P3 prototype at the GIF facility at CERN (preliminary results).

4.8.6 Aging

Three small (200 cm^2) one gap chambers have been assembled according to the current EMU CSC design and out of exactly the same materials envisioned for the final chambers. The chambers were flushed with one of the plausible gas mixtures ($Ar+CO_2+CF_4$ = 40+50+10) at a flow rate of 30 cc/min, and two wires of the first chamber were irradiated with a strong β-source (Figs. 4.8.34 and 4.8.35). The second chamber was not irradiated but its gas inlet was connected to the gas outlet of the irradiated chamber. The third chamber was used as a reference. The chambers were operating at the nominal operating point. During these aging tests, the gas gains (Fig. 4.8.36) and dark currents (Fig. 4.8.37) were measured at a few points in the two test chambers and compared with the reference chamber. One can see that even after accumulation of a total charge in excess of 2 C/cm/wire, neither gas gain nor dark current have changed. This total accumulated charge substantially exceeds the expected value of 0.1 C/cm after 10 years of LHC operation at the full luminosity. The results are very encouraging and not unexpected as we already knew of the aging preventive properties of CF_4 [4.38]. More details on the aging test setup and other results, including the ones with no CF_4 in the gas mixture, can be found elsewhere [4.39]. The aging test program will be continued.

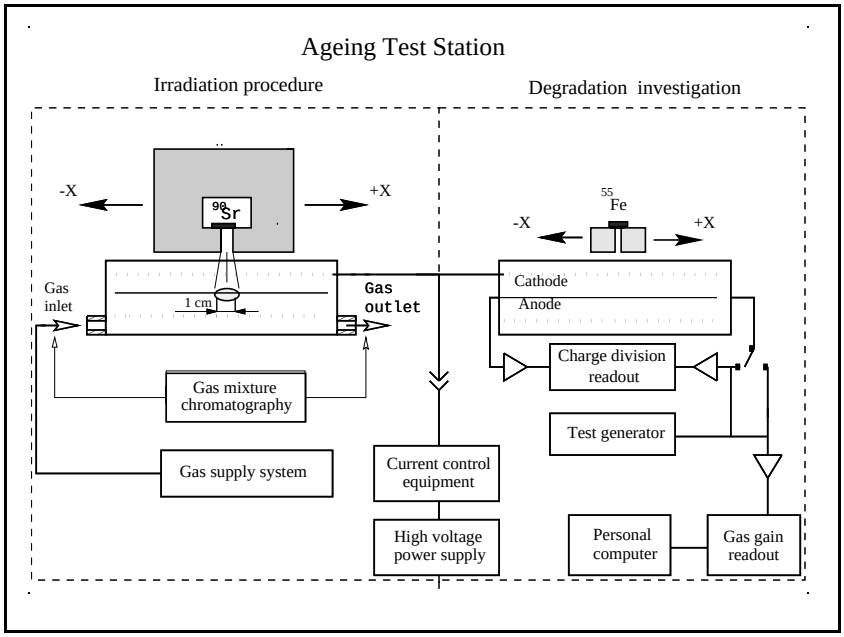


Fig. 4.8.34: Sketch showing the experimental setup for aging studies.

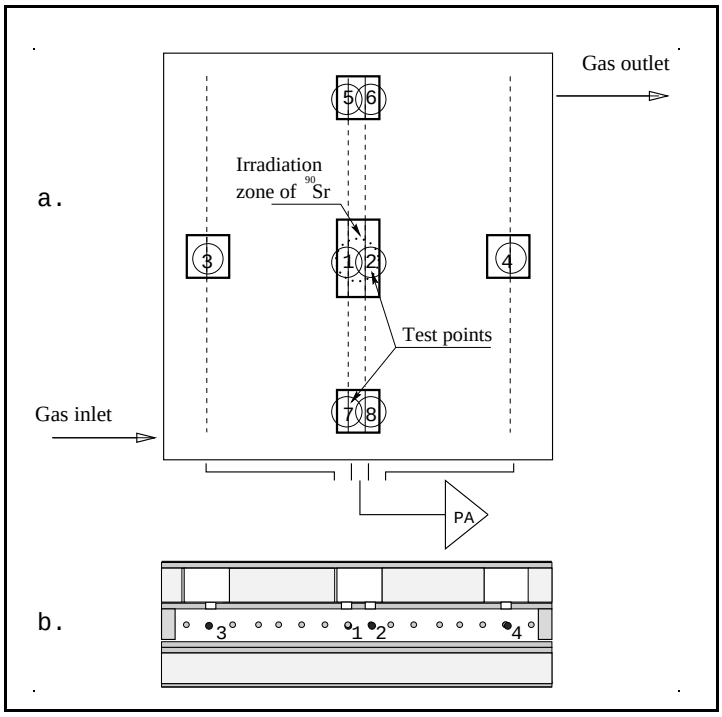


Fig. 4.8.35: Sketch showing test points of the chamber which was irradiated during aging studies. Only two points, 1 and 2, were irradiated, but all of the labelled points were monitored for any possible changes.

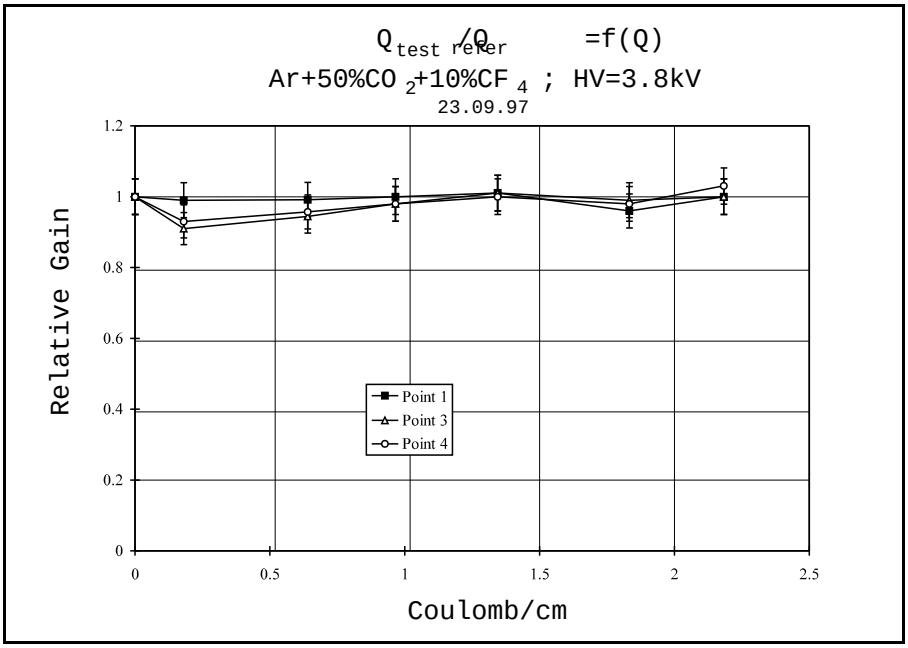


Fig. 4.8.36: Gas gain in the aged chamber has not shown any drop after accumulation of a total charge in excess of 2 C/cm/wire

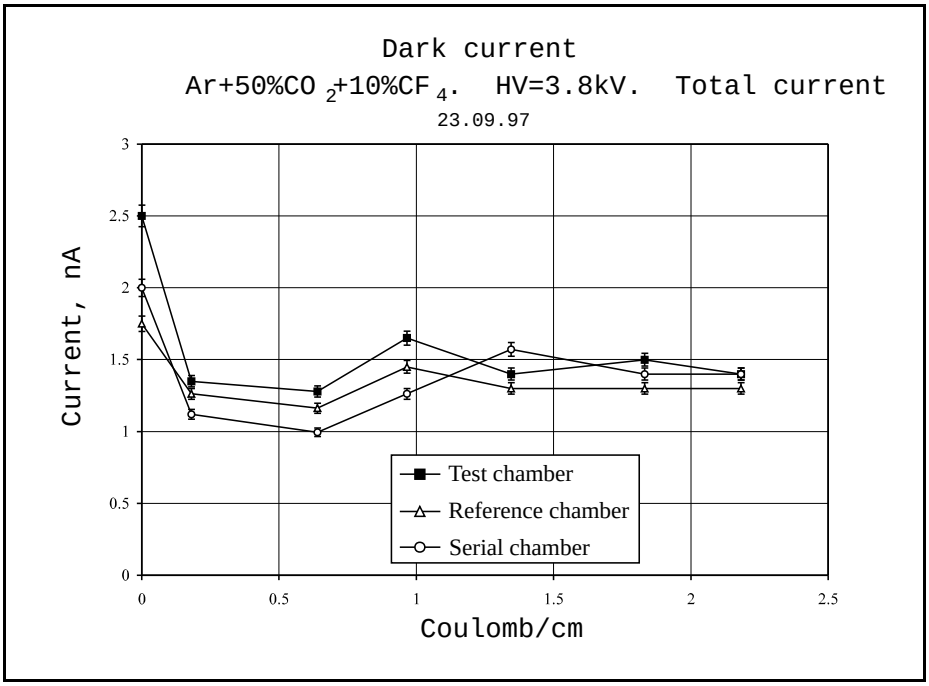


Fig. 4.8.37: Dark current observed over the entire period of aging

4.9 SIMULATION OF CSC DETECTOR AND ELECTRONICS RESPONSE

CMSIM is a general purpose CMS detector simulation package which is extensively used for optimization of the detector performance and its design. Below we discuss how CSCs are implemented in CMSIM.

4.9.1 Signal generation

When a CSC plane is entered or exited by any charged particle, the particle kinematic parameters, including those particles created in the tracking process, are saved for inclusion in the HITS bank.

Simulation of chamber hits begins by fetching the chamber hit positions from the HITS bank list. In addition to muon induced hits at this stage, extra hits from the superposition of background processes, such as minimum bias punchthrough and hits originating from neutrons, can be added to the hit list. These hits will have time-of-flight offsets that take their production beam crossing times into account. This allows for the realistic simulation of background hits in time.

As a first step, free electrons are produced in the gas gap and are transported to the anode wire. Free electrons are generated along a line between the gas volume entry and exit points fetched from the hit data banks. Free electron generation uses the atomic structure of the gas molecules in the calculation of the collision cross section. The differential cross section $d\sigma/dE$ is calculated from the complex dielectric constant of a material, which in the simplified model, contains the photoabsorption cross-section of the atom.

Each electron is then transported to the anode wire position independently. The electric and magnetic field vectors found at the electron's position are used to obtain the local drift velocity vector. In this fashion all electrons are transported incrementally to the wire with their different arrival times and Lorentz drift distances taken into account. The portion of the charge induced on the cathodes near the drifting electron's arrival position is determined following the Gatti parameterization (see discussion in section 4.1).

After summing the contributions from all electrons, electronic noise is randomly superimposed onto each strip and wire. It is important to note that the signal might contain contributions from drifting electrons due to background hits from other beam crossings. After simulation of the electronic response, the CSC cathode signal consists of the time profile of charge from all drifting electrons and the superimposed electronic noise for both the DAQ and trigger path signals on all strips. Simulation of the final digitizing step then proceeds.

4.9.2 CSC precision signal digitization (DAQ path)

The CSC front-end cathode readout includes a switched capacitor array (SCA) to store signals from strips. The signal shape is sampled at eight different times (the number is programmable) at 50 ns intervals and stored in capacitor cells in the SCA. Ultimately, after Lev-1 trigger signal arrives, signals of interest will be fetched form the SCA and digitized by 12-bit on-board ADCs. Actual algorithm of selecting which information is to be digitized and stored will depend on luminosity. For example, at very low luminosity all strip signals will be recorded, at very high luminosity only signals associated with LCTs will get to the tape. More complex algorithm are being discussed as well. Currently in the CMSIM, the precise cathode signal sampling is done and information is stored for five strips: the center strip that satisfied the

comparator and two strips on both sides. One can mask this information to simulate the ultimate DAQ selection algorithms.

4.9.3 CSC trigger primitive simulation

Trigger primitives in the endcap muon CSCs are charged track segments in a single superlayer, called local charged tracks (LCT). A collection of hits in adjacent gas gaps in a superlayer are matched to hit patterns that are produced by a single muon track. The spatial coordinates of the hits in the chamber give a global position and the matched pattern gives the local bending angle. A track segment hit position and bending angle characterize each endcap muon LCT. CSC volumes have both cathode strip and anode wire group measurements, yielding the precise ϕ coordinate and the coarse radial coordinate respectively. There is a track segment for each coordinate: a strip LCT and a wire group LCT.

Simulation of the strip LCT segments begins with the DIGI strip data. For each half-strip comparator hit, a 150 ns gate is opened. When a coincidence of four or more layers in a valid road pattern is encountered, the pattern of signals 100 ns later is sampled and checked for a valid LCT road. The collection of road patterns used assumes that tracks are straight lines within the CSC chamber. The patterns accept tracks with local bending angles that cover a range from zero up to five half-strip widths.

4.9.4 Cluster hit reconstruction

To recognize clusters of strip hits in a CSC layer, the strip with the greatest ADC count is found. Using this as the central strip, the charges from two strips on both sides are taken; the combination of these five strip charges is defined as a hit cluster. The five strips in a cluster are fit to the Gatti parameterization to determine the precise hit position. This is done by calculating the difference between the digitized charge distribution and the Gatti charge distribution for an assumed position x. A χ^2 is defined from this difference as

$$\chi^2 = \sum_{\text{strip}-2}^{\text{strip}+2} \frac{(Q_{\text{Gatti}} - Q_{\text{digi}})^2}{\sigma_Q^2}$$

where *strip* is the ID of the central strip in the cluster, Q_{Gatti} is the charge from the Gatti distribution for some position x, and Q_{digi} is the charge from the digitized CSC data. The position x and total charge are varied until χ^2 is a minimum. The resulting x value is used as the precise CSC hit position. When tracks pass close to the strip center, a similar amount of the cluster charge is distributed on each of the neighboring strips. The difference between the signals on the neighbors is then dominated by electronic noise, thus undermining the accuracy of the reconstructed hit position. The CSC position resolution thus depends on the distance of the precise hit position x from the strip center. It also depends on strip width and full gas gap. Fig. 4.9.1 summarizes CSC resolutions for different chambers as simulated in CMSIM.

The CMSIM has been verified against data obtained with prototypes in the muon beam. Since CSC intrinsic resolution is predominantly defined by electronics noise, it can be very well reproduced in simulation when signal and noise are properly taken into account. Fig. 4.9.2 shows the agreement between data and simulation explicitly.

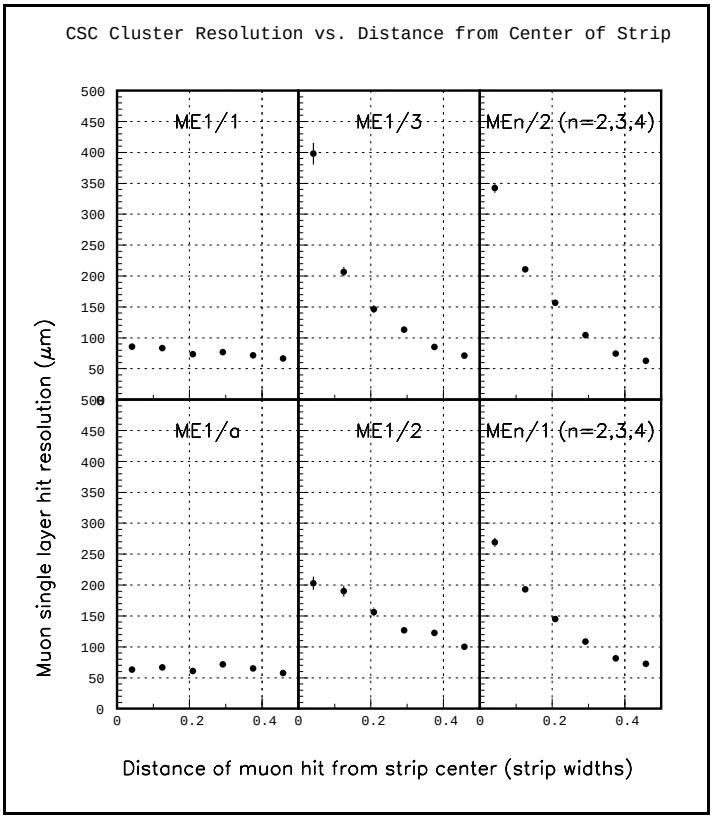


Fig. 4.9.1: CSC single layer resolution vs. distance from strip center for each muon station for 100 GeV muons. The x axis is the absolute value of the proportional distance from center, up to 1/2 strip width from center (0).

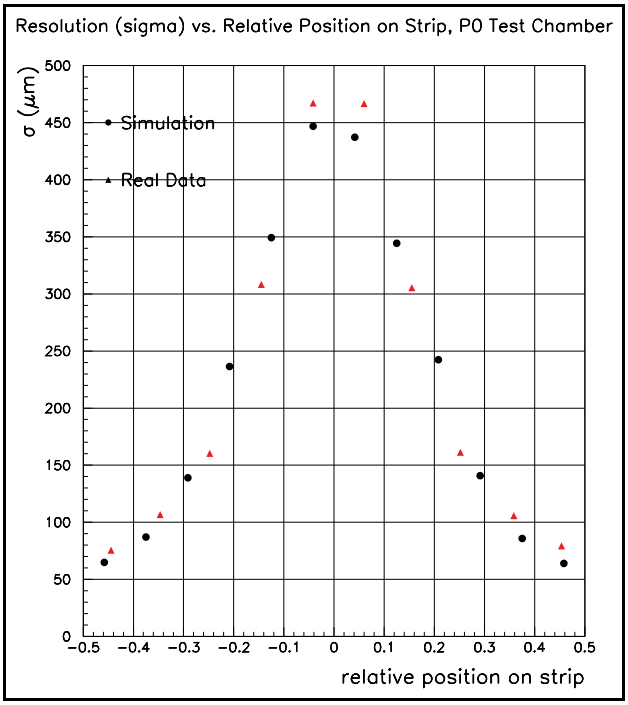


Fig. 4.9.2: Resolution of the US P0 prototype as obtained in the muon beam tests and simulated within the framework of the CMSIM package.

References

[4.1] E.Gatti et al., Nucl. Instr. and Meth. 163 (1979) 83.

[4.2] E.Mathieson and J.S.Gordon, Nucl. Instr. and Meth. 227 (1984) 277.

[4.3] G.Charpak et al., Nucl. Instr. and Meth. 167 (1979) 455.

[4.4] Yu.Fisyak, CMS TN/94-208, CMS technical note, 1994.

[4.5] I.Azhgirey and A.Uzunian "Background electrons track length distribution in CSCs," CMS TN/94-267, November 1, 1994,
C.Albajar et al., Nucl. Instr. and Meth. A364 (1995) p.473.

[4.6] C.Bradford et al, CMS-TN-95/094, CMS Technical Note, 1995.

[4.7] Plascore Inc., Zeeland, MI 49484, USA.

[4.8] M.Tavlet, "Material Test Report," TIS-CFM/MTR/95-07, 5 Apr 1995; (also see CMS EMU meeting proceedings, Apr 21, 1995, Maryland).

[4.9] Yu.Bonushkin, "CSC geometrical tolerances," to be published.

[4.10] A.Korytov, "Effect of crosstalks on 1/2-strip triger," CMS EMU meeting proceedings, July 11-12, 1997.

[4.11] Osram Sylvania, Towanda, PA 18848-0504, USA.

[4.12] M.Baarmand, "CSC wire tests," CMS EMU meeting proceedings, Nov 22-23, 1996, Riverside.

[4.13] Panasonic. Welding and Soft Beam and Assembly Robots, Franklin Park, IL 60131, USA.

[4.14] NA4 Collaboration, Nucl. Instr. and Meth. 176 (1980) 23,
Nucl. Instr. and Meth. 204 (1983) 333.

[4.15] D.Loveless, "CSC Panel bulging due to gas overpressure," CMS EMU meeting, June 1995.

[4.16] K. Kriesel, F. Feyzi, R. Loveless, CMS Note 1997/066.

[4.17] LumaMetall, Lumalampan AB, S-39127 Kalmar Sweden.

[4.18] L.S.Durkin, "CMS Modeling of Electron Signal for the Forward CSCs," CMS TN/95-194.

[4.19] J. Hauser, "Momentum Resolution Required for the Level 1 Muon Trigger," CMS TN/94-261.

[4.20] A.Korytov, "Analysis of valid hit patterns in CSCs," CMS TN/94-212.

[4.21] V. Karjavin, CMS TN/95-160.

[4.22] A. Zarubin et al., CMS DOC 1996-213.

[4.23] M.Gorski, et.al., "Clusters in RPC and Muon Trigger performance," CMS TN/95-107.

[4.24] J. Hauser, "Baseline Design for CSC based Endcap Muon Trigger," CMS TN/95-013.

[4.25] R. Breedon, Y. Fisyak, W. Ko, J. Rowe, "Background LCT Rates by CSC Type using the Forward Muon Trigger Simulation in CMSIM," CMS TN/96-070.

[4.26] Dubna P0 prototype results: notes and presentations- "Dubna 0.5 x 0.5 m2 RD5 CSC prototype 1993," in Milestones Report , CMS Collaboration, CERN/LHCC 93-48, p.70, 1993,
C.Albajar et al, Nucl. Instr. and Meth. A 364 (1995) 473-487.

[4.27] Dubna P1 prototype results: notes and presentations- “Study of Fundamental Properties of the Matter in Super High Energy Proton-Proton and Nucleus-Nucleus Interactions at CERN LHC. Participation in CMS Collaboration,” RDMS CMS Project. 96-85 CMS Document, CERN 1995,

Yu.Kiryushin, “MF1 status and milestones” in Proceedings of "First Annual RDMS CMS Collaboration Meeting", CERN, December , 1995 , CMS Document 96-89.

[4.28] Dubna P2 prototype results: notes and presentations - P.Moissenz “Simulation of MF1 CSC spatial resolution in endcap magnetic field” in: Proceedings of “First Annual RDMS CMS Collaboration Meeting,” CERN, Dec , 1995 , CMS Document 96-89,

A.Zarubin, “The MF1/1 Chambers,” Meeting with LHCC CMS Referees, 96-64 CMS meeting, May 28-29, 1996,

A.Chvyrov et al, “Bunch crossing identification study on MF1 prototype beam test data,” CMS TN/95-161,

A.Zarubin, “95 summer beam test” in: Proceedings of “First Annual RDMS CMS Collaboration Meeting,” CERN, December, 1995 , CMS Document 96-89,

A.Zarubin, “CMS Cathode Strip Chambers,” 6th topical Seminar on Experimental Apparatus for Particle Physics and Astrophysics, San Miniato, Italy, May 20-25, 1996, 1996-133 CMS TALK,

I.Gramenitsky, “Some results of the Integrated test” in: Proceedings of “Second Annual RDMS CMS Collaboration Meeting,” CERN, December 16-17, 1996 , CMS Document 1996-213,

V.Palichik, “Efficiency of muon track reconstruction in the Integrated” in: Proceedings of "Second Annual RDMS CMS Collaboration Meeting,” CERN, Dec 16-17, 1996, CMS Document 1996-213,

I.Golutvin, I Gramenitsky, P.Moissenz et al., “Muon track reconstruction efficiency of ME1/1 prototype in the integrated test,” CMS Note/1997-084,

A.Chvyrov et al, “Study of 'comparator' and 'digital' algorithms for muon trigger with MF1 prototype '95 test beam data,” CMS TN/95-160,

V.Karjavin, “Muon Trigger based on MF1 test results” in: Proceedings of “First Annual RDMS CMS Collaboration Meeting,” CERN, December , 1995, CMS Document 96-89.

[4.29] Dubna X-rays prototype results: notes and presentations:

A.Zarubin et al., “Status of MF1/1 and preliminary results of CSC rate capability,” CMS Collaboration Meeting, 1966-143, Aachen, Germany, September 11-12, 1996,

A.Zarubin et al., “MF1/1 Status report,” 1996-148 CMS meeting, Muons, CERN, October 7-10, 1996,

S.Movchan et al., “Dubna ME1/1 Status Report,” CMS Collaboration Meeting, 1966-191, CERN, December 11-12, 1996,

P.Moissenz, “Study of ME1/1 rate capability” in: Proceedings of “Second Annual RDMS CMS Collaboration Meeting,” CERN, December 16-17, 1996 , CMS Document 1996-213.

[4.30] Dubna P3 prototype results: notes and presentations:

Yu.Kiryushin “ME1/1 status and milestones” in: Proceedings of “Second Annual RDMS CMS Collaboration Meeting,” CERN, December 16-17, 1996 , CMS Document 1996-213,

Yu.Erchov, I.Golutvin, V.Karjavin et al., “Fabrication and test of the full-scale P3 prototype of the ME1/1 CSC,” CMS IN 1997/003, CERN, 1997

I.Golutvin, “RDMS participation in CMS, Second CMS Heavy Ion Meeting,” Feb.4-6, 1997, Dubna, Russia. CMS conference, 1997-011,

A.Zarubin et al. “Dubna P3 ME1/1 prototype high rate '97 tests with Minsk electronics (Preliminary results),” 14 September, 1997, Madison, Wisconsin.

[4.31] Dubna P4 prototype:

I.Golutvin, et al. “RDMS CMS 1996 Annual report,” CERN, March 28, 1997 , CMS Doc 1997-048.

[4.32] US T0 prototype:

A.Korytov, “T0 test setup and first experiences with it,” CMS EMU meeting, Feb 4-5, 1995,

O.Prokofiev, “Progress report on T0 prototype tests,” CMS EMU meeting, July 8, 1995, Boston,

O.Prokofiev, “Summary of T0 prototype tests at FNAL,” CMS EMU meeting, Sept 25 1995,

N.Bondar et al., “Study of T0 CSC prototype at FNA,” CMS TN/95-131.

[4.33] US P0+P0' prime:

D.Klem, “P0 timing results,” CMS EMU meeting, Feb 2, 1996, Gainesville,

L.Gorn, “P0 strip resolution,” CMS EMU meeting, Apr 11, 1996, Madison,

L.Gorn, “Half-strip comparator board: beam test results and simulation” CMS EMU meeting proceedings, Nov 22-23, 1996, Riverside,

L.Gorn, “Half-strips: comparator vs threshold schemes (beam test results with Si telescope),” CMS EMU meeting proceedings, CMS Week, March 1996,

P.Giacomelli, “P0' preliminary test beam results,” CMS EMU meeting, Feb 21, 1997, Houston,

M.Baarmand et al, “Tests of CSC Prototypes,” CMS Note 1997/72, to be published in Nucl. Instr. and Meth.

[4.34] US T1's:

O.Prokofiev, “T1 design report,” CMS EMU meeting proceedings, Apr 21, 1995, Maryland,

O.Prokofiev, “T1 construction and first results,” CMS EMU meeting, Nov 17, 1995, Fermilab,

A.Bujak, “Testing the T1 prototype,” CMS EMU meeting, Feb 2, 1996, Gainesville,

S.Medved, “Experience with shielding and grounding,” CMS EMU meeting, Mar 10, 1996, Madison,

A.Bujak, “T1: cathode electronics calibratio,” CMS EMU meeting, Mar 10, 1996, Madison,

A.Korytov, “CSC Q&A,” Meeting with referees at CERN, April 24-26, 1996, CMS Meeting 96-90.

[4.35] US P1A:

O.Prokofiev, “P1A design and construction,” CMS EMU meeting, Apr 11, 1996, Madison,

A.Bujak, S.Medved, O.Prokofiev, “P1A results,” CMS EMU meeting, June 17, 1996, Fermilab,

A.Bujak, S.Medved, O.Prokofiev, “P1A results.” CMS EMU meeting, Aug 29, 1996, Fermilab.

[4.36] US P1:

O.Prokofiev, V.Razmyslovich, “P1 design,” CMS EMU meeting, June 17, 1996, Fermilab,

O.Prokofiev, “First P1 tests,” CMS EMU meeting proceedings, Nov 22-23, 1996, Riverside,

D.Eartly et al., “Six-layer P1 CSC prototype,” CMS Note 1997/011,

A.Bujak, “P1 strip resolution,” CMS EMU meeting proceedings, Nov 14-15, 1997, Fermilab.

[4.37] US P2:

O.Prokofiev, “P2 design,” CMS EMU meeting proceedings, Feb 20, 1997, Houston.

[4.38] CF4 aging-preventive properties has been reported in:

R.Henderson et al., IEEE Trans. Nucl. Sci. NS-34 (35) (1988) 477,

R.Opershaw et al., IEEE Trans. Nucl. Sci. NS-36 (1) (1989) 567,

J.A.Kadyk, IEEE Trans. Nucl. Sci. NS-37 (1990) 478,

A.Korytov et al., Nucl. Instr. and Meth. A338 (1994) 375.

[4.39] CMS CSC aging test results have reported in (to be published):

G.Gavrilov et al., “Aging Test Station for Investigation of Gas-Filled Detector,”

Project Status Report No.1, Feb 28, 1997,

Project Status Report No.2, May 31, 1997,

Project Status Report No.2, Aug 31, 1997,

G.Gavrilov et al., “Recent Aging Results,” CMS EMU meeting, Nov 14-15, 1997, Fermilab.

5. RESISTIVE PLATE CHAMBERS

5.1 GENERAL DESCRIPTION

5.1.1 Overview

Resistive Plate Chambers (RPC) are gaseous parallel-plate detectors that combine good spatial resolution with a time resolution comparable to that of scintillators [5.1]. They are therefore well suited for fast space-time particle tracking as required for the muon trigger at the LHC experiments.

An RPC consists of two parallel plates, made out of phenolic resin (bakelite) with a bulk resistivity of 10^{10} - 10^{11} Ωcm, separated by a gas gap of a few millimeters. The whole structure is made gas tight. The outer surfaces of the resistive material are coated with conductive graphite paint to form the HV and ground electrodes. The read-out is performed by means of aluminum strips separated from the graphite coating by an insulating PET film.

So far, RPCs have been operated in streamer mode, i.e. the electric field inside the gap is kept intense enough to generate limited discharges localized near the crossing of the ionizing particle. However, the rate capability obtained in such operational conditions is limited (~100 Hz/cm^2) and not adequate for LHC.

A significant improvement is achieved by operating the detector in the so-called avalanche mode [5.2]; the electric field across the gap (and consequently the gas amplification) is reduced and a robust signal amplification is introduced at the front-end level. The substantial reduction of the charge produced in the gap improves by more than one order of magnitude the rate capability.

An RPC is capable of tagging the time of an ionizing event in times shorter than the 25 ns between two successive bunch crossings (BX). A fast dedicated muon trigger detector, based on RPCs can therefore identify unambiguously the relevant BXs with which the muon tracks are associated, even in the presence of the high rate and background expected at LHC. Signals from such detectors directly provide the time and the position of a muon hit with the required accuracy.

The trigger based on such a detector has to perform three basic functions simultaneously:

- identify candidate muon track(s);
- assign a bunch crossing to the candidate track(s);
- estimate their transverse momenta.

All these functions must be performed with high efficiency in an environment where due to the gamma and neutron background, the hit rates may reach 10^3 Hz/cm^2.

A total of six layers of RPCs will be embedded in the barrel iron yoke, two located in each of the muon stations MB1 and MB2 and one in each of the stations MB3 and MB4. The redundancy in the first two stations will allow the trigger algorithm to perform the reconstruction always on the basis of four layers, even for low p_T tracks, which may be stopped inside the detector.

In the forward region, the iron will be instrumented with four layers of RPCs to cover the region up to $\eta = 2.1$. However, a possibility for upgrading the system up to $\eta = 2.4$ is kept open. Figs. 5.1.1a and 5.1.1b show the RPC location in the R-Z view (both for barrel and endcap) and in the ϕ view (barrel only), respectively.

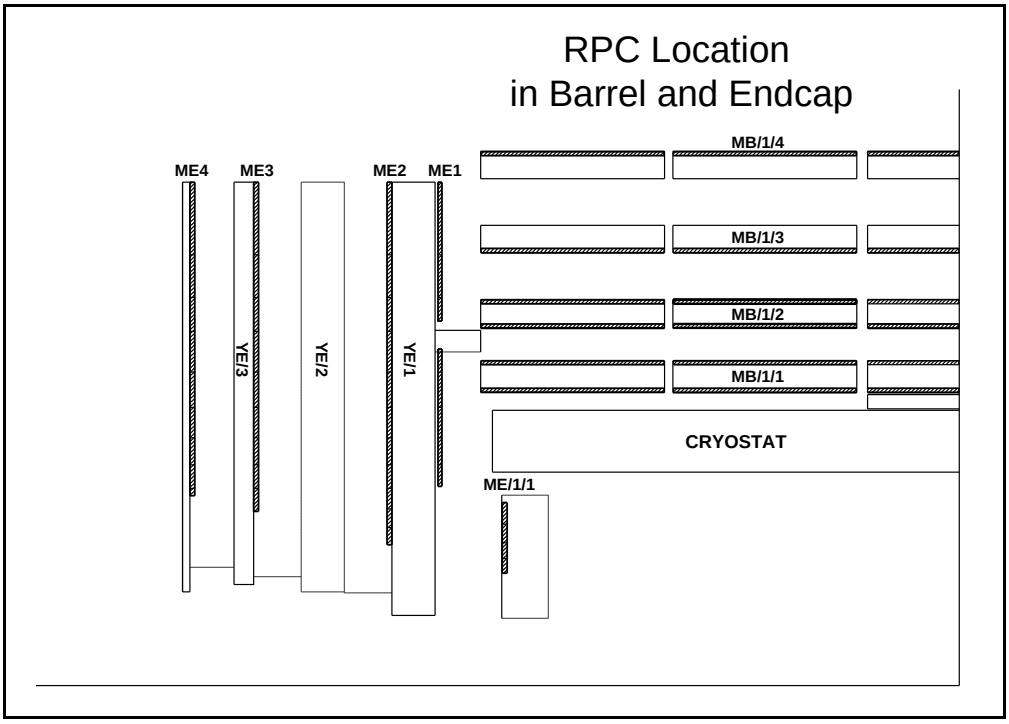


Fig. 5.1.1a: RPC location in R-Z.

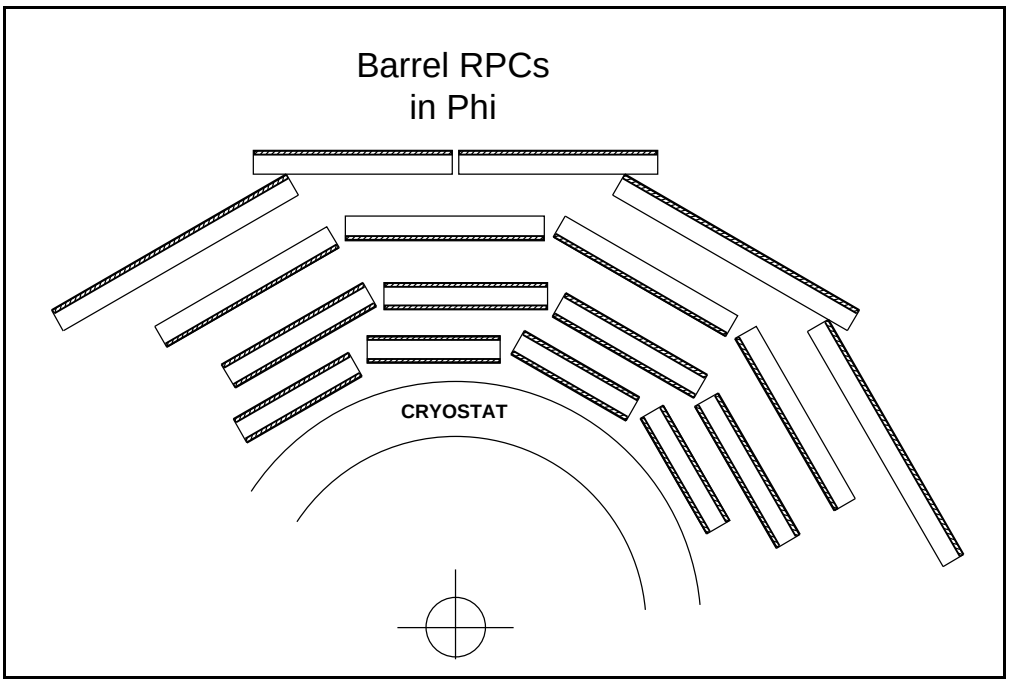


Fig. 5.1.1b: RPC location in ϕ (barrel only).

5.1.2 Specific conditions and requirements

The RPCs should fulfill some basic specific requirements: good timing, low cluster size, good rate capability. Moreover, they are expected to respond with high intrinsic efficiency and to withstand long term operation in high background conditions.

Good time performance is crucial for triggering with high efficiency. Muon identification within a 25 ns window requires not only a few nanoseconds resolution, but also that the tails of the signal time distribution stay within the window. This implies that the time walk due to the propagation of the signals along the strips and to the possible rate variation (which may affect the drift velocity), should be kept within a few nanoseconds. In CMS, long strips are used in the barrel region where rate effects are negligible, while very short strips are used in the endcap where the rate problem is more severe. The total tolerable time walk introduced by both effects should not exceed 4-5 ns.

In Fig. 5.1.2 the achievable trigger efficiency, computed using a full simulation of the CMS trigger detector [5.3], is shown as a function of the RPC time resolution and efficiency. Results only refer to muons generated in the region $-0.09 < \eta < 0.09$ with $50 < p_T < 70$ GeV/c and subject to a p_T^{cut} of 5 GeV/c. A more detailed discussion of the trigger algorithm performance will be presented in section 5.10.

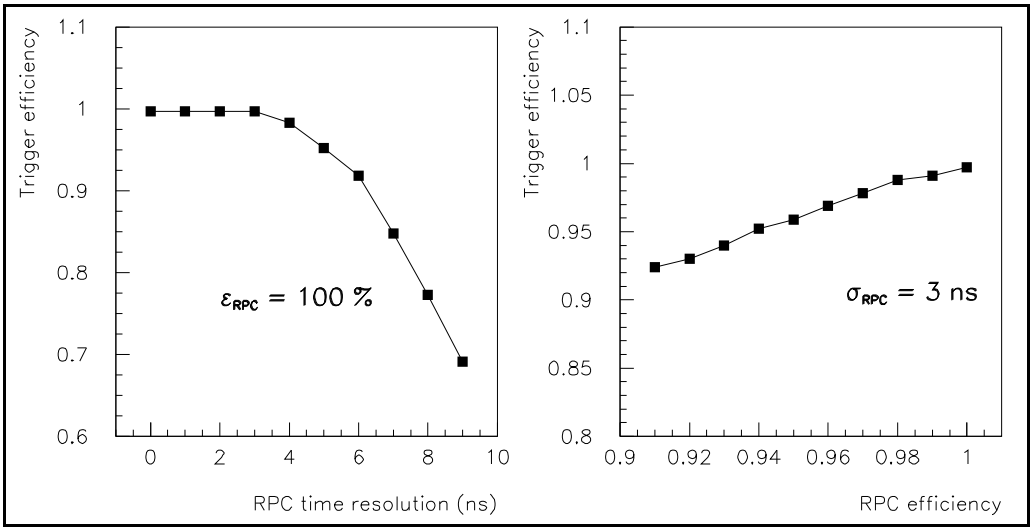


Fig. 5.1.2: Dependence of the trigger efficiency on the RPC time resolution (a) and on the RPC efficiency (b) for muons generated in the region $-0.09 < \eta < 0.09$ with $50 < p_T < 70$ GeV/c and subject to a p_T^{cut} of 5 GeV/c.

The cluster size (i.e. the number of contiguous strips which give signals at the crossing of an ionizing particle) should be small (≤ 2) in order to achieve the required momentum resolution and minimize the number of possible ghost-hit associations.

Finally, the rate capability should reach 1 kHz/cm^2 ($\varepsilon > 95\%$ at 1 kHz/cm^2). According to recent computations (as discussed in Chapter 2), the hit rate associated with the neutron and gamma background is 20 Hz/cm^2 in the barrel region and reaches a maximum of 250 Hz/cm^2 in the forward region at η=2.1. A reasonably safe estimate of 1 kHz/cm^2 gives therefore the highest rate at which the RPCs are expected to operate.

The full exploitation of the RPC time capability requires working at gains as high as 10^7. This makes the high rate operation sensitive to the resistance of the electrodes, because a sizable voltage drop is generated in the gas gap by the flow of the current across the resistive plates. This point will be discussed in detail in Section 5.2.2. Moreover, in a parallel plate chamber like an RPC, a large voltage has to be applied to generate a field intensity sufficient for electron multiplication; this makes the energy dissipated in the gas non-negligible. A limit not much larger than 2 W/m^2 should be achieved. This effect can be limited by an appropriate choice of the gas mixture and the gap width.

In Table 5.1.1 the main requirements are listed. It is also important to avoid, during the operation, the occurrence of streamers because the large amount of charge involved increases the current unnecessarily.

Table 5.1.1
CMS requirements for RPCs

Efficiency	> 95%
Time resolution	≤ 3 ns (98% within 20 ns)
Average cluster size	≤ 2 strips
Rate capability	≥ 1 kHz/cm^2
Power consumption	< 2-3 W/m^2
Operation plateau	> 300 V
# Streamers	< 10%

5.2 PRINCIPLES OF OPERATION

In this section the relevant detector parameters and the basic physical principles underlying the RPC signal formation will be briefly discussed. The electrode resistivity mainly determines the rate capability, while the gap width determines the time performance. Other parameters, such as the gas cluster density and the electrode thickness, are also important and should be optimized to achieve the best performance.

In Fig. 5.2.1 a simple model of the charge formation in an RPC is schematically presented: a cluster of n_0 electrons, produced by an ionizing particle, ignites the avalanche multiplication.

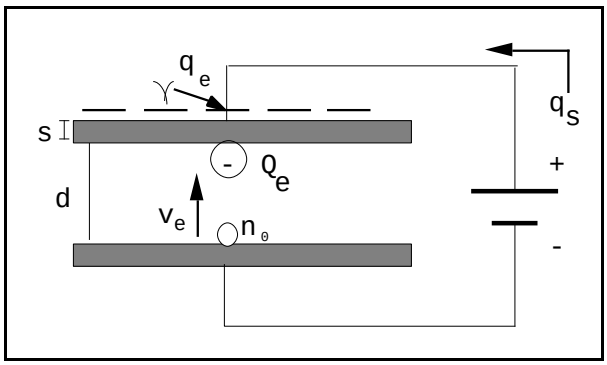


Fig. 5.2.1: Model of the charge formation in the RPC gap.

An electronic charge Q_e (d) is then developed inside the gap of height d. The drift of such charge towards the anode induces on the pick-up electrode the "fast" charge q_e, which represents the useful signal of the RPC.

The power supply has to move the charge q_s in the circuit outside the gap in order to compensate the charge collected on the electrodes. If α is the number of ionizing encounters per unit length undergone by one electron and the attachment coefficient β the number of attaching encounters per unit length, the effective ionization coefficient can be defined as $\eta = \alpha - \beta$.An RPC is said to work in "avalanche" or "low gain mode" if the condition $\eta d < 20$ is satisfied. It has been shown [5.4] that, in this case, the average fast charge q_e of a single avalanche can be evaluated as:

$$\langle q_e \rangle = \frac{k}{\eta d}\langle Q_e(d)\rangle = q_{el} n_0 \frac{k}{\eta d}\frac{\lambda}{\eta+\lambda}e^{\eta d} \qquad (5.1)$$

where $k= (\varepsilon_r d/s)/(\varepsilon_r d/s +2)$ is a constant depending on material parameters, and

- q_{el} is the electron charge,
- n_o is the average size of the primary cluster from which the avalanche originated,
- λ is the cluster density in the gas mixture (i.e. the number of primary clusters/unit length produced by an ionizing particle),
- ε_r is the relative dielectric constant of the electrode,
- d is the gap width,
- s is the electrode thickness.

For a given ηd, the factors k and λ should be as large as possible, in order to maximize the useful signal on the strip.

This simple model represents a valid approximation for our discussion. However, more clusters may develop in the gap. A better estimate of the average induced charge can be obtained by means of Monte Carlo simulations, where fluctuations of the avalanche can also be considered.

5.2.1 Simulation of avalanche growth and signal development

A detailed description of the simulation algorithms can be found in [5.5]; a comparison between model prediction and experimental results can also be found in [5.6].

The primary cluster positions and the avalanche growth are assumed to follow, respectively, simple Poisson statistics and the usual exponential law. After the simulation of the drifting avalanches, the total charge q_e, induced on the external pick-up electrodes (strips or pads) by the avalanches' motion, can be computed by means of the following formula:

$$q_e = \frac{k}{\eta d}Q_e(d) = \sum_{cluster} n_{0i}\, q_{el} M_i k\left[e^{\eta(d-xoi)} - 1\right]$$

where x_{0i} is the i-th cluster`s initial distance from the anode, n_{oi} is the number of initial electrons in the cluster, and M_i is the avalanche gain fluctuation factor [5.7].

In addition to q_e, (and more interesting) the current $i_{ind}(t)$ induced on the same electrodes (as a function of time) by the total drifting charge $Q_e(t)$ can also be computed [5.8]. The computation of $i_{ind}(t)$ provides complete information on the output from an RPC; it is possible

to input the simulated signals in simulated amplifiers, discriminators, etc., reproducing with accuracy the data-taking conditions of a real experiment.

Monte Carlo results on the charge spectrum and the efficiency of a 2 mm gap RPC, operated with an effective ionization coefficient η =8.3 mm^{-1} and a gas cluster density λ = 5.5 clusters/mm, are reported in Fig. 5.2.2. Experimental results, obtained with a small 50x50 cm^2 detector operated at equivalent conditions, are also superimposed. The experimental 1 mV amplitude threshold has been simulated with a 100 fC charge threshold.

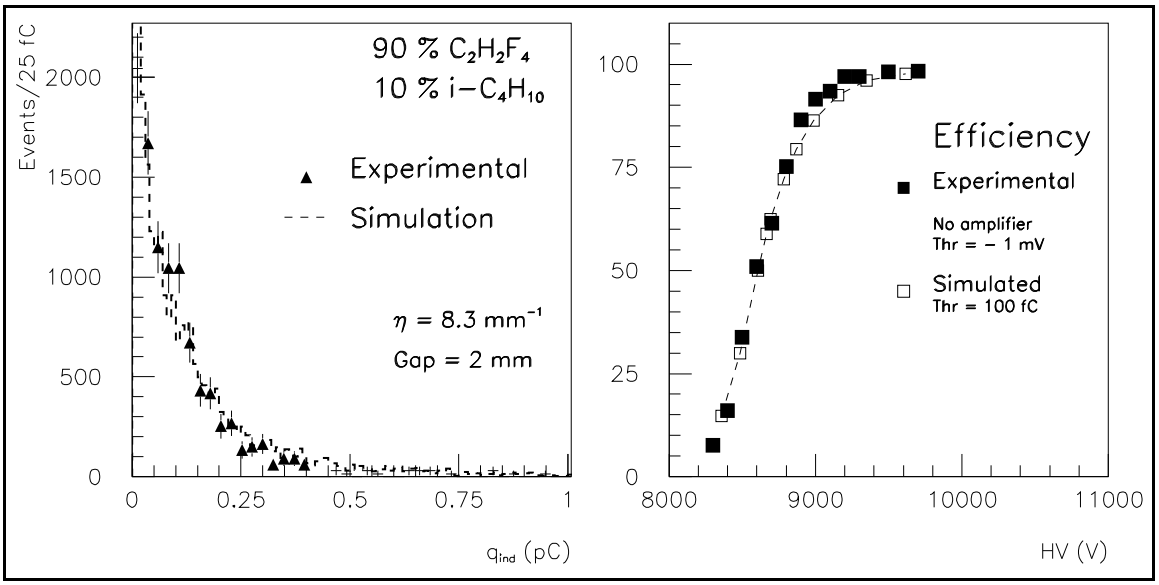


Fig. 5.2.2: Simulated and experimental results for the spectrum and the efficiency of a 2 mm RPC.

5.2.2 Material specification and basic parameters

5.2.2.1 Electrode composition and surface treatment

The resistive electrodes are usually made of bakelite (phenolic resin) plates covered with a thin layer of melamine. The bulk resistivity ρ of the bakelite plates should be optimized according to the required rate capability, which is strongly dependent on it. There are two main effects: first, the time constant $\tau = \varepsilon_0(\varepsilon_r+2)\rho$ of an elementary RPC cell involved in an avalanche process is smaller at lower resistivity; moreover, at very high rate, the flow of total current through the plates becomes important and produces a drop of voltage V_d across them. A lower "effective voltage" is therefore applied to the gas gap, resulting in a lower gas amplification. Both effects can be reduced by choosing an appropriate low value for the bulk resistivity. By simple electrostatic considerations [5.10], the voltage drop can be estimated as

$$V_d = 2\langle Q_e \rangle r\, s\, \rho$$

where r is the rate/cm^2, ρ is the bulk resistivity and the other quantities have already been introduced. Assuming, for example, $\langle Q_e \rangle$ = 25 pC and r = 10^3/cm^2, a value of ρ in the range 1-2*10^{10} Ωcm should be used to limit V_d to few tens of volts. A larger voltage drop would influence not only the rate capability, but also the pulse delay due to the change of drift velocity, as discussed later.

The surface quality of the electrode is crucial in reducing spontaneous discharges which might affect the rate capability of the chamber. Recently, a major improvement in the quality of the surface has been obtained by using more precise tools in the production procedure.

The "roughness" R_a, defined as the vertical deviation of the surface from its average profile, has been measured on different bakelite sheets. The values of R_a, averaged over the sampling length of a few millimeters, are shown in Fig. 5.2.3, at several arbitrary positions, for the following types of plates:

- standard Italian bakelite, used for the L3 and the BABAR RPC production,
- improved Italian bakelite, recently used by the CMS RPC group,
- bakelites used by other groups,
- melamine.

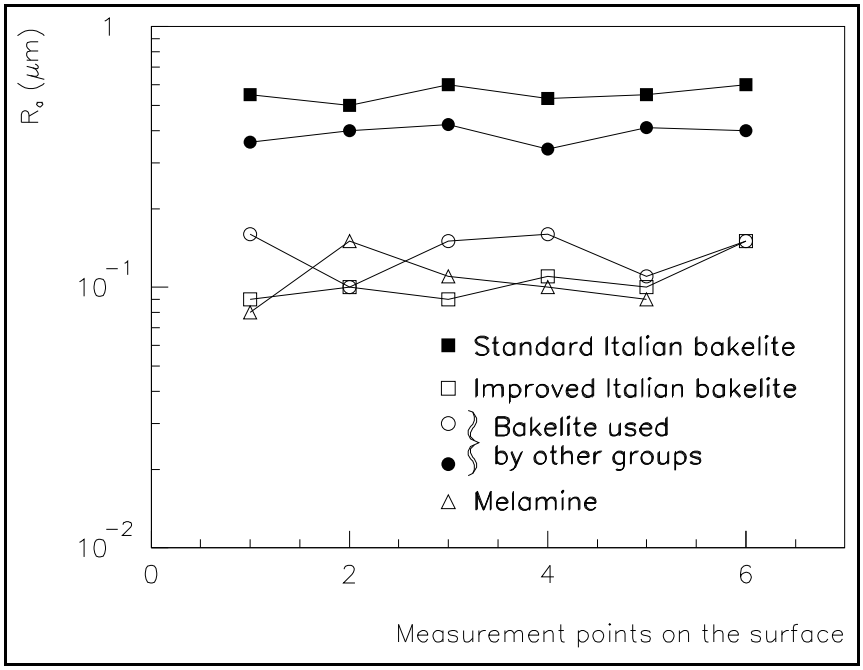


Fig. 5.2.3: Values of roughness R_a at several positions (1 cm apart) for different 10x10 cm^2 bakelite sheets.

Recent production has reduced the "roughness" of the surface by a factor of 6. The possibility of a quantitative characterization of the electrode surfaces can be exploited, during the production, to set up a control procedure. Encouraging results (see Section 5.9) on chamber performance have been obtained with these new electrodes. The linseed oil treatment [5.9], which has been traditionally employed to smooth the electrode surface, is not crucial for the detector operation, provided the bakelite plates have good surface quality and the assembly is cleanly and correctly done.

5.2.2.2 Gas mixture

The gas cluster density λ is crucial for exploiting the best detector performance. In principle, λ should be as large as possible to maximize the signal and to achieve high efficiency (see equation 5.1). Recently, 2 mm gap RPCs have been successfully operated with a $C_2H_2F_4$ based mixture (λ ~5 clusters/mm). Lower density gas mixtures (for example, argon-based

mixtures) have $\lambda \sim 2.5$ clusters/mm and do not allow high efficiency with low streamer contamination [5.10].

The drift velocity ofelectrons in different $C_2H_2F_4$ based mixtures at various electric fields has been recently measured [5.11,5.12]. In Fig. 5.2.4 the results for a 90% $C_2H_2F_4$, 10% i-C_4H_{10} mixture are shown. In the region of interest (streamer free operation) the drift velocity grows linearly with the applied electric field. At high rate, where the effective field applied to the gap is reduced, as discussed previously, the decrease of drift velocity may result in a longer response time. Again, a bakelite resistivity value in the range 1-2 $\cdot 10^{10}$ Ωcm will keep this effect within the requirements stated in Section 5.1.2.

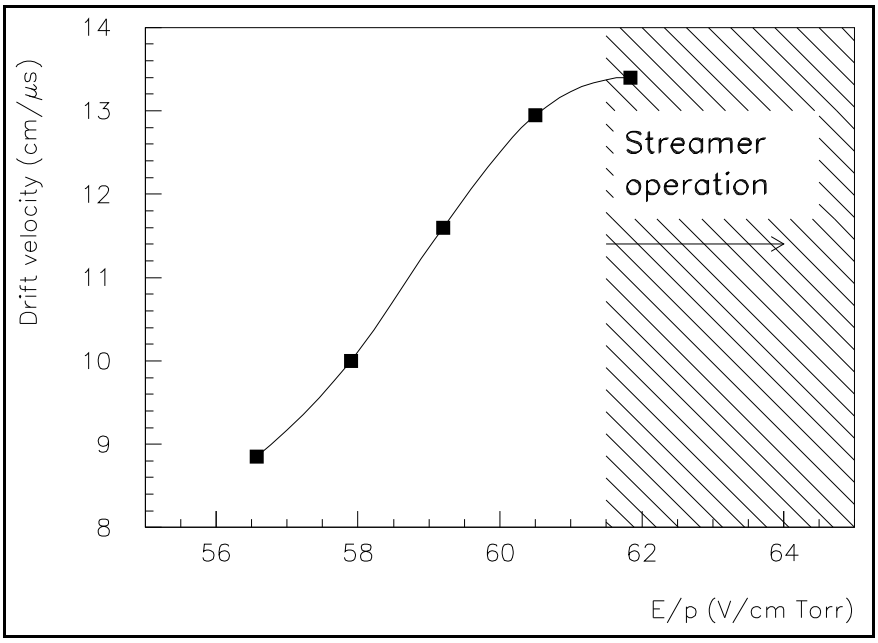


Fig. 5.2.4: Drift velocity for the 90% $C_2H_2F_4$, 10% i-C_4H_{10} gas mixture. The streamer operation region refers to a 2 mm gap RPC.

5.2.2.3 Gap width

The gap width affects the time performance of the detector. Fig. 5.2.5 shows the simulated achievable time resolution as a function of the gap width, assuming a gas cluster density $\lambda = 5$ clusters/mm and an electron drift velocity v= 130 μm/ns. Also the full width at the base (FWAB), defined as the time interval containing 95% of the events, is given. The performance, as expected, becomes poorer at wider gaps, due to the larger fluctuations present during the avalanche development. A 2 mm gap width seems the most appropriate choice.

5.2.3 The double-gap design

More gaps may be put together to increase the signal on the read out strip, which sees the sum of the single gap signals. This makes it possible to operate single-gaps at lower gas gain (lower high voltage) with an effective detector efficiency which is the OR of the single-gap efficiencies.

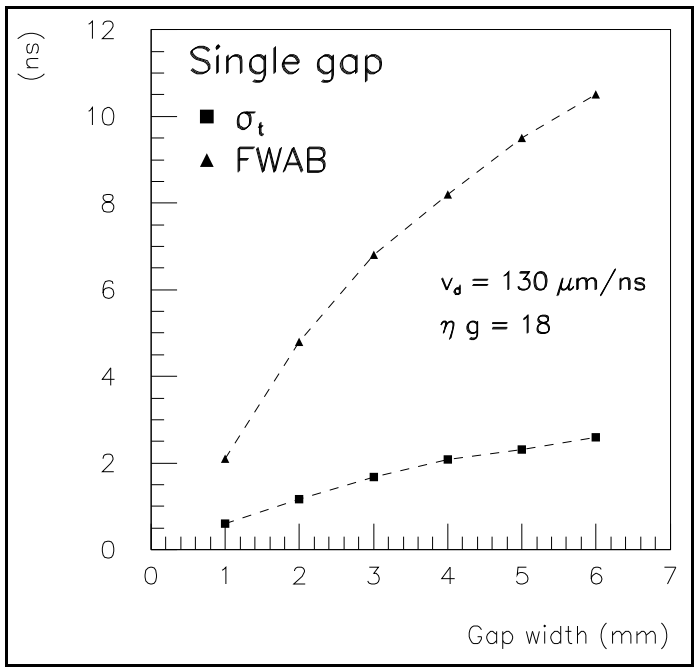


Fig. 5.2.5: Simulated time resolution as a function of the gap width.

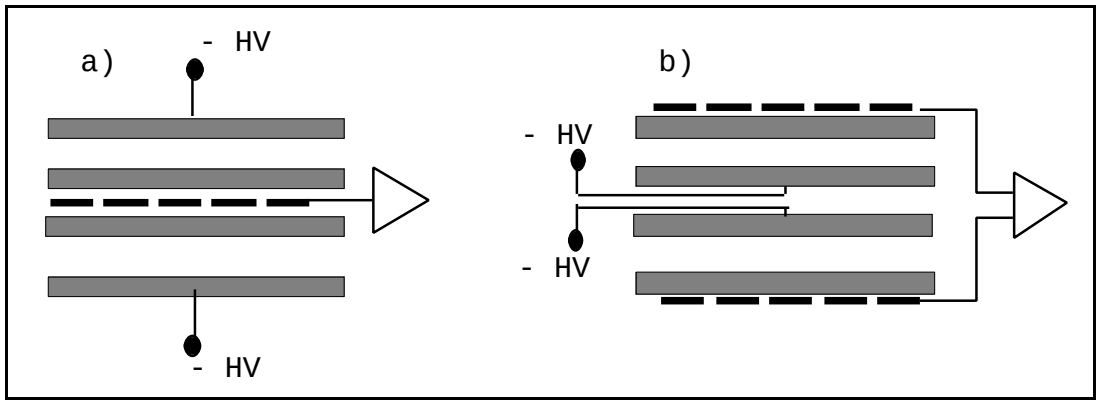


Fig. 5.2.6: Layout of a double-gap RPC: a) standard double-gap, b) double gap with two read-out planes.

The RPC proposed for CMS is made of two gaps with common pick-up strips in the middle (hereafter referred to as a double-gap RPC). A simplified layout of the double-gap design is shown in Fig. 5.2.6a. Alternatively, in the cases where the signal extraction is difficult, the layout shown in Fig. 5.2.6b could be adopted, with two independent read-out planes located externally and having their signals ORed, strip by strip, before entering the front-end. In both cases, the total induced signal is the sum of the two single-gap signals. Several studies on double-gap RPCs have been already reported in [5.4], [5.10] and [5.13].

The charge spectrum improves, as shown in Fig. 5.2.7, where also the single-gap spectrum (from Fig. 5.2.2) is shown for comparison (normalized to the area). Safer operation at higher threshold can therefore be achieved without loss of efficiency.

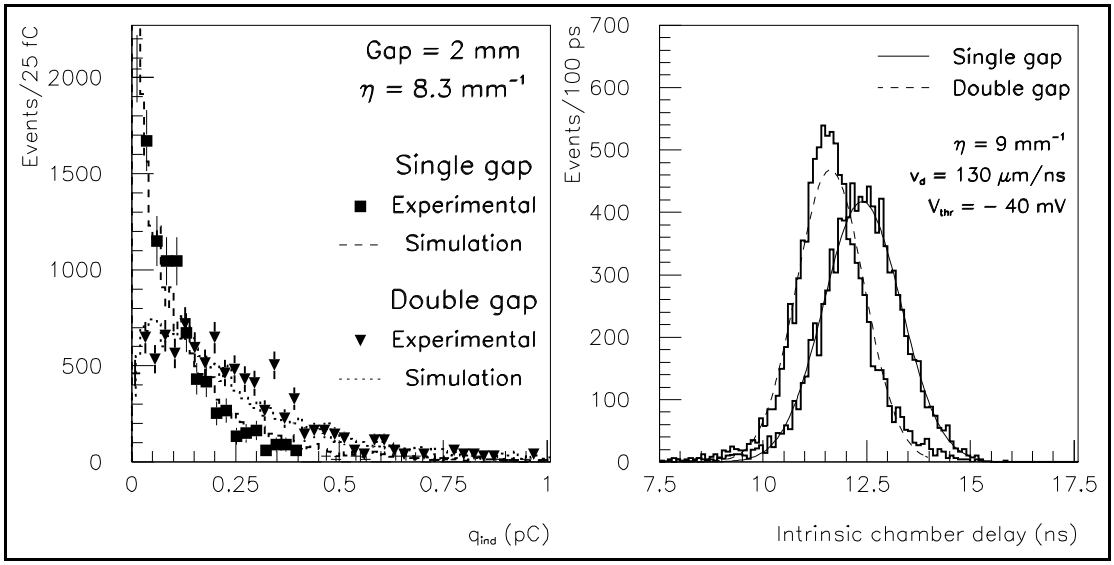


Fig. 5.2.7: Simulated and experimental charge spectra for a double-gap RPC.

Fig. 5.2.8: Simulated time distribution for single-gap and double-gap 2 mm RPCs

Also the time resolution is expected to improve, as shown in Fig. 5.2.8, where the results of the simulation for single-gap and double-gap (2 mm wide) RPCs are superimposed. These distributions refer to the case of $\lambda = 5$ clusters/mm. The arrival time is relative to the passage of the ionizing particle.

The predicted resolution of the 2 mm single-gap time response is about 1.4 ns. This value seems to be a lower limit, related to the statistical processes taking place during the avalanche development and to the walk produced by the signal amplitude fluctuations. However, other effects, such as electronic noise and local variations of electric field must be taken into consideration, to account for the realistic experimental resolution.

In Table 5.2.1 the basic construction and operating parameters of the CMS double-gap RPCs are given.

Table 5.2.1
Basic construction and operating parameters.

Bakelite thickness	2 mm
Bakelite bulk resistivity	$1\text{-}2 \cdot 10^{10}$ Ω cm
Gap width	2 mm
Gas mixtures	95% $C_2H_2F_4$, 5% i-C_4H_{10}
Operating High Voltage	8.5 - 9.0 kV
# Gaps	2

5.2.4 Aging studies

Three kind of aging effects should be considered:

- aging of the materials irrespective of the working conditions,
- aging due to the integrated dissipated current inside the detector,
- aging due to irradiation.

5.2.4.1 Aging of the materials

Resistive Plate Chambers have been used in various experiments since the 1970s, such as E771, WA92, E831 and RD5 [5.14]. The most recent one is L3 where a 600 m^2 detector has been successfully operated since 1994 as the muon trigger in the forward part [5.15]. BABAR has also decided to instrument the return yoke of its magnet with RPCs [5.16].

No experiment has reported any aging effect on the RPCs material over the period of time in which they have operated. Moreover, the efficiency and the time resolution of the chambers have remained constant over the running period.

5.2.4.2 Aging due to the integrated dissipated current inside the detector

Although all the mentioned experiments have operated RPCs in "streamer" mode, no degradation of the performance has been reported. The small charge (a factor 100 less with respect to the streamer) produced in the avalanche mode ensures safe long term operation.

5.2.4.3 Aging due to irradiation

One of the major concerns related to the neutron flux and dose rate in the experimental areas at LHC is the material radiation damage.

According to the energy of the neutrons, different processes can take place in organic materials such as those used in RPCs. In the reaction with the nuclei of an irradiated medium, fast neutrons transfer a considerable amount of their energy.

Thermal neutrons undergo nuclear capture and the resulting emitted radiation (gamma rays in the MeV range for the most probable reaction with hydrogenated compounds) is responsible for subsequent excitation and ionization via secondary processes (mainly Compton scattering and photoelectric effect).

The expected dose rate in the CMS barrel region does not exceed 1 Gy/year (100 Rad/year). A factor of 100 larger dose is expected in the forward region. A dose rate of 1 Gy/year is consistent with a particle dose of fast neutrons (> 1 MeV) equivalent to some 10^{10} n/cm^2.

In the case of bakelite, for example, the fluence of fast neutrons corresponding to a deposit of 100 Rads/cm^2 is $4.6*10^{10}$ n/cm^2. Similar fluences, for the same dose, are needed for Mylar ($6*10^{10}$ n/cm^2) and Polyethylene ($2.2*10^{10}$ n/cm^2).

Some preliminary irradiation tests have been carried out with the 250 kW Triga Mark II research reactor located in Pavia. Small bakelite samples have been exposed in the core of the reactor. An initial heavy irradiation (about 4.5 10^{16} thermal n/cm^2) has been performed in order to analyze the radioisotope content of the samples. More realistic exposures (10 LHC years equivalent) of the bakelite samples will be performed.

Complete tests planned for 1998 involve exposure of a small operating RPC to a fast neutron beam.

In parallel, an irradiation facility for long term aging tests is under development in the Bari Physics Department and INFN laboratory. A large RPC cosmic ray telescope, used in the past to study horizontal cosmic muons [5.17], has been upgraded to host an irradiation area, where large RPCs (1.0 x 1.5 m^2) can be located.

The telescope offers good tracking and pattern recognition capability through eight 2x2 m^2 additional RPCs situated at both ends of the irradiation area. On each side, two such chambers are read out with vertical strips and the remaining two with horizontal strips, in order to gain information both on x and y coordinates. The response of the irradiated detectors to the passage of an ionizing particle can be studied accurately and monitored during the operation for the whole chamber surface.

Three ^{137}Cs sources, 5 mCi each, have been installed. The chamber is uniformly irradiated at a hit rate of 500 Hz/cm^2, which is a factor of 2 larger than what is expected in the higher η region of CMS. Fig. 5.2.9 shows a layout of the telescope with the irradiation area. The operation started in October 1997, and it is scheduled to continue with no interruption for at least the next two years.

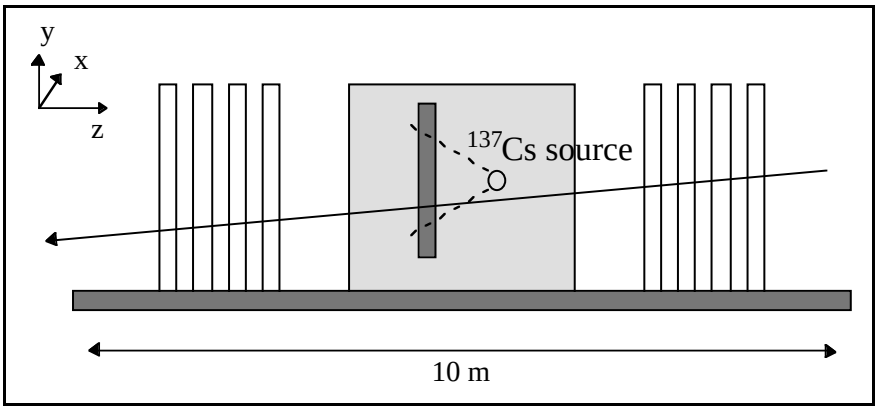


Fig. 5.2.9: Layout of the Bari irradiation facility.

5.3 RPC CONSTRUCTION AND TOOLS

Recent R&D results have shown that RPCs suitable for operation at low gain and high rate can be constructed using materials and technologies developed in the past and already employed for the L3 and BABAR mass productions. Only a few basic physical parameters (gas mixtures, plates resistivity, plate surface treatment) need to be adapted in order meet the CMS operation requirements.

The large production of RPCs for CMS can therefore be made on an industrial basis, following well established procedures developed several years ago by R. Santonico [5.1]. The construction requires two rectangular 2 mm thick bakelite plates kept at a fixed distance (2 mm $\pm$ 30 μm) by insulating spacers about 10 mm in diameter distributed over the entire surface in a square mesh of 100x100 mm^2. A schematic layout of an RPC is shown in Fig. 5.3.1.

The bakelite plates are first selected on the basis of their resistivity, which should be peaked around $2*10^{10}$ Ωcm and distributed over a wide range ($\pm 1*10^{10}$ Ωcm). At the same time, a sample surface roughness test is performed.

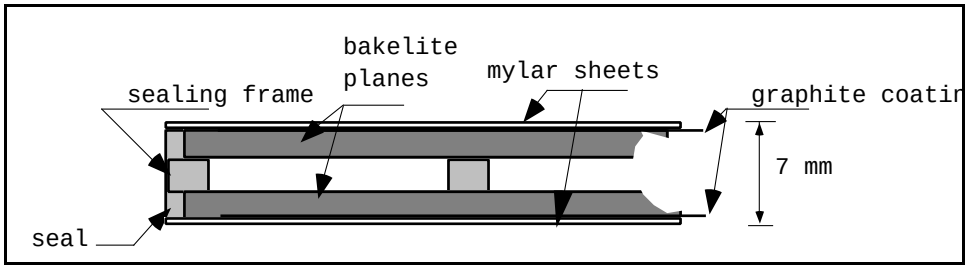


Fig. 5.3.1: Section of the end of a chamber (single-gap), showing plates, spacers, frame and seal of one gap.

Basic steps for the construction are:

- the bakelite plates are cut to the required dimensions.
- one side of each bakelite plane is painted with graphite (surface resistivity about 300 kΩ per square), by means of the facility shown in Fig. 5.3.2.
- on the graphite coated surface a 0.3 mm thick PET film is glued to provide HV insulation. This is done by means of a 'hot melt' facility, shown in Fig. 5.3.3.
- two such plates are glued together (graphite on the outside) with the spacer mesh on the inside, and a narrow (order of 7 mm) frame all around to form the basic chamber.

After drying, gas inlets are mounted at the four corners and an additional araldite seal is placed around the entire package. The construction of the single-gap chamber terminates with the connection of the HV cables. Then each chamber is tested for gas leaks, flushed for at least 48 hours and a first V/I plot is made, which is checked against the resistivity values measured at the beginning of the process.



Fig. 5.3.2: The RPC graphite spraying facility.



Fig. 5.3.3: The PET film gluing facility.

The production capability of the existing tools is about 15-20 large size single-gaps/day. An important constraint for the CMS detector design is determined by the maximum size of available bakelite plates (1.3 m in width and about 4 m in length). Also the tools have been developed to treat plates not larger than the quoted dimensions. The CMS design, therefore, should be optimized to contain RPC module sizes within the above limits.

Finally two single-gaps are superimposed to form a double-gap chamber with the spacers overlapped. Although this introduces some dead area, it ensures that, after the assembly, no deformation of the gaps is produced.

In parallel to the above steps, a special tool (Fig. 5.3.4) is devoted to the production of the read-out strip planes. They are made by milling a 40 μm aluminum sheet glued on a 100 μm thick PET film.

5.4 BARREL DESIGN

5.4.1 Station layout

In the barrel iron, the RPCs are arranged in six layers. Each layer is a dodecagon with full 2π coverage. Two layers are located in MB1, two in MB2, one in MB3 and one in MB4. There are a total of 360 rectangular stations, each one with a length in the beam direction dictated by the 2560 mm wheel length in the Z direction, and a width ranging from 2000 (MB1) to 4000 (MB4) mm.

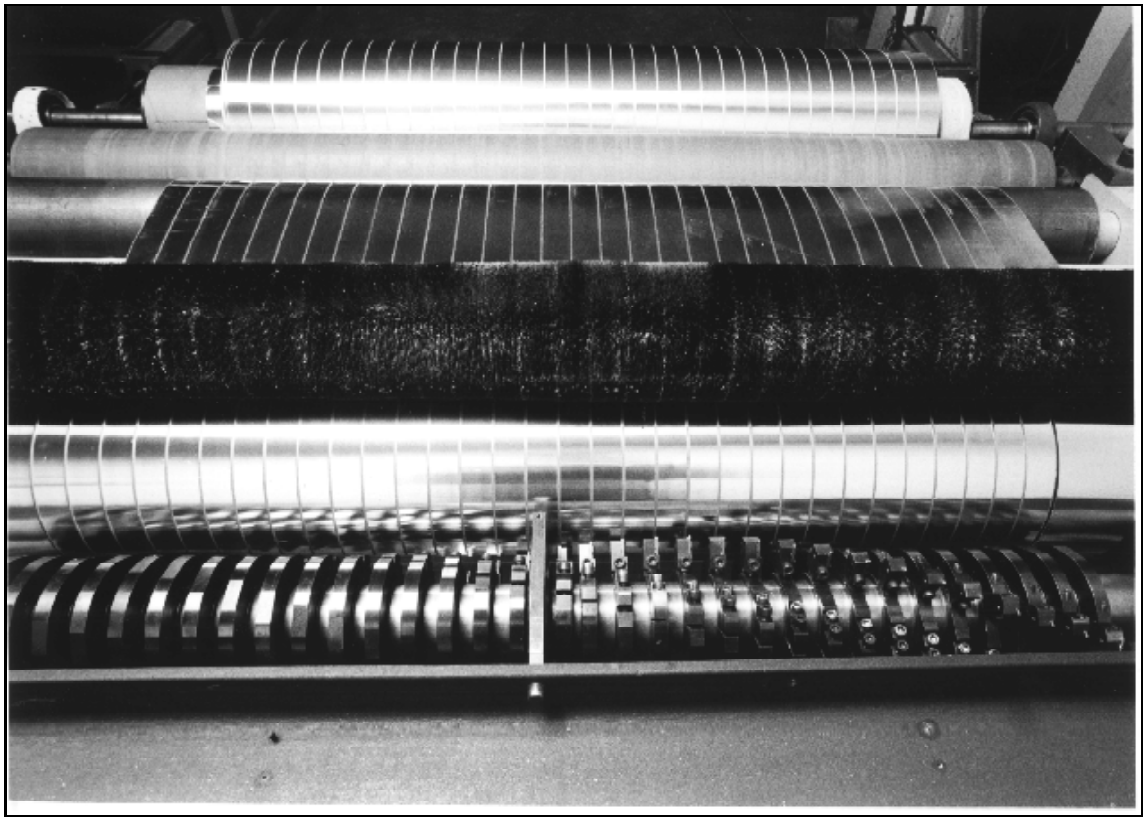


Fig. 5.3.4: The tool for the read-out strips production.

Physics requirements demand that in each station the strips, running always along the beam direction, be divided into two parts for stations MB1, MB3 and MB4. Station MB2, which represents a special case for the trigger algorithm, will have strips divided into three parts.

In each station, therefore, we have two (or three) double-gaps modules mounted sequentially along the beam direction to cover the whole area. In the case of two double-gaps, the strips will be 1300 mm long; in the case of three (only for one station in MB2), their length will be 850 mm. Fig. 5.4.1 shows a barrel station made of two (or three) double-gap modules.

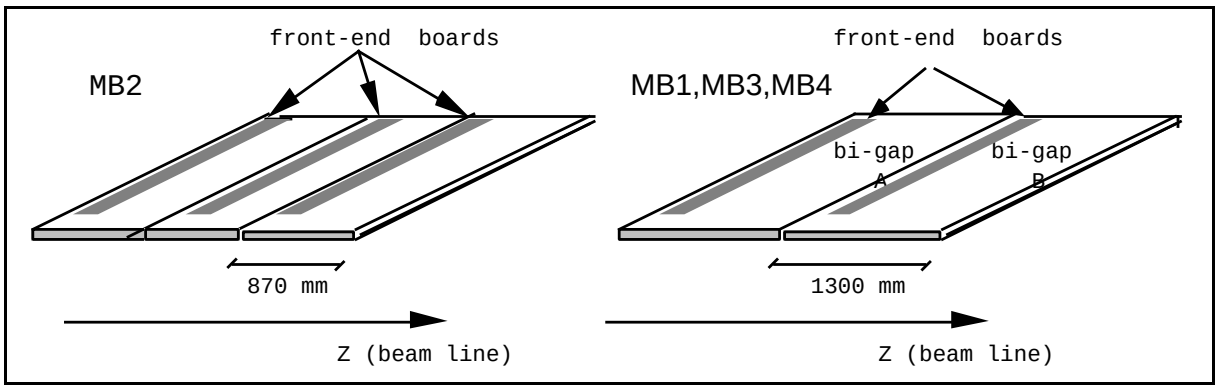


Fig. 5.4.1: Schematic layout of a barrel RPC station.

In each double-gap module, the front-end electronics board will be located at the strip end which minimizes the signal arrival time. For each double-gap 96 strips will be read out. Therefore, a total of 288 electronic channels are needed for each MB2 station and 192 for the other stations. The strip width will increase accordingly from the inner stations to the outer ones to preserve projectivity (each strip covers 5/16 degrees in ϕ). In Table 5.4.1 some global information on the barrel detector is given.

Table 5.4.1
Barrel detector totals.

Number of stations	360
Total surface area	2400 m^2
Number of double-gaps	840
Number of strips	80640

To reduce the effect of the dead zone produced along the line of contact, any station requiring only two sets of strips will be made of two double-gap chambers of different lengths (1230 or 1270 mm) with staggered single layers (see Fig. 5.4.4). Each double-gap will be assembled separately and completely covered with an Al sheet carrying the ground to the termination resistors and to the electronics. Figs. 5.4.2, 5.4.3 and 5.4.4 show schematically the layout of the front edge of the first double-gap (A), the far edge of the second double-gap (B) and the overlapping region.



Fig. 5.4.2: Double-gap module A.

Fig. 5.4.3: Double-gap module B.

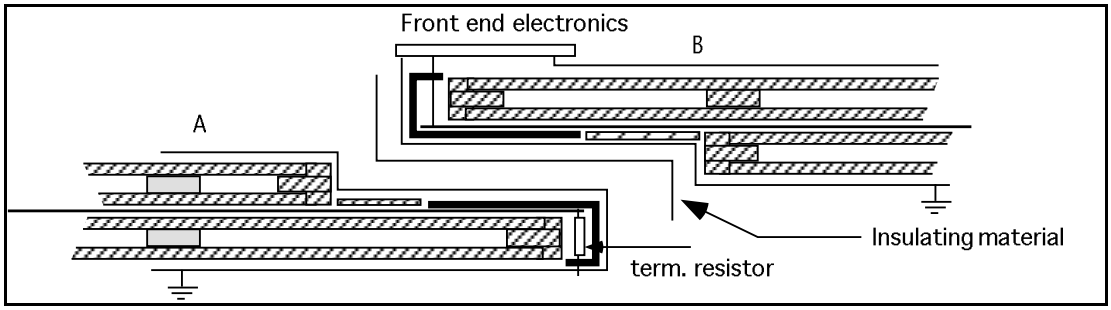


Fig. 5.4.4: Overlapping region.

5.4.2 Mechanical assembly and integration

As already stated, each barrel station has a rectangular surface; one side has constant length (2560 mm in the beam direction); the other ranges from 2000 to 4000 mm. Each station is self-supporting and therefore can be fastened in place by its edges only.

The RPCs alone, in the double-gap configuration, have a weight of 14 kg/m^2. Their mechanical structure does not have sufficient rigidity to remain flat over such large surfaces if supported only at the edges; in addition, a gentle pressure (on the order of 15 kg/m^2) must be applied to the external surfaces of the double-gap assembly to make sure that the strips, running between the two single-gaps, make good mechanical contact with them. This solution has been adopted in place of gluing the whole double-gap assembly for reasons of fragility, assembly time and costs.

Foam plates with thin Al skins glued on both sides, pre-loaded with a radius of curvature on the order of 10 m and squeezed flat over the two surfaces of the double-gaps, have been used up to now in test chambers to provide the necessary pressure. Unfortunately, this very attractive solution cannot be applied over sizes greater than 1000x1000 mm^2, because the pressure they can exert decreases as some power of the length. In addition, in the CMS barrel the effect of the chamber weight is different at different ϕ, so it is difficult to envisage the extension of this technique to provide pressure and support for all the barrel stations.

The solution adopted is based on experience with commercial Al bars. Rectangular 15x40x2 mm^3 bars, pre-loaded with a radius of curvature of ~10 m, have been shown to support flat a distributed weight of 20 kg/m^2 over a length of 2560 mm. Mounted on a rigid frame with different density over the two surfaces, they provide the necessary support and pressure, in all conditions, with an additional average weight of 2 kg/m^2.

In practice, in MB1 and MB2, where the chamber length perpendicular to the beam is less then 2500 mm, the mechanics will consist of a rectangular frame with two stainless steel C bars running along the two 2560 mm sides and connected with two (front-end) plates. The Al bars run parallel to the front-end plates and are anchored inside the Cs. The whole assembly is kept flat within a tolerance of a few millimeters and has a thickness of 55 mm. Fig. 5.4.5 is a schematic view of this assembly, where the relevant components are pictured.

In MB3 and MB4 the rectangular frame will be sturdier and the Al bars, on the face supporting the weight of the assembly, are mounted parallel to the C bars and are anchored to the front-end plates. In this case the front-end plates need to be supported at a few points on the iron yoke.

The pre-loaded bars are always mounted in correspondence with the spacers, to avoid deformations of the gap.

A full-scale prototype of both structures has been built and shown satisfactory behavior in both the horizontal and vertical position. The thickness of each station, could be kept within 55 mm with a maximum deviation from a plane surface of few mm. Details of the front-end plates (with gas , power and signal connections) are shown in Fig. 5.4.6.

Further studies are necessary to have a complete engineering design of the chamber. A full-size, operational prototype should be built by the end of 1998.

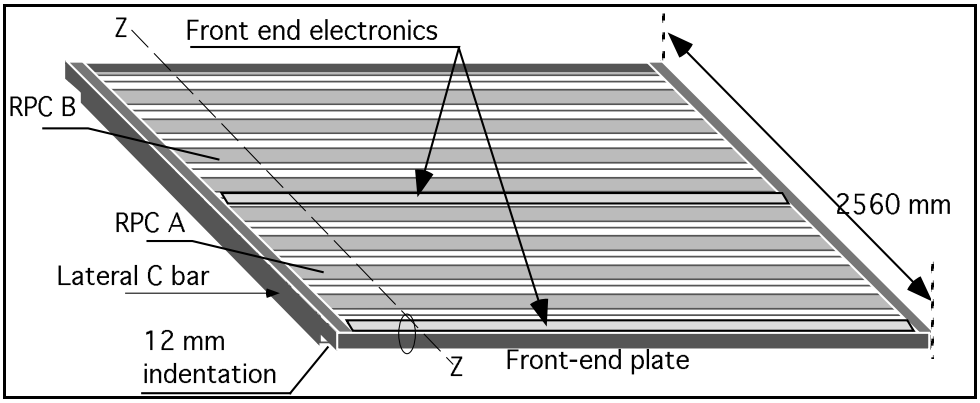


Fig. 5.4.5: Mechanical assembly of a station.

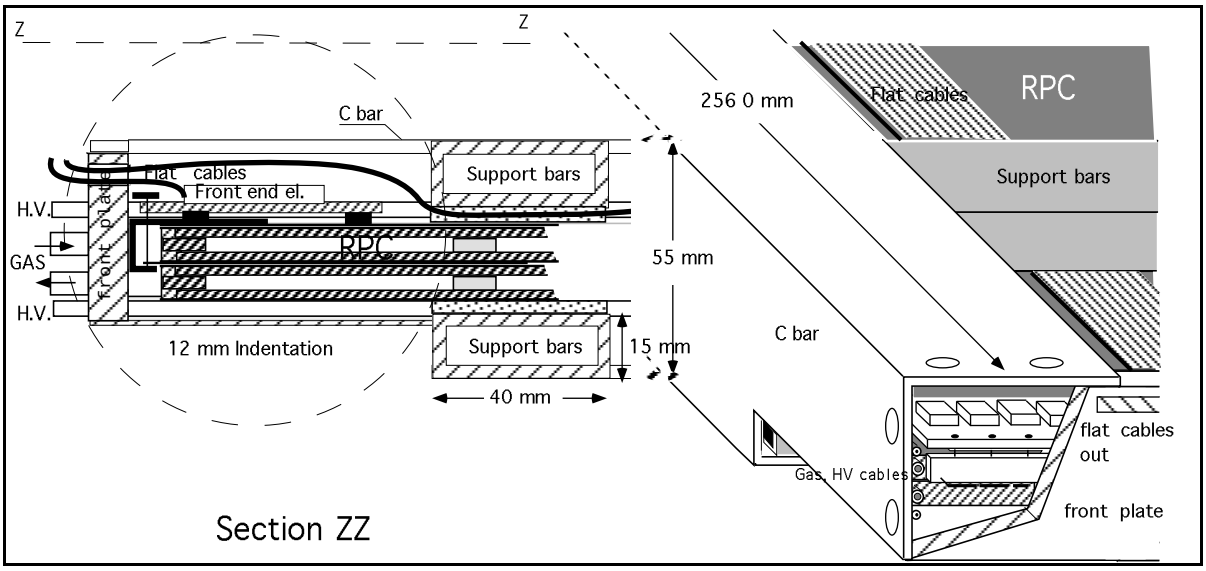


Fig. 5.4.6: Detail of ZZ section and front of circled zone in Fig. 5.4.5.

5.4.3 Production plans

To a large extent, the barrel RPC construction will be handled by industry, which has reliably produced chambers for the L3 and BABAR experiments. The necessary tooling for the basic single-gap production already exists and no modification is needed for the CMS production, which should follow the established standard procedure.

As a first step, all the bakelite electrodes will be produced at one time, to ensure equal characteristics, and then checked for resistivity and surface quality. This work will be the responsibility of the group in Pavia, where a test station is under construction. It should allow us to measure the bulk resistivity and the surface roughness at several positions on the plates in a fully automatic way.

The selected electrodes will then be transferred to industry, where the single-gap modules will be produced according to the procedure described in Section 5.3. At a rate of 15 single-

gap/day, the entire barrel (1680 pieces) could be produced in about 120 working days. However we plan to distribute the production over a period of 3 years, starting around the middle of 1999.

The double-gap assembly and the full station mechanical assembly will be done in parallel with the single-gap production.

Once completed, the stations will be transferred (at a rate of 10-15 per month) to the Bari Physics Department and Sezione INFN, where a large workshop (200 m^2) is being instrumented. In Bari, the front-end electronics will be mounted on the stations and exhaustive tests with cosmic rays will be performed before shipping them to CERN.

Recently, a group of universities from South Korea have expressed interest in joining the barrel RPC effort. Details of their participation are still under discussion, but it is likely that they will contribute significantly to the production, establishing a second assembly and testing line in Korea.

5.5 ENDCAP DESIGN

In the following, a design fully compatible with the required physical segmentation and with the constraints of the existing construction technology will be proposed and discussed.

A schematic R-Z view of the Endcap RPC system and the detector locations with respect to the iron walls is shown in Fig. 5.4.7. Four stations of RPCs are planned in the forward part of CMS (ME1, ME2, ME3, ME4) to cover the region up to η=2.1. The stations have a trapezoidal shape and the strips run along the radial direction.

In order to maintain projectivity, the strip shape is trapezoidal, so that in each η region its width always covers 5/16 degrees in ϕ. Also the strip length varies, according to the η region, from ~25 cm to ~100 cm. The endcap RPC stations will also be built using the double-gap concept. However, in the case of very short strips (especially true for ME1 and, in general, at high η), the use of the standard double-gap layout, where strips are embedded between the two gaps, has the problem that signals can not be extracted unless the chamber segmentation follows the strip length. Also the same limits on the bakelite plate dimensions, as discussed for the barrel part, must be considered for the design of the endcap, resulting in a severe constraint on the module size.

Different layouts, which avoid this limitation by placing the read-out strips on the external face of the detector, with a consequent increase of the module size, are also under consideration. Recently two chambers have been built and tested according to the alternative layouts shown in Fig. 5.2.6b and in [5.18], respectively. Their performances are presented in [5.19] and [5.21].

A basic concept of the design described below is to segment the stations in a way that strips, whose length should always cover one η region of Fig. 5.4.7, can be easily read out. This can be achieved by choosing the size of the double-gap modules to cover two η regions and by instrumenting them with two sets of strips, running from the center of the module to the edges, where signal can be extracted and fed into the front-end boards.

Of course different stations would require different strip lengths (to match the exact η segmentation) and, consequently, different module sizes. However, in order to simplify the detector design and the production procedure, it has been decided to maintain the same strip length and, therefore, the same module sizes in all the stations, according to the exact η

segmentation of ME2, as shown by the horizontal lines in Fig. 5.4.7. The choice of ME2 to determine the strip lengths is related to the trigger algorithm, which makes use of this station as a reference plane for the track finding process. Of course some minor differences are still present at very high η, and the case of the small ME1 chambers at $\eta > 1.65$ has to be specially treated.

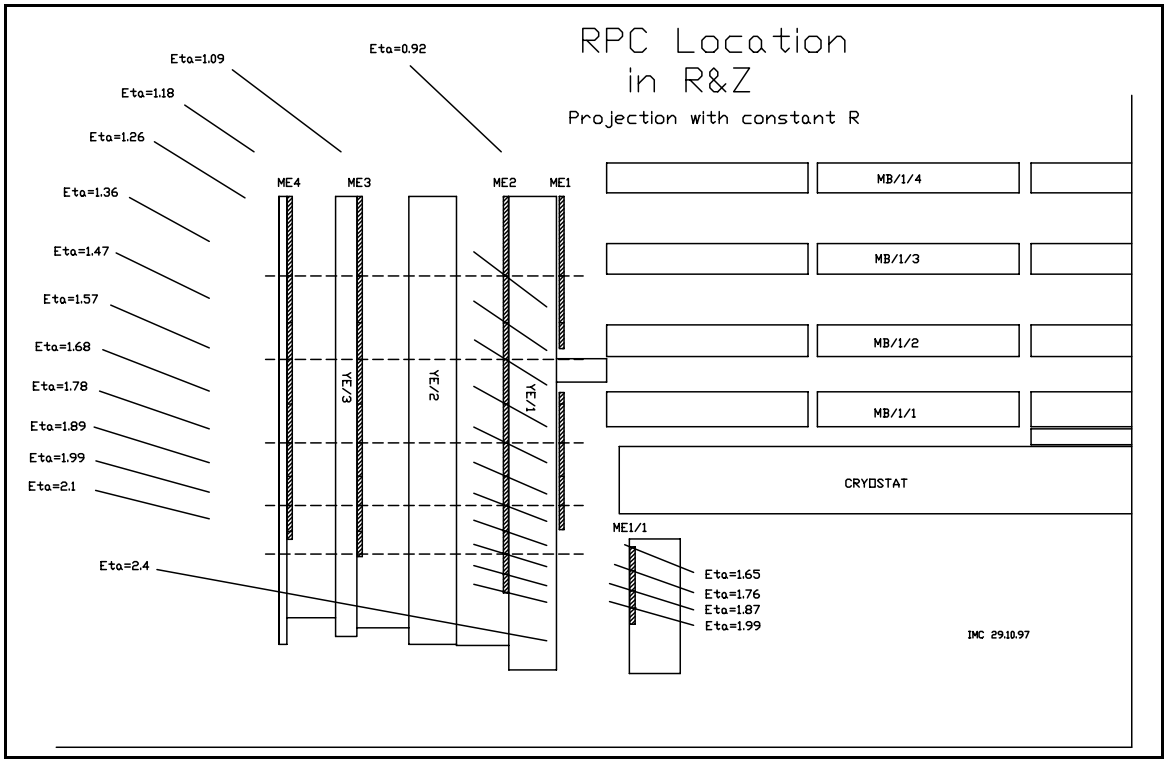


Fig. 5.4.7: Forward RPC location in the R-Z plane.

5.5.1 Layout and assembly of stations ME1

The station ME1 is the most demanding from the point of view of the design. It is divided into three chambers, which in the following will be referred to as ME1/1, ME1/2 and ME1/3. A front view of a small ϕ portion is shown in Fig. 5.4.8, where the station segmentation is evident.

The ME1/1 chambers cover 10^0 in ϕ and 4 η regions; they are composed of two double-gap modules, each one instrumented, as discussed above, with two sets of 32 radial strips. The double-gap modules are embedded between pre-loaded foams located on both faces and kept together by means of aluminum C bars.

To limit the dead area, two such chambers will be overlapped in ϕ according to the scheme shown in Fig. 5.4.9, ensuring that at least one single-gap is always present. The whole structure will be 60 mm thick.

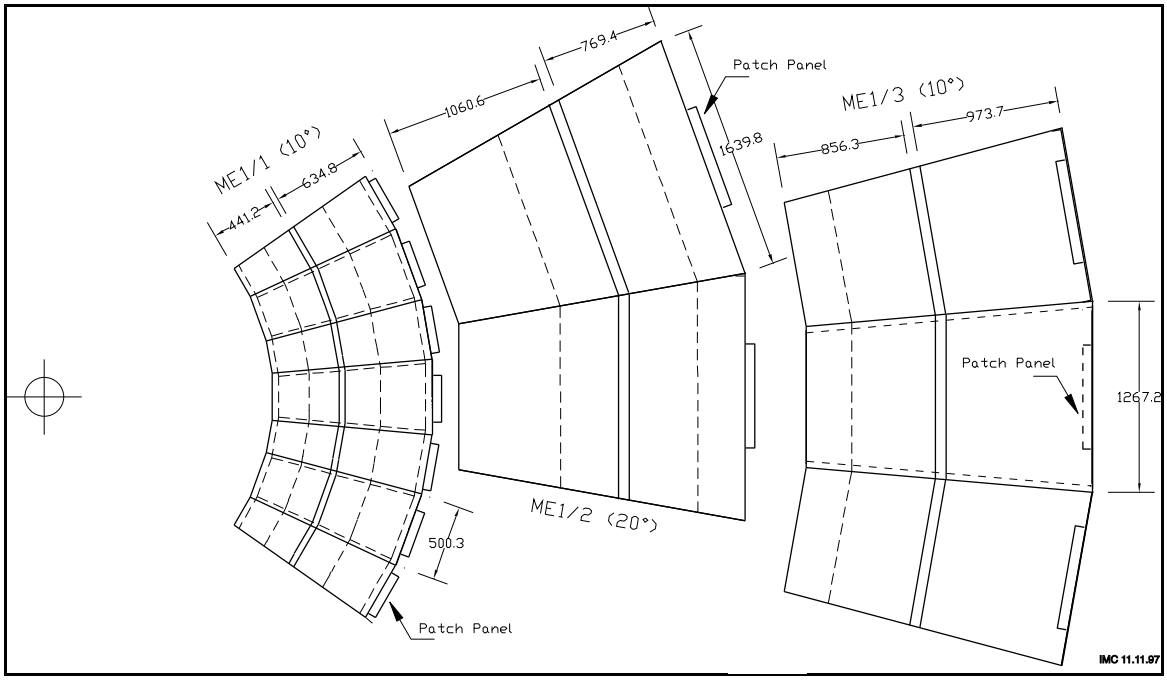


Fig. 5.4.8: Front view of a small ϕ portion of ME1. Dashed lines indicate η segmentation. The gap between ME1/1 and ME1/2 is only apparent, because they are located at different distances from the interacton point. Due to space limitations the ME1/2 RPCs have no overlap in ϕ.

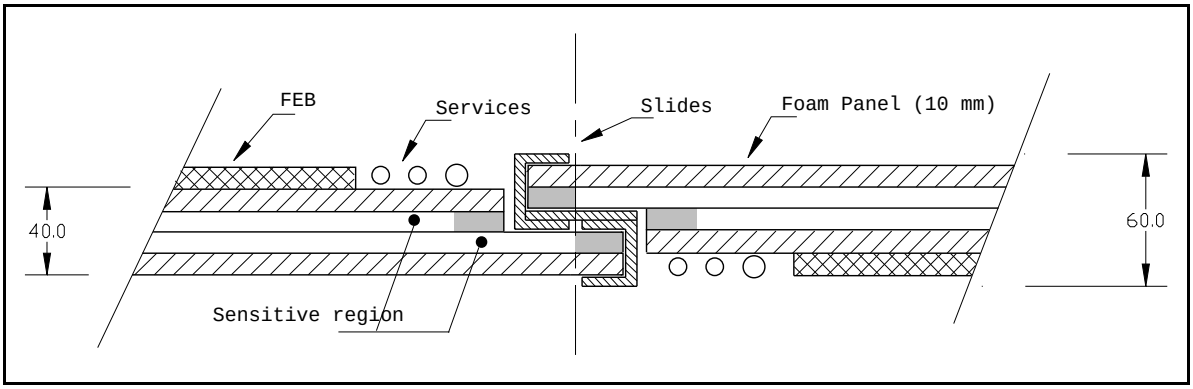


Fig. 5.4.9: Schematic detail of the ME1/1 chamber overlap in ϕ.

The same design concept will be used for both ME1/2 and ME1/3. However in the ME1/2 case, due to the severe space limitation in this region, each chamber will cover 20^0 and no overlap in ϕ will be possible.

While in the case of ME1/2 the details of the mechanical assembly are still to be defined, the ME1/3 stations will be assembled according to the same scheme proposed for the other ME/2 - ME/4 stations, which will be discussed in more detail in the following section. Table 5.5.1 lists some global parameters of the ME1 system.

Table 5.5.1
The ME1 RPC system totals.

	ME1/1	ME1/2	ME1/3	ME1 total
Number of stations	72	36	72	180
Total surface area	32 m^2	90 m^2	144 m^2	266 m^2
Number of bi-gaps	144	72	144	360
Number of strips	9216	9216	6912	25344

5.5.2 Layout of stations ME2, ME3, ME4

These stations will consist of several double-gap modules, whose dimensions will cover 30^0 in ϕ and two η regions. In each module two sets of 96 strips, for a total of 192 strips, run along the radial R direction and are read out at the edges. Only the last module, at the highest R, covers one η region and is instrumented with one set of 96 strips.

For example, Fig. 5.4.10 shows the layout of station ME2 with details of the segmentation. Each module comes with an independent enclosure and will be instrumented with the necessary electronics boards, located at the two edges and integrated in the mechanical structure. The strip lengths, and therefore the module's dimensions are determined according to the η segmentation, as given in Table 5.5.2.

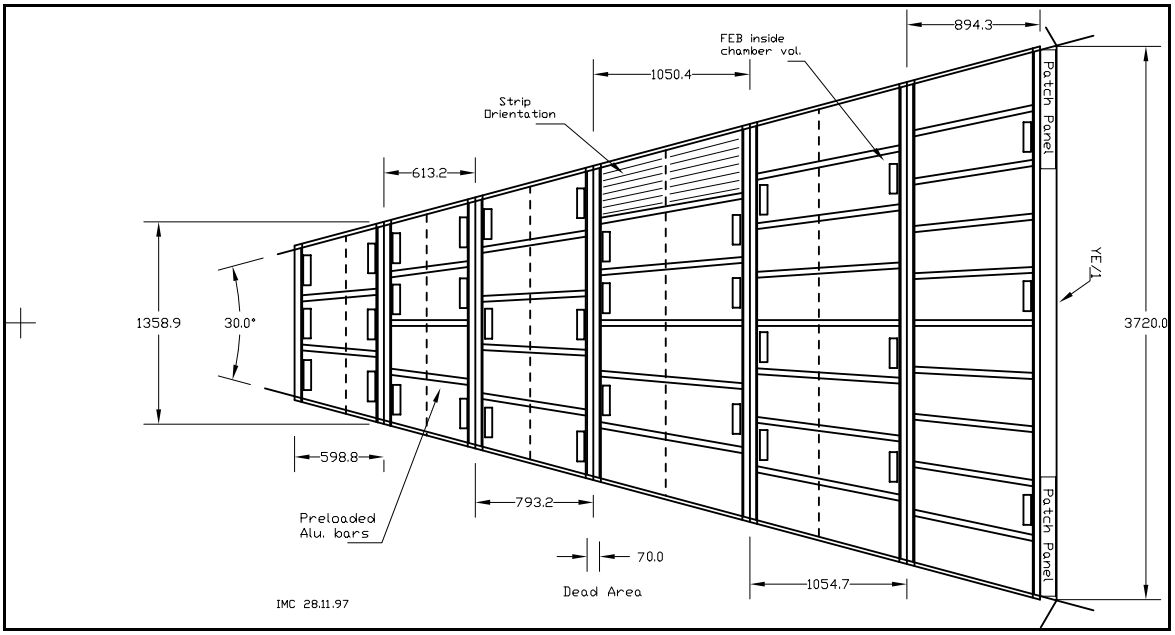


Fig. 5.4.10: Segmentation of station ME2. Location of the pre-loaded Al bars and the front-end boards locations is also shown.

Table 5.5.2
Station segmentation in η for RPC at ME2. Same strip length and module dimensions apply to ME3 and ME4 RPCs.

Module #	η_{min} η_{max}	Max. strip length (mm)	R_{min} R_{max} (mm) at center line	Dimension (mm^2)
1	2.10 1.99 1.99 1.89	313 220	1840 2437	599x1350
2	1.89 1.78 1.78 1.68	254 293	2442 3050	613x1678
3	1.68 1.57 1.57 1.47	339 394	3055 3843	793x2103
4	1.47 136 1.36 1.26	560 540	3848 4893	1054x2666
5	1.26 1.18 1.18 1.09	436 568	4898 5948	1054x3231
6	1.09 0.90	836	5950 6845	894x3710

The design of the other stations (ME3 and ME4) will be based on the same strip lengths and module size, as already discussed.

A set of pre-loaded Al bars running radially on both sides and embedded in two C bars, will stiffen the double-gap modules. The basic principle has already been described in detail for the barrel chambers. Since this layout will unavoidably produce some dead area in R between modules, an attempt will be made to avoid dead area also in ϕ. This is achieved by overlapping two corresponding 30^0 modules of adjacent stations, according to the scheme shown in Fig. 5.4.11. To limit the thickness in Z, only single gaps are overlapped. The total thickness of the RPC station is 6.7 cm.

Chamber counts for the ME2/3/4 system are given in Table 5.5.3.

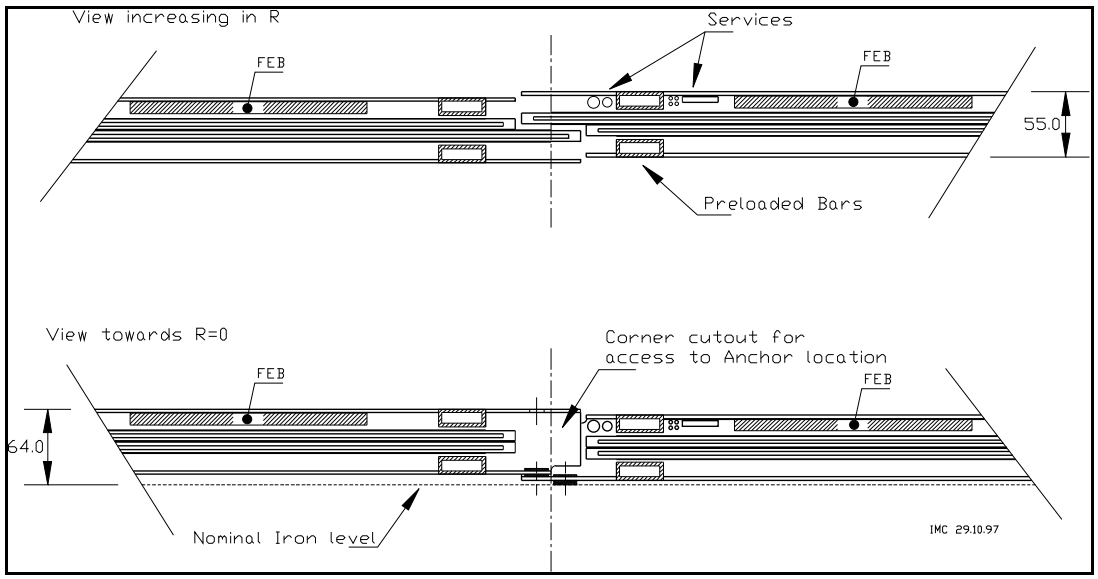


Fig. 5.4.11: Detail of the station overlap in ϕ.

Table 5.5.3
The ME2/3/4 RPC system totals.

Number of stations	72
Total surface area	750 m^2
Number of double-gaps	384
Number of strips	66818

5.5.3 Production plans

So far physicists from Florida, Rice, and Warsaw have played a major role in the R&D efforts for the forward RPC system. However very recently, three groups from South Korea, consisting of ten universities, have expressed strong interest in taking responsibilitiy for the construction of the forward RPCs and related readout electronics.

They are Cheju National Univ., Choongbuk National Univ., Kangwon National Univ., Wonkwang Univ., Chonnam National Univ., Dongshin Univ., Konkuk Univ., Korea Univ., Seoul National Univ. of Education, Seonam Univ.

Very fruitful contacts have already been established between this Korean Collaboration and the CMS muon community. A workshop on the forward RPC system was held in Seoul last February to trigger the discussion, and some Korean physicists have discussed at length the various options for the construction during a visit to the University of Bari, Italy, and to the RPC construction facilities existing in Italy.

Recently, the Korea Detector Laboratory (KODEL) has been established at the Korea University to co-ordinate all the research and construction RPC.

Two possible scenarios are under consideration:

- the establishment of complete production lines, including assembly of single-gaps. Bakelite production would, however, remain concentrated in one place (same as in the barrel case), to ensure uniform characteristic over the whole sample. It would be necessary to build a certain number of tools, according to the brief description reported in Section 5.3.
- only station assembly lines are set up to produce final chambers (including front-end electronics) from single-gap modules whichwould be industrially produced, preferably in one place (as in the barrel case) and distributed to the assembly centers.

It is worthwhile mentioning that a Chinese collaboration between groups from IHEP-Beijing and Peking University is also trying to find resources for a possible limited involvement in the forward RPC system.

5.6 FRONT-END ELECTRONICS

5.6.1 Design constraints

The choice of preamplifier configuration is determined by the electrical characteristics of the detector and by the shape of the signal to be processed. In the barrel RPC, the current signal comes from a strip-line 1.3 m long whose characteristic impedance R_0, for an RPC with 2-mm double-gap geometry and a strip width ranging from 2 to 4 cm, ranges from 40 to 15 ohms,

respectively. The corresponding strip capacitance goes from ~160 pF/m to ~420 pF/m. The propagation velocity is ~5.5 ns/m.

The shape of the current signal, induced by a single cluster, is described by the function $i_s(t)=i_o\exp(t/\tau)$. This is a good approximation to the real signal, since almost the whole induced current originates from the first two clusters. For the proposed $C_2H_2F_4$-based gas mixture, which has an electron drift speed v of ~130 micron/ns (as shown in Fig. 5.2.5), t is in the range $0 \leq t \leq 15$ ns. Furthermore, $\tau = 1/\eta v$ (η, effective Townsend coefficient) is the gas time constant that, at the nominal working point of the detector, is ~ 1 ns.

The total charge induced on the strip ranges typically from ~ 20 fC to more than 50 pC. However, such a wide linear dynamic range is not required.

Since the rise time of the induced signal is shorter than the propagation delay of the strip, the strip must be treated as a transmission line and properly terminated at both ends. One end is terminated by the input impedance of the preamplifier; the other, by an ohmic resistor. An active termination on both ends would be expensive and power consuming, yet yelding only a small decrease of noise. Terminating the strip with a resistor having a small and variable value requires AC coupling between strip and amplifier.

Simulations and past experience show that a threshold of about 20 fC allows the detector to achieve full efficiency with small streamer probability. This means that a noise sigma not exceeding 4 fC could be tolerated.

As will be discussed in Section 5.6.2, the timing error due to the walk (the only error that could be corrected with a constant fraction discriminator) is about 0.7 ns. Compared to the experimental total error (1.8 -2.0 ns), the walk contribution appears negligible. Thus, a leading-edge discriminator is adequate.

The preamplifier should preserve the fast rise time of the input signal to fully exploit it in leading-edge timing. A simple way to achieve this is to design an amplifier having a single dominant pole at relatively low frequency, while the next high frequency pole should be as far away as possible. The response will be a pulse having nearly the same fast rise as the input and a relatively long tail. Since we expect a singles rate of less than 200 kHz/channel (with the maximum strip area of 130x4 cm^2), a tail length below 50 ns would result in a negligible pile-up probability. Of course, the fast peaking time and the slow tail tend to affect the series and the parallel noise, respectively. This has been considered in the design in order not to exceed the required noise limit.

Often in an RPC, the avalanche pulse is accompanied by an after-pulse with a delay ranging from 0 to some tens of ns. Killing the possible second trigger is necessary. Thus, a one-shot must follow the discriminator. The choice of pulse length should take into account the trade-off between the possible second trigger and the dead time. A length of 100 ns, giving a dead time of 2%, is a good compromise

5.6.2 Electrical schematics

In the present version, the RPC front-end channel consists of a preamplifier, a leading edge discriminator plus one-shot, and a driver, as shown in the block diagram of Fig. 5.6.1.

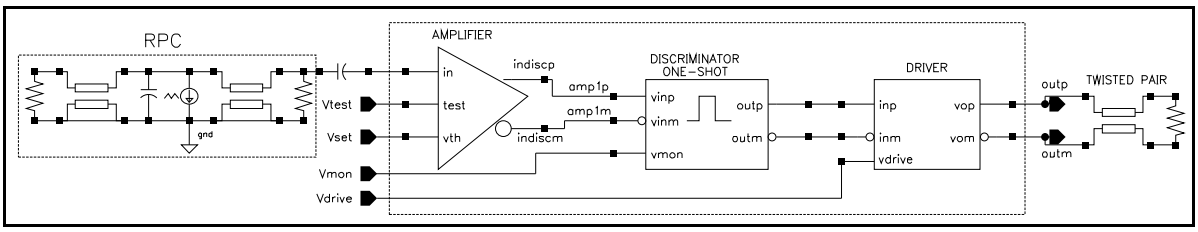


Fig. 5.6.1: Single channel block diagram of the front-end electronics.

The preamplifier starts with a transconductance stage, to match the characteristic impedance of the strip. An exact matching, independent of the signal charge, cannot be obtained; due to the wide dynamic range (the signal charge spans over 3-4 orders of magnitude), a low power amplifier is soon overloaded. Assuming the strip correctly terminated at the other end, impedance matching at the amplifier input is important for small signals, close to the threshold, where the reflections could affect the efficiency. However, looking at typical charge distributions, the probability of having signals around 20 fC is quite small. In the present version of the front-end, the input impedance is about 30 ohms at the signal frequencies (around 100 MHz).

The transconductance stage is followed by a gain stage that introduces the dominant pole at 20 MHz, giving a tail length of ~ 30 ns. The next high frequency pole is set by the input stage and is at 200 MHz, enough to preserve the leading edge. The charge sensitivity has been limited to 1.6 mV/fC, on the basis of past experience with RPCs. The equivalent noise charge (ENC) is ≤ 1.7 fC, in the worst case of a strip having R_o=15 Ω.

The power consumption of the preamplifier is 7 mW.

The threshold circuit is made of cascaded differential stages. The threshold can be adjusted between 10 and 300 fC using external voltage control. As already stated, the discriminator is followed by a one-shot circuit that gives a shaped 100 ns pulse.

The power consumption of the discriminator plus one-shot is also 7 mW per channel.

The driver has to feed a twisted pair cable with a signal level of 300 mV into 110 Ω, as required by the LVDS standard. The power consumption is 18 mW per channel. We are also considering the possibility of housing part of the readout electronics on the same PCB as the front-end chip. This solution would make the cable unnecessary, and the driver power could be decreased to 5 mW per channel. Because of this the chip has the possibility of reducing the driver output current.

Fig. 5.6.2 shows the time slewing (simulated) as a function of charge overdrive. The dominant contribution of the discriminator at small overdrives is due to the limited gain-bandwidth product of the circuit. However, the stable performance for overdrives down to 1 fC should be noted. Fig. 5.6.3 shows the slewing contribution to the time resolution, obtained by weighting the time slewing with the probability of occurrence of each charge value, given by the charge spectrum. The value σ_{t1} = 0.7 ns accounts for the effect of signal amplitude variations. This error could be reduced by a constant-fraction discriminator (CFD) or by simpler slewing correction techniques.

The intrinsic timing error of the amplifier is due to the noise and can be evaluated as follows. The total noise is σ_n < 3 mV rms at the discriminator input. The average signal slope

around the threshold is ~ 20 mV/ns. Thus, on average, σ_{t2} < 0.2 ns. Of course, a CFD would have no effect on this error.

Since the experimental σ_{tot} is 1.8 - 2.0 ns, the contribution of the time slewing and of the noise is marginal. The dominant timing error source is, for the moment, to be ascribed to the detector technology and would be unaffected by any slewing correction.

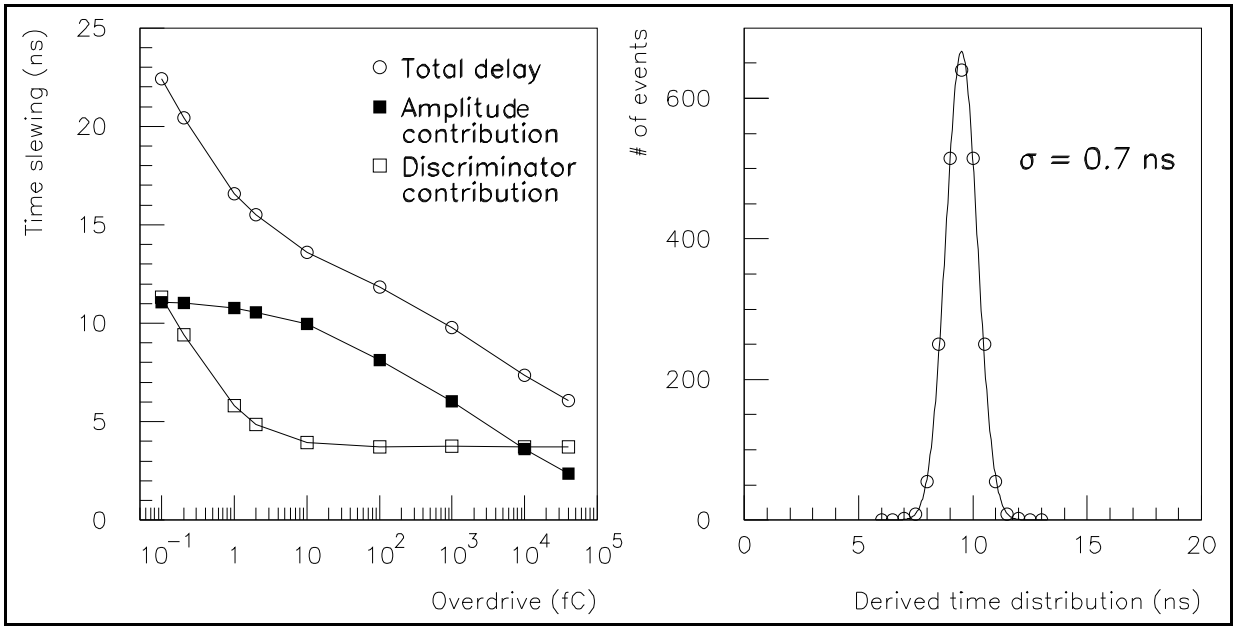


Fig. 5.6.2: Time slewing vs. charge overdrive. **Fig. 5.6.3:** Simulated time resolution.

5.6.3 The front-end chip

In the present version, the front-end chip (FEC) has been made using the semi-custom bipolar technology of Maxim. This process has been already used in many high energy physics experiments. In addition, its radiation hardness is well characterized and is considered adequate even at the highest radiation levels of LHC.

The FEC contains 6 channels (Fig. 5.6.4). For every 3 channels of a FEC there is a common test input and a common threshold setting. The number of channels was limited to 6, in order to optimize both the chip internal layout (component count) and the external connections to the strips. The required power supplies are +3V and -2V; the overall power consumption is around 30 mW/channel. The package is a quad-flat-pack, 64 pins, 10x10x2 mm^3.

Test bench measurements on the first prototype chips have shown good agreement with the simulation. Fig. 5.6.5 compares the simulated and measured slewing. A large RPC instrumented with this new electronics has been tested at the H2 muon beam. Results, which are encouraging, will be described in Section 8.1

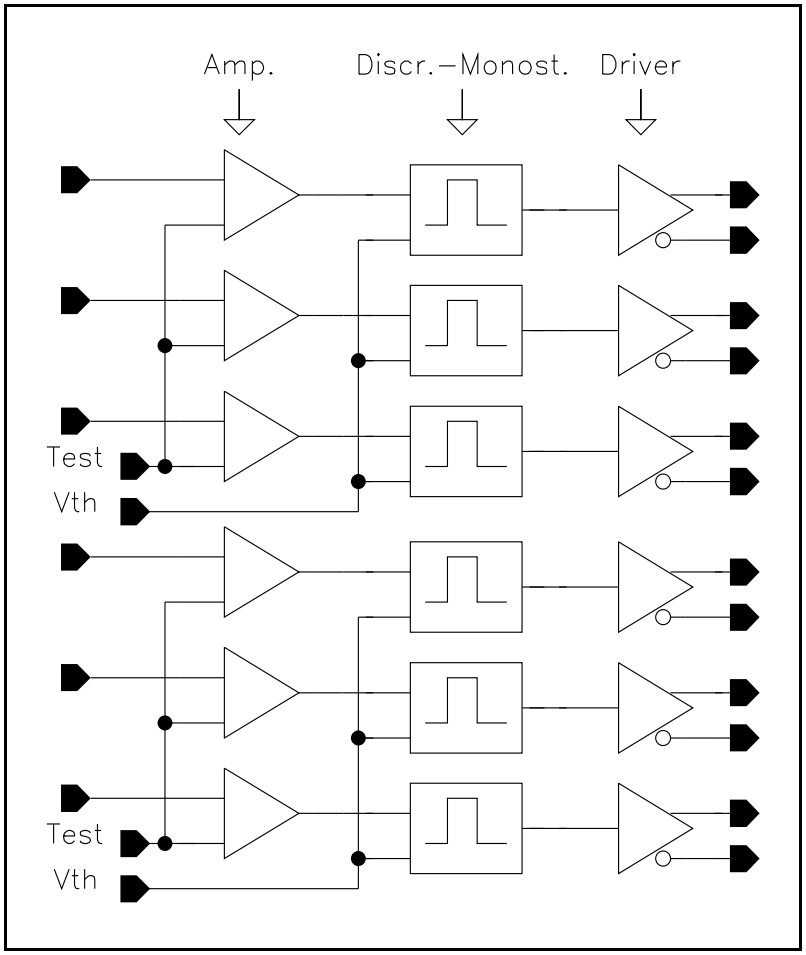


Fig. 5.6.4: Schematic of the Front-End Chip (FEC).

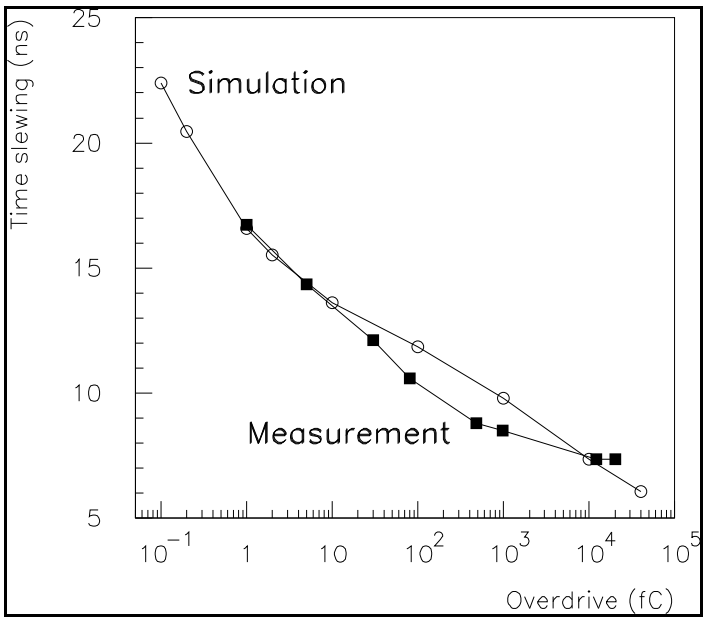


Fig. 5.6.5: Comparison between simulated and measured time slewing.

5.6.4 The front-end board

The Front-End Board (FEB) is connected directly to the RPCs and contains 24 channels of RPC front-end electronics. Its schematic is shown in Fig. 5.6.6. The physical size of a FEB is 24xW mm length (W being the strip pitch in mm), 50 mm high and 10 mm thick. Four FEBs belonging to the same RPC chamber are connected together.

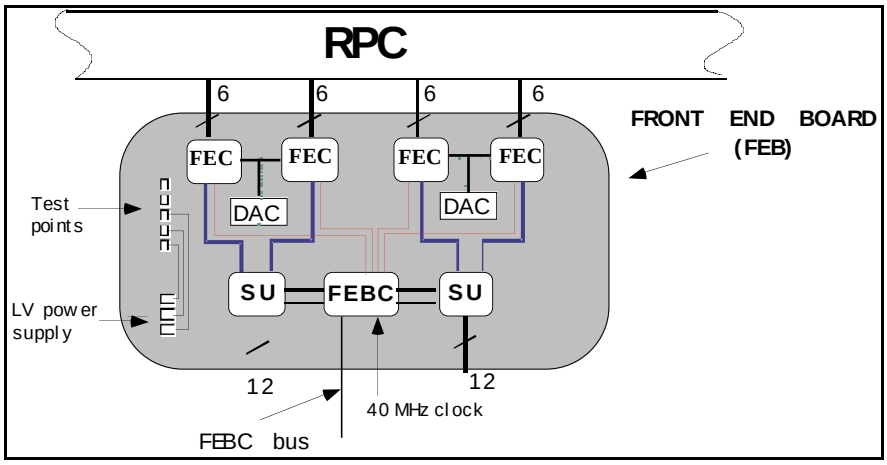


Fig. 5.6.6: Schematics of the Front-End Board (FEB).

The FEB accommodates:

- 4 FECs for a total of 24 channels,
- 2 Synchronization Units,
- 2 DACs for threshold setting,
- the Front-End Board Controller.

The Synchronization unit (SU) stores the FEC output data if they fall within a pre-defined time window within a bunch crossing period and synchronizes them with a selected bunch crossing period. The SU contains its own histogramming of rates for every data channel.

The Front-End Board Controller (FEBC) is a device controlling the front-end electronics. It will:

- store and distribute the threshold to the FECs,
- set the test pattern and test sequence and furnish them in a precise synchronous way as input to the FECs,
- set the time window properties for the SU,
- read out the SU test histograms.

The input threshold will fix the equivalent charge threshold value applied to the discriminator, varying between 10 fC and a maximum of 300 fC, with a resolution of 1.22 fC. An 8-bit DAC will be used to give the proper threshold value to the FEC discriminators. To set the correct DAC digital value, an 8-bit serial-to-parallel shift register will be loaded serially by the FEBC, and the analog output value of the DAC will be sent to an operational amplifier used as a buffer in order to provide a higher driver capability.

The test input is common to three channels, and its function is to apply a particular pattern to the amplifier input in order to check the channel connectivity and functionality.

A FIFO is planned to store the test patterns to be fed into the FEC; the same serial link used to load the DAC will be used to load the patterns into the FIFO.

5.7 GAS SYSTEM

The RPC chambers have a gas volume of 10 m^3 for the barrel region and about 8 m^3 for both endcaps. All chambers operate with a non-flammable gas mixture of $C_2H_2F_4$ and i-C_4H_{10} (95.5%/4.5%). The basic function of the gas system is to mix the two components in appropriate proportions and to distribute the clean gas mixture into the individual chambers at a pressure between 1 and 3 mbar above atmospheric pressure. The hydrostatic pressure gradient of the gas mixture is 0.3 mbar/m. The total height of the RCP's inside CMS is about 15 m which makes a compensation of hydrostatic pressure differences necessary.

The large detector volume and the use of a relatively expensive gas mixture makes a closed-loop circulation system unavoidable. The system proposed will consist of functional modules, which are designed as far as possible uniformly for all CMS gas systems (see Table 5.7.1). The component sizes and ranges are adapted to meet the specific requirements of the RPC system.

Table 5.7.1

Modules of the RPC gas system.

Module	*Situated in*
Primary Gas Supplies	SGX Building
Mixer	SGX Building
Inside closed circulation loop:	
Chamber Distribution Systems	UXC55 Cavern
Purifier	SGX Building
Pump and Return Gas Analysis	USC55 Area
C2H2F4 Recovery Plant (if economically justified)	SGX Building

5.7.1 Mixer

The flows of component gases are metered by mass flow controllers, which have an absolute precision of 0.3% in constant conditions (Fig. 5.7.1). Flows are monitored by a process control computer, which continually calculates and adjusts the mixture percentages supplied to the system. The medium-term stability in constant flow conditions is better than 0.1%: absolute stability will depend on the absolute precision of the analyzing instrument. The gas mixture is treated non-flammable, permanent mixture monitoring makes sure that this is the case. The gas flow is stopped automatically if the i-C_4H_{10} fraction increases beyond the flammability limit.

Running flows are typically about 30% of full-scale flow on the mass-flow-controllers. For fast detector filling the parallel rotameters will be used, yielding a complete volume renewal in about 8 hours.

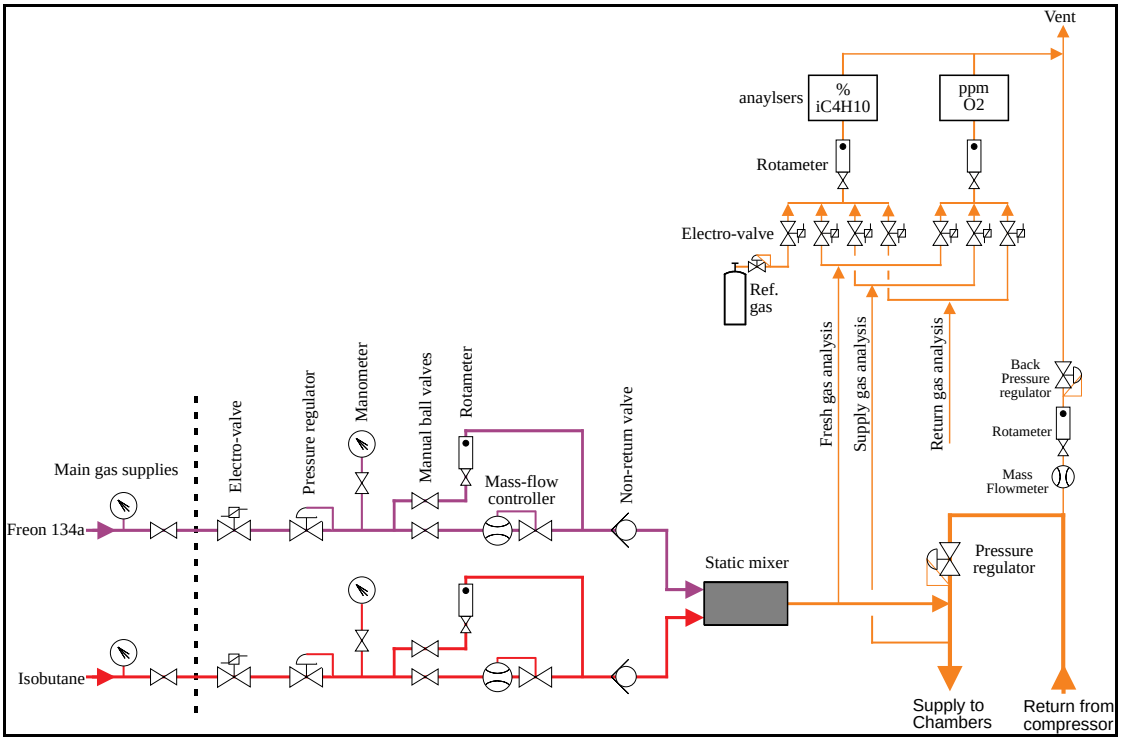


Fig. 5.7.1: $C_2H_2F_4$/i-C_4H_{10} mixer unit.

5.7.2 Closed circulation loop

The RPC gas is circulated in a common closed loop system for the barrel and both endcaps. With an expected regeneration rate of 90% and exchange rate of one volume in 24 hours the entire gas volume is re-newed ones every ten days.

As shown in Figure 5.7.2, the circulation loop is distributed over three different areas:

- purifier, gas input, and exhaust gas connections are situated in the SGX building on the surface
- pressure controllers, separation of barrel and endcap systems, compressor and analysis instrumentation are located in the USC service area and therefore accessible at any time
- the manifolds for the chamber gas supplies and channel flowmeters are mounted in distribution racks near the detector.

5.7.2.1 Barrel-chamber distribution system

The RPC detector in the barrel region consists of 360 chamber modules assembled on 5 distinct wheels. Every wheel is divided into 12 ϕ sections of 30° supplied by individual gas lines for each of the four muon stations (MS1 to MS4). Thus chambers are supplied individually or in groups of two leading to 240 independent gas channels for the full barrel detector. These gas lines are connected to five distribution racks situated on the bottom of each wheel.

5.7.2.2 Forward-chamber distribution system

The RPC detector in the endcap region is made of 372 chamber modules. Stations ME3 and ME4 are subdivided in 30° ϕ sectors, each sector being made of 5 chamber modules. Station ME2 is subdivided in 30° ϕ sectors, each sector being made of 6 chamber modules. In these three stations each chamber module has an independent gas connection. For the ME1 station the gas connections are such that chamber modules are grouped in 20° ϕ sectors, each sector having 6 independent gas connections. This means that, in stations ME1/1 and ME/1/3, two adjacent chamber modules in the phi direction are connected in series.

5.7.2.3 Pressure regulation system

The pressure regulation is independent for the barrel and the two endcaps, but the splitting in height is organised in the same manner. In order to correct for hydrostatic pressure differences in the upper, middle and lower section of the CMS detector (see Fig. 5.7.3 and Fig. 5.7.6)) the gas distribution is divided into three distinct height zones. In such a way relative pressure variations from chamber to chamber can be kept below 2 mbar during operation. Every height section has its own pressure control and pressure protection system. The latter uses bubblers situated in the distribution racks on the bottom of the wheels; the oil levels are adjusted to account for hydrostatic pressure differences in the three height zones. The mechanical stability of the chamber must, however, be sufficient to stand the full hydrostatic pressure of about 5 mbar for correct filling or purging of the chambers.

The pressure regulation is done from the USC area for the three height sections individually but in common for wheels. For that reason each of the wheel distribution racks is split into three distribution panels supplying gas for the different height zones. The panels of one height zone are connected then together to a common return pipe to the USC area (Fig. 5.7.7).

The pressure control is done using a pressure regulator on the inlet and a back-pressure regulator on the outlet. The outlet pressure at the regulator will be -1.0 mbar plus the hydrostatic pressure returned from the particular height zone connected; at nominal flow rate the pressure drop in the return line is < 2 mbar leading to a pressure between 1 and 3 mbar inside the chambers at operating conditions.

5.7.2.4 Gas distribution in the experimental cavern

A schematic layout of the gas distribution system to the chambers is shown in Fig. 5.7.5. Distribution racks are installed on the bottom of each wheel (5 for the barrel and 4 per endcap) housing 3 distribution panels for gas supply to the different height zones (see Fig. 5.7.4 and 5.7.7.). The distribution panels split into two manifold levels (radial stations and phi sections), the outer ones are equipped with remotely read flowmeters monitoring the flow in a radial sector. The flow measurement will be either differential or single, and can be used for possible leak detection and chamber flow adjustments using the needle valves at the inlets. In view of the large number of gas channels, and the fact that the instruments are in a zone with limited access, the flow metering technology must be simple, reliable and inexpensive. Currently two measurement principles are being considered: hot-wire anemometers and ultrasonic time-of-flight meters. A choice will be made on the basis of test results and a cost evaluation.

Every gas channel has a short flexible pipe with a self-sealing quick connector allowing gas channels to be individually disconnected from the circulation loop for flushing with inert gas. This facility is also very useful for leak tests on single gas channels.

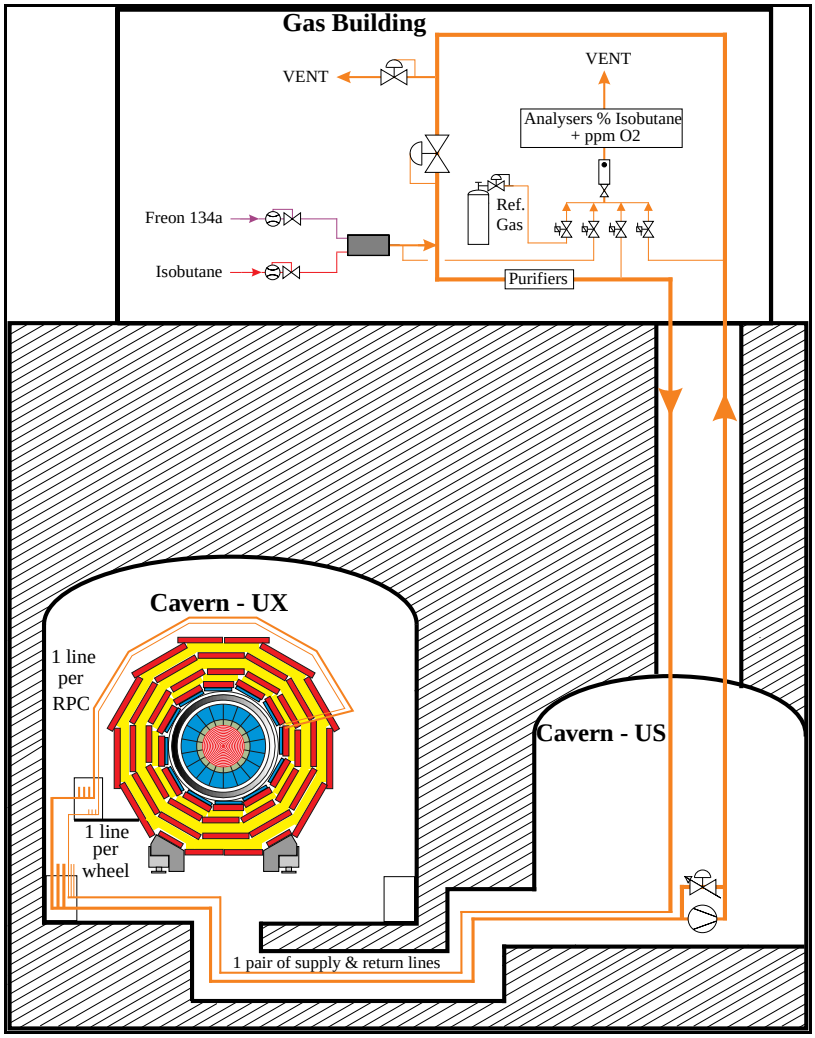


Fig. 5.7.2: Gas circulation loop.

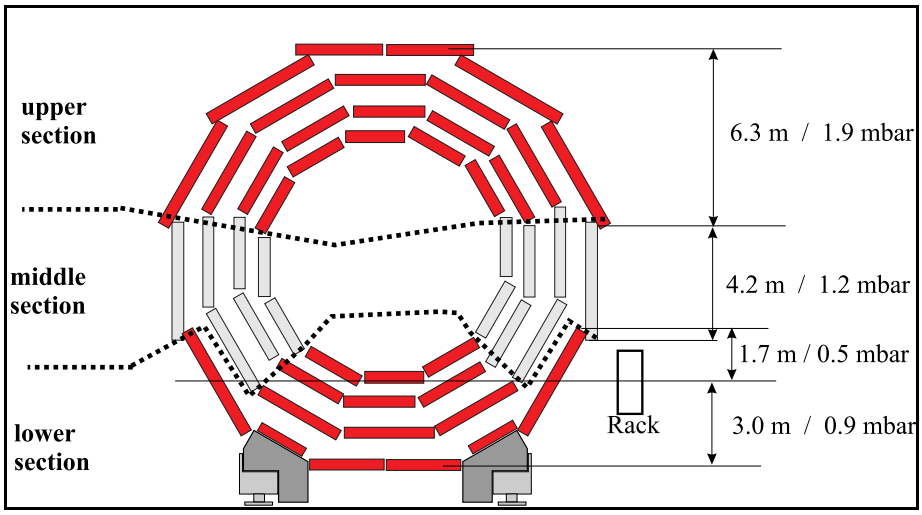


Fig. 5.7.3: Subdivision in 3 vertical zones (horizontal sections) of the RPC barrel gas distribution system.

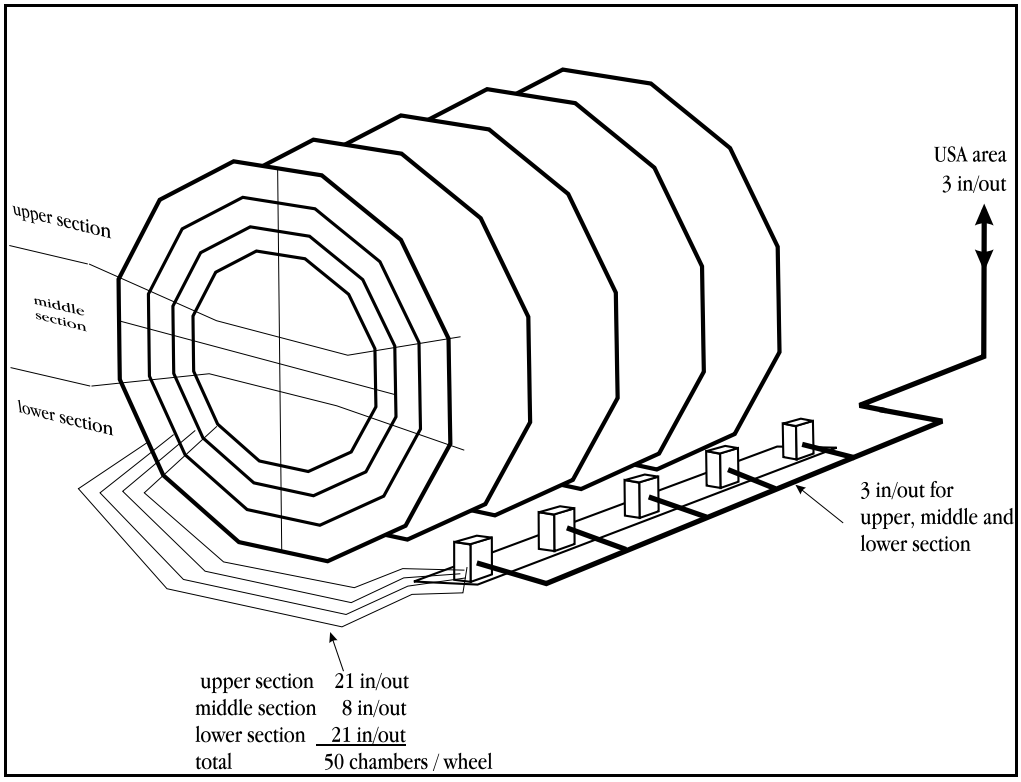


Fig. 5.7.4: Distribution system with station pressure regulation.

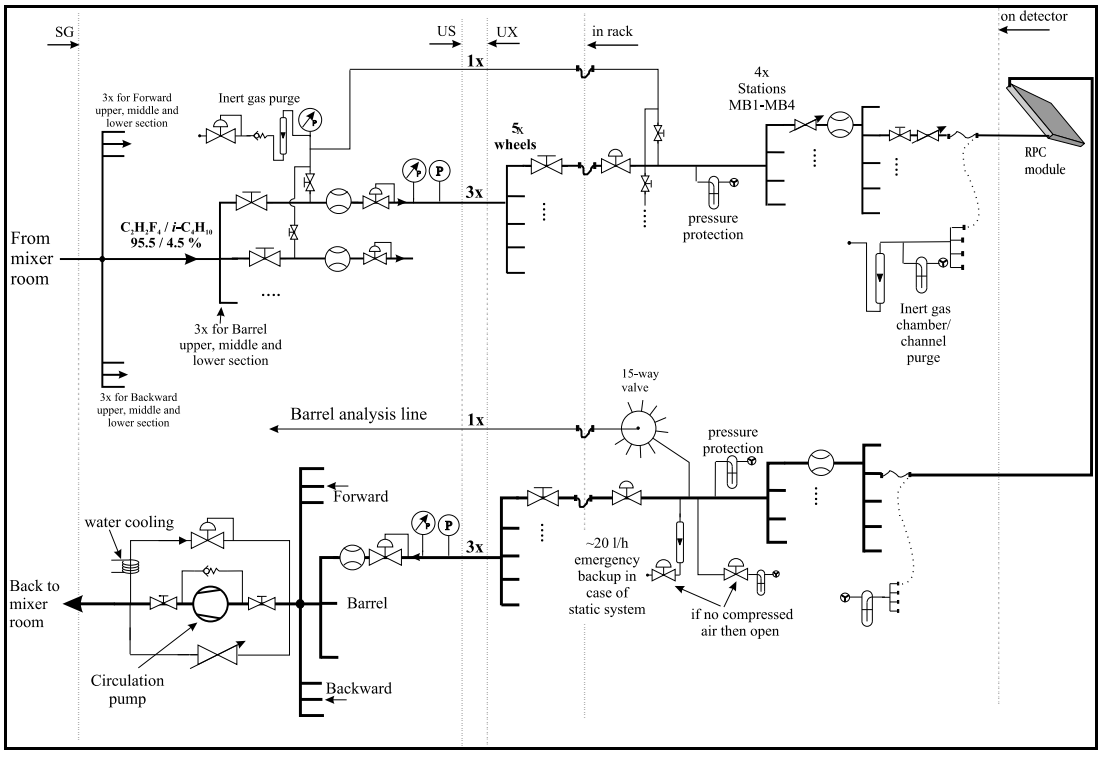


Fig. 5.7.5: Schematic diagram of the gas distribution system for parts of the barrel RPC's.

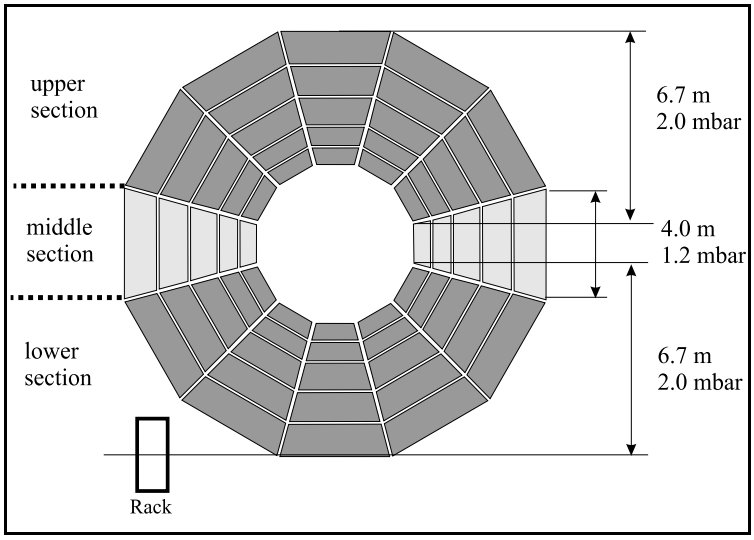


Fig. 5.7.6: Subdivision in three vertical zones of the forward RPC gas system.

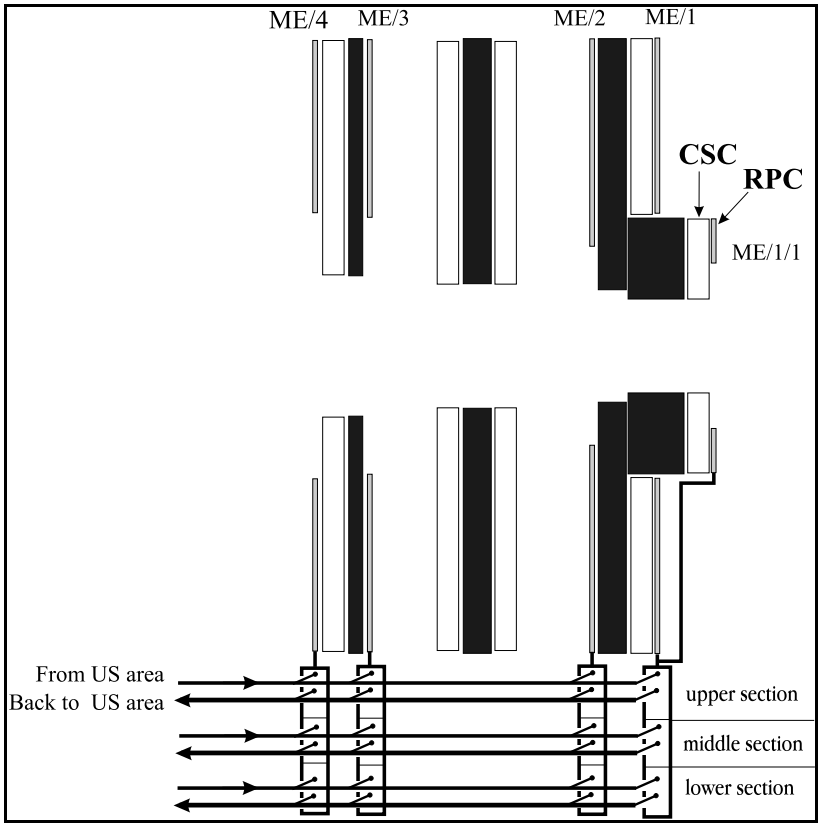


Fig. 5.7.7: Gas connections to the forward RPC stations subdivided in three horizontal sections.

It is planned to sample the chamber output gas on the distribution panels for gas analysis, this can be done for every channel or for a group of chambers. The sampled gas is returned to the USC area with a small pump. Thus, gas analysis instruments are accessible at any time and can be shared by several detector groups, if necessary.

5.7.2.5 Pump and return pipe pressure regulation

The gas from the distribution system must be compressed to approximately 100 mbar for return to the surface and recycling through the purifiers. At the same time, some of the return pipes from UXC55 may need slight under pressure (-2 to -5 mbar) in order to insure correct gas flow through the chambers situated in the bottom part of CMS. This pressure can be controlled by a regulation valve in parallel with the pump driven with the signal of a pressure transmitter in the main return pipe.

5.7.3 Purifier

Most closed-loop circulation systems need gas purification in the return line in order to achieve high recycling rates (usually 90%). For the RPC system, the gas purity requirements are not very high. The principal impurities that may harm are: nitrogen (<1%) and oxygen (<1%). A standard purifier using a twin column filled with e.g. activated copper can be used allowing water and oxygen removal. The compatibility of the $C_2H_2F_4$ with the cleaning agent remains to be tested; this will be done as soon as the proposed gas mixture is approved. The advantage of having two parallel cylinders is to run the gas mixture through one of them while the other one is regenerating. The activated copper can be regenerated by heating up the column to 180_C and flushing with an Ar/H_2 (93%/7%) mixture. The amount of oxygen to be removed is determined mainly by the leak rate of the chambers. The estimated oxygen levels in the return gas suggest a purifier with automated and in-line regeneration.

Nitrogen can only be removed in a gas recuperation plant after having separated the tetrafluoroethane from the isobutane. As a consequence the amount of N_2 penetrating into the circuit will give a limit to the achievable regeneration rate.

5.7.4 Distribution pipework

There will be one supply and one return pipe between the SGX building and underground service area USC. The barrel and both endcaps will have 3 supply and 3 return lines each, between the experimental cavern and the USC. Internal detector piping is planned in copper with inner diameters of 8 and 10 mm for supply and return line respectively.

5.7.5 Gas recovery

For the presently proposed gas mixture (95.5% $C_2H_2F_4$ + 4.5% i-C_4H_{10}), the expected gas cost for eight months of RPC operation are between 50 and 90 kCHF (gas prices of 1997). A gas recuperation plant separating the high value component, tetrafluoroethane, from isobutane, nitrogen and other residual impurities may reduce this expenditure to 50% or less. Thus, a recuperation plant may pay for itself after less than two years of operation. In case this gas mixture is confirmed in the future a feasibility study for the recovery of $C_2H_2F_4$ will be undertaken.

Table 5.7.2

Main gas specifications.

Gas volume	18 m^3
Concentration ratio $C_2H_2F_4$/i-C_4H_{10}	(95.5 ± 0.3): (4.5 ± 0.3)
Tolerable contamination: O_2	< 1%
H_2O	< 1%
Chamber pressure over atmospheric	< 3 mbar
Leak rate of the whole system	< 80 l/h
Maximum flow rate	2.2 m^3/h
Gas Flow rate at operating conditions	0.75 m^3/h
Fresh gas replenishing rate	< 0.15 m^3/h

5.8 CONTROL SYSTEM

5.8.1 Front-end control and monitoring

In Fig. 5.8.1, a general scheme for the front-end control system and the data transmission interface to the optical link is shown.

The data will be sent to a Link Board (LB) for zero suppression and transmission to the trigger processors. The LB will be located close to the detector and will be connected, via optical link, to the RPC Trigger Crates and to the network. It should also supply the LHC clock and broadcast test pulses to the FECs.

The LB board will have the dimension of a standard VME 6U module (160 x 233.35 mm^2) and its power consumption will be around some tens of watts.

Although a brief discussion of the LB issues related to RPC control is necessary, it should however be pointed out that this is part of the trigger electronics and it will be discussed in more detail in the appropriate section.

In the case of the barrel (shown in Fig. 5.8.1), one LB board serves a complete RPC station (192 channels in the case of MB1, MB3, MB4 and 288 channels in the case of MB2). In this last case, a maximum of 12 flat cables with 24 conductors (1 cable/FEB) will be necessary to bring the signals from the front-end electronics to the LB.

The RPC control system handles two aspects. The first concerns functions related to the detector operation, namely :

- control of low voltages on the FEBs,
- control of low voltages on the LBs,
- check of the thresholds of the FECs.

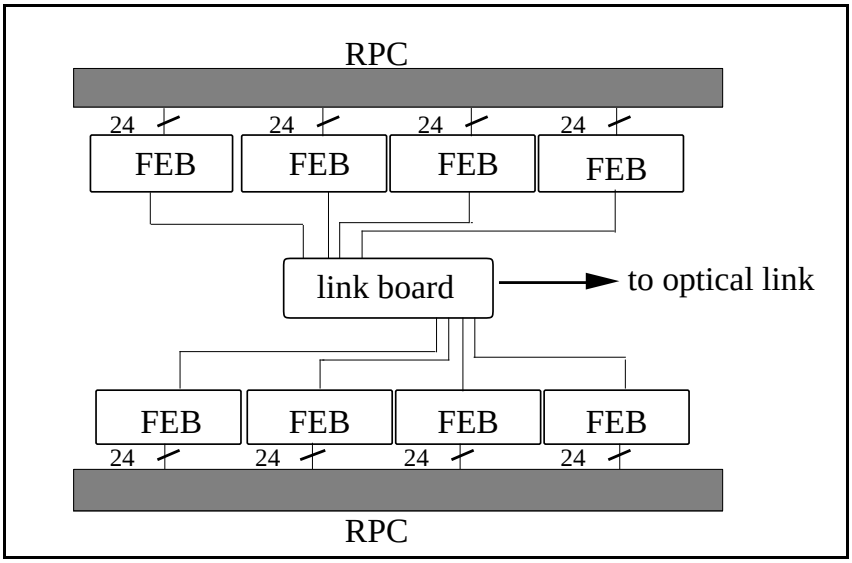


Fig. 5.8.1: General layout of the front-end system and transmission interface.

The second type of function is related to the slow data and trigger data path, which will make use of a slow clock frequency. It will:

- enable the test patterns to the FEC input,
- allow the setting of the thresholds for the FECs,
- allow the control and read-out of the SU histograms.

5.8.2 High voltage system

Each RPC gap must be operated at a maximum of 10 kV with a current limit of at most 200 μA. The very high number of single-gap modules with independent voltage connections, makes it difficult to build a system with a one-to-one correspondence between detectors and HV channels.

For example, in one barrel sector ($\Delta\phi$=30° of one wheel) 28 HV channels would be necessary for the 14 double-gap RPCs. This makes 336 HV channels/wheel and 1680 channels in total.

It is therefore important to provide a distribution bus to supply several detectors with a single HV channel. The bus should offer the possibility of switching off a particular noisy detector under a particular current draw condition (exceeding a pre-defined limit). Any HV module distributor should work with a full scale voltage of 15 kV, a voltage resolution of 4 V, a full scale current of ~10 mA and with a maximum ripple voltage peak-to-peak < 800 mV. The main HV crate will consist of a standard 19” Euro Crate which will house a Control Unit at the front end, and HV plug-in channels at the rear. The entire HV system will be located near the detector to minimize the cable lengths and the voltage drop over the cable. Moreover, a serial link is planned for controlling the voltage settings remotely.

5.8.3 RPC low voltage system

Each FEC needs two analog power supply voltages, +3V and -2V, with a tolerance of at most ±10% to operate properly within the design specification. Another digital +5V power

supply is required for the FEBC and SU. The same +3V power supply will be used for the DAC on the FEBC.

Switching and low noise low voltage power supplies will be distributed all around the detectors, 8 meters away from the RPC station, where the magnetic field of about 0.1 T can be shielded for appropriate working conditions. There are commercial devices with 8 Ch/±3V/3A and with 8 Ch/±12V/1.5A having current protection programmable per channel with a current resolution of 10 mA, a programmable voltage ramp-up and ramp-down and a maximum voltage ripple peak-to-peak at full load of < 5 mA, which are appropriate for this. Low drop-out linear regulators will also be put on the front-end boards. Fig. 5.8.2 shows a possible scheme for the LV connection.

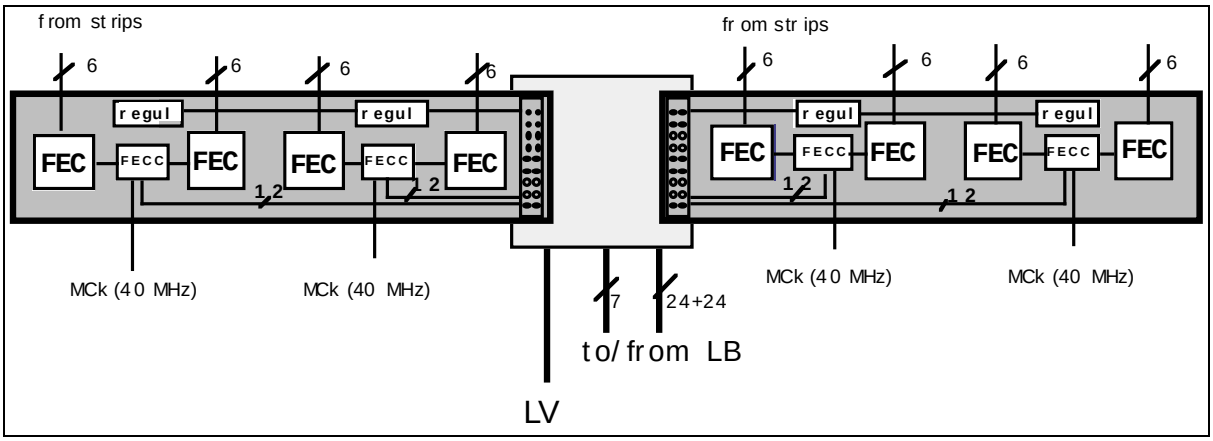


Fig. 5.8.2: LV connections.

One LV line will be distributed between two FEBs. Linear regulators can be connected between the internal power bus and the analog and digital sections of the board separately. The use of low drop-out devices is intended to keep the power dissipation to a minimum. For the scheme shown, a global consumption of 3 W and a current on the order of 0.5 A is expected. As in the case of the HV system, a distribution LV bus would be used to supply with a single LV channel an entire detector partition. Fuses rated at I > 2 A are necessary at each distribution point of the bus to protect the connector and input traces of each board.

5.9 RPC PERFORMANCE

Double-gap RPCs have been tested over the past years and results on the performance with different working conditions have been extensively reported in [5.4], [5.10] and [5.13]. These studies have shown the reliability of such detectors and have helped to highlight the main physical principles of their operation. The results from CMS related tests, which have been performed recently [5.20], [5.21], [5.22] will be presented here in a preliminary and more details will be given in forthcoming notes.

All results presented below have been obtained with a 90% $C_2H_2F_4$, 10% i-C_4H_{10} gas mixture. Although other non flammable mixtures were also tested, giving comparable results, extensive long term tests were done using the mixture mentioned.

Two main items will be discussed:

- global performance over a large surface,
- study of the rate capability.

5.9.1 Global performance

A 120x130 cm^2 double-gap RPC with 2 mm gas gap width, 130 cm long and 3.5 cm wide strips, has been exposed to the H2 SPS muon beam during the summer 1997 [5.20]. The strip size and length are typical of the barrel region. The bulk resistivity of the bakelite planes was $1\text{-}2*10^{11}$ Ωcm. The chamber was instrumented with boards employing the new Front-End Chip discussed in Section 5.6.3 and operated with a threshold of 30 mV (equivalent to ~20 fC).

In order to have different regions illuminated by ionizing particles, the chamber was displaced, during the test, by steps of 10 cm in the plane perpendicular to the beam. Displacements were arranged to ensure that the maximum of the beam profile was away from the spacers. A low intensity muon beam was used for this tests (200 Hz/cm^2 on a 2x2 cm^2 area).

Fig. 5.9.1 shows the efficiency vs. the applied high voltage when the beam is centered on the 10x10 cm^2 central region of the chamber. Also the in-spill drawn current (after subtraction of off-spill current) is given. In Fig. 5.9.2 the distribution of the signal arrival times is plotted at HV=8900 V. It is nicely fitted by a gaussian (σ =1.7 ns) and the base is within 20 ns. The cluster size is also measured at different voltages (Fig. 5.9.3).

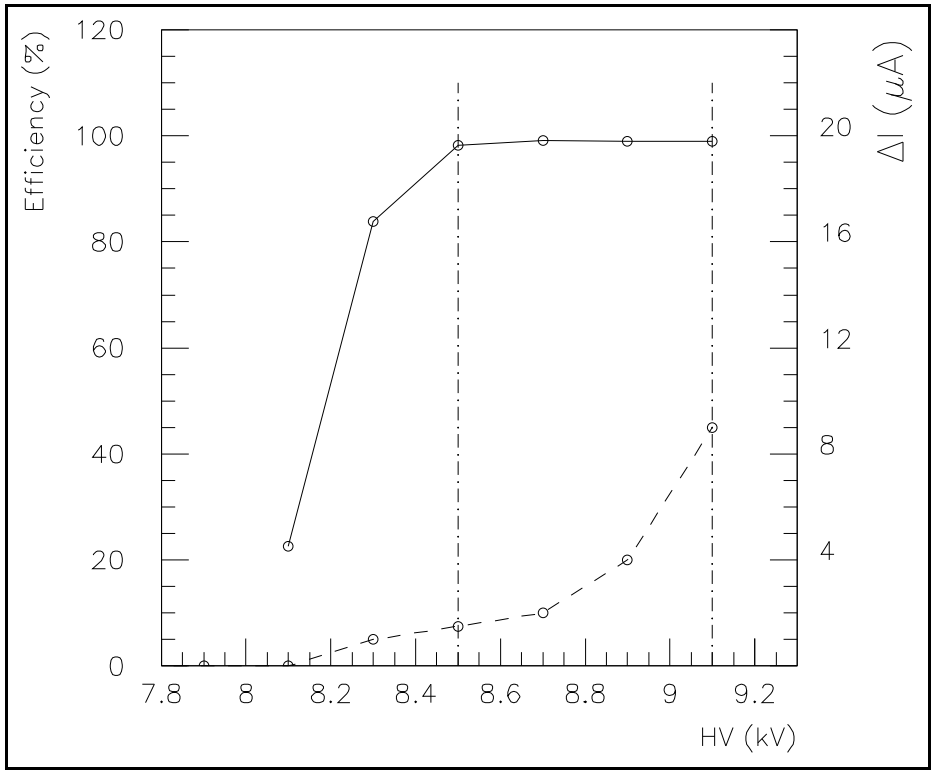


Fig. 5.9.1: Efficiency and in-spill current (off-spill current is subtracted) vs. the applied high voltage.

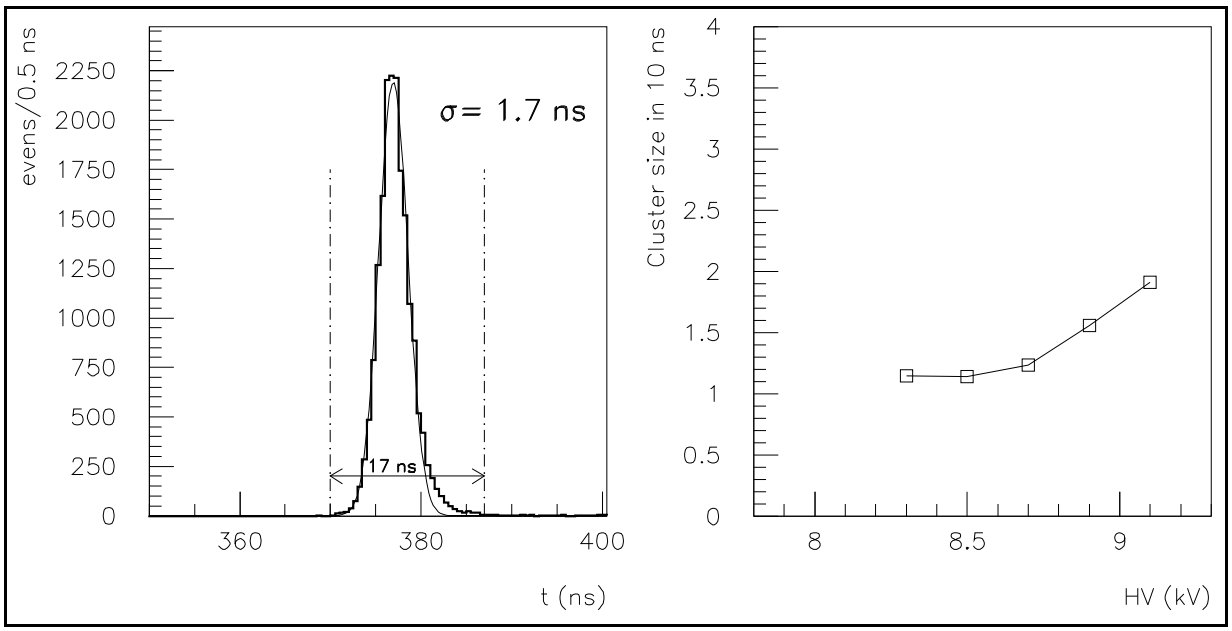


Fig. 5.9.2: Arrival time distribution at HV=8900 V (arbitrary zero).

Fig. 5.9.3: Cluster size (within a 10 ns window after the fastest strip) vs. high voltage.

It is, however, important to study the response uniformity over a large surface. A total of 18 different regions of the chamber were therefore illuminated and tested: 9 regions along the vertical direction (perpendicular to the strip direction) and 9 regions along the horizontal direction (parallel to the strip direction), each 10x10 cm^2 large, 10 cm away from the previous one and located along the central axes of the chamber.

In the following we will only discuss the vertical scanning, since the horizontal one gives very similar results.

Fig. 5.9.4 reports the efficiencies as a function of the position, at several high voltages. It can clearly be seen that, at increasing voltages the point-to-point fluctuations tend to become smaller, and eventually negligible at the detector working voltage.

The same behavior is observed for the average signal arrival time and its jitter. Both quantities are also computed at the different positions and high voltages.

In Figs. 5.9.5 the values, averaged over the different positions, of time of arrival and resolution are given as functions of the high voltage. The dashed lines select a region of 1 RMS around these mean values.

The chamber shows good uniform response over the whole surface for time related quantities as well.

5.9.2 Studies of rate capability

As discussed in Section 5.2.2, one of the critical parameters which could affect the performance at high rate is the bakelite bulk resistivity. To study this effect two small 25x25 cm^2 double-gap chambers (2.2 mm wide gap) of identical construction, but with bakelite of different resistivity, were illuminated with the high intensity pion beam at the H2 SPS line: in one case the resistivity was $\rho = \sim 5*10^{11}$ Ωcm; in the other $\rho \sim 5*10^{8}$ Ωcm. The low resistivity

material was developed on special request; further studies to understand the reproducibility and stability of this material are in progress [5.21].

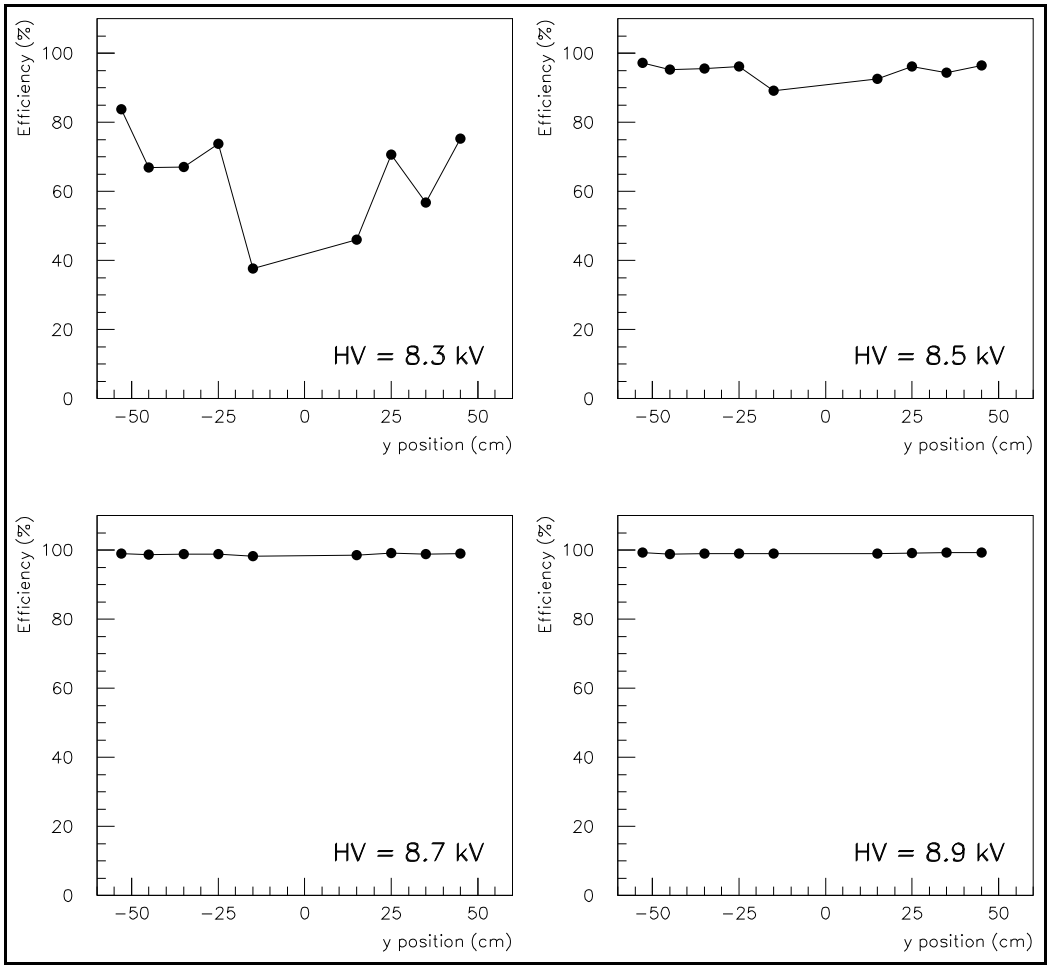


Fig. 5.9.4: Efficiency, as a function of the vertical position (perpendicular to the strip direction).

The strips read out were arranged according to the layout shown in Fig. 5.2.6b; they were 10 mm wide with a 12 mm pitch. A hybrid version of the amplifier already discussed in Section 5.6 was used as front-end electronics.

The two chambers were tested under the same experimental conditions (90% $C_2H_2F_4$ plus 10% i-C_4H_{10} gas mixture, 30 mV threshold, equivalent to 20 fC). The 150 GeV/c pion beam was de-focused in order to illuminate almost uniformly an area of 5 cm in diameter.

Tests were performed in a range of rates up to 7 kHz/cm^2, as measured by 4x4 cm^2 scintillators placed behind the two RPCs. Although they were carried on in pulse beam conditions, the 2.5 s SPS spill duration can reveal possible rate capability limitations.

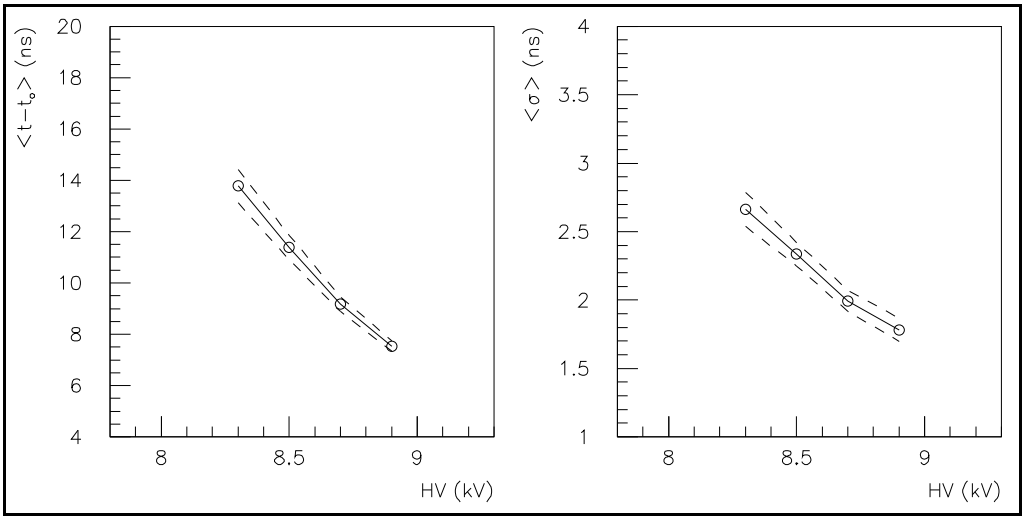


Fig. 5.9.5: Average arrival time (left) and average time resolution (right) vs the high voltage. The averages values are computed over the different vertical positions. Dashed lines select a 1 RMS region.

Figs. 5.9.6 show the average efficiency in the 2.5 s spill, as a function of the applied high voltage and the beam flux for the high and low resistivity RPCs.

The time resolution and the average signal arrival time are also shown in Fig. 5.9.7 for the low resistivity RPC. These results confirm that low electrode resistivity makes it possible to operate RPCs at high rate with practically no shift of the working point, with good timing and negligible time walk up to 7 kHz/cm^2.

The cluster size distributions for both low and high resistivity RPCs are shown in Fig. 5.9.8. In the range of resistivity studied no significant change is observed.

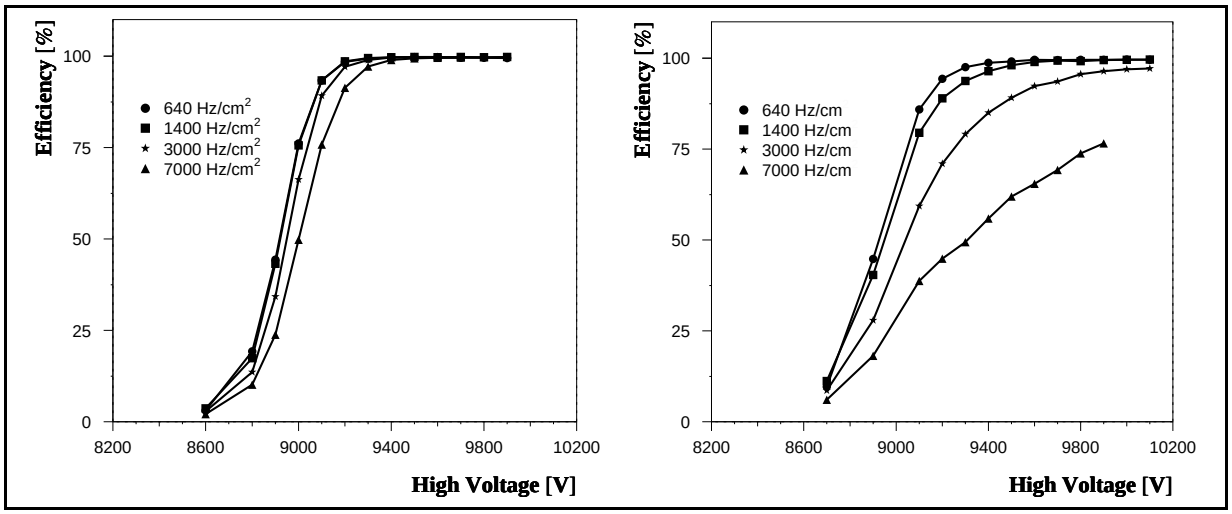


Fig. 5.9.6: Efficiency curves, at different rates, for the low resistivity RPC (top) and the high resistivity one (bottom).

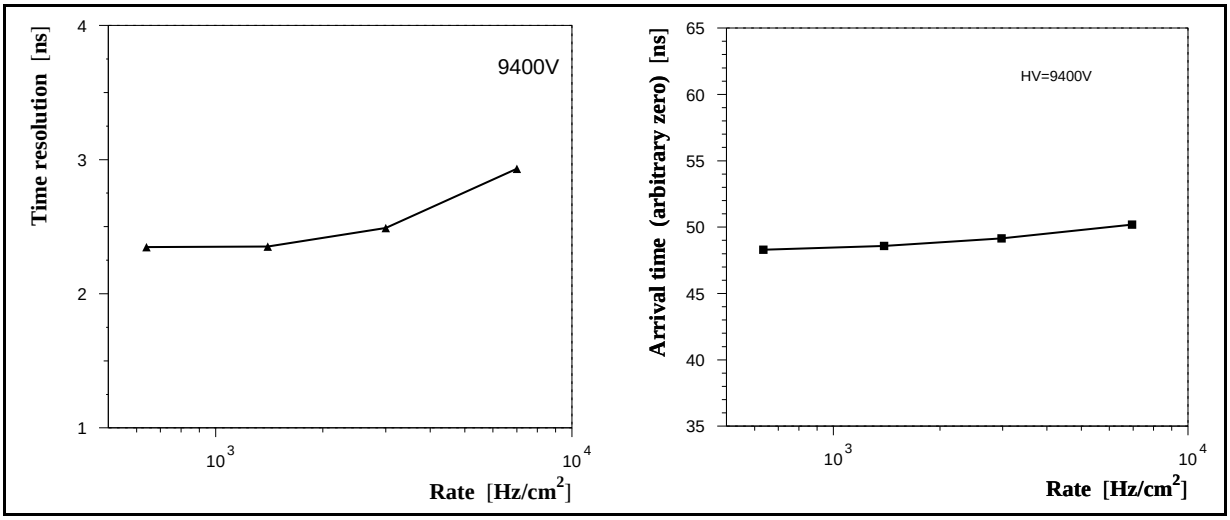


Fig. 5.9.7: Time resolution (left) and average signal arrival time (right) for the low resistivity RPC. Here the zero of the time scale is arbitrary.

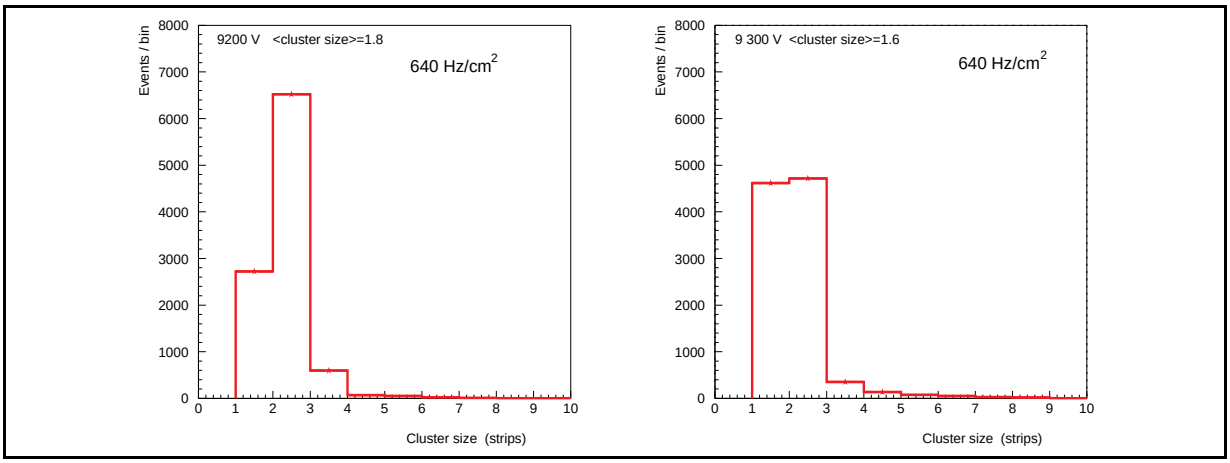


Fig. 5.9.8: Cluster size distributions for low resistivity (left) and high resistivity (right) RPCs, computed in a 10 ns window after the earliest signal.

The CMS requirements on rate capability can, therefore, be matched by tuning the resistivity to an appropriate value. For example, at the expected 1 kHz/cm^2 hit rate background, a resistivity of about 10^{10} Ωcm should guarantee a safe operation.

5.9.3 Test at the gamma irradiation facility

The Gamma Irradiation Facility (GIF) offers the possibility of studying the RPC performance in a high background environment, like LHC, by means of a powerful 15 Ci γ source located at the SPS X5 beam line. Efficiencies and time for minimum ionizing particles can, therefore, be studied with the detector uniformly irradiated. A system of several filters positioned in front of the source, and remotely controlled, allows varying background rates according to known factors. A precise calculation of the number of γs hitting, at a given absorption factor, a detector located in the area, deserves careful simulation and further studies.

Also the translation of the GIF γ rate to the LHC is not straightforward, because of the different energy spectrum, which may result in different detector sensitivity.

Two double-gap RPCs were irradiated during the 1997 test period late in the summer. The first was a 50x50 cm^2 chamber with 3 mm gas gap width, 25 cm long and 1.5 cm wide strips [5.22]. The strip size and length is typical of the endcap region. The bulk resistivity of the bakelite planes was ~ $2.0*10^{11}$ Ωcm (referred to as "high resistivity" in the following). It was positioned at a distance of 2 m from the source.

Also the low resistivity RPC, whose performance on the H2 beam line has already been described in the previous Section [5.21], was placed in front of the source, at a distance of 1.5 m.

Both chambers were instrumented with boards employing a "hybrid" version of the front-end amplifier discussed in Section 5.6.3 and were operated at a threshold of 30 mV (equivalent to ~20 fC) with a 90% $C_2H_2F_4$, 10% i-C_4H_{10} gas mixture.

In order to estimate the hit rate produced by the Compton electrons, a preliminary cluster-finding of the signals coming from different strips is necessary, because of the intrinsic detector cluster size and the electronics cross-talk. First, the single strip signals are sorted in time, starting from the fastest one; adjacent strips are then searched and clustered within a 250 ns time window.

The observed rate can be computed by simple cluster counting or, more accurately, by measuring the time differences between two subsequent clusters, in a given fiducial area, within the 64 μs time buffer of the TDC which was used.

The distribution of time differences follows an exponential law, whose slope gives the rate of clusters. Both methods give, within the errors, the same result: we observe a rate of about 2.2 kHz/cm^2 at absorption 1, and about 1.4 kHz/cm^2 at absorption 2, in the case of the RPC located 2 m away from the source.

Because of the double gap layout, the observed hit rate accounts for ionization taking place in both the gas gaps. Under the assumption that no ionization from a given γ goes from one gap to the other, a single gap rate half of the measured one should be considered as an estimate of the background.

Some care must be taken in the calculation of the efficiency. In a given time window, the number of observed events N_{ob} is:

$$N_{ob} = \varepsilon N_t + P_s(1- \varepsilon)N_t$$

where ε is the RPC efficiency, N_t is the number of triggers and P_s is the probability that a spurious hit appears in the chamber. The efficiency is therefore given by:

$$\varepsilon= [(N_{ob}/N_t) - P_s] / (1-P_s)$$

and P_s is determined by counting the hits in a time window delayed 500 ns after the trigger.

Fig. 5.9.9 show the efficiencies curves and the time resolutions at various absorption factors for the high resistivity RPC.

In Fig 5.9.10 the mean arrival time is also given at different voltages and rate conditions. In this last plot we prefer to consider the rates, as computed according to the method explained

above, instead of absorption factors. Even for the high value of resistivity, the chamber behavior is already satisfactory for CMS operation.

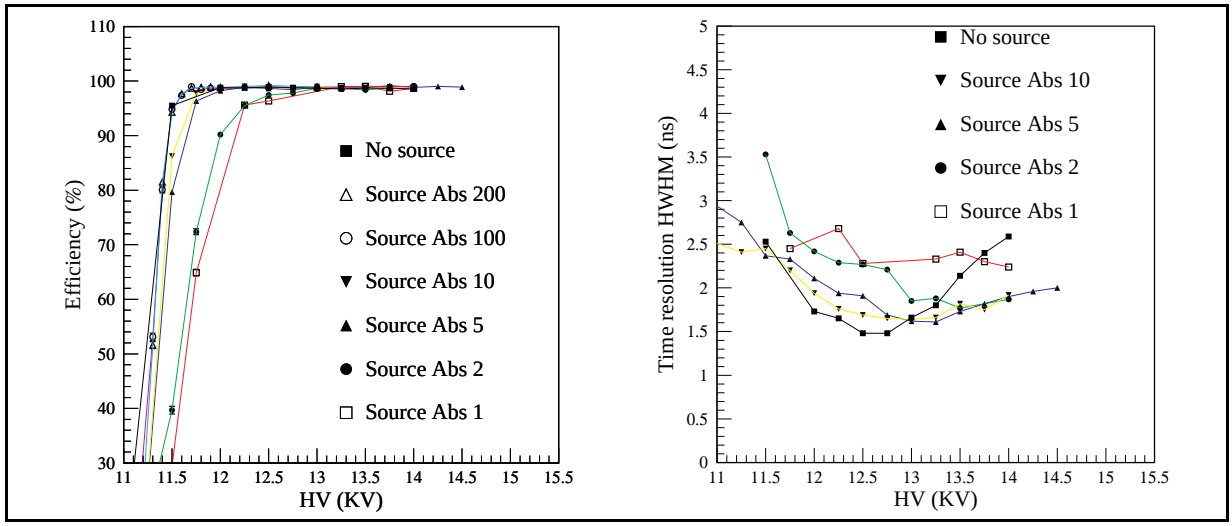


Fig. 5.9.9: Efficiencies (left) and time resolutions (right) for the high resistivity RPC at different rate conditions.

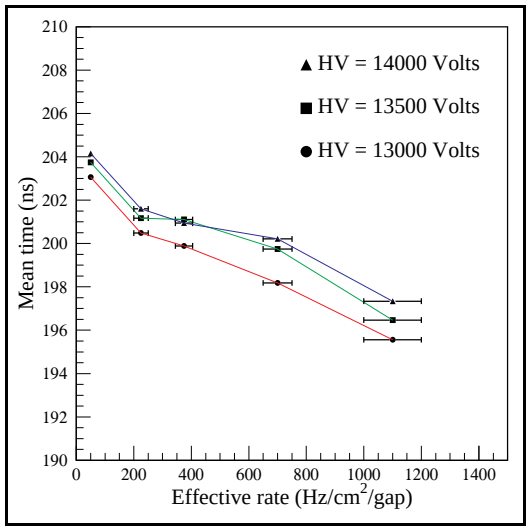


Fig. 5.9.10: Mean signal arrival time (arbitrary zero) as a function of the rate and the applied voltage for the high resistivity RPC.

Even better performances can be achieved by decreasing the resistivity of the electrodes, as already noted in the previous section. The efficiencies and the mean signal arrival times for the low resistivity RPC are shown in Fig. 5.9.11.

In this case, the rate conditions are even more severe, since the chamber was located closer to the source. The results are very encouraging, and allow us to conclude that, by choosing an appropriate low value of resistivity, RPCs can operate efficiently at very high rate. Of course a careful evaluation of the realistic rate conditions in the experiment is necessary to

tune the resistivity of the electrodes to an appropriate value, as required for the expected operational conditions.

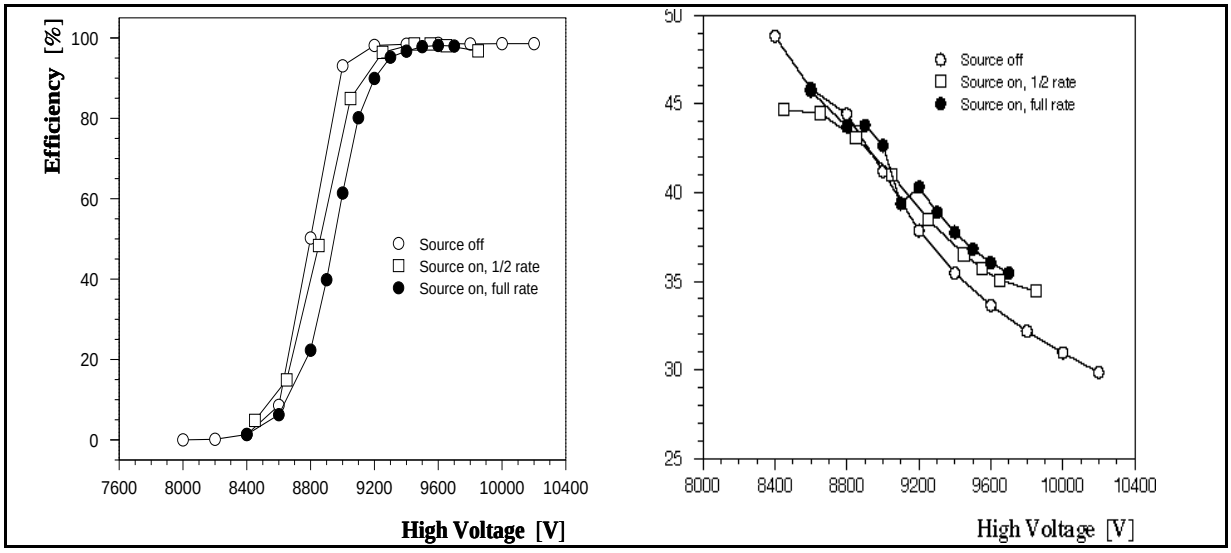


Fig. 5.9.11: Efficiencies (left) and mean signal arrival time (right) as a function of the rate and the applied voltage for the low resistivity RPC.

5.10 PATTERN COMPARATOR TRIGGER FOR RPC

This section contains the definition of the algorithms and a brief technical description of the RPC trigger electronics, for which we use the acronym PACT (Pattern Comparator Trigger). Detailed description of the system will be given in the forthcoming Trigger and Data Acquisition TDR. The dedicated detectors – RPCs – and their front end electronics were already described in the previous sections of this chapter. In Section 5.10.2 we describe the segmentation planned for the PACT trigger. Section 5.10.3 is devoted to a description of the trigger electronics. First, we present the general layout of the PACT electronics, and in the following subsections we discuss the basic components of the trigger system: optical fiber transmission with multiplexing / demultiplexing, layout of the trigger crates and the constituent trigger, sorter, timing and readout boards. We finish Section 5.10.3 with a description of the PAC processor, which is a kernel of the PACT trigger. Section 5.10.4 contains results of the PACT simulation.

5.10.1 The algorithm

The PACT algorithm has been described in detail elsewhere [5.23] but, for the sake of completeness, we recall here its basic features. Because of energy loss fluctuations and multiple scattering there are many possible hit patterns in the RPC chambers for muons of the same momenta emitted in a particular direction. In order to trigger on a muon with a particular hit pattern found in the RPCs, the PACT electronics performs two functions:

- requires the time coincidence of hits in several (3 or 4) muon stations, and
- matches the spatial distribution of these hits with one of many possible pre-defined hit patterns for muons of various momenta. This way both the bunch crossing and the momentum code of a muon are given.

Initially, the pre-defined patterns will be obtained from simulation, and programmed into Pattern Comparator (PAC) processors. The pre-defined patterns will be divided into classes with a momentum code assigned to a class. The more curved tracks will be assigned lower codes. The PACT trigger is a threshold trigger; it gives a momentum code if the actual pattern of hits is straighter than any of the pre-defined patterns with a lower code.

The number of pre-defined patterns which have to be compared with the actual one is large. To reduce this number we have taken two steps. Firstly, the RPC signals from neighboring strips are OR-ed together. This is done during the demultiplexing of RPC signals (see below for details). For very curved tracks of low momenta, we do not require high spatial resolution and we can perform the pattern matching on the OR-ed strips, thus reducing the number of pre-defined patterns. Presently, we envisage double (OR2) and quadruple (OR4) ORs. For the high momentum muons we use single (OR1) strips. Second, the design of the PAC processor implements the parallel matching of all pre-defined patterns which pass through a given strip in the reference RPC plane (Muon Station 2), thus saving processing time.

The algorithm described above will work very well in an ideal world, in which every muon always leaves one hit strip in every RPC station. In reality, however, there are both chamber inefficiencies and RPC cluster size to be taken into account. The realistic algorithm which accounts for these effects was called by us three-out-of-four (3/4). It requires three- or fourfold coincidence and pattern match. In the case of several matches in a given spatial region connected to one PAC processor (called segment, see the next section) a candidate with fourfold match, carrying a so-called quality bit set to one, is always preferred over that of a threefold match, with quality bit set to zero.

In case of equal quality bits, the candidate with the higher momentum code is chosen. Since one muon may result in several candidates in neighboring segments, the sorting and vetoing algorithm described in Sections 5.10.3.4 and 5.10.4.3 is then implemented.

5.10.2 Segmentation of the PACT trigger

It is useful to recall that the strip layout for the RPC chambers is designed to be projective in azimuth. Therefore the strip width varies with radius from about 10 mm at low radii at high η to about 40 mm at the outer radius of the CMS detector. In the other dimension, the strips length varies from about 1300 mm in the barrel to about 100 mm in the endcaps.

The currently planned segmentation in pseudorapidity is shown in Figure 5.10.1, together with a currently planned segmentation of the RPC chambers [5.24]. The size of each pseudorapidity ring - a projective region in pseudorapidity - is in the range 0.1-0.2. It is clear from this figure that the signals from several strips have to be brought together to form a projective ring structure.

The most basic logical unit of PACT is called a segment. It subtends approximately 2.5° in azimuth and 0.1 units in pseudorapidity. A segment subtends eight RPC strips in the reference plane in Muon Station 2, and the strips from wider areas in other stations are connected to it, forming a cone. The size of a cone was optimized by extensive simulations. In azimuth the cone size is 18, 18, and 22 strips for stations 1, 3 and 4 respectively. It is evident that the signal from a given strip in a non-reference plane of RPCs has to be shared between several segments in ϕ and between several rings in η. The difficult technical problem of realizing the large number of required reliable interconnections is still being studied.

The baseline design of the RPC system covers pseudorapidity range $|\eta|<2.1$. Provision is made for an upgrade up to $|\eta|=2.4$. The full η range is divided into 33 (baseline) or 39 (upgrade) rings. Each ring contains 144 ϕ-segments.

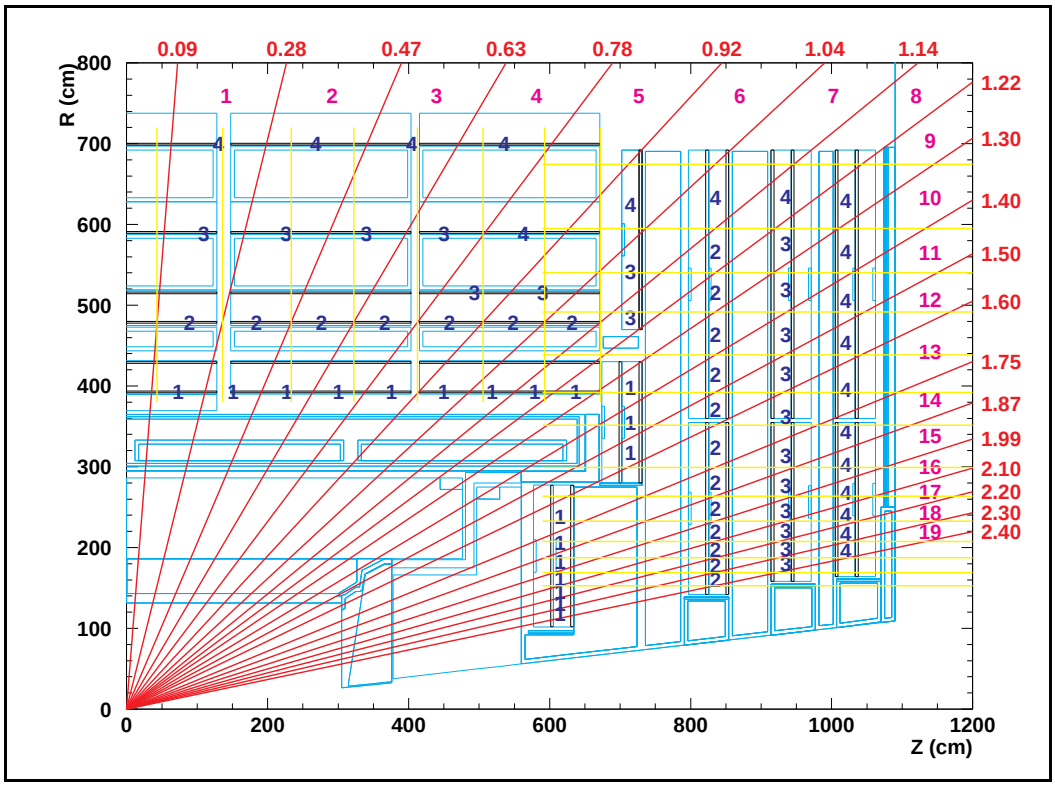


Fig. 5.10.1: PACT segmentation in pseudorapidity.

5.10.3 Technical description

5.10.3.1 General layout of the pattern comparator trigger (PACT)

The general layout of the PACT electronics is shown in Figure 5.10.2. There are two basic components: 1) the multiplexing and link system, and 2) the trigger crate.

The purpose of the multiplexing and link system is to transport the RPC signals from their front-ends on the detector to the trigger crates in the counting house 120 m away. Presently we envisage using a 1.2 Gbit/second optical link system.

The output of the trigger crates goes into two streams: to the DAS system through the Readout Board and to the Global Muon First Level Trigger (GMT LV1). The purpose of the latter is twofold: first, to perform final sorting of muon candidates in order to reduce the list of muon candidates to a manageable length and, second, to compare the PACT with the DT/CSC trigger and decide on the final list of muon candidates to be presented to the Global LV1.

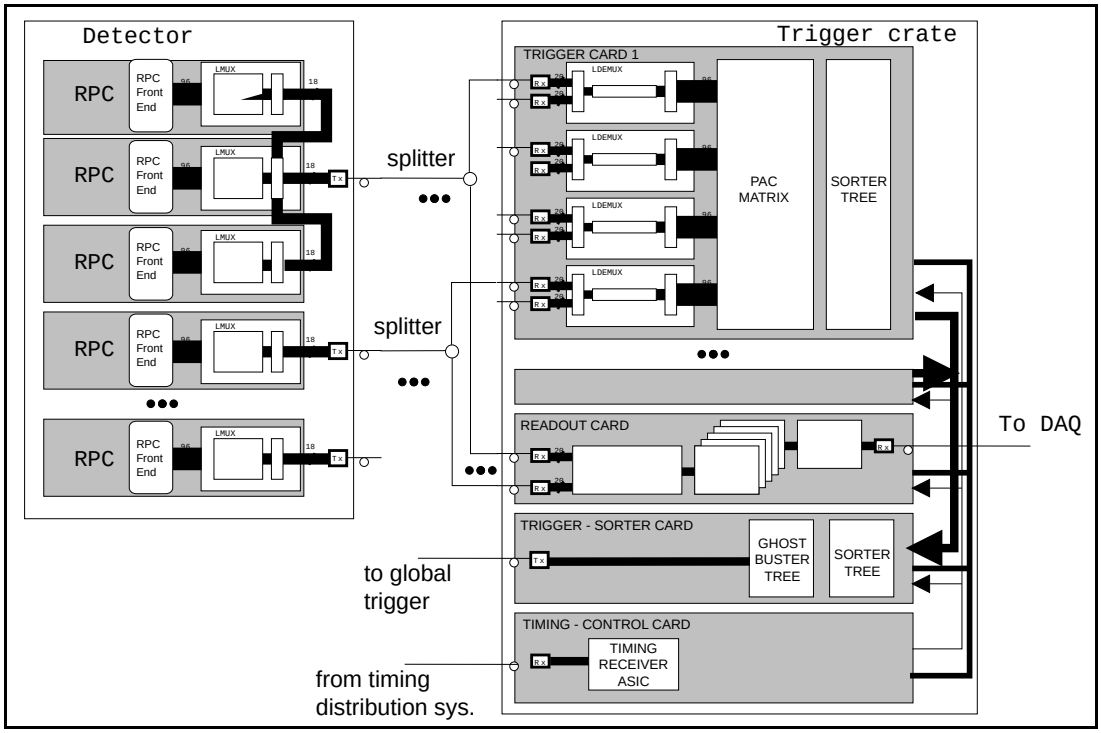


Fig. 5.10.2: General layout of the PACT trigger electronics. The optical link system joins the front-end electronics on the detector to trigger crates in the counting room. The incoming signals are split and transported to several Trigger Boards and/or Trigger Crates.

5.10.3.2 Optical fiber link and multiplexing/demultiplexing scheme

An optical link system is needed to transport the RPC signals from the detector to the trigger crates in the counting house. The transported data have to be multiplexed (and possibly packed) in order to efficiently utilize the bandwidth of the costly link system. This increases the latency of the PACT trigger. At present the cost of one transmitter / receiver with appropriate parallel-to-serial and serial-to-parallel converters having a bandwidth of 1.2 Gbit/second reaches 500 CHF; this is clearly one of the cost driving items of the PACT electronics [5.25].
The presently envisaged scheme shown in Figure 5.10.3 consists of the following steps:

a) the RPC signals on the detector are synchronized with a given bunch crossing and placed in the input buffer,
b multiplexing and serialization is performed on the data in the input buffer recognized as being from one bunch crossing, 3
c) serialized data are sent and received frame by frame,
d) demultiplexing and (possibly) resynchronization are performed.

We have performed simulations [5.26] of the scheme, taking into account recently calculated neutron and gamma background rates [5.27] and realistic cluster sizes in the RPCs. In order to minimize the cost we have assumed 2 RPC chambers / link in the low rate region of the barrel, one link per chamber for most of the remaining chambers, and 2 links per chamber in the small region of very high rates (pseudorapidity around 1.7 - 2.1 in ME1/1 and ME2/1). It turns out that for the 1.2 Gbit/s transmission speed one can have negligible transmission losses (at the level of one millionth of a bunch crossing, corresponding to a trigger efficiency loss of less than 1%) for the reasonably small buffer sizes (12 for the input, 8 for the output), and

modest increase in latency. Moreover, we have started the VHDL simulation of the multiplexing / demultiplexing circuit and we found that presently available ALTERA FPGAs are already capable of performing the task. Therefore we believe that this scheme is technically feasible. The optimization of the link system is, however, still not final because of the rapid progress in optical transmission technology which may result in drastic reduction of prices and/or faster transmission.

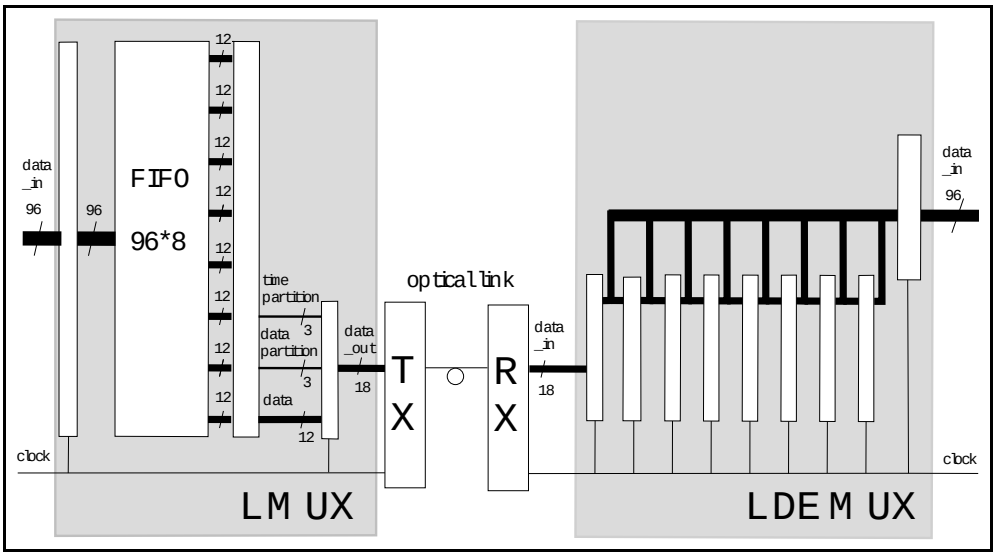


Fig. 5.10.3: Schematic diagram of the link and multiplexing/demultiplexing system for PACT.

5.10.3.3 Trigger crate

The trigger Crate (TC) is a functional unit working on RPC signals from one ring - a projective sector in pseudorapidity (approximately 0.1 units). Its main functions are:

- elaborating the PACT algorithm and producing a list of up to 4 muon candidates from the ring,
- providing the readout of the relevant RPCs,
- providing control, programming and calibration functions.
- One TC consists of:
- twelve Trigger Boards (TB), each of them serving 12 segments (i.e. one RPC chamber in the reference plane),
- one Sorter Board (SB),
- one Readout Board (including FED),
- one Timing and Control Board containing the TTC receiver chips, and
- one Crate Controller.

The input signals from the RPCs are brought to 12 Link Cards, sitting in the back of a crate. The necessary interconnections between segments are realized by:

- a custom design back-plane between Link Cards and the TB,
- optical fibers carrying the split signals from the Link Cards to the Trigger Boards,
- a TB PCB, and
- a small number of crate-to-crate flat cables.

The design of this aspect of PACT is still under way.

5.10.3.4 Trigger board

This board contains:

- demultiplexing, resynchronization and timing/delay circuits,
- PACT segment processors servicing 12 trigger segments,
- the layer of sorter/ ghost buster circuits [5.28], and
- necessary control and monitoring circuits.

It is not yet decided whether the demultiplexing ends of the link system will reside on the Trigger Boards or on the Link Cards at the back of the Trigger Crate (see previous subsection), but at the moment the latter seems to be the preferable solution. Since one segment receives signals from different muon stations, the need for resynchronization and proper time alignment is obvious. Therefore the Trigger Board is equipped with programmable delays. The PAC processor is discussed in more detail later in this chapter.

The necessity of sorting and vetoing of muon candidates found in the neighboring segments (both in azimuth and pseudorapidity) was already mentioned. The segment processors on one trigger board are connected to neighboring segments of strips in ϕ. The trigger board is a logical place to house the vetoing of ghosts in ϕ, realizing the ghost-buster (GB) algorithm [5.28].

This algorithm is based on the observation that most of the ghosts in ϕ found by the Pattern Comparator are either due to clusters in the RPCs or due to use of OR-ed signals. The GB algorithm detects contiguous regions in segment space with several candidates and selects one of them (that with the highest quality bit and / or highest momentum code). Therefore, the GB algorithm allows for at most 6 muon candidates from the initial 12 segments on a trigger board. The layer of GB is then followed by one sorter chip [5.29] to produce a list of at most four muon candidates from a trigger board. At this stage each candidate has the 8 bit address added to its 7 bit muon code. The vetoing of ghosts in pseudorapidity is done at the level of final sorting in the Global Muon LV1.

5.10.3.5 Sorter board

The basic function of this board is to reduce the number of candidate muons coming out from a trigger crate to four. Each of twelve trigger boards in this crate gives at most four muon candidates. Their addresses and momentum codes are passed to the Sorter Board, which contains four layers of sorter chips (10 chips). A detailed description of the sorter chip can be found in [5.29]. Here, we recall that the sorter chip selects the 4 muon candidates with the highest momenta (including the quality bit selection in the spirit of the 3/4 algorithm) out of eight input candidates.

5.10.3.6 Readout board

This board provides a standard interface - Detector Dependent Unit (DDU) between the detector dependent information and the Front End Driver, a data acquisition module being designed by the DAS group. The design of the DDU board has not yet started.

5.10.3.7 Synchronization and control board

The purpose of this board is:

- to provide the distribution of the Timing and Trigger Contol signals to the boards in a trigger crate, and
- to provide control and monitoring of various boards.

The board is in a very early stage of defining its specifications.

5.10.3.8 Pattern comparator (PAC) ASIC and PACT segment processor

The PAC is a fully custom ASIC which performs the matching of an actual RPC pattern to a set of pre-defined patterns programmed into it, and outputs the five bit muon candidate's momentum code, its sign and a quality bit. The size of a cone of strips in muon stations 1, 3 and 4 to be connected to a strip in the reference plane (muon station 2) was optimized by extensive simulations [5.23]. Presently, one PAC is connected to 4 RPC strips in the reference plane, and to 14, 14 and 18 strips in stations 1, 3 and 4, respectively. We envisage the possibility of setting some input strips artificially always on or off. Input strips could be masked in a programmable way. Presently we plan space for 160 programmable pre-defined patterns for each strip in the reference plane. The pre-defined patterns have to be chosen from the cone of $\pm$ 5, $\pm$ 5, $\pm$ 7 strips in stations 1, 3, and 4. Since several muon candidates with different momentum codes and quality bits could be found inside the chip, the final stage of the internal logic applies the 3/4 algorithm, described earlier, to produce the unique output code. The chip is equipped with a boundary scan circuit which, besides the usual diagnostic and debugging functions, is used for programming the masks for input strips, patterns and delays. The matching procedure occupies the time of 2 bunch crossings.

When designing the ASIC we found that the PAC described above is at the limit of 0.7 μm ES2 technology, with 800 000 transistors on a silicon surface of 80 mm^2 [5.30]. One PACT segment has to deal with OR1, OR2 and OR4 signals and it is connected to 8 OR1, 4 OR2 and 2 OR4 strips in the reference plane. That is why we presently need four PAC chips, connected in cascade, to form one PACT segment processor.

The PAC processors are designed to be connected in cascade; working in this mode the output code from one PAC is transmitted to the next PAC, where it is compared with the code produced internally. The 3/4 algorithm is then used to produce the new (joint) output code which is then again passed to the next PAC. This produces a unique 7 bit muon code from one PACT segment. Working in the cascade mode may require extra bunch crossings. Therefore, the output circuits of a PAC are equipped with a buffer of (programmable) 1 or 2 bunch crossings depth. Therefore, the total latency of a PACT segment processor may be 4 bunch crossings.

The pre-production PAC ASIC design is now complete. Before completing the design of a pre-prototype, the test chips with various PAC building blocks were produced and measured to check the reliability of the simulation and verify the design.. The series of pre-production prototypes will be available for tests late in 1997.

5.10.4 Simulated performance

5.10.4.1 CMSIM and MRPC

The three-out-of-four PACT trigger algorithm, described in detail in Sec. 6.2.3, is implemented in CMSIM [5.32] (from version 101 on) as a separate package called MRPC [5.33]. This package performs two major tasks: 1) simulation of the PACT trigger electronics response, and 2) preparation of a list of pre-defined patterns. The philosophy guiding the design of the MRPC package is to be as close as possible to the electronic realization of PACT.

The simulation of the PACT trigger electronics response consists of the RPC digitization, optionally taking into account chamber cluster size, and the implementation of full PACT algorithm with ghost busting, sorting and vetoing. There is a special routine which performs the

pattern recognition i.e. decides which segment (which pseudorapidity tower) contains a muon candidate. Multiple candidates (ghosts) caused by a single incoming muon are included.

The task of preparing a list of pre-defined patterns is for experts only. The list is required both by the PACT simulation and by the PAC processors, into which it is programmed. In the special runs, the simulated muons of given momenta are transported through the CMS muon system and their hits in the RPCs are digitized and recorded (on separate files for each incoming momentum). Then a special analysis program produces the list of all possible hit patterns and counts their frequency. The frequency tables from different momenta are then merged together, ordered, and some rare patterns are rejected.

The recent, most extensive simulation of single and double muon triggers is described in [5.34]. The results quoted below are mostly taken from there.

5.10.4.2 Efficiencies and rates

In the data presented in this subsection there are neither clusters nor inefficiencies assumed for the RPCs, and the ghosts are cut away by vetoing 8 segments in the ϕ-η plane surrounding a muon candidate. The results are therefore too optimistic: the rates are somewhat low. The more realistic case with clusters and ghosts will be discussed in the next subsection. The typical quality of the PACT trigger algorithm is shown in Figure 5.10.4, where the PACT-reconstructed transverse momentum of a muon from the sample of minimum bias events is shown as a function of its generated transverse momentum at the vertex, and in Figure 5.10.5 where the same variables are plotted for muons from a sample of Z^0 decays. The data in the above figures are for $|\eta| < 2.1$ i.e. for the whole range covered by the baseline PACT trigger. The plots reflect the PACT design, which always assigns the highest possible momentum code to a given pattern of hits. Therefore, most of the data on these two plots lie above the diagonal, and reasonably close to it.

Single muon trigger rates coming from different physical channels are shown in Figure 5.10.6. They are compared with the induced background rates in Figure 5.10.7. The muons from minimum bias events, shown in Figure 5.10.6 are those from (prompt) beauty and charm decays as well as those from pion and kaon decays in flight inside a tracker. There are two mechanisms which give rise to induced background: a random coincidence of background gamma/neutron hits in the RPCs, and a coincidence of a random gamma/neutron hit with a low momentum (stopping) muon track, which increases its apparent momentum.

The double muon trigger rates, simulated with the same assumptions, are shown in Figure 5.10.8. The second muon from a hard source like Z^0 or WW pair production may come from a pion or kaon decay. The detailed composition of the double muons from minimum bias events is shown in Figure 5.10.9. Most of them come from events with $b\bar{b}$ pair production, where the most energetic muon is typically coming from b decay while the second muon is most likely coming from a pion/kaon decay.

5.10.4.3 Clusters and ghosts

The three out of four algorithm, described in Sec. 6.2.3, has built-in ghost busting and vetoing procedures. These depend on the size of clusters in the RPCs, the declusterization algorithm implemented in the PACT electronics (presently envisaged to be done together with the demultiplexing and resynchronisation of link signals), and also on the RPCs segmentation and detailed connections to the particular Trigger Crates.

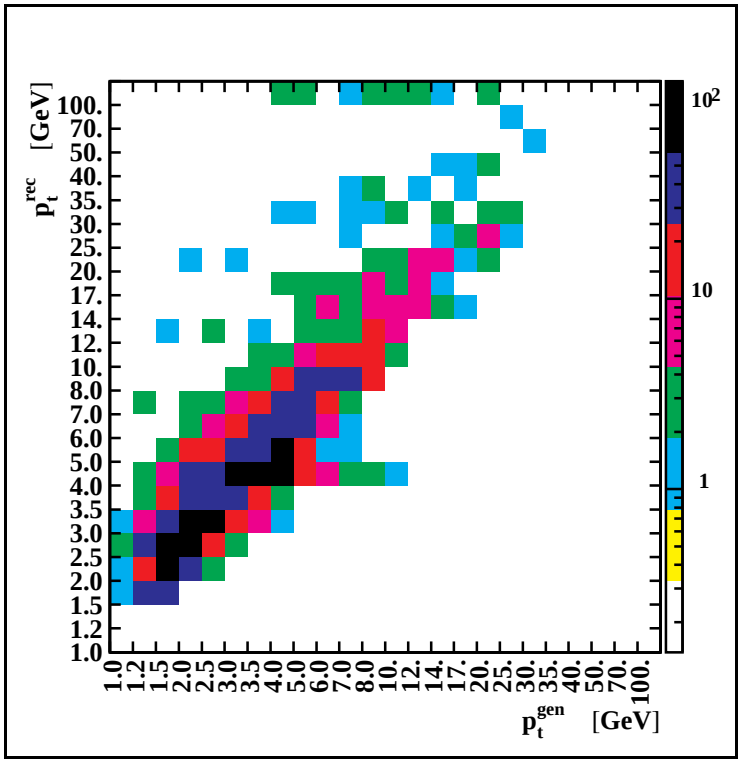


Fig. 5.10.4: PACT response to minimum bias events. The gray coding indicates the relative numbers of events.

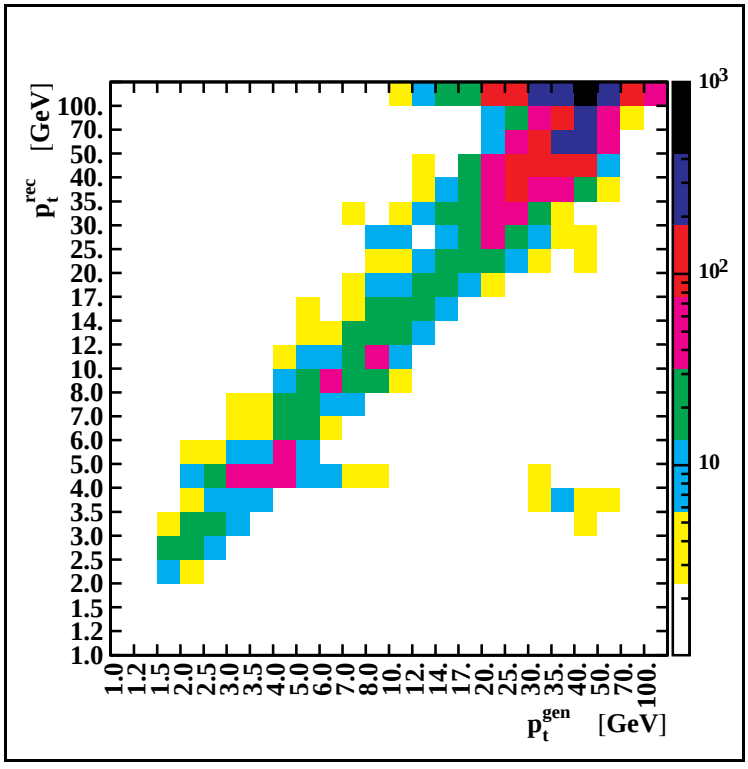


Fig. 5.10.5: PACT response to Z^0 events.

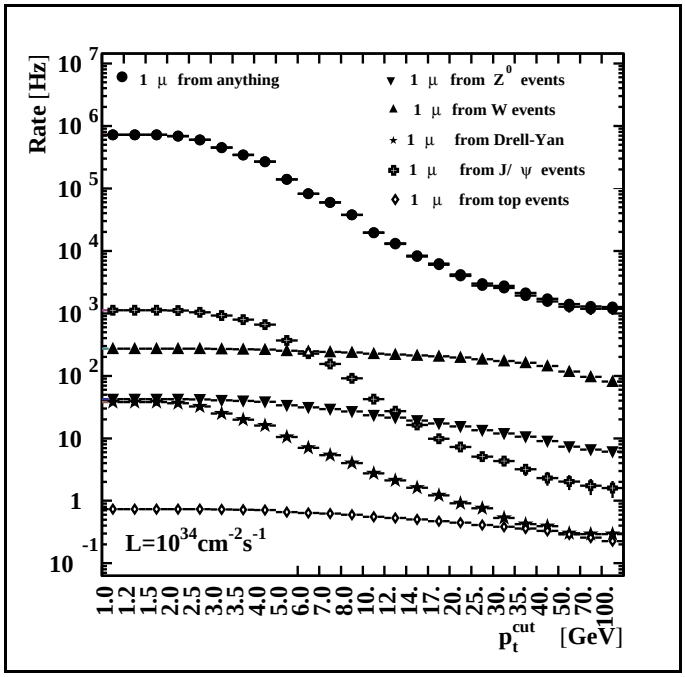


Fig. 5.10.6: Single muon trigger rates from physical sources for L= 10^{34} $cm^{-2}s^{-1}$.

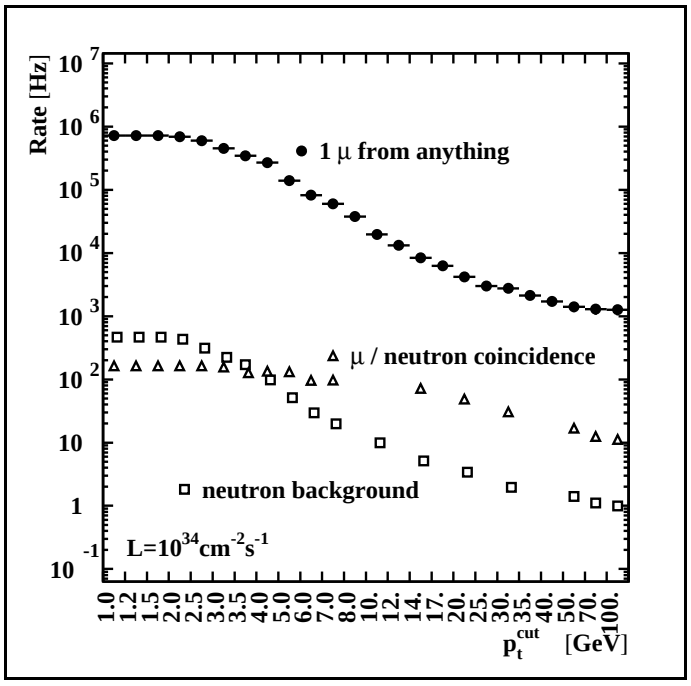


Fig. 5.10.7: Single muon trigger rates from physical signal channels and background (L= 10^{34} $cm^{-2}s^{-1}$).

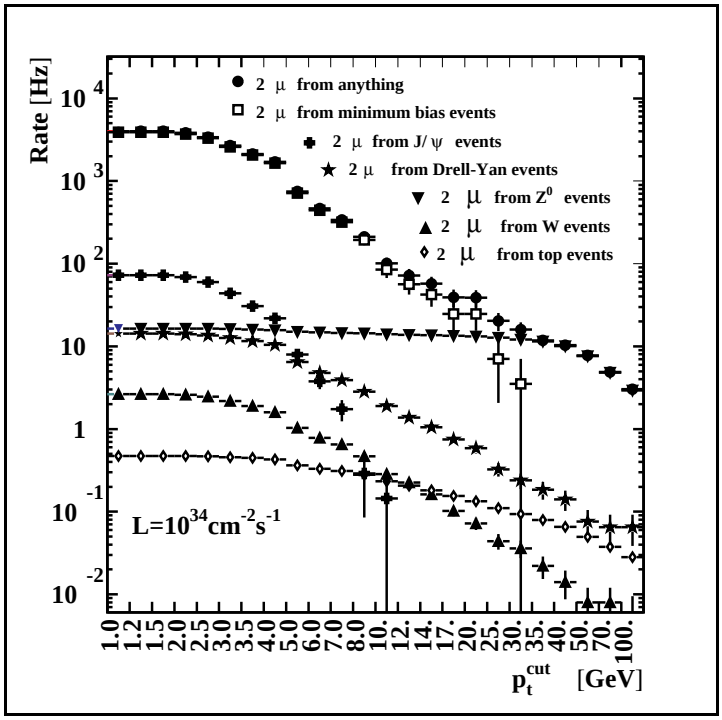


Fig. 5.10.8: Double muon trigger rates from physical sources for L= 10^{34} $cm^{-2}s^{-1}$.

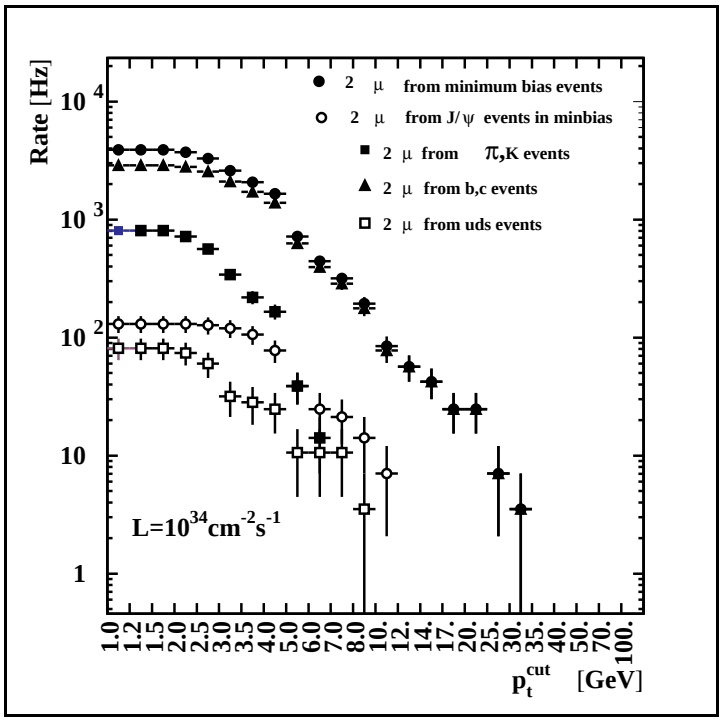


Fig. 5.10.9: Detailed composition of double muon minimum bias events.

In order to increase the PACT efficiency we implemented a threefold temporal and spatial coincidence between signals from the different RPC stations, on top of the fourfold one. We have also decided to use double or quadruple OR-ed signals in order to reduce the number of pre-defined patterns. These measures introduced ghosts – spurious muon candidates. An example of a severe ghost problem is shown in Figure 5.10.8, where the simulation of the old PACT algorithm with no ghost suppression results in a spurious double muon rate comparable to or higher than the real 2 μ rate.

They are mostly due to PAC finding candidates in three planes on top of some other candidate based on four planes. This is especially easy if the muon's passage through an RPC results in a cluster of hit strips. If both candidates are found within the same segment, its processor is able to deal with the problem (see Section 5.10.1 for details). If, however, the candidates are in different segments, we need some additional refinement to the algorithm - ghost busting and vetoing, described in more detail in Section 5.10.1.

While the final parameters of RPCs to be used in CMS are still being optimized, we have studied the trigger rate dependence on the cluster size and declusterization algorithm. Single muon rates for various cluster sizes and declustering algorithms are compared in Figure 5.10.11. The ghost busting algorithm was applied here. The curves for an average cluster size of 1.9 cm closely correspond to recent measurement of RPC prototypes [5.10]. With the present version of the GB algorithm, we keep ghosts at the 0.001 % level of single muon trigger rates. True and fake dimuon trigger rates, obtained with the improved simulation, are shown in Figure 5.10.12. Comparison with Figure 5.10.10 shows that the spurious dimuon rate went down to manageable proportions.

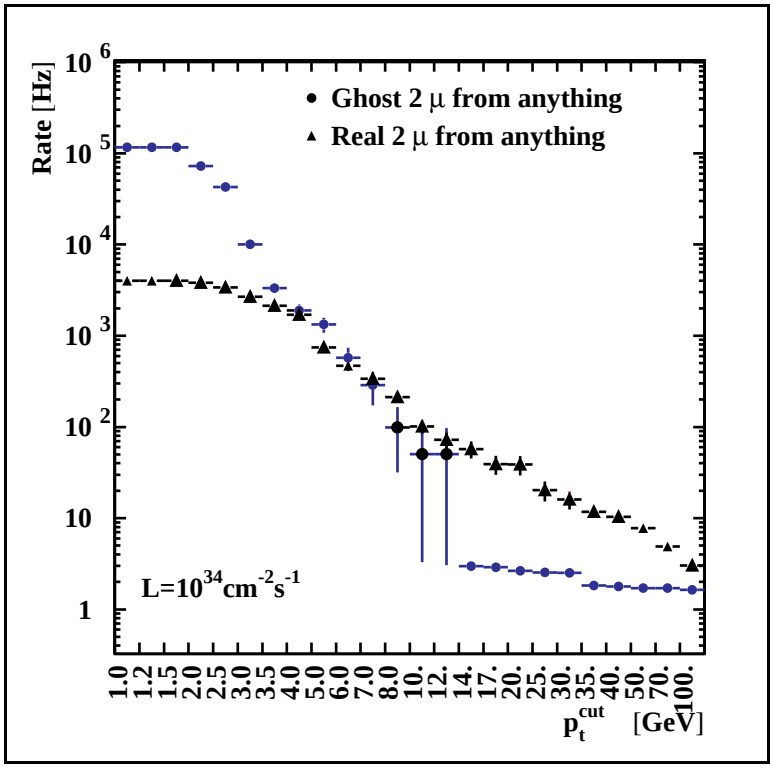


Fig. 5.10.10: Ghost rate of spurious double muon candidates compared to real double muon trigger rate. Early version of PACT algorithm (CMSIM 101).

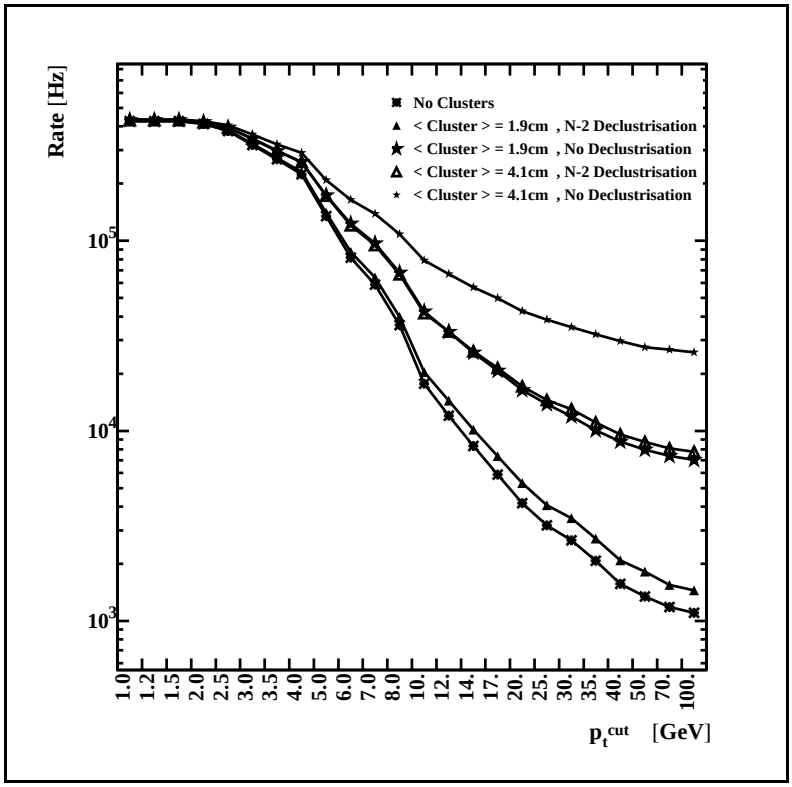


Fig. 5.10.11: Single muon rates for several average cluster sizes with and without declustering algorithm.

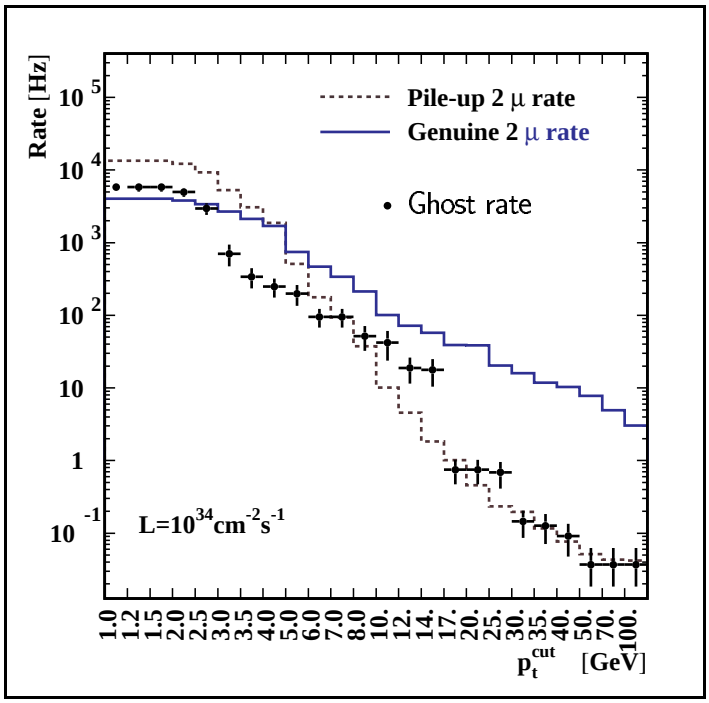


Fig. 5.10.12: True and fake dimuon rates.

References

[5.1] R.Santonico and R.Cardarelli, Nucl. Instr. and Meth. 187 (1981)377-380.

[5.2] R. Cardarelli et al., Nucl. Instr. and Meth. A 333 (1993) 399.
I. Duerdoth et al., Nucl. Instr. and Meth. A348 (1994) 303-306.
C. Bacci et al., Nucl. Instr. and Meth. A 352 (1995) 552.
I. Crotty et al., Nucl. Instr. and Meth. A 337 (1994) 370.

[5.3] G. Bruno, "A simulation study of the RPC muon trigger for CMS", CMS Note in preparation.

[5.4] M. Abbrescia et al., "Properties of $C_2H_2F_4$ based gas mixtures for avalanche mode operation of Resistive Plate Chambers", CMS Note 97/004. Nucl.Instr.Meth., in print.

[5.5] M. Abbrescia et al., "A Monte Carlo program for the simulation of RPC in avalanche mode", Bari-CMS internal note.
M. Abbrescia et al., "A model for the simulation of RPCs in avalanche mode", in Proceedings of the 4th International Workshop on Resistive Plate Chamber and Related Detectors, Napoli, Italy, 15-16 October 1997.

[5.6] M. Abbrescia et al., "Resistive Plate Chambers in avalanche mode: a comparison between model predictions and experimental results", in Proceedings of the 7th Meeting on Advanced Detectors, La Biodola, Italy, 25-31 May 1997.

[5.7] H. Genz, Nucl. Instr. and Meth. 112 (1973) 83-90.

[5.8] E. Gatti et al., Nucl. Instr. and Meth. 193 (1982) 651-673.

[5.9] P.Vitulo et al., "Properties of bakelite surfaces", in Proceedings of the 4th International Workshop on Resistive Plate Chamber and Related Detectors, Napoli, Italy, 15-16 October 1997.
M. Abbrescia et al., Nucl. Instr. and Meth. A 394 (1997) 13-20.

[5.10] M. Abbrescia et al., "Test beam results on Resistive Plate Chambers for the CMS experiment", CMS NOTE 1997/062.

[5.11] P. Bernardini et al., Nucl. Instr. and Meth. A355 (1995) 428.

[5.12] E. Gorini et al., "Drift velocity measurements in $C_2H_2F_4$ based mixtures", in Proceedings of the 4th International Workshop on Resistive Plate Chamber and Related Detectors, Napoli, Italy, 15-16 October 1997.

[5.13] M. Abbrescia et al., Nucl. Instr. and Meth. A392 (1997) 155-160.

[5.14] G. Bressi et al., Nucl. Instr. and Meth. A261 (1987) 449;
A. Antonelli et al., Nucl. Instr. and Meth. A337 (1993) 34;
M. Abbrescia et al., Nucl. Instr. and Meth. A336 (1993) 322;
L.Antoniazzi et al., Nucl. Instr. and Meth. A315 (1992) 92;
E. Petrolo et al., Nucl. Instr. and Meth. A315 (1992) 45;
C. Bacci et al., Nucl. Instr. and Meth. A315 (1992) 102;
M. Ambrosio et al., Nucl. Instr. and Meth. A344 (1994) 350.

[5.15] R. de Asmundis et al., "Performances of the RPC trigger system in L3", in Proceedings of the 3rd International Workshop on Resistive Plate Chambers and Related Detectors, Pavia 11-12 October 1995 (eds. S. Ratti and M.Merlo).

[5.16] The BABAR Collaboration, Technical Design Report (March 1995).

[5.17] M. Abbrescia et al., Nucl. Instr. and Meth. A 359 (1995) 603-609.

[5.18] E. Cerron Zeballos et al., Nucl. Instr. and Meth. A 392 (1997) 145.

[5.19] E. Cerron Zeballos et al.,"Micro-streamers and the Micro Gap RPC", submitted to Nucl. Instr. and Meth. A;

E. Platner, "Electronics for RPCs", in Proceedings of the 4th International Workshop on Resistive Plate Chamber and Related Detectors, Napoli, Italy, 15-16 October 1997.

[5.20] G. Pugliese et al., "Performances of a large double gap RPC", in Proceedings of the 4th International Workshop on Resistive Plate Chamber and Related Detectors, Napoli, Italy, 15-16 October 1997.

F. Loddo et al., "Front-end for the RPC detector in CMS", in Proceedings of the 4th International Workshop on Resistive Plate Chamber and Related Detectors, Napoli, Italy, 15-16 October 1997.

[5.21] W. Dominik et al., "High rate performance of inverted double gap RPCs", Proceedings of the 4th International Workshop on Resistive Plate Chamber and Related Detectors, Napoli, Italy, 15-16 October 1997.

[5.22] M. Maggi et al., "High rate performance of a standard double gap RPC", Proceedings of the 4th International Workshop on Resistive Plate Chamber and Related Detectors, Napoli, Italy, 15-16 October 1997.

[5.23] M. Andlinger et. al, Nucl. Instr. and Meth. A 370 (1996) 389.

[5.24] M. Konecki et al., "RPC geometry and muon trigger acceptance", CMS technical note CMS TN/95-120.

[5.25] CORE version 8**,** part 6.1.4.

[5.26] M. Cwiok et. al, "Data compression scheme for a data transfer from the RPCs to the muon trigger", CMS note in preparation.

[5.27] M. Huhtinen, G. Wrochna, "Estimation of the RPC trigger rates due to neutral particles", CMS technical note CMS TN/94-138.

[5.28] A. Fengler, P. Zalewski, "Ghost Buster for the CMS RPC muon Trigger", CMS note in preparation.

[5.29] G. De Robertis, A. Ranieri, I. M. Kudla, G. Wrochna, "The Sorting Processor Project", CMS technical note CMS TN/95-028.

[5.30] W. Kuzmicz, M. Niewczas, Z. Jaworski, "VLSI implementation of the RPC Pattern Comparator (PAC) ASIC – feasibility study", CMS technical note CMS TN/96-006.

[5.31] A. Kluge, W.H. Smith, "CMS Level 1 Trigger Latency", CMS technical note CMS TN/96-33.

[5.32] CMS Simulation Package — Users' Guide and Reference Manual, http://cmsdoc.cern.ch/~karimaki/manual/manual.ps.

[5.33] M. Konecki, J. Krolikowski, and G. Wrochna, "RPC Muon Trigger Software MRPC", CMS note in preparation, http://cmsdoc.cern.ch/~wrochna/mrpc/mrpc.ps.

[5.34] A. Fengler, "Double Muon Trigger Rates in CMS Experiment", University of Warsaw M.Sc. thesis, 1996, unpublished.

6. TRIGGER

Triggering is one of the basic tasks of the CMS Muon System. Therefore, for the completeness of the TDR we present in this chapter a brief description of the algorithms and their hardware implementation together with some simulation results. A detailed description of the Muon Trigger System will be presented in the "Trigger and Data Acquisition TDR."

Chapters 3, 4 and 5 were devoted to muon detectors: Drift Tubes (DT), Cathode Strip Chambers (CSC) and Resistive Plate Chambers (RPC). In CMS all of them are used for triggering. The idea of using both precise muon chambers and dedicated trigger detectors for the first level trigger emerges from the experience of previous experiments running in hadronic beams. At SPPS, UA1 was equipped with drift tubes and scintillation counters, but the number of detector layers and their granularity was not always enough to suppress the background in the forward region. ZEUS at HERA, in addition to drift tubes, uses two systems of dedicated detectors, one a plane of Time Of Flight (TOF) scintillators attached to the forward drift chambers, the other a Veto Wall consisting of 3 scintillator planes designed to reject beam halo background. H1, like ZEUS, uses TOF and Veto scintillator systems in addition to drift tubes. CDF at the Tevatron also uses a combination of scintillation counters and drift tubes in the forward region. Scintillators tag the crossing and drift tubes provide the p_T cut. The D0 trigger was initially based only on drift tubes. However it turned out to be necessary to upgrade the detector with scintillators for bunch crossing recognition and background rejection. In the case of CMS, high granularity of trigger detectors is required. This excludes scintillation counters and therefore Resistive Plate Chambers were proposed.

The trigger electronics which processes detector signals from Drift Tubes, Cathode Strip Chambers, and Resistive Plate Chambers was already described in Sections 3.4, 4.4 and 5.10 respectively. In this chapter we will describe how this information is combined in order to produce an efficient and robust trigger. Trigger requirements are derived from physics motivations in Section 6.1. Algorithms proposed to satisfy these requirements are presented in Section 6.2, together with their implementation. Expected "technical" performance is discussed in Section 6.3. The "physics" performance of the trigger was already presented in Section 2.4.

6.1 REQUIREMENTS

6.1.1 General requirements for trigger and DAQ

Particles to be studied at LHC can be divided into three classes, as shown in Table 6.1.1. Each class has different requirements for the trigger.

Table 6.1.1
Particles to be studied at LHC.

	Light	Medium	Heavy
Mass	<< 100 GeV	~ 100 GeV	>> 100 GeV
Particle	b-quark	t, W, Z, light Higgs	heavy Higgs, Z', W', SUSY particles
Luminosity	$10^{33}cm^{-2}s^{-1}$	$10^{33}cm^{-2}s^{-1}$, $10^{34}cm^{-2}s^{-1}$	$10^{34}cm^{-2}s^{-1}$

These particles can manifest themselves to the First Level Trigger (LV1) through their decay products. LV1 can recognize the following objects:

- muon
- electron/photon — the two are indistinguishable for LV1
- jet
- total deposited energy ΣE_T
- missing transverse energy E_T^{miss}

Most of the interesting physics processes produce at least two trigger objects [6.1]. Only a very few channels require *per se* single-object triggers. Those are:

- h, A,H $\rightarrow \tau\tau \rightarrow l^{\pm}\,\tau$-jet X
- $B^0_d \rightarrow \pi^+\pi^-$ with $b \rightarrow \mu_{tag}$ or $b \rightarrow e_{tag}$
- $B^0_s/B^0_s \rightarrow D^{\pm}_s,\ D^{\pm}_s \rightarrow \phi\ \pi^{\pm},\ \phi \rightarrow K^+K^-,\ b \rightarrow \mu_{tag}$
- inclusive W

In the first two channels one can still try to apply multi-object triggers looking at the τ-jet or treating the $\pi^+\pi^-$ pair as a kind of "minijet."

The fact that multi-object triggers are of primary importance at LHC has very substantial implications for the principle of the trigger operation. Different thresholds can be optimal for different combination of objects. Therefore one should not perform any cut on single objects at the level of muon or calorimeter trigger[i] These triggers can only recognize objects, estimate their p_T or E_T and send them to the Global Trigger. The Global Trigger is the only place where the objects are combined and the cuts are applied depending on a given combination.

It has been shown [6.2] that heavy and medium particles (see Table 6.1.1) can be effectively recognized applying a logical OR of the following conditions:

- single lepton or photon with p_T>60 GeV,
- two leptons or photons with p_T >15 GeV,
- E_T^{miss} >150 GeV.

The rate of processes selected by these criteria is dominated by standard physics background (Table 6.1.2) and it does not exceed 100 Hz. This does not include instrumental background and therefore the First Level Trigger rate can be much higher. However the instrumental background should be eliminated by higher trigger levels, and one can use the rate of 100 Hz to derive a first estimate of the capacity of mass storage devices (e.g. tape drives) that will be needed.

Table 6.1.2
Standard physics background at LHC for $L=10^{34}cm^{-2}s^{-1}$.

Condition	Process	Rate
1γ of E_T < 60 GeV	$\pi^0 \rightarrow \gamma\gamma$	10 Hz
2γ of E_T < 15 GeV	$\pi^0 \rightarrow \gamma\gamma$	10 Hz
$1l^{\pm}$ of p_T < 60 GeV	$W \rightarrow l$, jet $\rightarrow l$	10 Hz
$2l^{\pm}$ of p_T < 15 GeV	$Z \rightarrow l^+l^-$	20 Hz
E_T^{miss} > 150 GeV	QCD jets	10 Hz

[i] There are some instrumental limitations on detecting very soft particles, e.g. curling the tracks of p_T<0.7 GeV, etc.

Single-object triggers are used mainly to complete the efficiency of multi-object triggers. Therefore the criteria on their thresholds are not very strict. The actual working point should be chosen as a result of the trade off between efficiency and the LV1 rate. A reasonable upper limit is about 100 GeV. Beyond this point efficiency for various heavy objects is significantly degraded. The useful lower limit for $\mu/e/\gamma$ at $L=10^{34}cm^{-2}s^{-1}$ is about 20 GeV. Below this value one cannot further improve the efficiency for objects like W, Z or heavier, whereas the rate is dominated by leptons from quark decays (except the top quark). At this point, the rate of every single object is of the order of a kHz (see e.g. Figure 6.1.1). Adding all the channels together and leaving some room for an instrumental background, one can expect the total LV1 of the order of 10^4 Hz. Thus, in order to have some safety margin, the Second Level Trigger (LV2) should be able to receive ~10^5 Hz of events.

One can conclude this section with the following list of requirements:
- mass storage should be able to accept 100 Hz of events;
- input of the LV2 should be able to accept 100 kHz of events;
- muon and calorimeter LV1 recognize objects and estimate their p_T or E_T; cuts are applied by the Global LV1;
- expected thresholds for photons, electrons and muons are as shown in Table 6.1.3.

Table 6.1.3
Expected LV1 thresholds [GeV].

	e/γ	2 e/γ	e_b	2 e_b	μ	2 μ
$L=10^{33}cm^{-2}s^{-1}$	15–40	10	10	5	10	5
$L=10^{34}cm^{-2}s^{-1}$	20–100	15	—	—	20–100	10

6.1.2 Specific requirements for the first level muon trigger

The basic tasks of the CMS Muon Trigger are:
- muon identification,
- transverse momentum measurement,
- bunch crossing identification.

Genuine muon rates from various sources are given in Figures 6.1.1 and 6.1.2. The notation "2 μ from top events" means that at least one muon in each event comes from $\mathbf{t}$ or $\bar{\mathbf{t}}$ decay. The second one can come from another source.

Having this information, the requirements described in the previous chapter can be defined much more precisely for the specific case of the muon trigger. They are listed below together with justifications.

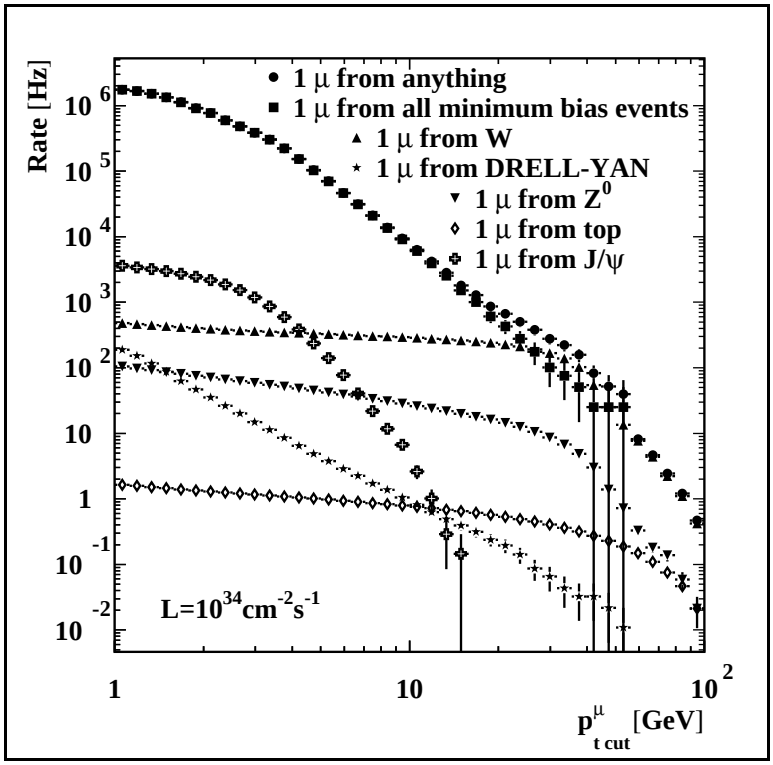


Fig. 6.1.1: Single muon rates ($|\eta| < 2.4$) [6.3].

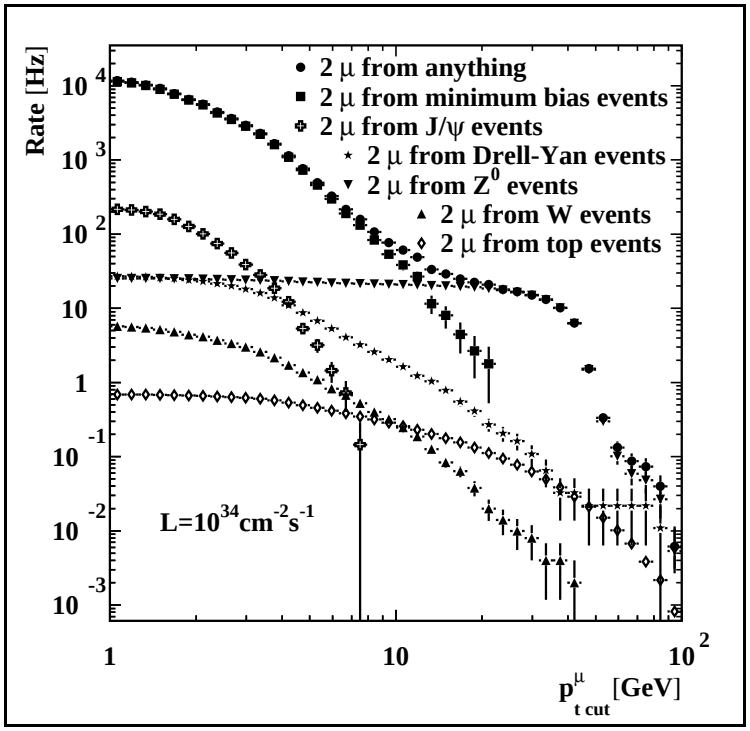


Fig. 6.1.2: Double muon rates ($|\eta| < 2.4$) [6.3].

Geometrical coverage: up to $|\eta| = 2.4$, in order to cover the entire area of the muon system.

Latency: < 3.2 μs.
Total trigger processing, including travel time over the 2×120 m of optical fibers (1.2 μs) to the control room and back, should stay within the length of the tracker pipelines, i.e., 128 bunch crossings (see Sec. 6.2.1). This implies that the trigger algorithms cannot be too complicated.

Trigger dead time: not allowed.
Every bunch crossing has to be processed in order to maintain the high efficiency crucial for many physics channels with low cross section.

Maximal output rate: < 15 kHz for luminosities < $10^{34}\,cm^{-2}\,s^{-1}$.
Maximal second level input rate is 100 kHz. Uncertainties in estimates of cross sections and luminosity variations during a single run requires a large safety margin. By design, the average first level output rate should not exceed 30 kHz, shared between muon and calorimeter triggers. About 5-10 kHz is assigned for the single muon trigger. This implies a rejection factor of ~10^{-5} at the highest luminosity.

Low p_T reach: should be limited only by muon energy loss in the calorimeters.
It is equal to about 4 GeV in the barrel and it decreases with $|\eta|$ down to ~2.5 GeV. This is required mainly for b-quark physics at L = $10^{33}\,cm^{-2}\,s^{-1}$.

The highest possible p_T cut: ~50-100 GeV.
The expected threshold needed to restrict the single muon trigger rate to 5–10 kHz at L = 10^{34} $cm^{-2}\,s^{-1}$ is 15–20 GeV. Uncertainties in estimates of cross sections and background levels requires a large safety margin. Increasing the threshold from 15–20 GeV to 50–100 GeV reduces the rate by an order of magnitude.

Background rejection: single muon trigger rate due to background should not exceed the rate of prompt muons from heavy quark decays at the nominal threshold (15-20 GeV).
This is necessary to maintain the rejection factor stated above. The prompt muon rate is irreducible except for channels where the isolation criterion can be applied (see below).

Isolation: transverse energy E_T deposited in each calorimeter region of $\Delta\eta\times\Delta\phi = 0.35 \times 0.35$ around a muon is compared with a threshold.
This function is needed to suppress the rate of background and prompt muons from heavy quark decays when triggering on muons not accompanied by jets. This is particularly useful in channels like $h,A,H \rightarrow \mu\mu$, $h,A,H \rightarrow \tau\tau$, $tt \rightarrow WW$, and gluino decays.

Output to the Global Trigger: up to 4 highest p_T muons in each event.
In principle, only 3 muons are necessary for the Global Trigger to perform single- and multi-object cuts including the three-muon trigger. By delivering 4 muons we reduce the probability that a low p_T isolated muon will not be selected because of the presence of higher p_t non isolated muons. This way we also reduce the probability of accepting ghosts instead of real muons.

6.2 TECHNICAL DESCRIPTION

6.2.1 CMS trigger and DAQ

Bunch crossings occur at LHC every 25 ns. The LV1 has to be able to analyze each crossing. The time of 25 ns is certainly not enough to recognize a trigger object and measure its p_T or E_T Therefore the CMS LV1 trigger utilizes a pipeline processor technique. Any trigger algorithm is divided in steps. Each step is performed in 25 ns by a trigger processor unit. At the end of the 25 ns period the result is sent to the next processor unit, and the data from the new bunch crossing are taken. In this way the trigger decision is delivered at the end of the chain every 25 ns, regardless the length of the chain.

Detector data must wait for the trigger decision in pipeline memories. The data from a given bunch crossing are shifted to the next memory unit every 25 ns. At the end of the pipeline they have to meet the trigger decision and they are either read out or discarded. Thus the length of the readout pipeline must be equal to the total LV1 latency.

Different detectors use either digital or analog pipeline memories. There are technical limitations on the length of analog pipeline memories. At present, memories as long as 120–150 bunch crossings are feasible. This implies that the total LV1 latency should not be longer than 3 μs.

The Second/Third Level Trigger division is flexible (Figure 6.2.1). One can even imagine a higher number of levels, depending on actual needs. This is because all higher level triggering is performed by a powerful farm of commercial processors called the *Event Filter Farm*.

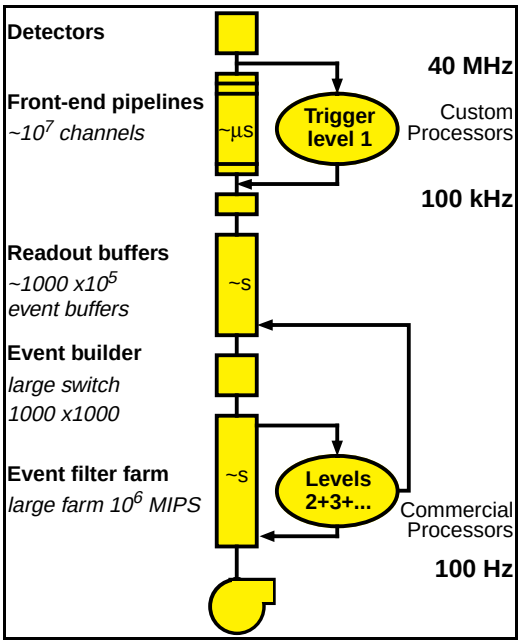


Fig. 6.2.1: Trigger and DAQ scheme of CMS.

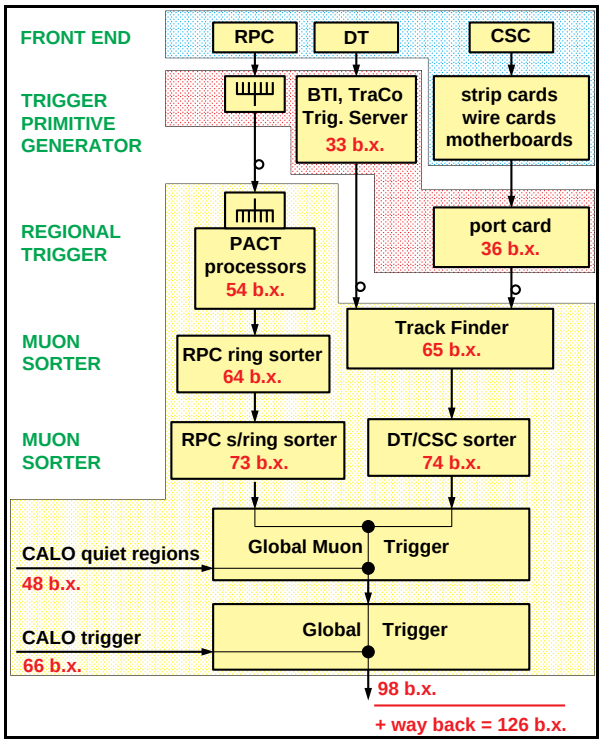


Fig. 6.2.2: Functional scheme of the Muon Trigger.

6.2.2 First level muon trigger

The First Level Muon Trigger of CMS uses all three kinds of muon detectors: Drift Tubes (DT), Cathode Strip Chambers (CSC) and Resistive Plate Chambers (RPC). The excellent spatial precision of DT and CSC ensures a sharp momentum threshold. Their multilayer structure provides the possibility of effective background rejection. RPCs are dedicated trigger detectors. Their superior time resolution ensures unambiguous bunch crossing identification. High granularity makes it possible to work in a high rate environment. Time information and both spatial coordinates of a detected particle are carried by the same signal, which eliminates ambiguities typical for wire detectors.

The complementary features of muon chambers (DT/CSC) and dedicated trigger detectors (RPC) allows us to build two trigger subsystems which deliver independent information about detected particles to the Global Muon Trigger. The advantages of having two such subsystems are numerous. The muon chambers and the dedicated trigger detectors deliver different information about particle tracks. They behave differently in difficult cases, and they respond in different ways to various backgrounds. Properly combining the information from both systems results in high efficiency and powerful background rejection. Two extreme cases of such combinations are the logical OR, which is optimized for efficiency, and the logical AND, optimized for background rejection. However, neither of these operations results in full use of the complementary functions of the muon trigger components and a more sophisticated algorithm should be used. This is possible because both the muon chambers and the dedicated trigger detectors deliver information about the quality of detected muon candidates.

Another important advantage of the two-component system is a possibility of cross checks and cross calibration. Trigger data from the two components collected by the DAQ can be compared online. This enables the quick discovery of possible problems and gives the possibility of immediate action. When studying cross sections, asymmetries etc., it is very important to know the trigger efficiency and acceptance. Usually this is done by running with thresholds much lower than the measurement range. A two-component system offers a unique ability to measure these quantities in a more unbiased way.

The block diagram of the Muon Trigger is shown in Figure 6.2.2. Cumulative latency is given in bunch crossing units. Three shaded backgrounds show the location of the electronics: at the chamber, in the experimental hall, and in the control room. Optical links of 1 Gbit/s, ~100 m long, are indicated by circles. Most of the Drift Tube trigger electronics is placed in the experimental hall, but an option is being considered to mount it directly on the chambers.

DT and CSC electronics (see Sections 3.4 and 4.4 respectively) first process the information from each chamber locally. Therefore they are called *local triggers*. As a result, a vector (position and angle) per muon station is delivered for each muon crossing the station. Vectors from different stations are collected by the Track Finder, (TF), which combines them to form a muon track and assign a transverse momentum value. This information is sent to the Muon Sorter. The TF plays the role of a *regional trigger*.

In the case of RPCs there is no local processing apart from synchronization and cluster reduction. Hits from all stations are collected by the PACT logic. If they are aligned along a possible muon track, a p_T value is assigned and the information is sent to the Muon Sorter.

The Muon Sorter selects the four highest p_T muons from each subsystem in several detector regions and sends them to the Global Muon Trigger which compares the information from TF (DT/CSC) and PACT (RPC). So-called *quiet bits* delivered by the Calorimeter Trigger

are used to form an isolated muon trigger. The four highest p_T muons in the whole event are then transmitted to the Global Trigger. Finally, transverse momentum thresholds are applied by the Global Trigger for all trigger conditions.

6.2.3 Track finder for DT and CSC

Drift Tube and Cathode Strip Chamber trigger electronics was described in Sections 3.4 and 4.4 respectively. They both deliver *track segments* (TS), namely position and angle of a track crossing a given muon station. This information is processed further by the Track Finder. Its task is to connect track segments into a full track and assign a p_T value to it.

The processing is done in sectors covering 30 degrees in ϕ and varying between 0.2 and 0.5 in η extent. The algorithm consists of three steps (Figure 6.2.3). First, track segments from different stations are matched by an extrapolation method. Then the matched pairs are combined into a full track. Finally unique values of ϕ, η and p_T are assigned to the track. This algorithm works well in the barrel. Preliminary simulation results (see Section 6.3.3) indicates that it can work also in the endcap and in the transition region, but it is still far from being optimized. The final design will be described in the Trigger and Data Acquisition TDR. Below we describe briefly the currently envisaged algorithm. More details can be found in [6.4].

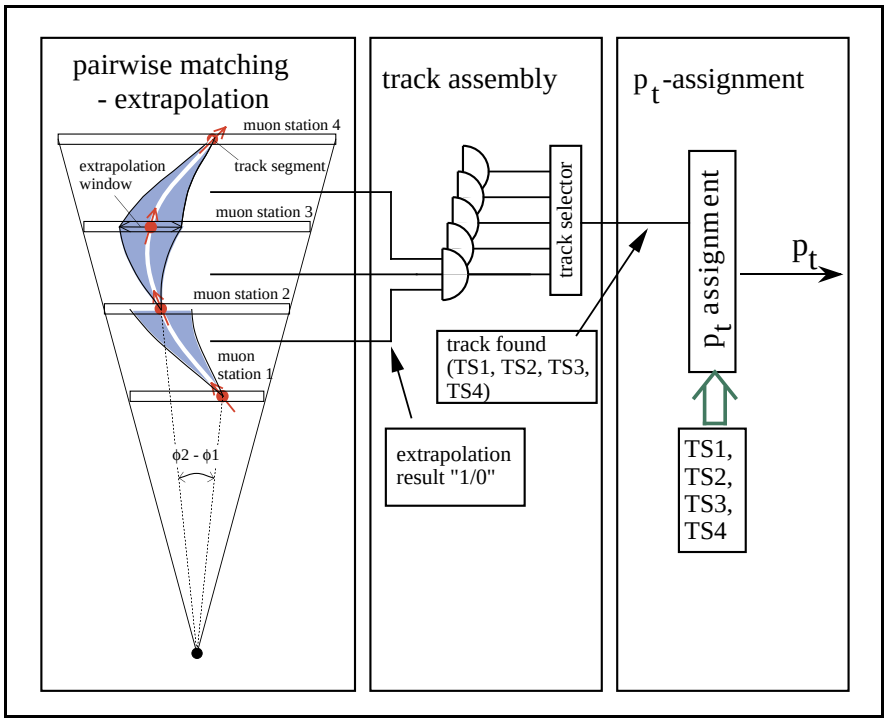


Fig. 6.2.3: Track Finder algorithm

The algorithm is performed by the following units (see Figure 6.2.4):

- Extrapolator
  - Extrapolation Unit (EU)
  - Extrapolation Result Selector (ERS)
- Track Assembler
  - Track Segment Linker (TSL)
    - TSL units
    - Single Track Selector (STS)
  - Track Selector (TSel)
    - Track Cancellation Logic (TCL)
- Track Router (TR)
- Assignment Units (AU)
  - quality, η, ϕ, and p_T

Their functionality will be described in the subsequent sections.

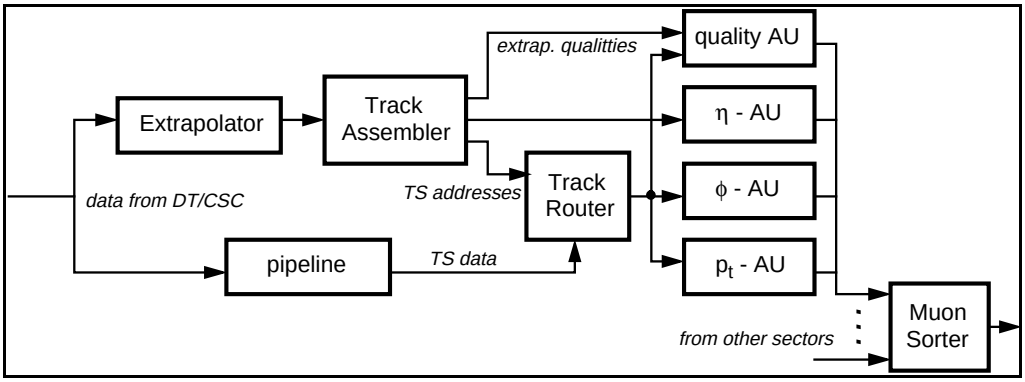


Fig. 6.2.4: Track Finder block diagram.

6.2.3.1 Extrapolator

With track segments in some of four muon stations, several extrapolations from one station to another are done in parallel by *Extrapolation Units* (EU). In the barrel they are: 1→2, 2→3, 4→3, 1→3, 2→4, and 1→4. The extrapolation is based on position ϕ and bend angle ψ of a track segment. The bend angle ψ is used as a starting direction and as a measure of p_T to find the track curvature. In the barrel the (p_T-ψ) relation is unique but in the forward region it depends also on η. A pair of track segments is considered as matched if the extrapolation of the first one coincides with the position (and possibly the angle) of the second one within a given accuracy. The two best extrapolations for each source track segment are selected by *Extrapolation Result Selector* (ERS).

6.2.3.2 Track assembler

The *Track Segment Linker* (TSL) attempts to combine all matched pairs into a full track. At least two matched track segments are required. The number of possible candidates is reduced by the *Single Track Selector* (STS) which selects only one candidate for each innermost source track of a given length. The selection is based on the quality of the two track segments.

Next steps are performed by the *Track Selector* (TSel). First *Track Cancellation Logic* (TCL) removes track candidates which are identical to parts of longer tracks. It also removes

shorter candidates having common segments with longer ones. Finally the two highest rank track candidates are selected. The rank is defined by two criteria (ordered by priority):

- Tracks consisting of higher number of track segments are preferred.
- Station 1 and 2 have preference over 3 and 4.

Track segments belonging to the selected tracks are sent to the *Assignment Unit* (AU) by the *Track Router* (TR).

6.2.3.3 Track router

Full information about track segments is stored in a pipeline memory during the processing time of the *Extrapolator* and the *Track Assembler* (TA). The TR extracts from the pipline the information related to the selected track segments, combines it with the output of the TA and transfers it to the AUa.

6.2.3.4 Assignment units

The last step is to assign a unique ϕ, η and p_T to the track. In most cases, the p_T is calculated as a function of the bend angle between two stations $\phi_i - \phi_j$. Only in the endcap, if one of the first two stations is missing, the local bend angle ψ of the track segment in the other station is used. In the forward region the η information must also be used. The resulting values are then transmitted to the Muon Sorter. A single sector processor can deliver up to 2 tracks. They are selected using p_T and quality bits.

6.2.4 Muon sorter

The Muon Sorter receives the information from the RPC PACT or the DT/CSC Track Finder in a form described in Table 6.2.1. One single sorter chip accepts up to eight muons on the input and delivers up to four muons on the output, sorted according to their quality and then according to p_T. In the RPC PACT part, a ghost suppression algorithm is applied (see below). The output data have the same format as the input (Table 6.2.1). A lack of a muon is indicated by $p_T = 0$. The sorting chips are arranged in the form of a tree, sorting out the four highest p_T muons among all candidates in several detector regions (see Figure 6.2.5). In total, 1065 sorting ASIC's are needed.

Table 6.2.1
Information about each muon handled by Muon Sorter
($\leq$ 8 tracks on input, $\leq$ 4 tracks on output).

Variable	Bits	Unit / Precision
η	6	~ 0.1 η
ϕ	8	2.5°
muon sign	1	—
p_T	5	nonlinear scale
quality bits	2	—

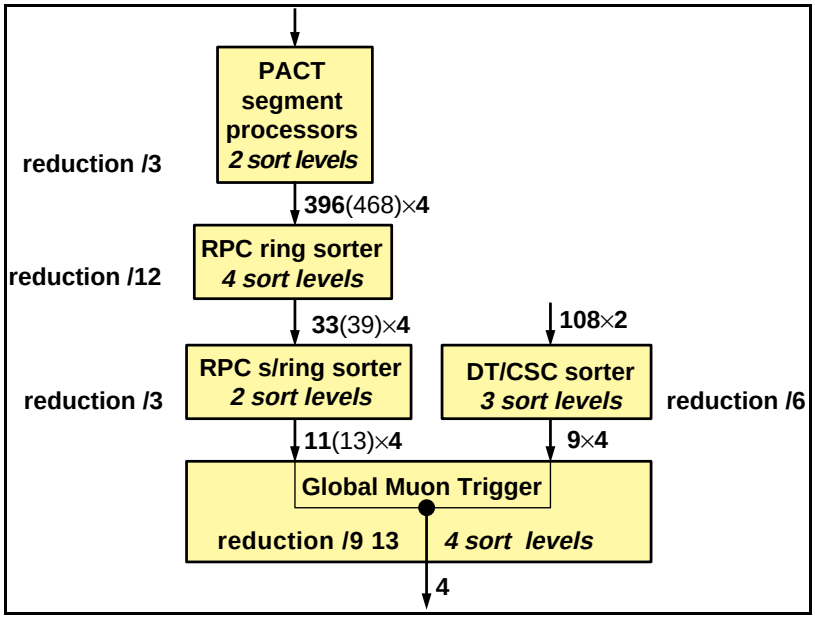


Fig. 6.2.5: Muon Sorter tree.

6.2.4.1 RPC PACT sorting tree

In the case of PACT, the first step of sorting is done already at *Trigger Boards* (TB) grouping 12 segment processors each. Their outputs (4 per TB) are further processed by 33 (or 39 in the case of an upgrade to $|\eta| = 2.4$) *ring sorters*, each covering a *ring* of $\Delta\eta \approx 0.1$ and $\Delta\phi = 360°$. Then the rings are grouped by 3 into 11 (or 13) *superrings* of $\Delta\eta \approx 0.35$ and $\Delta\phi = 360°$. Thus up to 11×4 (or 13×4) muons are delivered to the Global Muon Trigger. Details are given in Table 6.2.2.

6.2.4.2 DT/CSC sorting tree

The DT/CSC TF sectors are grouped into 9 regions of $\Delta\eta \approx 0.5$ and $\Delta\phi = 360°$ (5 in the barrel and 2 in each endcap) thus providing 9×4 muons at the Muon Sorter output. This segmentation is, however, still subject to optimization. Details of the DT/CSC sorting tree are given in Table 6.2.3.

6.2.5 Global muon trigger

In the previous sections we described the two systems for triggering on muons - one based on RPC chambers producing a pattern of hits in all muon stations, the other consisting of DT/CSC chambers which deliver track vectors at each station. They work independently up to the Global Muon Trigger. The purpose of the Global Muon Trigger (GMT) is to combine information from both systems in order to improve the overall muon trigger efficiency and rate capability. The GMT algorithm should make use of the complementarity of the subsystems, and is not a simple AND/OR combination of both. The design of the Global Muon Trigger presented below is the first attempt to implement such an algorithm. Its performance is discussed in Section 6.3.4. An improvement with respect to the stand-alone systems is clearly shown.

Table 6.2.2
RPC PACT sorting tree for baseline ($|\eta| < 2.1$) and upgrade ($|\eta| < 2.4$).

	Inputs		Reduction	Processing device
$\|\eta\|_{max}$	2.1	2.4	factor	
Trigger Board	4572 2376	+864 +432	1 / 2 2 / 3	ϕ Ghost Buster sorter ASIC
Ring Sorter	1584 792 396 264	+288 +144 +72 +48	1 / 2 1 / 2 2 / 3 1 / 2	sorter ASIC sorter ASIC sorter ASIC sorter ASIC
Super-ring Sorter	132 132 88	+24 +24 +16	1 / 1 2 / 3 1 / 2	η Ghost Buster sorter ASIC sorter ASIC
Global Muon Trigger	44 24 16 8	+8 +4	6 /11 2 / 3 1 / 2 1 / 2	sorter ASIC sorter ASIC sorter ASIC sorter ASIC
Global Trigger	4			

Table 6.2.3
DT/CSC sorting tree.

	Inputs	Reduction
DT/CSC Sorter	216 144	2 / 3 1 / 2
Global Muon Trigger	36 24 16	1 / 2 2 / 3 1 / 2
Global Trigger	4	

6.2.5.1 Global muon trigger design

The goal is to pass the best four muons of the event to the Global Trigger after combining the output of the RPC and DT/CSC based trigger systems [6.5]. The parameters used to evaluate a muon in addition to the transverse momentum p_T are based on information about the track's quality and presence in both systems. It is possible to assign different weights to all parameters. They are fully programmable and will be constantly optimized in order to obtain the best possible performance of the GMT.

The basic logical unit (segment) of the RPC trigger covers 0.12 units in η and 2.5 degrees in ϕ. In total there are 144 ϕ-segments in each of 39 η-towers covering the region $|\eta| < 2.4$. In the baseline design only the region $|\eta| < 2.1$ is equipped with RPCs. The logical segmentation in the DT/CSC is similar [6.6].

The standard input of both trigger systems to the GMT is given in Table 6.2.1. Five bits are foreseen to measure p_T. The definition of the p_T scale cannot be the same for RPCs and DT/CSC if we want to make use of the respective advantages of both systems as a function of p_T. The scale is approximately logarithmic as shown in Table 6.2.4. It designed in such a way that an increase of the threshold by one step should decrease the trigger rate by a constant factor of roughly 1.4. For the DT/CSCs the scale has more steps at the high-p_T end to reflect the more precise momentum measurement of these chambers with respect to the RPCs. There is still room for optimization of the scale definition. In addition, for the RPCs, quality bits will be sent indicating whether 3 or 4 planes have been hit. For the DT/CSCs there will be two to four quality bits. Their meaning is not yet fully defined and it will depend on the final GMT algorithm.

Table 6.2.4
Momentum scales of the RPC PACT (upper row)
and the DT/CSC Track Finder (lower row) in GeV.

2	2.5	3	3.5	4	5	6	7	8	10	12	14	17	20	25	30	35	40	-	-	70	-	100	-	-	-	-	-
2	2.5	3	3.5	4	5	6	7	8	10	12	14	17	20	25	30	35	40	50	60	70	80	100	120	140	170	200	250

In Figure 6.2.6 a block diagram of the Global Muon Trigger is shown. As the information from the RPC system arrives before that of the DT/CSC, *synchronization* logic aligns the two. The next step of the Global Muon Trigger algorithm is to convert the η, ϕ and p_T values of the tracks from the RPC and DT/CSC systems to comparable units. This is done with lookup tables. Then for every possible combination of muons, matching logic calculates the so called *match quality* to get a measurable criterion for the determination of whether muon candidates seen in both systems come from the same physical muon or not. First the differences in η and ϕ ($\Delta\eta$, $\Delta\phi$) are calculated. If one of the RPC or DT/CSC channels is empty, the difference is set to a maximum value. Then a function in (η, ϕ)-space is calculated to define the match quality. In Figure 6.2.6 the match quality is defined as a distance in (η, ϕ)-space where η carries a weight w which may differ from one. It may even be necessary to define the weights as a function of η to take into account the different resolutions of the different chamber systems. In any case, full programmability is foreseen to obtain the best possible performance.

The next step is the *pair logic* which uses the match qualities MQ_ij to find pairs of muon candidates. If MQ_ij is higher than that of its vertical and horizontal neighbors and if it exceeds a programmable threshold, then it represents the best match of two muon candidates. Only muons that are not disabled by one of their neighbors are included in this comparison. This last condition is necessary to find more pairs and therefore to suppress a small fraction of ghost muons in the output. The PAIR_ij bits flag pairs of muons.

Parallel to the matching and pair logic, a *single rank* is calculated for each muon candidate. In principal the single rank is proportional to p_T but its magnitude may be altered due to the detector type and part, due to missing or bad channels or due to background conditions, noise, and other possible causes of error. A lookup table will provide the necessary flexibility. Then all single ranks are compared to each other to select either the RPC or the DT/CSC candidate if both originate from the same physical muon. The comparator bits form the *select matrix*, e.g., if SEL_ij = 1 then the RPC muon is taken.

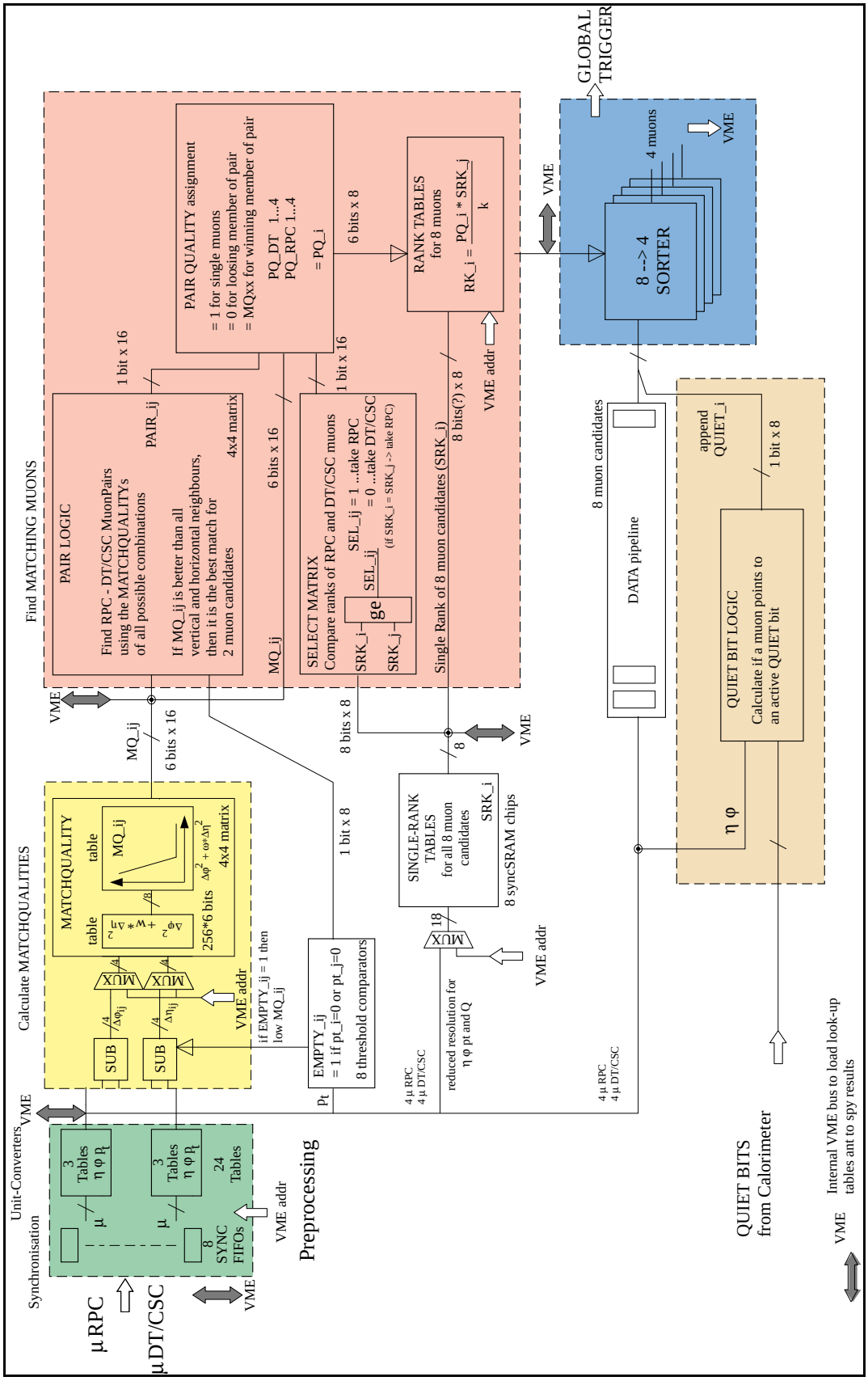


Fig. 6.2.6: Block diagram of the Global Muon Trigger.

Now the match qualities MQ_ij, the PAIR_ij bits and the SEL_ij values are used to assign a so-called *pair quality* for each RPC and DT/CSC muon candidate. PQ_ij = 1 for single muon candidates, PQ_ij = 0 for a losing member of a pair, and PQ_ij = MQ_ij for a winning member of a pair. The pair quality and the single rank are then used to calculate the *final rank* for each muon. In a first approach, muons found in both systems get a better rank than muons seen by one trigger system only. However, by changing the tables for the single rank and for the final rank calculations, the priority could be shifted more to the p_T values of muons, for example. Muon candidates that are losing members of a pair are eliminated. Finally all muon candidates are sorted according to their rank and the best four are passed to the Global Trigger.

6.3 TRIGGER PERFORMANCE

6.3.1 Simulation software

6.3.1.1 Event generation

For most of the study PYTHIA 5.7 was used as the event generator. Wherever possible default values of parameters were preserved. Particle distribution functions were calculated according to CTEQ2L parametrization.

Minimum bias events were simulated with parameter MSEL=1 which activates the following processes having in total a cross section of 55 mb:

$q_i\, q_j \rightarrow q_i\, q_j$ (where q_i = d, u, s, c, b)
$q_i\, q_i \rightarrow q_i\, q_i$
$q_i\, q_i \rightarrow g\, g$
$q_i\, g \rightarrow q_i\, g$
$g\, g \rightarrow q_i\, q_i$
$g\, g \rightarrow g\, g$
low p_T scattering.

This does not include diffractive and elastic scattering.

6.3.1.2 Detector simulation

Particle passed through the material of CMS detector and the detector response was simulated with CMSIM package [6.7]. It is based on GEANT and has interfaces to PYTHIA and other event generators.

The CMSIM package is under vigorous development. Below we briefly describe its current status as it was used to obtain results presented in the next sections.

6.3.1.3 Geometry definition

This part is relatively well advanced and the level of details is usually adequate to the questions addressed in the next sections. For example, muon chambers are described as composed of several material layers according to their technical designs. The biggest uncertainty is in the general layout of the barrel-endcap connection, where there are difficult mechanical mounts, many cables and other services, elements of the alignment system, etc. Therefore the design of this region is not yet fixed.

Another unknown is the effect of the dead area in the region of the cryogenic chimneys connecting the magnet cryostat with the helium tank and other equipment. They are not yet included in the simulation and one can expect that they will reduce the acceptance of the muon system in the barrel.

6.3.1.4 Particle tracking

This task is well covered by GEANT itself. Once the geometry is defined, the user only needs to provide a magnetic field map and set the proper cuts. The field map currently used is two-dimensional, calculated on a 10 cm grid. It is adapted to the polygonal shape of the return yoke by simple scaling and interpolation.

The set of cuts used for muon trigger studies is given in 6.3.1.

Table 6.3.1
GEANT cuts used in the simulation.

particle or process	GEANT var. name	far from muon chambers	close to muon chambers	inside muon chambers
γ	CUTGAM	100 MeV	10 MeV	10 keV
e	CUTELE	100 MeV	10 MeV	10 keV
n	CUTNEU	1 MeV	1 MeV	1 MeV
charged hadrons	CUTHAD	1 MeV	1 MeV	100 keV
μ	CUTMUO	10 MeV	10 MeV	100 keV
$e \rightarrow$ bremsstrahlung	BCUTE	10 MeV	10 MeV	10 MeV
$\mu \rightarrow$ bremsstrahlung	BCUTM	10 MeV	10 MeV	10 MeV
$e \rightarrow \delta$-rays	DCUTE	10 MeV	10 MeV	10 keV
$\mu \rightarrow \delta$-rays	DCUTM	10 MeV	10 MeV	10 keV
$\mu \rightarrow e^+e^-$ pair production	PPCUTM	10 MeV	10 MeV	10 MeV

6.3.1.5 Detector response

Phenomena inside Drift Tubes and CSC are simulated in great detail. A particle traversing the gas creates electrons by ionization. They develop a cascade in the electric field of the chamber. Charge collected by the electrodes creates a pulse which is shaped according to the electronics design.

In the case of RPCs such a level of detail is not needed because the measurement precision is only of the order of 1 cm, and the analog information is not needed. Thus taking the strip crossed by a particle as a cluster center is already a good approximation. However there is an effort going on to include in the simulation parametrized experimental results on the cluster size, chamber efficiency, and timing resolution.

6.3.1.6 Trigger algorithms

Drift Tube front end electronics, BTI, TRACO and Trigger Server are described in the simulation very precisely. Simulation results were checked against the test beam data taken with a chamber equipped with a BTI prototype. Very good agreement has been found.

CSC front end electronics including Anode and Cathode FEBs is simulated at the level of a behavioral model. Currently work is going on to design and simulate the Motherboard and Port Card.

The basic algorithm of the Track Finder is already coded and interfaced to the Drift Tube trigger output. Current effort concentrates on interfacing to the CSC output and on developing algorithms suitable for the endcap and for the barrel/endcap corner.

In the case of RPC PACT, the whole chain is precisely simulated. Current work concentrates on improving algorithms in the regions of low acceptance or weak bending.

6.3.2 Geometrical acceptance and low momentum reach

In principle the DT/CSC system can trigger with track segments in at least two muon stations. However background rejection is more powerful if three stations are required. Momentum measurement is the best if the first or the second muon station is among them. Acceptance for all these three cases is plotted in Figure 2.1.2. The white area below the curves corresponds to the coincidence of three stations, one of them being MB1, MB2, ME1 or ME2. If we accept the coincidence of any three stations we gain the dotted area. Finally, coincidence of any two stations is represented by the uppermost histogram. It is above 97% everywhere.

The RPC PACT trigger is based on four RPC planes and it requires coincidence of at least three of them. However, four planes provide better momentum measurement. These two cases we denote for short 3/4 and 4/4 respectively. Figure 6.3.1 shows the 3/4 acceptance in gray and 4/4 one in black. Upper plots present the local acceptance for a given η, whereas the lower ones present the acceptance average over trigger towers. The left plots correspond to the high p_T algorithm based on one RPC plane per station which is used for muons with $p_T > 5$ GeV in the barrel and for all muons in the endcap. The right plots correspond to the low p_T algorithm based on two RPC planes in the first station (denoted as MS1 and MS1')[ii] and two RPC planes in the second one (denoted as MS2 and MS2'). This algorithm is used only in the barrel.

The acceptance in Fig. 6.3.1 was calculated with straight lines in order to indicate better the origin of inefficiencies. There is a region ($|\eta| \approx 0.3$) with exceptionally low efficiency. This is due to the gap between the wheels of the CMS barrel. The gap is needed mainly for cables of inner tracker and calorimeters. In the current design it is 15 cm wide[iii] On top of that one should add 2×4 cm of dead RPC border. There are efforts to reduce these numbers, but it seems that the absolute lower limit is $15+2 \times 2$ cm. The impact of the gap on the muon trigger acceptance is better seen in Figure 6.3.2. The trigger acceptance (coincidence of 3 out of 4 planes) for muons with $4.5 < p_t < 5.0$ GeV is plotted for low (MS1, MS1', MS2, MS2') and high p_T (MS1, MS2, MS3, MS4) algorithms separately as well as for the logical OR of the two.

The minimal values of trigger threshold p_T^{min} achievable in CMS are plotted in Figure 6.3.3a. Because of Landau fluctuations of energy lost by muons, different p_T^{min} values are obtained for different required efficiencies. Because the detector design is not yet completely frozen, one can expect some small changes in the amount of absorber. However they should not be bigger than one nuclear interaction length λ. This is indicated in the figure by the "error bars". For comparison, the total momentum p^{min} is also plotted in Figure 6.3.3b.

Keeping in mind all the above mentioned uncertainties one can conclude that the lowest "triggerable" muon p_T is about 4 GeV in the barrel and it decreases down to ≈2 GeV in the endcaps if efficiency of 90% is required. One can, however, reduce p_T^{min} in the barrel down to ≈3.5 GeV relaxing the requirement on the efficiency down to 80%. Relaxing it further down to 50% allows us to trigger on muons with $p_T \approx 3.2$ GeV. This can be better seen from Figure 6.3.4a.

[ii] In this section we use the acronym MS for a generic Muon Station, which could be either MB or ME.
[iii] The acceptance plots are done for the previous design with the 20 cm gap.

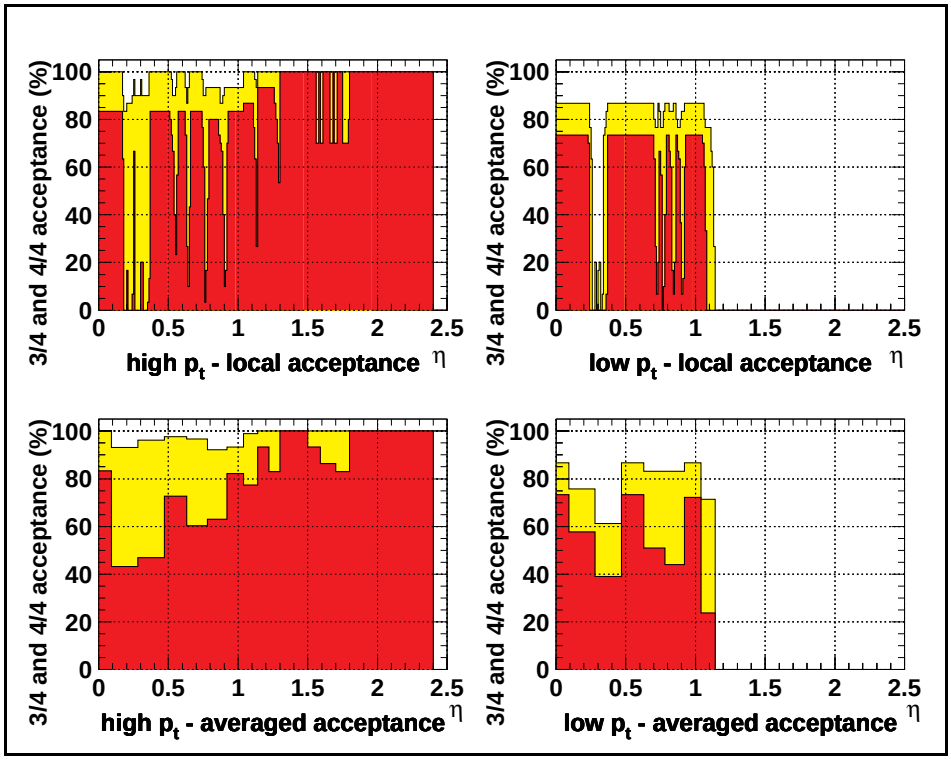


Fig. 6.3.1: Geometrical acceptance of the RPC system. "High p_T" denotes the standard algorithm based on 4 stations; "low p_T" denotes a special algorithm for p_T <5 GeV, based on 2 stations, used only in the barrel.

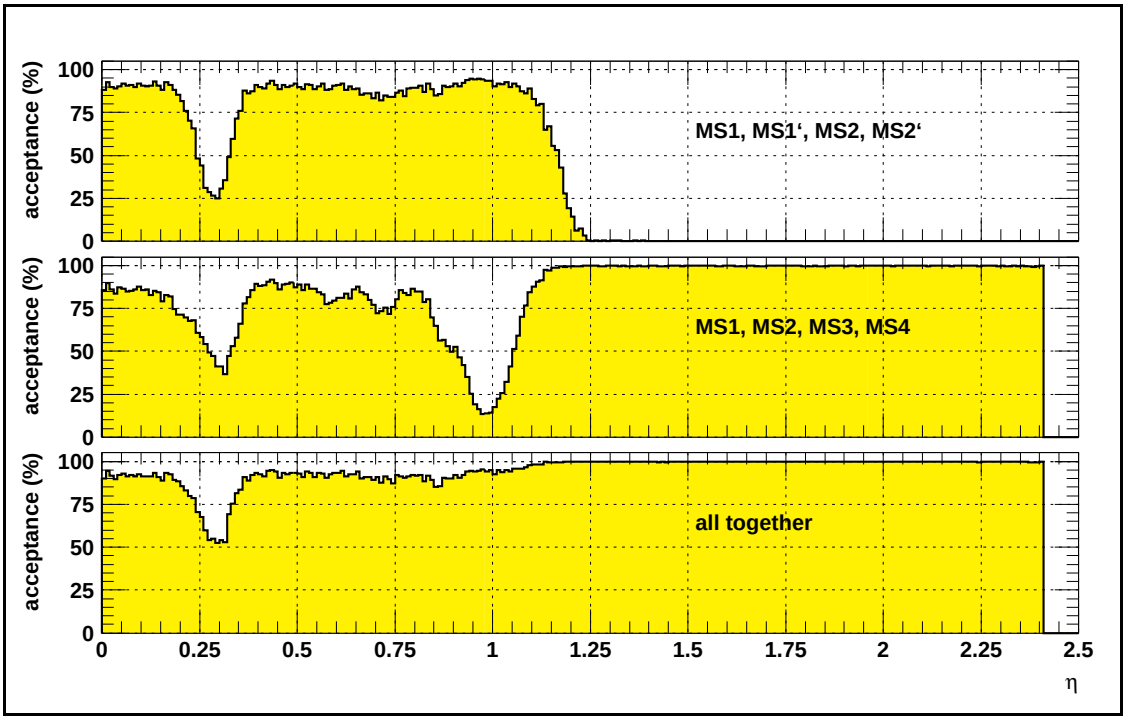


Fig. 6.3.2: Acceptance for muons with $4.5 < p_T < 5.0$ GeV.

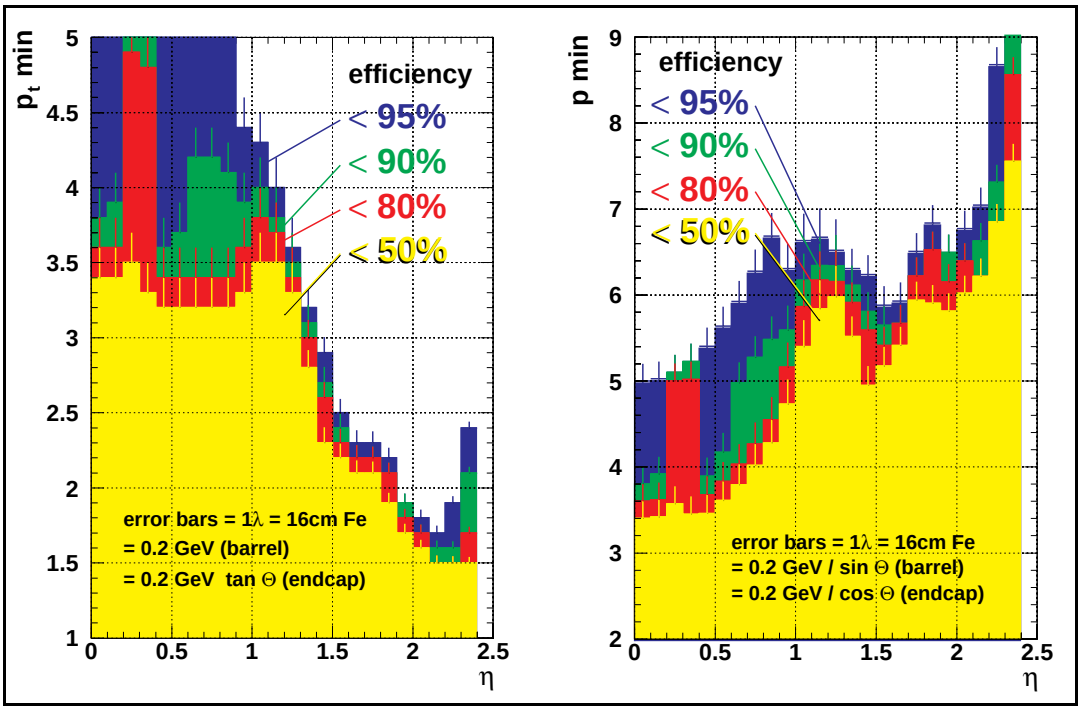


Fig. 6.3.3: The lowest possible p_T and p thresholds for various required efficiencies.

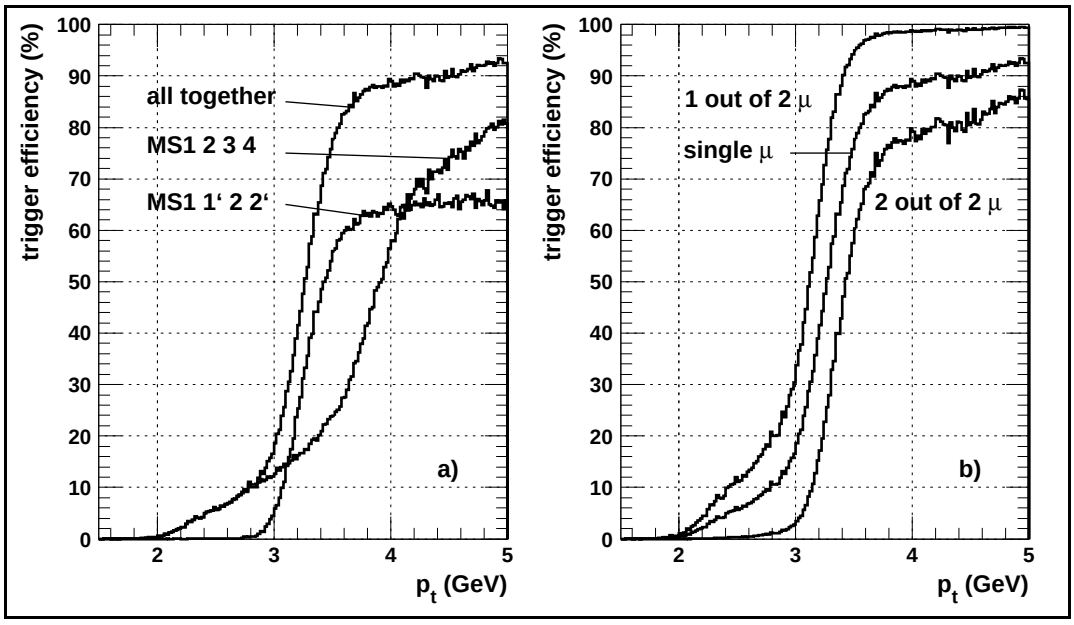


Fig. 6.3.4: Trigger efficiency for low p_T muons at $|\eta|<1.5$; a) single muons, b) muon pairs.

In most of the cases, we are interested in two-muon events (see Sec. 6.1.1). The requirement of two muons at the First Level Trigger strongly reduces the trigger rate, but also squares the single muon trigger efficiency. The result is shown as the lower curve in Figure 6.3.4b. In such a case the trigger is rather inefficient, especially at low p_T. If one can however trigger on any one of the two muons, then the inefficiency gets squared and the trigger performance became very good (the upper curve in Figure 6.3.4b). For example, it has been shown [6.8] that in the case of heavy ion physics with Pb-Pb collisions, this is a satisfactory solution because all the backgrounds amount to only 500 Hz. In the case of high luminosity p-p collisions, background rates are much higher and one has to raise the single muon threshold significantly. Nevertheless such a trigger is still very helpful to achieve the overall trigger efficiency.

6.3.3 Momentum resolution and efficiency curves

An ideal trigger should have efficiency equal 0 for muons with p_T below the threshold p_T^{cut} and 100% above it. In practice the momentum resolution is limited by multiple scattering and energy loss fluctuations at low p_T and by detector resolution at high p_T. Because of that, the efficiency curves $\varepsilon(p_T)$ have finite slopes proportional to the momentum resolution. Efficiency curves $\varepsilon(p_T)$ of RPC PACT and DT/CSC Track Finder have been calculated for various trigger thresholds p_T^{cut} in three detector regions: in the barrel (η=0), in the endcap (η=2), and in the transition region (η=1). They are shown in Figure 6.3.5. As expected, at p_T <20 GeV the curves for RPC and DT/CSC are almost identical. At higher momenta one can clearly see the superior resolution of DT and CSC. The effective trigger threshold can be provided by RPC PACT up to 70 GeV in the barrel and up to 50 GeV in the rest of CMS. The DT/CSC threshold can be effectively set at 80 GeV in the endcap and even above 100 GeV elsewhere. This fulfils the requirements given in Section 6.1.2.

6.3.4 Performance of the global muon trigger

The RPC and DT trigger systems have been tested together with an implementation of a Global Muon Trigger algorithm combining the results from the two systems to improve the overall muon trigger efficiency. A set of 100K events with a single muon (both charges) was generated with

- a flat distribution in p_T from 5 to 100 GeV
- an isotropic distribution in ϕ from 0 to 360 degrees
- a flat distribution in η from −1.0 to 1.0

The restriction to the barrel region was dictated by the incompatibility with the CSC trigger simulation software due to its preliminary stage of development.

After digitization the necessary trigger reconstruction information was extracted from the RPC PACT simulation routines and from a preliminary version of the muon Track Finder. Figure 6.3.6 shows the single muon efficiencies as functions of η, ϕ and p_T for the RPC and the DT in the region $|\eta| < 1$. Obviously in the regions of $|\eta| = 1$ and $|\eta| = 0.2$ both RPC and DT show inefficiencies. Geometrically this corresponds to crack positions, where two wheels carrying RPCs and DT chambers are fitted together. For $|\eta| > 0.8$ a rather different behavior for DTs and RPCs is observable. In this regime the overlap region with the forward muon system starts to be important especially for the DT system, since no CSC information was included in this study. Similarly there are inefficiencies in ϕ which appear every 30°, reflecting the layout of the detector planes.

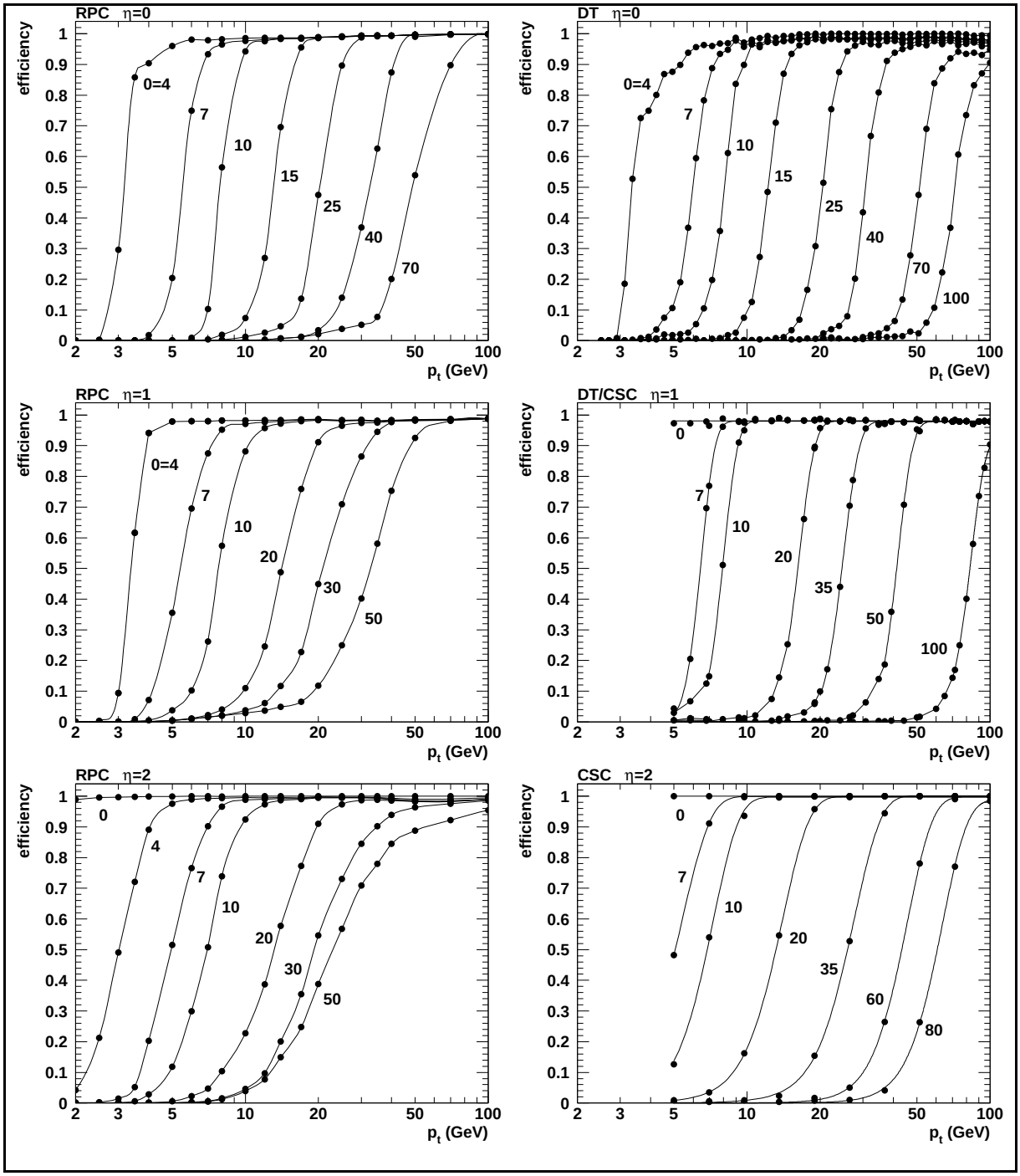


Fig. 6.3.5: Trigger efficiency curves $\varepsilon(p_T)$ of RPC PACT and DT/CSC Track Finder in different detector regions. Trigger threshold p_T^{cut} [GeV] is indicated next to each curve. Index "0" corresponds to the lowest possible p_T^{cut}, limited only by muon energy loss; "0=4" means that the lowest possible p_T^{cut} in this region is 4 GeV. The CSC Track Finder algorithm has not yet been simulated below p_T =5 GeV.

From Figure 6.3.6 it is clearly seen that the GMT algorithm not only improves the efficiency significantly but also it makes it more uniform over p_T, η and ϕ. The overall performance of the GMT algorithm is summarized in Table 6.3.2. One can see that the chosen logic of the Global Muon Trigger reduces the percentage of undetected muons drastically. Consequently the trigger efficiency is enhanced compared to the RPC and DT triggers alone. In addition, the resulting number of artificially created muons (ghosts) is smaller that the sum of ghosts from the two subsystems. This proves that the algorithm performs better than a simple AND/OR combination. In the case of a simple OR, one would expect improvement in efficiency at the price of many ghosts. In the case of an AND, ghosts would be suppressed at the expense of efficiency. In the algorithm presented, the efficiency is significantly improved without increasing the number of ghosts. The same conclusion is even better illustrated in Table 6.3.3, which presents the trigger response for muon pairs. The improvement of background suppression will be more manifest when other kinds of backgrounds are included and the simulation is performed also in the forward region where the number of RPC ghosts is higher. It should also be stressed that the system is very flexible, and there is a lot of room for optimization of the algorithm. The work on this subject is currently going on and the results will be presented in detail in the Trigger and Data Acquisition TDR.

Table 6.3.2
Trigger efficiencies for single muons.

$\|\eta\| < 0.8$	No muons found	1 muon found	>1 muon found
RPC	4.49 ± 0.10 %	95.49 ± 0.61 %	0.02 ± 0.01 %
DT	6.08 ± 0.11 %	93.70 ± 0.60 %	0.22 ± 0.02 %
GMT	1.04 ± 0.05 %	98.78 ± 0.70 %	0.18 ± 0.02 %

Table 6.3.3
Trigger efficiencies for muon pairs.

$\|\eta\| < 0.8$	No muons found	1 muon found	2 muon found	>2 muon found
RPC	0.24 ± 0.03 %	8.98 ± 0.22 %	90.72 ± 0.93 %	0.05 ± 0.02 %
DT	0.39 ± 0.04 %	12.75 ± 0.27 %	86.40 ± 0.90 %	0.46 ± 0.05 %
GMT	0.00 ± 0.01 %	2.70 ± 0.12 %	96.87 ± 0.98 %	0.42 ± 0.05 %

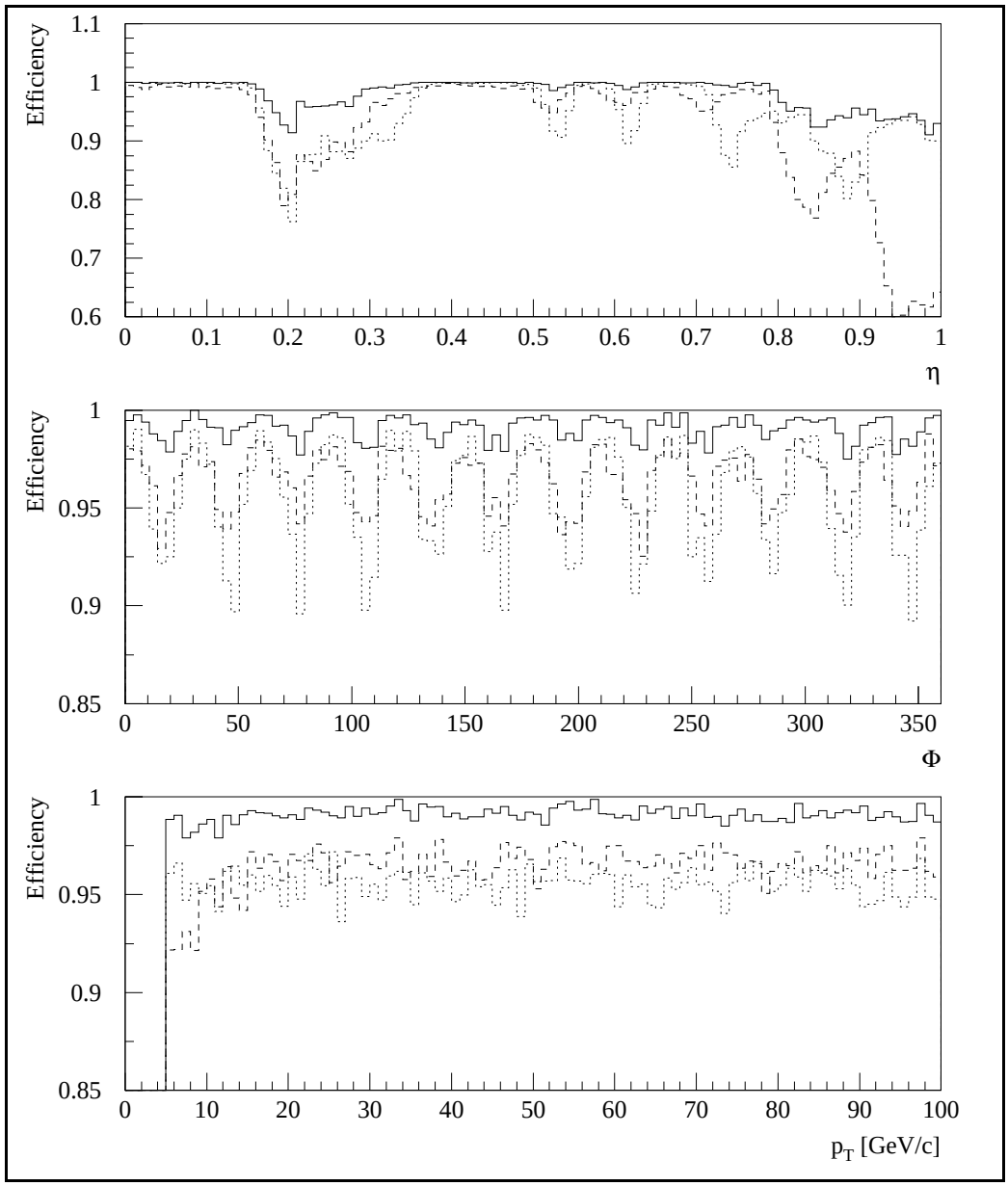


Fig. 6.3.6: Trigger efficiencies as functions of η, ϕ and p_T. The full line represents the GMT, the dashed line the DT and the dotted line the RPC.

References

[6.1] G. Wrochna, “Muon Trigger of the CMS detector for LHC,” CMS Note/97-096.

[6.2] C. Laurenço and J. Varela, “A Contribution for the Trigger Strategy of CMS,” CMS TN/95-025.

[6.3] A. Fengler, Double Muon Trigger Rates in CMS Experiment, University of Warsaw, M.Sc. thesis, 1996, unpublished.

[6.4] A. Kluge and T. Wildschek, “Track Finding Processor in the DTBX Based CMS Barrel Muon Trigger,” Proceedings of the First Workshop on Electronics for LHC Experiments (1995), p. 228.

[6.5] N. Neumeister, A. Taurok, C.-E. Wulz, F. Szoncso, “CMS Global Trigger,” CMS Note/97-009.

[6.6] N. Neumeister, P. Porth, H. Rohringer, “Simulation of the Global Muon Trigger,” CMS IN/97-023.

[6.7] CMS Simulation Package — Users' Guide and Reference Manual, http://cmsdoc.cern.ch/~karimaki/manual/manual.ps.

[6.8] G. Wrochna, “Muon Trigger for heavy ion physics,” CMS Note/97-089.

7. ALIGNMENT

7.1 INTRODUCTION

The optimal reach in momentum resolution for high-energy muons sets the required position accuracy of the muon chambers. Resolutions from 5 to 20% for 1 TeV muons (up to $\eta = 2.4$) will demand position accuracy comparable to the chamber resolution.

In CMS most of the muons bend through the full 4T magnetic field and reach the maximum curvature near the first muon station. This station gives the main contribution to the momentum measurement precision and leads to the most stringent requirements on chamber resolution and position accuracy. To set bounds on the required accuracy, the influence of the chamber misalignment on the momentum resolution has been studied for both barrel and endcap detectors [7.1]. The required accuracy, in $r\phi$, for the barrel detector is in the range of 150-350 μm (for MB1 -MB4 respectively), while for the endcap system it is 75-200 μm (for ME1-ME4). In both cases, looser requirements are set for muon identification and triggering.

Stability of the muon chambers at the 100 μm level is not guaranteed during detector operation. The expected movements and deflections of the muon spectrometer will exceed the requirements. To cope with movements, the detector is instrumented with an optical alignment system, which will allow continual measurement of the chambers position. The alignment information will be used for off-line correction in track reconstruction.

The system must provide accurate alignment of the barrel and muon detectors among themselves as well as alignment between them and the inner tracker detector. To fulfill these tasks the CMS alignment system is organized in three blocks:

- Internal alignment of the inner tracker to measure positions of the different tracker detector modules and monitor internal deformations. It will allow us to consider the tracker as a rigid body.
- Local alignment of Barrel and Endcap muon detectors to monitor the relative position of the muon chambers in the detector.
- A Link system to relate the muon (barrel and endcap) and tracker alignment systems, and allow a simultaneous monitoring of the detectors.

The full system is segmented in six ϕ planes (*active alignment planes*) to which the three tracking detectors are connected. Fig. 7.1.1 shows the muon alignment scheme for two radial opposite planes.

During detector operation, the system must track:

- Large changes from survey positions, due to the magnetic forces affecting the return yoke: the expected deflections are from a few mm to 1-2 cm [7.2].
- Long-term position stability of the detectors and changes due the thermal effects: with limited gradients (< 5 ^{o}C) across the muon detectors, the thermal expansion of the chambers and their iron supports are expected to be within the submillimeter range.

The range of movement to be monitored, and therefore the tolerances of the optical paths and dynamic range of the alignment elements, is mainly determined by the deflections produced when the magnet is turned on. During assembly, survey measurements based on photogrammetry techniques can provide accurate knowledge of the actual positions of the muon chambers and alignment components. Magnet tests foreseen during the installation period will provide information for detector position offsets. The survey measurements, and the possibility

to adjust the key elements of the magnet yoke and alignment system, will allow the efficient use of the full range of the sensors and optical passages of the alignment system.

It should be stressed that the proposed alignment system is not limited to the monitoring of local position changes with time, but provides an absolute measurement of the relative position of all components. Indeed, the actual measurement does not depend on previous measurements; the alignment system can be switched on and off without loss of precision.

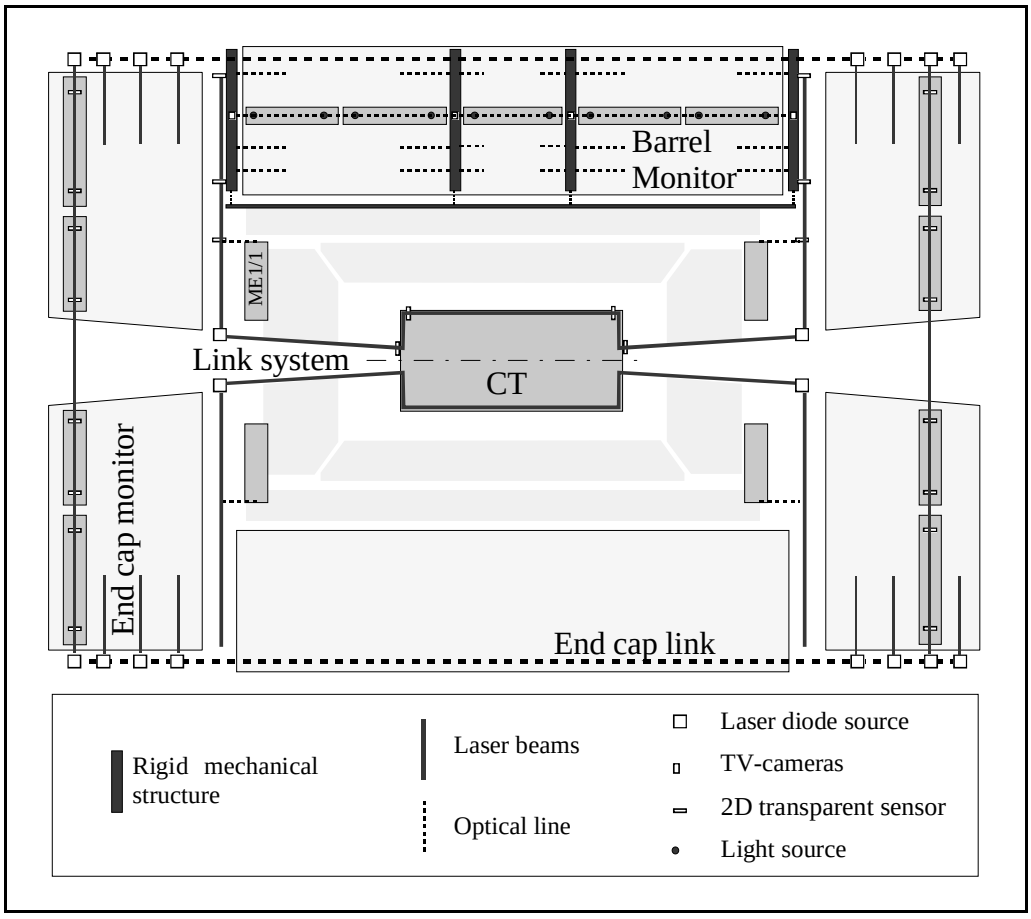


Fig. 7.1.1: Lateral view of the CMS detector, showing Barrel, Endcap and Link alignment systems.

7.2 ALIGNMENT SCHEME FOR THE BARREL

The position monitoring system for the barrel part [7.3] is designed to measure the positions of the barrel chambers with respect to each other (internal monitoring). The position of the whole barrel muon system is related to that of the Central Tracker and the Endcap muon system via the Link system.

7.2.1 Working principle of the internal barrel monitoring

The scheme of the barrel position monitor system is shown in Fig. 7.2.1 (color). It is based on the monitoring of the muon chamber positions with respect to a network of 36 rigid mechanical reference structures called MABs (Module for Alignment of Barrel). The MABs are

fixed to the barrel yoke forming 12 r-z planes parallel to the beam and distributed in ϕ. Six of them (called *active planes*) are connected to the link system. The other six planes (called *passive planes*) are connected to the active ones via diagonal connections.

The chambers are equipped with light sources on both sides. These light sources are mounted on frames rigidly attached to the chambers.

Each of the 36 MABs contains 8 camera boxes which observe light sources mounted on the muon chambers. The MABs also contain 4 light sources (on the active planes) or 4 camera boxes (on the passive planes) providing the diagonal connections. In addition, all 24 MABs of the 6 active planes are also equipped with cameras measuring the z positions by observing carbon-fiber bars called Z-bars installed on the vacuum tank of the CMS magnet.

All the 12 MABs that are connected to the link system (i.e. the outer MABs of the active planes) contain also elements belonging to the link and endcap systems. These elements and their functions are described in sections 7.3 and 7.4.

The MABs with all the elements mounted on them are considered to be rigid bodies with calibrated geometries having 6 degrees of freedom. The frames with the light sources mounted on the same frame are each considered to be one independent point-like object with 3 degrees of freedom. The Z-bars with the light sources mounted on them are also considered to be objects with 1 degree of freedom (movement along the z-axis). The total number of independent degrees of freedom in the stand-alone barrel position monitoring system is around 3000, while the number of independent observations is more than 4000 giving the desired redundancy to the system.

7.2.2 Measurement of the chamber positions with respect to the MABs

The position of the anode wires (knowledge of which is the primary aim from a physics point of view) cannot be monitored directly. Instead, positions of light sources rigidly fixed to the barrel muon chambers are monitored. The position transfer between the wires and the light sources is made by the measurement of the wire positions with respect to the outside fiducials during manufacturing and by the knowledge of the behavior of the chambers due to temperature changes. The transfer of the position from the outside fiducials to the light source will be made by precalibration of each chamber.

The principle of chamber position measurement with respect to the MABs is shown in Fig. 7.2.2. The frames with the light sources are mounted to the rigid honeycomb structures in the alignment passages (two on each side, 0.5 m from the corner). The position of a light source is determined by the calculation of the centroid of the light intensity distribution falling on the CCD matrix.

The r and ϕ positions are measured directly by the camera-box by measuring the corresponding light sources' positions. The z positions (only for the chamber corners close to camera-boxes) are measured by triangulation, measuring the relative positions of two light sources mounted on the same frame 20 mm from each other.

There are up to 3 sources per frame and up to 10 light sources per muon chamber. The r and ϕ coordinates are measured for all four corners of the chambers. The z measurement is provided for two corners.

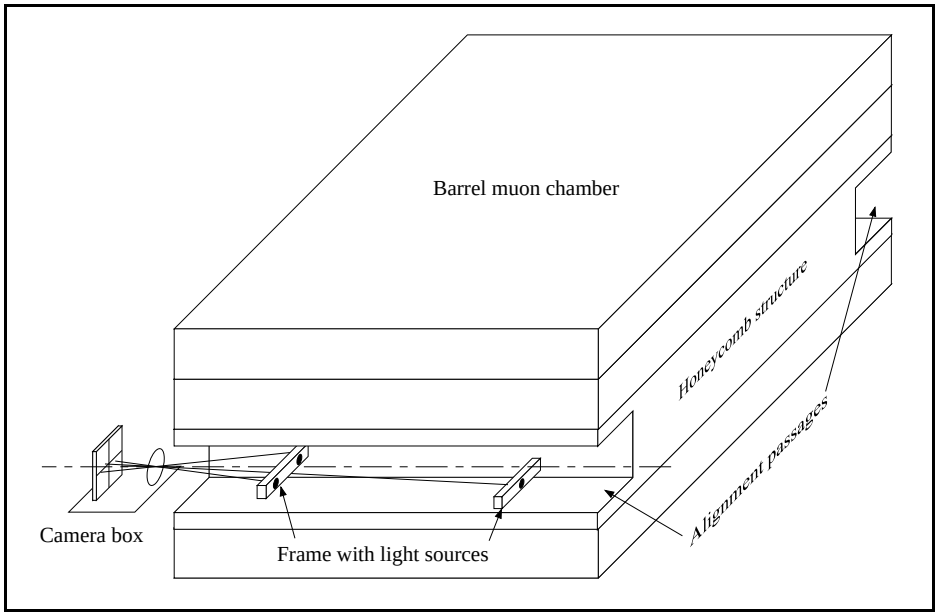


Fig. 7.2.2: Principle of chamber position measurement.

7.2.3 Measurement of the z positions of the MABs

The z position of a MAB of an active plane with respect to the other MABs of the same plane is measured by a light source - camera box pair. The optical connections for the z measurements are shown schematically in Fig. 7.2.1(color). The light sources are installed on carbon fiber bars (Z-bars) fixed on the vacuum tank parallel to the beam. The camera-boxes are fixed to the MABs.

As the rotation of MABs in the same plane is fully monitored by the eight connections through the camera measurements, one additional distance measurement provided by the Z-bars is sufficient to determine the location of the MABs (and the elements on the MABs) in the z direction.

7.2.4 Diagonal connections

The diagonal connections are also based on light source - camera-box pairs installed at the inner and outer radii of the MABs. The arrangement of the connections is also shown schematically in Fig. 7.2.1(color). In the figure, some elements of the barrel yoke and most of the muon chambers are not shown for better visibility of the connections. The same arrangement is repeated for the MABs mounted on wheels +1;+2 and -1;-2.

7.2.5 Elements of the system

In this section we describe the optical and mechanical characteristics of the elements of the system. Control and read-out is described in chapter 8.

MABs

The MABs are rigid structures made of carbon-fiber tubes and carbon-reinforced-carbon composite plates glued together. Each MAB is fixed to the barrel yoke at three points in an

isostatic way, allowing it to move without deformation. The rigidity is achieved by the construction, the choice of the material, and the assembly technology.

Each MAB is numbered following the CMS conventions: z/r/ϕ, where z is signed. Following this convention the numbering and mounting scheme of the MABs is shown in Table 7.2.1. As can be seen, no MAB is fixed to the central wheel.

Table 7.2.1

MAB numbering and mounting scheme (n = 1 to 12 corresponds to the 12 ϕ barrel sectors). The MAB number tells in which gap it is located, while the wheel number indicates to which wheel the MAB is attached.

MAB number	Wheel number	Wheel side
MAB/3/-/n (n=1,3,5,7,9,11)	+2	+Z
MAB/2/-/n (n=2,4,6,8,10,12)	+1	+Z
MAB/1/-/n (n=1,3,5,7,9,11)	+1	-Z
MAB/-1/-/n (n=1,3,5,7,9,11)	-1	+Z
MAB/-2/-/n (n=2,4,6,8,10,12)	-1	-Z
MAB/-3/-/n (n=1,3,5,7,9,11)	-2	-Z

Due to lack of rotational symmetry of the barrel muon system, the MABs have to be different. There is also a difference between the outer MABs connected to the link and endcap and the inner ones. As an example, the technical design of the MAB/3/-/1 is shown in Fig. 7.2.3.

In order to estimate the rigidity of the MABs and to choose the proper material, a simulation study has been carried out [7.4]. The calculations were made for the MAB/3/-/1, shown in Fig. 7.2.3, in its real (nearly horizontal) position in CMS. Two sources of deformations were studied : gravity and thermal expansion. The tilt of the CMS experimental hall (1.23% = 0.705 degree) was also taken into account in the calculation of the deformations due to gravity, and a 10 degree temperature difference across the MAB was assumed. The results are summarized in Table 7.2.2. which shows the values of the maximum deformations. As might be expected, the contribution of the thermal expansion is very small due to the carbon material used, and the rigidity of the MAB in its plane is much better than in the perpendicular direction. The overall rigidity of the MAB is satisfactory. It should also be noted that the chosen geometry and the material planned to be used for the plates are almost insensitive to humidity effects.

The mechanical stability and rigidity of the MABs under different conditions of load, temperature, and humidity will be tested at the specialized laboratory described in Section 7.6.1.

Table 7.2.2
Calculated values of the maximum displacements and deformations of the 3/-/1 MAB (see text).

Max. deformation	Gravity	Gravity + Thermal (10 degrees)
Displacement in x (μm)	13	9
Displacement in y (μm)	7	12
Displacement in z (μm)	39	39
Rotation around x (μrad)	20	20
Rotation around y (μrad)	61	61
Rotation around z (μrad)	26	28

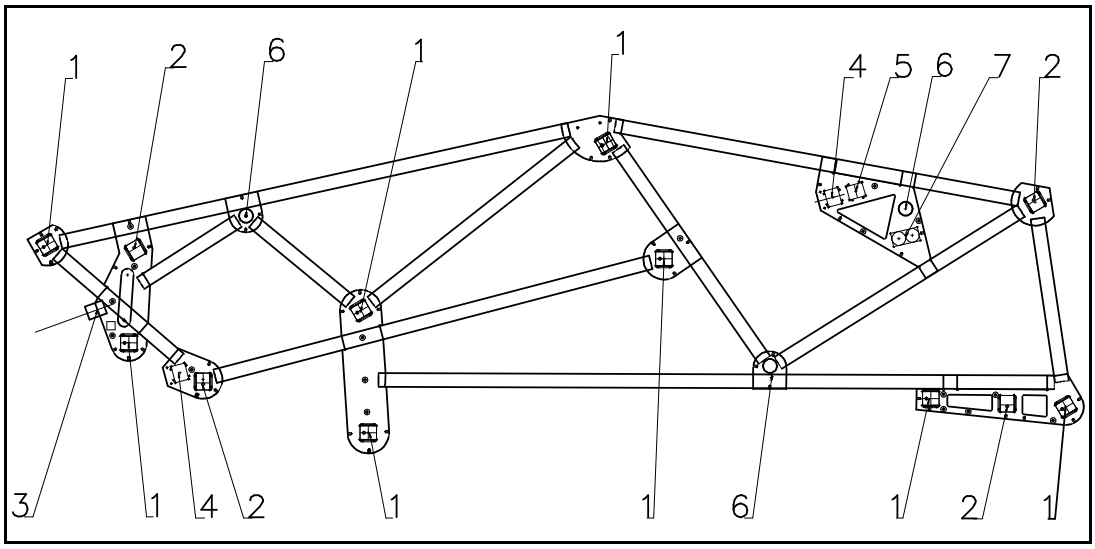


Fig. 7.2.3: The design of the 3/-/1 MAB. 1: Camera box for chamber measurement; 2: Camera box for diagonal connection; 3: Camera box for z measurement; 4: Transparent sensors for the link; 5: Tiltmeter; 6: Fixation; 7: Endcap link connection.

Camera-boxes

A camera-box consists of a CMOS video-sensor, optical elements (lens, prism or mirrors) and a mechanical box made of carbon-fiber material to minimize the deformation due to temperature effects and to reduce the weight. As the tests results show, the miniature video-sensor (312×287 pixels, $19.6 \times 16\ \mu m^2$ pixel size, $6.12 \times 4.59\ mm^2$ active area) used for the experiments (see section 7.5.1) is suitable for the given application.

There are four different camera boxes in the barrel position monitoring system. Two types are used to observe the chambers: the two-way and one-way cameras. The two-way camera box (its design is shown in Fig. 7.2.4) observes the muon chambers located on both sides of the MABs. These boxes are mounted on the inner MABs of the active planes and on the MABs of the passive planes (192 pieces in total). The one-way box monitors the muon chamber located

on one side of the MAB only; the second optical path is missing. These boxes are mounted on the outer MABs of the active planes (96 pieces).

A third type of camera is used for diagonal connections. The diagonal boxes are two-way camera boxes where the angle between the optical paths follows the directions of the diagonal connections (48 pieces).

The fourth type of box is used to measure the z positions of the MABs with the help of the Z-bars (24 pieces). These Z boxes are one-way camera boxes with simple geometry, optimized for the conditions of the z measurements (only one light source at short distance).

The total number of camera boxes is 360.

The design of the camera boxes (together with the parameters chosen for the light sources) can guarantee the field of observation adequate for the given task. The Table 7.2.3 shows the main parameters of the different types of cameras boxes.

Table 7.2.3
Main parameters of the camera boxes.

	One- and two-way Box	Diagonal box	Z-box
Focal length of the lens	50 mm	80 mm	20 mm
Aperture ∅	10 mm	10 mm	5 mm
Field of observation in length (in Z)	0.5 m - 7.5 m	3.2 m - 6.2 m	0.5 m
Field of observation	±40 mrad	±30 mrad	±140 mrad

As the radiation level in the barrel muon region is expected to be low (see chapter 10) there is no special need to use radiation hard equipment in the barrel monitor system.

Light sources

The muon barrel position monitoring system contains 2352 light sources (2208 of them are mounted on the chambers, 96 are on the MABs for the diagonal connections and 48 on the Z-bars). These light sources have to fulfill the following requirements:

- Good visibility (including their intensity) in the full longitudinal and transversal range of the measurements.
- Stable position of the centroid of the light intensity distribution.
- Long lifetime.
- Low price.

To fulfill all these requirements, LEDs have been chosen as light sources to be used in the barrel monitoring system. A simple mechanical design of the LED holder shown in section 7.5.1 seems to be adequate. The LED holders are glued in supports that are mounted on the chambers, MABs and Z-bars.

The number of optical and mechanical elements required for the Barrel alignment system is summarized in Table 7.2.4.

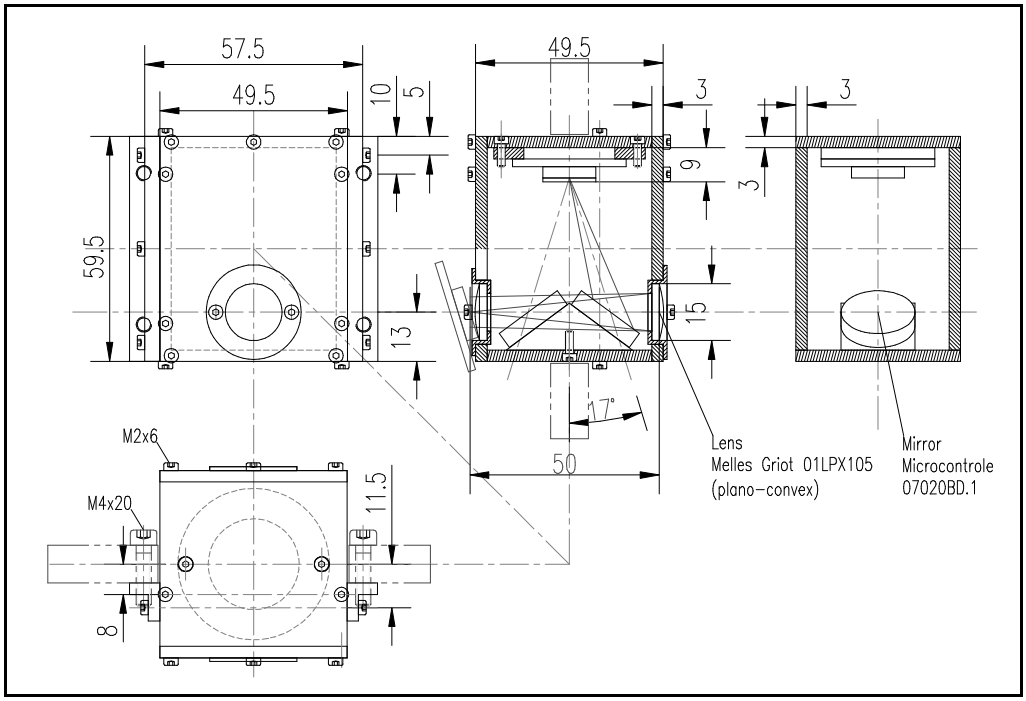


Fig.7.2.4: Design of the two-way camera box.

Table 7.2.4

The number of optical elements and mechanical structures in the barrel alignment system.

Element name	Number
Camera boxes	360
One-way camera	96
Two-way camera	192
Diagonal camera	48
Z-position camera	24
LED light source	2352
MAB structure	36
Z-reference bar	6

7.2.6 Quality control, assembly, calibration and installation.

The MABs will be built in a factory and tested before delivery. The camera boxes as well as the light sources will be built, assembled and tested in the participating laboratories. The MABs will be equipped with camera boxes, light sources, temperature sensors, and the necessary electronics at CERN.

Each complete MAB (containing the necessary number of survey fiducials) will be calibrated at a precise calibration bench. The error of the calibration of the critical points together

with the error due to deformation should not exceed 50 μm (in displacement) and 50 μrad (in rotation).

As the barrel system cannot observe the anode wire positions in the chambers directly, a calibration procedure is needed to relate the wires to the observable objects. This calibration is made in two steps:

- Measurement of the wire positions with respect to outside marks called reference blocks during the chamber production.
- Measurement of the positions of the survey fiducials and the alignment light sources with respect to the reference blocks on a calibration bench.

The schematic view of the chamber calibration bench [7.5] is shown in Fig. 7.2.5. The calibration bench is based on the same principle as the barrel monitoring system. Four cameras are used to measure the location of the positioning elements at each corner of the muon chamber. The four cameras are connected to each other by a stable laboratory network. The typical precision of the calibration bench is 60 μm in rϕ and 300 μm in z direction.

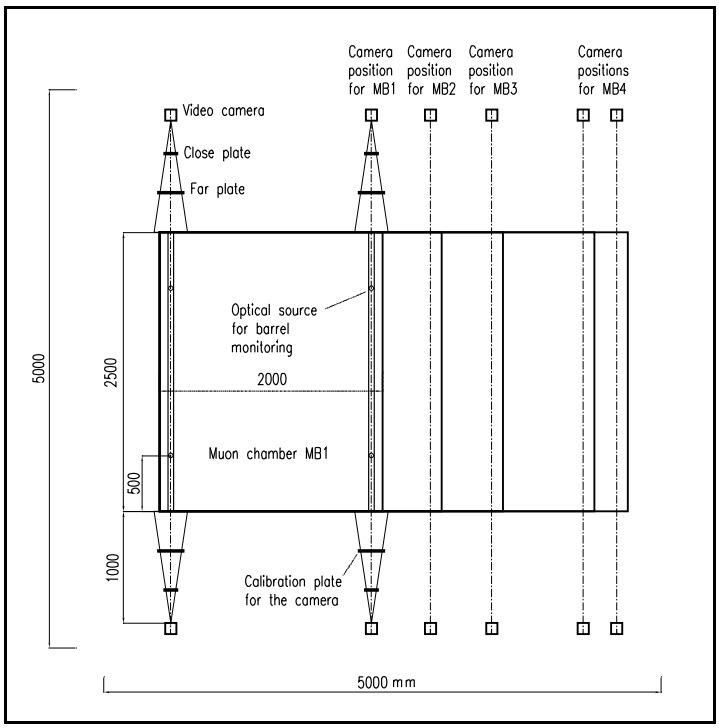


Fig. 7.2.5: Schematic view of the chamber calibration bench (units are mm).

The fully equipped MABs will be mounted on the barrel wheels after the insertion and fixation of the muon chambers located in the given wheel. The optimal position of the MABs will be achieved by adjustment at the fixation points measured by survey. The design of the barrel muon monitoring system permits a mispositioning of the elements of the system with respect to their nominal position of up to ±5 mm and a mispositioning between the wheels of up to ±10 mm.

Maintenance can be restricted to the replacement of broken elements. If a calibrated element has to be replaced, the corresponding MAB has to be demounted and recalibrated. The re-installation procedure is similar to that of the installation.

The light sources mounted on the chambers can be repaired/replaced when the chambers have to be removed for other reasons.

7.2.7 Simulation of the barrel alignment performance

A general purpose software program (UNIX, PC) called Simulgeo [7.6] has been developed for the simulation of the alignment system. It allows one to describe cameras, point sources, lasers, position sensitive detectors, tilt sensors and distance measurement devices. The software is object oriented and allows the user to study any system configuration.

The program was intensively used for the design of the barrel position monitor and for the laboratory tests with camera calibration (see section 7.5.1).

The study of the performance of the barrel monitoring system started by simulating the different parts of the system that can be considered as independent units : an active alignment plane, a passive plane, and the diagonal connections between planes.

Active plane:

A complete stand-alone active plane was simulated, containing the 4 MABs and 8 optical lines with 10 measurements. The outer MABs were equipped with tilt sensors.

The MAB rigidity and calibration precision is estimated to be 50 μm for translation and 50 μrad for rotation (from laboratory tests and finite element mechanical simulations). The precision of the matrix sensor of the cameras is about 1 μm (from laboratory tests). The tilt sensors give a connection between the two external MABs with an estimated precision of 20 μrad including calibration (see section 7.5.3).

The results show that the inner MABs are located with 50 μm precision with respect to the outer ones. This is achieved due to the strong connections between neighboring MABs: 8 lines of optical measurements, with 2 neighboring MABs observing the same optical source.

The position measurement precision for the light sources within an active plane is summarized in Table 7.2.6.

As a byproduct of the optical measurements the angles of the camera boxes are recalibrated. The simulation estimates an improvement of the calibrated angles by approximately 45%. The translation positions of the camera boxes do not benefit so much from the measurements but the MAB construction is adapted to a good stability of these translation parameters.

Table 7.2.6
The internal precision within an active plane.

	σ_{min}	$\sigma_{average}$	σ_{max}
$\sigma(r\phi)$ (μm)	47	69	86
$\sigma(r)$ (μm)	47	62	72

Passive plane:

A passive plane contains 2 MABs with 8 cameras observing 80 optical sources. The assumptions about MAB rigidity and sensor precision are the same as before. Two tilt sensors have been considered in each MAB to avoid torsion problems and to give "stand-alone" capability to the passive plane.

The results are summarized in Table 7.2.7. The measurement precision of the optical sources with respect to the reference is on average 80 μm (in rϕ). As in the case of the active plane the calibration of the camera angles improves by about 40 %.

Table 7.2.7
The internal precision within a passive plane.

	σ_{min}	$\sigma_{average}$	σ_{max}
σ(rϕ) (μm)	50	80	107
σ(r) (μm)	50	76	103

Diagonal connections between planes:

We have studied in detail the optical connection between planes with a complete simulation of 3 planes (2 active and 1 passive) including all the optical sources on the muon chambers and the optical characteristics of the diagonal connection.

The results show that the achievable precision in rϕ is about 100 μm and it is mainly determined by the precision of the calibration of the angle between the diagonal lines. In the simulation 20 μrad precision was used.

For r and z we obtained 100 and 300 μm. In this case the angular orientation of the diagonal box becomes relevant; for this study we used 50 μrad calibration precision. Contrary to the active and passive plane measurements, in this case the calibration precision cannot be improved by measurements due to the lack of redundancy. Due to this fact the initial calibration precision is more demanding.

Full barrel stand-alone system:

The previous studies have shown that the internal precision inside the planes is better than the measurement precision of the optical diagonal connections. Therefore, to simplify the simulation of the full system we have studied the global behavior fixing the performance of the active and passive planes as described above and simulating in detail the characteristics of the diagonal connections only.

A complete simulation of the barrel monitoring system (as a stand-alone system) is a closed loop between planes. The result of the simulation shows that the accuracy in the knowledge of the position of any active plane with respect to the others is in the range of 100 to 200 μm (in rϕ) depending on the distance between planes.

The final accuracy of the relative positions of the muon chambers is obtained by adding the precision of the diagonal connection and the accuracy of the optical measurements of the muon chamber positions (accuracy of an active or passive plane). The results are summarized in Table 7.2.8.

Table 7.2.8
Performance of the Barrel monitoring system.

	$\sigma(r\phi)_{min}$	$\sigma(r\phi)_{average}$	$\sigma(r\phi)_{max}$
Relative position of chambers in a barrel sector	112 μm	128 μm	146 μm
Relative position between barrel sectors	190 μm	200 μm	210 μm

7.2.8 Integration with the barrel resistive plate chambers

A low position monitoring accuracy, at the mrad level, is required to operate the Resistive Plate Chambers in the Barrel region.

The Resistive Plate chambers will be attached to the same mounts as the DT chambers, such that monitoring the muon chamber positions will also monitor the Resistive Plate Chamber positions within requirements. The chamber mounts will be measured by photogrammetry during detector assembly.

7.3 ALIGNMENT SCHEME FOR THE ENDCAP

For purposes of track matching and momentum measurement, the endcap muon system needs to be defined/monitored relative to the inner tracker detector. By connecting to the Link-Barrel system, the positions of the Endcap system can be defined relative to the tracker and barrel muon systems.

There is a need for instrumented position monitoring in the CMS endcap systems because each YEn return yoke iron plate, to which the muon cathode strip chambers (CSCs) will be directly attached, will change its shape under the extremely high magnetic field forces from the solenoid. Also there will be some thermal motion of the chambers. For these reasons, the muon chambers will shift in position and orientation relative to detector open, field free survey positions. In order to trigger on and define the correct position of passing particles (after software alignment correction), mechanical chamber positions and orientations need to be known with a reasonable tolerance, especially the r coordinates and angle rotations. The typical total error budget on these measurements is around 200 μm but is smaller at the ME1 muon momentum defining ring (75 μm).

The endcap muon position monitoring system [7.7] is schematically shown in Figs. 7.3.1 to 7.3.3. As shown in Fig. 7.3.1, critical tracker references (described in section 7.4) will be transferred to each of the endcap system detector layers at the CMS outer radial boundary. Twelve interleaved endcap Rasnik Straight Line Monitors (SLMs) are connecting the two endcaps. Going through the two outer end MABs these SLMs are also connected to the barrel muon system and linked to the inner tracker. The endcap Rasniks transfer 6 (rϕ, r) references to each CSC station. There is also an endcap z coordinate transfer system to all chamber layers. It consists of a concatenation of laser-detector triangulation distance measurements between the barrel end MABs and carbon fiber tubes/reference surfaces on the outer boundary of the YEn iron between all the layers of chambers. (Fig. 7.3.2). Thus diametrically opposing (rϕ, r, z) link points around the endcap iron are defined.

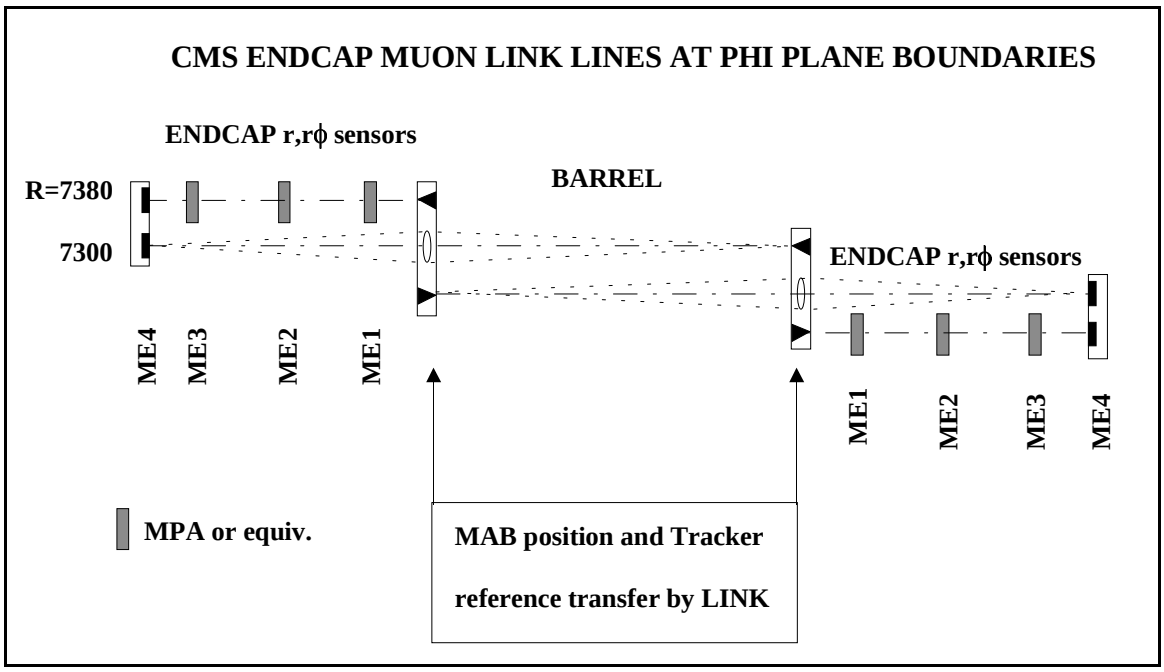


Fig. 7.3.1: Tracker transfer to the Endcap Muon System by the Link system.

Across each of the local planes (MEn/m) of the endcap cathode strip chambers, there will be three laser beamlines defined by the radially opposite link points. These are the chamber layer rϕ planes and z reference straight line monitors (SLMs).

These lines are defined by a laser source at one link point and a two dimensional detector at the opposite link point. These are referenced to the Rasnik detectors by rigid linkplate construction, CCM measurement of the linkplate assemblies, and θ, ϕ precision tiltmeters. Two transparent optical detectors mounted on each cathode strip chamber in each line will define these chamber positions (rϕ, z) relative to the laser beams. The four intermediate cathode strip chambers within each ring will be monitored using charged tracks in the overlapping cathode strips. In the ME1/3 ring where there is no overlap, the intermediate chambers in the ring will be measured in rϕ, r and z by low cost but high resolution optical distance sensors between chambers (at each radial end) and at ϕ plane boundaries. As costs allow, we will also apply these optical distance sensors to the ME1/2 and other overlapped chamber layers. To obtain r, there is a radial position measurement between the outer link references and the outer ring of cathode strip chambers, and between the outer and inner ring of cathode strip chambers. A schematic of the cathode strip chambers (inner and outer rings) with z, boundaries straight line monitors and r measurements is shown in Fig. 7.3.3.

7.3.1 Internal cathode strip chamber knowledge

Computer controlled milling/drilling of all the cathode strip panels will be done on one machine. All anode wire panels will be computer controlled milled and drilled on one machine. Each panel will have built-in external fiducialization and assembly alignment/transfer pinholes, so precision assembly tolerances and external measurements are achievable. All panels are processed at one location where cutting and measurement data will be logged. In addition, sample coordinate measuring machine (CMM) measurements (5-10 μm precision) of cathode and anode wire panels will be made and logged.

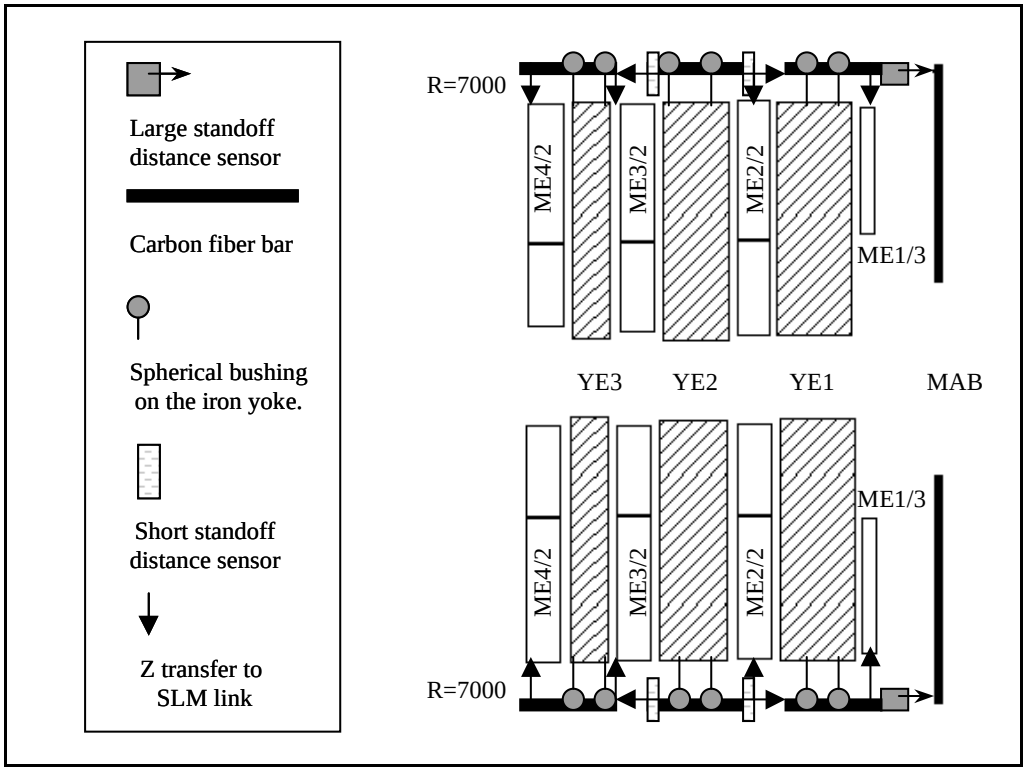


Fig. 7.3.2: Z coordinate transfer to (MEn/m) layers from references on the MABs.

Cathode strip position information

Both ends of the first and last cathode strip boundaries in each of the six planes are extended outside the gap frames to the edges of the chamber panels. After cathode strip chamber assembly with alignment pins, each strip plane will be measured externally relative to the alignment pins, fiducials, and alignment (position) sensor pins. This survey data will be logged to reference the SLM sensors. We are building a precision camera, scale, and motion system to automate this process.

Cathode strip chamber wire group position information

Wire position and pitch during winding is established by standard sets of precision wire locating combs on each edge of the panel. The wire support bars with precision etched solder pads and precision pinning holes are mounted and glued onto anode panels with precision drilled holes. These holes are located to fiducial marks near the outside edges of the panels which allow external measurement of the first/last wire positions. At the start of the winding, the first wire (comb groove) is carefully lined up on the center of the first pad and a completed winding can be checked to insure integrated wire pitch. We will measure sample windings with a coordinate measuring machine, by interference patterns against a precision printed mask of correct pitch, and with an optical laser position scanner or camera system.

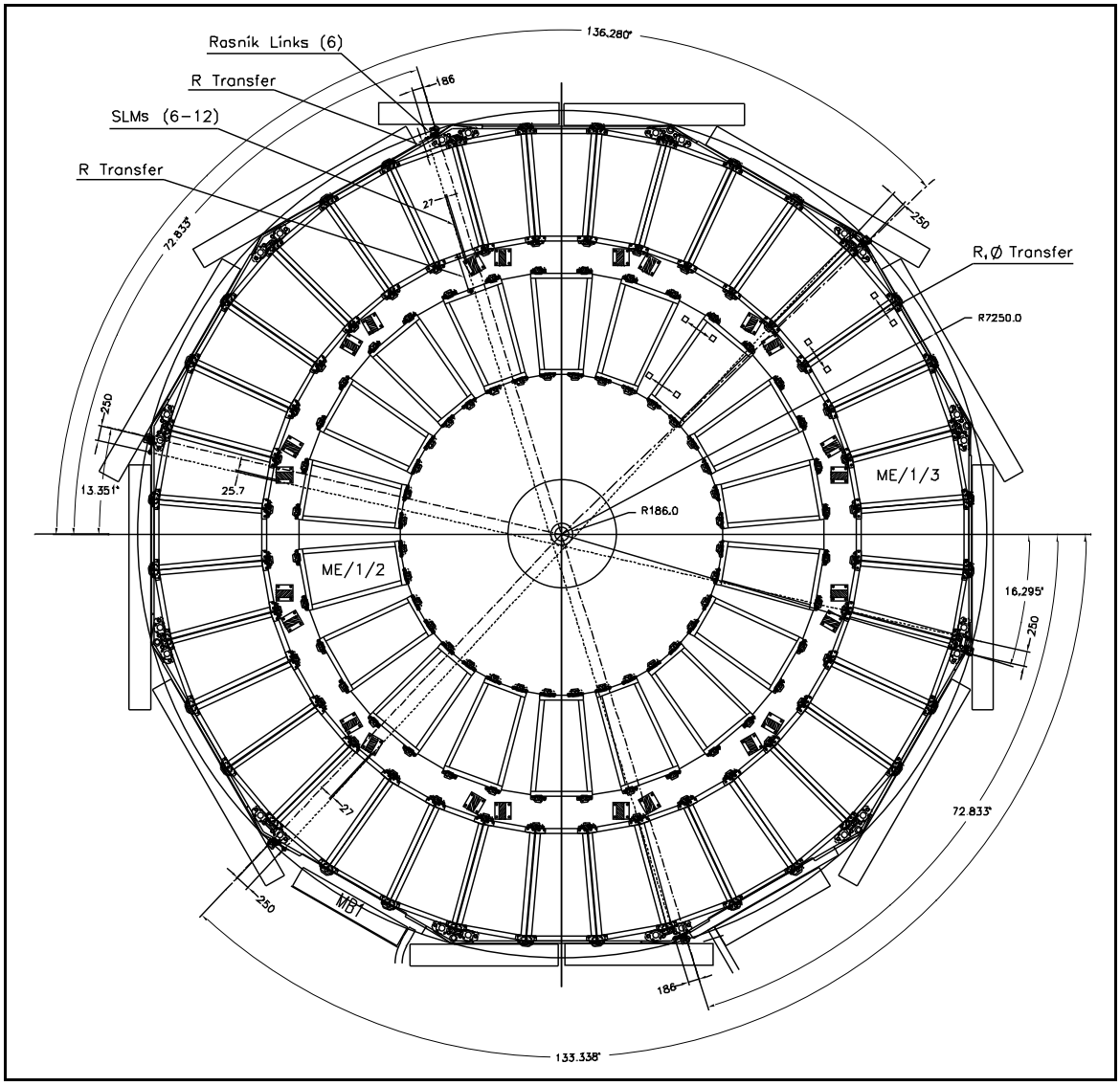


Fig. 7.3.3: Linking of the (MEn/m) layer: Straight Line Monitors.

Cathode strip chamber deformations

We have been making assembly mechanical deformation measurements in the development of support frames [7.8]. This will allow us to understand static deformations of the chambers in various configurations on their kinematic mounts. Studies have also been done on thermal distortion effects and gas bulging. We have been able to model mechanically our prototypes against the measurement. With the final production prototypes, extensive deformation tests will be done and the mechanical analysis refined to model the results. Then the model will be applied to the detector configuration to understand if there are any distortions we need to measure in survey (photogrammetry).

7.3.2 Cathode strip chamber monitoring

Local CSC layer rϕ, z straight line moniton (SLM)

We need to utilize a large number (48) of optical beam straight line monitors over a 14 m path with up to ten position sensors in the line. Low cost commercial 670 nm laser diode modules with fixed optics round beam profiles have been tested [7.9]. These provide a laser beam profile adequate for optical position measurement along a 14 m path in a magnetic field. With these sources located at the Endcap outer boundaries, each line is independent and the modules can be replaced with precalibrated substitutes in situ.

The system requires sensors with good optical response to simple light sources (low cost laser diode modules in magnetic fields), good intrinsic position resolution, 2 cm dynamic range, response uniformity, no internal calibration requirements, long term stability, and insensitivity to magnetic and radiation fields. The long term resolution requirement for the measurements is 25-50 μm. The detectors must have simple parameter calibration.

We have tested a transparent amorphous silicon detector with crossed x, y strip readout [7.9]. These detectors are under development at Max Planck Institute for ATLAS alignment [7.10]. The Multi-Point Alignment (MPA) sensors consist of a 64×64 grid of 300 μm wide (312 μm pitch) readout strip channels over a 20×20 mm^2 active area of 1 μm thick amorphous Si photodiode detector sensing a laser optical beam. These are adequate detectors that can be read out efficiently in long strings. Their characteristics are described in Section 7.4.3 and test results are given in Section 7.5.2.

We are also developing and testing an alternative digital CCD detector for the SLMs, which would avoid refraction, reflection, and beam absorption/scattering effects [7.11].

The accumulation of all estimated local errors in the local SLMs to the rϕ, r measurements is about 80 μm.

The process for precise sensor positioning on the cathode strip chambers is as follows: the chambers are mechanically supported by precision extrusion frames. The radial end frames are located on the precision alignment pins (each end of the centerline) used for the chamber assembly. These frames have CNC drilled pin locations for all the alignment sensors (SLM, radial, proximity) as indicated in Fig. 7.3.4. These pin/sensor locations are measured in the strip assembly survey. Photogrammetry targets will also be located in premeasured CNC holes/pins in the frames.

Radial position monitoring

The system will measure the radial position of the outer ring chambers near the SLM lines using simple cable extension linear potentiometers between the link fixture and the precision end frame of the cathode strip chamber. These potentiometers have been tested to have a 3 μm sensitivity and to yield a long term resolution of 25 μm [7.12]. They have a very small temperature dependence: dx/dT = 0.57 μm/°C/m. Near the same SLM lines, the inner ring cathode strip chamber MEn/1 (at its outer boundary) will be linked to the outer ring chamber by another linear potentiometer between the precision end frames. (Fig. 7.3.3).

The relevant temperature distribution of the cathode strip chambers, electronics, hardware, fixtures, etc. will be measured by simple current source transducers (AD592). We have been able to calibrate a large sample of these devices on a common heat sink to better than 0.2 °C. Assuming a 0.5 °C temperature uncertainty of the outer cathode strip chamber, this

corresponds to only a 37 μm error when used as an r connection. The accumulated local r measurement error of this measurement is about 80 μm.

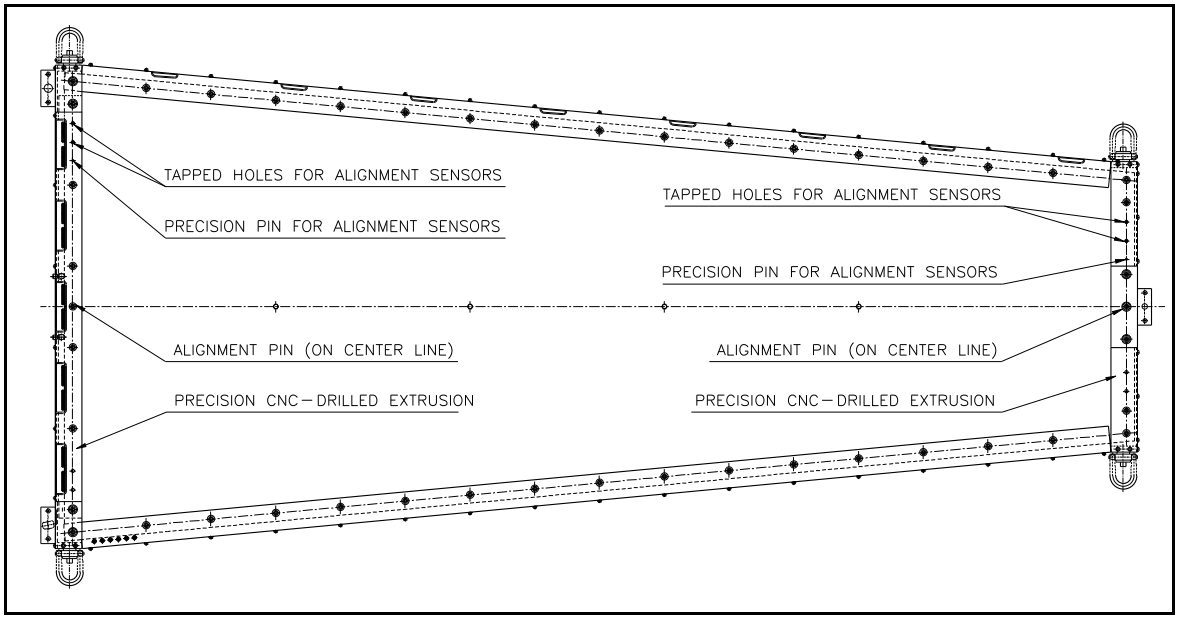


Fig. 7.3.4: Alignment references on precision end support frames of the CSC chambers.

Endcap muon rasnik system: Φ linking

Each Rasnik line (see Fig. 7.3.1) has a source on one barrel end MAB (reference point 1), a lens or pinhole on the opposite barrel end MAB (reference point 2) and a 2D sensor at the ME4 layer outer boundaries. This defines a known ME4 point which is transferred to a second sensor at ME4. The latter sensor is the endpoint of a second local Straight Line Monitor with transparent two dimensional sensors at each MEn layer and a known light source point on the MAB. We are testing a new laser diode/single mode fiber/collimator source (gaussian beam size =2cm at 13m distance) which may allow us to place all sensors MEn (n=1,4), along the primary Rasnik lines and eliminate the position transfers.

The endcap straight line monitors define six (rϕ, r) references that are transferred to each cathode strip chamber layer MEn.

We will build into each barrel end MAB structure a reference plate with an optical collimator source, a 25 mm lens subassembly or 1.2 mm pinhole mask, and a secondary line compact laser diode module. A model design of the (Z+) MAB Rasnik plate is shown in Fig 7.3.5. To limit non-linearity, insure long term stability, and allow exchange of elements, we will center and calibrate the source in a source-lens(s)-quad cell optical bench set-up where the test lens is displaced/rotated or the LED/laser is micrometer displaced. The source/lens assembly will be measured by a coordinate measuring machine. For the endpoint detectors at each of the endcap (MEn/m) layers, we would utilize the same transparent amorphous silicon detector with crossed x, y strip readout described for the local layer r SLMs. A prototype Rasnik system is under development and study at Fermilab (see section 7.5.2).

Endcap muon z transfer system : z linking

The z coordinate transfer system consists of a concatenation of laser-detector triangulation distance measurements between the barrel end MAB structures and carbon tubes/reference surfaces mounted on the outer boundary of theYEn iron between all the endcap layers (Fig. 7.3.2). The tubes are rigidly connected (referenced) to the link transfer fixtures and float (slide) in spherical bearing supports on the iron.

We have tested a commercial distance sensor (OMRON Z4MW40) that works on a 40 ± 10 mm stand-off with a long term resolution (3 week measurement periods) of 1-2 μm with a slow drift of less than 0.1 μm/day. This sensor has observed diurnal motions of 1 μm [7.13].

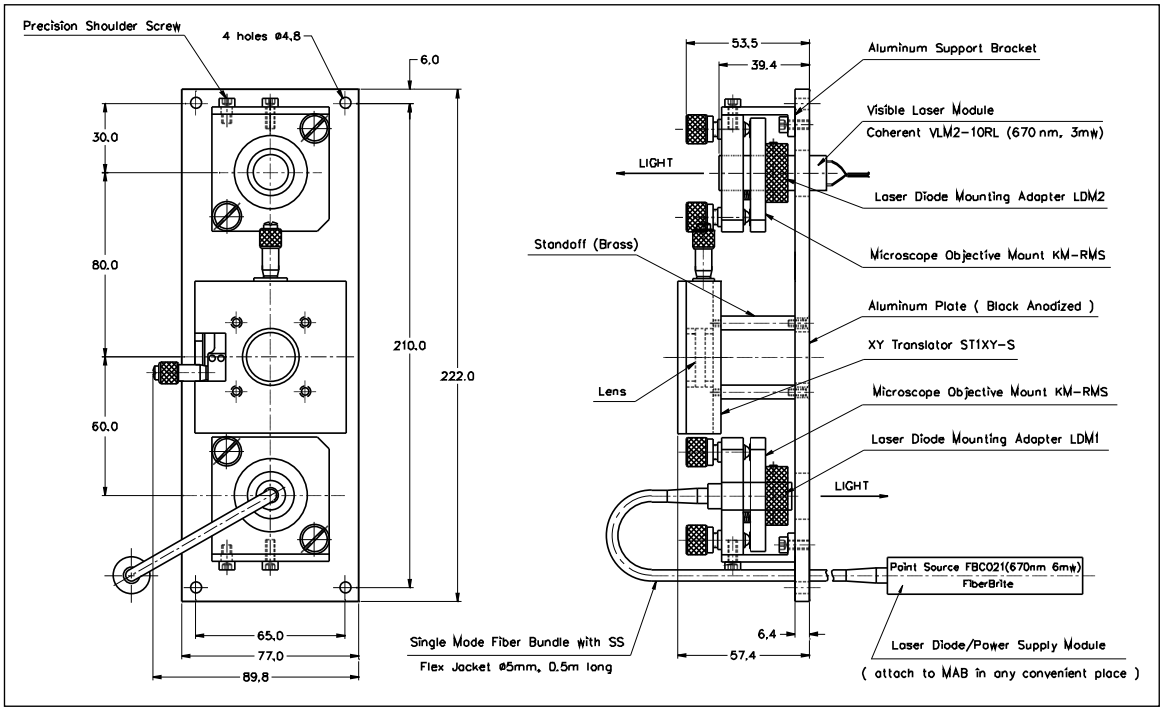


Fig. 7.3.5: A model design of the z (+) MAB Rasnik plates.

It is insensitive to light backgrounds, fringe magnetic fields, and is thermally compensated. It will be used to transfer a z reference surface on the MABs without touching them.

Between the outer boundaries of the Endcap iron discs there is a much smaller differential motion, so another low cost commercial distance sensor can be used. The OMRON Z4DA01 has a linear range of 2.5 mm at a 6 mm stand-off with a sensitivity of 2 μm and long-term stability (2 weeks) of 10 μm at a 20% duty cycle.

ME1/1 - ME1/2 chamber alignment

ME1/1 and ME1/2 chambers give the main contribution to the precision of the muon momentum measurement in the $1.3 > \eta > 2.4$ region. As mentioned before we aim for a position monitoring accuracy of 75 μm, compatible with their single hit position resolution.

Due to the special location of these chambers a direct position monitoring with respect to the tracker detector is foreseen. The aim is to improve the monitoring accuracy by avoiding the transfer errors introduced by the two step procedure of the endcap monitoring system.

ME1/1 ring alignment:

Precise knowledge of the chamber position during detector operation requires accurate chamber construction and installation procedures. Each chamber sector will be installed on precise, rigid fixtures in the return yoke, the frame of the chambers containing precise mechanical references for installation and survey purposes. This group of chambers will be located in the CMS coordinate system by optical connections to the link alignment system.

The alignment scheme used for the other MEn endcap wheels cannot be used here. The internal monitoring scheme currently under study is based on 3D measurements of the chamber position at the four corners of the chamber. Each corner can be instrumented with precise and low cost CCD video cameras and light sources facing each other at the overlap sectors. It can provide the required monitoring accuracy for this station of chambers: on the order of 50 μm in the transverse coordinate and ~ 200 μm in z.

ME1/2 ring alignment:

The position and coplanarity of the ME1/2 chamber ring will be monitored at six ϕ positions using the radial Link laser beams (or satellites) in order to have high precision rϕ reference lines.

Internally within the station, the relative rϕ position of the chambers will be monitored with proximity measurements at the two edges of the chamber. Furthermore, ME1 layer rϕ, z straight-line monitors also provide a secondary measurement of positions.

The number of components required for the endcap alignment system is summarized in Table 7.3.1.

7.3.3 Integration with the endcap resistive plate chambers

Measured reference targets around the perimeter of the endcap iron discs will allow survey of the closed system in the accelerator-CMS detector coordinate system network. No special monitoring is foreseen for these chambers. Nevertheless, monitoring the position of the CSCs mounted on the iron will provide information on the shape of the iron and the positions of the RPC chambers.

7.4 LINK BETWEEN TRACKER AND MUON SYSTEMS

The Link system is designed to relate the position monitoring systems of the inner tracker and muon detectors.

The system connects tracker and muon detectors creating six light paths accessible from both alignment references: tracker alignment wheels and MABs (to which barrel and endcap detectors are related). It provides a set of link points defined in the muon region (on the MAB structures) and in the tracker detector whose position is monitored with respect to common laser beam lines.

Table 7.3.1
Number of components required for the endcap alignment system.

Endcap Alignment Component	Number
Temperature sensor	468
Local CSC layer SLM	
MPA sensor	480
Laser diode module	48
Linear Potentiometer (Radial position monitor)	360
Optical distance sensor (RΦ proximity measurement)	936
Φ and Z Linking	
Rasnik system	12
Optical distance sensor (long range Z measurement)	12
Optical distance sensor (short range Z measurement)	48
ME1/1 - ME1/2 chambers	
CCD camera	300
LED source	1178

The light paths define planes in ϕ, every 60°, as shown in Fig. 7.2.1(color). This segmentation, although redundant, allows a direct reference of each barrel muon sector with the tracker detector and provides direct tracker references to the endcap monitoring system.

Fig. 7.4.1 shows a longitudinal cut of the CMS detector with the layout of the alignment lines. To minimize the interference with other subdetectors the light path follows the inner detector boundaries as shown in the figure and reaches the muon region through radial light channels in the endcap iron disks. The locations of the link points along the path are also indicated in the figure. Four primary points on the MAB structures are used to reference the barrel and endcap alignment systems in this plane. Because of the special location of the ME1 stations, extra link points (not shown) will be used to align these chambers.

7.4.1 The light path

The performance of the system depends mainly on the precise definition and stability of the light path. We describe here the geometry, the mechanical and optical components along the path as well as the constraints on the critical components.

Light beams are generated by two independent laser sources (at $z \sim \pm 6630$ mm, $r \sim \pm 660$ mm) attached to the endcap return yoke. Each source produces two laser beams at fixed angle ~ 94.7°.

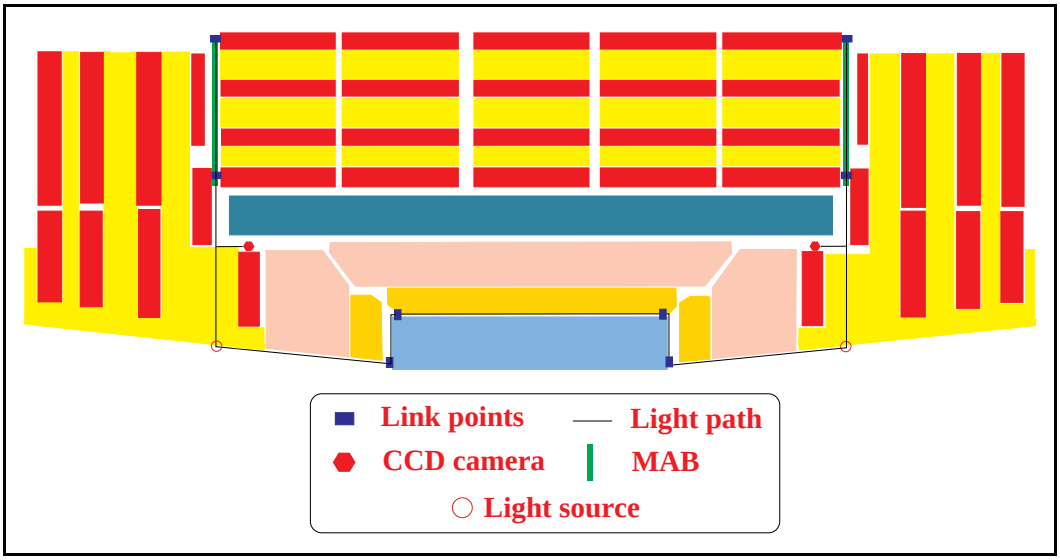


Fig. 7.4.1: Longitudinal cut of one half of the CMS detector showing the light path of the link system.

Due to high magnetic forces induced from the solenoid [7.2] the YN disk that supports the source (see Fig. 7.4.1), will deform and shift in position. Since the expected motion may exceed the range of the alignment active elements, the laser source platform will incorporate a precision remote control block to adjust the location and orientation of the laser beams. The expected distortions of the iron and the required source re-positioning accuracy are summarized in Table 7.4.1. Once the light is within the range of the sensors, the position and orientation of the rays are irrelevant for the monitoring method.

Table 7.4.1
Expected iron distortions and re-positioning accuracy requirements of the source.

Light source	B field on/off	Re-positioning accuracy
X / Y	~ 1 mm	±1 mm
Z	~ 14 mm	±1 mm
Rotations	≤ 2.5 mrad	≤ 1 mrad

Six radial light channels of 70 mm × 110 mm including clearance are machined in the YN2 plates of the iron noses at both ends of the detector to allow the laser beams reach the muon region. The required tolerances due to the shifts and distortions of the return iron under the magnetic forces determine the position and dimension of the channels. Carbon fiber light protecting tubes (or bars) along the channels, attached to the source platform, will also be used for radial distance measurements between the source and the muon link points that are housed on the external MAB structures (see Fig. 7.2.3), at the two ends of the barrel detector.

At r ~ 2630 mm the ME1/1 stations see the light path. Six lines of sight at $2630 < r < 2700$ mm, parallel to the CMS z-axis, allow us to refer these chambers to the muon alignment system.

At the inner detector part along the endcap detector boundaries, the optical lines are parallel to $\eta = 3$ and reach the tracker at r ~ 300 mm. On the tracker alignment wheels, radius periscopes shift the light path from $\eta = 3$ to match the alignment passages at the outer radius boundaries of the detector, allowing optical measurements across the tracker volume.

The current scheme of the tracker and link alignments consists of passages at the outer boundaries of the MSGC detectors as shown in Fig. 7.4.1. The final configuration of the tracker alignment system and radial position of the passages follows the design optimization of the tracker detector and will be described in the CMS Tracker Technical Design Report, to be published early next year (1998). While the ability to monitor the position across the tracker volume is crucial, the final radial position of the alignment passages is not relevant to the performance of the system.

Instead, the achievable accuracy of the system depends on unexpected variations of the light path shape introduced by the periscope. This imposes serious constraints on the calibration and stability of the periscope elements. Table 7.4.2 summarizes the positioning tolerances and stability requirements. The tolerances for the installation positioning of the periscope mirrors are defined by the location and the active area of the photo-sensors (20×20 mm^2) planned to be used in the system.

The requirements on the position stability of mirrors are set to limit the error contribution to position measurements at < 40 μm. As shown in the table, the position of the periscopes on the tracker wheel should be known to within 100 μrad, while the stability of the mirror's orientation must be a few μrad.

Table 7.4.2
Positioning tolerances and required stability of the periscope mirrors, for a periscope with main axis along y.

	Positioning tolerance	Stability requirement
Periscope Positioning		
Max. Rot (x)	10 mrad	(not critical)
Max. Rot (y)	10 mrad	2 mrad
Max. Rot (z)	6 mrad	0.1 mrad
Mirror's orientation		
Max. Rot (x)	0.7 mrad	0.005 mrad
Max. Rot (y)	1.4 mrad	0.010 mrad
Max. Rot (z)	1.4 mrad	0.010 mrad

Currently, we are considering the use of single unit periscopes consisting of a rod as support structure, with attached mirrors at both ends at fixed orientation. The chosen material for the structure is Ti-doped fused silica. The thermal and stability properties of this material under high rate irradiation exposures are excellent [7.14]. A reduced size prototype to test the construction, calibration procedure and stability of the mirrors is being studied.

The periscopes as well as the other alignment components (photo-detectors and tilt sensors) of the link system will be mounted on the tracker alignment wheels. The required calibration precision and stability of both alignment systems must be satisfied by the adequate choice of materials and wheel geometry.

Given the length of the light paths, temperature gradients along the light passages will distort the path, producing deflections of the light. Light protecting tubes and air flow through the passages together with the averaging over many measurements will help to reduce this effect.

7.4.2 Working principle

Linking the tracker to the barrel and endcap monitoring systems

The measurement of the MAB positions with respect to the tracker alignment wheels uses a total of eight linking points along each light path: four placed at the tracker ends and four at the MAB structures (2 per MAB).

At each z end, the measurement involves:

- The definition of the laser beam with respect to the tracker wheels: the position (x, y coordinates) is obtained at the intersection of the light ray with the 2-D sensors located at the tracker wheels, at $\eta \sim 3$. The origin of the beam from the tracker (z coordinate) is obtained by distance measurements along $\eta \sim 3$. The orientation of the laser beam relative to the tracker is determined by two 2-D measurements at the outer MSGC radial boundary.
- The definition of the MAB relative to the radial beam: 2-D position sensing detectors, located at the two link points defined on the MAB structure, measure the relative position and orientation laser beam-MAB. A radial distance measurement from the origin of the laser beam to the MAB give the r coordinate of the link points.

The ϕ orientation MAB-Tracker cannot be directly obtained with this geometry, so it is measured independently by laser levels (laser tilt sensors) placed on the MAB and tracker alignment wheels.

Position monitoring of the ME1 rings

The ME1/1 rings will be monitored at six points on the outer radius boundary of the ring and will require an extra reference (link point) in each light path at r ~ 2630 mm (the outer radius of the ring) seen by the ME1/1 chambers. To transfer the link coordinates to the ring we are currently considering using light sources (on the linking points) and CCD cameras sitting on the ME1/1 muon chambers.

CCD cameras like the ones described for the barrel alignment system have a large measurement field (~ 100 mrad) and assure the feasibility of measurements even if unexpected large uncorrelated distortions of the endcap return yoke occur in the region. A full reconstruction of the position (six measurements per station) will allow measuring the angular orientation of the cameras within the required precision.

The final method to align these chambers will be defined in the near future following the progress of the mechanical design and supports of the chambers in the return iron.

7.4.3 Elements of the system

Light source

The source consists of laser light from semiconductor laser diodes (in the red wavelength range, appropriate for the photosensors) coupled to single TEM_{00} mode optic fibers and collimator optics to guarantee diffraction limited laser beams with a gaussian profile over long distances. The light from each diode can be distributed to several positions using a commercial fiber splitter, such that the laser can be placed outside the detector and thus replaced without the need of access to the source assembly inside the detector.

Multi-Point Alignment sensors (MPA)

Semitransparent amorphous silicon sensors working in transparent mode are planned for use in the link and endcap alignments since both are based on multi-point measurements along laser beams. First tests of these sensors are summarized in 7.5.2.

The first semitransparent sensors were developed by H. Kroha et col. at the Max Planck Institute [7.10]. Two different transparent technologies were used in order to produce crystalline and amorphous silicon sensors. The crystalline sensors were rejected for alignment purposes. They shown large systematic errors and some resolution degradation near the edges. Besides this, the strips are built only on one surface, spoiling the precision on the transverse coordinate. In contrast, the amorphous silicon (aSi) films are fully active and position resolutions of 1 μm have been reported [7.10]. Both kinds are multilayer sensors.

The sensor layers are designed to be transparent to visible light with a sensitivity of 0.1 A/W at 690 nm and 0.01 A/W at 790 nm. The aSi sensors considered here consist of (see Fig. 7.4.2) a layer of hydrogenated amorphous silicon of 1 μm thickness sandwiched between two layers of 100 nm ITO (indium-tin oxide) electrodes segmented into a 2D transparent matrix of 64 × 64 electrodes. The sensor layers are deposited with chemical vapor deposition (CVD) techniques and are segmented using photolithography. The vertical electrodes are in the upper layer while the horizontal electrodes are two layers underneath, with the aSi layer in between. The three layers are deposited on a 0.5 mm thick glass substrate. The back and front surfaces of the sensor have different treatments to reflect and absorb respectively the red wavelength.

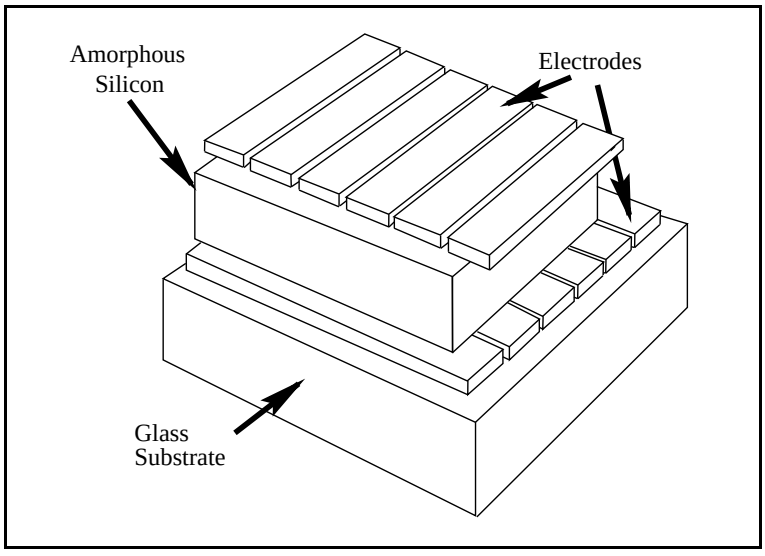


Fig. 7.4.2: 3D drawing of the layer arrangement in the sensor. The drawing is not to scale.

The laser light is partially absorbed by the aSi material, producing photocurrent on the strips.

The information obtained from the incoming beam consists of two orthogonal intensity profiles due to the particular geometry of the electrodes. Both profiles have a gaussian shape. The mean values of the distributions determine the beam light position.

The most important dimensions for these sensors are summarized in Table 7.4.3.

Table 7.4.3
Physical properties of the silicon strip sensors.

aSi thickness	≤ 1 μm
Strip thickness	100 nm
Glass thickness	500 μm
Number of strips	64×64
Active area	20×20 mm^2
Size	25×25 mm^2
Strip pitch	312 μm
Strip gap	10 μm

The sensors are expected to be insensitive to high radiation doses and high magnetic fields. Radiation and magnetic field tests and optical stability tests are planned.

Laser level

The angular ϕ orientation between the tracker and muon systems will be monitored using Laser Level boxes. A Laser Level box consists of a tilt sensor, a laser source with conditioning optics and, outside of the box, one or two transparent position detectors. The tilt sensor measures angular position and rotational movements with respect to the vertical *gravity vector* for the elements to which the sensor is attached. The laser source will extend the local measurement given by the tiltmeter through a ~ 3 m long structure (MABs and Tracker alignment wheel).

The operation of the tilt sensors is based on the fundamental principle that an enclosed bubble, suspended in a liquid, will always orient itself perpendicular to the gravity vector. The bubble (Fig. 7.4.3 (a)) is contained in a liquid-filled case, with three electrodes. When an AC voltage is applied across the two excitation electrodes, the AC output measured at the central pick-up electrode changes in linear proportion to the tilt angle. The conversion of AC current to DC current is obtained by means of a Signal Conditioning Unit (SCU). This unit also allows monitoring of the ambient temperature.

The sensors currently being considered are manufactured by Applied-Geomechanics Incorporated (AGI) and their main characteristics are summarized in Table 7.4.4. Calibration and test results are described in section 7.5.3.

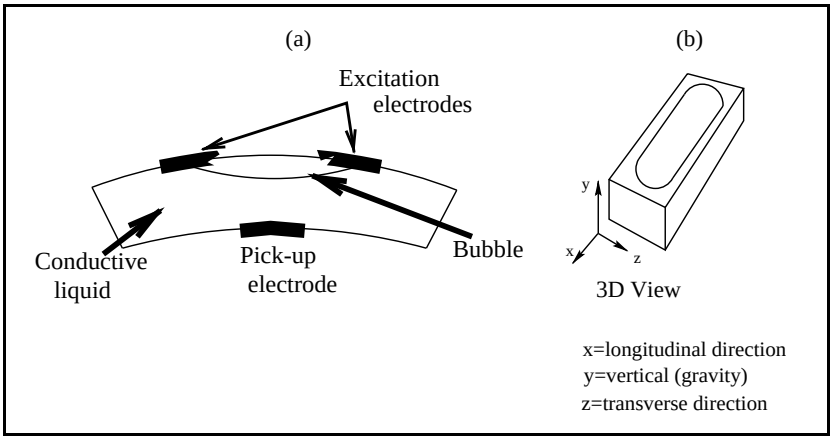


Fig. 7.4.3: (a) Working principle of a tiltmeter sensor. (b) Geometrical shape of the tilt sensors and axis definition.

Table 7.4.4
Characteristics of the 756 AGI-tilt sensors.

Total Range	±4 arc degrees (higher gain), ±10 (lower gain)
Resolution	1 μrad
Repeatability	5 μrad
Environmental	-25 °C to +70 °C operational, -30 °C to +100 °C storage, 0 to 100% humidity
Power requirements	±12 VDC @ 10 mA
Output voltage	±8VDC
Dimensions	50.8 × 15.7 × 15.7 mm
Mounting	Horizontal or vertical surface hole diameter = 4.3mm
Weight	42 g
Output connections	30 cm pigtails with tinned ends or mini connectors

The resistance to radiation has been tested up to 9.76 Mrad with a dose of about 0.08 Mrad/hour. The results indicated that the sensors will perform successfully in high-radiation environments, but that the signal conditioning electronics must operate in a non-irradiated area.

The sensor response is not affected by uniform magnetic fields. Nevertheless a sensitivity to field gradients along the sensor area was observed during the tests performed for SSC, where these kind of sensors were also considered. Only field gradients above 1.4 T/m between the ends of the sensors should be taken into consideration. For them, the reported specifications predict shifts in the output angle bigger than 10 μrad. In CMS, sensors at the region between Barrel and Endcap Muon detectors can be exposed to field gradients up to 1 T/m. If necessary, the effect of this field gradient can be parametrized and then subtracted from the output

response. The parametrization will be obtained from a detailed test using a well-known gradient field where the output shift from zero field gradient will be measured.

The scheme of the Laser Level box now under test is shown in Fig. 7.4.4. The figure shows the current arrangement for all the elements. The final design is still under development. The tilt sensor will be separated from the laser source by an insulator to minimize the effect of temperature changes. The laser light can be injected using a laser source inside the box (a solution that demands conditioning optics to bend the beam) or an optic fiber carrying the laser light.

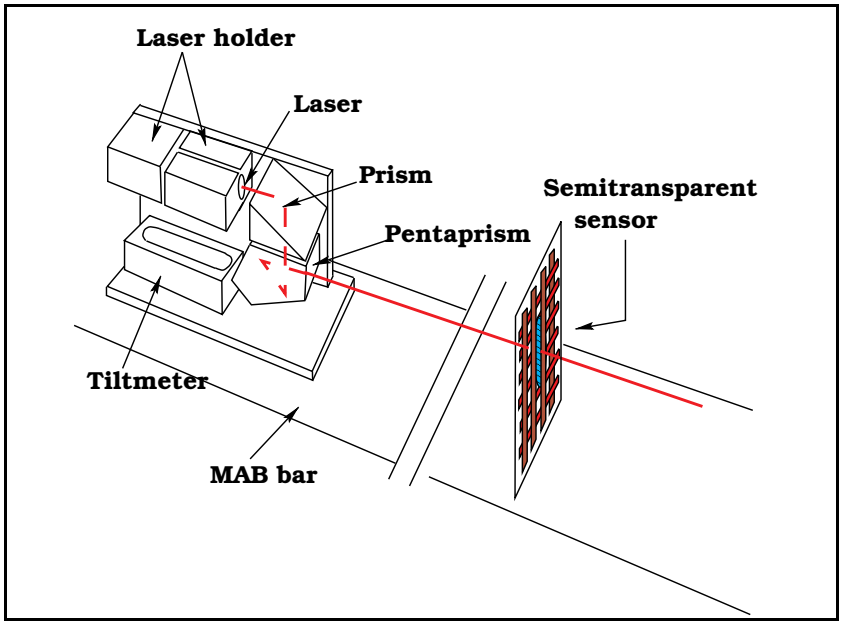


Fig. 7.4.4: A model design of the Laser Level box. The light beam has to cross one or two transparent position detectors. One of them is shown in the picture.

Distance measurements

Distance measurements between the laser source and the MAB or tracker alignment wheel are done using mechanically and thermally stable carbon-fiber bars along the light direction and long range proximity measurements between the alignment structures and the carbon-fiber bars. An optimized geometry, choice of material and type of fixation of the bar must guarantee minimal (≤ 50 μm) contribution to the measurement error.

The proximity sensors measure the displacement of objects with a high resolution using a semiconductor laser beam and a special optical system. Commercial displacement sensors, which provide a measurement range between 40 ± 10 mm (or 100 ± 40 mm) with a linearity better than 1% of the full range scale (respectively 1.5%), are planned to be used. The resolution is on the order of 2 μm (10 μm) at a response speed of 60 ms (500 ms). The measurement is stable even in inclined objects. The temperature fluctuation is on the order of 0.02-0.04% of full scale per °C.

Table 7.4.5 summarizes the active elements of the system.

7.4.4 Expected performance

Tests of the individual alignment elements are going on. Some are described in section 7.5. The estimated error contribution from the various components of the system is summarized in Table 7.4.6. The correct implementation of the link system at the tracker ends and in particular the calibration precision and stability of the periscopes can strongly affect the final accuracy of the system. The numbers quoted in the table must not be exceeded in order to guarantee the required ≤ 100 μm monitoring accuracy.

Table 7.4.5
Number of components of the link system.

Link Alignment component	Number
Laser diode module and optics	12
Temperature sensor	24
Elements mounted on the tracker	
2D-MPA sensor	30
Tilt sensors	6
Laser diode module	6
Optical distance sensor (long range Z measurement)	12
Elements for ME1/1	
LED	48
Video camera	12
Optical distance sensor (long range R and Z measurement)	24
2D-MPA sensor	12
Elements mounted on the MAB structure	
2D-MPA	24
Tilt sensors	12
Laser diode module	12
Optical distance sensor (long range R measurement)	12

Table 7.4.6
Expected error budget contribution.

Components	Estimated error
MPA sensor detection	5 μm/4 μrad
Sensor positioning	20-50 μm
Periscope mirrors	15 μrad
Periscope positioning	20 μrad
MAB rigidity	20 μm
Laser level	15 μrad
Laser opening angle	20 μrad
Distance measurements (r and z)	80 μm

7.5 EXPERIMENTAL TESTS

Due to the complexity and the scale of the muon alignment system, the strategy of the experimental tests is to:

- Check the elements of the proposed system and choose or develop the appropriate ones,
- Check the subparts of the system in the order of growing integration,
- Build and run the calibration bench for the MABs, on which also the MAB stability with respect to temperature, humidity, mechanical load, etc. will be checked,
- Build a full-scale test facility and check a set-up containing all the relevant elements of the whole system.

First tests of the basic components have been done at different laboratories to prove the feasibility of the chosen alignment techniques. The status and test results for the main components of the system are summarized here.

7.5.1 Calibration and measurements with camera boxes

A thorough study and a series of measurements have been carried out to test the proposed position measurement of the barrel muon chambers based on LED – camera box pairs and optimize their parameters. The final test set-up representing one connection line of half of an active plane [7.15] is shown in Fig. 7.5.1.

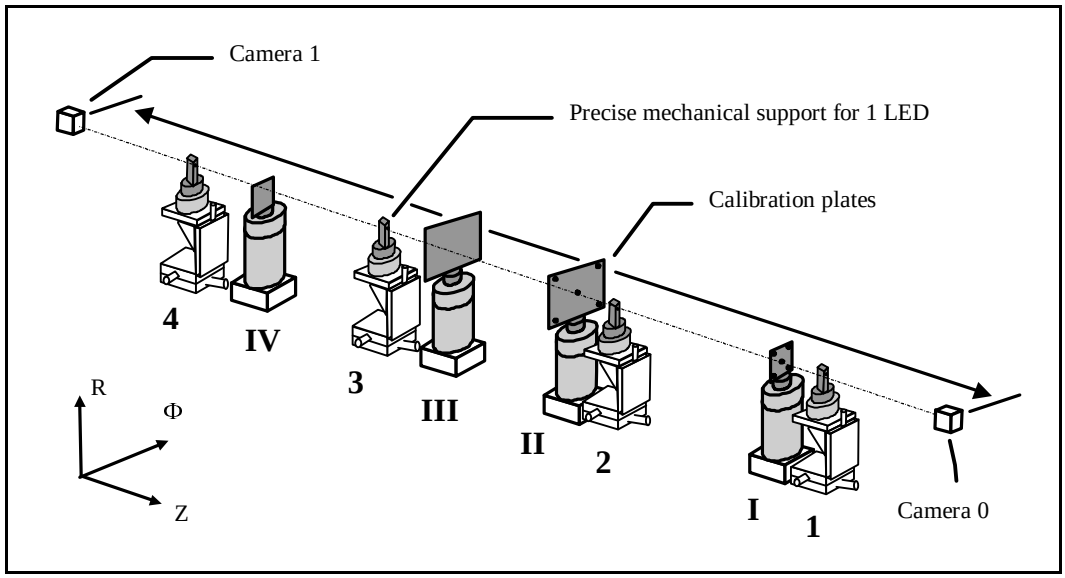


Fig. 7.5.1: 3D view of the bench: 4 movable single LED supports and 4 plates on rigid supports.

Two fixed camera boxes were placed on an optical bench at 5 m distance from each other (approximately the real CMS dimension). Four LEDs (corresponding to two barrel muon chambers) were mounted in precisely machined holders (standard survey sockets used at CERN) fixed on 3D moving tables. Next to each LED a calibration plate was placed in a similar holder. Two types of plates were used: small plates (I and IV, 74×43 mm^2 with 20 precise holes, Ø 10 mm), and large plates (II and III, 210×128 mm^2 with 41 holes). The machining

precision of plates is 5 μm from one hole to another. The cylindrical connection (30 mm diameter guidance) of the supports in the sockets permits 10 μm of repositioning precision for both the LED supports and the calibration plates.

The usage of survey sockets permitted us to measure the positions of the LEDs and also the calibration plates by various traditional survey methods such as theodolite triangulation, stretched wire measurement (distance from a point to a wire stretched between 2 reference points), horizontal distance measurement, and levelling (measurement of vertical coordinates with an optical level). The precision of the survey measurement was 20-30 μm in the ϕ direction, 40-50 μm in the R direction, and 150 μm in the z direction.

The LED light source was placed in a 10 mm diameter precise support (Fig. 7.5.2) which can be fixed at any hole of the plates or in the single source supports.

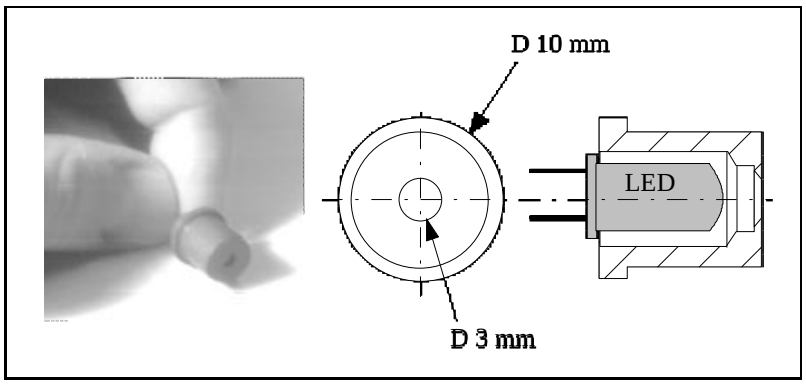


Fig. 7.5.2: The source is a LED fixed behind a 3 mm hole. The support diameter is 10 mm.

Standard 25 mm and 50 mm focal length video objectives were used as the imaging elements of the camera boxes. A low price CMOS CCD matrix (Peach mini camera from VideoCapteur, 312×287 pixels, 19.6×16 μm^2 each) providing standard CCIR video signal output was used as sensor element. The video acquisition card used is the primo card of the Euresys company (PC board) with an 8-bit ADC, local memory and processor with built-in image processing possibilities. The steps of the image processing are object detection (selection of a surface where illumination is higher than a threshold) and the calculation of the center of the light spot.

The calibration permits the sensor and the lens of a camera box to be located in the laboratory frame, which can be described by 9 independent parameters. To obtain these parameters a set of light sources with known positions have to be measured by the camera to be calibrated. To achieve the best calibration the light sources have to occupy the expected field of observation of the camera box both transversely and longitudinally. This was achieved by the 2 plates at 750 mm and 2300 mm distance (plates I and II for the camera box "0" and plates III and IV for the camera box "1"). Only half of the longitudinal field was used to have a compact calibration set-up.

The calculation of the 9 parameters describing the camera box was based on two sets of data: the survey measurement of the light source positions in the calibration plates, and the camera box measurement of the center of the light spot of each source. The calculation was done by the program Simulgeo [7.6]. The calibration was repeated under different conditions

(25 and 50 mm focal lengths, 1.8, 5.6 and 8 aperture values for the objectives; and 10 or 20 LEDs).

Finally, a set of measurements was made with light sources at different locations which was compared with the survey measurements (also any of the measurements made for calibrations could serve as reconstructed independent measurements).

The results of the tests are discussed in detail [7.15]. They can be briefly summarized as follows. Four sources of errors can be identified:

- Survey measurement precision
- Machining precision (holders, plates)
- Intrinsic precision of the camera-measurement
- Light source: difference between the mechanical and optical centers.

The intrinsic precision of the camera box (measured separately) is about 1 μm (5% of the pixel size). The machining precision did not exceed 5 μm. The dominating factors in the error budget were the survey precision and (mainly) the imperfection of the light sources used for the tests. These errors appear already at the calibration step, causing a systematic error during the measurements. For the same reason the test results are better for the reconstruction of points used in the calibration (50-80 μm) than for those not used (< 200 μm). The results also degrade outside the calibration zone, i.e. for distances more then 2300 mm (up to 300 μm systematic error).

Using the Simulgeo it was demonstrated that a realistic improvement in the survey measurements (from 30-40 μm to 20 μm) and the LED quality (10 μm max deviation between the optical and mechanical axes instead of 40-100 μm) would increase the precision by a factor of two. Inclusion of far points in the calibration would also decrease the degradation of the precision with distance.

The conclusions and consequences can be summarized as follows. The tests have proven the feasibility of building a monitor system based on light source – camera-box pairs that can fulfill the requirements of the barrel muon system. At the same time the tests have revealed some problems which need further attention, namely the high requirements on the calibration bench and the choice of the light source.

7.5.2 Multi-point alignment sensors: straight-line monitor test prototype

A test set-up/evaluation of six MPA 2D transparent sensors with simple light sources was completed at Fermilab in 1996. The detailed results are given in [7.9]. We found adequate stability, beam profiles, detector resolution, and gaussian fits in the application of simple laser diode-fixed optics modules. The source had little divergence (0.3 μrad). We utilized tunable collimator modules to control the profile on very long straight-line monitors across endcap CSC layers (collimators with distant foci as required are commercially available). However, the properties of the light and sensors set a limit on the number of detectors in a given beam. To overcome this problem a solution using beamsplitters to create linked optically opposing beamlines has been studied [7.16].

The results from short-term (few hours) stability tests of the string of six detectors in a *fixed* (stationary) laser diode module are summarized in Table 7.5.1. For this tests the sensors were placed on a granite table at S1 = 0.53 m, S2 = 0.94 m, S3 = 1.52 m, S4 = 2.11 m, S5 = 2.69 m, and S6 = 3.33 m from the laser source. We turned on the laser diode only during

measurement to avoid instabilities/changes in the optical response of the sensors and laser diode output. All elements remained in fixed mechanical positions and orientations.

Table 7.5.1
Short-term stability results for a string of 6 MPA transparent sensors.

Sensor #	σ (x) [μm]	σ (y) [μm]
S1	1.6	4.4
S2	2.9	2.0
S3	4.7	2.4
S4	10.6	6.4
S5	12.7	6.6
S6	15.3	10.7

In long-term (8 hours) stability measurement tests the detector response varied from 20-56 μm due to thermal and angular motions of the laser diode beam.

To understand long term stability in the endcap position monitoring system, we have set up a hardware test-bench at Fermilab in 1997 which connects a 14 m Rasnik line with a perpendicular, 6 m long, straight line monitor. Two different setups were used. The first setup linked a reference source to a (21 mm aperture) reference lens at 12 m distance, and to a MPA link sensor at 1.7 m. The second connected the reference source to a reference iris (1.2 mm diameter) at 13.4 m distance, and to a MPA sensor at 0.3 m downstream of the iris. The first case represents the link Rasnik of Fig. 7.3.1 and the second case corresponds to a ME1 link sensor in the primary Rasnik line scheme. The system also included a Z transfer setup between the lens (or iris) and a large range distance sensor Z4DA01, placed at ME2 distance. Current source temperature sensors are also distributed on critical items on the testbench. The MPA link sensor was mounted on a common structure with LD1 (the laser diode source for the 6 m layer straight line monitor) and the Z4DA01 sensor. The plate included Applied Geomechanics precision x, y inclinometers (tiltmeters). We measured the Rasnik lens/iris displacement range for both setups. In both cases the MPA sensor could track a 14 mm range of motion in r, rϕ. Typical RMS deviation of points from a linear fit was < 21 μm for the pinhole, and the resolution for a fixed beam position measurement in the link sensor was 11-12.6 μm. So, we concluded that we can establish a link transfer to the CSC layer Straight Line Monitor laser diode module sources within 30-40 μm uncertainty.

With temperature sensors read into 14 bit ADCs, we were able to track changes of 0.28 °C. Using a 1.54 m long aluminum z tube anchored at the ME2 end, we were able to observe and confirm the thermal expansion of the tube relative to a reference surface with a short term resolution of 1 μm, and with a long term resolution of 16 μm. In fact we believe that we can monitor temperature (with current source sensors) and correct for linear expansion of metal tubes as distinct from mechanical motions. This will avoid the difficulty of monitoring the expansion of carbon fiber structures due to humidity in coordinate transfers.

Long term stability tests of a 6 m long Straight Line Monitor (in a CMS like arrangement) were performed. Typical runs extended from 3 to 9 days. The tests included the study of transition effects during the warm-up period for the laser diode modules. We observed

variations over 250 μm of the beam position during the corresponding warm-up period, at the 6 m distant sensor. Measuring this effect at the distant sensor and properly correcting for it at the intermediate sensors, the instability of the setup was reduced to 16 μm. Thus, the unavoidable negative effect from the laser beam movements can be overcome by having a sensor at the far end. The position of this sensor is determined by the laser light coming from the opposite direction. These results confirmed our *design principle*, each Straight Line Monitor terminates in a laser beam monitoring sensor on the diametrically opposite link transfer fixture.

7.5.3 Calibration and tests of Laser Levels

The 756 Mid-range AGI tilt sensors (described in 7.4.3) have been calibrated and tested in the laboratory [7-17]. Although these sensors are intended to measure along their longitudinal direction (Fig. 7.4.4 (b)), they are slightly disturbed by tilts transverse to them. The relationship between longitudinal tilts and output voltage was measured and the effect of the transverse tilts on the longitudinal measurement was quantified within the expected working ranges (± 0.3 degrees) to be smaller than 5 μrad.

The test setup (Fig. 7.5.3) required a mechanism providing rotations on the order of μrad to cope with the accuracy of the sensors. A 450 mm long arm tripod which could move in steps of 0.5 μm (measured by a length gauge HEIDENHAIN with a resolution of 0.5 μm) was used. The tripod rests on three knobs that can be moved independently. The sensors were located on top of the longest arm, screwed to a platform that was the interface between the tripod and the sensors. The tripod, platform and sensors were placed on a stable bench.

Each sensor has its own calibration parameters and had to be separately calibrated. The longitudinal tilts of the sensors were reproduced with 5 μrad precision. The most important contribution to this error comes from the intrinsic position repeatability of the bubble inside the case. Temperature changes affect the magnitude of the calibration parameters typically by +0.0005/°C. This contribution will be corrected by measuring the temperature changes.

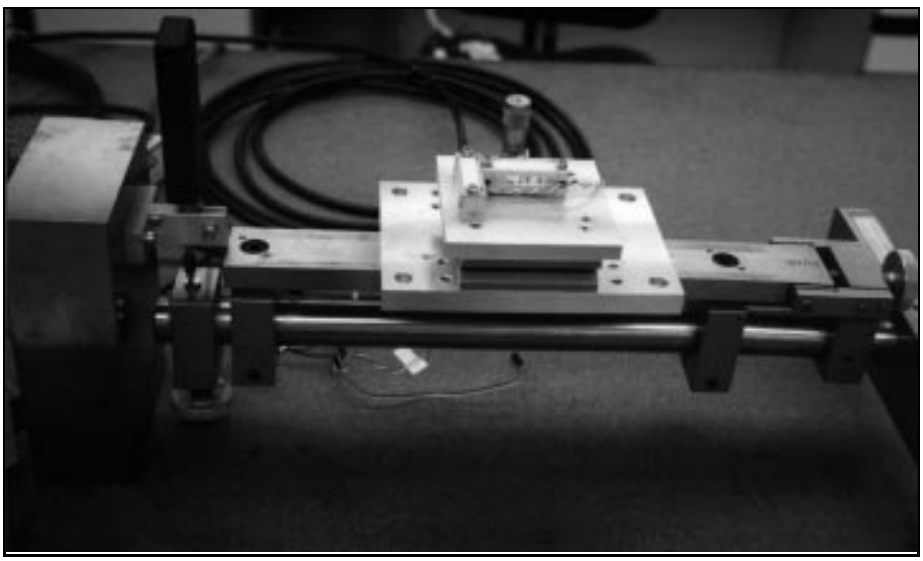


Fig. 7.5.3: Setup for calibration and test of AGI Tilt sensors.

7.6 VALIDATION OF THE MUON ALIGNMENT PERFORMANCE

The three subsystems, i.e. the Barrel (section 7.2), the Endcap (section 7.3) and the Link system (section 7.4) together constitute the full muon alignment system. All of them contribute to the final accuracy and also an incidental failure in any of them could affect the global performance. Therefore it is an indispensable step to study the system as a whole both experimentally and by simulation.

Due to the large scale, complexity and cost of the full system the experimental study has to be limited to a full-size minimum arrangement that contains all the relevant elements. The experimental setup for this test described in 7.6.1.

To validate the performance of the full system an extensive simulation study is in progress. The first results in this direction are discussed in 7.6.2. Further development of the simulation program will allow us to study the robustness and redundancy of the full system in detail, including the possible degradation of the full system, in case of failure of individual elements.

7.6.1 Full-scale test of the CMS position monitoring system

The planned full scale test laboratory setup is shown in Fig. 7.6.1. The aim of this facility is to verify the complete alignment concept and measure the precision of the system. It will allow us to study and develop the subparts of the system.

The setup is a simplified version of one CMS r-z plane containing all the elements relevant for the position monitoring: a Tracker zone, a Link line, one half of an active plane of the Barrel system and two Endcap lines (representing the two sides of the endcap) and the connection between them.

The measurement precision of the whole system will be obtained by comparison of the data provided by the system itself with direct survey measurements. For this reason a precise and redundant survey network will be built around the setup (not shown in Fig. 7.6.1). The CMS-ϕ direction has been set vertically, allowing the most precise survey measurements by optical levelling.

The test facility will also be used to optimize the organization of the slow control and the data acquisition of the monitoring system, to develop the data evaluation program capable of reconstructing the positions of the monitored elements based on the measured data and to make diagnostics of the system.

The laboratory, which will also house the calibration bench for the MABs, is being prepared at CERN and will be operational starting in 1998.

7.6.2 Performance of the global muon position monitoring system

The simulation program SIMULGEO, described in 7.2.7 is being used to study the performance and possible optimization of the system. Currently the simulation includes the inner tracker (so far described as a perfectly known rigid body), six linking optical lines on both sides of the detector and the barrel monitoring system.

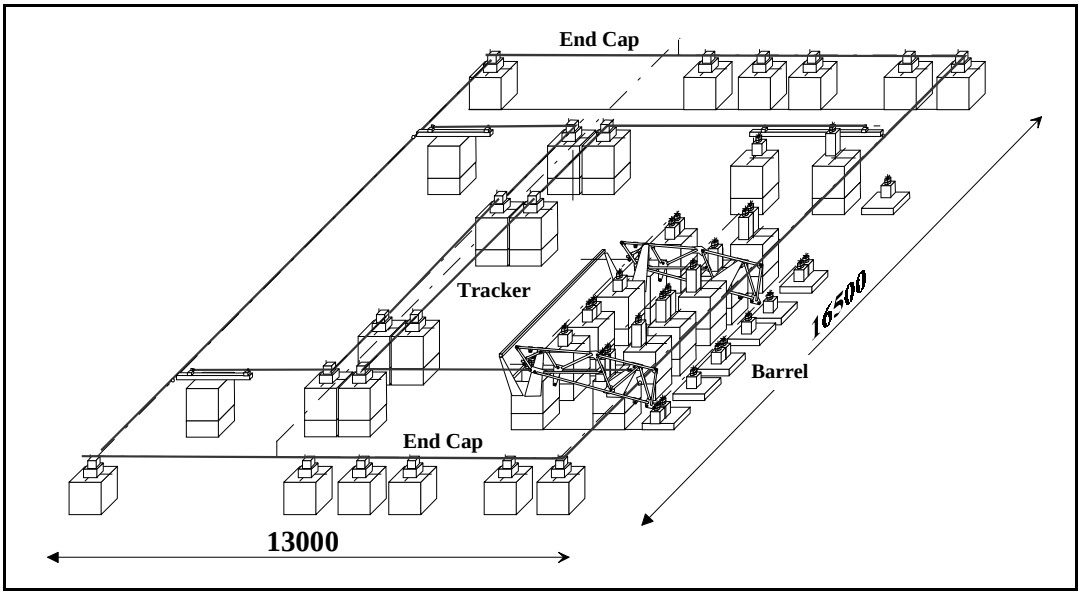


Fig. 7.6.1: Full-scale laboratory test setup of the CMS position monitoring system. The associated survey network is not shown.

The first results already show the improvement in precision due to the additional constraints introduced by combining the subsystems. As an example, at an initial 100 μm precision (link error), the active alignment planes of the barrel system can be located with a precision of 80 μm with respect to the inner tracker.

To characterize the alignment system performance we have extrapolated the current simulation results to estimate the final chamber positioning accuracy. Simple error propagation, based on the expected performance (and test results) of the alignment components as described in sections 7.2 to 7.4, indicates that the precision requirements can be achieved. The barrel chambers can be located with a precision better than 150 μm and the endcap chambers (ME2 to ME4 stations) in the range of 130-175 μm. The first endcap station will benefit from the six direct measurements from the link system. The overall system performance will depend on the final implementation of these measurements, which is not yet completely defined.

As it is designed the muon alignment system provides a rather uniform accuracy across the full muon system.

7.6.3 Validation and diagnostics in situ

During operation at LHC, it is essential that the alignment system be capable of providing, for each reconstructed coordinate, the corresponding error as derived from the data. It should also allow making diagnoses in case of large errors.

Further studies are needed to access the limits of this diagnostic capability and of the tolerable number of component failures in the system.

7.7 ALIGNMENT WITH MUON TRACKS

Alignment of this complex muon detector with tracks can only help as a validation of a set of predetermined parameters (although a detailed diagnosis, in case an error is found, remains

in general impossible). Tracks may also be useful when few local parameters are to be determined, as in the case of neighboring CSC chambers.

As a validation and possible refinement of the optical alignment measurements, a strategy of aligning the different components of the muon system using muon tracks is planned. This procedure must provide information on the different alignment steps: 1) alignment of chambers in the same sector; 2) sectors with respect to each other; 3) the barrel with respect to the endcap muon system; and 4) the muon system as a whole with respect to the central tracker.

Cosmic rays can be used during commissioning runs and for the barrel during data taking. Tunnel muons will also be useful for the endcap chambers during data taking, and prompt and decay muon production will also be used. Furthermore, it is planned to run with triggers selecting single muons above about 30 GeV (at $L = 10^{33}$ cm^{-2} s^{-1}) to 70 GeV (at 10^{34} cm^{-2} s^{-1}). The achievable precision of an offline alignment depends strongly on the lower bound in the momentum spectra of the tracks. Unfortunately a high cut-off is needed due to the systematic errors introduced by the uncertain knowledge of the magnetic field and material description inside the calorimeters, coil and return yoke. Thus tracks below 100 GeV have little or no use.

Based on the fact that each of the muon stations (together with the vertex information) as well as the central tracker provide full information on the muon trajectory, the track elements in one of these subdetectors can be compared with the extrapolation from the others. With a sufficiently large number of these events, offsets or rotations can be monitored. It is necessary that all elements be correctly matched, and for that, a previous alignment to the order of 1 mm is needed. For larger misalignments an iterative procedure has to be attempted.

The chambers in the same sector can be aligned by reconstructing the muon parameters using the first (closest to the interaction point) station together with the vertex constraint and extrapolating to the second one. A relative alignment of the first two stations to within 100 μm in rϕ can be achieved in a full year of data taking at low luminosity. Similarly, the third and fourth stations can be aligned with the first one to 120 and 150 μm in rϕ, respectively. For high luminosity better precision (50, 70 and 80 μm) can be reached. In principle, tasks (2) and (3) could be performed using tracks crossing different sectors or both barrel and endcap systems. However, the precision attained is relatively poor and a better result can be achieved with an individual alignment of all sectors with respect to the inner tracker.

In general, the expected precision provided by this method for a full year's data at low luminosity is expected to be comparable to that provided by the optical monitoring, allowing a good cross-check to be made. However, this applies only if the whole year's set of data can be used for this purpose.

References

[7.1] F. Matorras and A. Meneguzzo, CMS TN/95-069; V. Karimaki and G. Wrochna, CMS TN/94-199.

[7.2] CMS Magnet Technical Design Report 1997.

[7.3] L. Brunel, CMS TN/94-239; J. C. Gayde et al., CMS TN/94-250.

[7.4] C. Darve. Rapport de stage. PPE 1996.

[7.5] L. Brunel et al., "A calibration bench to measure the positioning elements of the barrel muon chambers for the CMS experiment", to be published as a CMS Note.

[7.6] L. Brunel CMS Note/96-018.

[7.7] Muon Alignment Group CMS TN/96-005.

[7.8] CMS Endcap Muon Meeting Proceedings (P1A Bulging Test, D. Eartly) Fermilab, June 1996.

[7.9] D. Eartly et al., CMS IN/97-005.

[7.10] W. Blumet al., Nucl. Instr. and Meth. A367 (1995) 413; Nucl. Instr. and Meth. A377 (1996) 404; Max-Plank Institute for Physics MPI-PhE/95-13.

[7.11] D. Eartly et al. CMS Note/96-021.

[7.12] D. Eartly, "Wire Potentiometer Tests", Proceedings CMS Endcap Muon Meeting Fermilab, November 1995.

[7.13] D. Eartly, "Z4MW40 Tests", Proceedings CMS Week Muon Alignment Meeting Aachen, September 1996.

[7.14] D.B. Hall, Vol 35, N10 Applied Optics 1673 (1996); C.I. Merzbacher et al., SPIE Vol. 1533, Optomechanics and dimensional stability (1991).

[7.15] L. Brunel CMS Note/96-019.

[7.16] D. Eartly et al., CMS IN/97-020.

[7.17] C. Burgos et al., "Calibration of AGI tiltmeters and study of the transverse tilts", to be published as a CMS Note.

8. CONTROLS AND MONITORING

8.1 OVERVIEW

Control and monitoring functions for all CMS detector subsystems will form a single control system to operate the detector. Design and implementation are coordinated by the Detector Control System (DCS) Group. Using guidelines provided by DCS, each of the subdetector groups defines and designs the data acquisition and control function needs for its subdetector. Data from the subdetectors are available to the global control system, which provides console hardware and software, as well as display, archiving and other higher level services. This section describes the control and monitoring of the MUON subdetector.

Parameters to be measured by the control system exist in four locations: the counting room, the side galleries of the cavern, on the detector, and inside the detector itself. Physically, the electronics outside the detector is housed in VMEbus crates. Inside the detector, electronics resides in readout boxes on the border or surface of each individual chamber. Access to data in the readout boxes will be via a network connection from dedicated DCS crates in the counting room to controller cards in the readout boxes. All VMEbus crates will include a DCS processor with a network connection to the higher system levels.

8.2 DCS OVERVIEW

8.2.1 Design principles

8.2.1.1 Hardware architecture

The DCS hardware architecture consists of three principal layers. At the top are operator workstations and general purpose computers which provide access to all of the DCS services. The front-end or bottom layer consists of a large number of distributed front-end processors (VME-based). The middle layer is a dedicated local network interfacing the other two layers. This network is segmented for availability purposes, and is connected to the general CERN network by a filtered access. The general CERN connection provides world wide access to authorised persons. The front-end layer connects to detector systems and equipment through direct I/O or through field buses. Figure 8.2.1 shows the architecture of the DCS network.

8.2.1.2 Software architecture

The software architecture is a cooperating network of dedicated control applications, DCS general services and gateways to other CMS and CERN systems. The dedicated control applications are the distributed controls for CMS detectors, which are composed of real time process control components and supervision components.

8.2.1.3 Operations

DCS services are needed for all operational phases of the experiment, from construction and commissioning to physics data taking runs, calibration tests and monitoring during shutdown periods. During the data taking phase, one or more operators will concurrently run the CMS detector. These functions will be carried out from control rooms, equipment rooms, or remotely under the filtering of the DCS access control.

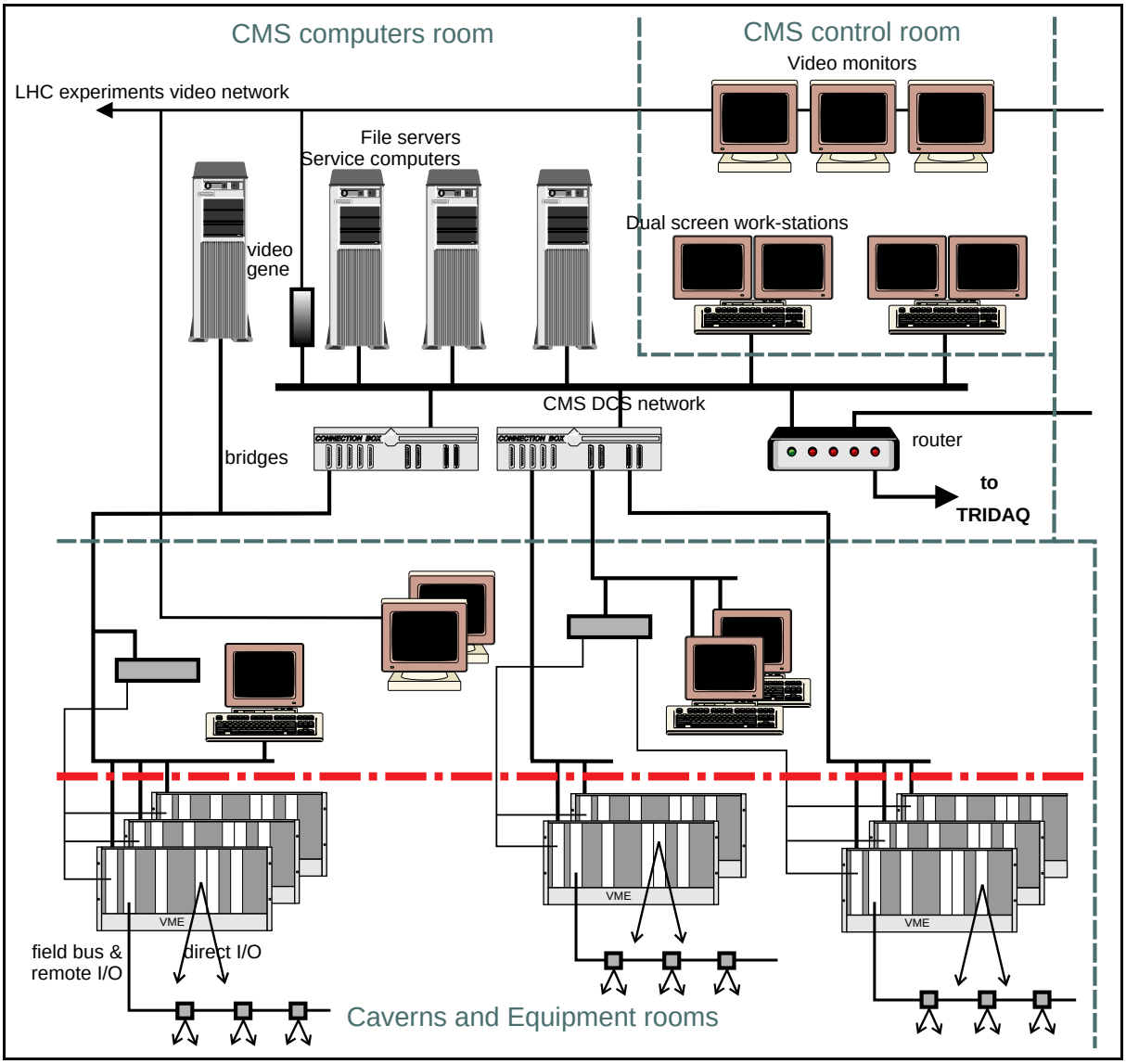


Fig. 8.2.1: DCS architecture.

8.2.1.4 DCS toolkit

DCS provides general services: Archiver, Logger, Alarms, Access controls, Central Repository, and a manager for the overall DCS activities. A toolkit is provided to build the dedicated control applications at the individual system level. The kit consists of drivers for the I/O hardware, a control kernel, generic applications and a set of libraries for specific applications.

8.2.2 Controls software system

The CMS collaboration has decided to implement a common general-services software approach using an existing controls package. Extension to a common approach for all four LHC experiments is presently under discussion as well. In CMS and ATLAS, the respective DCS groups are evaluating EPICS as a possible general software system and have demonstration

projects underway. EPICS is a highly developed software controls system that is widely used in the high energy and nuclear physics community and is supported by many laboratories.

To have a specific configuration and software environment to discuss, the remainder of this chapter will be based on the use of EPICS in its current VME implementation. In this context, the starting point for the individual detector subgroups is the EPICS Input-Output-Controller (IOC), a VMEbus based front-end crate containing a single-board computer running EPICS compatible software. At the present time, IOCs use the VxWorks real-time operating system running on Motorola processor boards. The data request protocol Channel Access (CA) allows upper level processors to read and set parameters in the IOC. At start-up, each IOC is downloaded with the programs and database entries needed to acquire and process locally the parameters associated with that particular IOC.

Because EPICS is used at many laboratories, software drivers are available for most commercial modules. The DCS group has indicated that they will recommend modules to use for standard analog and digital control system signals. This standardization goal is intended to minimize the software effort required to implement subdetector control and monitoring systems.

An important feature of the total EPICS/IOC software package is an extensive system for monitoring and reporting of analog and digital alarm conditions. Included in the alarms task is a provision for two-tier analog alarms, with independent settings for high and low values, plus high-high and low-low values to distinguish severe from off-normal alarm conditions. Using this capability, less severe out-of-tolerance conditions can be reported, allowing preventive maintenance to be performed before real hardware failures occur. Alarm system values are part of the data that are downloaded to each IOC at initialization time.

In EPICS, the database is a key element that allows the system to be adapted to different applications. Database records that are downloaded to the IOCs are processed at rates dictated by the records. Processing the records may be as simple as reading an analog value, but other operations such as state machines and PID control loops can also be implemented by configuring parameters of predefined database entries rather than writing special programs.

8.3 DATA FROM THE DRIFT TUBES

A summary of the control and monitoring data from the DTs is given in Table 8.3.1. Several items listed, as e.g. HV control and monitoring, are already included in other systems with their own DCS capability. The count of actual hardware links to the CAN bus is therefore much smaller.

8.3.1 Electrical system

On the DT chambers the frontend controller (FEC) allows the control of test pulse and preamplifier output to be done via masks, for each of the ~200,000 drift cells. The FECs also monitor the LV of the frontend electronics. For all these functions there will be only one link to the CAN bus for every DT chamber.

The number of channels shown for control and monitoring of the HV reflects a granularity of one HV line for over 60 drift cells and is limited by cost. HV and LV supplies, readout and trigger are foreseen to be located on the balcony of the CMS detector. These will be housed in about 200 crates, whose temperature and supply voltage and current will also be monitored.

Table 8.3.1
Control and monitoring data for the DTs. There are 250 DT chambers, each with 3 SLs.

Detector	Assume	Total number	Comment
LV status	1/DT ch.	250	logical bit; flags current consumption
TDC status	~7/DT ch.	1,700	one word per readout board
U_{thr}	1 / SL	750	preamplifier threshold
TP mask	1 / DT ch.	250	test pulse masks; address each cell
ROB commands	1 / DT ch.	250	mask preampl. output (1 bit / drift cell); power on/off and reset ReadOut Boards
HV: U & I	4 / SL (x3 voltages)	9,000	at input of HV cables; controlled by HV system itself
LV: U & I	1 / 4 DT ch.	60	LV supplies
Crate: U,I,temp.	1 / crate	200	all crates
Temperature	~9/DT ch.	2,200	including 2/DT ch. for electr. boards
Cooling fluid	2 / DT ch.	500	temperature In / Out
Cooling fans	1 / DT ch.	250	air flow present
Gas pressure	1 / DT ch. 2 / wheel	250 10	expensive; may have to reduce quantity
Gas flow	2 / DT ch. 5 / wheel	500 25	
n-way valves	1 / wheel	5	
Strain gauges	2 / DT ch.	500	deformation of DT
Oxygen in gas	1 / wheel	5	analyzer with digital output
Drift velocity	1 / wheel	5	is small 1-cell test chamber

Since the chamber temperature should be uniform and constant, to avoid deformations of the DT chamber and to have a precise knowledge of the drift cell position and of the drift velocity, cooling is built into the DT chamber and the temperature of the coolant monitored via two temperature sensors per chamber. The temperature of the gas inside the DT chamber is monitored via six sensors per chamber. A ventilation system will remove any further residual heat from the slot housing the chambers, and the presence of an air flow has to be monitored.

Possible deformations of the DT chamber will be also be directly monitored by a strain gauge mounted on each face of the chamber.

8.3.2 Gas system

There is an independent gas distribution system on each of the five barrel wheels, each requiring a pair of precision flowmeters and pressure gauges to be monitored. Since every DT chamber, i.e. a group of about 1,000 DTs, has an own gas tubing to the distribution panel, its gas flow will be monitored via a coarse flow measurement at the inlet and the outlet of the distribution panel, and the pressure will be measured by one gauge at the chamber.

The gas quality will be monitored by measuring the amount of oxygen impurity in the gas, and by measuring directly the drift velocity with a small reference drift cell. A remotely controlled N-way valve will serve as multiplexer, connecting the input or any of the 50 gas output lines to the analyzers.

8.4 DATA FROM THE CATHODE STRIP CHAMBERS

8.4.1 Electrical systems

Each CSC detector consists of 6 layers. Each layer is operated with a separate high voltage supply. The HV system assumes the use of a commercial multi-channel mainframe. The system will be able to fit all necessary HV channels in 27 crates, located in the control room. Each high voltage channel is controlled and monitored and the current is also monitored by DCS.

The cathode and anode electronics front-end boards (FEB) are mounted directly on the CSC detectors. Two low voltage supplies at +5 V and +3.3 V are required for each of the 540 CSCs. Each individual low voltage supply is monitored and controlled by DCS.

The CSC system will have an estimated heat load of 80 kW. The method chosen to remove this heat is a pressurized water system. The plan is to connect 3 CSCs in series to form a 20 degree f sector. The input and output water temperature will be monitored and controlled by DCS for each sector. The liquid pressure will also be monitored at each station.

8.4.2 Gas system

The three components of the CSC gas mixture are supplied by gas racks and are mixed by a mixer located in the SGX building under DCS control. The gas mixture is monitored by an analysis system to provide information on the mixing. The analysis system also monitors the return gas. The mixed gas is delivered to 10 racks (5 per endcap) residing in the detector cavern. Each rack supplies gas to a full station (two stations in the case of ME/2 and ME/3), consisting of 54 CSCs. The ME/1/1 CSCs are treated as a separate station. Within each station the gas is delivered to 3 CSCs connected in series covering a 20 degree f sector. The gas input pressure to each station is monitored by means of a flow meter and a control valve.

Each CSC detector needs gas pressure and flow monitoring by DCS. Four CO_2 sniffers per station are required. The gas mixture is monitored with an analysis line for every 20 degree f sector by means of one N-way (N=18 or 36) valve per station. Each N-way valve is controlled by DCS.

8.5 DATA FROM THE RESISTIVE PLATE CHAMBERS

8.5.1 Electrical systems

Each RPC gap will be fed by a high voltage channel supplied from a HV distribution bus. The HV distribution bus will be provided by commercial HV distributor modules housed in 50 crates residing in the detector cavern. Each distributor module will provide HV monitoring and control as well as current monitoring and will be interfaced to DCS.

Table 8.4.1
Control and monitoring data for the CSCs. There are 540 CSCs.

Detector	Assume	Total number	Comment
LV: U & I	2 / 3 CSC	300	for front-end (+5 V, +3.3 V)
Cooling	1 / 3 CSC	180	temperature In / Out
Liquid pressure	1 / station	10	
HV: U & I	6 / CSC	3,240	at input of HV cables; controlled by HV system itself
HV crates	27	27	
Gas pressure	1 / 3 CSC 1 / station	180 10	expensive; may have to reduce quantity
N-way gas valve	1 / station	8	
CO_2 sniffers	4 / station	40	
Fail-safe valves	1 / CSC	540	
Mass spectrograph	1	1	quantity limited by costs

The RPC front-end electronics requires two analog power supplies, +3 V and -2 V, as well as a digital +5 V supply for the FEBC and SU. One LV line will be shared by two FEBs. As for the HV system, a LV distribution bus will be used to supply an entire detector sector with a single LV channel. The LV system assumes the use of a commercial multi-channel mainframe and will be housed in 30 crates residing in the detector cavern. The LV to each RPC will be controlled and monitored by DCS through the mainframe supply.

The front-end electronics are interconnected to link boards (LB) which are housed in 40 VME crates located in the detector cavern. The LBs are connected via an optical link to the trigger electronics. The trigger electronics is contained in 22 VME crates located in the control room. All the crates are monitored by DCS.

The estimated heat load of the RPC front-end system is relatively limited and therefore does not require a cooling system. Each RPC will be equipped with a temperature sensor monitored by DCS.

8.5.2 Gas system

The two components of the RPC gas mixture are supplied by gas racks and are mixed under DCS control. The gas mixture is monitored by an analysis system to provide information on the mixing. The analysis system also monitors the return gas. The mixed gas is delivered to 15 racks (5 for the barrel and 5 per endcap) residing in the detector cavern. Each rack supplies gas to a full station (two stations in the case of ME/3 and ME/4), consisting of 54 RPCs. Within each station the various RPCs are grouped in 3 vertical groups to reduce the operational difference in pressure between the RPCs. The two layers of RPCs in the first and second station are connected in series and fed by the same gas input lines. Within each station the gas is delivered to a few (2 to 3) RPCs connected in series covering a 20 degree f sector. The gas pressure to one station is monitored by means of a flow meter and a control valve. The quality of the gas mixture is also monitored by means of 9 N-way valves.

Table 8.5.1
Control and monitoring data for the RPCs. There are 360 RPC detectors, each with 2 gaps in the barrel, and 744 RPCs, each with 2 gaps, in the endcap regions.

Detector	Assume	Total number	Comment
LV	1 / 48 ch.	4416	
U_{thr}	1 / RPC gap	2208	
HV: U & I	1 / RPC gap	2208	at input of HV cables; controlled by HV system itself
Crates		142	front-end readout, LV, HV and trigger electronics
Temperature	1 / RPC gap	2208	
Gas pressure	1 / vertical group	9	expensive; may have to reduce quantity
N-way valve	1 / vertical group	9	

8.6 DATA FROM THE ALIGNMENT

8.6.1 Barrel slow control

8.6.1.1 Read-out and control

From the control and read-out point of view, the barrel position monitor system is split into 36 units. One unit consists of

- one MAB with the camera-boxes mounted on it,
- a video multiplexer and optical fiber driver for these camera-boxes,
- temperature sensors mounted on it and the ADC for the sensors,
- all light sources (mounted on the chambers, on the Z-bars or on other MABs) that are observed by the cameras of the given MAB.

The total and the maximum number of elements/unit are given in Table 8.6.1.

Within one unit, the light sources are switched on and off in a synchronized way to avoid any ambiguity in the identification of the light source. The cameras provide standard video-signals, which are multiplexed and sent to the control room via optical fibers.

The speed and repetition rate of the individual measurements can vary from sensor to sensor. The system will be able to take a complete set of data every minute.

Due to the fact that the elements of one control/read-out unit are located on very different parts of the CMS detector, they cannot be interconnected locally. Their cabling will follow that of the given detector and the interconnection will be made in the control room.

The system needs low voltage only. The estimated power consumption including the LEDs (5V, 50 mA/LED), the cameras (9V, 20 mA/camera) and the electronics (multiplexers, ADC-s, fibre drivers, signal processing, crates) is about 4kW for the whole barrel monitor system.

Table 8.6.1
Total and maximum number of elements per control / read-out unit. There are 36 units.

Element name	Max number / unit	Total number
Camera boxes	12	360
Light sources	88	2352
Temperature sensors	4	144
16-channel Video-multiplexer	1	36
4-channel ADC	1	36

8.6.2 Endcap slow control

Table 8.6.2
Number of components required for the Endcap alignment system.

Endcap Alignment component	Number	Comment
Local CSC layer SLM		
MPA light sensor	480	2D transparent
Laser diode module	48	
Linear Potentiometer	360	Radial position monitor
Optical distance sensor	936	RF proximity measurement
F and Z Linking		
Rasnik system	12	light source + 2D detectors
Optical distance sensor	12	long range Z measurement
Optical distance sensor	48	short range Z measurement
ME1/1 - ME1/2 chambers		
CCD camera	300	
LED source	1178	
Temperature sensor	468	

8.6.3 Link Slow control

Table 8.6.3
Number of components required for the alignment Link system.

Link Alignment component	Number	Comment
Elements mounted on the CT		
MPA light sensor	30	2D, transparent
Laser diode module	6	
Tilt sensor	6	
Optical distance sensor	12	long range Z measurement
Elements mounted on the Endcap inner cone		
Laser diode module	12	
Elements mounted on the Endcap ME1/1 zone		
Video camera	12	
Optical distance sensor	24	long range R & Z measurements
Light source	48	
2D MPA sensor	12	2D, transparent
Elements mounted on the MABs		
MPA light sensor	24	2D, transparent
Tilt sensors	12	
Laser diode module	12	
Optical distance sensor	12	long range R measurement
Temperature sensor	24	

9. SAFETY

9.1 INTRODUCTION

9.1.1 Safety objectives

The overall objectives for the safety of the CMS, which apply to its components (projects) have been established as:

- protection of occupational and public health
- protection of major capital investments

The former includes the work-place and adjacent environment during construction, operation, maintenance and dismantling, and the latter refers to the experiment's success and the expectations of sponsors and users. These aspects are also supported, directly or indirectly in the CMS Constitution.

9.1.2 General principles

The safety requirements for experimental activities at CERN are generally described in the CERN document SAPOCO/42 which defines the safety policy. As a first step toward implementation of the provisions of the codes and instructions which emerge from this policy, the CMS collaboration has established a Safety Working Group with membership mainly drawn from the technical design staff of major subsystems. Coordination with the TIS Commission is ensured by three members from the TIS Division in this working group. The Group Leader in Matters of Safety (GLIMOS) of CMS chairs the group and sees to it that safety hazards are identified successively and in the early phases of the project, in order to eliminate or reduce them and control them.

Safety considerations, as reflected in design or specific measures for safety, in general have to follow the SAPOCO policy and the CERN Safety Codes and Rules resulting from it. In addition European and host-country Directives are taken into account, as well as European and/or internationally accepted codes and standards, such as for pressure bearing components (e.g. CODAP, ASME), structural aspects (e.g. EUROCODE 3, AISC), lifting equipment (e.g. FEM, the "Fédération Européenne de Manutention") and standards for cryogenics, chemicals, environment and radiation. In this connection recommendations of the International Organizations, such as IAEA, WHO, ILO and ISO will also be considered. In special cases the standards of the country of origin of the equipment may be used.

CERN's international status and safety prerogative on its own territory (see SAPOCO/42 for details) empowers it to settle differences between Swiss, French, international standards or its own experience and set its own safety standards to be applied uniformly to a particular site or experiment. A special requirements document for CMS is being established and will maintain a traceable written record on such settlements (see section 9.1.3). Special attention will be given to the correct functioning and reliability of any safety device of the muon system and supporting systems under the prevailing environmental conditions (magnetic field, electric fields, radiation, temperatures). Detection and alarm systems, interlocks, drives and controls of elevators, safety valves, circuit breakers, etc. will be examined for their reliability and redundancy, where needed.

A process of Initial Safety Discussions has been started for CMS and its Muon Project and has established many of the important safety features outlined below. A detailed worksheet

is used for these discussions as a guide to ensure that all aspects of hazards at accelerator facilities are covered. These are possible scenarios which could cause death, injury or occupational illness or damage to facilities, systems, equipment or the environment including those not routinely encountered by the public. Special hazards analyses and safety review meetings will focus on further details, some of them with the help of external expertise. Such analyses are either in progress or planned for the near future.

Results of initial hazard identification have already been considered below, along with mitigation strategies to reduce or eliminate risks. The technical solutions adopted or proposed to obtain the required high safety standards in the different disciplines and systems as well as some supporting organizational measures are outlined in the following chapters.

9.1.3 Safety documentation

As a complement to the existing set of TIS documents which have CERN-wide validity, a number of safety issues specific to CMS and its muon system are being summarized or recorded in the following documents:

- a follow-up list of open safety issues, which come up during design, manufacturing or testing, is maintained at the Project Office and pursued to resolution of items; particular inputs are the results from Initial Safety Discussions and the upcoming Hazard Analyses
- a CMS Safety Requirements document has been initiated with the purpose of providing clarified requirements to designers, collaborators, subcontractors and experimenters in a concise, controlled, written form; agreement from TIS has to be obtained for the contents. The Safety Working Group will be used for this
- a comprehensive CMS Safety Report will be issued in the last quarter of 1998.

9.1.4 Safety responsibilities

For the safety of the muon system the following established functions are important:

- the Group Leader in Matters of Safety as described in TIS documents (GLIMOS)
- the Technical Coordinator as described in the CMS Constitution
- the Division of Technical Inspections and Safety (TIS) for the setting of standards and rules, independent inspection and safety reviews and, in general, approval of all safety matters
- the individual designer and manufacturer with documented responsibility for delivery of a safe and reliable component or system commensurate with experimental and safety objectives and requirements
- important responsibilities have also been defined for gases and site-specific safety surveillance; they are described in the relevant TIS documents and are being coordinated with the GLIMOS functions.

9.1.5 Full-scale tests

At CERN and within the CMS Experiment certain proven-out rules are observed, by which major components and sometimes their subsystems are subjected to full-scale tests. The pre-production prototypes (PPP) have a special significance in this regard. These tests are usually performed at CERN facilities, with conditions of radiation, magnetic fields etc. similar to the expected operational CMS/LHC conditions. These important tests will not only answer final questions on design, feasibility and operational characteristics, but will also contribute

directly or indirectly to the confirmation of safety, as defined above. The ground rules for testing issued by TIS have to be followed.

9.2 MECHANICAL ASPECTS

9.2.1 General requirements

Structural integrity of the muon system and its components is essential to their safe and reliable operation during the life cycle of the CMS experiment. Mechanical design requirements comprise functionality over specified (relatively short) lifespans, mitigation of hazards and safety problems to the system, restraint of subsequent, consequential damages to human beings the environment and vital equipment, under all conceivable conditions during construction, operation and maintenance. Low-probability, high-risk events, such as earthquakes also have to be analyzed if major safety hazards are anticipated.

The policy adopted by the muon system engineering team calls for adequate safety factors for components, supports and major structures during normal operation, handling and maintenance (and, if necessary in the framework of hazards-analyses for emergencies). In today's environment of more accurate simulations by FE methods, safety factors of 1.5 against yield-strength (as stipulated by AISC) are common and acceptable; for less sophisticated analyses, factors of 2 would be more common. In addition, designs and design calculations are the subject of various reviews. A newly structured *final design review* is being added to the CMS technical review process, involving peers with relevant practical experience. Such reviews and the subsequent approvals shall be completed at the latest before commencement of fabrication.

While simple hand calculations can provide plausible checks on some design calculations, the software reliability issue is usually systematically addressed by requiring that numerical cross checks deal with potential input errors, modeling errors, or math errors by using a completely different finite element analysis code or by changing both the boundary conditions and the modeling in the same code. In addition a tolerance stack-up is performed for components to be integrated, to support design and installation feasibility and support safety with regard to assumed loads (forces) between components. This effort is performed with careful consideration of the actual operating conditions and loads, such as temperature, temperature gradients, pressures, moisture, and magnetic forces.

9.2.2 Applicable design codes and standards

In general the codes and standards will be taken directly from the relevant TIS documents. However, some major code applications will require more detail, careful review and possibly special consent from the relevant authorities, in order to determine relevant and advanced methodology for a pioneering experiment which operates at same time on the CERN premises and in France and may be manufactured in Russia or the USA, for example. While the French CODAP is generally the preferred choice, some ANSI, IEEE, AISC and, in particular ASME standards may be more explicit for the cases at hand; French authorities are known to have accepted justified usage of such foreign codes, and early agreement in that regard will be sought through TIS where this appears necessary.

9.2.3 Hoists, cranes, transport, and handling

This special discipline of mechanical design may require early attention in the project schedule because some installations are already required for the civil works. Although civil works and installation of the experiment are usually strictly separated (by contract and equipment) it may be cost-effective to use some of the hoists for both. Also the civil works will have their own safety issues to observe, in particular regarding personnel safety. A special safety coordinator has been engaged for the civil works on the site and will cooperate with the GLIMOS as much as necessary. Considering the unusually large, heavy and expensive loads to be handled for the experiment, the observation of the safety objectives (see section 9.1.2) in this area is particularly important and includes above all:

- Lifting equipment is to be designed to CERN Safety Code D1 and to be approved by TIS before operation, preferably before installation or even during the design phase.
- Particularly large and risky operations may require the additional consultation of more detailed or advanced standards, such as the ANSI/ASME B30.20 "Below-the-Hook Lifting Devices" or the German KTA - 3902, "Cranes in Nuclear Facilities"; TIS must be consulted on such applications.

9.2.4 Seismic design

For the rare event of earthquakes, 0.15 g accelerations generally have to be considered in all three dimensions. This is a quite severe criterion for a European site and is usually taken into consideration by making the addition to the basic static loads. Where such simple consideration imposes undue restrictions in the design of components which often have to be lean in their support structures, the designer should have additional options to fulfill safety objectives. One option is to carry out more sophisticated analyses, e.g. considering details such as applicable enveloping floor response spectra at various levels of the structure over the expected frequency range. This allows among other things the consideration of natural frequencies of components and their possible detuning to be moved outside the frequency range of the earthquake (as a simple tool for seismic protection). If the consequences of equipment damage are tolerable (e.g., low-cost replacement) and no risks to personnel result from failure, a second option would be to suspend special seismic strengthening for that component, provided agreement is obtained in the design review process, with the participation of TIS.

9.2.5 Magnetic fields in relays

The functioning of all magnetic parts of relays or of magnetic valves is checked against the influence of the prevailing strong magnetic fields from the solenoid (see also section 9.8). The external (experimental) fields in general must not exceed 10% of the field generated locally, by the field for the functioning of the relay for example.

9.2.6 Mechanical safety in specific components

Barrel drift tubes

The barrel DT chambers will weigh about 1000 Kg. The backbone consists of an aluminum honeycomb, 128 mm thick, a structure well suited for supporting the chambers. The Superlayers (3 per chamber, 4 layers per SL) are glued with Araldite AW106 to the honeycomb and the strength of these glue joints is currently being tested with mock-ups in order to ensure that an adequate safety factor in the chamber robustness exists.

Endcap CSCs

The mechanical safety issues which have been addressed for the large iron disks of the endcaps to be moved in and out one by one, are:

- support configuration changes from installation to operation, namely from a gravity loaded individual mode, on special supports, to a magnetic force dominated assembled structure without the special feet, as well as the transition between them
- distortion of the disks by magnetic forces
- necessity for consideration of seismic requirements when the disks are standing alone.

RPCs

Detailed FE stress analysis, supported by specific tests, has been performed for the bolts which are crucial for the support and attachment of the RPCs. High normal operational loads are incurred at the bolts and in their immediate surroundings; however, plastification of material in the most stressed zones will be avoided and an adequate safety factor (see section 9.2.1) observed. The RPCs will be placed in special cradles for transport and hoisting; the additional accelerations and forces which act during handling, including final installation, will be taken into account .

9.3 ELECTRICITY AND ELECTRONICS

9.3.1 Overview

The safety of conventional electrical systems for power and lighting in general is assured and controlled by adhering to well-developed rules and regulations in force at CERN, notably Safety Instructions IS23, IS24, IS26, IS28, IS33, and Safety Code C1. For electronics systems, the codes and handbooks for good safety practices are not quite as well developed; they therefore need more specific individual attention as to their safety. While electronics systems are typically characterized by low voltage DC power systems, 15 volts and lower, there are still significant hazards in connection with fire, thermal loads and radiation damage. Electricity as a cause for heating, short-circuit and fire cannot be totally excluded, mainly because of the high current capabilities of many of these systems. Low voltage power supplies in the range of several hundred amperes are not unusual. Once detector designs and above all the cabling and cooling arrangements are finalized these risks will be analyzed and appropriate measures taken.

Conversely there are a number of low-amperage high voltage systems needed for the operation of DTs, CSCs, and RPCs which need special attention and are treated under the electronics safety considerations in force at CERN. Voltages from 10 to 15 kV have to be coped with. Electrical components may also be directly or indirectly involved in the quenching of the magnet, and exceptional thermal, electrical and magnetic situations. Rapid transitions, induced fields and heat removal will be considered in hazard and safety analyses where relevant.

9.3.2 Overcurrent protection

World HEP experience has shown that lack of adequate overcurrent protection and of temperature monitoring in low-voltage high-current systems is a frequent cause of fires in experimental facilities. This is true to some extent for a whole range of modern high-tech installations. While considering adequate separation, cooling and quality of equipment, a

number of additional rules have been established to protect against overcurrents; corresponding review and inspection procedures for design and installation are being established and will also be reflected in the upcoming CMS Safety Requirements document. The draft CERN Design and Implementation Criteria for Low-Voltage High-Current Distribution Systems of April 1997 already covers the following major areas in this connection:

- Power Source Overcurrent Protection
- Connection to Single Load Conductor
- Connection to Multiple Load Conductors
- Material Matching and Connector Mechanics
- Power Rating Engineering.

9.3.3 Rack and crate protection

CMS planning calls for removal of waste heat from rack-mounted equipment by means of embedded air-to-water heat exchangers and forced ventilation. It is anticipated that some racks in the data acquisition system could produce up to 9 kW from electronics and corresponding low-voltage power supplies. Electrical ignition risks (i.e. from an arcing short circuit) can usually be prevented or reduced by proper fuses and circuit breakers. However, these risks may be compounded by thermal loads and water-leaks and must be analyzed further in the risk analyses.

A protective strategy against electrical risks has been developed by using the Detector Control System to monitor abnormal voltages, currents and temperatures. Detection of a minor fault would result in an abnormal condition alarm; a major fault would lead to a rack shutdown.

9.3.4 High voltage protection

High voltage direct current is required for the operation of all the types of chambers used in the experiment..Commensurate safety requirements have been developed following recommendations of the International Electrical Commission (IEC publication 479-1), concerning damage (namely lethality) to human beings. Safety limits are 10 mA for currents, 20 ms for exposure duration and 10 joules absorbed energy. Secondary effects, such as falls as a reesult of shock, will be taken into consideration below these limits. Above these limits, such measures as physical barriers and interlocks, as well as permit procedures for hazardous activities and mandatory lockout/tagout will be used. Most of the high-voltage components of the muon system fall orders of magnitude below the above limits.

9.3.5 Cooling systems

Pressurized water systems are the basis for a number of heat-removal tasks in the Muon System. These cooling systems are presently being checked for activation-levels of the water, depending on radiation fields it passes through and the take-up rate. Water systems also present a direct damage risk to nearby electrical equipment, especially energized electronics. Designing the cooling systems with adequate safety margins, quality assurance, leak-detection and proper arrangements (separation) to reduce vulnerability are essential mitigation measures which have been or will be implemented. Also the pressure, temperature and flow-rates of the water systems will be monitored to detect developments of abnormal conditions early. Shutdowns of water systems will be appropriately interlocked to power shutdowns to avoid overheating of uncooled components.

9.3.6 Specific component safety issues

On the barrel DT chambers there will be boards carrying front-end electronics; these boards are inside the gas volume, hence in a region of zero oxygen content. Every board will be individually fused so as not to rely, in case of a short circuit, on the protection of the low voltage power supply that will be located far from the chamber. In any case the power involved per chamber is quite limited (always below 100 W). The high voltage to the wires will be provided by a remotely located power supply; every line will have a limit of about 1 μA. The hardware limitation is about 100 μA and hence is unlikely to be a safety issue.

9.4 GASES

Non-flammable gases have been chosen for the muon system. The total quantity corresponds to about 340 m^3 in the project. The gas mixture chosen are also not highly toxic, although the oxygen levels in cases of leaks and the personnel safety issues have to be looked at in more detail. In the barrel DT chambers for example, the gas is an Argon/CO_2 mixture (85/15). For the RPCs the gas is 95.5% Tetrafluorethane and 4.5% Isobutane, thus a non-flammable mixture. Nevertheless, hazard analyses for possible leaks, which have been specified, will be performed soon with the help of external consultants.

Argon/CO_2/CF_4 proposed for use in the endcap CSCs, could be a candidate for recirculation because this gas is expensive.

9.5 FIRE PROTECTION

9.5.1 Prevention

In fire protection at accelerator facilities, emphasis is placed on four principal areas: safety of the operating personnel, program continuity, property protection and releases to the environment. The size and scope of the CMS detector presents important challenges to fire protection planning and engineering. By its very mission, the detector is not suitable for being partitioned into separate fire zones, as is common for large facilities. The deep underground location compounds some of the problems, in particular with regard to smoke venting and emergency egress (see section 9.10). On the other hand the situation is similar to other high-tech facilities where the cumulative amount of combustible materials is quite high and presents a large hazard, but the probability of ignition is kept low. Strict measures in that regard are taken in the protection of electrical circuitry (see section 9.3).

A significant portion of such combustible materials is made up of plastics used as carrier material in some scintillators and as shielding. However, many of these materials are either tightly sandwiched between metallic components or are specially protected by thin metal to prevent exposure to ignition sources. Another important source of combustible materials is the cables. By strictly observing the CERN Safety Instruction IS 23 the spread of corrosive and toxic gases is much reduced, ignition and propagation is inhibited and self-extinguishing is promoted. The choice of alternatives to PVC for barrel DT materials, in this case Mylar and Lexan, is an example of the compliance with this regulation. Stainless-steel cladding of flammable solids is being investigated. Also the choices of bakelite for chamber bodies and vetronite for the spacers are being studied with regard to fire-protection requirements. The gases present in the muon system are discussed in section 9.4. Combustible gases and also the presence of oxygen have been avoided in many cases.

9.5.2 Detection and suppression

Incipient detection is planned for all interior spaces within the detector and overhead spaces immediately above it. An aspiration, sample-draw smoke detection system is envisaged for the different internal layers, with consideration of natural openings, access ways for maintenance and loadings of combustible materials. Maximum use will be made of early warnings, assisted by sophisticated computer systems and an adequate multi-stage response starting locally. The diversity and redundancy of detector systems on one hand and the screening out of false alarms on the other is still under study. A complicating factor is the replacement of Halon 1211 and 1301, which are ozone depletants. Promising alternatives are being investigated, mainly based on fine mists of water, CO_2 and nitrogen.

In the event of a fire during accelerator operations, immediate access for human intervention is not possible. The beam can be aborted, but residual radiation activity from air and equipment may require a cooling down period of up to an hour. Certain shutdowns will have to be automatic, to switch off electrical supplies which could cause damage or suffer damage. Ventilation of smoke will be a priority in preparing extinguishing and recovery measures as well as facilitating egress. Loads of combustible materials and credible fire development scenarios may, however, be necessary to determine quantities of smoke and required ventilation rates.

9.6 LASERS

The laser-based positioning system is operated with low-energy lasers in the visible to infrared range. Nevertheless, beams are oriented such that they are normally directed into dead ends. In addition the leak tightness of these arrangements is under routine supervision, and interlocks, and warnings are provided for personnel safety, to prevent eye exposure. Possible interaction with other equipment, both as a source and as affected by radiation is being examined.

9.7 INDUCED RADIOACTIVITY

At LHC we will be confronted with two main mechanisms which induce radioactivity in materials: low energy neutron activation and inelastic hadronic interactions at high energy.

Of these the latter will dominate, unless the choice of materials is very unfortunate with respect to neutron activation. In the muon system possible cobalt impurities in the steel would lead to some long-lived activity due to thermal neutron activation. Therefore we foresee to use cobalt-free steel.

A proper treatment of induced radioactivity requires first the establishment of a full inventory of all created radionuclides and then following the time dependence of this set of nuclides. While this is relatively straightforward for neutron activation, where the cross-sections are well known, radionuclide production in high energy has been usually estimated with relatively simple parametrizations, expressed in the form of so-called ω–factors, [9.1]. For steel, which is the dominant material around the muon system, these ω–factors are rather well known.The ω–factors are based on the fact that effects due to individual nuclides are averaged out by the large amount of different nuclides which can be produced in high-energy interactions. Thus the gamma emission rate from a material due to the activity induced in it is directly proportional to the rate of inelastic hadronic interactions (stars) in the material. These emitted gammas then also have to represent the true photon spectrum in an average way.

Furthermore, in the spirit of this average treatment the time dependence of the dose rate ($\dot{D}$)in iron exposed to high-energy hadrons can be parametrized with the Overton-Sullivan formula [9.2].

$$\dot{D} \propto \ln \frac{t_I + t_C}{t_C},$$

where t_I is the duration of the irradiation and t_C is the time since the end of the irradiation. For a typical irradiation time of 60 days the dose rate drops rapidly immediately after the irradiation, but decreases very slowly for decay times in excess of about one day.

A folding of the Overton-Sullivan formula with the expected LHC operation schedule shows that the dose rate after machine shutdown remains for several months within a factor of three from the dose rate scaled to t_I = 60 days (assuming continuous irradiation at an average luminosity of 5×10^{33} cm^{-2} s^{-1} and t_C = 1 day. In addition, the dose at t_I = 60 days and t_C = 1 day provides a good estimate for the dose a few days after machine stop when LHC has been operating long enough so that the activity has reached the saturation level.

The star density rate multiplied by the ω–factors gives the dose equivalent rate. A typical value for the ω–factor in iron is 10^{-8} (Sv h^{-1})/(star cm^{-3} s^{-1}) [9.3]. But the dose obtained with the ω–factors is defined to be in contact with a semi-infinite slab of uniformly activated material. For the relatively small objects and highly non-uniform irradiation which we encounter at CMS, this is a severe restriction. In particular, the ω–factors themselves do not give the dose at a distance from the activated object.

A ray-tracing method to calculate the dose rate at any given position in an activated environment is implemented in the FIASCO-code [9.2], which is a subroutine package to be used with FLUKA. The code uses the star densities calculated with FLUKA and the latest fits of the ω–factors. The ω–factors used in FIASCO are by a factor of 2-3 lower than the classical values [9.1]. The difference arises from the fact that the older values have been obtained with simulation codes with less complete physics, i.e. fewer stars. Other effects are due to the accurate buildup model in FIASCO, which increases the estimated penetration compared to rougher calculations.

Thus 10^{-8} (Sv h^{-1})/(star cm^{-3} s^{-1}) is a proper value for fast estimation of dose equivalent rate in contact with activated iron or copper, but it is expected to provide always upper estimates, about a factor of 2-3 higher than those produced by FIASCO. Therefore safety margins should always be added on top of the FIASCO results.

The FIASCO-estimates of dose equivalent rates in the region of the endcap muon system, are shown in Fig. 1. Some activated elements, in particular the beam pipe, have been excluded from the calculation, because such thin objects need a special treatment and cannot be reliably handled with the FIASCO code. Furthermore, it has been assumed that the forward calorimeter is moved to its garage, which will be the case during any access to the endcap chambers.

We observe relatively low-dose rates in the whole endcap area. Inside of the forward $\eta = 3$ cone at z > 6 m the dose remains at the level of few tens of μSv/h, but it should be emphasized that these values will depend on the final choice of the shielding material closest to $\eta = 3$. In all chamber slots the dose remains under 1 μSv/h.

These estimates show that the dose rates from the activation of the endcap yoke and the muon system itself are very moderate. It has to be taken into account, however, that during access other subdetectors with much higher activity might be in the same area. The forward calorimeter will be in its garage in all scenarios which allow access to the muon chambers, but

the endcap ECAL and HCAL will reside in the area, and at their $\eta = 3$ corner the dose rate reaches to about 500 μSv/h, which will require special shielding precautions.

Also the iron nose of the forward shielding, i.e. the shielding element immediately surrounding the collimator, has to be considered when planning the access to the endcap muon stations. When the endcaps are fully retracted without disconnecting individual disks the nose will be covered by the endcap iron. But if the endcap is only partly retracted while the rotating shielding is open, part of this nose remains unshielded. Such a situation is created also when the endcap disks are disconnected to allow access to the inner endcap chambers. The highly active collimator itself is enclosed in the nose. In front of the nose the dose rate is expected to be about 500 μSv/h. On the lateral surface of the nose the present estimates indicate doses up to 70 μSv/h.

Detailed studies to assess the need of additional radiation shielding in different access scenarios, including the effects due to the iron nose, will be done soon. Other refinements of the calculations will include a detailed follow-up of the time development of the dominating radionuclides.

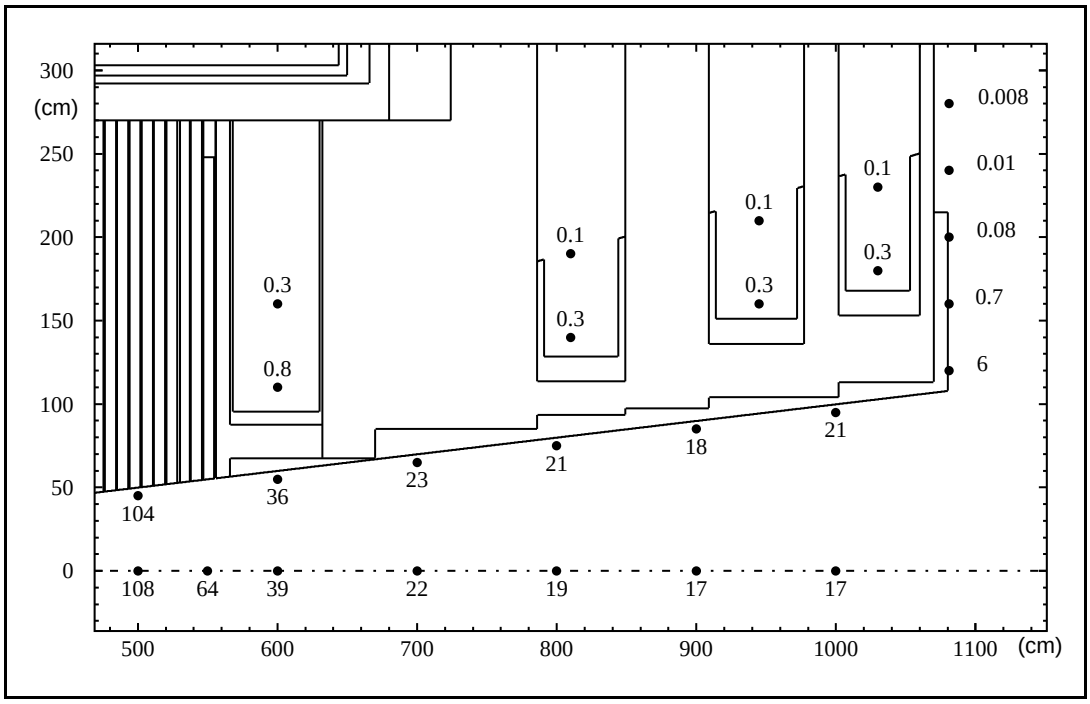


Fig. 9.1: Estimated dose rate in μSv/h in the region of the CMS endcap muon system due to induced radioactivity. The values are plotted for an irradiation time of 60 days and a cooling time of 1 day. The average luminosity during the irradiation is assumed to be 5×10^{33} cm^{-2} s^{-1}.

9.8 MAGNETIC FIELDS

Currently still valid international standards [9.4] report that professional and medical short-term exposures of human beings in the Tesla-range have not had any measurable negative health effects. This could mean that short-term access might even be possible with the field on. On the accessible outside areas (like the control room) fields in the milli-Tesla range are not expected to present health risks for longer stays.

Besides the risks of structural failure mentioned earlier, a potential risk for human beings would be secondary effects, like flying tools, accelerated by the strong fields. Effective control measures for tools carried into the area are being studied together with ATLAS, by looking into corresponding organizational and instrumental measures in other accelerators, and in the nuclear and aircraft industries.

9.9 SOFTWARE SAFETY

In addition to the software packages used for design calculations (see section 9.2.1) other essential pieces of software are going to be subjected to a verification and design review process to ensure that no safety hazards could result from this increasingly important component in modern technology.

The fire- and gas-protection system with software priority and hardware backup (not yet decided) and/or the Detector Control System (already decided) may be such deviations from hard-wired safety-systems and will thus be scrutinized for their reliability in reviews and tests.

9.10 ACCESS AND EGRESS

9.10.1 Access

Somewhat different conditions and requirements rule the normal come and go on one hand and emergency evacuation on the other. Both items are related to safety but also bear heavily on other items such as site security, efficiency, design and costs. Finding and evacuating people and not leaving tools behind (see section 9.8) are important for personnel safety, and rules to deal with this are being refined.

As an amendment and detail to the safety objectives defined in section 9.1.1, facility security from accidental or willful interference of unauthorized persons has to be considered, as well as efficiency of construction, maintenance and operation. Finally, the supervision man-hours and equipment expenses for access control have to be taken into consideration.

Based on the experience gained with LEP and SPS, and considering the size and radiation levels of LHC, the third EST-LEA Safety Forum made major recommendations on improving access control, namely:

- All underground access during operation, maintenance and dismantling phases will require radiation protection badges, to be checked at all available above-ground entrances (pits).
- Automatic turnstiles and entrance times in the 10 second range per person are planned, with additions as needed, pending clarification of the following items:
- the potential problem of unnoticed access of a double-person (piggy-back) package is to be sufficiently addressed by modern automatic personnel detection methods or by human supervision, possibly only in a limited number of sites at one time
- visitors whose access can be effectively limited to non-radiating areas may obtain dummy badges (without films) to operate the automatic access gates
- all other control measures, such as key-access and personal identification, are recommended to be administered below ground, depending on the facility, task and phase of operation, i.e., technical stop, short shutdown (with search facility intact), long shutdown

- how many and which measures of access control are adequate before the start-up of the facilities (during construction) have yet to be elaborated.

9.10.2 Egress

Whereas check-out from experimental facilities also has to be formalized according to proven procedures, specific provisions for emergency evacuation will be developed. They will use as input the more precise loading with various combustible materials, the new fire-extinguishing substances to be used, and results from hazard analyses, exercises and safety reviews. Specific emergency scenarios will be developed and used to design, establish and teach emergency egress procedures.

References

[9.1] R. Thomas and G. Stevenson, *Radiological Safety Aspects of the Operation of Proton Accelerators*, IAEA Technical Report Series 283 (1988).

[9.2] A. Sullivan and T. Overton, Health Physics 11 (1965) 1101.

[9.3] M. Huhtinen, *Method for Estimating Dose rates from Induced Radioactivity in Complicated Hadron Accelerator Geometries*, to be published as CERN TIS Divisional Report (1997).

[9.4] Environmental Health Criteria 69, Magnetic Fields, World Health Organization, Geneva, 1987.

10. RADIATION ENVIRONMENT

10.1 LHC PARAMETERS

10.1.1 Luminosity

The usually quoted LHC luminosity of 10^{34} $cm^{-2}s^{-1}$ is in fact the design value at the beginning of the fill when the machine is operating at its nominal parameters. During the fill the beam intensity goes down due to various loss processes and the luminosity decreases correspondingly. No final decision on the number of fills per day has been taken, but it has been shown that about the same day-averaged luminosity can be reached with either one or two fills. In both cases this average is roughly half of the nominal value [10.1].

10.1.2 Assumed operation schedule

Depending on the detector type and the expected radiation effects, we have to consider either integrated or instantaneous values of fluxes or dose rates. Detector occupancies, for instance, depend only on the instantaneous particle rate, whereas radiation damage is often a cumulative effect. For the estimation of induced activity even differences in the irradiation histories have to be considered. This is due to the fact that residual nuclides are produced proportionally to the integrated luminosity, but the decay of radioactive isotopes takes place simultaneously and, for a given nuclide, is only a function of time. Therefore an assumption of the machine schedule has to be included in some of the calculations.

Following the suggestion of Hoefert et al. [10.2], we assume three periods of 60 days of pp operation per year. These periods would be separated by ten-day shutdowns. Following a 17-day shutdown would come a heavy-ion operation period of 6 weeks. Under these conditions and including a low-luminosity start-up phase, we can expect to integrate about 5×10^5 pb^{-1} over ten years of LHC operation. This corresponds to 5×10^7 seconds of operation at LHC peak luminosity.

The peak luminosity in the Pb–Pb mode will be 1.95×10^{27} $cm^{-2}s^{-1}$. Compared to the proton–proton operation, the inelastic cross section and the average multiplicity are estimated to be larger by factors of about 35 and 200, respectively. Even so, the average background from Pb–Pb operation remains about three orders of magnitude below that of the high luminosity pp-collision mode. The instantaneous particle rate resulting from a central Pb–Pb collision, however, will be about 50 times larger than from an average proton–proton bunch crossing.

10.2 GENERAL FEATURES OF THE RADIATION ENVIRONMENT

The nominal luminosity of LHC, 10^{34} $cm^{-2}s^{-1}$, combined together with the 7 TeV beam energy will create a very hostile radiation environment. It has been known since the first LHC pre-studies that the inner tracker and very forward calorimeters of LHC experiments will have to deal with unprecedented radiation levels. More recently it has been shown that also the endcap calorimeters and the muon spectrometer will suffer from the environment. In CMS, due to the strong solenoidal field and the massive iron yoke, the barrel calorimetry and barrel muon spectrometry are least affected by background and radiation damage effects.

Although radiation issues have become a principal design parameter for LHC detectors, most of them are connected with low-energy phenomena, which are the same at almost all hadron accelerators. But at LHC the high-beam energy combined with the extreme luminosity

results in numerous intense cascades, which all end up as an immense number of low energy particles. In fact, particle energies exceeding some 10 GeV are very rare in the minimum bias background even at LHC. Therefore the radiation studies have to focus on the energy range around 1 GeV and below. Often, physics simulations do not fully account for all low energy background effects so these have to be addressed in specialized radiation environment simulations.

We can distinguish three regions with quite different characteristics from the shielding point of view:

1. The main detector, up to $\eta = 3.0$. Here we have to deal with the secondaries from pp collisions directly, and also with neutron albedo and hadronic punchthrough.
2. The region $\eta = 3.0–5.3$, covered by the HF. Cascades developing here mainly affect the HF itself and its electronics, but any leakage would also be of concern for the endcap muon system.
3. At pseudorapidities beyond the acceptance of the HF comes the collimator, which protects the superconducting quadrupoles. Cascading in this region is the dominant source of radiation background in the experimental cavern outside of the detector. Assuming a 34 mm aperture for the collimator, particles with $\eta > 7.8$ will not be captured in the experimental area and therefore do not contribute to the radiation background around the detector.

The muon system gets significant contributions from all of these three sources and therefore requires the most complicated shielding of all CMS subdetectors.

Table 10.2.1 shows the estimated energy flow into the different η-regions described above.

Table 10.2.1

Average total energy distributed by inelastic minimum bias events into different pseudorapidity region, according to predictions from the DPMJET-II event generator. The magnetic field and particle decays are neglected.

η region	0 – 3 (Main detector)	3 – 5.3 (HF)	5.3 – 7.8 (Collimators)	> 7.8 (Leaving area)
Average energy	100 GeV	760 GeV	4200 GeV	8900 GeV

10.3 SOURCES OF BACKGROUND IN MUON STATIONS

Muons and charged hadrons traversing a muon station will generate a hit with almost 100% probability. These particles originate mainly from calorimeter punchthrough (in ME1/1 and MB1), but for the forward muon system also from leakage out of the calorimeter edge at $\eta = 3.0$ and from interactions in the beam pipe [10.3,10.4].

Another source of background is often referred to as “neutron background.” This term is somewhat misleading, because most of the actual background hits are caused by the electrons (positrons) at the end of the reaction chain

$$\text{Thermal neutron} \rightarrow \gamma \rightarrow e^{+}e^{-}$$

where the thermal neutron is captured by a nucleus and the emitted photon undergoes one of the possible electromagnetic reactions. If the chamber gas contains hydrogen a signal can also be

due to a recoil proton produced in (n,p) scattering, but it is estimated that this process is insignificant compared to the photon reactions [10.5]. Thus although the neutrons are the underlying source of the background, the hits themselves are actually induced by soft electrons. This aspect is important, since it means that the emphasis of shielding should not only be on reducing the neutron flux, but also on reducing the photon flux and softening the photon energy spectrum [10.6].

The neutron flux can be suppressed by first thermalizing the neutrons with a moderator so that their capture cross section rises. Most of the photons are produced in thermal neutron capture and the photon energy is characteristic for the capturing nucleus. For instance, hydrogen emits 2.2 MeV photons, whereas the photons from boron-10 have an energy of only 470 keV. Some materials, like iron, have several emission lines. Typically the capture photon energies range from virtually zero up to about 10 MeV.

The sensitivity of the muon chambers to the photon flux depends on the incident energy spectrum. A low energy photon can generate only a relatively soft electron, which is able to penetrate only a few chamber walls [10.7]. Thus most photons lead to hits in single chamber layers or short track segments. Only electrons produced by high-energy photons will be able to penetrate the whole chamber in the same way as the fast charged particles.

Neutrons are produced in most hadronic interactions and their main sources for the muon system are the interactions in the beam pipe and the lower endcap, the HF and the collimator region. For ME1/1 neutrons produced in the HE also play an important role. Most of the neutrons are produced during the nuclear evaporation process following a high-energy hadronic interaction. These evaporation neutrons have typical energies around 1 MeV.

Another important source of neutrons is the intranuclear cascade, which produces neutrons with energies up to several hundred MeV. A general feature of neutron–nucleus cross sections is a minimum at neutron energies around 100–200 MeV, followed by a slow rise. When a neutron flux propagates through material this minimum is translated into a maximum of the neutron flux at an energy of about 70 MeV. Usually this maximum is less pronounced than the evaporation peak at 1 MeV. In a well-shielded region, however, these high–energy neutrons, which due to their small cross sections are very penetrating, can dominate the neutron flux.

10.4 SHIELDING STRATEGIES AND MATERIALS

Studies to find the optimum shielding for the CMS muon system started four years ago. Several shielding designs have been proposed [10.4,10.5,10.8–10.12]. After the first dramatic suppression [10.5] the background has not been significantly reduced even though the shielding has evolved. This is mainly due to the fact that the improvements in the shielding have merely been compensating for the—usually disadvantageous—changes introduced by increasingly realistic detector geometry and, in particular, by a better understanding of all unavoidable cracks and service channels.

Due to the limited space inside the detector, the calorimeter punchthrough in ME1/1 cannot be reduced by any additional shielding. The same is true for all of the barrel muon system except for MB4, where some fluxes can be suppressed by shielding external to the detector.

10.4.1 Beam pipe design

It has been shown that the beam pipe is one significant source of background for the endcap muon system and therefore has to be designed taking background issues into account [10.3]. Even with the best design invented so far, the beam pipe is the source of roughly half of the background in ME1/1 [10.3].

In addition to the background, the beam pipe geometry is also restricted by considerations of vacuum stability, mechanical rigidity, RF-power capture, and the requirement to have a feasible procedure to insert the pixel detector. In addition, care has to be taken that the beam pipe does not interfere with the detector opening scenarios or jeopardize the performance of the HF.

A conical beam pipe has been shown to be the optimum solution for background issues, and designs have been presented which fulfill all requirements [10.3]. The exact geometry however is still under study.

10.4.2 Shielding at $\eta = 3$

Most of the radiation entering the endcap muon chambers comes from the high-η region. This background comes from the beam pipe, the calorimeter edges and to some extent from the forward calorimeter albedo. Thus the shielding in this region is critical for the muon system. The muon system itself extends only up to $\eta = 2.4$, but the central calorimeters are extended up to $\eta = 3$ in order to provide space for shielding between the muon system and the HF at $\eta = 3$ [10.5].

The spectrum of neutrons and charged hadrons hitting the $\eta = 3$ cone between $z = 5.7$ m and $z = 11$ m is shown in Fig. 10.4.1. It is important to note that the albedo from the material at $\eta < 3$ is not included in these spectra, thus it does not represent the flux spectrum at $\eta = 3$, but only the spectrum of the incident particle current.

A significant effort has been devoted to the optimization of the shielding configuration in the region $\eta = 2.4– 3$. The task is far from trivial, since space is very limited and the radiation field is highly heterogeneous, comprising both low and high-energy components. In addition, the number of different shielding materials is large and the number of reasonable combinations and layer thicknesses is almost unmanageable.

One constraint is provided by the fact that the endcap disks have to be connected at their inner radius by 20 cm thick steel joints, which carry the mechanical load and the magnetic flux. The optimization studies [10.11] have shown that 15 cm of space is needed between these joints and the chambers for hydrogenated material to absorb low-energy neutrons, which penetrate the iron relatively easily. This hydrogenated shielding should continue as a 5 cm thick layer along both faces of the chambers down to $\eta = 2.15$. Thermal neutron capture by a nucleus is usually accompanied by prompt photon emission. These photons are much more harmful for the chambers than the neutrons themselves and need to be suppressed. This can be achieved by adding a layer of high-Z material on top of the neutron moderator where most captures occur.

Unfortunately, in a high-energy environment most heavy elements, lead in particular, tend to multiply the incident neutron flux. Thus a medium-A element like copper appears to be the most suitable photon shielding. Another possibility is to reduce the emission probability or the energy of the capture photons by admixing to the neutron moderator an isotope with a high

neutron capture cross section and no (lithium-6) or only low-energy (boron-10) gamma emission.

The two methods are clearly complementary, e.g., borated polyethylene can be covered with copper to obtain even better shielding. Another recently proposed possibility is to admix both photon absorber and neutron capturer directly into the neutron moderator. Thus the same material takes care of suppression of both the neutron and photon flux. One such material has been proposed [10.13] and looks very promising. It is essentially a polymer with a relatively high hydrogen content of 0.083 g/cm^3. An additional 0.147 g/cm^3 of lithium suppresses photons emission, and most importantly 2.1 g/cm^3 of lead efficiently attenuates photons. The full composition can be found in [10.11].

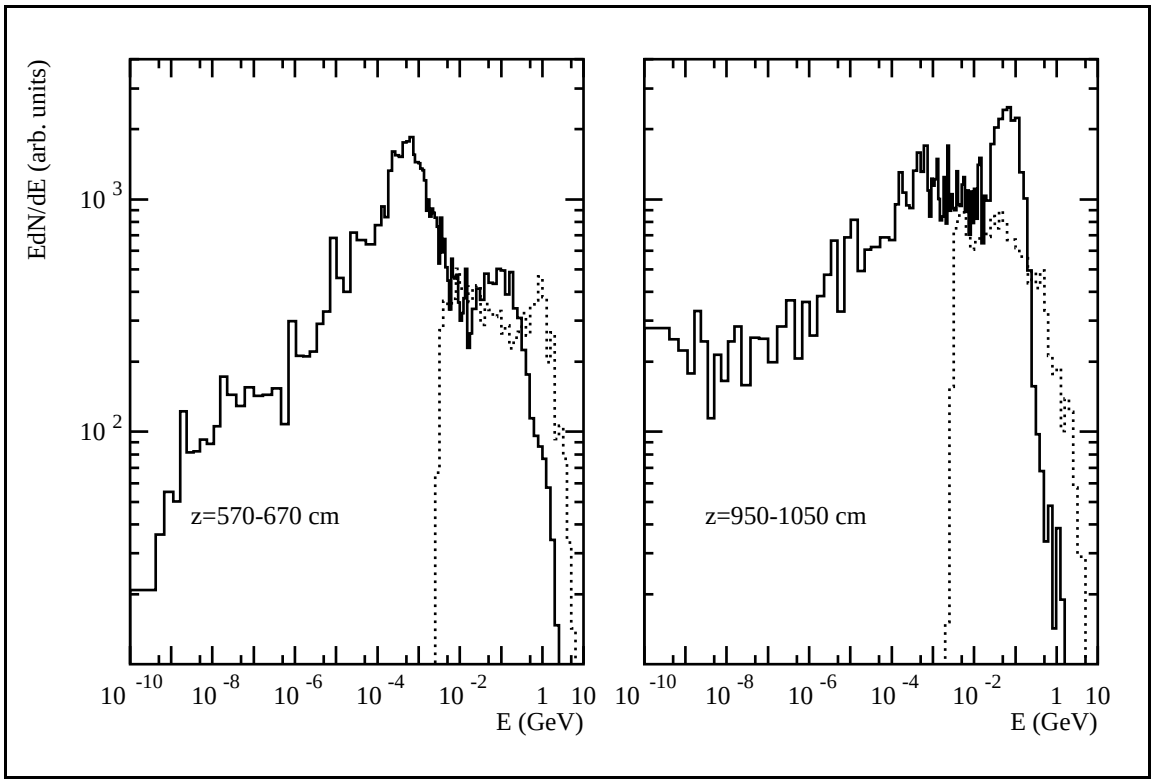


Fig. 10.4.1: Neutron (solid line) and charged hadron (dashed line) spectra incident on the $\eta = 3$ cone for two z-ranges. The big relative difference between the 70 MeV and the 1 MeV peaks in the neutron spectrum is to be noted. The effect appears because the albedo, which is mostly around 1 MeV, has been artificially killed in the simulation for the $\eta = 3$ cone; for the HF it is shielded by 20 cm of polyethylene, but for the HE it is unshielded. The curves include no normalization by area.

Some space remains available at the inner radius of the joints. The shielding material for this region has been extensively studied and it has been shown that the best solution is to have a relatively thin layer (5–10 cm) of hydrogenated material below the joints. Exactly what this material should be is not yet finally decided, but it should contain enough hydrogen to absorb most of the incident low-energy neutrons that would penetrate relatively far into the steel. The main issue, however, is to suppress the high-energy components. This requires maximizing the amount of steel. The hydrogenated layer closest to $\eta = 3$ will consist only of pieces which are

easy to remove in order to access the bolts which tie the endcap disks together. The layout of the shielding in this region, as it is used in the FLUKA simulations, is shown in Fig. 10.4.2.

One important aspect is the interface with the HF and its shielding. After ME4 we have an iron ring extending from $\eta = 3$ out to at least the same radius as the HF shielding. The thickness of this ring is 10 cm. Another ring of the same size, but consisting of hydrogenated material (e.g. polyethylene) is attached to this iron ring.

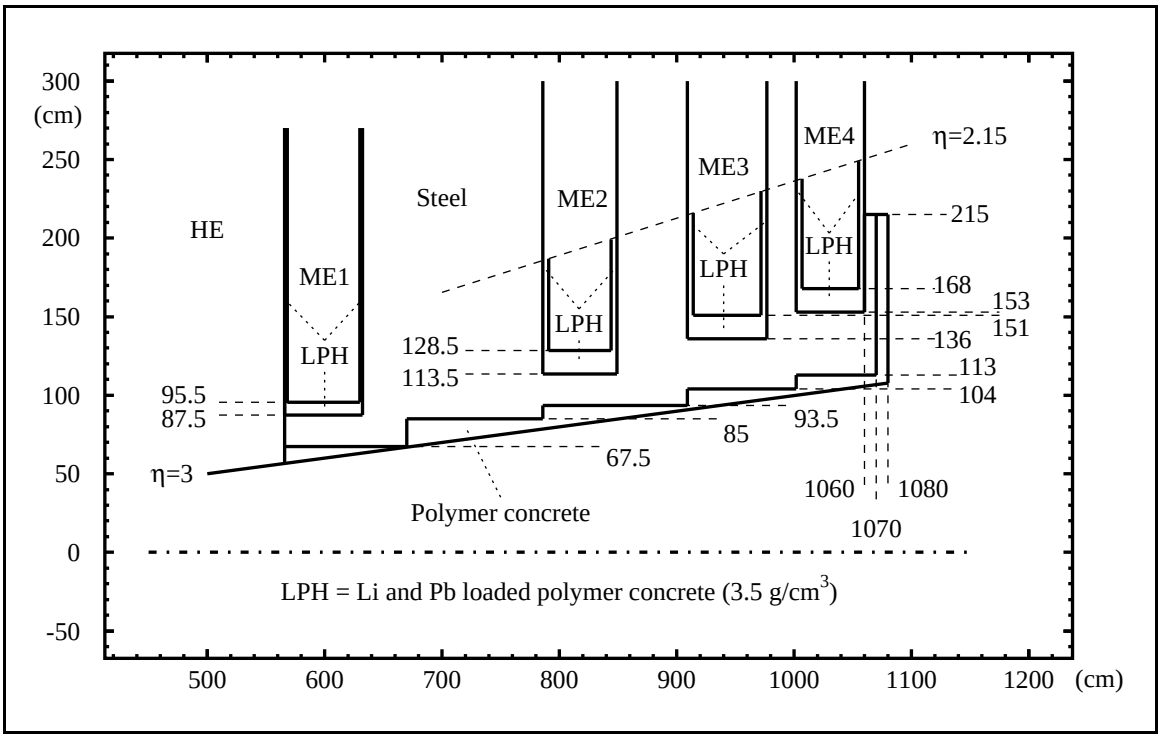


Fig. 10.4.2: Shielding near the $\eta = 3$cone as described in the radiation simulations. The geometry is as described in the text, but due to space restrictions only 2 cm of Li-Pb-polyconcrete is used alongside ME1/1 instead of 5 cm.

10.4.3 Shielding around the HF

One important shielding function is to suppress the neutron albedo from the HF back into the $\eta = 3$ cone. This is best achieved by using material with high hydrogen density per unit volume. In this respect polyethylene is the best, closely followed by water and paraffin. It can be shown that for a typical accelerator spectrum, which includes both a large amount of evaporation neutrons and high energy components, pure polyethylene provides better shielding than borated polyethylene and should be preferred if capture gamma emission is not an issue. Beyond a thickness of about 20 cm, however, polyethylene becomes essentially useless as shielding, since all low energy components of the spectrum are removed and attenuation of high energy neutrons depends mainly on the density of the shielding material. This determines the optimum moderator in front of the HF to be 20 cm of pure polyethylene.

Above the $\eta = 3$ line the interface between the HF shielding and the endcap is of crucial important for the background in ME4/1 and has been discussed above.

The outermost muon chambers, MB4 and especially ME4, are subject to the radiation leaking out of the HF and the collimator region. It was shown at a very early stage that a big crack between the endcap and the HF would be detrimental to both of these chambers [10.5,10.12]. Thus it has been agreed that the design goal for this crack is 3 cm.

The shielding of the HF is limited by the weight that can be supported on the platform, but also by the size so that the HF with all its shielding fits into the garage. Fig. 10.4.3 shows the layout of the HF shielding as described for the FLUKA simulations. Going out laterally, starting at a radius of 145 cm, we have 30 cm of steel, 30 cm of borated magnetite concrete and 10 cm of borated polyethylene. At the end of the HF the steel is replaced by borated magnetite concrete. It should be emphasized that the composition of this concrete is not very critical if the density is maintained, but the addition of boron is important since it is required to suppress the capture photons. This lateral shielding is deliberatelly slightly overdesigned, because particles escaping the HF laterally would be the most dangerous for ME4.

At the back of the HF we have a plug consisting of steel and borated magnetite concrete, which is covered by borated polyethylene. Here the boron is required to protect the HF electronics, not the muon system. Between the lateral shielding and the end plug a shielding ring of steel and polyethylene will be inserted to protect the HF electronics and reduce the particle flow through this gap.

10.4.4 The rotating shielding

An enormous amount of energy is incident on the collimator, situated at $z = 19-20.8$ m. Thus we expect the most intense hadronic cascades in this region and need substantial shielding to achieve tolerable background levels in the experimental area, including muon stations ME4 and MB4.

The collimator is surrounded by a fixed iron cone, which fits into the endcap opening of CMS when the endcaps are retracted for maintenance. This fixed iron is by far insufficient to suppress all leakage from the collimator. Therefore it is surrounded by a rotating shielding, which extends from the back of the HF to the block house at $z = 21.6$ m. This shielding can be opened to allow the CMS endcaps to be retracted in order to provide access to the central detector.

For the rotating shielding weight is a more severe restriction than size. The mass of one half-shell is limited to 75 tons. The high energy cascades are only partially contained inside the iron at the inner radii. Thus the iron is followed by borated magnetite concrete ($\rho = 3.65$ g/cm^3), which further attenuates the high energy components and simultaneously reduces also the neutron flux. The top layer consists of 10 cm of borated polyethylene to absorb the low energy neutrons. As for the lateral shielding of the HF, borated polyethylene and concrete is better than pure material because the 2.2 MeV capture gammas from hydrogen are more harmful for ME4 than the 470 keV photons emitted by boron. The rotating shielding and the block house as described in the FLUKA simulations are shown in Fig. 10.4.4

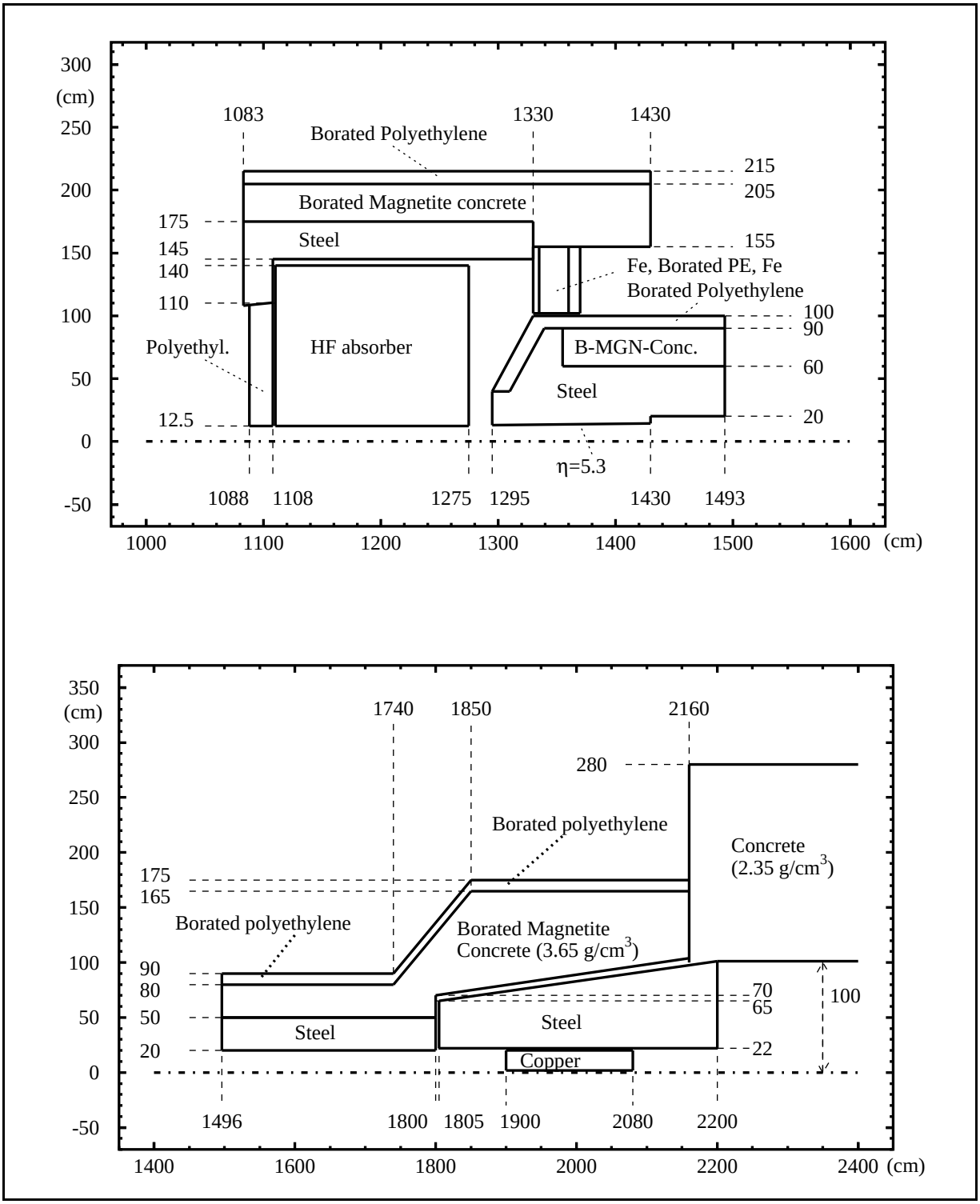


Fig. 10.4.3: Shielding around the HF as described in the radiation simulations.

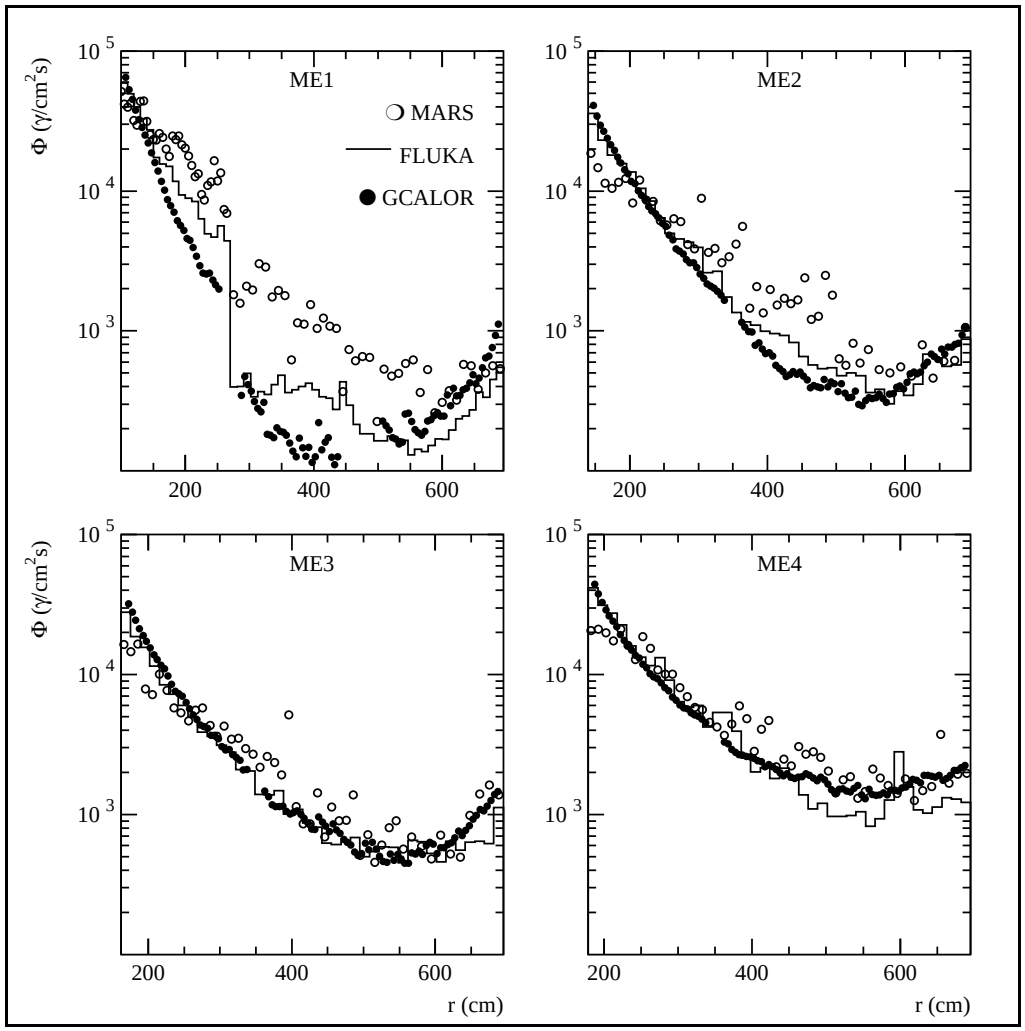


Fig. 10.4.4: Rotating shield and block house as described in the radiation simulations.

10.4.5 The block house

At z > 21.6 m the last machine quadrupole Q1 is surrounded by a block house. Here size and weight are much less restricted and the present design is 1.8 m thick walls of conventional concrete.

In addition to the suppression of particles emerging laterally from Q1, the block house has another important function of sealing the tunnel mouth. Thus it suppresses most of the hadronic and electromagnetic background created in beam-gas interactions and beam particle losses. If these were allowed to enter the hall they would increase the background in ME4 substantially.

10.4.6 The ME4 wall

In order to manage with the moderate weight required by the concept of the rotating shielding, a somewhat unorthodox shielding strategy had to be adopted; the forward shielding still allows some radiation to stream into the experimental hall. The escaping high energy particles are predominantly directed towards the end of the experimental hall, i.e. away from the

detector. When they interact in the cavern walls they generate a relatively soft albedo. While a shielding of the high energy radiation emerging from the source would require roughly 40 cm of steel for each order of magnitude reduction in flux, the low energy albedo components can be shielded with significant layers of material.

The CMS iron yoke already protects all inner chambers from the low energy albedo, leaving only ME4 openly exposed. It is mainly the photon background in the hall which might be at a critical level for ME4.

This photon flux can be reduced by adding a 10 cm thick steel disk on the outer surface of ME4, as a kind of fourth endcap disk. Such a photon shield also suppresses some of the softer hadron and muon background in the hall. In addition, it provides some safety against unforeseen cracks and other imperfections in the forward shielding. In particular, it gives a rather good shielding against particles leaking through the small (3 cm) crack between the endcap and the HF shielding.

This shielding philosophy of not attempting a perfect shielding of the source automatically also gives some safety against cracks and other imperfections in the shielding, since their percent contribution to the total leakage is likely to remain smaller.

10.5 SIMULATION METHODS

10.5.1 Event generators

The radiation environment simulations are based on minimum bias events obtained from the DPMJET-II or DTUJET93 event generators [10.14,10.15]. DPMJET-II is the most recent of the Dual Parton Model generators, which are specially suited for simulation of minimum bias hadronic collisions. As one of the updates with respect to the older DTUJET93 program, DPMJET-II includes a complete description of charm production. High-p_T physics, which is important when estimating the punchthrough effects on the barrel chambers, has been further complemented by adding the proper fraction of pure b-events from PYTHIA [10.16] to the DPMJET-II events. Differences between the DPMJET-II and DTUJET93 event sets used are mainly in high-p_T and diffractive events.

The global scaling parameter for the radiation levels at the LHC is the inelastic interaction rate, which is defined by the luminosity discussed above and by the inelastic cross section. For the latter a value of 80 mb will be assumed. This includes a sizable fraction of diffractive events. Double diffraction is a relatively rare process and as far as the radiation environment is concerned it will be essentially equivalent to normal inelastic collisions. Some 15% of the collisions are expected to be single diffractive. In these events one participating proton continues with only a small sideways deflection, much like in elastic scattering, and only the dissociated proton contributes to the radiation background in the experimental area.

The DPMJET-II minimum bias event file used for the simulations includes 2000 events. From PYTHIA 500 pure b-events were extracted into a separate file. The cross section for b-production was assumed to be 0.35 mb. In order to obtain sufficient statistics for the high-p_T events selection from the b-event file was favoured. Adjusting the statistical weight of the selected particles compensated for this. For radiation studies, the 25 ns bunch structure of the LHC is not significant and even the correlations within a single event can be neglected. This allows both files to be randomized, i.e. the secondaries were randomly reordered, resulting in a

smoother source at the cost of destroying the event structure. The average total multiplicity per event, which is used to scale the simulation results to the proper luminosity, is 124.

10.5.2 Radiation transport codes

Most of the radiation simulations are independent of the general detector performance simulations and are performed with simulation codes that are specially designed for radiation physics. FLUKA [10.17] is the baseline code for the radiation environment simulations of CMS, but MARS [10.18] and GCALOR [10.19] have also been used for the muon system radiation background studies. MARS13 [10.20] is used for the accelerator-related background simulations [10.21].

Requirements for a modern radiation simulation code include:

- Proper hadronic event generators from the Coulomb barrier up to the full LHC energy;
- Proper treatment of particle capture by a nucleus;
- Nuclear evaporation and de-excitation with explicit photon emission;
- Transport of low energy neutrons and explicit generation of capture gammas;
- An accurate model for electron, positron and photon transport;
- Accurate tracking in thin layers and magnetic fields taking multiple scattering rigorously into account;
- Proper treatment of Bremsstrahlung and pair production by heavy charged particles;
- Proper accounting for ionization loss of charged particles including low energy and relativistic effects.

At the high-energy end these requirements are fulfilled by all three codes, but in FLUKA and MARS special emphasis has been put on effects occurring around the energy of few GeV and below. In particular, FLUKA includes a sophisticated pre-equilibrium cascade model for inelastic interactions below 1.3 GeV and for capture reactions at rest. Both FLUKA and MARS use a multigroup approach for the neutron transport, whereas GCALOR uses point cross section data. MARS13 includes the most sophisticated models for high-energy muon physics and is therefore best suited for the LHC background simulations.

In addition both FLUKA and MARS, but not GCALOR, provide very powerful variance reduction possibilities, which are essential in order to obtain sufficient statistics in well-shielded regions of phase space.

10.5.3 General geometry description

A substantial effort has been devoted to finding the best parameters and approximations to describe the CMS system that are feasible to implement with the geometry routines of FLUKA and MARS. Roughly 1000 volumes are needed to achieve this for the full CMS detector including shielding and the surrounding hall. Each detector has been described with only the minimum accuracy, which was considered sufficient. Due to the complexity of the radiation field, studies for the muon system require a relatively accurate description of the whole detector, the beam pipe, the forward shielding and the machine elements in the hall.

A major approximation is that everything is assumed to have cylindrical symmetry. This is because only with cylindrical symmetry can azimuthal averaging be applied to get results with sufficient statistics.

10.5.4 Energy cuts and transport parameters

In the FLUKA simulations, the lower threshold for neutron transport was set to thermal energy, which at 293° K corresponds to a mean energy of 0.025 eV. The transport cut for charged hadrons was set to 100 keV. Anti-neutron transport was stopped at 50 MeV, which is dictated by the available cross section data. Energy cuts for electromagnetic particles are more problematic, because of the intolerable increase of computing time if cuts are set too low. Therefore, the energy thresholds for photon, electron and positron transport were adjusted according to the region. The absolute lower cut was 100 keV for electrons and 30 keV for photons, which was used in most of the sensitive detectors and their surroundings—including all muon chambers. Sufficiently deep inside non-sensitive regions and in the HCAL these cuts were raised to 300 keV and 100 keV, respectively. The scoring of photon flux in the muon system, however, was done with a threshold of 100 keV.

The full two-dimensional (azimuthally symmetric) magnetic field map of CMS was used in the region of the main detector. A correct field map was also used in the machine quadrupole Q1.

Multiple scattering was performed down to the Moliere limit. Inside and close to the chambers, delta-electrons were produced above a threshold of 100 keV. Pair production and Bremsstrahlung were explicitly simulated for high energy muons and charged hadrons.

10.5.5 Estimation of error margins

All simulations have been divided into several independent batches of equal size. These have been used to estimate the statistical errors arising from fluctuations in the event sampling and during cascade simulation. Only these statistical error estimates are indicated in the figures as 1-σ error bars. Systematic errors are usually more important.

A first uncertainty arises from the extrapolation of existing data to the inelastic proton-proton cross section at 14 TeV. A further uncertainty concerning the event multiplicities and momentum distributions comes on top of this. We should therefore expect an underlying uncertainty of about 30 percent from the pp events alone [10.22] which probably cannot be reduced before LHC minimum bias data are available. This error is the dominant one as far as charged hadron fluxes at the CMS tracker are concerned. In all other regions uncertainties in the cascade development overwhelm this 30 percent.

The accuracy of the cascade simulation is affected by approximations in the geometry description and the incompleteness of physics models and cross section data sets.

FLUKA, MARS13 and GCALOR have been benchmarked in several shielding experiments [10.23,10.24]. The agreement with measurements is typically on the order of a few tens of percent even after several attenuation lengths of shielding.

At CMS we can expect major uncertainties to arise from the modelling of the geometry and the assumptions made concerning material compositions. These uncertainties are very difficult to estimate properly, but an idea of their magnitude can be obtained by repeating the simulations with different codes used by different groups. Since most cross section data have a common origin, this procedure cannot account reliably for all physics aspects. However, it gives a measure of the uncertainty that arises from the accuracy with which the detector geometry can be implemented in the simulation codes.

A comparison among FLUKA, MARS and GCALOR was performed on a non-optimized baseline shielding configuration of CMS. The results for photon fluxes in the endcap stations are shown in Fig. 10.5.1. The discrepancies in neutron flux were similar. For charged particles the statistics reach of the study was insufficient to allow any firm conclusions. Several minor discrepancies in the geometries were identified after the studies, and it was finally concluded that about a factor of three should be a reasonable estimate of the systematic uncertainty on results of carefully performed simulations.

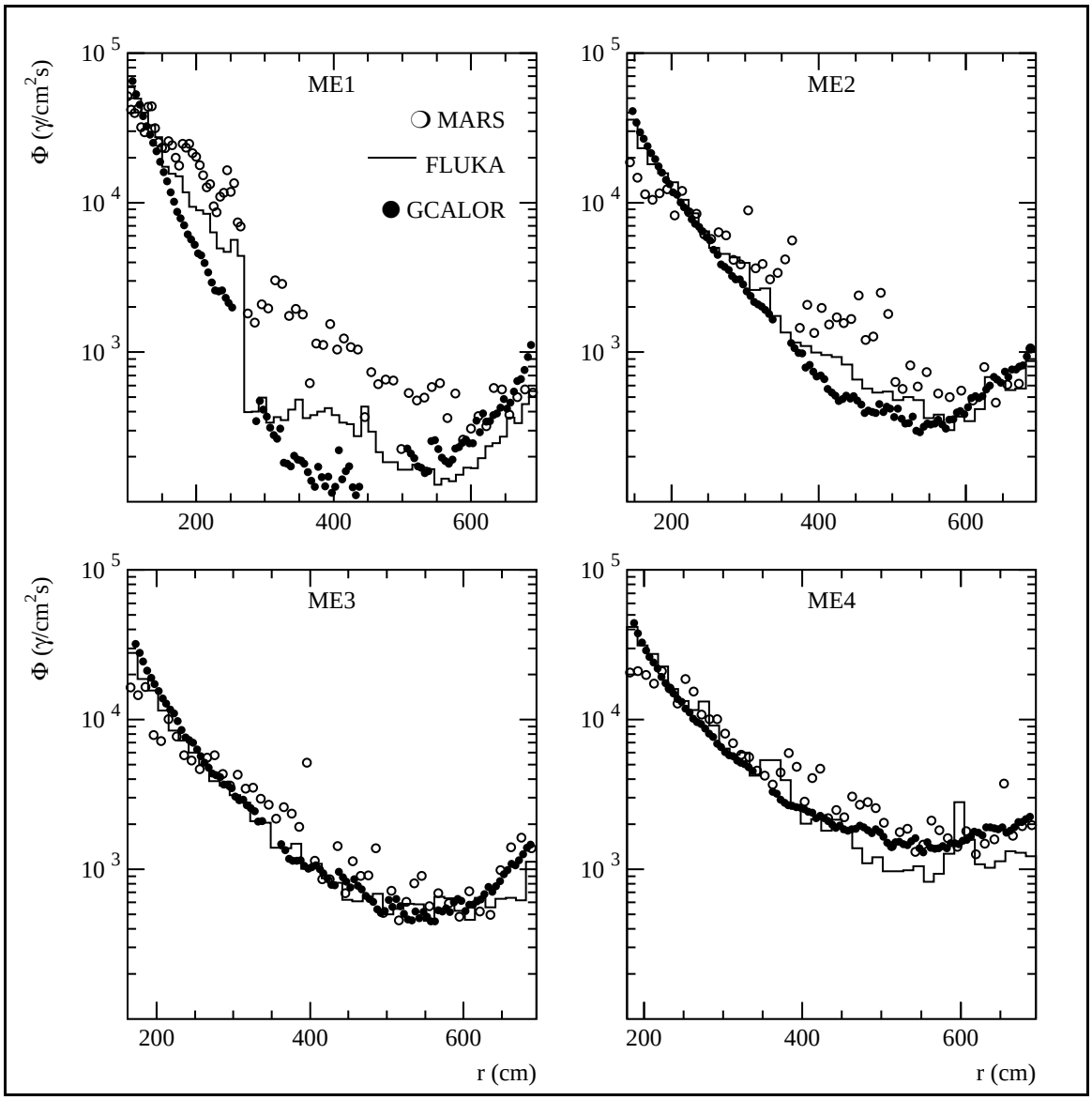


Fig. 10.5.1: Comparison of photon fluxes obtained by FLUKA, MARS and GCALOR. These results are based on a non-optimized baseline shielding of the detector [10.25].

10.6 PARTICLE FLUXES IN THE MUON CHAMBERS

An overview of the radiation environment with the most recent shielding version can be found in Figs. 10.6.1a (color), 10.6.1b (color) and 10.6.1c (color), where the neutron, charged particle and photon fluxes in the whole CMS area are shown. It can be seen from Fig. 10.6.1b (color) that at fluxes below 1 $cm^{-2}s^{-1}$ the statistical significance of the results starts to get lost since single particles can give dominant contributions and thus lead to large fluctuations.

For the photon flux, shown in Fig. 10.6.1c (color), it is important to note that the transport cuts for electromagnetic particles were raised deep inside non-sensitive material. This creates unphysical photon minima in the affected regions. Only the values in the air of the experimental hall, the material in the chamber slots and the surface layers of all adjacent shielding material correspond to the photon cut of 30 keV.

It can be seen that the inner barrel chambers are very well shielded by the iron. Forward chambers suffer mainly from the relatively thin shielding above the $\eta = 3$ line and ME4/2 gets the main contribution from the particles leaking through the rotating shielding.

An important point to notice is the pronounced directionality of the charged flux—most particles are directed towards the end of the cavern.

Figure 10.6.2 shows the fluxes of fast charged particles (hadrons and muons), electrons and positrons, neutrons and photons in the CMS barrel drift tubes and Fig. 10.6.3 gives corresponding data for the endcap CSC chambers. The neutron, photon and charged fluxes are averaged over the whole chamber, whereas the electron fluxes are obtained in the sensitive gas only. It is to be noted that the flux values should not be confused with actual hit rates in the chambers, since this relation is complicated and depends on the chamber geometry. Flux is the total track length per unit time in a given volume divided by this volume, thus it is completely independent of chamber geometry and orientation.

In both Figs. 10.6.2 and 10.6.3 we observe large fluctuations in the charged particle fluxes. These correspond to the individual particles that can be observed in Fig. 10.6.1b and are a sign that the statistics is becoming insufficient for a reliable flux determination.

It is particularly interesting to note that for instance in ME4, the background photon flux of about 10^6 $cm^{-2}s^{-1}$ for a completely unshielded system [10.5] has been reduced with the shielding to a range between $0.8–5 \times 10^3$, i.e. by roughly three orders of magnitude. An idea of the importance of relatively small details in shielding optimization can be obtained by comparing the photon fluxes in Fig. 10.6.3 with those in Fig. 10.5.1.

Figure 10.6.4 shows the energy spectra of neutrons, photons and electrons in the gas of the barrel drift tubes of muon stations MB1 and MB2. Corresponding data for ME1/1, ME 2/1 and ME4/2 are given in Fig. 10.6.5.

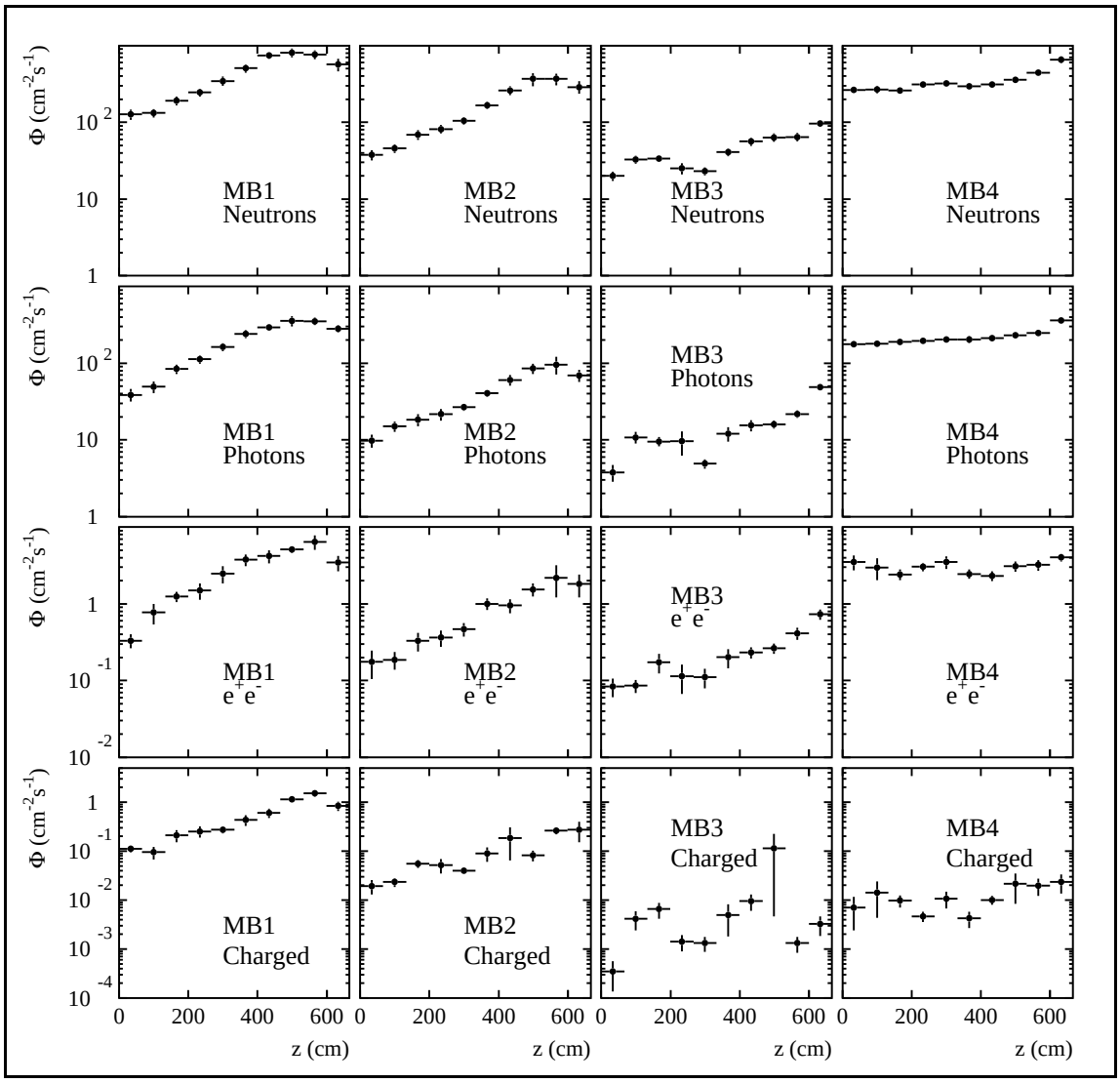


Fig. 10.6.2: Particle fluxes in the CMS barrel muon chambers. For this and the following figure, the data are from latest FLUKA simulations and correspond to LHC peak luminosity (10^{34} cm^{-2}s^{-1}).

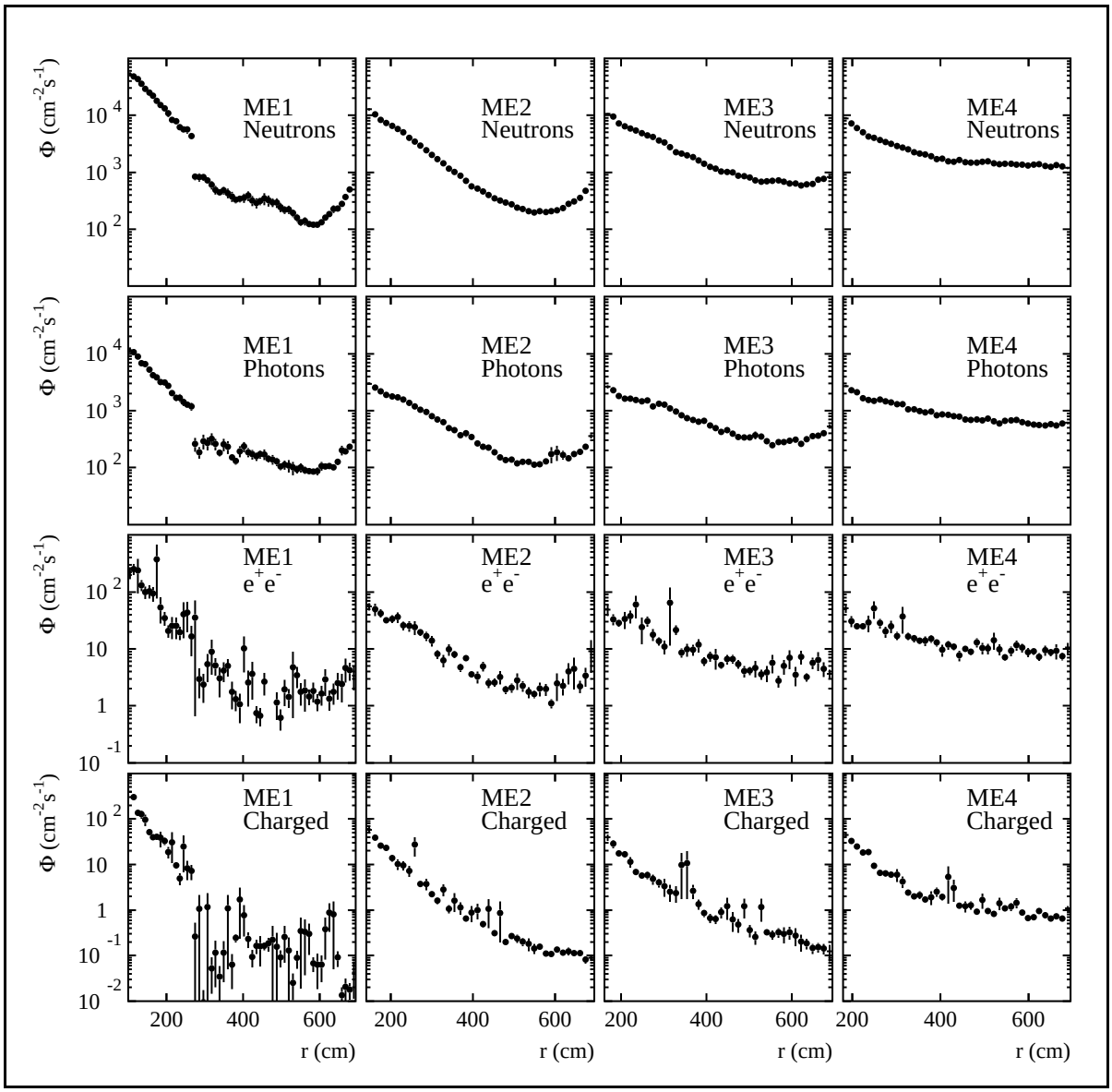


Fig. 10.6.3: Particle fluxes in the CMS endcap muon chambers.

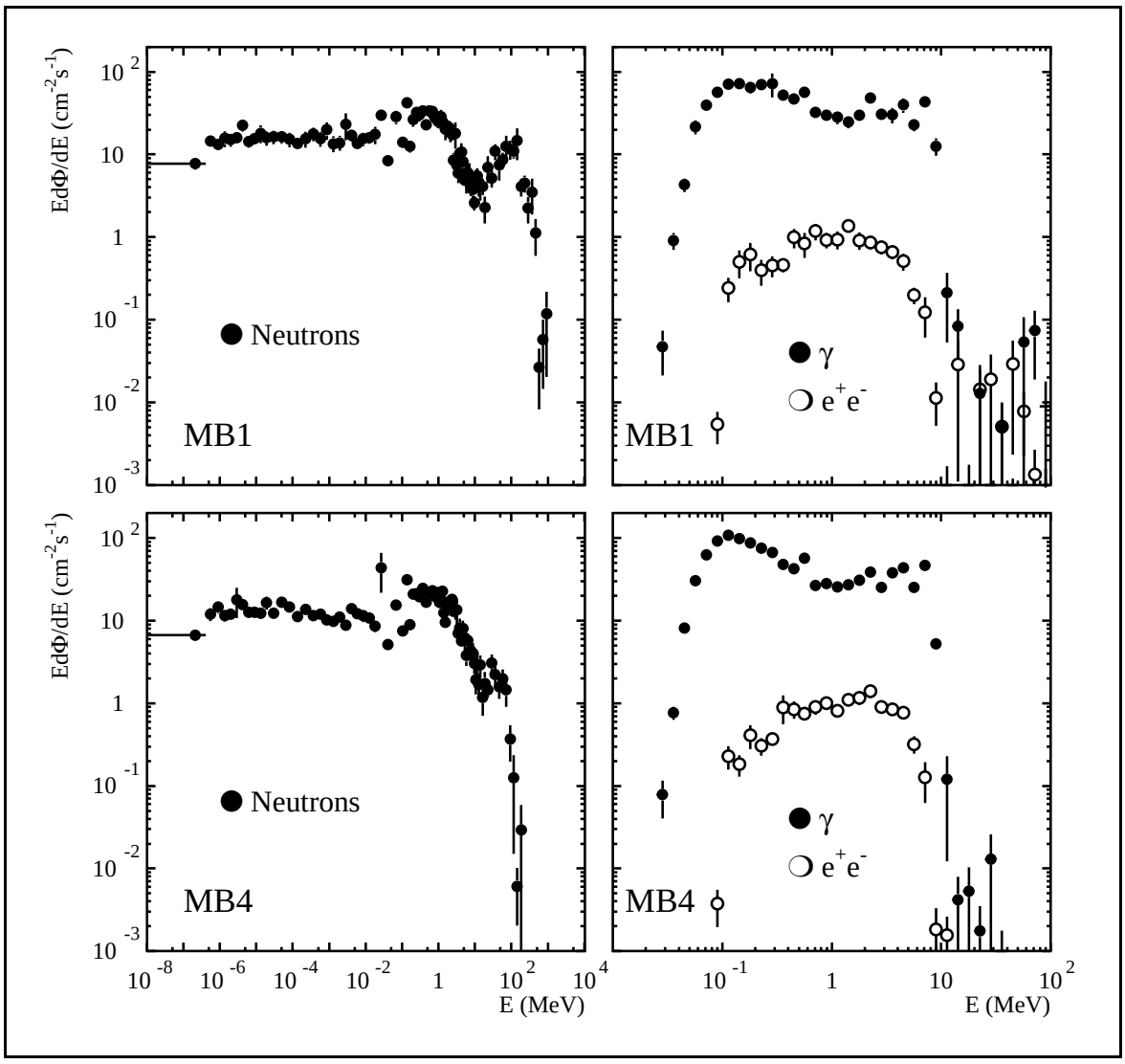


Fig. 10.6.4: Particle spectra in the drift tube gas layers of MB1 and MB4. For this and the following figure, the photon transport cut is at 30 keV and the electron cut at 100 keV. Values correspond to LHC peak luminosity of 10^{34} $cm^{-2}s^{-1}$.

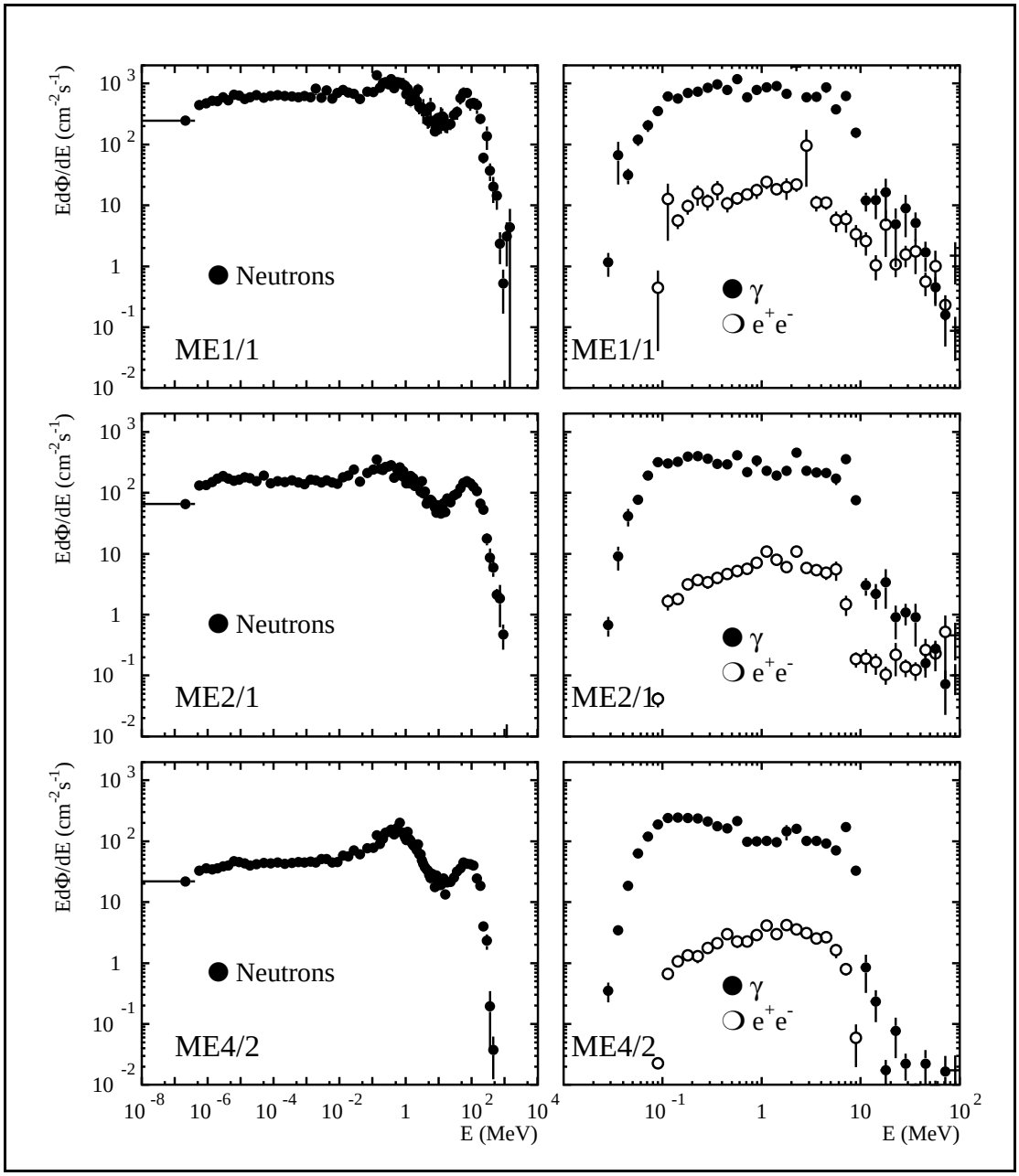


Fig. 10.6.5: Particle spectra in the CSC gas layers of ME1/1, ME 2/1 and ME4/2.

10.7 MACHINE BACKGROUND

Beam losses in the LHC machine, due to beam-gas scattering and at limiting apertures, give rise to backgrounds in CMS. Hadronic and electromagnetic components are mostly absorbed locally, but high energy muons are a matter of special concern. These muons, which can have energies up to several TeV, are emitted tangentially to the ring. Several independent studies, done in collaboration with LHC machine designers, have addressed the problem [10.21,10.26], and it has been shown that the most critical places for muon production are beam-gas scattering in the dispersion suppressor and interactions of beam halo in the straight section before the experiment. We expect a beam-gas interaction rate of 2×10^4 $m^{-1}s^{-1}$ in the cold dispersion suppressor and 500 $m^{-1}s^{-1}$ in the warm straight section. The dangerous regions for beam loss are at β_{max} in the final focus quadrupoles (~50 m) and in the neutral beam absorber (TAN) at 149.5 m. The long drifts in the D1-Q4 region are also important for muon production.

Hadronic and electromagnetic components of the machine background are mostly absorbed by the block house, which hermetically covers the whole tunnel entry of the CMS area. But even the relatively massive forward shielding of CMS is not able to attenuate significantly the muon flux. The high-η ends of the forward chambers are the most exposed to these muons. It has been shown [10.21], and can be seen from Fig. 10.7.1, that in ME3 and ME4 the muon flux emerging from the machine is about equal to the muon flux due to pp collisions at nominal LHC parameters. However, in the inner chambers the muon flux from pp collisions is significantly higher, whereas the machine muons give in all chambers a flux of about 1 $cm^{-2}s^{-1}$. In addition, the charged hadron background due to pp operation is much higher than the muon background in all chambers.

Therefore, at nominal LHC parameters, the machine background amounts to only 1-10% of the pp−background. It is important to note, however, that the pp−background depends on luminosity and the machine background on current. Thus we can expect that during the low-luminosity phase the machine background will be relatively more important. It is also very likely that during the first years LHC will not be as clean a machine as has been assumed in the simulations. This would further increase the fraction of machine background. This should be tolerable, however, since the total occupancy of the muon system will be lower during the low-luminosity phase [10.21].

10.8 RADIATION DAMAGE

In all parts of the CMS muon system, background minimization requirements impose such low particle fluxes that we do not expect any significant radiation damage. At its maximum, in ME1/1, the radiation dose over 10 years reaches about 100 Gy, see Fig. 10.8.1 (color). The requirements this imposes on the radiation tolerance of electronics are not very severe. In most parts of the forward muon system and in all of the barrel 10-year integrated doses remain below 1 Gy.

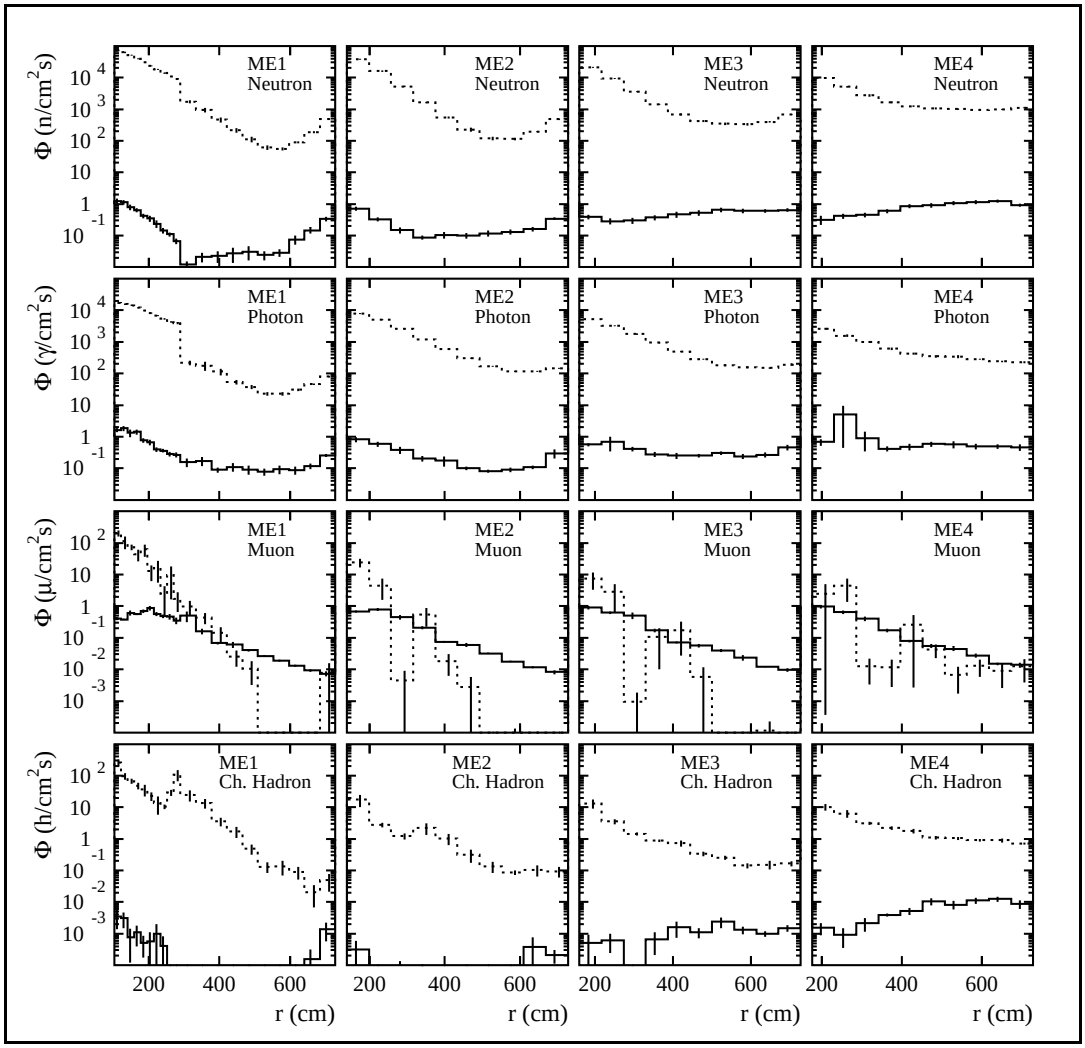


Fig. 10.7.1: Particle fluxes in the CMS endcap muon system due to pp-collisions (dashed lines) and LHC background (solid lines) [10.21]. The values correspond to an older version of the CMS shielding [10.8] and of the LHC lattice, but should nevertheless be indicative.

10.9 INDUCED RADIOACTIVITY

10.9.1 Personnel safety

Induced radioactivity is a major concern at the LHC. We can assume that each inelastic hadronic interaction results in a residual nucleus, which can be almost anything below the target mass and charge. As for radiation damage, the low particle fluxes in the muon system mean that there will be no problem of induced radioactivity in the vicinity of the muon system itself. The elements of the muon system with the highest induced activity are the inner edges of the endcap disks and the steel joints between them. Close to them we expect dose equivalent rates of the order of 50-100 μSv/h. The dose equivalent rate from the yoke iron at radii larger than 2 m is less than the expected natural background of 0.2 μSv/h.

However, for maintenance of the endcap muon system, we need to take into account that the endcap and forward calorimeters will be highly activated objects reaching dose equivalent rates of the order of 1 mSv/h. Their activation and possible shielding is described in the relevant technical design reports.

10.9.2 Detector background

While only relatively long- lived nuclides need to be considered when assessing personnel safety aspects, the detectors get contributions from all radionuclides, no matter what their life-time is. Local activation, i.e. close to the chambers, by high-energy charged hadrons cannot be a problem, because each hadron would itself generate a signal, so the excess hit rate from possible activity would always remain a small fraction of the charged hadron rate. Excess background by neutron activation can be avoided by avoiding materials with high activation cross sections in the vicinity of the muon chambers.

All CMS detectors require significant cooling and the cooling pipes from all inner detectors pass close to several barrel and endcap chambers. Since hadron fluxes in the tracker are several orders of magnitude higher than in these chambers, we have to carefully consider the effect of the induced activity in the cooling fluids on the backgrounds in these chambers.

The induced activity in the forward shielding and the cavern walls will add to the photon background in ME4, but it is not expected that this will be a significant contribution. In particular, the possible wall in front of ME4 would suppress these external photons.

References

[10.1] K. Potter and G.R. Stevenson, Average interaction rates for shielding specification in high-luminosity LHC experiments, CERN LHC Note 310 (1995).

[10.2] M. Hoefert, K. Potter and G.R. Stevenson, Summary of design values, dose limits, interaction rates, etc. for use in estimating radiological quantities associated with LHC operation, CERN TIS-RP/IR/95-19.1 (1995).

[10.3] M. Huhtinen and P.A. Aarnio, Report HU-SEFT-R-1994-07 (1994).
M. Huhtinen, A. Rubbia and P.A. Aarnio, Nucl. Instr. and Meth. A351 (1994) 236.
P.A. Aarnio and M. Huhtinen, CERN CMS IN/1997-025 (1997).

[10.4] I. Azhgirey, V. Talanov and A. Uzunian, Second Annual RDMS CMS Collaboration Meeting, CMS Document 1996-213 (1996) p. 59.

[10.5] M. Huhtinen and P. A. Aarnio, Nucl. Instr. and Meth. A363 (1995) 545.

[10.6] I. Azhgirey and A. Uzunian, CERN CMS TN/94-265 (1994).

[10.7] I. Azhgirey and A. Uzunian, CERN CMS TN/94-267 (1994).

[10.8] M. Huhtinen, Proceedings of the 2nd workshop on simulating accelerator radiation environments, CERN 9-11 Oct. 1995, CERN/TIS-RP/97-05 (1997).

[10.9] R. Breedon and Y. Fisyak, CERN CMS TN/96-035 (1996).
Y. Fisyak, CERN CMS TN/96-076 (1996).

[10.10] CMS Collaboration, CMS Technical Proposal, CERN/LHCC 94-38 (1994).

[10.11] M. Huhtinen and P.A. Aarnio, CERN CMS IN/97-024 (1997).

[10.12] The CMS Collaboration, CMS Status reports and Milestones, CERN LHCC 93-48 (1993).

[10.13] L.N. Zaitsev, Dubna Report JINR-R14-95-104, 1995.

[10.14] J. Ranft, Phys. Rev. D51 (1995) 64.
J. Ranft, DPMJET-II, A Dual Parton Model event generator for hadron-hadron, hadron-nucleus and nucleus-nucleus collisions, Presented at SARE 2 workshop, CERN, 9-11 October 1995, Proceedings: CERN/TIS-RP/97-05 (1997).

[10.15] P. Aurenche et al., Computer Physics Commun. 83 (1994) 107.

[10.16] H. Bengtson and T. Sjöstrand, Computer Physics Commun. 43 (1987) 43.

[10.17] P.A. Aarnio et al., FLUKA86 user's guide, CERN TIS-RP/168 (1986).
P.A. Aarnio et al., Enhancements to the FLUKA86 program (FLUKA87) CERN TIS-RP/190 (1987).
A. Fassò et al., FLUKA: present status and future developments, Proc IV Int. Conf. on Calorimetry in High Energy Physics, La Biodola, Sept. 20-25, 1993, Ed. A. Menzione and A. Scribano, World Scientific (1993) p. 493.
A. Fassò et al., FLUKA: performances and applications in the intermediate energy range, Specialists' Meeting on Shielding Aspects of Accelerators, Targets and Irradiation Facilities, Arlington, Texas, April 28-29, 1994.

[10.18] I. Azhgirey, I. Kurochkin and V. Talanov, Development of MARS Code Package for Radiation Problems: Solution of Electro-Nuclear Installations Design, Proc. XV Conf. on Charged Particles Accelerators, Protvino, October 1996.

[10.19] C. Zeitnitz and T.A. Gabriel, Nucl. Instr. and Meth. A349 (1994) 106.

[10.20] N. V. Mokhov, The MARS Code System User's Guide, version 13 (95), FNAL-FN-628 (1995).

[10.21] A. I. Drozhdin, M. Huhtinen and N.V. Mokhov, Nucl. Instr. and Meth. A381 (1996) 531.

[10.22] M. Huhtinen and C. Seez, CERN CMS/TN 95-133.

[10.23] A. Fassò et al, Nucl. Instr. and Meth. A332 (1993) 459.
C. Birattari et al, Nucl. Instr. and Meth. A338 (1994) 534.

[10.24] Y. Nakane et al., Intercomparison of Neutron Transmission Benchmark Analyses for Iron and Concrete Shields in Low, Intermediate and High-Energy Proton Accelerator Facilities, SATIF-3, Tohoku University, Sendai (1997).

[10.25] M. Huhtinen, Presentation at the CMS Collaboration Meeting, 11. December 1996.

[10.26] I. Azhgirey, V. Talanov and A. Uzunian, CERN CMS TN/95-202 (1995).

11. PROJECT ORGANIZATION AND COSTS

The CMS Muon Project consists of two largely independent parts; the Barrel Muon Project and the Endcap Muon Project. It is organized according to the rules of CMS. There are 49 institutions widely distributed around the world and 369 physicists and engineers who are working together to construct this muon measurement system. Major institutions involved in the Barrel Muon Project come from Germany, Italy, and Spain; for the Endcap Muon Project they come from China, Korea, Russia, and the United States. The major technical tasks are constructing the following subsystems: (1) the drift tubes (barrel), (2) the cathode strip chambers (endcap and ME1/1), (3) the resistive plate chambers (barrel and endcap), and (4) the alignment system (barrel, endcap, and link).

11.1 PARTICIPATING INSTITUTES

Austria, HEPHY, HEPHY, Wien
A. Kluge, N. Neumeister, P. Porth, H. Rohringer, F. Szoncso, G. Walzel, T. Wildschek, C.-E. Wulz

Belarus, MINSK-NCPHEP, National Centre of Part. and HEP, Minsk
V. Chekhovsky, O. Dvornikov, A. Khomich, A. Panfilenko, S. Reutovich, N. Shumeiko, A. Solin, V. Stepanets, Y. Yurenya, F. Zyazyulya

Bulgaria, SOFIA-INRNE, Inst. for Nuclear Research and Nuclear Energy, Sofia
I. Atanasov, L. Dimitrov, V. Genchev, G. Georgiev, I. Ivanov, V. Penev, I. Vankov

Bulgaria, SOFIA UNIV., Faculty of Physics, Sofia
L. Litov, P. Petev, R. Tsenov

China, IHEP, Inst. of High Energy Physics, Beijing
Y. Chen, G.M. Chen, B.S. Cheng, Y.N. Guo, J.T. He, Z.J. Ke, J. Li, W.G. Li, X.N. Li, J. Liu, B.W. Shen, C.Q. Shen, P.R. Shen, H.Y. Sheng, H.Z. Shi, X.F. Song, Y.Y. Wang, Y.R. Wu, R.S. Xu, B.Y. Zhang, S.Q. Zhang, W.R. Zhao, J.P. Zheng, G.Y. Zhu

China, PEKING UNIV., Dept. of Physics, Beijing
Y. Ban, J.E. Chen, H. Liu, S. Liu, B. Lou, S. Qian, Y. Ye

Germany, AACHEN-3A, RWTH, III. Physik. Inst. A, Aachen
S. Bethke, O. Biebel, H. Faissner, H. Fesefeldt, D. Rein, H. Reithler[1], H. Schwarthoff, V. Sondermann, V. Tano, H. Teykal, M. Tonutti, J. Tutas, M. Wegner

Hungary, BUDAPEST, KFKI Res. Inst. for Part. & Nucl. Phys., Budapest G. Bencze[2], G. Vesztergombi

[1] Also at CERN
[2] Also at CERN

Hungary, DEBRECEN-IEP, Kossuth Lajos Univ., Debrecen
T. Bondar, L. Brunel, S. Juhasz, G. Marian, P. Raics, J. Szabo, Z. Szabo, S. Szegedi, Z. Szillasi, T. Sztaricskai, G. Zilizi

Italy, BARI, Univ. di Bari e Sez. dell' INFN, Bari
M. Abbrescia, A. Colaleo, G. Iaselli, F. Loddo, M. Maggi, B. Marangelli, S. Natali, S. Nuzzo, G. Pugliese, A. Ranieri, F. Romano, F. Ruggieri, G. Zito

Italy, BOLOGNA, Univ. di Bologna e Sez. dell' INFN, Bologna
A. Benvenuti, P. Capiluppi, F. Cavallo, M. Cuffiani, I. D'Antone, G.M. Dallavalle, F. Fabbri, P.L. Frabetti, G. Giacomelli, P. Giacomelli[3], C. Grandi, M. Guerzoni, S. Marcellini, P. Mazzanti, A. Montanari, F. L. Navarria, F. Odorici, A. Perrotta, A.M. Rossi, T. Rovelli, G. Siroli, G. Valenti

Italy, PADOVA, Univ. di Padova e Sez. dell' INFN, Padova
M. Benettoni, G. Busetto, R. Carlin, S. Centro, P. Checchia, E. Conti, M. De Giorgi, A. De Min, U. Dosselli, C. Fanin, F. Gasparini, U. Gasparini, P. Guaita, I. Lippi, R. Martinelli, A.T. Meneguzzo, M. Pegoraro, L. Pescara, P. Ronchese, A. Sancho Daponte, P. Sartori, L. Stanco, E. Torassa, L. Ventura, P. Zotto[4], G. Zumerle

Italy, PAVIA, Univ. di Pavia e Sez. dell' INFN, Pavia
S. Altieri, V. Arena, G. Belli, G. Bonomi, G. Gianini, M. Merlo, S.P. Ratti, C. Riccardi, L. Viola, P. Vitulo

Italy, TORINO, Univ. di Torino e Sez. dell' INFN, Torino
M. Arneodo, F. Bertolino, M. Bigi, R. Cirio, M. Costa, F. Daudo, M. I. Ferrero, S. Maselli, E. Migliore, V. Monaco, C. Peroni, M. C. Petrucci, A. Romero, R. Sacchi, A. Solano, A. Staiano

Korea, CHEJU, Cheju National University, Cheju
Y.J. Kim

Korea, CHONNAM, Chonnam National University, Kwangju
H.I. Jang, J.Y. Kim, T.I. Kim, I.T. Lim

Korea, CHOONGBUK, Choongbuk National University, Chongju
Y.U. Kim

Korea, DONGSHIN, Dongshin University, Naju
M.Y. Pac

Korea, KANGNUNG, Kangnung National University, Kangnung
Y. Ho, K.S. Kang, D.W. Kim, D.S. Kim, S.-C. Lee

Korea, KANGWON, Kangwon National University, Chungchon
S.K. Nam

[3] Also at Univ. of California, Riverside
[4] Also at Politecnico di Milano

Korea, KONKUK, Kon-Kuk University, Seoul
J.T. Rhee

Korea, KOREA, Korea University, Seoul
B.S. Hong, S.J. Hong, Y.S. Kim, K.S. Lee, S.K. Park, K.-S. Sim

Korea, KYUNGPOOK, Kyungpook National University, Taegu
H. Jeon, D. Kim, W.Y. Kim, I.H. Park, D. Son

Korea, POHANG, Pohang Univ. of Science and Technology, Pohang
G.N. Kim

Korea, SEONAM, Seonam University, Namwon
S.J. Lee

Korea, SEOUL, Seoul National University of Education, Seoul
D.G. Koo

Korea, WONKWANG, Wonkwang University, Iri
S.Y. Bahk

Latvia, RIGA, Inst. of Elec. and Comp. Science, Riga - Salaspils
Y. Bilinskis

Poland, WARSAW-IEP, Institute of Experimental Physics, Warsaw
M. Cwiok, W. Dominik, A. Fengler, M. Konecki, J. Krolikowski, I. Kudla, P. Majewski, K. Pozniak

Poland, WARSAW-INS, Soltan Institute of Nuclear Studies, Warsaw
R. Gokieli, M. Gorski, P. Zalewski

Russia, DUBNA, Joint Inst. for Nuclear Research, Dubna
D. Belosludtsev, A. Chvyrov, Y. Erchov, I. Golutvin, N. Gorbunov, I. Gramenitsky, V. Karjavin, S. Khabarov, V. Khabarov, Y. Kiryushin, A. Koutov, V. Lyssiakov, G. Mechtcheriakov, I. Melnichenko, P. Moissenz, S. Movchan, V. Palichik, V. Perelygin, S. Selunin, D. Smolin, A. Zarubin

Russia, ST-PETERSBURG, Petersburg Nucl. Phys. Inst., Gatchina (St Petersburg)
N. Bondar, G. Gavrilov, A. Golyash, O. Kisselev, O. Prokofiev[5], E. Orichtchine, V. Razmyslovich[6], V. Sedov, D. Seliverstrov, V. Sknar, I. Smirnov, S. Sobolev, V. Soulimov, I. Tkach, G. Velitchko, A. Vorobyov

[5] Also at Fermilab
[6] Also at Fermilab

Spain, CIEMAT, Centro de Investigaciones Energeticas Medioambientales y Tecnologicas, Madrid
M. Aguilar-Benitez, J. Alberdi, J.M. Barcala, J. Berdugo, C. Burgos, M. Cerrada, N. Colino, M. Daniel, M. Fernandez, A. Ferrando, M.C. Fouz, M.I. Josa, P. Ladron De Guevara, J. Marin, F. Martin Suarez, J. Mocholi, A. Molinero, J. Navarrete, J.C. Oller, J.L. Pablos, L. Romero, J. Salicio, C. Willmott

Spain, SANTANDER, IFCA-Instituto de Fisica de Cantabria, CSIC-Univ. de Cantabria, Santander
C.F. Figueroa, N. Garcia, I. Gonzalez, J.M. Lopez, J. Marco, F. Matorras, T. Rodrigo, A. Ruiz, I. Vila

Switzerland, CERN, European Laboratory for Particle Physics, Geneva
J. Christiansen, D. Dattola, D. Peach, J. Potier, J. C. Santiard, G. Wrochna

USA, ALABAMA, Univ. of Alabama, Tuscaloosa, AL
L. Baksay[7], B. Fenyi, J. Huang, J. Rodin

USA, UC DAVIS, Univ. of California, Davis, CA
R. Breedon, Y. Fisyak, B. Holbrook, W. Ko, F. Lin, J. Rowe, J. Smith

USA, UCLA, Univ. of California, Los Angeles, CA
K. Arisaka, Y. Bonushkin, F. Chase, D. Cline, J. Hauser, M. Lindgren, C. Matthey, S. Otwinowski, J. Park, Y. Pischalnikov, H.C. Shankar, P. Schlein, Y. Shi, B. Tannenbaum

USA, UC RIVERSIDE, Univ. of California, Riverside, CA
D. Chrisman, I. Crotty[8], J.W. Gary, W. Gorn, J.G. Layter, B.C. Shen

USA, CARNEGIE MELLON, Carnegie Mellon Univ., Pittsburgh, PA
A. Engler, T. Ferguson, R. Kraemer, M. Procario, J. Russ, H. Vogel

USA, FERMILAB, Fermi National Accelerator Lab., Batavia, IL
N. Chester, D. Denisov, D.P. Eartly, M. Lamm, K. Maeshima, N. Mokhov, V. Yarba

USA, FLORIDA, Univ. of Florida, Gainesville, FL
D. Acosta, P. Avery, R.D. Field, L. Gorn[9], J. Konigsberg, S. Klimenko, A. Korytov, G. Mitselmakher[10], A. Nomerotski, P. Ramond, J. Yelton

USA, STONY BROOK, State Univ. of New York, Stony Brook, NY
M.M. Baarmand, R. Engelmann, K.-K. Ng, J. Steffens, S.-Y. Yoon

USA, NORTHEASTERN, Northeastern Univ., Boston, MA
E. von Goeler, J. Moromisato.

[7] Also at Kossuth Lajos Univ., Debrecen
[8] Also at CERN
[9] Also at CERN
[10] Also at Fermilab

USA, PURDUE, Purdue Univ., Task D, West Lafayette, IN
A. Bujak, D. Carmony, L. Gutay, S. Medved

USA, OHIO STATE, The Ohio State Univ., Columbus, OH
B. Bylsma, L.S. Durkin, J. Hoftiezer, R. Hughes, M. Johnson, D. Larsen, T.Y. Ling, C.J. Rush, V. Sehgal, B. Winer

USA, RICE, Rice Univ., Houston, TX
D.L. Adams, M. Corcoran, G. Eppley, H.E. Miettinen, B.P. Padley, E. Platner, J. Roberts, P. Yepes

USA, TEXAS-DALLAS, Univ. of Texas at Dallas, Dallas, TX
R.C. Chaney, E.J. Fenyves

USA, WISCONSIN, Univ. of Wisconsin, Madison, WI
D. Carlsmith, F. Feyzi, R. Loveless, D. Reeder

11.2 ORGANIZATION

The organization of the Muon Project is structured similar to the CMS Collaboration. This organization is completely described by the Constitution of the Muon Group, which was ratified by the entire muon group in Sept. 1995. The present organization chart of the Muon Project is shown in Fig. 11.2.1.

11.2.1 Institution board (IB)

This is the highest decision-making body in the Muon Group and must ratify all important decisions. In particular, it must assess the costs of the muon subsystem and balance these against the expected funding. Each institute involved in the construction of the muon subsystem has a member on the IB. In addition, the Project Managers and Technical Coordinators are also members of the IB. The Chairman and Deputy Chairman of the IB are elected by the members of the IB for a term of two years.

11.2.2 Project managers

The Project Manager of the muon system is appointed by the Spokesman of CMS as are the Project Managers of the Barrel and the Endcap Muon Projects. The Technical Coordinators for the Barrel and Endcap Projects are nominated by the respective Project Managers and appointed jointly by the CMS Spokesman and the Project Managers.

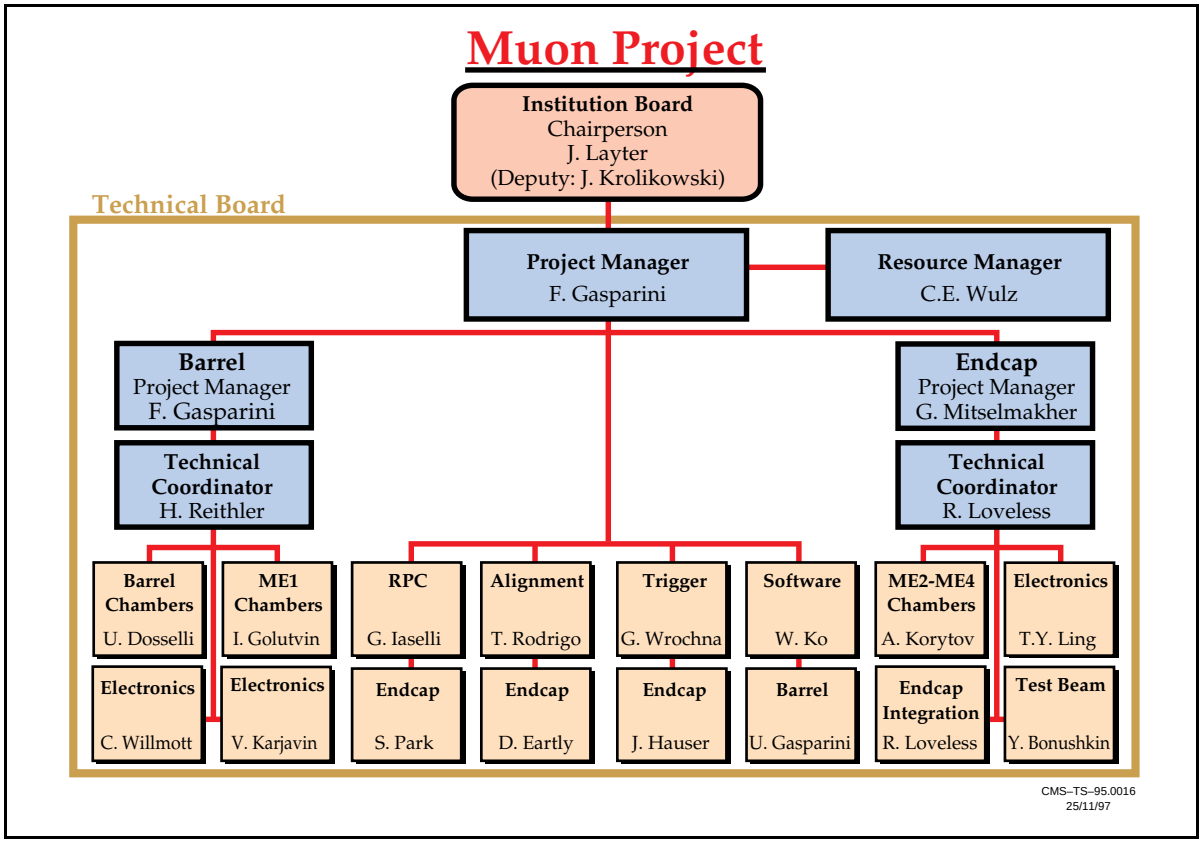


Fig. 11.2.1: Organization chart of the CMS Muon Project.

11.2.3 Muon technical board

The Muon Technical Board is composed of the Muon Project Managers, the Technical Coordinators, and by all the Coordinators of the various subsystems. Two largely independent subsections of this Board exist; the Barrel and Endcap Technical Boards. Members are the respective Project Managers, Technical Coordinators, and the Barrel and Endcap Subsystem Coordinators. The Technical Boards provide a forum for technical discussions and formulate proposals and recommendations to the Muon Institution Board.

11.3 CONSTRUCTION RESPONSIBILITIES

The construction of the muon system is a large task requiring the efforts of many institutions. In the tables below we delineate the responsibilities for each phase of the construction**.**

Table 11.3.1
Responsibilities for the Barrel Muon subsystem

Item #	Barrel Muon Chambers	Institutes
5.1.1		
	Detector and components	Aachen, Bologna, CIEMAT, Padova, Torino
	Tooling	Aachen, Bologna, CIEMAT, Padova, Torino, Wien
	Part production	Aachen, Bologna, CIEMAT, Padova, Torino, Wien
5.1.2		
	Front-End electronics	Aachen, Bologna, CIEMAT, Padova
	Readout electronics	Aachen, Bologna, CERN, CIEMAT, Padova, Torino
	Trigger electronics	Bologna, Padova
	HV and HV distribution	Aachen, Bologna, CIEMAT, Padova, Torino
	LV	Aachen, Bologna, CIEMAT, Padova
5.1.3	Fixation	Aachen, Bologna, CIEMAT, Padova, Torino, Wien
5.1.4	Transportation & Cabling	Aachen, Bologna, CIEMAT, Padova, Torino
5.1.5	Slow control	Aachen, Bologna, CIEMAT, Torino
5.1.6	Service systems	Aachen, CIEMAT
-	Other participating Insts.	IHEP-Beijing, Debrecen, Korea, Peking Univ

Table 11.3.2
Responsibilities for the Endcap Muon subsystem

Item #	Endcap Muon Chambers	Institutes
5.3.1		
	Detector and components	IHEP-Beijing, UC Davis, UCLA, UC Riverside, Fermilab, Florida, PNPI-St. Petersburg, Purdue, Wisconsin
	Tooling	Fermilab
	Part production	IHEP-Beijing, Fermilab, PNPI-St. Petersburg
5.3.2		
	Front-End electronics	CMU, OSU, PNPI-St. Petersburg
	Readout electronics	UC Davis, OSU, Rice
	Trigger electronics	UCLA, CERN, OSU, Rice
	HV and HV distribution	Florida
	LV	Wisconsin
5.3.3	Mechanical structure	Wisconsin
5.3.4	Transportation & Cabling	IHEP-Beijing, Fermilab, UC Davis, UCLA, UC Riverside, Florida, PNPI-St. Petersburg
5.3.5	Slow control	Wisconsin
5.3.6	Service systems	Wisconsin
-	Other participating Insts.	Alabama, MIT, SUNY-SB, Texas-Dallas

Table 11.3.3
Responsibilities for the ME1/1 Muon subsystem

Item #	Endcap Muon Chambers	Institutes
5.2.1		
	Detectors & components	JINR Dubna
5.2.2		
	Front-end electronics	JINR Dubna, NCPHEP Minsk (in cooperation with Ohio State & other US groups)
	HV & HV distribution	JINR Dubna, INRNE Sofia, SU Sofia
	LV	JINR Dubna, INRNE Sofia, SU Sofia
5.2.3	Mechanical structure	JINR Dubna,
5.2.4	Transportation & Cabling	JINR Dubna
5.2.5	Slow control	JINR Dubna, INRNE Sofia, SU Sofia
5.2.6	Services	JINR Dubna,

Table 11.3.4
Responsibilities for the RPC subsystem

Item #	RPC Chambers	Institutes
5.4.1	Barrel chamber construction	Bari, Kangnung, Kyungpook, Pohang
5.5.1	Endcap chamber construction	Cheju, Choongbuk, Kangwon, Chonnam, Dongshin, Konkuk, Korea, Seoul, Seonam, Wongkwang
5.4.2, 5.5.2	Electronics	Bari, Korea, Pavia
	High voltage	Bari, Korea, Pavia
5.4.6, 5.5.6	Services	Bari, Korea, Pavia
-	Other participating Insts.	IHEP-Beijing, Peking Univ., Rice, Warsaw

Table 11.3.5
Responsibilities for the Alignment subsystem

Item #	Alignment task	Institutes
5.6.1		
	MABs	CERN
	Video cameras (mech., electr.)	CERN, Debrecen
	LEDs (mech., electr.)	CERN
5.6.2	Endcap	Northeastern, Fermilab
5.6.3	Link	CIEMAT, Santander

11.4 MUON SCHEDULE AND MILESTONES

The planning for the Muon System has been developed in coordination with CMS planning to minimize conflicts with other subsystems during installation and commissioning. The overall CMS plan has the iron return yoke constructed from 2001 to 2003 in the above-ground assembly building. Once some of the barrel rings and endcap disks have been assembled, installation of muon chambers can begin. We expect to install a majority of chambers in the above-ground hall prior to the magnet test which is scheduled for the third quarter of 2003. Once the magnet tests and mapping are complete, the first endcap return yoke will be lowered into the hall. Then each of the five barrel rings will be lowered, and finally the last endcap during the first quarter of 2004. During the remainder of 2004 the muon group will install the final chambers and perform the commissioning of the system.

The schedules for the construction of the CMS Muon System are given in Figs. 11.4.1-5.

11.4.1 Prototypes

11.4.1.1 Barrel subsystem

A full-size drift tube chamber (MB96) was completed in early 1997 using precision tooling intended for the production run. Another large prototype of 3 m x 1 m, with all 12 layers, was tested under LHC conditions in 1997. The results of these prototypes tests are presented in section 3.9. A final preproduction prototype (MB98) will be completed at the end of 1998.

11.4.1.2 Endcap subsystem

The endcap subsystem has developed a number of prototypes (see chapter 4) including a large (3.3 m long) CSC during ‘96 and a full-size CSC during ‘97. During 1998 we plan to build a preproduction ME2/2 CSC chamber using the tooling developed for the factory production. We also plan to build a 2-layer prototype of the ME2/1 20-degree chamber at Fermilab and a full-size version of ME2/1 at PNPI (St. Petersburg). During 1999 prototypes of ME1/2 and/or ME1/3 will be built.

11.4.1.3 ME1/1 station

The ME1/1 group has developed a number of prototypes (see chapter 4) including the P3 full-size CSC during 1996 and the P4 preseries prototype during 1997 using the major mass production facility. During 1998 the P4 prototype will be tested and development will continue on the mass production tooling.

11.4.1.4 RPC subsystem

A large size barrel chamber was produced and tested in 1997; results are presented in section 5.9. During 1998 full-size MB1 and ME2 chambers will be built using mass production tools. Full details of the front-end board location and services will be studied and fixed.

11.4.1.5 Alignment subsystem

Prototypes of the individual components have been built and tested in the participating institutes. A full-scale test of the alignment system is scheduled for 1998. It will be done at CERN where an alignment stand will be built to integrate the different parts of the system.

11.4.2 Production of chambers

11.4.2.1 Barrel subsystem

The barrel drift tube chambers will be assembled at three sites: CIEMAT (Madrid, Spain), INFN LNL (Padova, Italy), and RWTH (Aachen, Germany). Assembly of the 250 chambers will start in the second half of 1999. The anticipated time for construction is 4.5 years. Assembled chambers will be sent to CERN after basic tests at the assembly sites. They will be installed according to the CMS installation schedule.

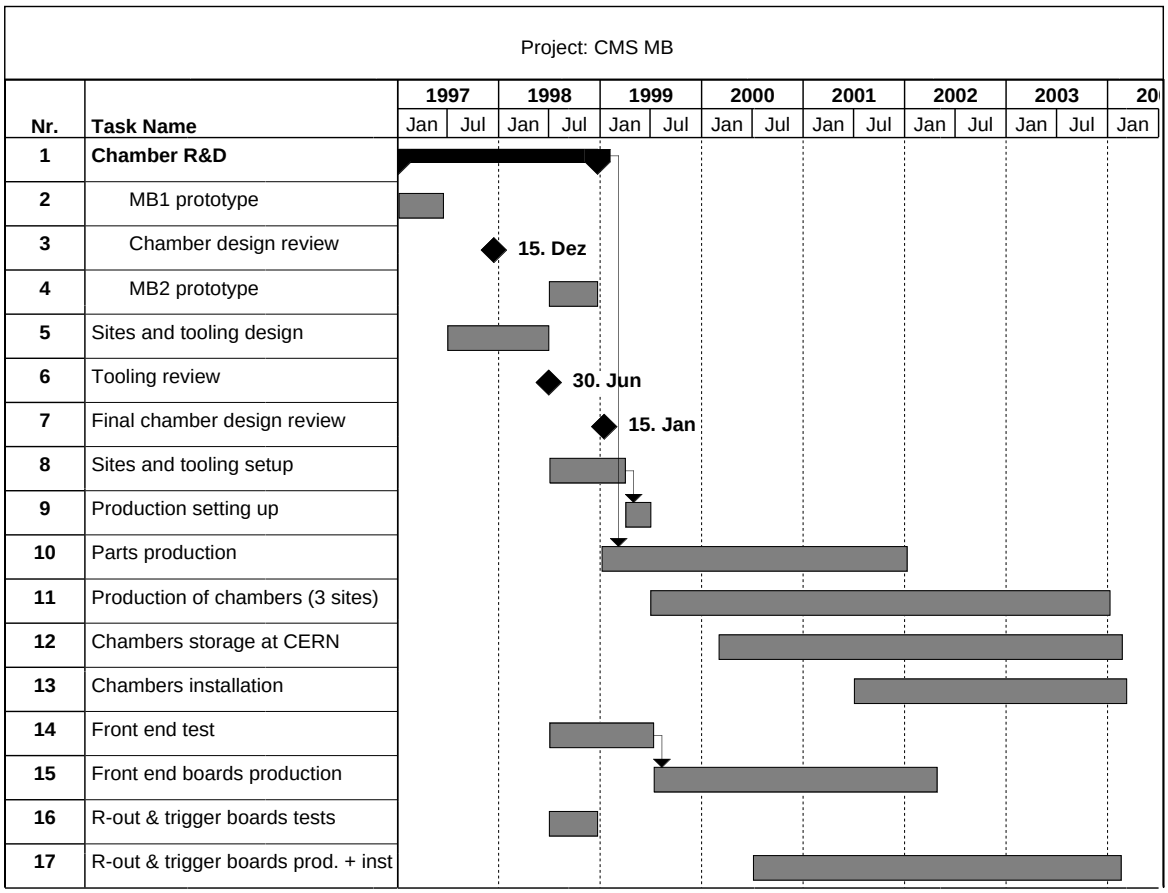


Fig. 11.4.1: Schedule for the barrel muon drift tube production.

11.4.2.2 Endcap subsystem

All panels will be produced at Fermilab beginning in early '99 and shipped to the various assembly sites.

Assembly of the 220 ME234/2 CSC chambers will begin at Fermilab during 1999. The production is estimated to take roughly four years and be finished around mid-2003. Since the initial rampup is expected to go slowly, we must plan to complete a chamber every three to four days during the height of production.

As the chambers are completed they are shipped to the FAST sites, UCLA and Florida, where the electronics will be added and the chambers tested. The chambers will be shipped to CERN as the installation schedule requires.

At PNPI (St. Petersburg) the assembly and testing of the ME2/1(36), ME3/1(36), ME4/1(36) will begin late in 1999 and be finished by mid-2003. At IHEP (Beijing) the assembly and testing of ME1/2 (72) and ME1/3 (72) chambers will begin in 2000 and finish near the end of 2003. All chamber parts, electronics, and critical tooling will be provided by the US institutes to the assembly sites.

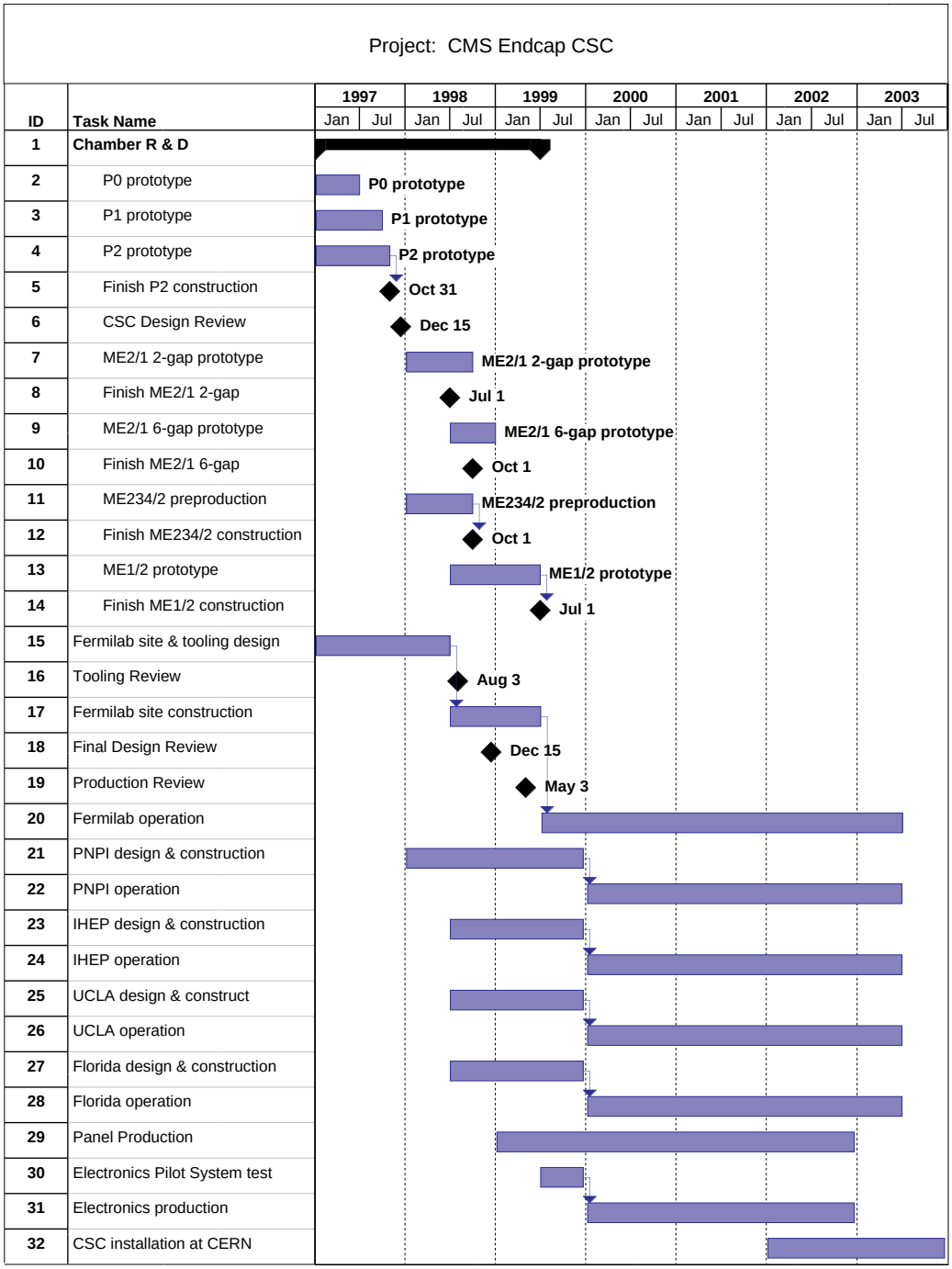


Fig. 11.4.2: Schedule for the endcap muon CSC production and installation.

11.4.2.3 ME1/1 station

The production of 75 ME1/1 CSC chambers will begin in Dubna during 1999. The production will take roughly four years and will be finished in 2003. The chambers will be instrumented with electronics and tested in Dubna. The chambers will be shipped to CERN according to the CMS installation schedule.

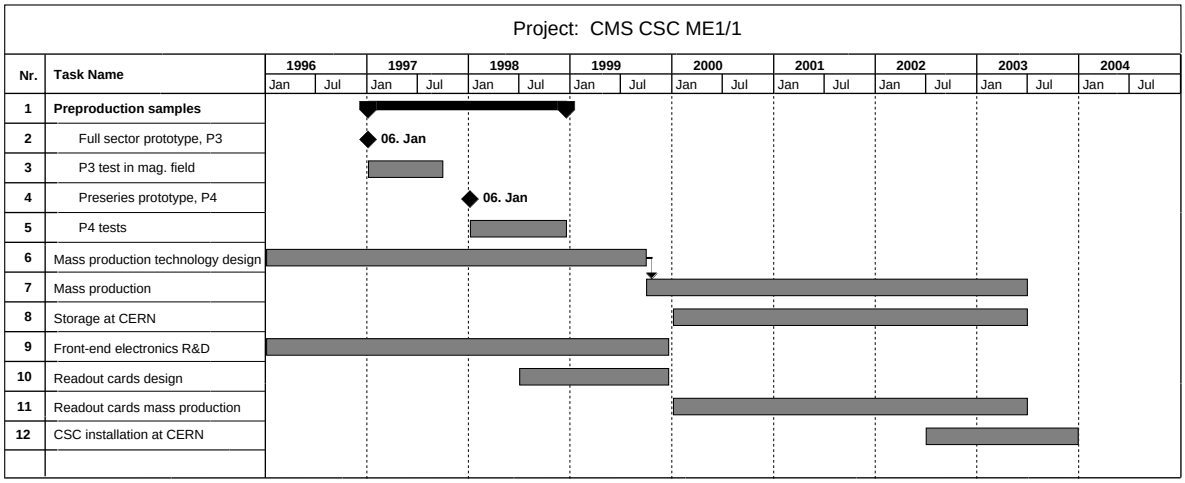


Fig. 11.4.3: Schedule for the ME1/1 production and installation.

11.4.2.4 RPC subsystem

The full RPC barrel production of 300 chambers will be produced by an industrial vendor. The front-end installation and final testing will be done in Bari. Recent interest of Korean and Chinese groups could eventually lead to barrel RPC production outside Europe. The endcap RPC chambers will be produced in Korea, where a major endcap RPC production facility will be established. It is possible that China may also contribute to the production. Endcap RPC production will start in the middle of 1999 and finish in about three years.

11.4.2.5 Alignment subsystem

The alignment components will be built, tested, and calibrated at the participating institutes. Calibrated elements will be mounted on the chambers at each chamber construction site. Assembly and calibration of the alignment structures will be done at CERN and they will be installed in CMS according to the installation schedule.

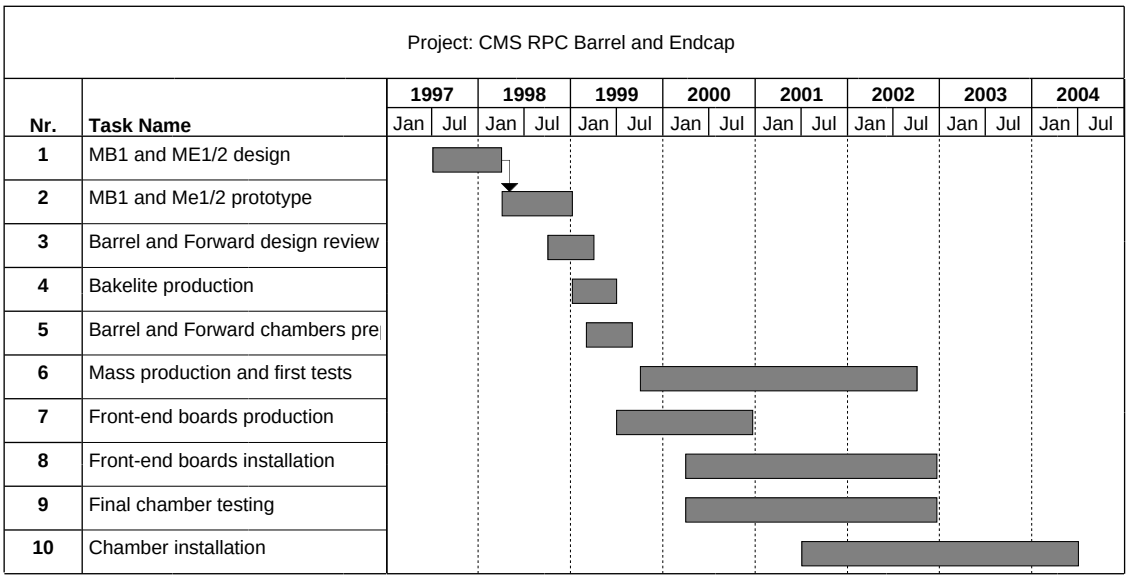


Fig. 11.4.4: Schedule for the RPC production and installation.

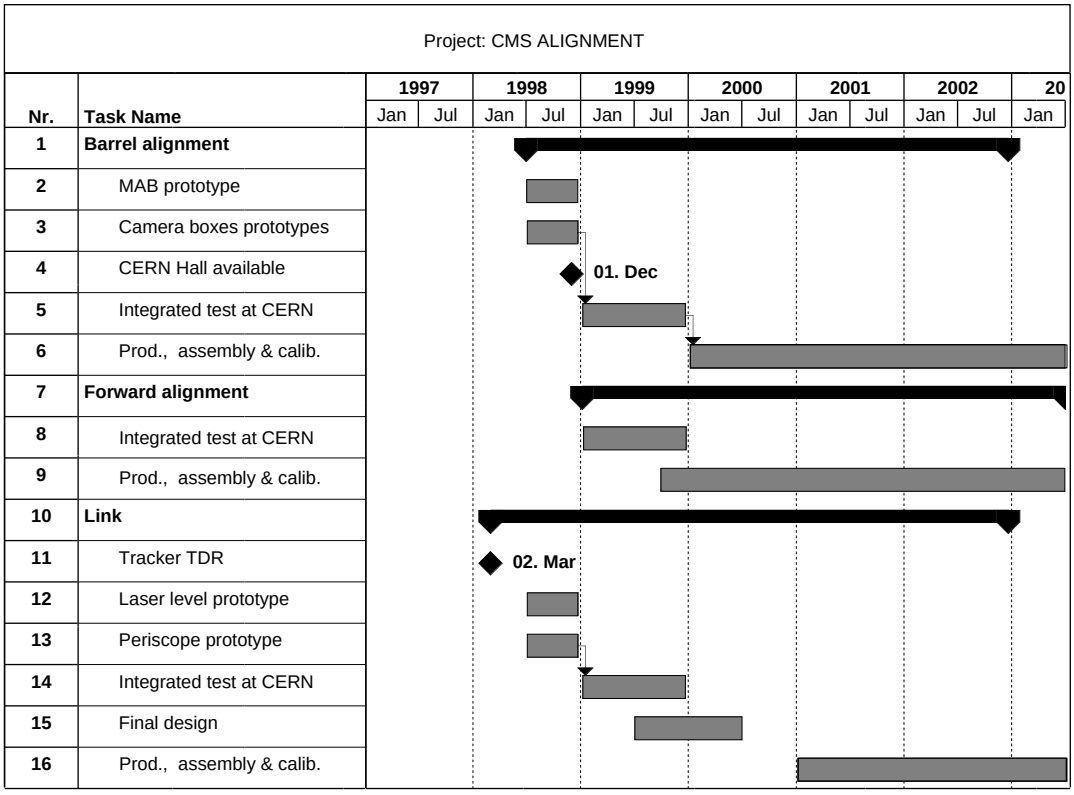


Fig. 11.4.5: Schedule for the muon alignment subsystem.

11.4.3 Muon milestones

Table 11.4.1
Key milestones for the Muon System

Milestone	Date
Drift Tubes (Barrel)	
Prototype	1st quarter '99
Begin production	3rd quarter '99
Begin installation	3rd quarter '01
Finish installation	2nd quarter '04
CSC (Endcap)	
Final CSC design review	Dec '98
System test of electronics	1st quarter '00
Begin Fermilab production	3rd quarter '99
Begin PNPI production	1st quarter '00
Begin electronics production	1st quarter '00
Begin IHEP production	1st quarter '00
Begin CSC installation	1st quarter '02
Finish installation	1st quarter '04
CSC (ME1/1)	
Test P4 prototype	4th quarter '98
Begin production	4th quarter '99
Begin installation	3rd quarter '02
Finish installation	1st quarter '04
RPC	
Full-size prototype	1st quarter '99
Begin production	4th quarter '99
Begin installation	3rd quarter '01
Finish installation	3rd quarter '04
Alignment	
Begin full-scale prototype test	1st quarter '99
Begin production	1st quarter '00
Finish installation	3rd quarter '04

11.5 ESTIMATED COSTS

Table 11.5.1
Estimated costs for the Muon System

Item #	Item	Total Cost (kCHF)	Institute Manpower (man years)
5.1	**Barrel drift tubes**	**22330**	**250**
5.1.1	detectors & components	8630	199
5.1.2	electronics	11600	27
5.1.3	mechanical structure & supports	500	2
5.1.4	assembly/installation	700	12
5.1.5	monitoring	500	5
5.1.6	service systems	400	5
5.2	**ME1 station**	**5160**	**58**
5.2.1	detectors & components	1793	-
5.2.2	electronics	2579	20
5.2.3	mechanical structure & supports	210	3
5.2.4	assembly/installation	428	30
5.2.5	monitoring	50	3
5.2.6	service systems	100	2
5.3	**Endcap CSCs**	**23633**	**301**
5.3.1	detectors & components	10807	201
5.3.2	electronics	11423	62
5.3.3	mechanical structure & supports	490	3
5.3.4	assembly/installation	230	27
5.3.5	monitoring	33	1
5.3.6	service systems	650	7
5.4	**Barrel RPCs**	**4378**	**19**
5.4.1	detectors & components	2247	-
5.4.2	electronics	1401	-
5.4.3	mechanical structure & supports	210	-
5.4.4	assembly/installation	340	13
5.4.5	monitoring	60	3
5.4.6	service systems	120	3
5.5	**Endcap RPCs**	**2574**	**17**
5.5.1	detectors & components	939	-
5.5.2	electronics	1083	10
5.5.3	mechanical structure & supports	150	-
5.5.4	assembly/installation	242	5
5.5.5	monitoring	40	1
5.5.6	service systems	120	1
5.6	**Alignment**	**3235**	**30**
5.6.1	barrel alignment	1300	12
6.6.2	endcap alignment	929	10
5.6.3	link system	1006	8
5	**Total Muon System**	**61310**	**675**

Glossary of Terms

AL	Alignment (TDR Chapter 7)
ALR Model	Version of Standard Model extension with additional gauge bosons
Altera	Manufacturer of programmable logic devices
AMI	Integrated circuit foundry and process (1.2 μ)
AMS	Integrated circuit foundry and process (Europe)
ANSI	American National Standards Institute
ANSYS	Computer program for FEA
ASD8	Fast preAmplifier-Shaper-Discriminator ASIC developed for SDC straw-tube chambers
ASIC	Application Specific Integrated Circuit
ASME	American Society of Mechanical Engineers
ATLAS	A Toroidal LHC ApparatuS Collaboration
BABAR	Experiment at SLAC B-factory
BE	Muon Barrel Electronics (TDR Chapter 3)
BiCMOS	Bipolar CMOS technology
BMU	Barrel MUon Group
BTI	Bunch and Track Identifier (BE)
BUCKEYE Chip	CSC front end preamplifier-shaper chip designed by Ohio State University (The Buckeye is the nut of the state tree of Ohio and is the nickname of the university.)
BW	Band Width
BX	Beam Crossing
BXID, BxID	BX Identification
CAD	Computer Aided Design
CAE	Computer Aided Engineering
CCD	Charge Coupled Device (analog storage device)
CFD	Constant Fraction Discriminator
CHI	Version of Standard Model extension with additional gauge bosons
CK	Clock signal on BE bus
CMOS	Complementary Metal Oxide Silicon
CMM	Coordinate Measuring Machine (AL)
CMS	The Compact Muon Solenoid Collaboration
CMSIM	GEANT-based simulation package for CMS
CNC	Computer Numerical Control
COPS	CCD Optical Position Sensor
CODAP	French pressure vessel code (COnstruction Des Appareils a Pression)
CSC	Cathode Strip Chamber
CSP	Charge Sensitive Preamplifier (BE)

DAC	Digital to Analog Converter
DAQ	Data AcQuisition
DAS	Data Acquisition System
DLL	Delay Locked Loop (BE)
DT	Drift Tube
DTBX	Drift Tube with Beam Crossing ID capability
ECL	Emitter Coupled Logic (differential signal)
EE	Endcap Electronics (TDR Chapter 4)
EMPMS	Endcap Muon PMS
EMI	Electromagnetic Interference
EMU	Endcap Muon Group
ENC	Equivalent Noise Charge
ERS	Extrapolation Result Selector
ETA	Version of Standard Model extension with additional gauge bosons
EU	Extrapolation Units (TR)
FBT	"First Best Trigger" (BE)
FEA	Finite Element Analysis
FE	Front-End, Finite Element
FEB	Front-End Board
FEC	Front-End Chip
FEBC	Front-End Board Controller (BE, RPC)
FED	Front-End Driver
FET	Field Effect Transistor
FIFO	First In, First Out buffer
FLT	First-Level Trigger (Cf. LV1)
FLUKA	Computer program for hadron shower calculations
FPGA	Field Programmable Gate Array
FR4	Fiberglass Epoxy construction material with fire retardant
GARFIELD	Computer program for electromagnetic field calculation
GB	Ghost Buster (TR)
GBW	Gain BandWidth product
GCALOR	Computer program for background calculations
GEANT	Computer program for detector modeling and simulation
GIF	Gamma Irradiation Facility (CERN SPS)
GLIMOS	Group Leader In Matters Of Safety
GMT	Global Muon Trigger
GND	Ground line on BE bus
GPM	Gallons Per Minute
G10	Fiberglass Epoxy construction material

HE	Endcap Hadron Calorimeter
HF	Forward Hadron Calorimeter
HH, HL, etc	Combinations with HTRG and LTRG (BE)
HP	Hewlett-Packard integrated circuit foundry and process (1.2 μ)
HV	High Voltage
HTRG	High Quality Trigger (BE)
H2	Beam test area at SPS used by CMS/RD5
IAEA	International Atomic Energy Agency
IEEE	Institute of Electrical and Electronics Engineers
ILO	International Labor Office
ISO	International Standards Organization
I5	CMS experimental area in LHC ring
JTAG	IEEE 1149.1 (Joint Test Action Group) serial protocol for boundary scan testing of electronic systems
Kalman Filter	Computational method for fitting tracks using candidate points
LAA	Laboratory for Accelerator Applications (CERN)
LB	Link Board (RPC)
LCT	Local Charged Track (EE)
LDEMUX	Link Demultiplexer
LDM	Laser Diode Module (AL)
LED	Light Emitting Diode
LHC	Large Hadron Collider
Lexan	Plastic construction material
LO	Leading Order (said of a calculation)
LMUX	Link Multiplexer
LRM	Version of Standard Model extension with additional gauge bosons
LTRG	Low Quality Trigger (BE)
LTS	Low Trigger Suppression (TR)
LUT	Look Up Table
LV	Low Voltage
LVDS	Low Voltage Differential Signal
LV1, Lev-1	Level-1 Trigger
L3	LEP experiment at CERN
MAB	Module for Alignment of Barrel (AL)
MARS	Computer program for background simulation
MB	Mother Board (EE)
MB1, MB2, MB3, MB4	Muon Barrel stations 1 through 4 "
MB96	Full size prototype of Muon Barrel chambers

ME1/1, ME1a	Endcap Muon Chamber stations (Fig. 4.1.1)
ME1/2, ME1/3	"
ME2/1, ME2/2	"
ME3/1, ME3/2	"
ME4/1, ME4/2	"
MGRPC	Multi Gap RPC
MIP	Minimum Ionizing Particle
MOSIS	Non-profit company run by University of Southern California to facilitate experimental chip development
MPA	Multi Point transparent Alignment sensor (AL)
MS1, MS2,	Generic reference to a muon station in either barrel or endcap
MS3, MS4	"
MT	Mean Timer (BE)
MTF	Muon Track Finder (TR)
MWPC	Multi Wire Proportional Chamber
ORBIT	Integrated circuit foundry and process (US)
PAC	PAttern Comparator ASIC
PACT	PAttern Comparator Trigger (RPC, TR)
PC, PCB	Printed Circuit, PC Board
PET	Polyethylene Terephthalate
PLL	Phase Locked Loop (BE)
PMS	Position Monitoring System (AL)
PSI	Version of Standard Model extension with additional gauge bosons
PVC	Poly Vinyl Chloride
Pythia	Computer program for simulation of particle production and decay
P0, P0'	Designations for prototype CSC chambers
P1, P2,	"
RAM	Random Access Memory
Rasnik	Three-point Relative Alignment Scheme from NIKHEF (AL)
RB	Readout Board
RDMS	Russia and Dubna Member States
RD5	R&D experiment in SPS H2 beam line used by CMS detector components
RF	Radio Frequency
ROB	Read-Out Board (BE)
ROS	Read-Out Server (BE)
RPC	Resistive Plate Chamber, dedicated trigger element for the Muon System
RTV	Room Temperature Vulcanizer (latex-based glue)
R/W	Read/Write signal on BE bus
SAPOCO	CERN SAfety POlicy COmmittee
SBT	Second Best Trigger (BE)

SCA	Switched Capacitor Array, an analog storage device (EE)
SGX	Surface Building at I5
SL	Super Layer, a 4-layer assembly of drift tubes in the barrel
SLM	Straight Line Monitor (AL)
SPICE	Computer program for circuit analysis
SPS	Super Proton Synchrotron accelerator at CERN
STS	Single Track Selector (TR)
SU	Synchronization Unit (RPC)
T	Temperature monitoring line on BE bus
TB	Trigger Board
TC	Trigger Crate
TCL	Track Cancellation Logic (TR)
TDC	Time to Digital Converter
TDR	Technical Design Report
TE	Track Encoder (EE)
TF	Track Finder (EE)
THR	Threshold signal on (BE) bus
TIS	CERN Technical Inspection and Safety Commission
TP	Technical Proposal (CERN/LHCC 94-38 for CMS)
TP	Test Pulse signal on BE bus
TRACO	TRAck COrrelator, a processor in the muon barrel trigger system that selects the best track from candidates supplied by the BTI (BE)
TRG	Strobe signal on BE bus
TS	Track Segment
TSel	Track Selector,
TR	Track Router, Trigger (TDR Chapter 6)
TSL	Track Segment Linker (BE)
TSM, TSS	Track Sorter Master, Slave (BE)
TSθ, TSϕ	θ, ϕ view Trigger Server (BE)
TTC	Timing and Trigger Control
T1,T2	Designations for prototype CSC chambers
US, USC55	Underground Service building at I5
UX, UXC55	Underground eXperimental building at I5
WBS	Work Breakdown System, DOE-supported cost accounting system
WHO	World Health Organization
XILINX	Manufacturer of FPGAs
YE1, YE2, YE3	Large iron disks in the endcaps
YN1, YN2	Small iron disks in the nose of the endcaps